

THE UNIVERSITY OF CHICAGO

FLUORESCENCE-ENCODED INFRARED SPECTROSCOPY FOR SINGLE-MOLECULE
VIBRATIONAL INVESTIGATION IN SOLUTION

A DISSERTATION SUBMITTED TO
THE FACULTY OF THE DIVISION OF THE PHYSICAL SCIENCES
IN CANDIDACY FOR THE DEGREE OF
DOCTOR OF PHILOSOPHY

DEPARTMENT OF CHEMISTRY

BY

LUKAS WHALEY-MAYDA

CHICAGO, ILLINOIS

DECEMBER 2022

Contents

List of Figures	ix
List of Tables	xvii
Acknowledgements	xviii
Funding	xxii
Abstract	xxiii
1 Introduction	1
1.1 Interrogating single molecules: what can they tell us and how can we ask?	1
1.1.1 The single-molecule advantage	1
1.1.2 Fluorescence: the workhorse of SM detection	3
1.2 Studying chemistry at the SM level with vibrational spectroscopy	5
1.2.1 SM vibrational detection in the optical near-field	6
1.2.2 Circumventing the near-field: Vibrational detection by double-resonance fluorescence spectroscopy	7
1.3 Fluorescence-encoded infrared spectroscopy	8
1.4 Thesis outline	10

2	Theory of FEIR Spectroscopy	13
2.1	Introduction	13
2.2	Vibronic coupling	16
2.2.1	Multimode vibronic Hamiltonian	16
2.2.2	Transition dipole moments	24
2.2.3	Franck-Condon factors	27
2.3	Nonlinear action spectroscopy	40
2.3.1	Fluorescence as action spectroscopy	40
2.3.2	Response function formulation of time-dependent perturbation theory	44
2.3.3	Response functions for coherent vs. action spectroscopy	49
2.3.4	Odd vs even in coherent vs action: Consequences of inversion symmetry	61
2.3.5	Material pathways in the action response function	66
2.3.6	Diagrammatic notation, the rotating wave approximation, and signal isolation strategies	72
2.4	FEIR as fourth-order action spectroscopy	81
2.4.1	Overview	81
2.4.2	Response function	84
2.4.3	Two- and three-pulse signals and FEIR spectra	86
2.4.4	Single-mode population response	89
2.4.5	Multimode coherence	93
3	Finite-pulse effects	99
3.1	Overview	99
3.2	Mixed time-ordering in the response function convolution integrals	103
3.3	Pulse characteristics	114

3.4	Numerical evaluation by Monte Carlo integration	117
3.4.1	Two-pulse signal	120
3.4.2	Three-pulse signal and FEIR spectrum	121
3.5	Finite-pulse effects in a two-mode system	124
3.6	Lineshape distortions during pulse-overlap	132
3.7	IR + visible two-photon excited fluorescence	134
4	Experimental implementation of FEIR spectroscopy	143
4.1	Overview	143
4.2	Generation of femtosecond mid-IR pulses at 1 MHz repetition-rate	147
4.2.1	Introduction	147
4.2.2	Mid-IR nonlinear crystals for Yb laser pumping	149
4.2.3	Design and performance of the mid-IR OPA	151
4.2.4	Operational details and challenges	157
4.3	Mach-Zehnder interferometer and visible encoding line	159
4.3.1	Mach-Zehnder interferometer	159
4.3.2	Visible encoding line	160
4.4	The FEIR microscope	160
4.4.1	Microscope body and optical layout	160
4.4.2	IR and visible focal characterization and sample region	168
4.5	Detection of IR and fluorescence signals	171
4.5.1	Data acquisition architecture	171
4.5.2	Continuous stage ‘fastscanning’ with Position Synchronized Output (PSO)	175
4.5.3	Fourier transform spectral artifacts from periodic stage position errors	179

4.5.4	Correction to photon count rates for pile-up error	184
4.6	Temporal pulse characterization and instrument response	188
4.6.1	IR pulse characterization by interferometric autocorrelation	188
4.6.2	IR/Vis temporal pulse overlap characterized by two-photon-excited fluorescence	190
4.6.3	Uncertainties in assigning $\tau_{\text{enc}} = 0$	192
4.7	Acquisition and processing of bulk FEIR signals	194
4.7.1	Two-pulse experiments	194
4.7.2	Three-pulse Fourier transform experiments	195
4.7.3	IR and visible power dependence	199
4.8	Bulk heating effects	202
4.8.1	Thermal modulation of the detected fluorescence intensity	202
4.8.2	Immersion oil heating	205
4.8.3	Spectral artifacts caused by thermal modulation along τ_{IR}	207
4.9	Time-resolved fluorescence detection	217
4.9.1	Data acquisition with time-correlated single-photon counting	217
4.9.2	Fluorescence lifetime-resolved FEIR spectra	218
4.9.3	Using fluorescence lifetime-resolved FEIR spectra to disentangle mul- ticomponent systems: hydrogen-bonded thiourea and coumarin het- erodimers	220
5	Principles of fluorescence and FEIR correlation spectroscopy	225
5.1	Overview	225
5.2	Evaluation of the correlation function for diffusion and chemical reaction	227
5.2.1	General method	227

5.2.2	Separation of diffusion and reaction	235
5.2.3	Diffusion through a 3D Gaussian observation volume	236
5.2.4	Two-state equilibrium	239
5.3	FEIR correlation spectroscopy	242
6	Demonstrating single-molecule sensitivity with FEIR correlation spectroscopy	247
6.1	Introduction	247
6.2	FEIR resonance and signals from Coumarin 6	249
6.3	Time-gated detection for background reduction in the small-signal regime . .	251
6.4	SM determination by FEIR-CS	255
6.4.1	FEIR-CS data acquisition and processing	255
6.4.2	FEIR-CS experiments on nanomolar C6 solutions	257
6.5	Discussion and Outlook	262
7	Influence of resonance conditions on detection quality and single-molecule sensitivity	264
7.1	Introduction	264
7.2	Experimental Methods	267
7.2.1	Steady-state spectroscopic characterization of coumarin FEIR dyes .	267
7.2.2	FEIR measurements	268
7.3	Theoretical principles of signal and background size	270
7.3.1	FEIR Brightness	271
7.3.2	FEIR cross-section	276
7.3.3	Background	277

7.4	Results and Discussion	278
7.4.1	Electronic absorption and fluorescence spectra	278
7.4.2	FTIR absorption spectra	283
7.4.3	Brightness analysis of high concentration FEIR data	285
7.4.4	Signal to background in the SM regime	293
7.5	Conclusions	300
7.A	Appendix: Supplementary material	303
7.A.1	Low-frequency electronic absorption tails	303
7.A.2	Complete coumarin series high concentration FEIR data and acquisition details	304
7.A.3	Instrument-dependent uncertainty in brightness values	306
7.A.4	Brightness vs. extinction on linear axes, FEIR brightness at signal maximum, and correlation incorporating ε_{IR}	308
7.A.5	C6 and C7 concentration and visible intensity dependent data	312
7.A.6	Limiting concentrations of the coumarin series	316
7.A.7	Details of encoding transition saturation behavior	317
7.A.8	Visible intensity dependence for C30 and C314	319
7.A.9	FEIR-CS on 1 nM C6 solution	320
8	Interpreting early encoding-delay FEIR signals	322
8.1	Overview	322
8.2	Coumarin 6	325
8.3	Coumarin 153	334
8.A	Appendix: Coumarin series τ_{enc} -dependent FEIR data with $\omega_{\text{IR}} = 1620 \text{ cm}^{-1}$	341

9	Polarization-dependent FEIR spectroscopy	346
9.1	Overview	346
9.2	Orientational response	348
9.2.1	Orientational averaging	348
9.2.2	FEIR orientational response for population and coherence pathways .	353
9.2.3	Polarization-dependence of signals and the FEIR anisotropy.	356
9.3	Polarization-dependent FEIR experiments	360
9.3.1	Polarization-dependence and anisotropy decay of a single-mode system: coumarin 337 nitrile stretch	360
9.3.2	Anisotropy in a multimode system: coumarin 334 carbonyl and ring vibrations	364
10	Vibrational relaxation through the lens of FEIR spectroscopy	367
10.1	Overview	367
10.2	Encoding-resonance dependent long-time relaxation behavior in coumarins .	369
10.3	Reshaping of the FEIR spectrum at late encoding delays	374
10.4	Discussion and outlook	376
10.A	Appendix: Fitting of two-pulse transients	379
	Bibliography	380

List of Figures

1.1	Performing time-dependent experiments at the ensemble and single-molecule levels.	2
1.2	Principle of FEIR spectroscopy and experimental schematic for detection in the single-molecule regime.	9
2.1	Forms of FC coupling in the harmonic limit.	21
2.2	Selected DHO FC factors and their squares as a function of dimensionless displacement d and Huang-Rhys factor $S = d^2/2$	31
2.3	Effect of frequency changes on the $\langle 0^e 1^g \rangle$ FC factor (FCF).	34
2.4	Duschinsky transformation for a two-mode system.	35
2.5	Effect of Duschinsky mixing on the $\langle 0_1^e 0_2^e 1_1^g 0_2^g \rangle$ FC factor (FCF).	38
2.6	Diagrammatic representation of the constituent correlation functions making up (a) the coherent response function $R_C^{(3)}$ and (b) the action response function $R_A^{(4)}$	53
2.7	Generation of (a) the 3 rd -order polarization and (b) the 4 th -order population with generalized pulse sequences and relevant perturbation-theoretic time variables.	57
2.8	Liouville space coupling diagram illustrating all 4 th -order pathways ending in a population.	68

2.9	Rules for pairing a complex field phase factor to a transition in a material pathway for DSF and ladder diagrams.	74
2.10	Comparison of DSF and ladder diagrams for two example pathways contributing to a three-level system's 4 th -order action response.	76
2.11	Energy level diagram, pulse sequence, and target population in an FEIR experiment.	82
2.12	Pulse sequences with experimental delays and perturbation-theoretic interaction time variables for (a) the two-pulse and (b) three-pulse signals.	87
2.13	(a) Double-sided Feynman diagrams and (b) ladder diagrams for the unique pathway contributing to each correlation function for a three-level system.	90
2.14	Vibrational coherence pathways and their τ_{enc} -dependent spectral signatures.	95
2.15	Interference between population and coherence contributions of positive or negative sign.	97
3.1	Pulse-specific interaction time variables τ_α and their relationship to the fully time-ordered light-matter interaction times t_i and time-delays τ_i	105
3.2	Diagrams (excluding complex conjugates) for all contributing orderings of light-matter interactions for a three-level system.	110
3.3	Finite-pulse calculation of the two-pulse signal for a single-oscillator system.	122
3.4	Finite-pulse calculation of the $\tau_{\text{enc}} = 500$ fs three-pulse signal and FEIR spectrum for the same single-mode system as Figure 3.3.	123
3.5	Spectral characteristics of the two-mode model system and its FEIR resonance conditions.	125
3.6	Two-pulse FEIR signals from the two-mode system in (a) the impulsive limit and (b) with finite pulses.	127

3.7	Comparison of the impulsive and finite-pulse τ_{enc} -dependent FEIR spectrum for the two-mode system.	128
3.8	Effect of IR spectral filtering and pump-normalization on FEIR spectra of the two-mode system.	130
3.9	IR/Vis pulse-overlap lineshape phase distortion for a single-mode population feature, and its dependence on the IR-vibrational detuning $\Delta = \omega_{\text{IR}} - \omega_{10}$. . .	132
3.10	Appearance of the three-pulse-resolved TPA signal in the time-domain. . . .	137
3.11	Frequency-resolved TPA signals $S^{\text{TPA}}(\omega, \tau_{\text{enc}})$ with corresponding IR and visible temporal intensity profiles and cross-correlations for a variety of relative pulse durations and values of $\gamma_{\text{IR},2}$	139
4.1	Schematic overview of the primary components of the FEIR instrument. . . .	144
4.2	(a) LGS mid-IR absorption and (b) Type I phase-matching angles for a 1033 nm pump.	151
4.3	Schematic of the OPA.	152
4.4	SC seed spectrum and mid-IR idler tuning range and pulse characteristics. . .	155
4.5	Layout of the FEIR microscope.	161
4.6	(a) Top view of the FEIR microscope detection area with principle components labelled, and (b) illustration of an Airy pattern from an idealized diffraction-limited spot in the objective's focal plane.	163
4.7	Spectral characteristics of the epifluorescence filter set.	164
4.8	Cofocusing of the counter-propagating IR and visible beams and characterization of their focal spots.	167
4.9	Fluorescence Z profiles of multiple samples on linear (a) and logarithmic (b) vertical scales, indicating typical variations in apparent thickness.	170

4.10	Signal acquisition architecture using the DAQ card.	172
4.11	IR detection with continuous stage motion.	176
4.12	Fastscan acquisition of an IR pulse interferogram.	177
4.13	Fluorescence detection with continuous stage motion.	178
4.14	Tracking stage position errors with the HeNe tracer interferogram.	180
4.15	Removal of spectral satellites with the stage position correction.	183
4.16	Model for pile-up error.	184
4.17	Experimental evaluation of the pile-up correction.	187
4.18	IR Pulse spectra and interferometric autocorrelations at (a)-(b) $\omega_{\text{IR}} = 1620$ cm^{-1} (6.17 μm) and (c)-(d) $\omega_{\text{IR}} = 2235 \text{ cm}^{-1}$ (4.47 μm).	189
4.19	TPA signals from C343 and C6 with vibrationally off-resonant IR pumping. .	191
4.20	Coupling of the relative IR/Vis timing and Z position in the sample.	193
4.21	Two-pulse signal from C6 in acetonitrile-d3.	195
4.22	Signal contributions in a three-pulse experiment and projection slice relation- ship.	196
4.23	Acquisition and processing of the three-pulse signal to a spectrum.	198
4.24	IR and visible power dependence of the FEIR signal.	200
4.25	Solvent dependence of the thermal effect.	202
4.26	Thermal modulation with different sample configurations for a 30 μM C6 solution in acetonitrile-d3.	203
4.27	Heating effects in immersion media.	206
4.28	Experimental and modelled steady-state thermal signatures in an FEIR spec- trum.	209
4.29	Model of thermal modulation with fastscanning of the IR delay	213

4.30	Thermal signatures in three-pulse FEIR data with stepscan and fastscan acquisition.	214
4.31	Scan speed dependence of the thermal spectral artifact.	215
4.32	Microtime-resolved photon count data for a two-pulse FEIR measurement . .	217
4.33	Microtime-resolved three-pulse FEIR signal and spectrum.	219
4.34	IR and electronic spectral characteristics of C6 and thiourea association in C ₂ Cl ₄	221
4.35	Microtime-resolved three-pulse FEIR signal and spectrum.	223
5.1	Reaction propagating functions $Y_{AA}(\tau)\langle C_A \rangle$ and $Y_{AB}(\tau)\langle C_B \rangle$ for a two-state exchange reaction.	241
5.2	Cartoon illustrating the concept of FEIR-CS and strategies for achieving selective IR resonance for a vibration undergoing a frequency shift in response to two-state chemical exchange process.	243
6.1	Resonance conditions and FEIR data on C6 in acetonitrile-d ₃	249
6.2	Concentration dependence of FEIR signal and background for C6.	252
6.3	Time-gated fluorescence detection for background reduction.	253
6.4	SPAD afterpulsing distribution and removal in photon correlation.	255
6.5	FEIR and FEIR-CS experiments at SM equivalent concentrations.	258
6.6	Dependence of the FEIR-CS amplitude on time-gating to remove scattering background.	260
6.7	Concentration dependence of the total photon count rate for the time series underlying the FEIR-CS correlation functions.	261

7.1	Energy-level diagram for FEIR excitation of a single vibration coupled to the electronic transition.	272
7.2	Electronic absorption and emission characteristics of the coumarin dye series in acetonitrile.	279
7.3	FTIR spectra of the coumarin series in acetonitrile-d3 with the IR pulse spectrum used for each FEIR measurement overlaid.	284
7.4	Bulk FEIR data in brightness units.	286
7.5	Correlations between effective FEIR and one-photon cross-sections and electronic absorption spectrum.	288
7.6	Concentration dependence of the FEIR signal and background for C6 and C7.	294
7.7	Saturation of the encoding transition.	297
7.A.1	Low-frequency electronic extinction spectra (black circles) for each coumarin on a log y-scale, with fits of the Urbach region to an exponential (red).	303
7.A.2	Exponential decay parameter k_{edge} from the fits to the low-frequency absorption edge in Figure 7.A.1.	304
7.A.3	Complete coumarin series data in brightness units.	305
7.A.4	Integration time per bin (T_{bin} , left axis) and total experimental acquisition time (T_{total} , right axis) for (a) the two-pulse transients and (b) spectra shown in Figure 7.A.3.	306
7.A.5	Experimental uncertainty in brightness values.	307
7.A.6	Brightness and electronic extinction correlations on linear axes.	309
7.A.7	Effect on the q/ϕ vs. $\varepsilon_{\text{el}}(\omega_{\text{IR}} + \omega_{\text{vis}})$ correlation when alternately using the signal maximum (triangles, regression line in red) instead of the averaged signal as in Section 7.4.3 (circles, regression line in black).	311

7.A.8 q/ϕ vs. $\epsilon_{\text{IR}} \times \epsilon_{\text{el}}(\omega_{\text{IR}} + \omega_{\text{vis}})$ on (a) linear and (b) log-log axes	312
7.A.9 C6 concentration and I_{vis} dependent two-pulse FEIR data.	314
7.A.10 C7 concentration and I_{vis} dependent two-pulse FEIR data.	315
7.A.11 Integration time per bin (T_{bin} , left axis) and total experimental acquisition time (T_{total} , right axis) for the measurements on (a) C6 and (b) C7.	316
7.A.12 C_{lim} (Eq. 7.19) for the coumarin series.	316
7.A.13 Details of the encoding transition saturation behavior.	318
7.A.14 Super-linear visible intensity dependence for C30 and C314.	320
7.A.15 1 nM C6 FEIR-CS measurement with updated sample configuration.	321
8.1 Early-time two-pulse FEIR signals measured for 10 coumarin dyes with ω_{IR} $= 1620 \text{ cm}^{-1}$ (same data as in Chapter 7).	324
8.2 C6 experimental FTIR absorption spectrum and normal modes calculated by DFT.	326
8.3 Comparison of (a)-(c) experimental and (d)-(f) calculated τ_{enc} -dependent FEIR spectra of C6.	329
8.4 Comparison of experimental and calculated two-pulse signals from C6.	330
8.5 Comparison of impulsive and finite-pulse calculations for the C6 model system.	332
8.6 C153 experimental IR absorption spectrum and relevant normal modes calcu- lated by DFT.	334
8.7 Comparison of (a)-(c) experimental and (d)-(f) calculated τ_{enc} -dependent FEIR signals of C153.	336
8.8 Comparison of impulsive and finite-pulse calculations for the C153 model sys- tem.	339
8.A.1 Coumarin 525 experimental τ_{enc} -dependent FEIR data	341

8.A.2 Coumarin 30 and 314 experimental τ_{enc} -dependent FEIR data	342
8.A.3 Coumarin 153 and 337 experimental τ_{enc} -dependent FEIR data	343
8.A.4 Coumarin 343 and 334 experimental τ_{enc} -dependent FEIR data	344
8.A.5 Coumarin 7 and 6 experimental τ_{enc} -dependent FEIR data	345
9.1 Orientational correlation functions for two and three independent transition dipoles.	354
9.2 Polarized FEIR pulse sequence.	357
9.3 Anisotropy for single-mode population response.	358
9.4 Polarization-dependent FEIR signals from the coumarin 337 nitrile stretch. .	361
9.5 C334 FEIR spectrum anisotropy.	365
10.1 Dependence of the two-pulse slow decay component on detuning between the electronic energy gap and encoding frequency ω_{vis}	370
10.2 Schematic representation of vibrational cooling and how the FEIR resonance condition influences how the resulting quasi-thermal distribution is sampled. .	373
10.3 Comparison of FEIR spectra at early and late encoding delays with the IR pump-scaled FTIR spectrum for selected coumarins.	375
10.A.1 Bi-exponential fits (red) of the late-time portion of two-pulse decay tran- sients (black dots).	379

List of Tables

3.1	RWA conjugated pathways for each pulse interaction order and their corresponding time arguments in terms of pulse interaction delays.	109
4.1	Nonlinear crystals for phase-matching 3-8 μm generation by OPA with a 1033 nm pump.	150
4.2	Tube lens standards for different objective manufacturers.	166
7.1	$S_0 \rightarrow S_1$ spectroscopic parameters of the coumarin dye series.	281
7.2	Saturation curve fit parameters for the exponential model $c(1 - \exp(-I_{\text{vis}}/I_S))$ including 95% confidence intervals from the fitting routine.	298
7.3	FEIR and one-photon background brightnesses	308
8.1	Response function parameters for C6.	327
8.2	Response function parameters for C153.	335
9.1	Elements of the orientational averaging tensor for isotropic media.	352
9.2	Experimental ($\tau_{\text{enc}} = 1$ ps) and calculated C337 nitrile FEIR anisotropy and relative transition dipole angle.	363
9.3	Experimental ($\tau_{\text{enc}} = 0.5$ ps) and calculated FEIR anisotropy and relative transition dipole angles for selected modes in C334.	366

Acknowledgements

Upon joining the seven-year club and receiving its dubious honor, I can now confirm the words of another member: seven years is, indeed, a long time. First I would like to thank Andrei for being a wonderful advisor through it all. It is hard to express just how important Andrei's calm, steady presence and mentorship has been for me over the course of my time in his group. Andrei granted me an incredible amount of freedom to explore and develop while always being available for discussion and guidance. His curiosity-driven approach to science is a constant source of inspiration and energy, and has provided me with much needed optimism in the darkest moments. Additionally, his clear presentation of his science and high bar for excellence represent an ideal worth striving for, as does his fearlessness in approaching high-risk high-reward research. I could always count on an extra dose of 'Andrei magic' to improve any publication, talk, or proposal. Perhaps most importantly, I am incredibly thankful for Andrei's profound commitment to developing his students and postdocs into independent scientists. It is clear he cares deeply about everyone in his group and is invested in their success throughout their careers. As long as people like Andrei are around, I am uncautiously optimistic about the future of the scientific community.

Sam Penwell joining the group as a postdoc at the end of my first year was the best thing that could have happened to me. Sam is the most technically gifted scientist I've had the pleasure to work with, and he patiently taught me everything I know about designing and building experiments. It is safe to say that without Sam, the work in this thesis could not have happened. He took me under his wing as we set off on developing the rather outrageous instrumentation of the FEIR experiment, and mentored me through over two and a half years of close work together. Throughout the process, Sam showed me the importance of insisting

on a good work-life balance, as well as approaching work with a calm, patient, and good-natured attitude. Oftentimes when posed with a problem in the lab, I ask myself, “What would Sam do?” While I’m not sure I always land upon the truest answer, it is always worth asking. Thank you.

My journey through the PhD was shaped and enhanced by so many former and current group members. Although we did not overlap for very long, Luigi De Marco had a big impact when I first joined the lab by taking it upon himself—while writing up his thesis, no less—to give me a small building project in the Water Lab. I remember receiving a handshake and “You’re a spectroscopist now” when the very first signal came in (impulsive Raman scattering off phonons in a CaF_2 window). While my path soon led me out of E018, I am grateful to have had the experience of working with Luigi in his element and learning from him the simple joys of slapping together some optics on the table. Paul Stevenson was someone whose group meetings I always anticipated with great pleasure, and he thereby instilled in me the value of giving an absolute banger of a talk (something I would like to accomplish someday). Paul Sanstead was a wonderful figure to be around in the group. He represented a model for careful, high-quality work, strong mentorship, and dedication to good science, all while being able to absolutely kill with an exquisitely placed joke on a moment’s notice. Joe Fournier was a postdoc who I looked up to for his seemingly effortless ability to craft a great scientific story out of the data he collected. He also looked out for us younger students as we tried to figure out how to develop a project, and always made sure the group had lunch at noon on the dot.

Memo Carpenter was a role model as well as a good friend for the majority of my time in the group. It was inspiring to see him grow into his role as a senior student with calm confidence and emerge as an excellent scientist with so many accomplishments. Outside of

lab he introduced me to all the good spots for nature and food in and around Chicago. A particularly critical experience early on was a camping trip Memo organized to help me recover mentally after my candidacy exam (it worked). Our many late-night food adventures after work, often accompanied by Chi-Jui Feng, provided release from the stress of research as well as a chance to get a broader perspective on what the point of it all was. Chi-Jui's earnest and deeply knowledgeable approach to any question I asked him helped overcome so many stumbling blocks throughout my time in the group. Nick Lewis demonstrated by example what true mastery is: technical capability, theoretical rigor, clarity of analysis, and deep physical intuition. Even though we did not work directly together, Nick's presence in the group and his generosity with his time has done more to help my growth as a scientist than I could have appreciated, as I'm sure it will continue to do for future students.

More recently I have come to greatly admire Brennan Ashwood's work and look forward to discussions with him on science, music, and the mysterious qualities of Iowa. I am excited to see what he accomplishes next. John Hack's calm and thoughtful approach to explaining his science has been a pleasure to experience, and I have enjoyed seeing his work in the Water Lab develop over the years. Ram Itani always brings an lively energy that seems to instantly improve the mood in the office. The conversations I've had with Melissa Bodine in the office, usually filled with wry commentary and excellently devastating sarcasm, have done much to keep me sane while writing my thesis, and I thank her for that. Yumin Lee has both brought excellent science and made a huge positive impact on the quality of group life. I wish I had been able to overlap more with her. As one of the group's newest students, Sam Knight's excitement about embarking on his scientific path has been refreshing, and I wish him all the best.

It has been a great pleasure to introduce Abhirup Guha, and more recently Seung Yeon

Lee, to the Flour Lab. I am particularly glad to see them becoming a team together, and I am very much looking forward to see where they take FEIR. Of all the group members who read and gave comments on chapters of my thesis (thank you all, you know who you are), Abhirup heroically read through the most, which I appreciate immensely. I would also like to thank Abhirup for sharing his extensive DFT calculations on coumarins and other FEIR fluorophores, some of which are used in Chapters 8 and 9.

I am grateful for the steady support of my parents and sister. They provided encouragement along my path through graduate school, even though my Dad still asks why it took so long given that I was doing ‘femtosecond experiments’. Finally, I need to thank Chloe Lindeman for her companionship, support, adventure-sharing, and just being in my life over these past years.

Funding

I would like to acknowledge support by the National Science Foundation (Grant Nos. CHE-1856684 and CHE-2155027) who funded the work in this thesis. Additionally, all steady-state electronic absorption and fluorescence measurements would not have been possible without use of the shared facilities at the University of Chicago Materials Research Science and Engineering Center, supported by the National Science Foundation under Award No. DMR-2011854.

Abstract

Single-molecule methods have revolutionized molecular science, but techniques possessing the bond-level structural sensitivity required for chemical problems—e.g. vibrational spectroscopy—remain difficult to apply in solution. This thesis describes a new approach, fluorescence-encoded infrared (FEIR) spectroscopy, that couples IR-vibrational absorption to a fluorescent electronic transition to achieve high-sensitivity vibrational detection in solution with conventional far-field optics. Our approach uses a double resonance scheme that first excites vibrations by resonant IR absorption, followed by an electronically pre-resonant visible excitation (‘encoding’) that selectively brings the molecule to its fluorescent excited state. Femtosecond IR and visible pulses are used to make these transitions coincident within the picosecond vibrational lifetime, while splitting the IR pulse into a pulse-pair with an interferometer enables Fourier transform measurements of FEIR vibrational spectra.

An FEIR instrument is described that combines design principles of ultrafast IR spectroscopy with single-molecule fluorescence microscopy to achieve high detection sensitivity. Specifically, a trade-off in repetition-rate between the requirements of efficient fluorescence photon counting and intense, femtosecond mid-IR pulse generation is satisfied by employing a 1 MHz Yb fiber laser to pump the experiment, and the IR pulse delivery is integrated into a confocal fluorescence microscope configuration. FEIR correlation spectroscopy, an IR-vibrational analogue of fluorescence correlation spectroscopy, is introduced to demonstrate single-molecule sensitivity in solution. Potential applications of this method as a vibrational probe of dynamic solution-phase chemical processes are proposed. The role of FEIR resonance conditions and other practical experimental factors in achieving single-molecule sensitivity are discussed through a comparative study of coumarin fluorophores.

To aid in understanding the spectroscopic information content of FEIR experiments, a theoretical description based on fourth-order response functions for the electronic excited population is developed. Incorporating the effect of finite pulses and inter-mode vibrational coherence explains the appearance and encoding-delay dependence of FEIR signals in our measurements. Polarization-dependent FEIR experiments that probe the relative orientation of the vibrational and electronic transitions, as well as the manifestation of vibrational relaxation phenomena in FEIR signals, are discussed.

Chapter 1

Introduction

1.1 Interrogating single molecules: what can they tell us and how can we ask?

1.1.1 The single-molecule advantage

Single-molecule (SM) methods have had a profound impact on how we describe molecular phenomena in chemistry, biology, materials science, and beyond. Studying the behavior of molecules one at a time offers the unique ability to access their distinct individual characteristics—information which would otherwise be lost within the ensemble average in a conventional bulk experiment. The nature of this ‘hidden’ information and how it is revealed can take many forms, and speaks to the wide diversity of research areas revolutionized by SM approaches, as well as their continually expanding potential. Variations in each molecule’s internal configuration, their interactions with each other, or their local nanoscale environment invariably lead to heterogeneity across a macroscopic sample. From a static perspective, the distribution of this disorder can be directly probed by collecting observations on many distinct individuals, while an ensemble measurement might only provide the mean, or else

give ambiguous results as to the true extent and origin of the disorder.

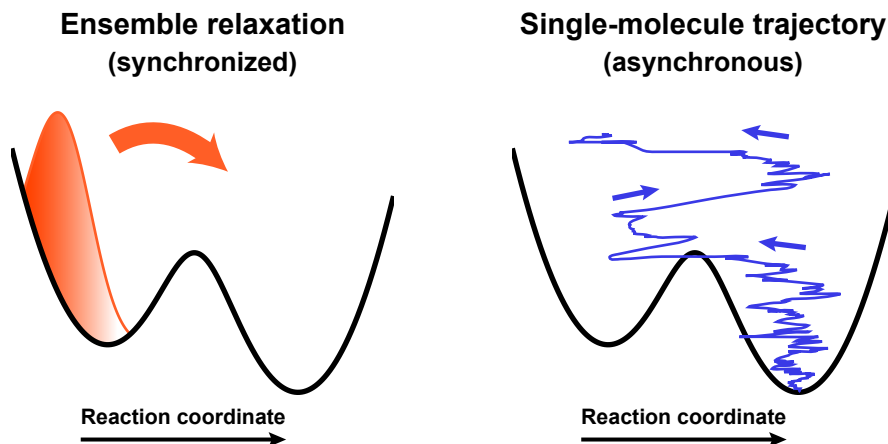


Figure 1.1: Performing time-dependent experiments at the ensemble and single-molecule levels.

From a time-dependent perspective, SM observation can reveal the trajectory of a molecular observable as it freely explores its configurational space. The simple power of this idea has profound implications for the experimental study of dynamical problems, and is illustrated in Figure 1.1. To observe time-dependent phenomena in an ensemble, molecules across the entire sample must be synchronized so that a transient signal can be measured. In practice, this requires some form of perturbation which either triggers the process of interest, or prepares the ensemble in a non-equilibrium state. While the time-course of the signal in principle follows the evolution of the ensuing molecular dynamics, it is also influenced by the heterogeneity in the sample, and information is lost as the individual molecular trajectories diverge. On the other hand, simply observing one of the molecules continuously at equilibrium can often provide this dynamical information directly without the need for synchronization. In fact, provided sufficient time-resolution and sampling, such trajectory

measurements represent the purest form of studying kinetics and dynamics in that the residence times within, transitions between, and overall history of states visited are directly accessible.

1.1.2 Fluorescence: the workhorse of SM detection

The first demonstration of SM observation in 1989 by Moerner *et al* was accomplished by measuring the optical absorption by a molecule's electronic transition at cryogenic temperatures.¹ Capturing the minute change in the probe beam's optical energy due to absorption by an individual molecule was an incredible feat of experimental design, and can be appreciated by considering the highly sophisticated double-modulation approach that was required to pull out the tiny SM signature. Shortly after this tour de force experiment, another method for observing single molecules was demonstrated by Orrit *et al* (on the same sample, no less!), this time by simply monitoring their fluorescence emission in response to the optical excitation.² The clear, fundamental advantage of the fluorescence detection approach is striking upon comparison—namely, due to the molecule's Stokes shift, the emitted fluorescence is at a longer wavelength than the excitation light and can be isolated by a spectral filter, thereby creating an intrinsically background-free signal. Even if only a handful of photons are emitted, they can be registered on a sensitive detector, whereas the analogous situation in an absorption experiment requires measuring the *loss* of a few photons from the intense and—due to the inherent shot noise at the photon level—noisy excitation beam.

Launched by this powerful background-free advantage, fluorescence excitation has gone on to become the most widely adapted method for SM detection and spectroscopy. Further advantages of fluorescence detection became evident as new capabilities emerged,^{3,4} including transient observation of single-molecules in room-temperature solution⁵, direct imaging

of single-molecules at room temperature in the optical near-field,^{6–8} and then the far-field using confocal, wide-field, and total internal reflection configurations.^{9,10} The transition from the optical near-field—characterized by the use of structures smaller than the wavelength of light to influence its coupling into and out of a molecule within the same sub-wavelength region—into the far-field—where the molecule is many wavelengths away from any optical elements—is especially significant. With all far-field optics, the molecule can be left unperturbed in its natural environment, rather than needing to be placed in nanometer proximity to the specially fabricated metallic nanostructures required for near-field probing. With advances in microscopy tools and methodologies, far-field fluorescence detection has become compatible with SM observation in increasingly complex environments, ranging from free solution, polymer matrices, and molecular glasses, to the interior of living cells and even biological tissues.

This adaptability to complex molecular environments has played a large part in the huge success of SM fluorescence methods for studying biological problems through the investigation of macromolecules like proteins and nucleic acids.^{11–13} These experiments use the fluorescence of probe chromophores, either intrinsic to the target biomolecule or as extrinsic labels, to report on some aspect of the biomolecule’s state. The primary challenge of experimental design is therefore how to encode the desired molecular properties into the fluorophore’s absorption or emission characteristics. One common strategy uses the change in fluorescence brightness induced by binding to a specific site or structural motif, or resulting from a biomolecule-catalyzed reaction.^{14,15} Fluorescence lifetime can be used to sense differences in solvent exposure or quencher proximity during conformational changes or folding,¹⁶ or the fluorescence polarization can be used to follow reorientation or rotational motion.¹⁷ Another highly successful approach is to employ Förster resonance energy transfer (FRET)

between a pair of fluorophores to monitor nanometer-scale distance.^{18–21}

A second, more incisive, reason SM fluorescence has been so impactful in molecular biology may have become clear from considering the character of the fluorescence observables in the examples above. Namely, the information content accessible from the fluorescent probe is by and large limited to conformational coordinates greater than the size of the chromophore, changes that influence its surroundings in an averaged way, or the outcome of reaction events that change its chemical identity in a binary fashion. This lack of sensitivity to the finer levels of chemical structure is fundamentally related to the delocalized character of the electronic states at play in fluorescence, and sets a limit on the molecular resolution that can be obtained. In the study of large biological macromolecules, much of the interesting phenomena occur on these larger nanometer length scales, so fluorescence can (and continues) to provide a wealth of valuable information. However, fluorescence spectroscopy consequently has much more limited utility for situations requiring knowledge of structural information at the level of chemical bonds within a molecule—that is, the study of chemistry.

1.2 Studying chemistry at the SM level with vibrational spectroscopy

Addressing the problems of chemistry, i.e. those determined by the specific structure, interactions, and reactivity of molecules, requires access to local chemical structure information. Vibrational spectroscopy provides a direct view into chemical structure in that a molecule's normal modes of vibration encode the connectivity and strength of the bonds linking its constituent atoms. Beyond reporting on a molecule's static intramolecular composition, probing its vibrations offers sensitivity to the formation and breaking of intermolecular contacts as

well as other angstrom-scale changes in its structure—the dynamic molecular events that drive chemical phenomena. Following the pioneering work in SM fluorescence spectroscopy, a concurrent development of SM vibrational methods emerged to apply the SM advantage in the problems of chemistry. While this combination of capabilities offers enormous potential, SM vibrational detection presents unique technical challenges that compound the difficulty of experiments, and continues to be developed in many different forms.

1.2.1 SM vibrational detection in the optical near-field

The primary difficulties associated with the optical detection of molecular vibrations are their small light-matter interaction cross-sections and fast non-radiative relaxation rates, precluding any kind of luminescent emission that could serve as a background-free signal. Currently, the most prevalent approaches employ near-field optical effects to both amplify the light-matter interaction and reduce the observation volume to the point where SM detection is possible. The most important examples are surface- and tip-enhanced Raman spectroscopy (SERS and TERS) which achieve near-field signal enhancement through nanometer proximity or direct adsorption to a metallic nanostructure, and have been used extensively for SM spectroscopy for over two decades.^{22–26} Infrared (IR) techniques based on scattering-type scanning near-field microscopy (IR s-SNOM), atomic force microscopy (AFM-IR), and other near-field schemes can isolate signals from small ensembles of oscillators at nanometer length scales,^{27,28} and are being developed toward SM detection with some recent success.²⁹ Non-optical methods based on scanning tunnelling microscopy (STM) have also been used to probe the vibrations of individual molecules, and similarly rely on sub-nanometer localization with a metallic probe.³⁰ However, the necessity for contact with a surface, nanostructure, or probe imposes severe restrictions on the types of samples that can be studied with these

methods. Critically, molecular systems in solution or other condensed-phase environments where these requirements are too perturbative remain out of reach.

1.2.2 Circumventing the near-field: Vibrational detection by double-resonance fluorescence spectroscopy

An alternative approach that circumvents the optical near-field is to couple the ground-state vibrational spectroscopy to a fluorescence read-out signal. Using the by now well-developed far-field microscopy methods of SM fluorescence, this signal can be detected from molecules left unperturbed in their natural environments, with all the detection sensitivity advantages of fluorescence working in its favor. This idea long predates SM spectroscopy and was explored in the work of Laubereau, Seilmeier, and Kaiser, who in 1975 introduced a double-resonance method employing a picosecond IR pulse followed by a picosecond UV/Vis pulse to resonantly excite vibrations and then selectively bring those molecules to their fluorescent electronic excited state.³¹⁻³⁴ Critical to this approach is the use of pulses that are of similar duration to or shorter than the typically picosecond vibrational lifetime, ensuring that the sequential double-resonance process is competitive against the vibration's population relaxation. In fact, the original motivations for this approach were not necessarily of chasing high detection sensitivity, but rather just as a way to investigate the up till then unstudied relaxation dynamics of molecular vibrations in liquids with the newly-pioneered picosecond IR laser pulses (presumably because IR detector technology lagged considerably behind). However, the original demonstration of this idea, which was termed the 'two-pulse fluorescence' experiment, showed sensitivity down to low μM concentrations, which is still a remarkable $\sim 2\text{-}3$ orders of magnitude below most modern time-resolved IR spectroscopies!

A similar double-resonance approach using stimulated Raman excitation instead of IR absorption was proposed by Wright,³⁵ and later explored theoretically by Orrit and co-workers as a potential technique for SM vibrational detection.³⁶ Min and coworkers successfully established this double-resonance Raman method—stimulated Raman excited fluorescence (SREF) spectroscopy—using modern high repetition-rate laser sources and microscopy tools. With this approach, they demonstrated the first SM vibrational detection operating entirely in the far-field.^{37,38} Like the IR-pumped method pioneered by Kaiser and co-workers, using picosecond pulses is crucial for achieving sufficient overall excitation efficiencies.

1.3 Fluorescence-encoded infrared spectroscopy

The work in this thesis describes an effort to take the concept of Laubereau, Seilmeier, and Kaiser’s ‘two-pulse fluorescence’ experiment and develop it into a method for SM vibrational spectroscopy in solution and soft-matter. In lieu of a compelling name from its historical development, we term this approach fluorescence-encoded IR, or FEIR, spectroscopy. FEIR is a mixed vibrational/electronic technique that operates on fluorescent molecules. As in its original implementation described above, FEIR spectroscopy functions by the double resonance scheme depicted in Figure 1.2(a). An IR pulse resonantly drives vibrations into their first excited state, after which an electronically pre-resonant visible pulse selectively brings the fluorophore to its electronic excited state. The resulting fluorescence emission intensity is therefore dependent on the excited vibrational population created by the IR field on the ground electronic state, and is used as an action signal that encodes vibrational information.

In practice, the weak IR-vibrational absorption cross-sections and picosecond lifetimes

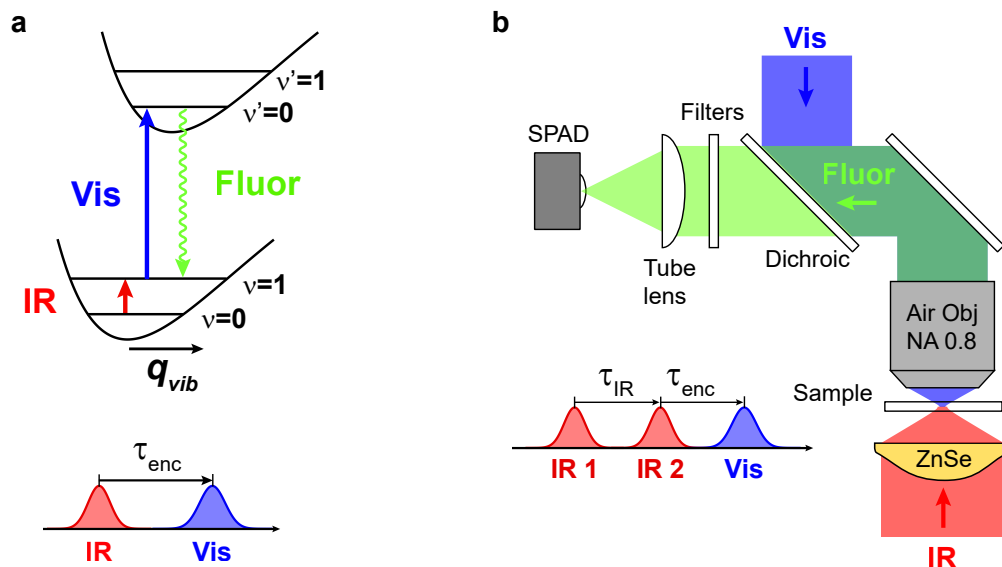


Figure 1.2: Principle of FEIR spectroscopy and experimental schematic for detection in the single-molecule regime. (a) Energy level diagram for FEIR spectroscopy. (b) Schematic of the FEIR microscope and pulse sequence used for the experiments described in this thesis.

necessitate short, intense pulses of mid-IR light, and a similarly short visible encoding pulse. Our implementation of FEIR spectroscopy uses femtosecond pulses, making it an ultrafast time-domain technique sensitive to the vibrational dynamics occurring during the encoding delay τ_{enc} . The short IR pulse duration corresponds to a large spectral bandwidth, which we used to our advantage by performing Fourier transform measurements of the vibrational spectrum. As shown in Figure 1.2(b), this is accomplished by splitting the IR pulse into a pulse-pair and measuring the FEIR signal as a function of their relative delay τ_{IR} , after which the molecule's FEIR vibrational spectrum is recovered by Fourier transformation.

Our group's initial entry into FEIR spectroscopy used the conventional instrumentation of modern ultrafast IR spectroscopy, based on 1 kHz repetition-rate Titanium:Sapphire laser technology with table-top optics. These experiments demonstrated the principle of ultrafast

and Fourier transform FEIR vibrational measurements at the high concentrations characteristic of bulk IR methods.^{39,40} In this thesis we describe a new experimental approach specifically tailored towards the goal of SM measurements that more fully integrates the methodologies of ultrafast IR spectroscopy with those of fluorescence microscopy. Critical to this approach is the use of a much higher 1 MHz pulse repetition-rate that enables efficient single-photon counting detection of the small FEIR signals from individual molecules. As stressed earlier in Section 1.2.2, the advantage of dealing with a fluorescence signal is the availability of advanced, well-developed far-field microscopy tools to help with achieving sensitive detection. In keeping with this philosophy, we adapt a confocal fluorescence microscope configuration (shown in Figure 1.2(b)) with the IR and visible beams incident from either side of the sample to achieve tight focusing, a small observation volume in solution, and efficient collection of the fluorescence signal.

1.4 Thesis outline

This thesis is organized as follows. In Chapter 2 we discuss the general theoretical background for FEIR spectroscopy. The time-domain modality of our measurements is most naturally handled by the nonlinear response function framework common to ultrafast and multidimensional spectroscopy. Using this formalism connects FEIR spectroscopy to this larger field, allowing us to draw upon decades of knowledge and practice to understand the detailed workings of our experiments. The 4th-order response function description we develop is closely related to nonlinear action methods gaining increasing popularity in the multidimensional electronic spectroscopy community.

Chapter 3 is an extension of the theoretical development in Chapter 2 to incorporate

the effect of finite pulses. While the spectroscopic information content can largely be understood from the molecular response function alone, the actual appearance of real data can be strongly influenced by the temporal and spectral pulse characteristics. As every photon counts for an SM measurement, understanding each and every detail of the signal in this way is worthwhile.

In Chapter 4 we discuss the details of the FEIR instrumentation, including the overarching technical design principles, generation of femtosecond mid-IR and visible pulses, FEIR microscope, signal acquisition, and data processing.

Chapter 5 describes some of the concepts and theoretical principles of correlation spectroscopy, a class of quasi-SM methods exemplified by fluorescence correlation spectroscopy (FCS) that leverage SM sensitivity to extract dynamic information from the equilibrium fluctuations of an ensemble. Specifically, we discuss the implementation of FEIR correlation spectroscopy (FEIR-CS) as an IR-vibrational analogue of FCS, and propose its potential application to studying time-dependent chemical phenomena in solution.

Chapter 6 demonstrates experimentally that FEIR spectroscopy can achieve SM sensitivity in solution. Our method for doing so is to perform proof-of-principle versions of the FEIR-CS experiments introduced in Chapter 5. Although these measurements do not probe interesting chemical reaction phenomena—only observing the diffusion of molecules through the microscope’s observation region—they demonstrate the viability of FEIR spectroscopy for SM vibrational investigation while providing quantitative benchmarks for SM FEIR signal levels.

Chapter 7 provides a more detailed investigation into the practical experimental factors involved in achieving SM sensitivity, as well as the general quality of an FEIR measurement in terms of contrast and signal-to-noise. Particular emphasis is given to the role of the FEIR

double-resonance condition (Figure 1.2(a)) as one of the central properties that must be optimized for a successful experiment. These studies are carried out on a series of coumarin FEIR fluorophores that are used throughout the remainder of the thesis.

Chapter 8 discusses the detailed interpretation of FEIR signals at early encoding delays. Here we put the theoretical methods developed in Chapters 2 and 3 to use by comparing response function simulations with real data.

Chapter 9 treats polarization-dependent FEIR spectroscopy, which interrogates the orientational response of the molecule to yield information on the relative arrangement of its vibrational and electronic transition dipoles. The theoretical framework is closely related to the orientational response in 3rd-order coherent spectroscopies, and similar experimental observables like the polarization anisotropy are useful under appropriate conditions. We describe some examples of polarization-dependent FEIR experiments that could be used to gain further structural insight.

Finally, in Chapter 10 we discuss how vibrational relaxation phenomena manifest in FEIR spectroscopy. Perhaps it is fitting to come back full circle in this way to this original arena of FEIR spectroscopy as conceived by Laubereau, Seilmeier, and Kaiser nearly five decades ago. Consistent with their original measurements and many other time-resolved vibrational experiments since then, our results suggest a picture of rapid picosecond depopulation of the initial vibrational population through intramolecular vibrational energy redistribution into a quasi-thermal distribution of the molecule's low-frequency modes, which then cools by dissipation into the solvent. This process results in an interesting dependence of the observed signal relaxation during τ_{enc} on the FEIR double-resonance conditions, as well as suggesting a potential mechanism for FEIR signal generation based on vibrational energy transfer.

Chapter 2

Theory of FEIR Spectroscopy

2.1 Introduction

In introducing the concept of FEIR spectroscopy, we have put forward a qualitative picture consisting of three sequential molecular events: (1) excitation of the vibration by resonant IR absorption, (2) upconversion to the excited electronic state (i.e. ‘encoding’) by resonant visible absorption, and (3) emission of the fluorescence photon. Underlying these events are fast system dynamics, which makes the problem of understanding and modelling the FEIR process intrinsically time-dependent as well as nonlinear. Specifically, a key experimental principle is the use of ultrashort pulses for vibrational excitation and encoding to ensure the overall process is efficient in the presence of picosecond vibrational relaxation processes ubiquitous in the condensed phase. A theoretical description of FEIR spectroscopy that can adequately describe the details of our measurements must therefore be rooted in the dynamical nature and time-domain modality of the technique.

Before delving into the spectroscopy, we highlight that the encoding transition (step (2)) is contingent on the existence of coupling between the molecule’s vibrational and electronic

degrees of freedom. Vibrational-electronic (i.e. vibronic) coupling is therefore the key molecular property that enables FEIR detection, or conversely, is the molecular observable most sensitively revealed in FEIR measurements. Given the central importance of vibronic coupling, as well as the wide variety of different physical effects that can give rise to it, we will begin this chapter with a discussion of its theoretical description and its influence on the spectroscopic transitions in an FEIR experiment.

An important simplification in describing the overall FEIR process arises from the large separation of timescale between the femtosecond to picosecond vibrational dynamics and the nanosecond electronic relaxation that gives rise to fluorescence emission. Namely, we can assume that the processes of FEIR excitation (i.e. steps (1) and (2)) and fluorescence emission (step (3)) are essentially independent. Our approach is to describe the excitation process using the nonlinear response function formalism widely employed in the theory of ultrafast spectroscopy, and then treat the emission process phenomenologically. This theoretical strategy is characteristic of action spectroscopy—the general class of techniques where the detected observable is an indirect read-out of the spectroscopic excitation. Formally, action observables are proportional to the population of an excited state or set of states that the system is driven into by the excitation method. Action-based techniques, especially those using fluorescence, are gaining wider popularity in the field of ultrafast and multidimensional spectroscopy, and there is much useful insight to be gained by setting up our treatment of FEIR spectroscopy within this wider context. We will therefore devote some time to introducing the perturbative response function formulation of nonlinear action spectroscopy, and discuss how it differs from its more familiar form in coherent spectroscopy. Specifically, we will explore a fundamental correspondence between a system’s coherent and action responses occurring at n and $n + 1$ orders of nonlinearity, respectively. This correspondence is by now

well established in the link between 3rd-order coherent techniques like two-dimensional (2D) spectroscopy, and their 4th-order action-based counterparts.

Casting the FEIR excitation process in perturbation theory language requires developing the light-matter interaction to 4th-order, as two interactions each are required to describe the transfer of population in steps (1) and (2). In terms of nonlinear response, FEIR spectroscopy is therefore on par with existing 4th-order action-detected spectroscopies, and by the correspondence mentioned above also to 3rd-order coherent techniques. We will use the resulting conceptual and technical analogies to our advantage by describing FEIR experiments in the well-developed language of these ultrafast nonlinear methods. Specifically, FEIR as performed in this thesis is a three-pulse (IR-IR-visible) experiment, in which the delay between the first two pulses (τ_{IR}) is scanned to resolve the vibrational excitation frequency via Fourier transformation, while the delay before the third pulse (τ_{enc}) acts as a waiting time in which the system evolves before the encoding step. These aspects of the experiment are directly analogous to 2D spectroscopy, although FEIR does not go on to resolve a second coherence period and conjugate frequency after the waiting time. As such, many direct similarities exist in the spectroscopic information content and how it is visualized, as well as in the practicalities of how measurements are conducted and data is processed. Mixed IR/visible techniques such as 2D vibrational-electronic spectroscopy are especially closely related.⁴¹⁻⁴³

While these analogies are useful, it is also important to keep in mind that the primary motivations for developing FEIR spectroscopy—namely, for performing single-molecule experiments—are different in many ways from those of ultrafast and multidimensional spectroscopies and lead to different priorities in experimental design. Along these lines, we will be less concerned with how FEIR spectroscopy can probe ultrafast system dynamics or reveal

the correlation between multiple transitions, but rather with how one-dimensional vibrational spectra can be measured with the highest possible detection sensitivity. Nevertheless, this richness in spectroscopic information content is still important to understand, as it can have a major impact on the appearance of these apparently simple spectra and their interpretation. Some examples of the information ‘beyond linear spectroscopy’ that appears in FEIR experiments are vibrational relaxation dynamics, inter-mode vibrational coherence and dephasing, and the relative orientation of vibrational and electronic transition dipoles. Of particular importance is the contribution of vibrational coherence, and specifically how these coherent signal contributions affect the appearance of spectra at early encoding delays. The orientational dependence of the vibrational and electronic transition dipole moment directions and resulting polarization-dependence of FEIR signals will be treated in Chapter 9, while vibrational relaxation phenomena are discussed in Chapter 10. The effect of the real pulse characteristics used in experiment can also have a significant impact on measured signals, and will be treated in Chapter 3. In short, the details matter, and the aim of the present chapter is to provide the basic framework for incorporating all these various factors into a unified theoretical description.

2.2 Vibronic coupling

2.2.1 Multimode vibronic Hamiltonian

Before embarking on developing response function expressions for FEIR experiments, it will be useful to describe in some detail a model Hamiltonian for the types of systems studied with FEIR spectroscopy. Of central importance is the coupling of the vibrational and electronic degrees of freedom, as without such coupling the encoding transition cannot occur and any

FEIR signal vanishes. At the outset it is worth noting that the term vibronic coupling is used in various contexts to describe many different types of physical effects.⁴⁴ Here we will work within the Born-Oppenheimer framework, where the adiabatic separation of electronic and nuclear coordinates is always assumed to hold. As such, non-adiabatic coupling effects will not be considered.⁴⁵ We will largely describe vibronic coupling within the Franck-Condon approximation where spectroscopic transitions between adiabatic electronic surfaces proceed with the nuclei fixed, although we will briefly discuss non-Condon effects in the form of Herzberg-Teller coupling. In the Franck-Condon picture, vibronic coupling manifests through the differences in the relaxed nuclear geometries of the initial and final electronic states, which influence how their respective nuclear wavefunctions overlap, or, from a time-dependent perspective, how a nuclear wavepacket evolves on the final electronic surface.^{46,47} Due to the core importance of these wavefunction overlaps, i.e. the Franck-Condon factors, in determining transition moments, we will devote some time to their calculation for our model system.

We consider a two-level electronic system consisting of ground (g) and excited (e) levels coupled to multiple harmonic vibration modes. Restricting ourselves to harmonic vibrations is largely for convenience and analytic tractability. Importantly, the FEIR experiments explored in this thesis only access singly-excited vibrational levels, and are therefore not directly sensitive to vibrational anharmonicity in the way that degenerate nonlinear IR techniques like 2D IR spectroscopy are. The system Hamiltonian is

$$H_S = |g\rangle H_g \langle g| + |e\rangle (H_e + \hbar\omega_{eg}^0) \langle e| \tag{2.1}$$

where H_g and H_e are the nuclear Hamiltonians for the electronic ground and excited states,

respectively, and $\hbar\omega_{eg}^0$ is the energy difference between electronic states. These nuclear Hamiltonians are intended to describe the spectroscopically accessible vibrations of the system. Mostly what we have in mind by this are the chromophore’s high-frequency intramolecular vibrations resonant with the IR pulses in an experiment, although it is also possible to consider low-frequency vibrations not within the window of the pulse spectrum. An analogous Hamiltonian could be used to describe the nuclear coordinates comprising the bath that arise either from the molecule’s unobserved intramolecular coordinates or the solvent environment, which would lead to a Brownian oscillator model that describes the electronic energy gap dynamics and resulting lineshape.⁴⁸ However, we will not pursue this approach here. The nuclear modes are described by a set of normal coordinates q_i and conjugate momenta p_i . In general, the normal coordinates are linear combinations of the mass-weighted atomic Cartesian coordinates

$$q_i = \sum_k L_{ik} \sqrt{m_k} (x_k - x_{0k}) \quad (2.2)$$

relative to the equilibrium geometry x_{0k} , where L_{ik} is the normal mode transformation.⁴⁹ In these coordinates the ground-state Hamiltonian is

$$H_g = \sum_i \frac{p_i^2}{2} + V_g(\{q_i\}) \quad (2.3)$$

with the ground-state potential

$$V_g(\{q_i\}) = \sum_i \frac{1}{2} \omega_i^2 q_i^2 \quad (2.4)$$

where ω_i is frequency of the i^{th} -normal mode coordinate. It is also convenient to switch to dimensionless coordinates

$$Q_i = (\omega_i/\hbar)^{1/2}q_i \quad (2.5a)$$

$$P_i = (\hbar\omega_i)^{-1/2}p_i, \quad (2.5b)$$

in which the Hamiltonian is rewritten as

$$H_g = \sum_i \frac{1}{2}\hbar\omega_i P_i^2 + V_g(\{Q_i\}) \quad (2.6a)$$

$$V_g(\{Q_i\}) = \sum_i \frac{1}{2}\hbar\omega_i Q_i^2. \quad (2.6b)$$

As we will see, both the conventional normal mode coordinates and their corresponding dimensionless versions will be useful in various contexts. The excited-state nuclear Hamiltonian is

$$H_e = \sum_i \frac{1}{2}\hbar\omega_i P_i^2 + V_e(\{Q_i\}), \quad (2.7)$$

where the excited-state potential is expressed in terms of the ground-state coordinates as

$$V_e(\{Q_i\}) = \sum_i \frac{1}{2}\hbar\omega_i Q_i^2 - \sum_i \hbar\omega_i d_i Q_i + \frac{1}{2} \sum_{i,j} U_{ij} Q_i Q_j. \quad (2.8)$$

In writing this expression we have taken the perspective of treating the effect of changing the electronic state as a perturbation to the ground state potential, which acts to couple to electronic and nuclear degrees of freedom in the molecule. We will generally refer to this

form of vibronic coupling as Franck-Condon (FC) coupling, to distinguish it from Herzberg-Teller coupling, which will be discussed briefly in Section 2.2.2. Specifically, moving from the ground to excited state induces changes in the nuclear structure described by the difference potential

$$V_e - V_g = - \sum_i \hbar\omega_i d_i Q_i + \frac{1}{2} \sum_{i,j} U_{ij} Q_i Q_j, \quad (2.9)$$

which separates effects due to linear FC coupling, described by d_i , and quadratic FC coupling, described by U_{ij} . More generally, higher order coupling terms could be included, which would result in an anharmonic excited state. However, we will restrict our model to purely harmonic effects.

Keeping only the linear term (i.e setting $U_{ij} = 0$) results in the displaced harmonic oscillator (DHO) model (Figure 2.1(a)), which is the most commonly adopted model for FC vibronic coupling due to its simplicity, and, as we will see later, its analytic tractability.^{48,50} Specifically, the linear term displaces the minimum of the excited state potential relative to the ground state by the dimensionless shift d_i along the i^{th} -coordinate, which is evident by completing the square in Eq. 2.8,

$$V_e = \sum_i \frac{1}{2} \hbar\omega_i (Q_i - d_i)^2 - \sum_i \frac{1}{2} \hbar\omega_i d_i^2. \quad (2.10)$$

As we can see, this displacement also comes with a constant decrease in excited state energy by $\frac{1}{2} \hbar\omega_i d_i^2$, known as the reorganization energy associated with mode i . Many descriptions of the displaced harmonic oscillator define the excited state Hamiltonian with this shift added in so that the minimum of the potential does not change energy as it gets displaced along the nuclear coordinate.⁴⁸ In that picture, the value of the excited-state potential at

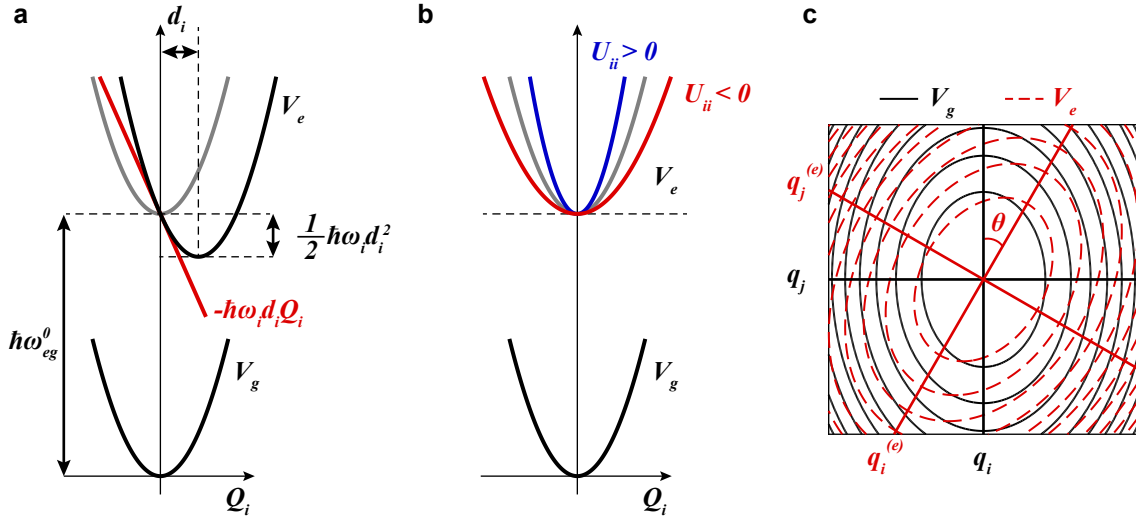


Figure 2.1: Forms of FC coupling in the harmonic limit. (a) Linear FC coupling resulting in a DHO model. The linear coupling term (red) is shown for the case of a positive displacement $d_i > 0$, superimposed over the excited potential in the absence of coupling (gray). The minimum of the resulting excited potential (black) is also shifted down in energy by the reorganization energy $\frac{1}{2}\hbar\omega_i d_i^2$. (b) Frequency changes of the excited-state potential resulting from quadratic FC coupling. (c) Duschinsky rotation of the normal coordinates for a two-dimensional potential as a result of off-diagonal quadratic FC coupling. The ground and excited potentials are represented by solid black and dashed red contours, respectively. The ratio of mode frequencies is $\omega_i/\omega_j = 2$, with no associated frequency changes in the excited state. The modes are mixed by an angle of $\theta = -30^\circ$, as indicated by the relative rotation of the ground- and excited-state normal coordinate axes (solid black and red lines, respectively).

the ground-state equilibrium geometry $V_e(Q_i = 0)$ is consequently raised above ω_{eg}^0 by the reorganization energy, while in our current description it remains unchanged. The Huang-Rhys factor, defined as

$$S_i = \frac{1}{2}d_i^2 \quad (2.11)$$

is a particularly convenient dimensionless parameter to describe the strength of the linear FC coupling, as will become evident in Section 2.2.3 when calculating FC wavefunction overlap.

The quadratic FC coupling terms are responsible for two other classes of physical effects: (1) changes in mode frequency, and (2) mixing of the normal mode coordinates, commonly referred to as Duschinsky mixing or rotation.⁵¹ When the off-diagonal quadratic couplings are neglected ($U_{i \neq j} = 0$), the remaining diagonal terms U_{ii} can be seen to impart frequency changes of

$$\Delta\omega_i = \omega_i^{(e)} - \omega_i^{(g)} = U_{ii}/\hbar \quad (2.12)$$

upon promotion to the excited state. As shown in Figure 2.1(b), the potential correspondingly softens for $U_{ii} < 0$ and hardens for $U_{ii} > 0$.

The off-diagonal coupling terms $U_{i \neq j}$ mix the ground-state coordinates Q_i in the excited state. Without loss of generality, we require that $U_{ij} = U_{ji}$. Because the resulting excited-state potential is still quadratic, however, a set of new, un-mixed excited-state coordinates $Q_i^{(e)}$ can be found by diagonalizing H_e . The result is a rotation of the normal coordinates between the ground and excited states. Geometrically, we can see this explicitly for the case of a two-dimensional potential with ground-state coordinates Q_1 and Q_2 , in which the rotational transformation

$$\mathbf{R} = \begin{pmatrix} \cos \theta & -\sin \theta \\ \sin \theta & \cos \theta \end{pmatrix}, \quad (2.13a)$$

with

$$\theta = \frac{1}{2} \tan^{-1} \left(\frac{2U_{12}}{\hbar\omega_1 + U_{11} - \hbar\omega_2 - U_{22}} \right) \quad (2.13b)$$

transforms the ground-state normal coordinates into the excited-state normal coordinates.⁵²

Figure 2.1(c) shows the ground and excited potentials for this case with $\theta = -30^\circ$ and no frequency changes ($U_{11} = U_{22} = 0$). For an arbitrary number of modes, this transformation is accomplished by the so-called Duschinsky matrix J_{ij} , which by convention is usually defined to express the ground-state coordinates in terms of the excited-state coordinates and is typically expressed with respect to the dimensional normal coordinates

$$q_i = \sum_j J_{ij} q_j^{(e)}. \quad (2.14)$$

Formally, the Duschinsky matrix can be expressed in terms of the normal mode transformations (Eq. 2.2) for the ground (L_{ij}) and excited ($L_{ij}^{(e)}$) potentials,⁵³

$$J_{ij} = \sum_k (L^{-1})_{ik} L_{kj}^{(e)}. \quad (2.15)$$

In terms of dimensionless coordinates, the Duschinsky matrix is modified by the square root of the frequency ratios between modes⁵⁴

$$Q_i = \sum_j \tilde{J}_{ij} Q_j^{(e)} \quad (2.16a)$$

$$\tilde{J}_{ij} = \sqrt{\omega_i^{(g)}/\omega_j^{(e)}} J_{ij}. \quad (2.16b)$$

We note that while J_{ij} is an orthogonal transformation ($(J^{-1})_{ij} = J_{ji}$), \tilde{J}_{ij} is in general not due to these frequency scalings. For our two-mode system the Duschinsky matrix is the inverse of the rotation matrix in Eq. 2.13a, i.e. $J_{ij} = (\mathbf{R}^{-1})_{ij}$. We note that in the presence of off-diagonal quadratic coupling, frequency changes are no longer simply given by Eq. 2.12, and are instead influenced in more complicated ways by the diagonalization procedure.

2.2.2 Transition dipole moments

Spectroscopically, the coupling of vibrational and electronic degrees of freedom is most prominently manifested through modifications to the transition dipole moments connecting vibronic states. Here we describe some of these effects for our model system Hamiltonian, with an emphasis on the transitions relevant for FEIR spectroscopy. Within the Born-Oppenheimer approximation the total system dipole operator is the sum of electronic and vibrational contributions

$$\mathbf{M}(\mathbf{r}, \mathbf{Q}) = \mathbf{M}_{\text{elec}}(\mathbf{r}) + \mathbf{M}_{\text{vib}}(\mathbf{Q}), \quad (2.17)$$

which depend on the set of all electronic and nuclear coordinates, for brevity denoted by \mathbf{r} and \mathbf{Q} , respectively. The vibronic eigenstates are taken to be adiabatic Born-Oppenheimer wavefunctions

$$|a(\mathbf{r}, \mathbf{Q})\rangle = |\psi_a(\mathbf{r}, \mathbf{Q})\rangle|\chi_a(\mathbf{Q})\rangle \quad (2.18)$$

where the nuclear part χ_a is independent of the electronic coordinates and the electronic part ψ_a depends only parametrically on the nuclear coordinates. The transition dipole moment connecting vibronic eigenstates a and b is therefore

$$\begin{aligned} \mathbf{M}_{ba} = & \langle \chi_b(\mathbf{Q}) | \langle \psi_b(\mathbf{r}, \mathbf{Q}) | \mathbf{M}_{\text{elec}}(\mathbf{r}) | \psi_a(\mathbf{r}, \mathbf{Q}) \rangle | \chi_a(\mathbf{Q}) \rangle \\ & + \langle \psi_b(\mathbf{r}, \mathbf{Q}) | \psi_a(\mathbf{r}, \mathbf{Q}) \rangle \langle \chi_b(\mathbf{Q}) | \mathbf{M}_{\text{vib}}(\mathbf{Q}) | \chi_a(\mathbf{Q}) \rangle. \end{aligned} \quad (2.19)$$

Vibrational transitions

When $|a\rangle$ and $|b\rangle$ belong to the same electronic state, $|\psi_a\rangle = |\psi_b\rangle$ and the first term in Eq. 2.19 vanishes, assuming the system does not have a permanent electronic dipole moment. The transition dipole moment then reduces to a pure vibrational transition dipole moment

$$\mathbf{M}_{ba} = \langle \chi_b(\mathbf{Q}) | \mathbf{M}_{\text{vib}}(\mathbf{Q}) | \chi_a(\mathbf{Q}) \rangle. \quad (2.20)$$

FEIR spectroscopy deals only with the pure vibrational transitions on the electronic ground state. The vibrational coordinate dependence of \mathbf{M}_{vib} may be expanded in a power series

$$\mathbf{M}_{\text{vib}}(\mathbf{Q}) = \boldsymbol{\mu}^{(0)} + \sum_i \boldsymbol{\mu}_i^{(1)} Q_i + \frac{1}{2} \sum_{i,j} \boldsymbol{\mu}_{ij}^{(2)} Q_i Q_j + \dots \quad (2.21)$$

where the coefficients $\boldsymbol{\mu}^{(0)} = \mathbf{M}_{\text{vib}}(\mathbf{Q}_0)$, $\boldsymbol{\mu}_i^{(1)} = \left(\frac{\partial \mathbf{M}_{\text{vib}}}{\partial Q_i} \right)_0$, $\boldsymbol{\mu}_{ij}^{(2)} = \left(\frac{\partial^2 \mathbf{M}_{\text{vib}}}{\partial Q_i \partial Q_j} \right)_0$ are evaluated at the equilibrium geometry \mathbf{Q}_0 . The constant term $\boldsymbol{\mu}^{(0)}$ can be ignored, as the accompanying wavefunction overlap $\langle \chi_b | \chi_a \rangle = 0$ in Eq. 2.20. The linear term $\boldsymbol{\mu}_i^{(1)}$ produces the usual IR harmonic selection rule $\Delta \nu_i = \pm 1$, while $\boldsymbol{\mu}_{ij}^{(2)}$ and higher-order nonlinear terms describe electrical anharmonicity of the vibrational dipole moment and are responsible for multi-quantum overtone or combination band transitions. In this work we will only retain the linear term, and denote the pure vibrational dipole moment of the i -th mode on the ground state as $\boldsymbol{\mu}_i$.

Vibronic transitions

On the other hand, when $|a\rangle$ and $|b\rangle$ belong to different electronic states, $|\psi_a\rangle$ and $|\psi_b\rangle$ are orthogonal and the second term in Eq. 2.19 vanishes. We will examine the case most relevant

to FEIR spectroscopy where $|a\rangle \in |g\rangle$ and $|b\rangle \in |e\rangle$. The remaining term is

$$\mathbf{M}_{ba} = \langle \chi_b(\mathbf{Q}) | \mathbf{M}_{eg}(\mathbf{Q}) | \chi_a(\mathbf{Q}) \rangle, \quad (2.22)$$

where the vibrational coordinate-dependence to the electronic transition moment comes from the parametric dependence of the electronic wavefunctions in the integral

$$\mathbf{M}_{eg}(\mathbf{Q}) = \langle \psi_e(\mathbf{r}, \mathbf{Q}) | \mathbf{M}_{elec}(\mathbf{r}) | \psi_g(\mathbf{r}, \mathbf{Q}) \rangle. \quad (2.23)$$

This \mathbf{Q} -dependence can be similarly developed in a power series expansion

$$\mathbf{M}_{eg}(\mathbf{Q}) = \boldsymbol{\mu}_{eg}^{(0)} + \sum_i \boldsymbol{\mu}_{eg,i}^{(1)} Q_i + \dots \quad (2.24)$$

where $\boldsymbol{\mu}_{eg}^{(0)} = \mathbf{M}_{eg}(Q_0)$ is the pure electronic transition dipole moment at the equilibrium nuclear geometry, while $\boldsymbol{\mu}_{eg,i}^{(1)} = \left(\frac{\partial \mathbf{M}_{eg}}{\partial Q_i} \right)_0$ describes linear coordinate-dependence through the dipole derivative along the i -th mode. The Condon approximation neglects all vibrational coordinate-dependence to the electronic transition dipole moment, keeping only the $\boldsymbol{\mu}_{eg}^{(0)}$ term. The resulting Franck-Condon vibronic transition matrix element is

$$\mathbf{M}_{ba} = \boldsymbol{\mu}_{eg}^{(0)} \langle \chi_b | \chi_a \rangle, \quad (2.25)$$

that is, simply the product of $\boldsymbol{\mu}_{eg}^{(0)}$ with the vibrational wavefunction overlap, i.e. the FC factor. The $\boldsymbol{\mu}_{eg,i}^{(1)}$ term produces Herzberg-Teller (HT) coupling, which allows modes with zero FC overlap to be active, i.e. gain or lose vibrational quanta, in the electronic transition.⁵⁵ Similarly, dipole-forbidden electronic transitions, i.e. for which $\boldsymbol{\mu}_{eg}^{(0)} = 0$, may gain intensity

through HT coupling to vibrations of appropriate symmetry. Specifically, by developing the derivative $\boldsymbol{\mu}_{eg,i}^{(1)}$ as an expansion over all electronic states, it can be shown that the HT-active vibration acts to couple the forbidden $g \rightarrow e$ transition to other allowed electronic transitions, thereby facilitating “intensity borrowing”.^{56,57} HT coupling is consequently often important for weakly allowed electronic transitions, but less prevalent or obvious for the strong, dipole-allowed electronic transitions that are mostly of interest for generating bright signals in sensitive FEIR spectroscopy experiments. While exceptions to this observation exist, in this work we will largely describe vibronic coupling in the FC approximation, and only keep the $\boldsymbol{\mu}_{eg}^{(0)}$ term in Eq. 2.24 which we will henceforth simply denote by $\boldsymbol{\mu}_{eg}$.

In terms of transition dipole orientation, an important consequence of the FC limit is that the vibronic transition moments are necessarily aligned along the pure electronic moment $\boldsymbol{\mu}_{eg}$, as the FC factor in Eq. 2.25 is a just scalar that modifies the magnitude of the transition. On the other hand, HT coupling can influence the orientation of the vibronic transition moment through the vectorial dipole derivatives $\boldsymbol{\mu}_{eg,i}^{(1)}$. In some cases, this form of coupling can fully rotate the transition orientation by 90° .⁵⁸

2.2.3 Franck-Condon factors

Here we calculate some FC factors relevant to FEIR spectroscopy for our vibronic Hamiltonian, and demonstrate how they depend on the various forms of FC coupling discussed in Section 2.2.1. We note that some authors reserve the term FC factor for the square of the wavefunction overlap $|\langle\chi_b|\chi_a\rangle|^2$, however we will use this term to refer to the overlap $\langle\chi_b|\chi_a\rangle$ itself. We will consider the case discussed above where $|\chi_a\rangle$ and $|\chi_b\rangle$ are the ground- and excited-state nuclear wavefunctions, respectively. As our model potentials

are harmonic, these wavefunctions are multidimensional products of 1D harmonic oscillator wavefunctions,^{59,60} e.g. for the ground state

$$\chi_a(\mathbf{Q}) = \prod_{i=1}^K N_{\nu_i^g} H_{\nu_i^g}(Q_i) e^{-Q_i^2/2} = |\nu_1^g \cdots \nu_i^g \cdots \nu_K^g\rangle \quad (2.26)$$

where ν_i^g is the number of quanta in the i^{th} -mode, K is the total number of normal modes, $H_{\nu_i^g}(x)$ is the Hermite polynomial of degree ν_i^g , $N_{\nu_i^g}$ is a normalization factor, and we recall that Q_i is dimensionless (Eq. 2.5). The second equality indicates the notation for this wavefunction in terms of the number of quanta in each mode. The excited-state nuclear wavefunction is given by an analogous expression, but rather using the excited-state coordinates $Q_i^{(e)}$ and their occupation numbers ν_i^e ,

$$\chi_b(\mathbf{Q}^{(e)}) = \prod_{i=1}^K N_{\nu_i^e} H_{\nu_i^e}(Q_i^{(e)}) e^{-(Q_i^{(e)})^2/2} = |\nu_1^e \cdots \nu_i^e \cdots \nu_K^e\rangle. \quad (2.27)$$

The FC factor is the multi-dimensional overlap integral⁶¹

$$\langle \chi_b | \chi_a \rangle = \langle \nu_1^e \cdots \nu_K^e | \nu_1^g \cdots \nu_K^g \rangle = \int \chi_b^*(\mathbf{Q}^{(e)}) \chi_a(\mathbf{Q}) d\mathbf{Q}, \quad (2.28)$$

where here we have expressed the integration over the ground-state coordinates, although it would be equally valid to use the excited-state coordinates. In either case, it is necessary to express one set of coordinates in terms of the other, which is accomplished by the following linear transformation, often referred to as the Duschinsky transformation,

$$Q_i = \sum_j \tilde{J}_{ij} Q_j^{(e)} + d_i. \quad (2.29)$$

Here \tilde{J}_{ij} is the dimensionless version of the Duschinsky matrix from Eq. 2.16 and d_i is the dimensionless displacement. We note that the Duschinsky transformation is more typically expressed in terms of the dimensional normal mode coordinates⁵³

$$q_i = \sum_j J_{ij} q_j^{(e)} + \sqrt{\hbar/\omega_i} d_i. \quad (2.30)$$

The interpretation of this expression is that the excited state normal modes are first rotated (via J_{ij}), and then displaced to match up to the ground state normal modes. To perform the integrals in Eq. 2.28, the inverse Duschinsky transformation would be used to express $Q_i^{(e)}$ in terms of Q_i ,

$$Q_i^{(e)} = \sum_j (\tilde{J}^{-1})_{ij} (Q_j - d_j), \quad (2.31)$$

that is, the ground-state modes are first displaced, and then rotated. We note that because the vibrational wavefunctions in the integral are real-valued, the FC factor is consequently also real and satisfies $\langle \chi_b | \chi_a \rangle = \langle \chi_a | \chi_b \rangle$.

In the absence of mode mixing ($U_{i \neq j} = 0$), the Duschinsky matrix is the identity, and the multidimensional overlap integral can be separated into the products of 1D integrals over each normal coordinate,

$$\langle \nu_1^e \cdots \nu_K^e | \nu_1^g \cdots \nu_K^g \rangle = \prod_i \langle \nu_i^e | \nu_i^g \rangle, \quad (2.32)$$

which greatly simplifies the situation and allows for relatively straightforward closed-form expressions. Below, we discuss 1D FC factors first in the case of mode displacements without frequency changes, yielding the well-known DHO FC factors, and then address the effects

of frequency changes. Finally, we will return to the multidimensional treatment required for incorporating the effects of mode-mixing.

Mode displacement

The case of purely linear FC coupling ($U_{ij} = 0$), i.e. the DHO model, results in the following simple closed-form expressions for 1D overlap integrals⁶²

$$\langle \nu^e | \nu^g \rangle = \begin{cases} \sqrt{\frac{\nu^e!}{\nu^g!}} \left(\frac{d}{\sqrt{2}}\right)^{\nu^g - \nu^e} L_{\nu^e}^{\nu^g - \nu^e} \left(\frac{d}{\sqrt{2}}\right) \langle 0^e | 0^g \rangle, & \nu^g \geq \nu^e \\ \sqrt{\frac{\nu^g!}{\nu^e!}} \left(-\frac{d}{\sqrt{2}}\right)^{\nu^e - \nu^g} L_{\nu^g}^{\nu^e - \nu^g} \left(\frac{d}{\sqrt{2}}\right) \langle 0^e | 0^g \rangle, & \nu^g \leq \nu^e, \end{cases} \quad (2.33a)$$

where d is the dimensionless displacement (Eq. 2.10) and the 0-0 FC factor is

$$\langle 0^e | 0^g \rangle = e^{-d^2/4}, \quad (2.33b)$$

and $L_n^k(x)$ are the associated Laguerre polynomials.⁶³ The first few of these polynomials are

$$L_0^k(x) = 1 \quad (2.33c)$$

$$L_1^k(x) = -x + (k + 1) \quad (2.33d)$$

$$L_2^k(x) = x^2 - 2(k + 2)x + \frac{(k + 1)(k + 2)}{2}. \quad (2.33e)$$

Figures 2.2(a)-(b) show these FC factors for $\nu^g = 0$ and 1 and $\nu^e = 0, 1$, and 2 as a function of the dimensionless displacement d . Here we see that achieving a non-zero FC factor with $\nu^g \neq \nu^e$ requires having a non-zero mode displacement, which is also evident in the general case from Eq. 2.33a. These FC factors have the following symmetry when

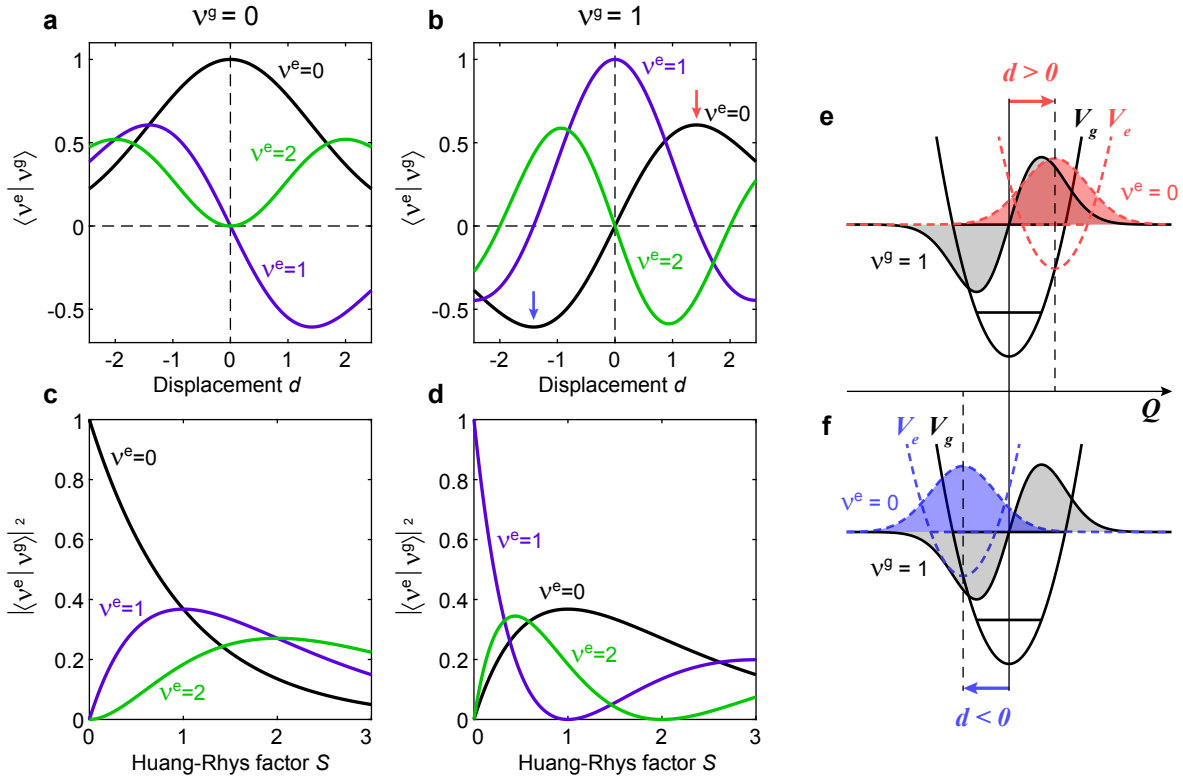


Figure 2.2: Selected DHO FC factors and their squares as a function of dimensionless displacement d and Huang-Rhys factor $S = d^2/2$. FC factors with (a) $\nu^g = 0$ and (b) $\nu^g = 1$ for $\nu^e = 0, 1, 2$ as a function of d . (c) and (d) show the squares of the FC factors in (a) and (b), respectively, as a function of S . The x axis range of $[0, 3]$ in (c) and (d) corresponds to the positive half of $[-\sqrt{6}, \sqrt{6}]$ in (a) and (b). (e)-(f) Overlap of the ground-state (solid) and excited-state (dashed) nuclear potentials and wavefunctions involved in the $\langle 0^e | 1^g \rangle$ FC factor for displacements of $d = \sqrt{2}$ and $d = -\sqrt{2}$, respectively ($S = 1$). The corresponding values of $\langle 0^e | 1^g \rangle$ are indicated in (b) with red and blue arrows, respectively. In both cases the ground and excited potentials are vertically positioned so that the $\nu^g = 1$ and $\nu^e = 0$ wavefunctions share a common zero-level.

exchanging ground- and excited-state vibrational quantum numbers

$$\langle \nu^e = l | \nu^g = k \rangle = (-1)^{l-k} \langle \nu^e = k | \nu^g = l \rangle. \quad (2.34)$$

Figures 2.2(c)-(d) show the corresponding squares of the FC factors in panel (a) and (b) as

a function of the Huang-Rhys factor $S = d^2/2$. In the special case where either $\nu^e = 0$ or $\nu^g = 0$, the squares of the FC factors are given by a Poisson distribution

$$\langle n^e = n | 0^g \rangle^2 = \langle 0^e | n^g = n \rangle^2 = \frac{S^n e^{-S}}{n!} \quad (2.35)$$

with the Huang-Rhys factor playing the role of the Poisson parameter. Of special importance in FEIR spectroscopy is the 1-0 FC factor $\langle 0^e | 1^g \rangle$, which nominally controls the strength of the encoding transition that brings the vibrationally excited molecule to the electronic excited manifold under typical resonance conditions. In the DHO model, its square takes the simple form $|\langle 0^e | 1^g \rangle|^2 = S \exp(-S) \approx S$, where this final approximation holds for small S . Typical Huang-Rhys factors for vibronically active modes on electronic chromophores range from $S \sim 0.01$ to 0.5 .⁶⁴⁻⁶⁶ In general, the following sum rule

$$\sum_{n=0}^{\infty} |\langle n^e = n | n^g \rangle|^2 = \sum_{n=0}^{\infty} |\langle n^e | n^g = n \rangle|^2 = 1 \quad (2.36a)$$

holds for any n^g and n^e , respectively, which simply reflects the normalization of the harmonic oscillator wavefunctions.

In addition to the absolute magnitude, in some cases the sign of an FC factor depends on d . Specifically, FC factors for which $|\nu^g - \nu^e|$ is odd are odd functions of d , that is, they will invert sign when d inverts sign. This can be seen graphically for $\langle 1^e | 0^g \rangle$, $\langle 0^e | 1^g \rangle$, and $\langle 2^e | 1^g \rangle$ in Figures 2.2(a) and (b). Notably, the FEIR-relevant 1-0 FC factor exhibits this sign inversion. The physical rationale for the sign inversion can be seen by considering the parity and overlap of the initial and final wavefunctions, and is shown specifically for $\langle 0^e | 1^g \rangle$ in Figures 2.2(e)-(f). For positive displacement (panel (e)), the equilibrium position of the coordinate lengthens in the excited state, resulting in overlap of $|0^e\rangle$ with the positive lobe

of $|1^g\rangle$. Similarly, for negative displacements (panel (f)), the coordinate shortens, leading to overlap of $|0^e\rangle$ with the negative lobe of $|1^g\rangle$. As we will see later when calculating FEIR signals in Section 2.4.5, this sign change can produce a dramatic effect in the appearance of FEIR spectra in the presence of vibrational coherence.

Frequency changes

Next we consider the effect of a change in mode frequency between the ground and excited state induced by diagonal quadratic coupling (U_{ii}). A general expression for $\langle\nu^e|\nu^g\rangle$ with arbitrary displacement and frequency change may be found in Ref. [62], however here we will specialize to the FEIR-relevant $\langle 0^e|1^g\rangle$ FC factor. Explicitly,

$$\langle 0^e|1^g\rangle = \frac{2d\beta^2\sqrt{1-\beta^2}}{\sqrt{2(1+\beta^2)(1-\beta^4)}}\langle 0^e|0^g\rangle, \quad (2.37a)$$

$$\langle 0^e|0^g\rangle = \sqrt{\frac{2\beta}{1+\beta^2}} \exp\left(\frac{-d^2\beta^2}{2(1+\beta^2)}\right), \quad (2.37b)$$

where $\beta^2 = \omega^{(e)}/\omega^{(g)}$ is the ratio of excited- to ground-state frequency. In the limit $\beta^2 \rightarrow 1$, direct substitution shows that $\langle 0^e|0^g\rangle$ reverts to its DHO value of $\exp(-d^2/4) = \exp(-S/2)$. Similarly, $\langle 0^e|1^g\rangle$ is seen to achieve its corresponding DHO value of $(d/\sqrt{2})\exp(-d^2/4) = \text{sgn}(d)\sqrt{S}\exp(-S/2)$, where $\text{sgn}(d)$ denotes the sign of d , with the help of the limit $\lim_{x \rightarrow 1} \sqrt{1-x^2}/\sqrt{1-x^4} = 1/\sqrt{2}$. Figure 2.3(a) shows the magnitude of this FC factor as a function of both S and β^2 . Importantly, the FC factor is zero for $S = 0$ regardless of the frequency ratio, i.e. displacement is required for the mode to be FC active. Physically, this reflects the fact that $|0^e\rangle$ always has equivalent overlap with the positive and negative lobes of $|1^g\rangle$ for $S = 0$ independent of the frequency change which simply stretches or compresses

the wavefunctions with respect to each other.

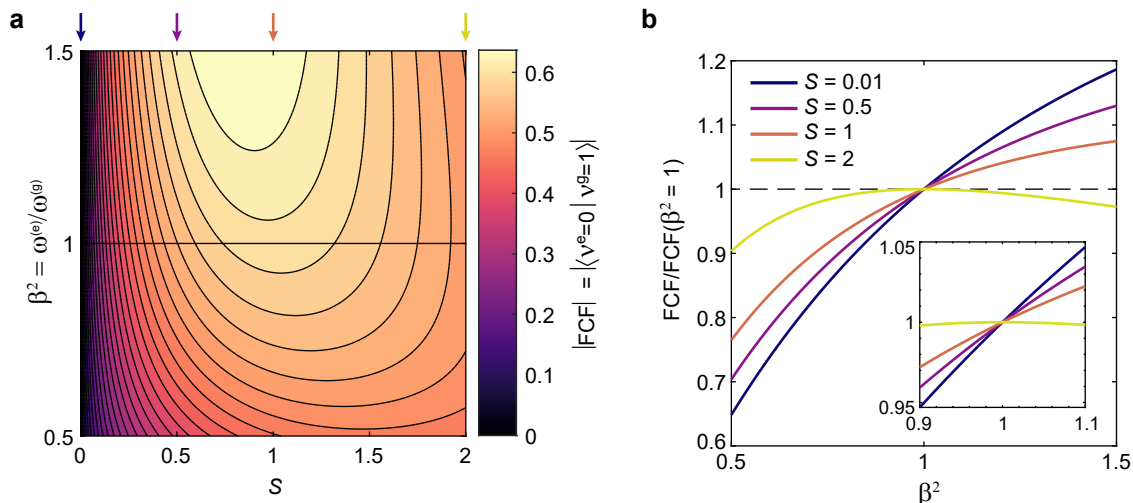


Figure 2.3: Effect of frequency changes on the $\langle 0^e | 1^g \rangle$ FC factor (FCF). (a) Absolute value of the FCF as a function of S and β^2 . (b) Ratio of the FCF to its $\beta^2 = 1$ value as a function of β^2 for selected S values (indicated in (a) by arrows). The inset shows the region around $\beta^2 = 1$.

For non-zero $S < 2$, the FC factor's magnitude increases for $\beta^2 > 1$ (higher excited-state frequency) and decreases for $\beta^2 < 1$ (lower excited-state frequency). Figure 2.3(b) shows the ratio of the FC factor for variable β^2 against its $\beta^2 = 1$ value for a range of S values. The change is most significant for small S , but is overall a small effect given that frequency changes for the high-frequency modes in electronically conjugated molecules are often below 10%. The inset shows that the changes to the FC factor are less than 5% within this range.

Mode-mixing

To demonstrate the effect of Duschinsky mixing, we analyze the two-mode system discussed earlier in Section 2.2.1, as the physical geometry of the problem can be easily visualized. We will consider the case where Q_1 is the vibration of interest being interrogated in an FEIR

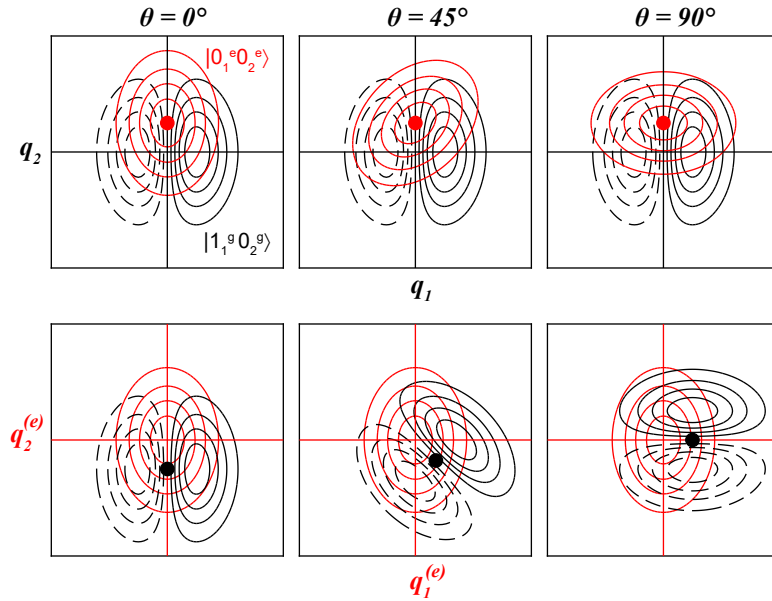


Figure 2.4: Duschinsky transformation for a two-mode system. (a) Ground-state (black) and excited-state (red) wavefunctions for various mixing angles plotted in the ground-state coordinate frame (top row) and excited-state coordinate frame (bottom row). Solid and dashed contours denote positive and negative wavefunction amplitude, respectively. Black and red dots denote the origin of the ground and excited coordinates frames, respectively.

experiment, while Q_2 is another system mode (of lower or higher frequency) that is not being excited, i.e. a ‘spectator’ mode. The relevant FC factor in this scenario is $\langle 0_1^e 0_2^e | 1_1^g 0_2^g \rangle$. Without mode-mixing this integral is separable, and we recover our earlier results: namely, displacement along Q_1 (e.g. linear FC coupling) is required for the FC factor to be non-zero. Of special interest is the question of whether mode-mixing can alter this state of affairs, i.e. can Q_1 become vibronically active even without any displacement of its own? As demonstrated in Figures 2.4 and 2.5, the answer is yes, mode-mixing can make this FC factor non-zero under certain conditions that we will discuss below.

It is useful to begin at a qualitative level by visualizing the wavefunctions involved in the overlap integral, and how they are influenced by the mode-mixing. Figure 2.4 shows

the ground- and excited-state nuclear wavefunctions represented as contour plots for mixing angles of $\theta = 0^\circ, 45^\circ$ and 90° . In this example we have set $d_1 = 0$ and $d_2 = \sqrt{2}$, and the modes have a relative frequency ratio of $\omega_2/\omega_1 = 1/2$ with no frequency changes between the ground and excited states. In order for the relative difference in frequency between the modes to be visible (e.g. evident in the ellipticity of the $|0_1^e 0_2^e\rangle$ contours), we have employed dimensional normal coordinates q_i , rather than the frequency-scaled dimensionless coordinates Q_i . The Duschinsky transformation is shown both from the perspective of the ground-state coordinates (top row) and the excited-state coordinates (bottom row). Starting in the ground-state coordinate frame, $|0_1^e 0_2^e\rangle$ is first displaced along q_2 by $\sqrt{\hbar/\omega_2}\sqrt{2}$, then rotated by $-\theta$. From the excited-state perspective, $|1_1^g 0_2^g\rangle$ is first rotated by θ , then displaced (along the new rotated q_2 axis) by $-\sqrt{\hbar/\omega_2}\sqrt{2}$. The resulting relative positioning of the two wavefunctions can be seen to be equivalent in both frames.

For $\theta = 0^\circ$ and 90° , $|0_1^e 0_2^e\rangle$ symmetrically covers both the positive and negative lobes of $|1_1^g 0_2^g\rangle$, leading to zero overlap. However, for $\theta = 45^\circ$ we see that due to the partial rotation, there is more overlap of $|0_1^e 0_2^e\rangle$ with the negative than the positive lobe of $|1_1^g 0_2^g\rangle$, resulting in a non-zero FC factor. One way to frame this is that mode-mixing has caused Q_1 to “borrow” FC activity from Q_2 .

Calculating FC factors for multi-dimensional harmonic systems with mode-mixing is most conventionally done by way of recursion relations that build up arbitrary FC factors from the 0-0 overlap,^{53,67-70} although analytic expressions (of substantial complexity) can be found for low-dimensional cases.⁷¹⁻⁷³ As our problem consists of one quantum of excitation in a single mode in the ground state, the recursion method is thankfully very convenient. Here we provide the relevant expression for the case of K modes^{74,75}, which we will evaluate numerically for our two-mode system. Using the notation $|\mathbf{0}^e\rangle = |0_1^e \cdots 0_l^e \cdots 0_K^e\rangle$ and $|\mathbf{0}^g +$

$$1_l^g \rangle = |0_1^g \cdots 1_l^g \cdots 0_K^g \rangle,$$

$$\langle \mathbf{0}^e | \mathbf{0}^g + 1_l^g \rangle = \frac{1}{\sqrt{2}} B_l \langle \mathbf{0}^e | \mathbf{0}^g \rangle. \quad (2.38a)$$

The recursion factor is the l^{th} element of the vector

$$\mathbf{B} = 2\mathbf{d} \left(\mathbf{1} - \boldsymbol{\Omega}_g^{1/2} \mathbf{J} \mathbf{X}^{-1} \mathbf{J}^{-1} \boldsymbol{\Omega}_g^{1/2} \right), \quad (2.38b)$$

with

$$\mathbf{X} = \mathbf{J}^{-1} \boldsymbol{\Omega}_g \mathbf{J} + \boldsymbol{\Omega}_e, \quad (2.38c)$$

where \mathbf{d} is a column vector of the dimensionless displacements, \mathbf{J} is the Duschinsky matrix, $\mathbf{1}$ is the identity matrix, and $\boldsymbol{\Omega}_g$ and $\boldsymbol{\Omega}_e$ are diagonal matrices of the ground- and excited-state frequencies. The 0-0 overlap is

$$\langle \mathbf{0}^e | \mathbf{0}^g \rangle = (\det \boldsymbol{\Omega}_g \det \boldsymbol{\Omega}_e)^{1/4} \left(\frac{2^N \det \mathbf{J}}{\det \mathbf{X}} \right)^{1/2} \exp \left[-\frac{1}{2} \mathbf{d}^T \mathbf{d} + \frac{1}{2} \mathbf{Y}^T \mathbf{X}^{-1} \mathbf{Y} \right], \quad (2.38d)$$

with

$$\mathbf{Y} = \mathbf{J}^{-1} \boldsymbol{\Omega}_g^{1/2} \mathbf{d}. \quad (2.38e)$$

Using this expression, Figure 2.5(a) shows the value of the $\langle 0_1^e 0_2^e | 1_1^g 0_2^g \rangle$ FC factor as a function of θ and d_1 for $d_2 = \sqrt{2}$. As in Figure 2.4, the frequency ratio is $\omega_2/\omega_1 = 1/2$ with no frequency changes between the ground and excited states. The case of $d_1 = 0$ we have been considering is indicated by a dashed line, and shown explicitly in Figure 2.5(c). The three

angles depicted in Figure 2.4 are indicated by arrows. The FC factor has 180° periodicity in the mixing angle, which can be inferred by visual inspection of the wavefunctions. The maximum value achieved by the FC factor in Figure 2.5(b) is near 0.1, a non-negligible fraction of the 1D overlap $\langle 0_2^e | 1_2^g \rangle = e^{-1/2} \approx 0.61$ if the “spectator” mode was being excited.

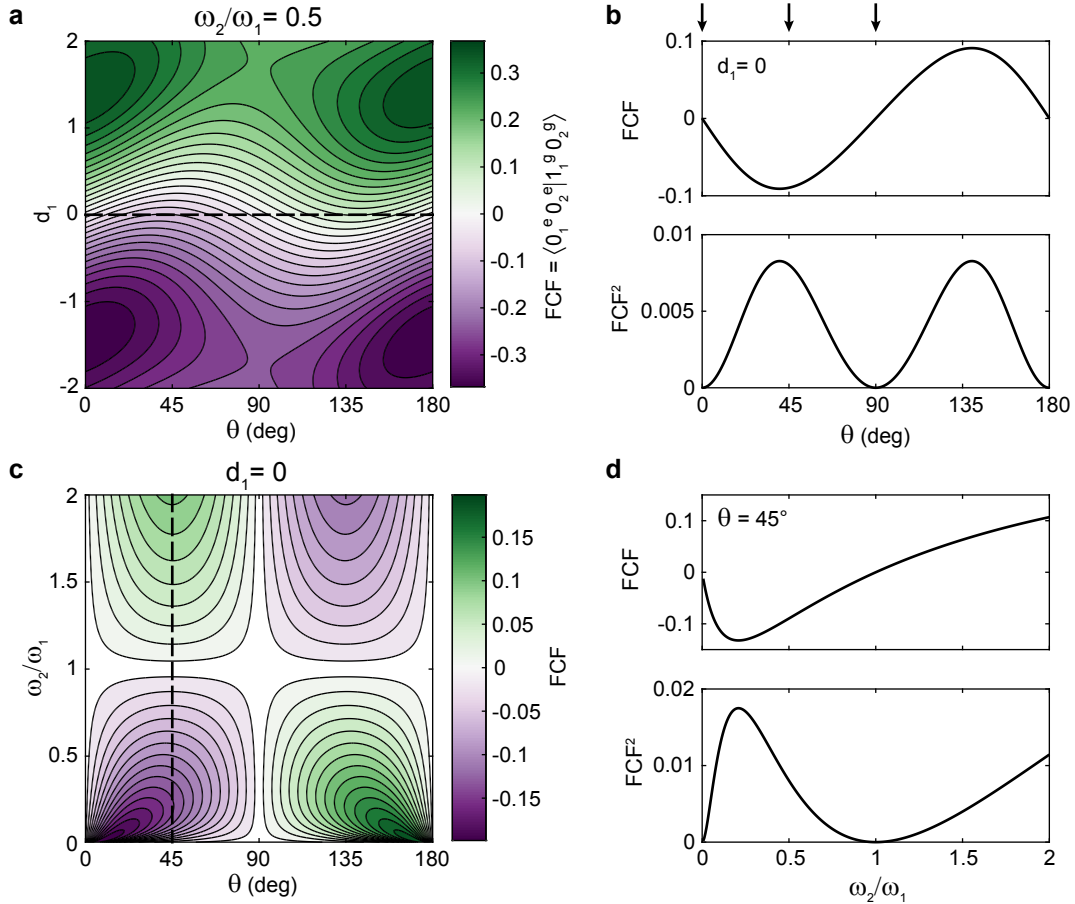


Figure 2.5: Effect of Duschinsky mixing on the $\langle 0_1^e 0_2^e | 1_1^g 0_2^g \rangle$ FC factor (FCF). (a) FC factor as a function of θ and d_1 for $\omega_2/\omega_1 = 1/2$. (b) Slice along $d_1 = 0$ of the FC factor (top panel) and its square (bottom panel). (c) FC factor as a function of θ and ω_2/ω_1 for $d_1 = 0$. (d) Slice along $\theta = 45^\circ$ of the FC factor (top panel) and its square (bottom panel).

A crucial factor in facilitating this mixing-induced FC activity are the relative frequencies of the two modes. Figure 2.5(c) shows the FC factor for the case of $d_1 = 0$ as a function of θ

and the frequency ratio ω_2/ω_1 . As we can see, for a given mixing angle the FC factor increases in absolute magnitude as the frequency ratio departs from unity, e.g. Figure 2.5(d) shows the slice along $\theta = 45^\circ$. In terms of the wavefunctions in Figure 2.4, this can be understood by the improved selectivity of overlap between $|0_1^e 0_2^e\rangle$ and the positive or negative lobe of $|1_1^g 0_2^g\rangle$ with increasing ellipticity of the wavefunctions. The FC factor vanishes as ω_2/ω_1 approaches unity, and when the modes are degenerate Duschinsky rotation is no longer well defined. The sign of the FC factor flips when the frequency ratio switches from $\omega_2/\omega_1 < 1$ to $\omega_2/\omega_1 > 1$. For $\omega_2/\omega_1 > 1$, the maximum FC factor magnitude always occurs at a mixing angle of $\theta = 45^\circ$, while for $\omega_2/\omega_1 < 1$, it moves to increasingly lower mixing angles.

Overall, we have seen that mode-mixing can cause an undisplaced mode to gain FC activity (i.e. achieve a non-zero 1-0 FC factor) if it mixes with a displaced mode of different frequency in the excited state. The magnitude of the effect is highly dependent on the mixing angle and relative frequency, and the example discussed here uses rather extreme cases of these parameters. The importance of these effects are therefore highly system dependent, and should be evaluated for the vibration and molecule at hand. For example, quantum chemical calculations for the coumarin dyes used in the thesis show very little mode mixing between the S_0 and S_1 states, while excited-state frequency changes are also small ($< 5\%$).⁷⁴ Therefore, the DHO model is likely a good model with which to understand vibronic coupling as it pertains to the FEIR spectroscopy of these molecules.

2.3 Nonlinear action spectroscopy

2.3.1 Fluorescence as action spectroscopy

Give the ubiquity of fluorescence as a tool in molecular science—or indeed as a basic phenomenon observed in everyday life—it may appear somewhat surprising that a satisfactory, fully self-consistent physical picture of the emission process is rather elusive.⁷⁶ Fluorescence, or the spontaneous emission of light from an electronically-excited molecule, is difficult to describe rigorously with the typical semi-classical methods found in a physical chemist’s theoretical tool-box. Part of the subtlety arises from a rigorous description of photons, which requires a fully quantum-mechanical treatment of the electromagnetic field,^{77,78} and is notoriously fraught with confusion and miscommunication.⁷⁹ The interaction of such a quantum field with the spectroscopic system of interest is a further complicating factor that goes beyond the typical formalism that chemists such as myself would prefer to use. Specifically, the radiative relaxation of the excited level and associated emission of a photon is ultimately governed by the interaction of the material system with the vacuum state of the radiation field, although even this statement might elicit an indignant response from practitioners of quantum optics.^{80–82}

One solution to describing fluorescence-detected experiments in the face of these theoretical complexities is to simply ignore them. More precisely, if the details of the measurement don’t explicitly reveal the quantum electrodynamical nature of spontaneous emission, a simple phenomenological treatment is likely sufficient or even desirable. This approach of theoretical agnosticism about the physical processes underlying the detection method can be classified under the umbrella of ‘action spectroscopy’. Specifically, action spectroscopy refers to any method whereby the spectroscopic signal is read out from the system by indirect

means. Here our meaning of ‘indirect’ is defined in contrast to the situation in conventional spectroscopy where excitation and signal generation can be treated on essentially the same footing, e.g. directly monitoring absorption, scattering, interference, or amplification of the interrogating electromagnetic field. The indirect response detected in an action experiment is assumed to arise in a proportional manner from the spectroscopic excitation, but its details are not explicitly treated and can often involve substantial microscopic complexity. In addition to fluorescence, some examples of action observables include the detection of photocurrent, photoelectrons, ions produced by photofragmentation, mechanical motion, or temperature changes and thermal gradients.

The term action spectroscopy is used in a variety of contexts with slightly different meanings. It seems to have originated in the field of photosynthetic biology, where an action spectrum measures the frequency-dependent effect of light on some biological response in an organism.^{83,84} In fact, this idea dates back to the remarkable work of Engelmann in the 1880’s, who measured the first action spectrum by monitoring the accumulation of aerotactic (i.e. oxygen-seeking) bacteria around photosynthetic algae on a plate illuminated by spectrally-dispersed light.^{85,86} The amount of oxygen produced by the algae in different regions of the plate depended on the strength of photosynthetic response induced by the particular incident color, which was correspondingly read out by the sizes of bacterial colonies which congregated in the different regions. The resulting ‘bacterial accumulation’-detected spectrum (quite the complicated action observable!) looks remarkably similar to the optical absorption spectrum of chlorophyll.

Modern usage of the term action spectroscopy in physical chemistry is common in the gas-phase community, where it refers mostly to techniques that detect ions produced by dissociation proceeding optical absorption.⁸⁷ Our usage of the term is aligned with that in

ultrafast and multidimensional spectroscopy, where action detection formally refers to the measurement of a specific excited state population by proxy through a proportional quantity. Fluorescence is perhaps the most common mode of action detection in ultrafast spectroscopy, which has roots in linear wave-packet interferometry experiments involving phase-controlled femtosecond pulses,⁸⁸⁻⁹⁰ and is by now widespread in multidimensional experiments.⁹¹⁻⁹⁴ Other more recent examples of action methods involve the detection of photocurrent,⁹⁵⁻¹⁰¹ photoelectrons,¹⁰² and mass-resolved ions,¹⁰³⁻¹⁰⁶ to name a few. Fluorescence-detected action spectroscopies are often referred to as ‘incoherent’, because the fluorescence emission from the sample does not retain a coherent temporal phase-relationship to a macroscopic polarization set up in the sample by the driving fields. Indeed, the creation of such a macroscopic polarization is not required for the success of the experiment, and in fact does not even occur at the relevant nonlinear order for spatial symmetry reasons that will be discussed later in this section.

In the case of fluorescence, multiple types of information are in principle available beyond intensity, including emission spectrum, polarization, and emission kinetics. In many cases these can be incorporated in the action framework through phenomenological strategies. In describing the FEIR experiments in this thesis, however, we will mostly be concerned with intensity. Despite the theoretical subtleties mentioned above, we will use the term ‘photon’ liberally in this thesis. In the context of light detection what we really have in mind is a click on a photon-counting detector, the accumulation of which describes the fluorescence intensity.

The principle of action spectroscopy can be illustrated in the context of the following simple and widely used phenomenological model for fluorescence emission. In this model, electronically excited molecules can decay back to the ground state either by emitting a

photon with the radiative rate constant Γ_r or through nonradiative relaxation with rate constant Γ_{nr} . The number of excited molecules at time t therefore obeys the linear rate law

$$\frac{dN(t)}{dt} = -(\Gamma_r + \Gamma_{nr})N(t), \quad (2.39)$$

and considering an ensemble of molecules excited impulsively at $t = 0$, the solution is

$$N(t) = N(0)e^{-(\Gamma_r + \Gamma_{nr})t}. \quad (2.40)$$

The number of photons emitted in the interval $[t, t + dt]$ is determined by the radiative rate

$$F(t)dt = \Gamma_r N(t)dt. \quad (2.41)$$

The signal typically measured is the time-integrated fluorescence output (in practice scaled by factors involved in the instrument's detection efficiency)

$$F = \int_{t_0}^{t_1} F(t)dt \quad (2.42)$$

where the integration bounds can in principle be set by a fast time-gated detector. In a pulsed experiment, the excitation process occurs over and over again at the repetition-rate of the laser system, and this signal is therefore more conveniently represented as the pulse-train averaged photon count rate rather than the total number of photons collected. Taking the integration bounds to cover the entire decay profile, we have

$$F = \int_0^{\infty} F(t)dt = \frac{\Gamma_r}{\Gamma_r + \Gamma_{nr}} N(0). \quad (2.43)$$

This defines the fluorescence quantum yield

$$\phi = \Gamma_r / (\Gamma_r + \Gamma_{nr}), \quad (2.44)$$

which dictates the probability that an excitation decays by photon emission. In action spectroscopy language, the signal measured in experiment is sufficiently well-described by Eq. 2.43, that is, only with knowledge of the initial excited population $N(0)$ and the quantum yield ϕ . In other words, the physical processes and dynamics that actually give rise to the emission of the photon do not need to be known in detail to calculate or analyze the signal as detected in experiment. This perspective is useful for the FEIR experiments discussed in this thesis, where for the most part the spectroscopic information is wrapped up in excitation process, and the intensity of fluorescence emission merely acts to “read out” this excitation. From a theoretical standpoint this means our efforts can go into simulating the excitation process, i.e. calculating $N(0)$, and the remainder of this chapter is devoted to this task.

When considering single molecules, rather than an ensemble, we can interpret the expressions above in terms of probability densities, rather than populations. Making the substitution $N(t) \rightarrow P_{\text{excited}}(t) = N(t)/N_{\text{tot}}$ where N_{tot} is the total number of molecules in the ensemble, Eq. 2.40 is the probability density an initially excited molecule is still in the excited state at time t , assuming a homogeneous ensemble.

2.3.2 Response function formulation of time-dependent perturbation theory

Response functions provide a convenient method for calculating the response of a system observable to an external perturbation within the framework of time-dependent perturbation

theory. The modern origins of this approach can be traced to the work of Kubo in developing methods for treating non-equilibrium dynamics.¹⁰⁷ In the context of optical spectroscopy, the external perturbation is the light-matter interaction between the incident electromagnetic field controlled by the experimenter and the system being interrogated. The system's response is developed order-by-order in a perturbative expansion of the interaction, and the resulting response function at the appropriate order of nonlinearity is used to describe the nonlinear signals measured in experiment. This formulation is especially well suited to time-domain experiments using multiple short pulses, as the correspondence between the theoretical response functions and spectroscopic data can be made particularly direct under appropriate conditions. Indeed, largely thanks to the highly influential work of Mukamel,⁴⁸ the response function formalism is deeply embedded in the modern field of ultrafast spectroscopy down to the very language used in the interpretation and design of experiments.

It is useful to provide a brief overview of the response function approach as it is typically applied to nonlinear spectroscopy. This method uses a semiclassical treatment of the light-matter interaction in which the material system is described quantum-mechanically, while the electromagnetic field is a classical function obeying Maxwell's equations. Response functions are most naturally represented when using the density matrix to describe the system and its dynamics. The density matrix evolves according to the Liouville-von Neumann equation

$$\frac{\partial \rho(t)}{\partial t} = -\frac{i}{\hbar} [H(t), \rho(t)]. \quad (2.45)$$

The Hamiltonian is expressed as

$$H(t) = H_0 + V(t), \quad (2.46)$$

where H_0 is the time-independent matter Hamiltonian describing the system and its environment, and the perturbation $V(t)$ is the light-matter interaction taken in the dipole approximation,^{108–110}

$$V(t) = -\mu E(t). \quad (2.47)$$

Here μ is the system dipole operator, $E(t)$ is the incident electric field (a classical, real-valued function), and to simplify the notation for the time being, we have ignored their vector qualities. The vectorial nature of these quantities is, however, critical for describing polarization-dependent spectroscopy, and will be built back into the response function later on. Working in the interaction picture, a solution for the time-dependent density matrix can be developed in a series expansion

$$\rho(t) = \rho_0 + \rho^{(1)}(t) + \rho^{(2)}(t) + \rho^{(3)}(t) + \dots . \quad (2.48)$$

Each successive term is found by plugging the previous back into the Liouville-von Neumann equation, yielding

$$\rho^{(n)}(t) = \left(-\frac{i}{\hbar}\right)^n \int_{t_0}^t dt_n \int_{t_0}^{t_n} dt_{n-1} \cdots \int_{t_0}^{t_2} dt_1 [V(t_n), [V(t_{n-1}), \cdots [V(t_1), \rho_0] \cdots]], \quad (2.49)$$

where the initial state of the system (and hence 0th-order term in the perturbation) is $\rho(t_0) = \rho_0$. The expectation value of any system observable O can then be expressed order-by-order

as

$$\langle O(t) \rangle = O^{(0)}(t) + O^{(1)}(t) + O^{(2)}(t) + O^{(3)}(t) + \dots, \quad (2.50a)$$

$$O^{(n)}(t) = \text{Tr}\{O(t)\rho^{(n)}(t)\}. \quad (2.50b)$$

Plugging in Eq. 2.49, the n^{th} -order contribution is

$$\begin{aligned} O^{(n)}(t) &= \text{Tr}\{O(t)\rho^{(n)}(t)\} \\ &= \left(-\frac{i}{\hbar}\right)^n \int_{t_0}^t dt_n \int_{t_0}^{t_n} dt_{n-1} \cdots \int_{t_0}^{t_2} dt_1 \\ &\quad \times \text{Tr}\{O(t)[V(t_n), [V(t_{n-1}), \cdots [V(t_1), \rho_0] \cdots]]\} \end{aligned} \quad (2.51)$$

$$\begin{aligned} &= \left(\frac{i}{\hbar}\right)^n \int_{-\infty}^t dt_n \int_{-\infty}^{t_n} dt_{n-1} \cdots \int_{-\infty}^{t_2} dt_1 E(t_n)E(t_{n-1}) \cdots E(t_1) \\ &\quad \times \text{Tr}\{O(t)[\mu(t_n), [\mu(t_{n-1}), \cdots [\mu(t_1), \rho_0] \cdots]]\}, \end{aligned} \quad (2.52)$$

where in the last line we have also sent $t_0 \rightarrow -\infty$, taking ρ_0 to be the equilibrium density matrix. Next, the integration variables are changed from absolute interaction times t_n, t_{n-1}, \dots, t_1 to the time intervals between interactions $\tau_n = t - t_n, \tau_{n-1} = t_n - t_{n-1}, \dots, \tau_1 = t_2 - t_1$, yielding

$$\begin{aligned} O^{(n)}(t) &= \left(\frac{i}{\hbar}\right)^n \int_0^\infty d\tau_n \int_0^\infty d\tau_{n-1} \cdots \int_0^\infty d\tau_1 \\ &\quad \times E(t - \tau_n)E(t - \tau_n - \tau_{n-1}) \cdots E(t - \tau_n - \cdots - \tau_1) \\ &\quad \times \text{Tr}\{O(t)[\mu(t - \tau_n), [\mu(t - \tau_n - \tau_{n-1}), \cdots [\mu(t - \tau_n - \cdots - \tau_1), \rho_0] \cdots]]\}. \end{aligned} \quad (2.53)$$

The trace's invariance to cyclic permutation means we can arbitrarily shift the absolute origin of time inside the trace, e.g. for any set of operators A_1, \dots, A_n

$$\begin{aligned}
 \text{Tr}\{A_1(t)A_2(t)\cdots A_n(t)\} &= \text{Tr}\{\mathcal{U}_0(\tau)\mathcal{U}_0^\dagger(\tau)A_1(t)\mathcal{U}_0(\tau)\mathcal{U}_0^\dagger(\tau)A_2(t)\mathcal{U}_0(\tau)\cdots\mathcal{U}_0^\dagger(\tau)A_n(t)\} \\
 &= \text{Tr}\{\mathcal{U}_0^\dagger(\tau)A_1(t)\mathcal{U}_0(\tau)\mathcal{U}_0^\dagger(\tau)A_2(t)\mathcal{U}_0(\tau)\cdots\mathcal{U}_0^\dagger(\tau)A_n(t)\mathcal{U}_0(\tau)\} \\
 &= \text{Tr}\{A_1(t+\tau)A_2(t+\tau)\cdots A_n(t+\tau)\}, \tag{2.54}
 \end{aligned}$$

where $\mathcal{U}_0(\tau) = e^{-iH_0\tau/\hbar}$ is the free time-evolution operator. Applying such a transformation to Eq. 2.53, we set $t = \tau_n + \dots + \tau_1$, which removes the spurious t -dependence from inside the trace by referring the origin of time to the first light-matter interaction. The n^{th} -order response then appears in the following form,

$$\begin{aligned}
 O^{(n)}(t) &= \int_0^\infty d\tau_n \int_0^\infty d\tau_{n-1} \cdots \int_0^\infty d\tau_1 E(t - \tau_n)E(t - \tau_n - \tau_{n-1}) \cdots E(t - \tau_n - \dots - \tau_1) \\
 &\quad \times R^{(n)}(\tau_n, \tau_{n-1}, \dots, \tau_1), \tag{2.55a}
 \end{aligned}$$

where we have defined the n^{th} -order response function

$$\begin{aligned}
 &R^{(n)}(\tau_n, \tau_{n-1}, \dots, \tau_1) \\
 &= \left(\frac{i}{\hbar}\right)^n \theta(\tau_n) \cdots \theta(\tau_1) \text{Tr}\{O(\tau_n + \dots + \tau_1)[\mu(\tau_{n-1} + \dots + \tau_1), \dots [\mu(\tau_1), [\mu(0), \rho_0]] \cdots]\} \\
 &\tag{2.55b}
 \end{aligned}$$

$$\begin{aligned}
 &= \left(\frac{i}{\hbar}\right)^n \theta(\tau_n) \cdots \theta(\tau_1) \text{Tr}\{[[\cdots [O(\tau_n + \dots + \tau_1), \mu(\tau_{n-1} + \dots + \tau_1)] \cdots, \mu(\tau_1)], \mu(0)]\rho_0\}. \\
 &\tag{2.55c}
 \end{aligned}$$

These two alternate forms of the nested commutators inside the trace are related by repeated

application of the identity $[A, [B, C]] = [[A, B], C]$. Although the Heaviside step functions $\theta(\tau_i)$ are redundant in light of the integration bounds in Eq. 2.55a, their inclusion reminds us of the strict sequential time-ordering of the n light-matter interactions when working with $R^{(n)}$ in isolation.

2.3.3 Response functions for coherent vs. action spectroscopy

The response function framework can be used to calculate any system observable, and therefore can be adapted to describe experiments using various detection strategies. Here we will make a general comparison between coherent and action techniques from the formal perspective of their response functions. In coherent spectroscopy, the experimentally measured quantity is the electric field radiated from a material polarization induced by the incident laser fields. This signal field is an intense, classical electric field, for which the details of generation, propagation, and detection are described by the laws of classical electrodynamics independently of the molecular response. The object of interest is therefore the source polarization, which is usually expressed via the expectation value of the system dipole operator

$$P(t) = \langle \mu(t) \rangle. \tag{2.56}$$

This source polarization is really a macroscopic polarization density extended over the sample by many wavelengths of light, and the right-hand side of this expression should be understood as the density of microscopic dipole moments at a certain location averaged over a spatial region much smaller than this wavelength.

On the other hand, in action spectroscopy the experimental observable is assumed to be proportional to the population of a specific excited state or set of excited states. This

population is intrinsically a property of an individual molecule or particle, and does not depend on the spatial arrangement of the macroscopic sample. The system observable to be calculated is therefore a projection operator

$$N = |f\rangle\langle f| \tag{2.57}$$

where for simplicity we consider a single relevant excited state $|f\rangle$ which we will call the target state. In general, there could be multiple target states to consider, each of which might contribute to the resulting action signal with unequal weights. This case will be addressed briefly at the end of this section. Evaluating the expectation value of the projection operator is equivalent to calculating the density matrix element corresponding to the target population $\langle N \rangle = \text{Tr}\{N\rho\} = \rho_{ff}$.

The response function approach calculates the n^{th} -order contributions $P^{(n)}(t)$ and $N^{(n)}(t)$ via Eq. 2.55 with the observed system operator $O = \mu$ and $O = N$, respectively. Crucially, in the coherent case both the perturbation and the system observable involve the dipole operator, and the n^{th} -order response function is therefore made up of terms involving products of $n + 1$ dipole operators. This is not the case for action detection, where the n^{th} -order response function only contains products of n dipole operators. However, increasing the perturbative order to $n + 1$ for the action response function consequently reproduces these same number of dipole operators found in the n^{th} -order coherent response function. This association forms the mathematical basis for the correspondence between coherent and action-based nonlinear techniques. For spatial symmetry reasons that will be discussed below in Section 2.3.4, even-order contributions to the nonlinear polarization vanish in isotropic media like free solution, and therefore coherent spectroscopies that probe the bulk are odd-order techniques. As a result, the corresponding action versions are described by even order response functions,

which produces some formal distinctions worth mentioning.

For both coherent and action response functions, expanding the n nested commutators inside the trace in Eq. 2.55b produces 2^n total terms, called Liouville pathways. Because each commutator represents the choice of placing a dipole operator on the left-side (associated with a positive sign) or the right-side (negative sign) of the equilibrium density operator, every pathway carries an overall sign given by $(-1)^k$, where k is the number of right-side dipole interactions. Each pathway has a complex conjugate partner (not considering overall sign) formed by reversing the left/right choice for each of the n dipoles. In the coherent case, the final $(n+1)^{\text{th}}$ dipole operator at time $\tau_n + \dots + \tau_1$ is not considered as it is not associated with a commutator. Therefore there are effectively 2^{n-1} independent complex terms, which as shown below are formally multi-time dipole correlation functions.

To see how these terms play out, we examine the specific case of the 3rd-order coherent response and the corresponding 4th-order action response. Using Eq. 2.55b, the coherent 3rd-order response function is

$$\begin{aligned} R_C^{(3)}(\tau_3, \tau_2, \tau_1) &= \left(\frac{i}{\hbar}\right)^3 \theta(\tau_3)\theta(\tau_2)\theta(\tau_1) \text{Tr}\{\mu(\tau_3 + \tau_2 + \tau_1)[\mu(\tau_2 + \tau_1), [\mu(\tau_1), [\mu(0), \rho_0]]]\} \\ &= \left(\frac{i}{\hbar}\right)^3 \theta(\tau_3)\theta(\tau_2)\theta(\tau_1) \sum_{\alpha=1}^4 \left[R_\alpha(\tau_3, \tau_2, \tau_1) - R_\alpha^*(\tau_3, \tau_2, \tau_1) \right] \end{aligned} \quad (2.58)$$

where the $2^{3-1} = 4$ constituent correlation functions are

$$\begin{aligned} R_1 &= \text{Tr}\{\mu(\tau_3 + \tau_2 + \tau_1)\mu(0)\rho_0\mu(\tau_1)\mu(\tau_2 + \tau_1)\} \\ &= \langle \mu(\tau_1)\mu(\tau_2 + \tau_1)\mu(\tau_3 + \tau_2 + \tau_1)\mu(0) \rangle, \end{aligned} \quad (2.59a)$$

$$\begin{aligned} R_2 &= \text{Tr}\{\mu(\tau_3 + \tau_2 + \tau_1)\mu(\tau_1)\rho_0\mu(0)\mu(\tau_2 + \tau_1)\} \\ &= \langle \mu(0)\mu(\tau_2 + \tau_1)\mu(\tau_3 + \tau_2 + \tau_1)\mu(\tau_1) \rangle, \end{aligned} \quad (2.59b)$$

$$\begin{aligned}
 R_3 &= \text{Tr}\{\mu(\tau_3 + \tau_2 + \tau_1)\mu(\tau_2 + \tau_1)\rho_0\mu(0)\mu(\tau_1)\} \\
 &= \langle\mu(0)\mu(\tau_1)\mu(\tau_3 + \tau_2 + \tau_1)\mu(\tau_2 + \tau_1)\rangle,
 \end{aligned}
 \tag{2.59c}$$

$$\begin{aligned}
 R_4 &= \text{Tr}\{\mu(\tau_3 + \tau_2 + \tau_1)\mu(\tau_2 + \tau_1)\mu(\tau_1)\mu(0)\rho_0\} \\
 &= \langle\mu(\tau_3 + \tau_2 + \tau_1)\mu(\tau_2 + \tau_1)\mu(\tau_1)\mu(0)\rangle.
 \end{aligned}
 \tag{2.59d}$$

Here the bracket notation denotes an equilibrium average, i.e. for any operator A , $\langle A \rangle = \text{Tr}\{A\rho_0\}$, and going between the first and second version of each expression is accomplished by cyclically permuting the dipole operators so that ρ_0 is the final member of product. We note that taking the difference between complex conjugate terms in Eq. 2.58 results in the coherent 3rd-order response function begin given by the imaginary parts of its correlation functions.

Each pathway (i.e. a correlation function or its complex conjugate) can be given a diagrammatic shorthand in a number of well-established ways,^{48,111} and in Figure 2.6(a) we show a version that represents all the mathematical information present so far. We note that these diagrams do not yet include information about the incident fields, which will be incorporated later in Section 2.3.6 along with an expansion over system eigenstates to produce so-called double-sided Feynman diagrams and ladder diagrams. Here a pathway is represented by a double vertical line with time increasing in the upward direction. Each left (i.e. ket) side dipole interaction is represented by an black node and line on the left, while the right (i.e. bra) side interactions are red nodes and lines on the right. The time intervals τ_i between these interactions are indicated by the vertical spacing between successive nodes, and the time-ordering of the interactions is represented by the sequence in which they progress from bottom to top. The final dipole operator (of which the expectation value is begin taken) is shown in grey to distinguish it from the perturbation-theoretic light-matter

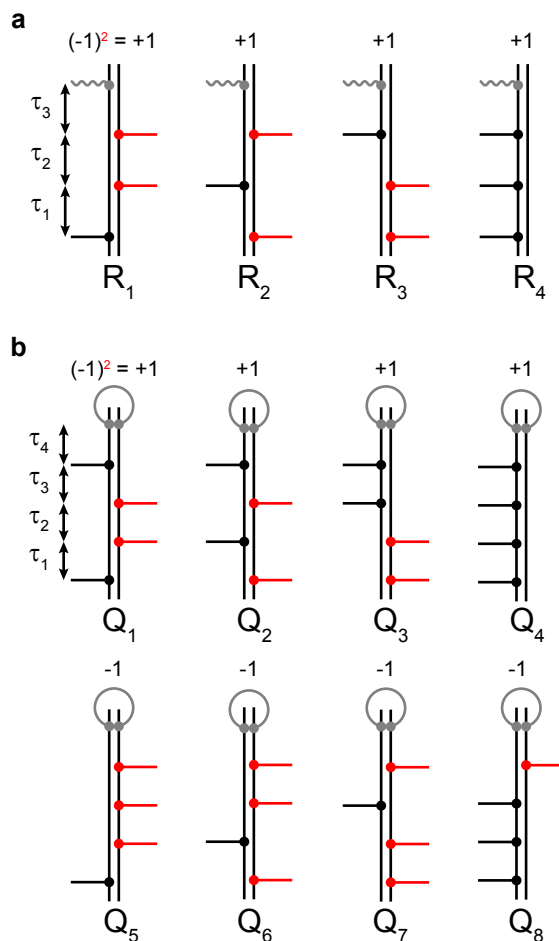


Figure 2.6: Diagrammatic representation of the constituent correlation functions making up (a) the coherent response function $R_C^{(3)}$ and (b) the action response function $R_A^{(4)}$. See text for details.

interactions. Due to the cyclic invariance of the trace, it could be placed on either side of the diagram without changing its mathematical meaning, but by convention it is placed on the left (ket) side. The overall sign of the pathway is indicated above each diagram. The diagram for a pathway's complex conjugate is found by reflecting the original diagram across the vertical, with the exception of the final grey node.

As mentioned above, the 3rd-order response function is proportional to the imaginary

parts of its constituent correlation functions. This is a general feature of the odd-order, while for even-order the response function is proportional to the real parts of its constituent correlation functions. This arises because for odd n the complex conjugate pairs of pathways have opposite signs, while for even n they have the same sign, producing purely imaginary or real results when summed, respectively. To see this, we note that if the overall sign of a pathway is $(-1)^k$ where k is the number of right-side interactions, then its conjugate's sign is

$$(-1)^{n-k} = (-1)^n / (-1)^k = \begin{cases} -(-1)^k & n \text{ odd} \\ (-1)^k & n \text{ even.} \end{cases} \quad (2.60)$$

The prefactor $(i/\hbar)^n$ is imaginary for odd n and real for even n , so the response function always works out to be purely real, as is required by Eq. 2.55a.

This distinction between odd and even order can be seen when comparing the results above for 3rd-order coherent response with the 4th-order action response function

$$\begin{aligned} R_A^{(4)}(\tau_4, \tau_3, \tau_2, \tau_1) &= \left(\frac{i}{\hbar}\right)^4 \theta(\tau_4)\theta(\tau_3)\theta(\tau_2)\theta(\tau_1) \\ &\times \text{Tr}\{N(\tau_4 + \tau_3 + \tau_2 + \tau_1)[\mu(\tau_3 + \tau_2 + \tau_1), [\mu(\tau_2 + \tau_1), [\mu(\tau_1), [\mu(0), \rho_0]]]]\} \\ &= \left(\frac{i}{\hbar}\right)^4 \theta(\tau_4)\theta(\tau_3)\theta(\tau_2)\theta(\tau_1) \sum_{\alpha=1}^8 [Q_\alpha(\tau_4, \tau_3, \tau_2, \tau_1) + Q_\alpha^*(\tau_4, \tau_3, \tau_2, \tau_1)] \end{aligned} \quad (2.61)$$

which has $2^{4-1} = 8$ constituent correlation functions

$$Q_1 = \text{Tr}\{N(\tau_4 + \tau_3 + \tau_2 + \tau_1)\mu(\tau_3 + \tau_2 + \tau_1)\mu(0)\rho_0\mu(\tau_1)\mu(\tau_2 + \tau_1)\}$$

$$= \langle \mu(\tau_1) \mu(\tau_2 + \tau_1) N(\tau_4 + \tau_3 + \tau_2 + \tau_1) \mu(\tau_3 + \tau_2 + \tau_1) \mu(0) \rangle \quad (2.62a)$$

$$\begin{aligned} Q_2 &= \text{Tr}\{N(\tau_4 + \tau_3 + \tau_2 + \tau_1) \mu(\tau_3 + \tau_2 + \tau_1) \mu(\tau_1) \rho_0 \mu(0) \mu(\tau_2 + \tau_1)\} \\ &= \langle \mu(0) \mu(\tau_2 + \tau_1) N(\tau_4 + \tau_3 + \tau_2 + \tau_1) \mu(\tau_3 + \tau_2 + \tau_1) \mu(\tau_1) \rangle \end{aligned} \quad (2.62b)$$

$$\begin{aligned} Q_3 &= \text{Tr}\{N(\tau_4 + \tau_3 + \tau_2 + \tau_1) \mu(\tau_3 + \tau_2 + \tau_1) \mu(\tau_2 + \tau_1) \rho_0 \mu(0) \mu(\tau_1)\} \\ &= \langle \mu(0) \mu(\tau_1) N(\tau_4 + \tau_3 + \tau_2 + \tau_1) \mu(\tau_3 + \tau_2 + \tau_1) \mu(\tau_2 + \tau_1) \rangle \end{aligned} \quad (2.62c)$$

$$\begin{aligned} Q_4 &= \text{Tr}\{N(\tau_4 + \tau_3 + \tau_2 + \tau_1) \mu(\tau_3 + \tau_2 + \tau_1) \mu(\tau_2 + \tau_1) \mu(\tau_1) \mu(0) \rho_0\} \\ &= \langle N(\tau_4 + \tau_3 + \tau_2 + \tau_1) \mu(\tau_3 + \tau_2 + \tau_1) \mu(\tau_2 + \tau_1) \mu(\tau_1) \mu(0) \rangle \end{aligned} \quad (2.62d)$$

$$\begin{aligned} Q_5 &= -\text{Tr}\{N(\tau_4 + \tau_3 + \tau_2 + \tau_1) \mu(0) \rho_0 \mu(\tau_1) \mu(\tau_2 + \tau_1) \mu(\tau_3 + \tau_2 + \tau_1)\} \\ &= -\langle \mu(\tau_1) \mu(\tau_2 + \tau_1) \mu(\tau_3 + \tau_2 + \tau_1) N(\tau_4 + \tau_3 + \tau_2 + \tau_1) \mu(0) \rangle \end{aligned} \quad (2.62e)$$

$$\begin{aligned} Q_6 &= -\text{Tr}\{N(\tau_4 + \tau_3 + \tau_2 + \tau_1) \mu(\tau_1) \rho_0 \mu(0) \mu(\tau_2 + \tau_1) \mu(\tau_3 + \tau_2 + \tau_1)\} \\ &= -\langle \mu(0) \mu(\tau_2 + \tau_1) \mu(\tau_3 + \tau_2 + \tau_1) N(\tau_4 + \tau_3 + \tau_2 + \tau_1) \mu(\tau_1) \rangle \end{aligned} \quad (2.62f)$$

$$\begin{aligned} Q_7 &= -\text{Tr}\{N(\tau_4 + \tau_3 + \tau_2 + \tau_1) \mu(\tau_2 + \tau_1) \rho_0 \mu(0) \mu(\tau_1) \mu(\tau_3 + \tau_2 + \tau_1)\} \\ &= -\langle \mu(0) \mu(\tau_1) \mu(\tau_3 + \tau_2 + \tau_1) N(\tau_4 + \tau_3 + \tau_2 + \tau_1) \mu(\tau_2 + \tau_1) \rangle \end{aligned} \quad (2.62g)$$

$$\begin{aligned} Q_8 &= -\text{Tr}\{N(\tau_4 + \tau_3 + \tau_2 + \tau_1) \mu(\tau_2 + \tau_1) \mu(\tau_1) \mu(0) \rho_0 \mu(\tau_3 + \tau_2 + \tau_1)\} \\ &= -\langle \mu(\tau_3 + \tau_2 + \tau_1) N(\tau_4 + \tau_3 + \tau_2 + \tau_1) \mu(\tau_2 + \tau_1) \mu(\tau_1) \mu(0) \rangle. \end{aligned} \quad (2.62h)$$

These are depicted in Figure 2.6(b) using analogous diagrammatic notation. The only important difference in the diagrams is that the action of the final projection operator N within the trace is represented by a loop connecting the left and right sides, indicating that a population is being computed, rather than a transition dipole connecting two different states. Another consequence of the conjugate pathway pairs having the same sign for even n is that the correlation functions cannot uniformly be defined to be positive, as is the case for

odd n in which the positively signed pathway of a conjugate pair is conventionally defined as the correlation function. For example, the ‘Four-wave mixing’ naming convention for the 3rd-order coherent correlation functions R_α used in Eq. 2.59 and Figure 2.6(a) is well established.^{48,112–115} However, the naming convention for 4th-order correlation functions Q_α is intrinsically more ambiguous, because it is no longer possible to choose the positively signed pathways as the correlation functions. In practice, multiple different schemes are used, e.g. by authors describing fluorescence-detected 2D electronic spectroscopy.^{93,116,117} Here, we have chosen a naming scheme designed to highlight the correspondence with $R_C^{(3)}$: Q_1 - Q_4 have the same first three interactions as R_1 - R_4 with a fourth interaction on the ket side, while Q_5 - Q_8 instead have the fourth interaction on the bra side.

The final remaining difference between the coherent and action response functions is in the interpretation and treatment of the final time argument denoting the delay between the last light-matter interaction and the evaluation of the system observable. In the 3rd-order coherent case, the radiation of the detected signal field is driven by the oscillation of the material polarization

$$\tilde{E}_{\text{sig}}(t) = i\tilde{P}^{(3)}(t) \quad (2.63)$$

where in this expression, a complex representation denoted by a tilde has been used to indicate a $\pi/2$ phase-shift. The time-dependence of the polarization is in turn determined by the response function and incident fields via the multiple convolution integrals

$$\begin{aligned} P^{(3)}(t) = & \int_0^\infty d\tau_3 \int_0^\infty d\tau_2 \int_0^\infty d\tau_1 R_C^{(3)}(\tau_3, \tau_2, \tau_1) \\ & \times E(t - \tau_3)E(t - \tau_3 - \tau_2)E(t - \tau_3 - \tau_2 - \tau_1), \end{aligned} \quad (2.64)$$

This process is depicted schematically in Figure 2.7(a) for the case where the three light-matter interactions occur with three short, well-separated pulses. We see that it is the coherent system evolution during τ_3 that produces the oscillating polarization.

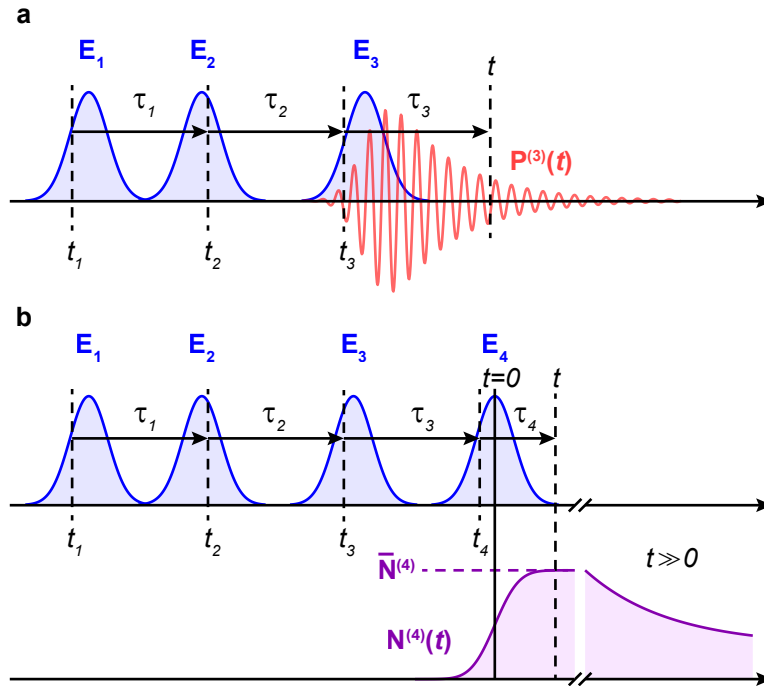


Figure 2.7: Generation of (a) the 3rd-order polarization and (b) the 4th-order population with generalized pulse sequences and relevant perturbation-theoretic time variables. The limiting final target population $\bar{N}^{(4)}$ after the action of the last pulse is indicated. Also shown is the eventual relaxation of the target population on a time-scale much longer than the pulse durations and time-delays.

In the 4th-order action case, an additional light-matter interaction promotes the system to the target excited population. If a fourth short pulse is used for this interaction, as depicted in Figure 2.7(b), the same coherent evolution in τ_3 can be encoded in the time-delay between pulses 3 and 4. This is the strategy adopted by essentially all action-detected 2D spectroscopy techniques. However, formally we still have the last time interval τ_4 to deal with. Specifically, the structure of the response function framework is set up to calculate

$N^{(4)}$ at any time t , i.e.

$$\begin{aligned}
 N^{(4)}(t) = & \int_0^\infty d\tau_4 \int_0^\infty d\tau_3 \int_0^\infty d\tau_2 \int_0^\infty d\tau_1 R_A^{(4)}(\tau_4, \tau_3, \tau_2, \tau_1) \\
 & \times E(t - \tau_4)E(t - \tau_4 - \tau_3 - \tau_2)E(t - \tau_4 - \tau_3 - \tau_2)E(t - \tau_4 - \tau_3 - \tau_2 - \tau_1).
 \end{aligned}
 \tag{2.65}$$

The time-dependence of the target population is characterized by relaxation under the free system plus bath Hamiltonian, and is in principle described by the τ_4 -dependence of $R_A^{(4)}$. While this relaxation is important—in fact critically so, as it is a consequence of the very process giving rise to the action signal being detected—it is in general difficult to describe microscopically, and more importantly its details usually do not directly influence the experimental observable. As discussed in Section 2.3.1, here is where the motivating principle of action spectroscopy comes into play. We will simply use the initial population of the target state created by the excitation fields as a proxy for whatever kind of experimental signal is eventually recorded. In practice, this means we wish to calculate the value of $N^{(4)}$ “right after” the last light-matter interaction. In the impulsive limit where the electric fields envelopes are much shorter than any system dynamics and $N^{(4)}$ is directly proportional to the response function, this is simply accomplished by setting $\tau_4 = 0$. However, when using arbitrary finite duration pulses a different approach is necessary to make this procedure mathematically sound.

Our approach is to assume that the relaxation timescale of the target state is much longer than the pulse durations (e.g. as in Figure 2.7(b)), and then calculate the limiting “final” population created after the last pulse has finished interacting, i.e. $\bar{N}^{(4)} \equiv N^{(4)}(t \gg \tau_p)$, where $t = 0$ is set at the center of the last pulse and τ_p is the pulse duration (Figure 2.7(b)). Taking this limit is most convenient in terms of the absolute time of the last interaction

$$t_4 = t - \tau_4,$$

$$\begin{aligned} N^{(4)}(t) &= \int_{-\infty}^t dt_4 \int_0^\infty d\tau_3 \int_0^\infty d\tau_2 \int_0^\infty d\tau_1 R_A^{(4)}(t - t_4, \tau_3, \tau_2, \tau_1) \\ &\quad \times E(t_4)E(t_4 - \tau_3)E(t_4 - \tau_3 - \tau_2)E(t_4 - \tau_3 - \tau_2 - \tau_1). \end{aligned} \quad (2.66)$$

This assumption lets us make two approximations. First, because the target population's relaxation is slow, N is approximately a constant of the motion under free evolution so that $N(\tau_4 + \tau_3 + \tau_2 + \tau_1) = N$ in Eq. 2.61. Second, the upper integration limit of the t_4 integral can be safely extended to $t \rightarrow \infty$, as the product of the four electric fields will be essentially zero for these t_4 values. This also takes care of causality, so the step function $\theta(t - t_4)$ can be dropped from the response function. The result is

$$\begin{aligned} \bar{N}^{(4)} &= \lim_{t \rightarrow \infty} N^{(4)}(t) = \int_{-\infty}^\infty dt_4 \int_0^\infty d\tau_3 \int_0^\infty d\tau_2 \int_0^\infty d\tau_1 R_{A,\text{eff}}^{(4)}(\tau_3, \tau_2, \tau_1) \\ &\quad \times E(t_4)E(t_4 - \tau_3)E(t_4 - \tau_3 - \tau_2)E(t_4 - \tau_3 - \tau_2 - \tau_1). \end{aligned} \quad (2.67)$$

with

$$\begin{aligned} R_{A,\text{eff}}^{(4)}(\tau_3, \tau_2, \tau_1) &= \left(\frac{i}{\hbar}\right)^4 \theta(\tau_3)\theta(\tau_2)\theta(\tau_1) \text{Tr}\{N[\mu(\tau_3 + \tau_2 + \tau_1), [\mu(\tau_2 + \tau_1), [\mu(\tau_1), [\mu(0), \rho_0]]]]]\}. \end{aligned} \quad (2.68)$$

This effective action response function does not depend on τ_4 , and only on the time intervals between the four successive light-matter interactions. The corresponding correlation functions are likewise given by Eq. 2.62 with the time dependence of N removed. The resulting action signal intensity can then be taken to be simply proportional to $\bar{N}^{(4)}$.

For fluorescence detection, the proportionality factor is the quantum yield ϕ which arises from the relaxation dynamics of N , e.g. via the phenomenological treatment in Section 2.3. Specifically, accounting for the repetition-rate of the experiment r and overall detection efficiency of a fluorescence photon η , the fluorescence count rate from the sample is

$$F = r\eta\phi\bar{N}^{(4)}. \quad (2.69)$$

In the case of multiple target states, more complicated relaxation dynamics like fast equilibration between excited levels can occur. However, in terms of the detected signal, the effect of these dynamics can be described through a set of different quantum yields specific to the various target states.^{93,117,118} These can then be included directly in the projection operator to give an effective ‘action observable’

$$A = \sum_f \phi_f |f\rangle\langle f|, \quad (2.70)$$

which can be used in place of N in Eq. 2.68. This approach has been especially important in modelling fluorescence-detected 2D spectroscopy signals from multi-chromophoric systems, where processes like exciton annihilation control the yield from different excited states and thus play a crucial role in re-weighting different excitation pathways.^{94,119} However, for the FEIR experiments performed and analyzed in this thesis, we will assume a single target state can be used to account for the emission process.

2.3.4 Odd vs even in coherent vs action: Consequences of inversion symmetry

The previous discussion laid out some of the differences in the structure of nonlinear response functions at odd and even perturbative orders (specifically, 3rd and 4th-order, respectively), which was motivated by the fact that only the odd-order coherent response can contribute in media with inversion symmetry, also called centrosymmetry. As the corresponding action response occurs at even order, does this same symmetry argument preclude its existence in isotropic solution, where ensemble-averaged quantities necessarily have inversion symmetry? Clearly the answer is no, as demonstrated by the success and general acceptance of 4th-order theories of action-based 2D spectroscopy applied to isotropic systems. The explanation is related to the fact that action response functions calculate system populations that, unlike the material polarization, do not need to transform spatially with the coordinate system chosen for the problem. However, this does not mean that nonlinear action response functions are immune to the spatial symmetry properties of the system. On the contrary, inversion symmetry in fact dictates that it is the *odd-order* contributions to the action response that vanish in centrosymmetric media.

To discuss these points, here we examine the constraints imposed on nonlinear response functions by inversion symmetry from a more rigorous standpoint. The following is based on an argument laid out by Ippen for the nonlinear susceptibility,¹²⁰ and can also be found in the text by Butcher and Cotter.¹²¹ As a spatial symmetry property that has to do with how the system ‘looks the same’ in opposing directions, inversion symmetry must be analyzed with the vector nature of the system dipole moment and electric fields explicitly included.

Updating Eq. 2.47, the light-matter interaction is

$$V(t) = -\boldsymbol{\mu} \cdot \mathbf{E}(t) \quad (2.71)$$

where bold-face notation denotes a Cartesian vector. By Eq. 2.56, the n^{th} -order material polarization $\mathbf{P}^{(n)}$ is also a vector, and the n^{th} -order coherent response function $\mathbf{R}_C^{(n)}$ that relates $\mathbf{P}^{(n)}$ to the n incident fields is therefore a Cartesian tensor of rank $n + 1$. Suppressing the time-dependence and multiple time convolution integrals, the vector components of $\mathbf{P}^{(n)}$ are expressed as

$$P_i^{(n)} = \sum_{j \cdots s} R_{C,ij \cdots s}^{(n)} E_j \cdots E_s, \quad (2.72)$$

where each of the indices i, j, \dots, s runs over the three lab-frame Cartesian components X, Y, Z . The particular choice of lab-frame coordinates used to describe the system is arbitrary, and any new coordinate system formed by an orthogonal transformation, i.e. one that merely rotates or reflects the coordinate system, is in principle equally good. Such a coordinate change may be effected by a transformation matrix \mathbf{T} with the orthogonality property

$$T_{ij} = T_{ji} = (T^{-1})_{ij}. \quad (2.73)$$

Applying such a transformation to the polarization and fields expresses them in the new coordinate system denoted by primed indices and components

$$P_{i'}^{(n)'} = \sum_i T_{i'i} P_i^{(n)} \quad (2.74a)$$

$$E_{j'} = \sum_j T_{j'j} E_j. \quad (2.74b)$$

The orthogonality condition 2.73 means the inverse transformation back to the original coordinates is also given by the same transformation matrix

$$P_i^{(n)} = \sum_{i'} T_{i'i} P_{i'}^{(n)'} \quad (2.75a)$$

$$E_j = \sum_{j'} T_{j'j} E_{j'}. \quad (2.75b)$$

Plugging Eqs. 2.75 into Eq. 2.72 yields

$$P_{i'}^{(n)'} = \sum_{j' \dots s'} R_{C, i' j' \dots s'}^{(n)'} E_{j'} \dots E_{s'}, \quad (2.76)$$

where

$$R_{C, i' j' \dots s'}^{(n)'} = \sum_{ij \dots s} T_{i'i} T_{j'j} \dots T_{s's} R_{C, ij \dots s}^{(n)} \quad (2.77)$$

are the components of the transformed tensorial response function. This equation simply demonstrates how the response function transforms, and is always true for any situation. The specific case of inversion is described by the following orthogonal transformation that

sends each coordinate to its negative

$$T_{ij} = (-1)\delta_{ij}, \quad (2.78)$$

where δ_{ij} is the Kronecker delta. When the material system has inversion symmetry, however, it and its relationship to the external fields must be *invariant* to this transformation, meaning the tensor components of the response function must remain unchanged even as the fields and polarization invert. Namely, applying Eq. 2.78 to Eq. 2.77, this constraint results in

$$R_{C,ij\dots s}^{(n)} = R_{C,i'j'\dots s'}^{(n)'} = (-1)^{(n+1)} R_{C,ij\dots s}^{(n)}. \quad (2.79)$$

For even n this relation is only satisfied when every element is identically zero, i.e. the even-order coherent response function vanishes for centrosymmetric media.

So what is different in the case of the action response? The target population is a scalar quantity, so the n^{th} -order action response function $\mathbf{R}_A^{(n)}$ that connects $N^{(n)}$ to the n incident fields is only a tensor of rank n . Using similar notation as before

$$N^{(n)} = \sum_{ij\dots r} R_{A,ij\dots r}^{(n)} E_i E_j \cdots E_r. \quad (2.80)$$

Repeating the same argument as above shows that the tensorial action response function transforms in exactly the same way, just with one less copy of the transformation matrix (n rather than $n + 1$)

$$R_{A,i'j'\dots r'}^{(n)'} = \sum_{ij\dots r} T_{i'i} T_{j'j} \cdots T_{r'r} R_{A,ij\dots r}^{(n)}. \quad (2.81)$$

Therefore, for a medium with inversion symmetry, the components must satisfy

$$R_{A,ij\dots r}^{(n)} = R_{A,i'j'\dots r'}^{(n)'} = (-1)^n R_{A,ij\dots r}^{(n)}, \quad (2.82)$$

that is, the odd-order action response function vanishes!

The lesson of this analysis is that the tensorial properties of the material system's response functions must encode its spatial symmetries. The switching of the even-odd inversion symmetry rule between nonlinear coherent and action spectroscopies is due to their respective dependence on $n + 1$ and n dipole operators, which makes their corresponding n^{th} -order response functions tensors of rank $n + 1$ and n , respectively. In fact, given the correspondence of microscopic information content between n^{th} -order coherent and $(n + 1)^{\text{th}}$ -order action response functions, this switching should appear rather unremarkable. Namely, in order to encode similar information, the n^{th} -order coherent and $(n + 1)^{\text{th}}$ -order action response functions had better vanish together if required by the symmetry of the system. We note that the tensorial properties of the response functions analyzed here are specific to the dipole-approximation, and higher multipolar light-matter interactions will result in different symmetry considerations.¹²¹

It is worth making some comments on how action techniques fit into the convention of classifying nonlinear spectroscopies based on the order of nonlinear susceptibility that they 'belong' to. The nonlinear susceptibility $\chi^{(n)}$ is the frequency-domain analogue of the coherent response function, and relates frequency components of the nonlinear polarization to those of the driving electric fields.^{48,121} Because the susceptibility is fundamentally associated with the material polarization, the statement that a given action-detected experiment "is $\chi^{(n)}$ " is therefore not especially meaningful. However, along the lines of the correspondence between n^{th} -order coherent and $(n + 1)^{\text{th}}$ -order action response functions analyzed in this

chapter, the most preferable statement would be that an n^{th} -order action experiment is $\chi^{(n-1)}$. Some authors have used the term $\chi^{(3+1)}$ when describing 4th-order fluorescence-detected 2D electronic spectroscopy to emphasize the correspondences and differences with coherent 3rd-order 2D electronic spectroscopy.¹²² The perspective advocated in this thesis, however, is that it would be more correct (and useful) to say that such a 4th-order action experiment, of which FEIR spectroscopy is an example, is a $\chi^{(3)}$ technique.

2.3.5 Material pathways in the action response function

Progressing further with calculating the spectroscopic response for a given experiment requires knowledge of the material system’s internal Hamiltonian including its interaction with its environment, and is usually accomplished by expanding over a set of spectroscopically relevant eigenstates. Here we return to the 4th-order action response function $\mathbf{R}_A^{(4)}$, specifically the ‘effective’ version where the target state’s population dynamics are not included (Eq. 2.68). Overall, with the exception of the final projection onto the target state, the 4-point dipole correlation functions that make up $\mathbf{R}_A^{(4)}$ are common to the 3rd-order coherent response, and the same strategies and methods can be used to evaluate them. The aim of this section is to develop analogous expressions and notation for $\mathbf{R}^{(4)}$ (we will henceforth drop the subscript A) and discuss how the desired signals arise from the system’s response. These expressions will form the basis for describing FEIR experiments in Section 2.4.

Expanding over system eigenstates first requires making a distinction between system and bath by partitioning the material Hamiltonian as

$$H_0 = H_S + H_B + H_{SB}. \quad (2.83)$$

Here, H_S is the system Hamiltonian describing the spectroscopically accessible coordinates (e.g. the multimode vibronic Hamiltonian discussed in Section 2.2), H_B describes the bath which is assumed not to interact with the incident fields, and H_{SB} describes the system-bath interaction. To illustrate this process, we develop expressions for the correlation function Q_1 in Eq. 2.62, which as we will see in Section 2.4 plays an important role in FEIR spectroscopy. Indexing the system eigenstates independently by each a, b, c , and d , the correlation function is expanded as follows,

$$\mathbf{Q}_1(\tau_3, \tau_2, \tau_1) = \sum_{a,b,c,d} \delta_{fc} \boldsymbol{\mu}_{dc} \boldsymbol{\mu}_{cb} \boldsymbol{\mu}_{ad} \boldsymbol{\mu}_{ba} P(a) \left\langle \mathcal{G}_{cd}(\tau_3) \mathcal{G}_{bd}(\tau_2) \mathcal{G}_{ba}(\tau_1) \right\rangle_B. \quad (2.84)$$

Here $P(a) = \langle a | \rho_0 | a \rangle$ is the equilibrium population of the initial state $|a\rangle$, $\mathcal{G}_{ij}(t)$ is the Liouville-space propagator for the ij system density matrix element, and the average $\langle \dots \rangle_B$ denotes a trace over the equilibrium bath degrees of freedom. Explicitly, the propagator is defined by its action on any bath operator A as $\mathcal{G}_{ij}(t)A = \exp(-iH_i t/\hbar)A \exp(iH_j t/\hbar)$, where $H_i = \langle i | H_0 | i \rangle$ is the bath and system-bath coupling Hamiltonian associated with the system eigenstate $|i\rangle$. Specifically, H_i is a matrix element with respect to the system sub-space, but an operator over the bath sub-space.¹²³ The transition dipole moment $\boldsymbol{\mu}_{ij} = \langle i | \boldsymbol{\mu} | j \rangle$ connecting systems states $|i\rangle$ and $|j\rangle$, is assumed to be independent of the bath coordinates. The Kroenecker delta δ_{fi} is the effect of the projection operator N : the final state $|i\rangle$ must be the target state $|f\rangle$, or belong to the target subsystem if there are multiple target states.

Each of the 8 correlation functions and their complex conjugates can be represented on the Liouville-space coupling diagram in Figure 2.8.^{48,124} Each node corresponds to the propagator of a specific system density matrix element according to Eq. 2.62, and evolves for the time interval the separates successive nodes. The segments connecting nodes represent the dipole

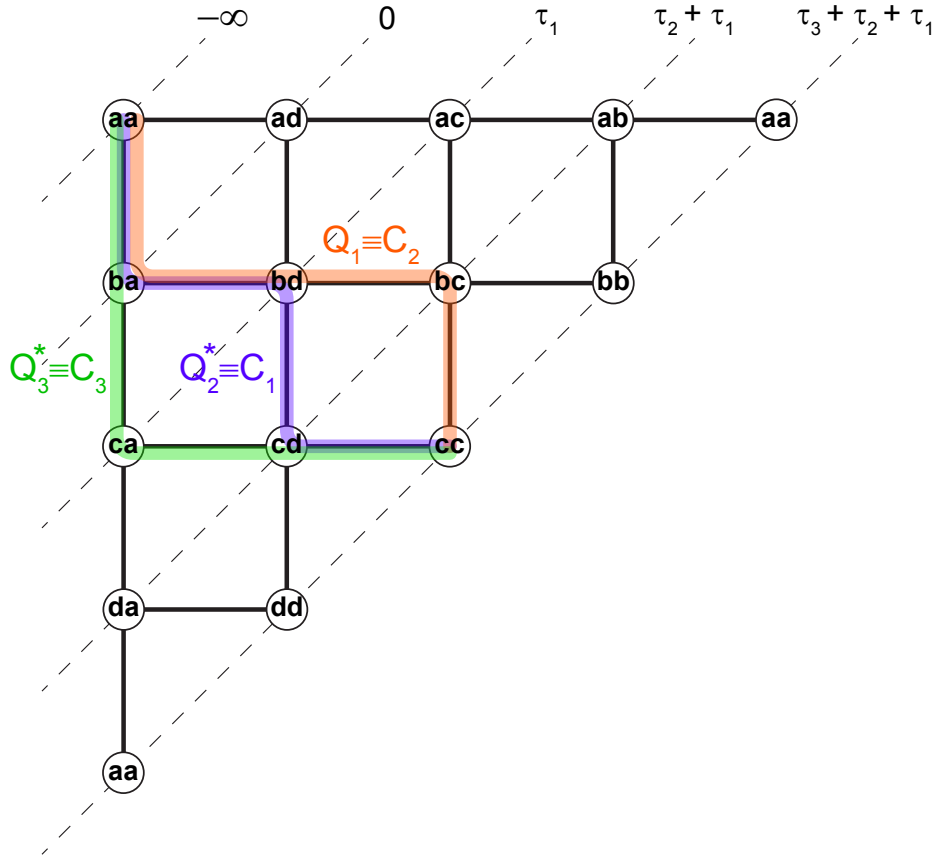


Figure 2.8: Liouville space coupling diagram illustrating all 4th-order pathways ending in a population. The three pathways Q_1 , Q_2^* , and Q_3^* are overlaid, which are respectively the correlation functions C_2 , C_1 , and C_3 relevant for FEIR spectroscopy, as discussed in Section 2.4. Their complex conjugates can be found by reflection across the diagonal perpendicular to the dashed lines indicating the interaction times.

interactions, with left-side interactions that change the ket state going down, and right-side interactions that change the bra state going to the right. As we can see, the requirement of ending in a population after four interactions has fixed the number of independent eigenstate indices that label the nodes at four (a, b, c, d) , just as in the coherent 3rd-order response. The pathway Q_1 as well as two others that are relevant in FEIR spectroscopy are outlined.

The homogeneous limit

In the homogeneous limit where the bath dynamics are sufficiently fast to decorrelate on the shortest system timescales, the bath averages of the propagators factorize,¹¹³ for example in \mathbf{Q}_1

$$\left\langle \mathcal{G}_{cd}(\tau_3) \mathcal{G}_{bd}(\tau_2) \mathcal{G}_{ba}(\tau_1) \right\rangle_B = \left\langle \mathcal{G}_{cd}(\tau_3) \right\rangle_B \left\langle \mathcal{G}_{bd}(\tau_2) \right\rangle_B \left\langle \mathcal{G}_{ba}(\tau_1) \right\rangle_B. \quad (2.85)$$

We can then use phenomenological models for the propagators $G_{ab}(t) \equiv \langle \mathcal{G}_{ba}(t) \rangle_B$ independently in each evolution period, e.g. in the so-called optical Bloch model^{48,125}

$$G_{ba}(t) = \theta(t) \exp(-i\omega_{ba}t - \Gamma_{ba}t). \quad (2.86)$$

Here, $\omega_{ba} = (E_b - E_a)/\hbar$ is a system eigenfrequency, and Γ_{ba} is a population relaxation rate for $a = b$ and the dephasing rate for $a \neq b$. This overall dephasing rate is related to the population relaxation via

$$\Gamma_{ba} = \Gamma_{ab} = \frac{1}{2}(\Gamma_{bb} + \Gamma_{aa}) + \hat{\Gamma}_{ba}, \quad (2.87)$$

where $\hat{\Gamma}_{ba}$ is the pure dephasing rate. For a single transition, the inverse of the overall dephasing rate is often referred to as the T_2 time, the inverse population relaxation rate is called the T_1 time, and the inverse pure dephasing rate is termed T_2^* .^{126–128}

The homogeneous limit breaks down when the timescale of bath-induced fluctuations in the system energy levels are intermediate or slower than the time-resolution of the experiment, nominally given by the pulse durations. This situation is, in fact, typically the norm in femtosecond vibrational and electronic spectroscopies in the condensed phase. Indeed, much

of the power of these methods, exemplified by the various flavors of 3rd-order and higher multidimensional techniques, derives from the sensitivity of the multi-time correlation functions to persistent heterogeneity which prevents their factorization. This general case can be approached by pulling out the contribution oscillating at the system eigenfrequencies and treating the remainder as a dephasing function $F_\alpha^{a,b,c,d}(\tau_3, \tau_2, \tau_1)$ for $\alpha = 1, \dots, 8$, which does not factorize into terms depending on single time intervals, e.g. for the average in Eq. 2.85

$$\left\langle \mathcal{G}_{cd}(\tau_3) \mathcal{G}_{bd}(\tau_2) \mathcal{G}_{ba}(\tau_1) \right\rangle_B = \exp(-i\omega_{cd}\tau_3 - i\omega_{bd}\tau_2 - i\omega_{ba}\tau_1) F_1^{a,b,c,d}(\tau_3, \tau_2, \tau_1). \quad (2.88)$$

Analytic expressions for the dephasing functions can be derived for some models of the bath and its interaction with the system, notably the multimode Brownian oscillator model.^{48,123} However, the aim of this thesis is to illustrate the basic spectroscopic features of FEIR experiments, and we will largely adopt the homogeneous limit to simplify the expressions and their calculation.

Separation of vibronic and orientational contributions

The vectorial transition dipole moment connecting system eigenstates $|a\rangle$ and $|b\rangle$ can be written as

$$\langle b | \boldsymbol{\mu} | a \rangle = \mu_{ba} \hat{\boldsymbol{\mu}}_{ba}, \quad (2.89)$$

where $\hat{\boldsymbol{\mu}}_{ba}$ is the unit vector along the direction of the transition dipole and μ_{ba} its magnitude. Given that the system wavefunctions can in general be complex-valued, the transition dipole matrix elements can also be complex quantities. However, it can be shown that if the system Hamiltonian H_S is time-reversal symmetric, its eigenfunctions can always be chosen to be

real, ensuring that the dipole matrix elements in the energy eigenbasis are also real.^{108,129} It is worth noting that Eq. 2.89 has some redundancy if the magnitude of the scalar part is allowed to be positive or negative, as a change in sign in μ_{ba} has the same effect as inverting the unit vector $\hat{\boldsymbol{\mu}}_{ba}$. We will allow for this redundancy, as it is convenient to describe the magnitude of Franck-Condon vibronic transitions through the scalar factor, which as we saw in Section 2.2 can be positively or negatively signed.

Assuming independence of the vibronic and rotational degrees of freedom, i.e.

$$H_S = H_{\text{vibr}} + H_{\text{rot}}, \quad (2.90)$$

the fourth-rank tensorial correlation functions can be separated into products of scalar pathways describing the vibronic dynamics, and fourth-rank tensors describing the orientational dynamics.¹³⁰ In components,

$$(Q_\alpha)_{IJKL}(\tau_3, \tau_2, \tau_1) = \sum_{a,b,c,d} (Y_\alpha)_{IJKL}^{a,b,c,d}(\tau_3, \tau_2, \tau_1) Q_\alpha^{a,b,c,d}(\tau_3, \tau_2, \tau_1), \quad (2.91)$$

where I, J, K , and L each refer to the lab-frame Cartesian coordinates X, Y, Z , and $\alpha = 1, \dots, 8$ indexes the 8 correlation functions. The orientational dynamics are conventionally treated classically, and the resulting orientational response functions will be addressed in Chapter 9. Therefore we will henceforth use H_S to refer specifically to the vibronic part of the system Hamiltonian. The scalar vibronic terms of \mathbf{Q}_1 expressed in the homogeneous limit are

$$Q_1^{a,b,c,d}(\tau_3, \tau_2, \tau_1) = \delta_{fc} \mu_{dc} \mu_{cb} \mu_{ad} \mu_{ba} P(a) \exp(-i\omega_{cd}\tau_3 - i\omega_{bd}\tau_2 - i\omega_{ba}\tau_1) \\ \times \exp(-\Gamma_{cd}\tau_3 - \Gamma_{bd}\tau_2 - \Gamma_{ba}\tau_1). \quad (2.92)$$

The corresponding orientational correlation function elements are

$$(Y_1)_{IJKL}^{a,b,c,d}(\tau_3, \tau_2, \tau_1) = \sum_{ijkl} \tilde{Y}_{IJKL}^{ijkl}(\tau_3, \tau_2, \tau_1) \left[\hat{\boldsymbol{\mu}}_{dc} \cdot \hat{i} \right] \left[\hat{\boldsymbol{\mu}}_{cb} \cdot \hat{j} \right] \left[\hat{\boldsymbol{\mu}}_{ad} \cdot \hat{k} \right] \left[\hat{\boldsymbol{\mu}}_{ba} \cdot \hat{l} \right] \quad (2.93)$$

where $\hat{i}, \hat{j}, \hat{k}$, and \hat{l} are the unit vectors along the Cartesian coordinates in the molecular frame and $\tilde{Y}_{IJKL}^{ijkl}(\tau_3, \tau_2, \tau_1)$ performs the orientational average to transform to the lab-frame, and will be discussed in Chapter 9.

2.3.6 Diagrammatic notation, the rotating wave approximation, and signal isolation strategies

So far we have developed expressions for the system response function, but have not examined the role of the driving electric fields. Time-domain nonlinear experiments use the characteristics of the pulse sequence to control the set of light-matter interactions encoded in the response function. Depending on the type of experiment, the various ‘controls knobs’ of the pulse sequence available to the experimenter could include inter-pulse delays and ordering, field frequency and resonance, propagation wavevector, or field phase. Two well-established systems of diagrammatic notation, known as double-sided Feynman (DSF) diagrams and ladder diagrams, respectively, are employed to indicate how these field characteristics are imprinted in the spectroscopic response.^{48,50,111,131,132} Here we give a brief overview of these notations, and how their usage is specified to action spectroscopy.

DSF diagrams build off of the diagrammatic notation for the correlation functions introduced earlier in Section 2.3.3, while ladder diagrams explicitly show the system’s energy level structure. Both types of diagram explicitly indicate the sequence of system eigenstates that a given pathway from the response function progresses through, as well as information

on the electric field that drives each transition. Specifically, the total electric field which appears in the convolution integrals (e.g. in Eq. 2.67), is given by the sum of individual pulse electric fields E_j

$$E(t, \mathbf{r}) = \sum_j E_j(t - T_j, \mathbf{r}), \quad (2.94)$$

where T_j is the arrival time of the j -th pulse, \mathbf{r} is position in the sample, and we have ignored the fields' vectorial character. These fields are real-valued, as is the overall response function. However, an exceptionally useful simplification that captures the effect of resonance, known as the rotating wave approximation (RWA), comes about from breaking the fields into their complex positive and negative frequency components. Explicitly, each field is expressed as

$$E_j(t, \mathbf{r}) = E_j^+(t, \mathbf{r}) + E_j^-(t, \mathbf{r}) \quad (2.95a)$$

$$E_j^+(t, \mathbf{r}) = \frac{1}{2}e_j(t) \exp(-i\omega_j t + i\mathbf{k}_j \cdot \mathbf{r} + i\phi_j) \quad (2.95b)$$

$$E_j^-(t, \mathbf{r}) = (E_j^+(t, \mathbf{r}))^*. \quad (2.95c)$$

The positive frequency complex component E_j^+ is formally the complex analytic representation of the field,¹³³ and more about this decomposition will be said in Chapter 3. The utility of this representation arises from the separation of the pulse's field into a slowly-varying envelope $e_j(t)$ and a phase factor $\exp(-i\omega_j t + i\mathbf{k}_j \cdot \mathbf{r} + i\phi_j)$ that depends on the carrier frequency ω_j , wavevector \mathbf{k}_j , and possibly an additional constant phase ϕ_j . For simplicity, this expression assumes that each pulse propagates spatially as a plane wave.^{121,134}

Within the convolution integrals, all possible permutations of products between these positive and negative field components and the complex material pathways making up the

response function are present. The RWA amounts to only selecting those products in which the integration variable-dependent phase factors from the fields approximately cancel out with (i.e. are RWA conjugate to) those in the material pathways.^{48,135} Doing so results in an integrand which varies slowly and therefore survives the convolution integrals. This cancellation is only possible on resonance, i.e. when the field's carrier frequency is similar in magnitude to the transition energy gap. An explicit example of this cancellation can be found in Section 3.2 of Chapter 3, where we see the RWA in action when evaluating the convolution integrals.

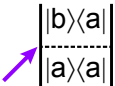
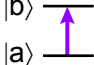
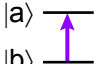
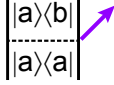
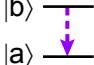
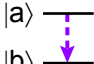
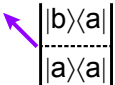
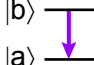
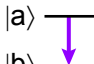
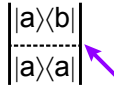
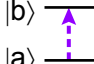
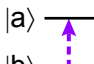
Complex field factor	Double-sided Feynman diagram	Ladder diagram	Role under RWA
$E_j^+ \sim e^{-i\omega_j t} e^{+i\mathbf{k}_j \cdot \mathbf{r}} e^{+i\phi_j}$	Ket-side 	$\omega_{ba} > 0$ 	absorption
		$\omega_{ba} < 0$ 	not allowed
	Bra-side 	$\omega_{ba} > 0$ 	not allowed
		$\omega_{ba} < 0$ 	emission
$E_j^- \sim e^{+i\omega_j t} e^{-i\mathbf{k}_j \cdot \mathbf{r}} e^{-i\phi_j}$	Ket-side 	$\omega_{ba} > 0$ 	not allowed
		$\omega_{ba} < 0$ 	emission
	Bra-side 	$\omega_{ba} > 0$ 	absorption
		$\omega_{ba} < 0$ 	not allowed

Figure 2.9: Rules for pairing a complex field phase factor to a transition in a material pathway for DSF and ladder diagrams. All possible combinations of E_j^+ vs. E_j^- , ket-side vs. bra-side, and upward ($\omega_{ba} > 0$) vs. downward ($\omega_{ba} < 0$) are shown, and their resulting roles within the RWA are indicated.

DSF and ladder diagrams explicitly incorporate the RWA in a visually intuitive way, which allows for straightforward book-keeping of the relevant terms. Figure 2.9 provides a legend for how each field interaction is incorporated into both types of diagram, while Figure 2.10 shows examples of two different pathways contributing to the 4th-order action response in both styles. DSF diagrams are ‘filled-in’ versions of the correlation function diagrams in Section 2.3.3, where time progresses upwards, the system density matrix elements before and after each light-matter interaction are indicated, and the intervening evolution periods correspond to the propagators $\mathcal{G}_{ij}(\tau_k)$. An interaction driven by E_j^+ (E_j^-) is denoted by a right (left) pointing arrow. The net result is that the field’s temporal phase evolution is RWA conjugate to that in the material pathway for an inward pointing arrow (E_j^+ on the ket-side or E_j^- on the bra-side) when the pathway transitions upwards in energy ($\omega_{ba} = (E_b - E_a)/\hbar > 0$ in Figure 2.9), or for an outward pointing arrow (E_j^+ on the bra-side or E_j^- on the ket-side) for a downward transition ($\omega_{ba} < 0$).

This state of affairs naturally suggests the terminology that an upward transition driven by an inward pointing arrow is absorption, while a downward transition driven by the outward arrow is stimulated emission. While this nomenclature is useful, it is important to note that we are not actually keeping track of the system’s or field’s energy after each interaction, so these terms cannot be taken too literally. Indeed, individual diagrams do not describe the actual time-evolving state of the system during the pulse sequence, nor do they correspond to real physical processes. In this context, the labels absorption and emission should be thought of as direct consequences of the RWA and reflect the resonant nature of the light-matter interactions. It is instructive to consider the field/pathway combinations that do not survive the RWA, e.g. involving a downward transition with an inward pointing arrow or the other disallowed cases shown in Figure 2.9. In these cases, the diagram ‘looks wrong’,

which works well as a visual guide to screen them out in a calculation within the RWA.

Ladder diagrams encode the same information, and have the advantage of simultaneously displaying the system's energy-level structure. In a ladder diagram, time progresses from left to right, and ket- or bra-side interactions are represented by solid or dashed arrows, respectively. The upward or downward direction of the arrow corresponds to the inward or outward direction of the corresponding arrow in a DSF diagram, i.e. not directly to E_j^+ vs. E_j^- , which could be considered a disadvantage. Another disadvantage of ladder diagrams is that the propagators for the evolution periods between interactions are less evident than in the DSF representation.

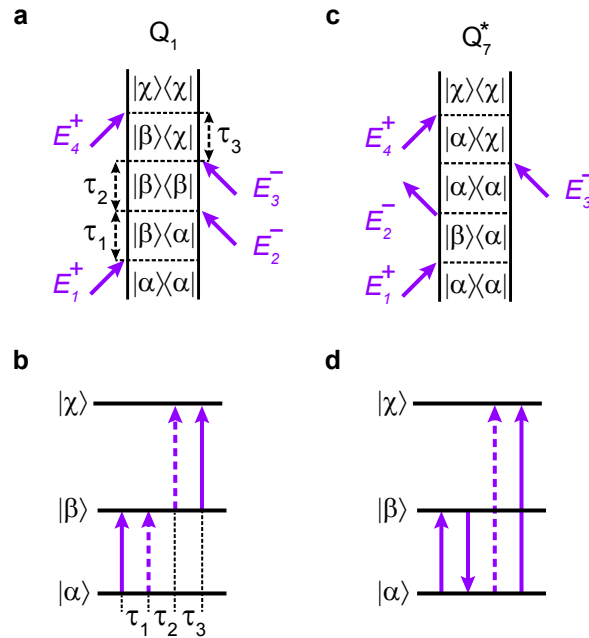


Figure 2.10: Comparison of DSF and ladder diagrams for two example pathways contributing to a three-level system's 4th-order action response. (a) and (b) are equivalent DSF and ladder diagrams, respectively, for an excited-state pathway belonging to Q_1 , while (c) and (d) represent a ground-state bleach pathway in Q_7^* .

Figure 2.10 compares both types of diagrams for two example pathways contributing

to the 4th-order action response of a three-level system with eigenstate energies ordered as $E_\alpha < E_\beta < E_\chi$, and in which $|\chi\rangle$ is the target state. The pathway shown in panels (a) and (b) belongs to Q_1 and can be labelled as an excited-state absorption pathway progressing through the intermediate state $|\beta\rangle$. All four interactions are absorptive, and the pathway has rephasing character, meaning the sign of the pathway's phase evolution in τ_1 is opposite that in τ_3 . As we will discuss in Section 2.4, this pathway is relevant to FEIR spectroscopy, where it is one of a set of pathways that represent the sequential excitation of the vibration followed by the encoding transition. Figures 2.10(c) and (d) show a pathway belonging to Q_7^* . Notably, the sequence of RWA-conjugate field factors E_j^\pm are the same as in panels (a) and (b), however the second transition is emissive, and the resulting diagram represents a ground-state bleach. This type of pathway will not contribute to the FEIR signal under typical resonance conditions. Both pathways end in the target population $|\chi\rangle\langle\chi|$, as required in order to contribute to the action response.

In both styles of diagram, we have only shown the four perturbation-theoretic light-matter interactions leading to the population of the target state, as this is formally the full extent of what is being calculated. However, it is common practice for DSF diagrams in action spectroscopy (particularly fluorescence-detected techniques) to additionally include a final pair of squiggly arrows emanating from both sides of the diagram,^{94,136,137} or alternatively a horizontal arrow above the top to indicate the 'signal emission'.^{93,138} One reason for doing this is to highlight the correspondence to diagrams for 3rd-order coherent spectroscopy in which the trace against the final dipole operator is depicted as an outgoing squiggly arrow (i.e. as in Figure 2.6). However, in the action case the final projection onto the target population is already explicitly indicated in the DSF diagram (e.g. by $|\chi\rangle\langle\chi|$ after the final rung). Therefore, while these additional arrow(s) are perhaps visually compelling, they

do not contribute any new mathematical meaning to the diagram within the scope of the formalism presented here. As the primary goal of the diagram is to directly represent a mathematical term in the response calculation, we will therefore avoid this convention.

Signal isolation: Phase-matching vs. phase-cycling and phase-modulation

Before concluding this section, it is worth making some comments on the differences in the type of signal isolation strategies that are possible in coherent vs. action techniques. The crucial distinction involves the spatially-extended nature of the macroscopic polarization central to coherent spectroscopy, which is tied to the phenomenon of phase-matching. Phase-matching refers to how the wavevector of the nonlinear polarization, and therefore the emitted signal field (Eq. 2.63), is related to those of the driving fields. Specifically, the propagation wavevector for a signal field radiated by the 3rd-order polarization is given by

$$\mathbf{k}_{\text{sig}} = \pm\mathbf{k}_1 \pm \mathbf{k}_2 \pm \mathbf{k}_3, \quad (2.96)$$

where the individual choice of plus or minus for each field wavevector depends on whether E_j^+ or E_j^- is RWA conjugate for each interaction, respectively. In this way, the wavevector of the signal a given pathway will contribute to can be directly read off of its diagram. Isolating the contribution from a subset of desired pathways can therefore be aided through control of the incident fields' wavevectors, for example by employing a fully non-collinear beam geometry where each pulse propagates toward the sample along a unique wavevector.

Phase-matching is the result of alternating constructive and destructive interference between radiation from the countless microscopic dipole oscillations making up the polarization density across the sample.^{48,121,139} The successful operation of coherent techniques is therefore intimately tied to the polarization's macroscopically-extended and possibly spatially-varying

structure. For example, in 2D spectroscopy performed in the BOXCARS geometry, the result of the first two pulses is to imprint the system's coherent τ_1 phase evolution in an excited population grating extended over the beam overlap region, which helps explain why measurements can be made at waiting times much longer than the transitions' dephasing timescale (often by many orders of magnitude for electronic transitions).¹⁴⁰ In the pump-probe geometry, these first two pulses are collinear and the resulting spatial profile of excited population is uniform (i.e. the grating wavevector is zero).^{129,141} However, signal generation is still a phase-matched process requiring the coherent addition of radiation from the ensemble of dipoles in order to produce a field strong enough to noticeably modulate the probe beam's intensity through interference.

In action spectroscopy, on the other hand, the macroscopic polarization is not involved in signal generation, and, as discussed previously in Section 2.3.4, its relevant nonlinear component in fact vanishes in centrosymmetric media due to the even perturbative order. Furthermore, in the case of fluorescence detection, photon emission from individual molecules is random and uncorrelated across the ensemble, so the net fluorescence signal from the sample is incoherent. Phase-matching is therefore not a viable strategy for pathway isolation. On the contrary, for phase-sensitive action experiments it is required that the relative phases of the driving fields be constant over the spatial region from which the action signal is being detected, so that the interferometric resolution is not washed away when collecting the aggregate incoherent emission. For example, the implementation of fluorescence-detected 2D electronic spectroscopy by De et al¹²² employed a mildly non-collinear geometry, which resulted in a spatial grating of target population in the sample. Successful detection of the 2D signal was only possible by selectively monitoring emission from the grating's central fringe through confocal imaging. As a result, nonlinear action spectroscopies—including our

present implementation of FEIR spectroscopy—employ fully collinear beam geometries in most cases, although for the reason mentioned in the previous paragraph the pump-probe geometry is also viable for 4th-order experiments.¹⁴² A crucial feature of not having to rely on the sample’s macroscopic polarization for signal generation is the applicability (in principle) of action-based methods to single-molecule or single-particle detection. Indeed, this is often one of the principle motivations cited for developing fluorescence-detected nonlinear action techniques, and is central to our approach with FEIR spectroscopy. Femtosecond linear and nonlinear fluorescence-detected methods have been applied to study the electronic spectroscopy of single-molecules in a variety of contexts.^{143–149}

Signal isolation in nonlinear action spectroscopy is usually accomplished through various flavors of phase control. In general, for a 4th-order experiment the additional constant phase of ϕ_j in each incident field (Eq. 2.95) is imprinted in the signal via

$$\phi_{\text{sig}} = \pm\phi_1 \pm \phi_2 \pm \phi_3 \pm \phi_4, \tag{2.97}$$

where the choice of plus or minus is determined in the same way as in the case of phase-matching above. Such a constant phase may be added to each pulse electric field by acousto-optic modulation or pulse-shaping techniques.¹⁵⁰ Phase-cycling is a strategy that involves taking the linear combination of successive measurements with the ϕ_j set at different values such that unwanted contributions cancel out, revealing the desired signal.^{91,116,122,151,152} Phase-modulation is a similar approach in which the different ϕ_j are continuously swept at unique frequencies, and the desired signal is recovered by demodulating the total response by a reference constructed from the appropriate linear combination of sweeping frequencies.^{90,92,153–155}

As it turns out, for the FEIR experiments discussed in this thesis we will not need to

explicitly employ phase-cycling or phase-modulation to extract the desired signal contributions (although employing such approaches could offer important improvements). We will instead rely on the resonance conditions to reduce the number of pathways that contribute. As discussed in Section 2.4.3, there is a close analogy with how signal components appear in the total response between our implementation of FEIR spectroscopy and 2D spectroscopy performed in the pump-probe geometry. This analogy is also useful in aspects of the experimental design and data processing strategies which will be discussed in Chapter 4.

2.4 FEIR as fourth-order action spectroscopy

2.4.1 Overview

The physical picture for FEIR excitation is a sequential, double-resonance process consisting of the absorption of an IR photon by the vibration, followed by the absorption of a visible photon by a vibronic transition from the vibration's excited level to the excited electronic manifold. Putting this into perturbation theory language requires two light-matter interactions for the IR-vibrational transition and two for the visible-vibronic transition, resulting in a 4th-order description. Here, we will develop a theoretical description for FEIR excitation based on the 4th-order action response function introduced in Section 2.3. While a 4th-order response function formulation may at first seem unnecessarily complicated for understanding the basic features of FEIR experiments, understanding all the details requires such a treatment, and this development will be well worth it.

Just as resonance plays a critical role in successful experimental FEIR detection, it also greatly simplifies the theoretical response function expressions by imposing strict conditions on which pathways can contribute. Figure 2.11(a) shows a generalized energy level diagram

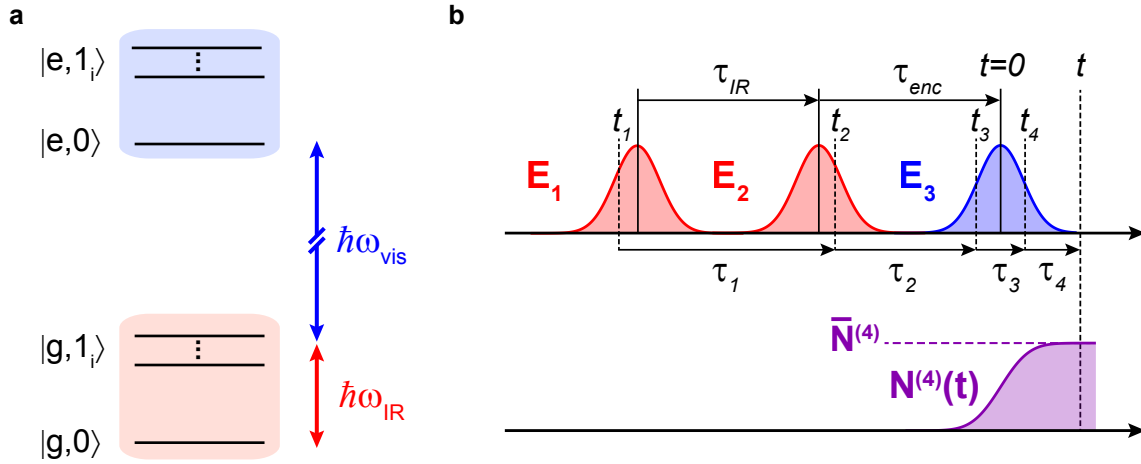


Figure 2.11: Energy level diagram, pulse sequence, and target population in an FEIR experiment. (a) Generalized energy level diagram for FEIR excitation. Relative energy gaps are not to scale. (b) Pulse sequence, excited target population, and relevant time variables for the calculation of the system response.

relevant to FEIR spectroscopy for the two-level electronic system coupled to multiple high-frequency vibrations discussed in Section 2.2. Because there are only 2 IR-vibrational light-matter interactions and the target state is only reached by two-photon material resonances, only the singly-excited levels of the oscillators can be accessed. Specifically, neither overtone nor combination states, e.g. in the notation of Section 2.2 $|2_i^g 0_j^g\rangle$ or $|1_i^g 1_j^g\rangle$, need to be considered. We can therefore adopt the simplified level structure and notation where the electronic ground state is composed of the global ground state $|g, 0\rangle$ with zero quanta in all vibrational oscillators, and the manifold of singly-excited vibrational states $|g, 1_i\rangle$ in which the i -th mode has one quantum of excitation while all others remain in the ground state. These system vibrational frequencies are assumed to be substantially higher than $k_B T/\hbar$ so that the one-quantum manifold is not appreciably populated at equilibrium. Similarly, the excited electronic state has the zero-quantum level $|e, 0\rangle$ and corresponding manifold of one-quantum levels $|e, 1_i\rangle$.

The IR field (photon energy $\hbar\omega_{\text{IR}}$ indicated by red arrow) is tuned to resonance with the vibrational fundamentals, and has sufficient bandwidth to cover multiple transitions. The visible encoding field (blue arrow) is tuned to be resonant with the transitions from $|g, 1_i\rangle$ to $|e, 0\rangle$. Critically, the visible frequency ω_{vis} is below resonance with any transitions from the equilibrium ground state $|g, 0\rangle$ to the electronic excited state, as otherwise one-photon excitation, e.g. to 2nd-order in the light-matter interaction, would dominate. As a consequence of this resonance condition, transitions between the $|g, 1_i\rangle$ and $|e, 1_i\rangle$ manifolds are also out of resonance. Therefore, the target state for action detection can simply be taken to be $|e, 0\rangle$, and the higher vibrational levels can be ignored. In general, the visible field should also be narrowband with respect to the electronic linewidth to ensure good spectral selectivity of double-resonance FEIR vs. one-photon excitation.

The pulse sequence used in an FEIR experiment is depicted in Figure 2.11(b). Explicitly, the incident electric field is

$$\mathbf{E}(t) = \mathbf{E}_3(t) + \mathbf{E}_2(t + \tau_{\text{enc}}) + \mathbf{E}_1(t + \tau_{\text{enc}} + \tau_{\text{IR}}), \quad (2.98)$$

where \mathbf{E}_1 and \mathbf{E}_2 are a pair of IR pulses separated by delay τ_{IR} , and \mathbf{E}_3 is the visible encoding pulse delayed with respect to \mathbf{E}_2 by the encoding delay τ_{enc} . These pulses propagate collinearly, and their parallel wave-vectors will therefore be left out of the notation. Two light-matter interactions with the visible field are required to reach the target excited state, and in the case of well-separated pulses shown in Figure 2.11(b) they must be sequential. In what follows, we denote the total system dipole operator generically by \mathbf{M} as in Section 2.2.2 to allow specific notation for vibrational and vibronic transition moments later on. For well-separated pulses in the ‘proper’ ordering shown in Figure 2.11(b), the 4th-order contribution

to the target population is

$$\begin{aligned} \bar{N}^{(4)} \equiv \lim_{t \rightarrow \infty} N^{(4)}(t) &= \int_{-\infty}^{\infty} dt_4 \int_0^{\infty} d\tau_3 \int_0^{\infty} d\tau_2 \int_0^{\infty} d\tau_1 \mathbf{R}^{(4)}(\tau_3, \tau_2, \tau_1) \\ &\quad \times \mathbf{E}_3(t_4) \mathbf{E}_3(t_4 - \tau_3) \mathbf{E}_2(t_4 - \tau_3 - \tau_2) \mathbf{E}_1(t_4 - \tau_3 - \tau_2 - \tau_1), \end{aligned} \quad (2.99)$$

where the multiplication of the tensorial response function with the field vectors is understood as a tensor contraction. Here we have used the limiting procedure described by Eqs. 2.66-2.68 with the effective action response function

$$\begin{aligned} &\mathbf{R}^{(4)}(\tau_3, \tau_2, \tau_1) \\ &= \left(\frac{i}{\hbar}\right)^4 \theta(\tau_3) \theta(\tau_2) \theta(\tau_1) \text{Tr}\{N[\mathbf{M}(\tau_3 + \tau_2 + \tau_1), [\mathbf{M}(\tau_2 + \tau_1), [\mathbf{M}(\tau_1), [\mathbf{M}(0), \rho_0]]]]\}, \end{aligned} \quad (2.100)$$

where $N = |f\rangle\langle f|$ is the projection onto the target state $|f\rangle$. We will treat the effects of finite pulse duration, including different pulse interaction orderings that occur during their temporal overlap in Chapter 3. The remainder of this chapter describes the basic features of FEIR spectroscopy in the impulsive limit.

2.4.2 Response function

The system's level structure and resonance conditions dictate that the target state is only accessible through two-photon material resonances, specifically involving the singly-excited vibrational states as intermediates. In terms of Liouville pathways for the response function, this means that two bra and ket side interactions each are required to arrive in the target state. This requirement immediately excludes all correlation functions in Eqs. 2.61-2.62 and Figure 2.6 except for Q_1 , Q_2 , and Q_3 . For convenience and to establish specificity to FEIR

spectroscopy, we will rename these correlation functions $C_1 \equiv Q_1^*$, $C_2 \equiv Q_2$, and $C_3 \equiv Q_3^*$. Each of these correlation function is depicted in Figure 2.8. Explicitly, the response function is written as

$$\mathbf{R}^{(4)}(\tau_3, \tau_2, \tau_1) = \frac{1}{\hbar^4} \theta(t_3) \theta(\tau_2) \theta(\tau_3) \sum_{\alpha=1}^3 \left[\mathbf{C}_\alpha(\tau_3, \tau_2, \tau_1) + \mathbf{C}_\alpha(\tau_3, \tau_2, \tau_1)^* \right] \quad (2.101)$$

with

$$\mathbf{C}_1(\tau_3, \tau_2, \tau_1) = \text{Tr}\{N\mathbf{M}(\tau_2 + \tau_1)\mathbf{M}(0)\rho_0\mathbf{M}(\tau_1)\mathbf{M}(\tau_3 + \tau_2 + \tau_1)\} \quad (2.102a)$$

$$\mathbf{C}_2(\tau_3, \tau_2, \tau_1) = \text{Tr}\{N\mathbf{M}(\tau_3 + \tau_2 + \tau_1)\mathbf{M}(0)\rho_0\mathbf{M}(\tau_1)\mathbf{M}(\tau_2 + \tau_1)\} \quad (2.102b)$$

$$\mathbf{C}_3(\tau_3, \tau_2, \tau_1) = \text{Tr}\{N\mathbf{M}(\tau_1)\mathbf{M}(0)\rho_0\mathbf{M}(\tau_2 + \tau_1)\mathbf{M}(\tau_3 + \tau_2 + \tau_1)\}. \quad (2.102c)$$

The scalar vibronic terms in these correlation functions expressed in the homogeneous limit are

$$\begin{aligned} C_1^{a,b,c,d}(\tau_3, \tau_2, \tau_1) &= \delta_{fc} M_{dc} M_{cb} M_{ad} M_{ba} P(a) \exp(-i\omega_{cd}\tau_3 - i\omega_{bd}\tau_2 - i\omega_{ba}\tau_1) \\ &\quad \times \exp(-\Gamma_{cd}\tau_3 - \Gamma_{bd}\tau_2 - \Gamma_{ba}\tau_1) \end{aligned} \quad (2.103a)$$

$$\begin{aligned} C_2^{a,b,c,d}(\tau_3, \tau_2, \tau_1) &= \delta_{fc} M_{cb} M_{dc} M_{ad} M_{ba} P(a) \exp(-i\omega_{bc}\tau_3 - i\omega_{bd}\tau_2 - i\omega_{ba}\tau_1) \\ &\quad \times \exp(-\Gamma_{bc}\tau_3 - \Gamma_{bd}\tau_2 - \Gamma_{ba}\tau_1) \end{aligned} \quad (2.103b)$$

$$\begin{aligned} C_3^{a,b,c,d}(\tau_3, \tau_2, \tau_1) &= \delta_{fc} M_{dc} M_{ad} M_{cb} M_{ba} P(a) \exp(-i\omega_{cd}\tau_3 - i\omega_{ca}\tau_2 - i\omega_{ba}\tau_1) \\ &\quad \times \exp(-\Gamma_{cd}\tau_3 - \Gamma_{ca}\tau_2 - \Gamma_{ba}\tau_1), \end{aligned} \quad (2.103c)$$

while the corresponding orientational tensor elements are

$$(Y_1)_{IJKL}^{a,b,c,d}(\tau_3, \tau_2, \tau_1) = \sum_{ijkl} \tilde{Y}_{IJKL}^{ijkl}(\tau_3, \tau_2, \tau_1) \left[\hat{\mathbf{m}}_{dc} \cdot \hat{i} \right] \left[\hat{\mathbf{m}}_{cb} \cdot \hat{j} \right] \left[\hat{\mathbf{m}}_{ad} \cdot \hat{k} \right] \left[\hat{\mathbf{m}}_{ba} \cdot \hat{l} \right] \quad (2.104a)$$

$$(Y_2)_{IJKL}^{a,b,c,d}(\tau_3, \tau_2, \tau_1) = \sum_{ijkl} \tilde{Y}_{IJKL}^{ijkl}(\tau_3, \tau_2, \tau_1) \left[\hat{\mathbf{m}}_{cb} \cdot \hat{i} \right] \left[\hat{\mathbf{m}}_{dc} \cdot \hat{j} \right] \left[\hat{\mathbf{m}}_{ad} \cdot \hat{k} \right] \left[\hat{\mathbf{m}}_{ba} \cdot \hat{l} \right] \quad (2.104b)$$

$$(Y_3)_{IJKL}^{a,b,c,d}(\tau_3, \tau_2, \tau_1) = \sum_{ijkl} \tilde{Y}_{IJKL}^{ijkl}(\tau_3, \tau_2, \tau_1) \left[\hat{\mathbf{m}}_{dc} \cdot \hat{i} \right] \left[\hat{\mathbf{m}}_{ad} \cdot \hat{j} \right] \left[\hat{\mathbf{m}}_{cb} \cdot \hat{k} \right] \left[\hat{\mathbf{m}}_{ba} \cdot \hat{l} \right] \quad (2.104c)$$

These orientational correlation functions differ only in the order in which the transition dipole unit vectors appear, and will be treated in Chapter 9. For the remainder of this chapter we will restrict ourselves to analyzing the scalar vibronic response. Specifically, the vibronic correlation functions are the sum over all material pathways

$$C_\alpha(\tau_3, \tau_2, \tau_1) = \sum_{a,b,c,d} C_\alpha^{a,b,c,d}(\tau_3, \tau_2, \tau_1) \quad (2.105)$$

for $\alpha = 1, 2$, and 3 .

2.4.3 Two- and three-pulse signals and FEIR spectra

The full pulse sequence shown in Figure 2.11(b) and reproduced here in Figure 2.12(a) facilitates the measurement of Fourier transform (FT) vibrational spectra as a function of encoding delay. The total FEIR signal F is proportional to the final target population $\bar{N}^{(4)}$ via Eq 2.69, and is the sum of the following three contributions

$$F(\tau_{\text{IR}}, \tau_{\text{enc}}) = F_{12}(\tau_{\text{IR}}, \tau_{\text{enc}}) + F_1(\tau_{\text{IR}} + \tau_{\text{enc}}) + F_2(\tau_{\text{enc}}). \quad (2.106)$$

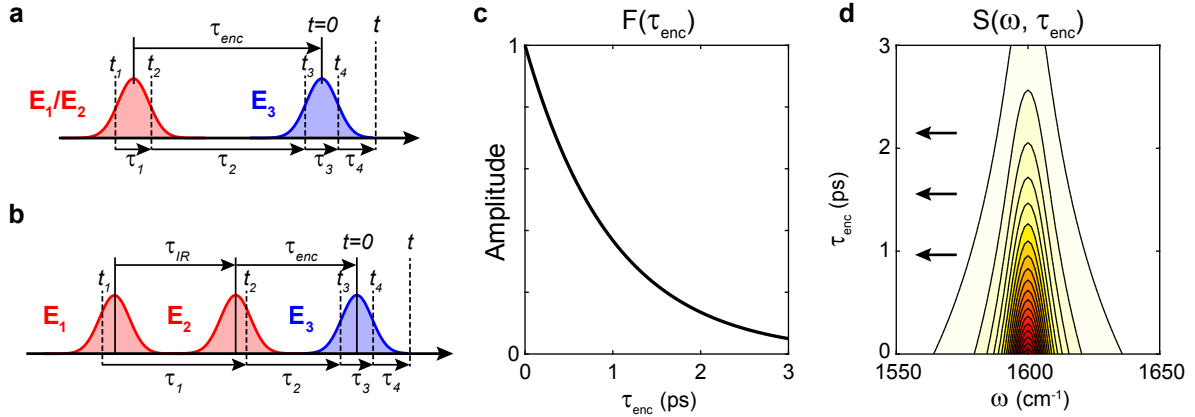


Figure 2.12: Pulse sequences with experimental delays and perturbation-theoretic interaction time variables for (a) the two-pulse and (b) three-pulse signals. (c) Projection-slice relationship between the τ_{enc} -dependent FEIR spectrum $S(\omega, \tau_{\text{enc}})$ derived from the three-pulse signal (left panel) and the two-pulse signal $F(\tau_{\text{enc}})$ (right panel) for a single lifetime-broadened vibrational mode at 1600 cm^{-1} with 1 ps population relaxation calculated in the impulsive limit. Explicitly, the two-pulse signal could be either $F_1(\tau_{\text{enc}})$ (i.e. with $\tau_{\text{IR}} = 0$), $F_2(\tau_{\text{enc}})$, or $F(\tau_{\text{IR}} = 0, \tau_{\text{enc}})$.

The contribution $F_{12}(\tau_{\text{IR}}, \tau_{\text{enc}})$ is due to one interaction each with \mathbf{E}_1 and \mathbf{E}_2 and two with the encoding field \mathbf{E}_3 (Figure 2.12(a)), and is therefore termed the three-pulse signal. The three-pulse signal resolves the vibrational free-induction decay in τ_{IR} and is consequently the desired signal for measuring vibrational spectra. $F_1(t) = F_2(t)$ are two-pulse signals where both IR-vibrational interactions occur with either \mathbf{E}_1 or \mathbf{E}_2 , respectively (2.12b). This situation is analogous to 2D spectroscopy experiments performed in the pump-probe geometry, where the 2D signal (analogous to F_{12}) must be separated from the pump-probe signals (analogous to F_1 and F_2).^{129,141,156,157} Explicit expressions for these contributions in terms of convolution integrals of the response function and pulse electric fields will be given

in Chapter 3. By symmetry, the two- and three-pulse signals are related via

$$F_{12}(\tau_{\text{IR}} = 0, \tau_{\text{enc}}) \propto F_1(\tau_{\text{enc}}) = F_2(\tau_{\text{enc}}). \quad (2.107)$$

The FEIR spectrum at a given encoding delay is given by the FT of the three-pulse signal

$$S(\omega, \tau_{\text{enc}}) = \text{Re} \int_0^\infty F_{12}(\tau_{\text{IR}}, \tau_{\text{enc}}) e^{i\omega\tau_{\text{IR}}} d\tau_{\text{IR}}. \quad (2.108)$$

The two-pulse signal measures the encoding delay dependence of the integrated vibrational resonances projected onto the τ_{enc} -axis, as described formally by the projection-slice theorem

$$F_{12}(\tau_{\text{IR}} = 0, \tau_{\text{enc}}) = \int_{-\infty}^\infty S(\omega, \tau_{\text{enc}}) d\omega \quad (2.109)$$

in conjunction with Eq. 2.107. This relationship between the spectrum and two-pulse signal is demonstrated in Figure 2.12(c) for the case of a single vibrational mode, discussed below in Section 2.4.4.

In practice, the two-pulse signal can be measured either by blocking \mathbf{E}_1 (measuring $F_2(\tau_{\text{enc}})$), or setting $\tau_{\text{IR}} = 0$ (measuring $F_{12}(\tau_{\text{IR}} = 0, \tau_{\text{enc}}) + F_1(\tau_{\text{enc}}) + F_2(\tau_{\text{enc}})$). Due to the effect of constructive interference, this latter method produces a 4 times larger signal size than the former, as will be demonstrated experimentally in Chapter 4. For brevity, we will refer to the two-pulse signal simply by $F(\tau_{\text{enc}})$.

2.4.4 Single-mode population response

To describe the basic spectroscopic features in a typical FEIR measurement we first address the simplest case of a single vibrational oscillator coupled to the electronic transition. Referring to the generic level structure in Figure 2.11(a), this system can be represented by a three-level system consisting of the global ground state $|0\rangle \equiv |g, 0\rangle$, first vibrational excited state $|1\rangle \equiv |g, 1\rangle$, and zero-quantum level of the excited electronic state $|e\rangle \equiv |e, 0\rangle$ which is the target state. Assuming only the ground state $|0\rangle$ is initially populated at equilibrium, this model produces one unique material pathway per correlation function (or its complex conjugate), which are shown in Figure 2.13 as both double-sided Feynman diagrams and ladder diagrams. The corresponding complex conjugate pathways are found by switching each ket-side interaction to bra-side interaction, and vice versa. The red or blue color of the arrows indicate interaction with an IR or visible field, respectively. Each of these pathways involves only two unique transition dipole moments.

In the language of 2D or pump-probe spectroscopy, pathways C_1 and C_2 represent excited-state absorption, while C_3 has the character of a double quantum coherence pathway. In each case, all four interactions are absorptive, and every pathway carries an overall positive sign due to having two bra-side interactions, and consequently contributes a gain in fluorescence output from the molecule. This should come as no surprise, as we specifically restricted the response function to such terms to describe the double-resonance excitation process. Likewise, the lack of ground-state bleaching or stimulated emission pathways is a consequence of the level structure and resonance conditions. Filling in the eigenstate indices according to Eq. 2.103, the single-mode pathways $C_1^{0,1,e,1}$ and $C_2^{0,1,e,1}$ will be referred to as population pathways, as they report on the excited population of the vibration being pumped.

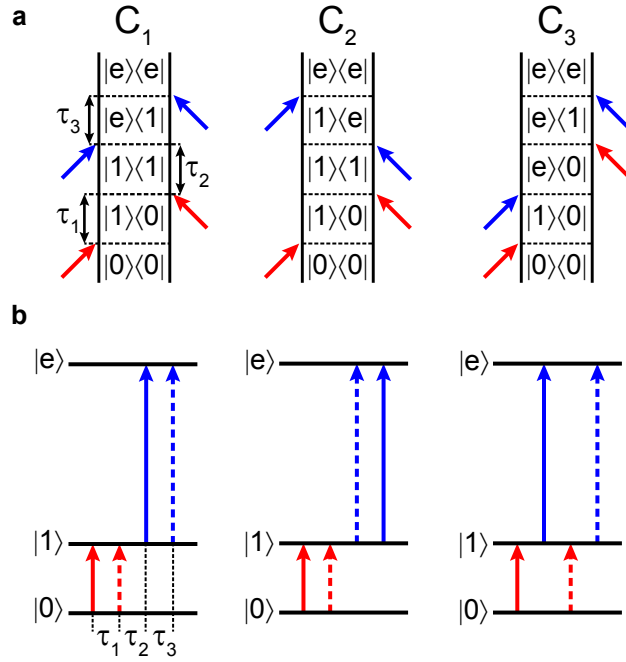


Figure 2.13: (a) Double-sided Feynman diagrams and (b) ladder diagrams for the unique pathway contributing to each correlation function for a three-level system. Red and blue arrows indicate IR and visible field interactions, respectively.

In the homogeneous limit (Eq. 2.103), the vibronic correlation functions C_1 and C_2 are

$$C_1^{0,1,e,1} = |M_{e1}|^2 |M_{10}|^2 \exp \left[(-i(\omega_{e0} - \omega_{10}) - \Gamma_{e1})\tau_3 - \Gamma_{11}\tau_2 + (-i\omega_{10} - \Gamma_{10})\tau_1 \right] \quad (2.110a)$$

$$C_2^{0,1,e,1} = |M_{e1}|^2 |M_{10}|^2 \exp \left[(i(\omega_{e0} - \omega_{10}) - \Gamma_{e1})\tau_3 - \Gamma_{11}\tau_2 + (-i\omega_{10} - \Gamma_{10})\tau_1 \right]. \quad (2.110b)$$

Here Γ_{11} is the vibrational population relaxation rate, and Γ_{10} and Γ_{e1} are the dephasing rates of the $|0\rangle \rightarrow |1\rangle$ vibrational fundamental and $|1\rangle \rightarrow |e\rangle$ vibronic transition, respectively. Both pathways' magnitude is given by the square of both the vibrational and vibronic transition dipoles, M_{10} and M_{e1} , respectively. The vibronic transition dipole is only non-zero in the presence of some form of vibronic coupling, which as discussed in Section 2.2 could arise

from Franck-Condon activity or more generally from a non-Condon vibrational coordinate-dependence to the electronic transition moment. Specifically, in the Condon approximation

$$|M_{e1}|^2|M_{10}|^2 = |\mu_{eg}|^2\langle 0^e|1^g\rangle^2|\mu_{10}|^2, \quad (2.111)$$

where $\langle 0^e|1^g\rangle$ is the Franck-Condon overlap between the nuclear wavefunctions of the $|1\rangle$ and $|e\rangle$ states. Because the squared electronic transition matrix element $|\mu_{eg}|^2$ will always be present in any pathway's amplitude, we will call the product $\langle 0^e|1^g\rangle^2|\mu_{10}|^2$ the (Condon approximation) FEIR activity of the vibration. Within a given molecule, the FEIR activity is a simple indicator of the strength of a vibration's FEIR response, although orientational factors will also contribute (discussed in Chapter 9). The τ_1 and τ_3 dependence describe the frequency and linewidth of the vibrational and vibronic transitions, respectively, while vibrational population relaxation during τ_2 causes the response to decay and represents a loss channel for the overall FEIR excitation probability.

While the C_3 pathway satisfies the resonance conditions, it involves the mixed IR-Vis-IR-Vis ordering of light-matter interactions, and therefore can only contribute during the temporal overlap of the IR and visible fields when $|\tau_{\text{enc}}| \lesssim \tau_p$, where τ_p is the duration of the IR/Vis pulse cross-correlation. Explicitly,

$$C_3^{0,1,e,1} = |M_{e1}|^2|M_{10}|^2 \exp\left[(-i(\omega_{e0} - \omega_{10}) - \Gamma_{e1})\tau_3 - (-i\omega_{e0} - \Gamma_{e0})\tau_2 + (-i\omega_{10} - \Gamma_{10})\tau_1\right]. \quad (2.112)$$

This pathway involves a rapidly oscillating electronic $|e\rangle\langle 0|$ coherence during τ_2 , which typically dephases within tens of femtoseconds. As discussed in Chapter 3, it typically will not survive the pulse convolution integrals and can be safely neglected.

In the impulsive limit, the τ_1 -dependence is mapped out in the IR pulse-pair delay τ_{IR} , τ_2 becomes the encoding delay τ_{enc} , and $\tau_3 = 0$ as the two interactions with \mathbf{E}_3 become time-coincident. Similarly, $C_3 \propto \delta(\tau_{\text{enc}})$ and therefore vanishes for positive τ_{enc} . Figure 2.12(d) shows the τ_{enc} -dependent FEIR spectrum $S(\omega, \tau_{\text{enc}})$ calculated from the impulsive three-pulse signal

$$\begin{aligned} F_{12}(\tau_{\text{IR}}, \tau_{\text{enc}}) &\propto \theta(\tau_{\text{enc}})\theta(\tau_{\text{IR}}) \left[C_1(0, \tau_{\text{enc}}, \tau_{\text{IR}}) + C_2(0, \tau_{\text{enc}}, \tau_{\text{IR}}) + c.c. \right] \\ &\propto \theta(\tau_{\text{enc}})\theta(\tau_{\text{IR}}) |M_{e1}|^2 |M_{10}|^2 \exp(-\Gamma_{11}\tau_{\text{enc}}) \cos(\omega_{10}\tau_{\text{IR}}) \exp(-\Gamma_{10}\tau_{\text{IR}}) \end{aligned} \quad (2.113)$$

with $\omega_{10} = 1600 \text{ cm}^{-1}$ and $\Gamma_{10} = \Gamma_{11} = 1 \text{ ps}$. The FEIR spectrum resolves the vibrational fundamental's frequency and lineshape, and decays in τ_{enc} due to population relaxation of the $|1\rangle$ state. The two-pulse signal

$$\begin{aligned} F(\tau_{\text{enc}}) &\propto \theta(\tau_{\text{enc}}) \left[C_1(0, \tau_{\text{enc}}, 0) + C_2(0, \tau_{\text{enc}}, 0) + c.c. \right] \\ &\propto \theta(\tau_{\text{enc}}) |M_{e1}|^2 |M_{10}|^2 \exp(-\Gamma_{11}\tau_{\text{enc}}) \end{aligned} \quad (2.114)$$

correspondingly tracks this relaxation directly without resolving the lineshape via the projection-slice relationship.

The C_1 and C_2 pathways differ only in the sign of their τ_3 phase evolution. The C_1 pathway has the same sign of phase evolution during τ_1 and τ_3 and can therefore be classified as a non-rephasing pathway, while the C_2 pathway exhibits opposite signs and is consequently a rephasing pathway. The presence of correlated heterogeneity between the vibrational and electronic frequencies will therefore affect these pathways differently, although the large mismatch in magnitude of the vibrational and electronic transition frequencies precludes strong

echo behavior.¹⁵⁸ However, because both the third and fourth light-matter interaction occur with the same pulse, the phase evolution in τ_3 is not directly monitored. These pathways are therefore not distinguishable in experiment, and contribute similarly to the measured signals (although perhaps with different magnitudes in the presence of heterogeneity). The consequence is that FEIR spectroscopy as performed in this thesis is not directly sensitive to heterogeneity in the way that related non-degenerate 3rd-order techniques like 2DVE and 2DEV are. The rephasing/non-rephasing terminology is however still useful for bookkeeping purposes when setting up finite-pulse calculations in Chapter 3.

2.4.5 Multimode coherence

When multiple vibrational modes are covered within the bandwidth of the IR pulses, pairs of fundamentals may be excited coherently if the vibrations are coupled. To describe these vibrationally coherent signals we add in a second vibrational oscillator, resulting in a four-level system with the ground state $|0\rangle \equiv |g, 0_m, 0_n\rangle$, singly-excited vibrational states $|m\rangle \equiv |g, 1_m, 0_n\rangle$ and $|n\rangle \equiv |g, 0_m, 1_n\rangle$, and the target excited state $|e\rangle \equiv |e, 0\rangle$. In addition to the population pathways residing in either $|m\rangle\langle m|$ or $|n\rangle\langle n|$ during τ_2 described above, there is the possibility for pathways residing in an $|m\rangle\langle n|$ or $|n\rangle\langle m|$ coherence during τ_2 . Each correlation function has a pair of coherence pathways formed by exchanging the roles of the two vibrations n and m , i.e. which differ by which mode is excited first. Such a pair of pathways is shown for C_1 in Figure 2.14(a), while the analogous pair for C_2 would be found by switching the order of the final two interactions with the visible field. Explicitly,

$$C_1^{0,m,e,n} = M_{en}^* M_{em} M_{n0}^* M_{m0} \\ \times \exp\left((-i(\omega_{eg} - \omega_{n0}) - \Gamma_{en})\tau_3 + (-i\omega_{mn} - \Gamma_{mn})\tau_2 + (-i\omega_{m0} - \Gamma_{m0})\tau_1\right), \quad (2.115a)$$

$$C_1^{0,n,e,m} = M_{em}^* M_{en} M_{m0}^* M_{n0} \times \exp((-i(\omega_{eg} - \omega_{m0}) - \Gamma_{em})\tau_3 + (-i\omega_{nm} - \Gamma_{nm})\tau_2 + (-i\omega_{n0} - \Gamma_{n0})\tau_1). \quad (2.115b)$$

Both pathways exhibit oscillatory behavior in τ_2 at the difference frequency ω_{mn} or ω_{nm} between the vibrational fundamentals. Specifically, the oscillating part of the τ_2 -dependence acts as a phase-shift $\phi_{mn}(\tau_2) = \omega_{mn}\tau_2$ on the vibrational lineshape encoded in the τ_1 -dependence. This phase has opposite sign for the two pathways in a coherence pair, $\phi_{mn}(\tau_2) = -\phi_{nm}(\tau_2)$. The resulting contribution of the pair of coherence pathways to the FEIR spectrum is shown in Figure 2.14(b), with the coherence dephasing $\Gamma_{nm} = \Gamma_{mn} = 0$ for purposes of illustration. At $\tau_2 = 0$ the coherence phase is zero, and $C_1^{0,m,e,n}$ and $C_1^{0,n,e,m}$ produce absorptive vibrational lineshapes centered at ω_{m0} and ω_{n0} , respectively. As τ_2 increases the phase evolves with opposite signs over each resonance, leading to dispersive lineshapes with overlapping negative lobes at $\phi_{mn} = -\phi_{nm} = \pi/2$, inverted absorptive lineshapes at $\phi_{mn} = -\phi_{nm} = \pi$, and then dispersive lineshapes with overlapping positive lobes at $\phi_{mn} = -\phi_{nm} = 3\pi/2$.

The coherence contribution decays away in τ_{enc} due to dephasing processes characterized by the rate Γ_{nm} , shown for the impulsive FEIR spectrum and two-pulse transient in Figures 2.14(c) and (d), respectively. As discussed in Section 2.3.5, this overall dephasing rate has contributions from both energy relaxation (i.e. the concomitant decay of the excited $|m\rangle$ and $|n\rangle$ populations) and phase relaxation (pure dephasing). The pure dephasing component of Γ_{nm} is determined by environmentally induced fluctuations in the energies of each level. In general when the vibrations are uncoupled, e.g. on different molecules where the use of a common ground state is not meaningful, these fluctuations must be completely uncorrelated so that the coherence pathway cannot survive the equilibrium average of Eq. 2.84 and will

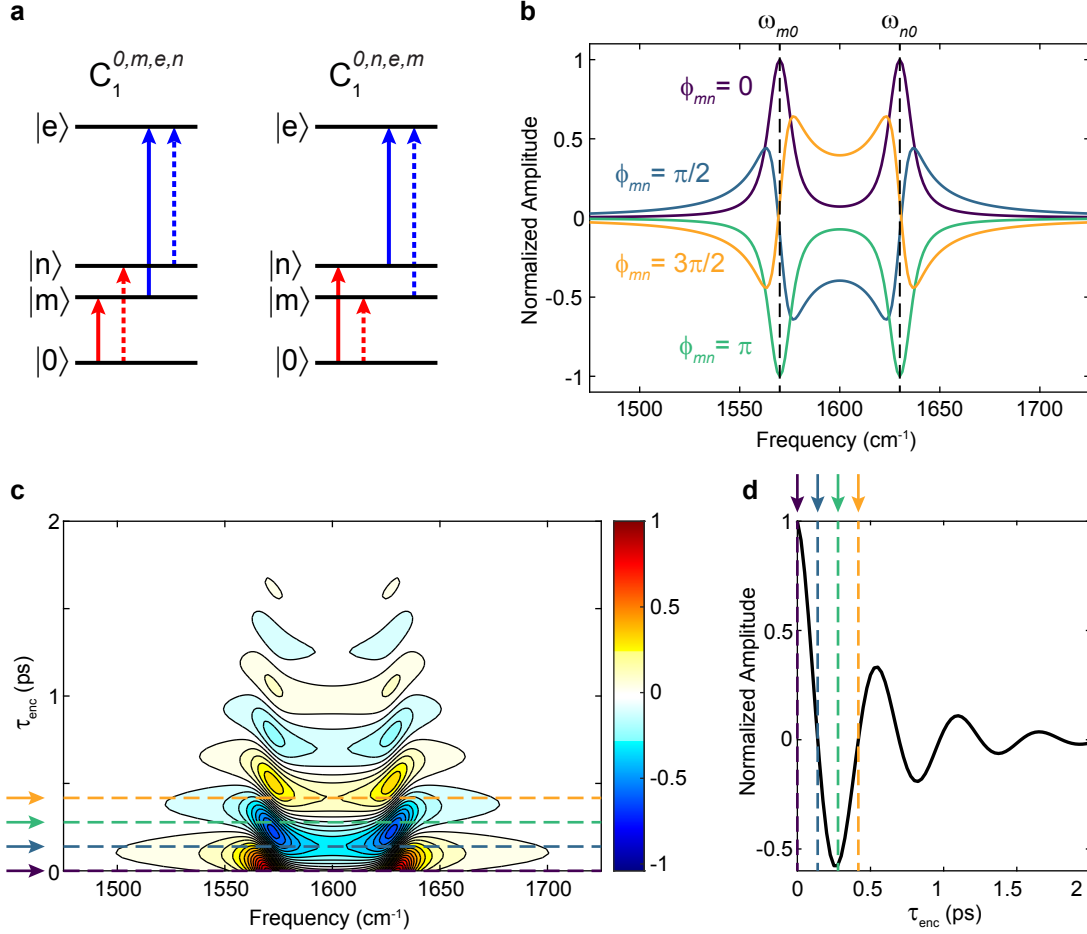


Figure 2.14: Vibrational coherence pathways and their τ_{enc} -dependent spectral signatures. (a) Ladder diagrams for a pair of coherence pathways connecting fundamentals m and n . (b) Lineshapes of a positive coherent pathway pair after acquiring phases of $\phi_{mn} = 0, \pi/2, \pi, \text{ and } 3\pi/2$ through τ_{enc} -evolution, respectively. The fundamentals have frequencies $\omega_{m0} = 1570 \text{ cm}^{-1}$ and $\omega_{n0} = 1630 \text{ cm}^{-1}$, and are lifetime-broadened with $\Gamma_{m0}^{-1} = \Gamma_{n0}^{-1} = 1000 \text{ fs}$. The coherence dephasing Γ_{nm} has been set to zero. (c) Isolated contribution of the coherence to the impulsive τ_{enc} -dependent FEIR spectrum, with $\Gamma_{nm}^{-1} = 500 \text{ fs}$. Color-coded dashed lines indicate the τ_{enc} values corresponding to the different coherence phases in (b). (d) Contribution of the coherence to the impulsive two-pulse transient, with analogous dashed lines showing the τ_{enc} values corresponding to the coherence phases in (b).

not contribute to the signal. The presence of coherence in a measurement is therefore a marker of coupling between the vibrations.

The amplitudes of the two pathways in a coherence pair are always the same due to the reality of the transition dipole moments. Specifically, in the Condon approximation this amplitude is

$$M_{en}^* M_{em} M_{n0}^* M_{m0} = M_{em}^* M_{en} M_{m0}^* M_{n0} = |\mu_{eg}|^2 \langle 0^e | 1_n^g \rangle \langle 0^e | 1_m^g \rangle \mu_{n0} \mu_{m0}. \quad (2.116)$$

The transition dipole moments of both vibrations and their respective FC factors contribute to the pathway pair's magnitude. As such, the strength of the coherence can be thought of as being determined by a 'mixture' of both vibration's FEIR activity. Crucially, as the signs of these four matrix elements could be variable, the overall coherence amplitude can be positive or negative. Along the lines of our discussion on the separation of vibronic and orientational effects in Section 2.3.5, without loss of generality we take the vibrational matrix elements μ_{m0} and μ_{n0} to be positive, and let their dipole unit vectors in the orientational correlation function assume any direction. However, in the Condon approximation the vibronic transitions must be aligned along the bare electronic transition dipole unit vector $\hat{\mu}_{eg}$ (Eq. 2.25). Therefore we set both the vibronic transition dipole unit vectors to be $\hat{\mu}_{eg}$ in the orientational correlation function, and let their FC factors $\langle 0^e | 1_n^g \rangle$ and $\langle 0^e | 1_m^g \rangle$ vary freely in sign. Indeed, we saw in Section 2.2 how the sign of these FC factors depends in various ways on the nature of the vibronic coupling. The result of assuming this convention is that the sign of the coherence amplitude in the vibronic response function (Eq. 2.116) is sensitive to the relative sign of two mode's FC factors. The relative orientation of the electronic and two vibrational transitions can also affect the sign of the coherence through the orientational correlation function, as will be discussed in Chapter 9.

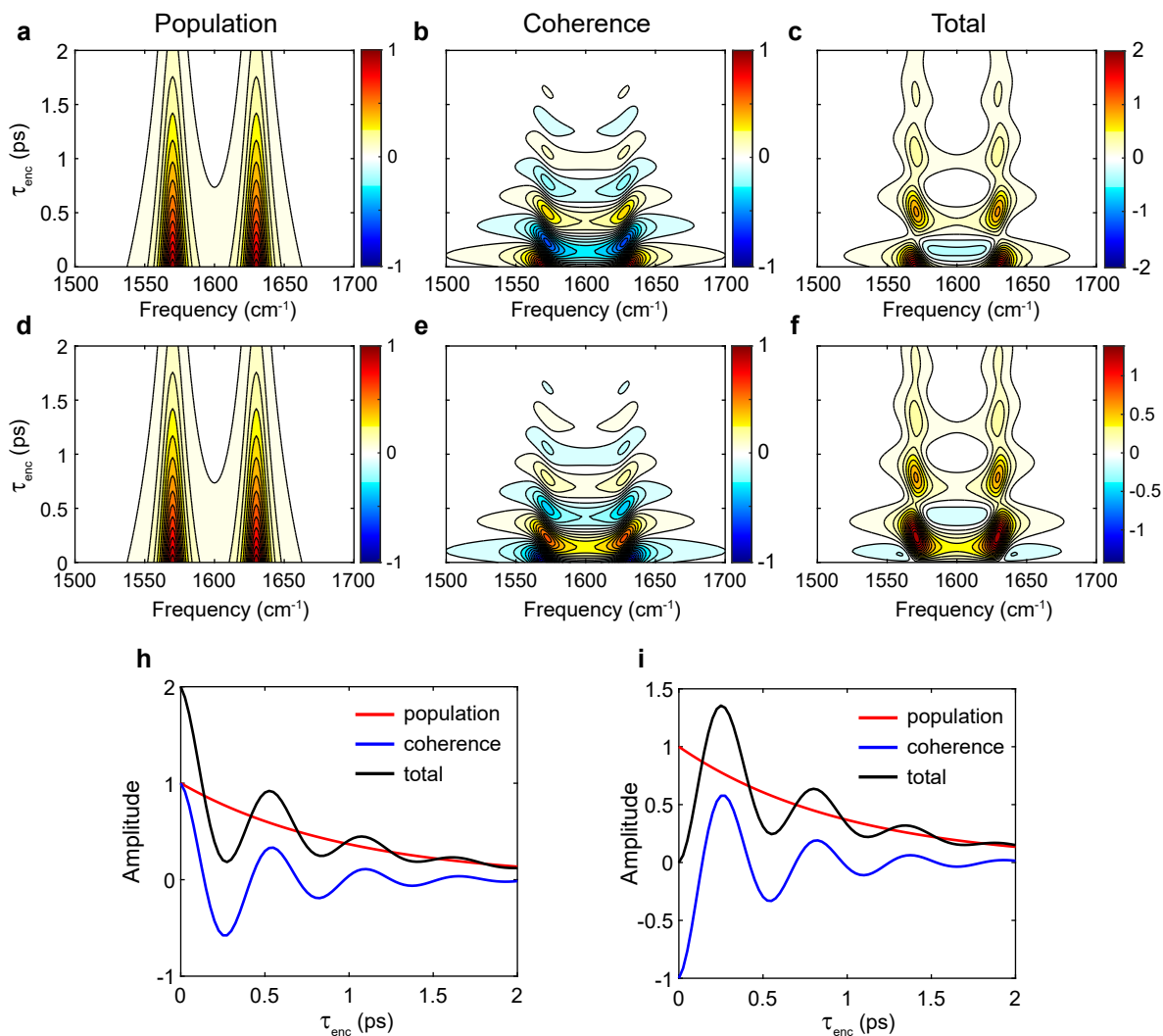


Figure 2.15: Interference between population and coherence contributions of positive or negative sign. Contributions to the impulsive-limit τ_{enc} -dependent FEIR spectrum from (a) population pathways and (b) coherence pathways, and (c) the total spectrum in the case of a positively-signed coherence. (d)-(f) show the analogous case for a negatively-signed coherence. (h) and (i) show the corresponding two-pulse signal and its population and coherence contributions for a positively- and negatively-signed coherence, respectively.

This overall sign sensitivity has dramatic consequences for the way in which the population and coherence contributions interfere in the total FEIR signal, as demonstrated in Figure 2.15. Panels (a), (b), and (c) show the contribution of the population pathways, coherence pathways, and the resulting total τ_{enc} -dependent FEIR spectrum for the two-mode system in the case where both FC factors have the same sign, resulting in a positive coherence amplitude at $\tau_{\text{enc}} = 0$ fs. This is the situation shown previously in Figure 2.14. At $\tau_{\text{enc}} = 0$ fs the positive absorptive coherence lineshape interferes constructively with the population features, leading to maximally intense, absorptive lineshapes in the spectrum. This constructive interference correspondingly leads to a signal maximum at $\tau_{\text{enc}} = 0$ fs in the two-pulse signal, shown in Figure 2.15(h).

The case of oppositely signed FC factors resulting in a negatively-signed coherence is shown in Figures 2.15(d)-(f) and (i). The population features are unchanged (c.f. panel (a)), as they depend on the square of matrix elements (i.e. the vibrations' respective FEIR activities). However, the coherence amplitude is inverted, which could equivalently be described as a π phase-shift to the coherence evolution cycle depicted in Figure 2.14. As a result, the total spectrum is subject to destructive interference between the population and coherence features at $\tau_{\text{enc}} = 0$ fs. In this example the modes have equal FEIR activity, so this destructive interference is complete, as can be seen by the total cancellation of two-pulse signal at $\tau_{\text{enc}} = 0$ fs in Figure 2.15(i). Instead, the two-pulse signal is peaked at the first half-cycle of the coherence phase evolution near $\tau_{\text{enc}} \sim 250$ fs, where the spectrum's lineshape is also fully absorptive.

Chapter 3

Finite-pulse effects

3.1 Overview

So far we have discussed the theoretical description of FEIR signals within the impulsive limit, that is, with pulses that are essentially infinitely short compared to the system and bath dynamics encoded in the response function. This was done by simply isolating the desired pathways from the response function and replacing the relevant evolution times by the experimental inter-pulse delays. Formally, this procedure involves first selecting the pathways that contribute to the signal under the RWA (while discarding the rest), and then assigning delta function pulse envelopes to the electric fields in the multiple convolution integrals. Assuming the impulsive limit, as is commonly done in modelling ultrafast time-domain nonlinear experiments, is for the most part a convenience that simplifies the problem, rather than a good physical approximation. In fact, the effect of the actual pulses used in experiment can have an enormous impact on the appearance of the measured signals. Some of the most apparent effects are caused by the pulses' finite spectral bandwidth, which effectively windows the system response in the frequency domain and thereby distorts spectra,^{141,159,160}

or their finite duration, which modifies the apparent system dynamics measured in the time-domain.^{64,161–163} These two types of effects are in general connected by a Fourier transform relation, and occur simultaneously in a measurement. Perhaps less intuitive, but no less important, are effects involving distortions due to non-uniform spectral phase, i.e. when pulses are not transform-limited.^{164–166} Another class of artifacts emerges from the presence of ‘improperly’ time-ordered light-matter interactions, most notably occurring when pulses overlap in time and the desired sequentiality of interaction cannot be enforced. Some examples are the perturbed free-induction decay contribution and “coherence spike” in transient absorption spectra,^{167–169} or various distortions to absorptive 2D spectra from the spurious mixing of rephasing, non-rephasing, and double-quantum coherence pathways.^{160,170–172}

Coherently-detected nonlinear experiments are also often affected by other signal contributions not originating from the spectroscopic response of the system of interest, for example arising instead from the solvent or sample cell substrates. These contributions are often non-resonant with the incident fields, and therefore occur during pulse overlap where they can overwhelm the desired experimental signal. Some common examples include cross-phase modulation of the probe field,¹⁷³ and multi-photon absorption or stimulated Raman scattering from the solvent and/or windows.^{174,175} As these processes are not described by the response function of the system in question, they present an additional layer of complexity in the task of achieving quantitative agreement between the measured and modelled data, and therefore limit the utility and pay-off of incorporating finite pulse effects for realistic simulation of early-time signals.

It is often claimed that action-based techniques, specifically those employing fluorescence detection, are immune to these non-resonant pulse-overlap artifacts because the fluorescence signal comes unambiguously from the spectroscopic system being targeted.^{94,117,137,142,176}

While it is true that this ability to selectively sample the system does preclude many of the pulse-overlap artifacts mentioned above and is an important advantage of fluorescence-detected experiments, it is still possible for undesired processes to influence the system’s target population—and hence fluorescence signal—during pulse-overlap. One important example is multi-photon excitation proceeding through virtual states, i.e. non-resonant with the real intermediate system states that are of spectroscopic interest. Therefore it can still be difficult to interpret early-time data in the pulse-overlap region, especially when also considering the misordered system response. In FEIR spectroscopy, vibrationally-nonresonant IR + visible two-photon absorption is an example of such a pulse-overlap artifact that can contribute to early-time data, and will be discussed in Section 3.7.

Understanding the effects of real pulses in FEIR experiments is especially important for a number of reasons. First and foremost, the aim of single-molecule detection sensitivity dictates achieving the largest possible signal levels, which invariably occur at early encoding delays—often within the pulse-overlap region—before the vibrational excitation has significantly relaxed. Data in this early-time region is most susceptible to the combination of finite-pulse effects introduced above, and its interpretation therefore benefits the most from incorporating these effects into response function simulations. Specifically, the problem of where the largest signal is located along the encoding delay, which is strongly influenced by the interference of population and coherence contributions in multimode measurements, is especially sensitive to finite-pulse effects.

Second, the 150-350 fs IR and visible pulses used in our FEIR experiments—durations longer than those typically used in modern ultrafast spectroscopies in both the IR and visible regions—are in practice not all that much shorter than some of the vibrational dynamics of the chromophores being studied. As a result, finite-pulse effects are expected to be quite

dramatic in the measured signals. While the choice of pulse durations for our FEIR experiments is partly constrained from a practical standpoint by the instrumentation currently at hand, in general it would not be desirable to use significantly shorter pulses. Specifically, a fundamental limitation arises from the correspondingly broad spectral bandwidth of the visible encoding pulse, which would degrade the spectral selectivity of FEIR against direct one-photon excitation due to its overlap with the red-wing of the electronic absorption line-shape. As a result, high-quality FEIR experiments cannot be done with, for example, the truly ultrafast ~ 10 fs visible pulses with corresponding bandwidths well over 1000 cm^{-1} now standard in femtosecond electronic spectroscopy.

Along similar lines, a third reason to understand finite-pulse effects is to explore avenues for maximizing single-molecule FEIR efficiencies through optimal pulse design. The primary importance of maximizing overall efficiency alters the fundamental strategy in FEIR excitation from that typical of conventional ultrafast spectroscopies—that is, to approach the impulsive limit with the shortest possible pulses in order to directly measure the unadulterated system response function. In contrast, an FEIR excitation scheme that optimizes the excitation rate per molecule at the expense of imprinting the pulse characteristics into the data would in principle be desirable, provided that the resulting signal can still be interpreted to reveal the sought after molecule information.

Incorporating finite-pulse effects into a response function calculation presents two main challenges: (1) accounting for all possible time-orderings of light-matter interactions supported by the pulses at any given set of inter-pulse delays, and (2) evaluating the multiple time-convolution integrals of the pulse electric fields against the response function. For fully-degenerate techniques, this first consideration is a combinatorial problem that can often become overwhelming. In contrast, the resonance conditions of FEIR spectroscopy

significantly limit the number of pathways that can contribute, which greatly simplifies this mixed time-ordering situation. We address this first aspect of the problem in Section 3.2 by transforming to a set of pulse-specific time variables introduced by Jonas and co-workers.¹²⁹ Section 3.3 describes the relevant finite pulse characteristics and lays out notation for their incorporation in the calculation. The second issue of performing the integration is computationally challenging due to its high dimensionality. Specifically, four nested convolution integrals are required to compute the target population in FEIR. Our approach, described in Section 3.4, is to use a numerical Monte Carlo integration procedure. In principle, Monte Carlo integration with optimized sampling schemes can greatly outperform conventional deterministic integration in high dimensional problems. However, our current approach uses simple uniform sampling and is advantageous primarily due to its simplicity. Section 3.5 then demonstrates some of the most salient finite-pulse effects from calculations on a simple two-mode model system, while Section 3.6 discusses a lineshape distortion that occurs within the IR/Vis pulse-overlap region.

3.2 Mixed time-ordering in the response function convolution integrals

Calculating the final target population, and hence FEIR signal, generated by finite-duration pulses requires evaluating the multiple convolution integrals against the response function

$$\begin{aligned} \bar{N}^{(4)} \equiv \lim_{t \rightarrow \infty} N^{(4)}(t) &= \int_{-\infty}^{\infty} dt_4 \int_0^{\infty} d\tau_3 \int_0^{\infty} d\tau_2 \int_0^{\infty} d\tau_1 R^{(4)}(\tau_3, \tau_2, \tau_1) \\ &\quad \times E(t_4)E(t_4 - \tau_3)E(t_4 - \tau_3 - \tau_2)E(t_4 - \tau_3 - \tau_2 - \tau_1). \end{aligned} \quad (3.1)$$

Here we have reverted to the most general case where the four fields in the product each represent the sum of all pulses, in order to allow for all possible time-orderings to contribute to the response (c.f. Eq. 2.99 in Chapter 2). For simplicity of notation we have suppressed the tensorial nature of the response function and electric fields vectors.

We recall that the perturbation-theoretic delays τ_i in this expression are fully time-ordered, e.g. the τ_2 interval must always proceed the τ_1 interval etc., regardless of the sequence of the pulse envelopes. To separate the different time-ordered contributions permitted for an arbitrary set of inter-pulse delays and durations, we will recast the integration in terms of partially time-ordered ‘pulse-specific’ light-matter interaction time variables (Figure 3.1).¹²⁹ First, to avoid confusion between the identities of each pulse when considering their different possible orderings, we will rename each pulse electric field in the sequence as follows: the IR pulse from the moving arm of the interferometer $E_1 \equiv E_a$, the IR pulse from the stationary arm $E_2 \equiv E_b$, and the visible encoding pulse $E_3 \equiv E_c$. The total electric field is given by

$$E(t) = E_c(t) + E_b(t + \tau_{\text{enc}}) + E_a(t + \tau_{\text{enc}} + \tau_{\text{IR}}). \quad (3.2)$$

As shown in Figure 3.1, the pulse-specific interaction delay τ_α for $\alpha = a, b, c$ specifies the time-delay between the perturbation-theoretic light-matter interaction facilitated by pulse E_α and the final interaction with the encoding pulse E_c at time t_4 . Each pulse-specific delay is causally restricted to positive values, however they can assume any relative ordering among themselves. The final interaction time t_4 is not a causally restricted interval, and occurs anywhere within the profile of E_c . The relationship between these pulse-specific interaction delays and the conventional, fully-time-ordered variables t_i and τ_i introduced early are shown in Figure 3.1a in the case of a well-separated, properly-ordered pulse sequence.

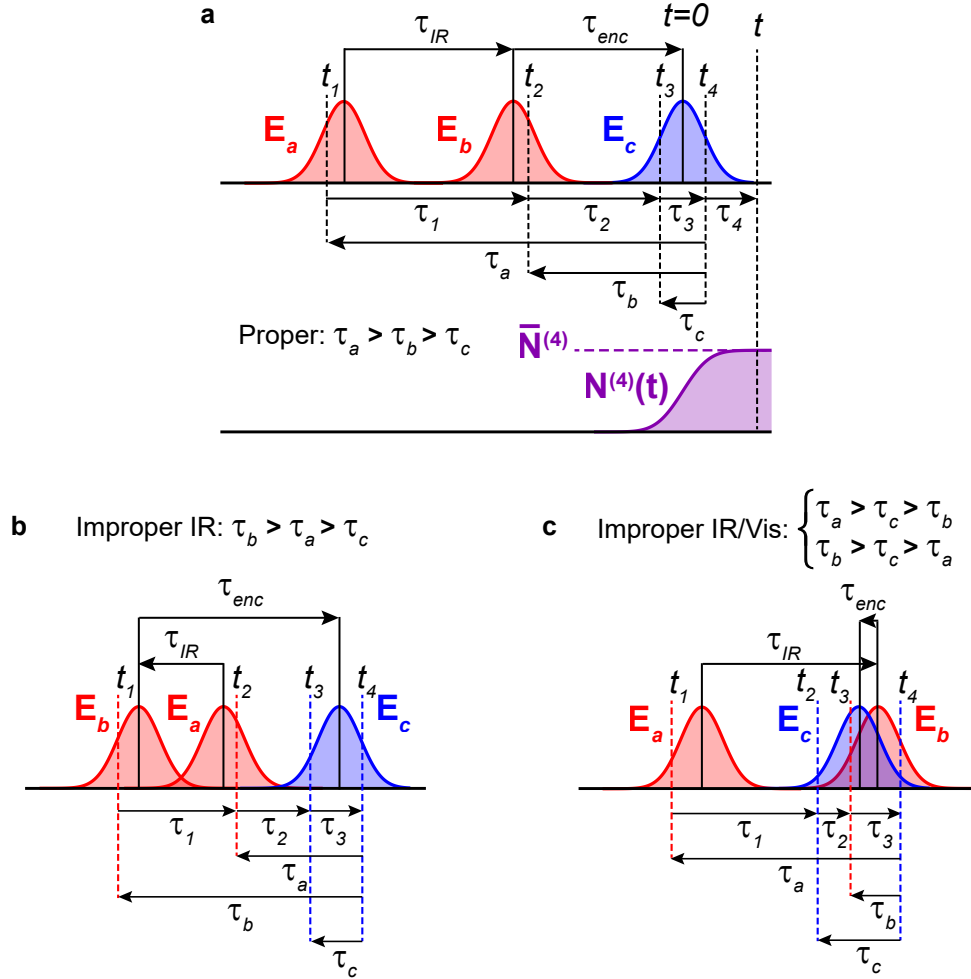


Figure 3.1: Pulse-specific interaction time variables τ_α and their relationship to the fully time-ordered light-matter interaction times t_i and time-delays τ_i . (a) Relationship between all sets of time variables in the properly time-ordered case $\tau_a < \tau_b < \tau_c$ with well-separated pulses obeying $\tau_{IR} > 0$ and $\tau_{enc} > 0$. (b) Improperly-ordered IR interactions $\tau_b < \tau_a < \tau_c$ with $\tau_{IR} < 0$. (c) Improperly-ordered IR-vis-IR-vis interaction when $|\tau_{enc}| < \tau_p$, where τ_p is the longer of the IR and visible pulses. Specifically shown is the case $\tau_a > \tau_c > \tau_b$ with $\tau_{enc} < 0$ and $\tau_{IR} > |\tau_{enc}|$.

Two IR and two visible light-matter interactions are always required in FEIR, so the product of real-valued electric fields in Eq. 3.1 can be written in terms of pulse-specific

delays as

$$E_c(t_4)E_c(t_4 - \tau_c)E_b(t_4 + \tau_{\text{enc}} - \tau_b)E_a(t_4 + \tau_{\text{enc}} + \tau_{\text{IR}} - \tau_a). \quad (3.3)$$

Specifically, this field product describes the three-pulse signal $F_{12}(\tau_{\text{IR}}, \tau_{\text{enc}})$ (Eq. 2.106), where each of the two IR pulses contributes one interaction. However, as the two IR pulses are identical copies, to calculate the two-pulse signal we can simply set $\tau_{\text{IR}} = 0$ in Eq. 3.3 (i.e. using Eq. 2.107). With the pulse-specific time variables, this field product handles all possible time-orderings of light-matter interactions allowed by the resonance conditions and system level structure. The task of keeping track of these different time-orderings is in turn accorded to the response function and will be tackled next.

As discussed in Chapter 2, to apply the RWA we decompose each real-valued pulse electric field into its complex positive and negative frequency components

$$E_\alpha(t) = E_\alpha^+(t) + E_\alpha^-(t), \quad (3.4a)$$

$$E_\alpha^+(t) = \frac{1}{2}e_\alpha(t)e^{-i\omega_\alpha t}, \quad (3.4b)$$

$$E_\alpha^-(t) = (E_\alpha^+)^*, \quad (3.4c)$$

where ω_α is the center frequency, $e_\alpha(t)$ is the (in general complex) pulse envelope, and $\alpha = a, b, c$. Specifically,

$$\omega_a = \omega_b = \omega_{\text{IR}}, \quad (3.5)$$

$$\omega_c = \omega_{\text{vis}}. \quad (3.6)$$

The specific characteristics of these fields, including temporal profile, spectrum, and spectral

phase, will be discussed in Section 3.3. In general, we will assume that each field's temporal envelope $e_\alpha(t)$ is a pulse of characteristic duration $\sim \tau_{p,\alpha}$.

Expanding each real-valued field in Eq. 3.3 into its pair of counter-rotating complex parts via Eq. 3.4 yields $2^4 = 16$ terms. Our analysis of the FEIR response function in Chapter 2 established that each response pathway must involve four absorptive interactions: one bra/ket-side pair resonant with the IR and the other bra/ket-side pair resonant with the visible. As a result there are only two unique choices (up to complex conjugation) of the product of four complex fields that can contribute within the RWA, which we will term E_I and E_{II} :

$$\begin{aligned}
 E_I(\tau_{\text{IR}}, \tau_{\text{enc}}, t_4, \tau_c, \tau_b, \tau_a) &\equiv E_c^+(t_4)E_c^-(t_4 - \tau_c)E_b^-(t_4 + \tau_{\text{enc}} - \tau_b)E_a^+(t_4 + \tau_{\text{enc}} + \tau_{\text{IR}} - \tau_a) \\
 &= e_c(t_4)e_c^*(t_4 - \tau_c)e_b^*(t_4 + \tau_{\text{enc}} - \tau_b)e_a(t_4 + \tau_{\text{enc}} + \tau_{\text{IR}} - \tau_a) \\
 &\quad \times e^{-i\omega_{\text{vis}}\tau_c}e^{i\omega_{\text{IR}}(\tau_a - \tau_b)}e^{-i\omega_{\text{IR}}\tau_{\text{IR}}}, \quad (3.7a)
 \end{aligned}$$

$$\begin{aligned}
 E_{II}(\tau_{\text{IR}}, \tau_{\text{enc}}, t_4, \tau_c, \tau_b, \tau_a) &\equiv E_c^-(t_4)E_c^+(t_4 - \tau_c)E_b^-(t_4 + \tau_{\text{enc}} - \tau_b)E_a^+(t_4 + \tau_{\text{enc}} + \tau_{\text{IR}} - \tau_a) \\
 &= e_c^*(t_4)e_c(t_4 - \tau_c)e_b^*(t_4 + \tau_{\text{enc}} - \tau_b)e_a(t_4 + \tau_{\text{enc}} + \tau_{\text{IR}} - \tau_a) \\
 &\quad \times e^{i\omega_{\text{vis}}\tau_c}e^{i\omega_{\text{IR}}(\tau_a - \tau_b)}e^{-i\omega_{\text{IR}}\tau_{\text{IR}}}. \quad (3.7b)
 \end{aligned}$$

These field combinations differ in the ordering of the two oppositely-signed encoding field carriers.

The total response $\bar{N}^{(4)}(\tau_{\text{IR}}, \tau_{\text{enc}})$ is then expressed as the sum of the two real-valued contributions which result from these two field combinations

$$\bar{N}^{(4)}(\tau_{\text{IR}}, \tau_{\text{enc}}) = \bar{N}_{\text{I}}^{(4)}(\tau_{\text{IR}}, \tau_{\text{enc}}) + \bar{N}_{\text{II}}^{(4)}(\tau_{\text{IR}}, \tau_{\text{enc}}), \quad (3.8a)$$

$$\begin{aligned} \bar{N}_{\text{I}}^{(4)}(\tau_{\text{IR}}, \tau_{\text{enc}}) = & \int_{-\infty}^{\infty} dt_4 \int_0^{\infty} d\tau_c \int_0^{\infty} d\tau_b \int_0^{\infty} d\tau_a \\ & \times S_{\text{I}}^{(4)}(\tau_c, \tau_b, \tau_a) E_{\text{I}}(\tau_{\text{IR}}, \tau_{\text{enc}}, t_4, \tau_c, \tau_b, \tau_a) + c.c., \end{aligned} \quad (3.8b)$$

$$\begin{aligned} \bar{N}_{\text{II}}^{(4)}(\tau_{\text{IR}}, \tau_{\text{enc}}) = & \int_{-\infty}^{\infty} dt_4 \int_0^{\infty} d\tau_c \int_0^{\infty} d\tau_b \int_0^{\infty} d\tau_a \\ & \times S_{\text{II}}^{(4)}(\tau_c, \tau_b, \tau_a) E_{\text{II}}(\tau_{\text{IR}}, \tau_{\text{enc}}, t_4, \tau_c, \tau_b, \tau_a) + c.c. \end{aligned} \quad (3.8c)$$

The ‘mixed’ response functions $S_{\text{I}}^{(4)}$ and $S_{\text{II}}^{(4)}$ (explicit expressions given in Eq. 3.9) are piecewise functions of the different time-orderings of pulse-specific delays that account for the switching between pathways depending on the sequentiality of field interactions. Table 3.1 summarizes the ‘recipe’ for their construction in terms of the correlation functions and fully time-ordered interaction delays, while Figure 3.2 shows every double-sided Feynman diagram (excluding complex conjugates) contributing to $\bar{N}_{\text{I}}^{(4)}$ and $\bar{N}_{\text{II}}^{(4)}$ for the single-oscillator system discussed in Section 2.4.4 of Chapter 2.

In general, there are 6 permutations for ordering the delays τ_a, τ_b , and τ_c . We will first consider the two orderings in which both IR interactions precede the visible encoding interactions. The *abc* ordering, i.e. $\tau_a > \tau_b > \tau_c$, represents the ‘proper’ sequence of interaction which occurs for well-separated pulses with $\tau_{\text{IR}} > 0$ and $\tau_{\text{enc}} > 0$ (Figure 3.1a). Measuring Fourier transform FEIR spectra via the three-pulse signal uses one-sided time-domain data with $\tau_{\text{IR}} > 0$, so this situation reflects the dominant ordering, and is the only ordering that needs to be considered in the impulsive limit. For this ordering, contribution I is

Interaction order	RWA conjugate to E_I	RWA conjugate to E_{II}	τ_1	τ_2	τ_3
$\tau_a \geq \tau_b \geq \tau_c$	$C_2(\tau_3, \tau_2, \tau_1)$	$C_1(\tau_3, \tau_2, \tau_1)$	$\tau_a - \tau_b$	$\tau_b - \tau_c$	τ_c
$\tau_b > \tau_a \geq \tau_c$	$C_1^*(\tau_3, \tau_2, \tau_1)$	$C_2^*(\tau_3, \tau_2, \tau_1)$	$\tau_b - \tau_a$	$\tau_a - \tau_c$	τ_c
$\tau_a \geq \tau_c > \tau_b$	0	$C_3(\tau_3, \tau_2, \tau_1)$	$\tau_a - \tau_c$	$\tau_c - \tau_b$	τ_b
$\tau_b > \tau_c \geq \tau_a$	$C_3^*(\tau_3, \tau_2, \tau_1)$	0	$\tau_b - \tau_c$	$\tau_c - \tau_a$	τ_a
$\tau_c \geq \tau_a > \tau_b$	0	0	$\tau_c - \tau_a$	$\tau_a - \tau_b$	τ_b
$\tau_c > \tau_b > \tau_a$	0	0	$\tau_c - \tau_b$	$\tau_b - \tau_a$	τ_a

Table 3.1: RWA conjugated pathways for each pulse interaction order and their corresponding time arguments in terms of pulse interaction delays.

comprised of rephasing pathways (C_2), while contribution II is non-rephasing (C_1). This can be seen, for example, by inspection of the diagrams in Figure 3.2. The *bac* ordering, i.e. the ‘improper IR’ ordering when the stationary IR pulse E_b contributes the first interaction, dominates for $\tau_{IR} < 0$ (Figure 3.1b). As stated above, the $\tau_{IR} < 0$ range is not used when processing three-pulse data, because the τ_1 and τ_2 evolution periods are being varied simultaneously. However, the *bac* ordering does contribute to the measured signal within the IR pulse-pair overlap region when $0 < \tau_{IR} \lesssim \tau_{p,a} = \tau_{p,b}$, and therefore cannot be ignored. Here the rephasing/non-rephasing identity of I and II are switched, as the ordering of the two IR interactions are reversed (Figure 3.2).

Next, we have the two mixed IR-Vis-IR-Vis orderings *acb* and *bca*. Both orderings can only occur during IR/Vis pulse overlap, i.e. for $|\tau_{enc}| \lesssim \tau_p$ (Figure 3.1c). Both involve the double-quantum coherence correlation function C_3 , which is a fundamentally different kind of excitation pathway compared to the ‘proper’ FEIR pathways C_1 and C_2 . Importantly, because the two visible interactions occur with the same pulse but are not directly sequential, the system evolution periods are no longer simply connected to the experimentally-controlled

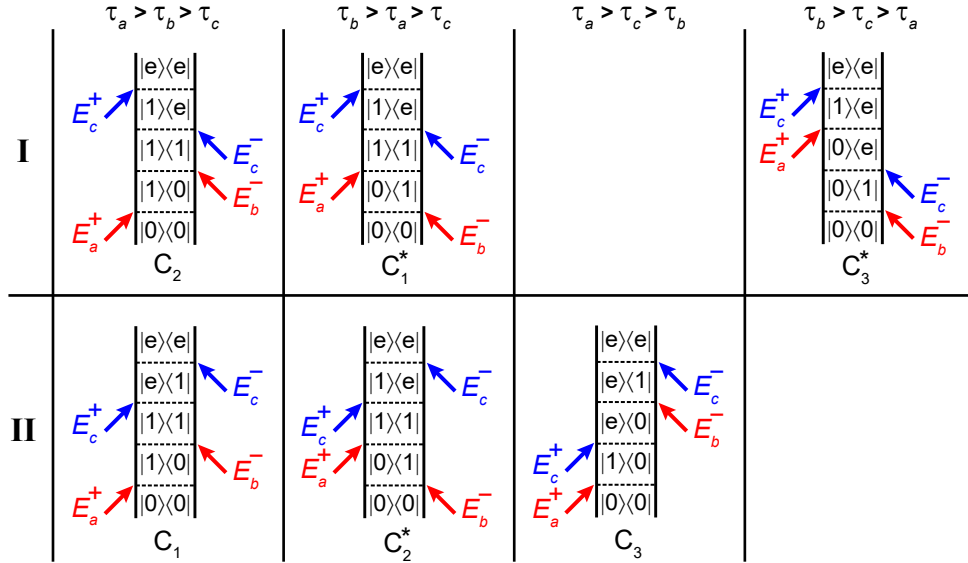


Figure 3.2: Diagrams (excluding complex conjugates) for all contributing orderings of light-matter interactions for a three-level system. For a generic multimode system more diagrams exist within each correlation function, but this general structure holds.

inter-pulse delays. As we will see, these contributions will generally not survive the convolution integrals under typical conditions. Finally, the orderings cab and cba involve the visible field interacting first, and therefore do not contribute under FEIR resonance conditions and can be ignored. For completeness, we give explicit expressions for the mixed response functions below:

$$S_{\text{I}}^{(4)}(\tau_c, \tau_b, \tau_a) = \frac{1}{\hbar^4} \left\{ \begin{array}{ll} C_2(\tau_c, \tau_b - \tau_c, \tau_a - \tau_b) & \tau_a > \tau_b > \tau_c \\ C_1^*(\tau_c, \tau_a - \tau_c, \tau_b - \tau_a) & \tau_b > \tau_a > \tau_c \\ 0 & \tau_a > \tau_c > \tau_b \\ C_3^*(\tau_b, \tau_c - \tau_b, \tau_a - \tau_c) & \tau_c > \tau_a > \tau_b \\ 0 & \tau_c > \tau_a > \tau_b \\ 0 & \tau_c > \tau_b > \tau_a \end{array} \right. , \quad (3.9a)$$

$$S_{\text{II}}^{(4)}(\tau_c, \tau_b, \tau_a) = \frac{1}{\hbar^4} \left\{ \begin{array}{ll} C_1(\tau_c, \tau_b - \tau_c, \tau_a - \tau_b) & \tau_a > \tau_b > \tau_c \\ C_2^*(\tau_c, \tau_a - \tau_c, \tau_b - \tau_a) & \tau_b > \tau_a > \tau_c \\ C_3(\tau_b, \tau_c - \tau_b, \tau_a - \tau_c) & \tau_a > \tau_c > \tau_b \\ 0 & \tau_c > \tau_a > \tau_b \\ 0 & \tau_c > \tau_a > \tau_b \\ 0 & \tau_c > \tau_b > \tau_a \end{array} \right. . \quad (3.9b)$$

The positive-valued integration ranges of the τ_α enforce causality, so the usual heaviside step-functions do not need to be included.

The RWA is fully incorporated in the integrands of the I and II contributions. For example, we can see this by considering the explicit expression for contribution I

$$\begin{aligned}
 \bar{N}_I^{(4)}(\tau_{\text{IR}}, \tau_{\text{enc}}) &= e^{-i\omega_{\text{IR}}\tau_{\text{IR}}} \int_{-\infty}^{\infty} dt_4 \int_0^{\infty} d\tau_c \int_0^{\infty} d\tau_b \int_0^{\infty} d\tau_a \\
 &\quad \times S_I^{(4)}(\tau_c, \tau_b, \tau_a) e^{-i\omega_{\text{vis}}\tau_c} e^{i\omega_{\text{IR}}(\tau_a - \tau_b)} \\
 &\quad \times e_c(t_4) e_c^*(t_4 - \tau_c) e_b^*(t_4 + \tau_{\text{enc}} - \tau_b) e_a(t_4 + \tau_{\text{enc}} + \tau_{\text{IR}} - \tau_a) + c.c.,
 \end{aligned} \tag{3.10}$$

and specifically examining the *abc* time-ordering where $S_I^{(4)}(\tau_c, \tau_b, \tau_a) = C_2(\tau_c, \tau_b - \tau_c, \tau_a - \tau_b)$. For our three-level system (Eq. 2.110) this correlation function oscillates as $\exp[i(\omega_{e0} - \omega_{10})\tau_c - i\omega_{10}(\tau_a - \tau_b)]$, while the complex field phase-factors oscillate as $\exp[-i\omega_{\text{vis}}\tau_c + i\omega_{\text{IR}}(\tau_a - \tau_b)]$. On resonance when $\omega_{\text{IR}} \approx \omega_{10}$ and $\omega_{\text{vis}} \approx \omega_{e0} - \omega_{10}$, these complex phase oscillations approximately cancel out, leaving behind a slowly varying function of the integration variables that therefore survives the integration.

We also note that Eq. 3.10 (and the analogous expression for $\bar{N}_{\text{II}}^{(4)}(\tau_{\text{IR}}, \tau_{\text{enc}})$) is modulated by the IR carrier phase $\omega_{\text{IR}}\tau_{\text{IR}}$ outside of the integrals, which reflects the interferometric excitation by the IR pulse-pair. Explicitly, we can write these expressions for $m = \text{I}$ or II as

$$\bar{N}_m^{(4)}(\tau_{\text{IR}}, \tau_{\text{enc}}) = \mathcal{N}_m^{(4)}(\tau_{\text{IR}}, \tau_{\text{enc}}) e^{-i\omega_{\text{IR}}\tau_{\text{IR}}} + \left(\mathcal{N}_m^{(4)}(\tau_{\text{IR}}, \tau_{\text{enc}})\right)^* e^{i\omega_{\text{IR}}\tau_{\text{IR}}} \tag{3.11a}$$

where

$$\begin{aligned} \mathcal{N}_I^{(4)}(\tau_{\text{IR}}, \tau_{\text{enc}}) &= \int_{-\infty}^{\infty} dt_4 \int_0^{\infty} d\tau_c \int_0^{\infty} d\tau_b \int_0^{\infty} d\tau_a \\ &\quad \times S_I^{(4)}(\tau_c, \tau_b, \tau_a) e^{-i\omega_{\text{vis}}\tau_c} e^{i\omega_{\text{IR}}(\tau_a - \tau_b)} \\ &\quad \times e_c(t_4) e_c^*(t_4 - \tau_c) e_b^*(t_4 + \tau_{\text{enc}} - \tau_b) e_a(t_4 + \tau_{\text{enc}} + \tau_{\text{IR}} - \tau_a) \end{aligned} \quad (3.11b)$$

$$\begin{aligned} \mathcal{N}_{II}^{(4)}(\tau_{\text{IR}}, \tau_{\text{enc}}) &= \int_{-\infty}^{\infty} dt_4 \int_0^{\infty} d\tau_c \int_0^{\infty} d\tau_b \int_0^{\infty} d\tau_a \\ &\quad \times S_{II}^{(4)}(\tau_c, \tau_b, \tau_a) e^{i\omega_{\text{vis}}\tau_c} e^{i\omega_{\text{IR}}(\tau_a - \tau_b)} \\ &\quad \times e_c^*(t_4) e_c(t_4 - \tau_c) e_b^*(t_4 + \tau_{\text{enc}} - \tau_b) e_a(t_4 + \tau_{\text{enc}} + \tau_{\text{IR}} - \tau_a). \end{aligned} \quad (3.11c)$$

These functions $\mathcal{N}_m^{(4)}(\tau_{\text{IR}}, \tau_{\text{enc}})$ can be interpreted as the complex analytic envelopes of the $m = \text{I}$ or II contributions to the three-pulse signal. In practice, to calculate the three-pulse signal we only need to calculate its complex envelope,

$$\mathcal{N}^{(4)}(\tau_{\text{IR}}, \tau_{\text{enc}}) = \sum_{m=\text{I,II}} \mathcal{N}_m^{(4)}(\tau_{\text{IR}}, \tau_{\text{enc}}), \quad (3.12)$$

which evolves slowly in τ_{IR} and can therefore be sampled much more sparsely. Specifically, the sampling interval only needs to be Nyquist for the difference frequency between the highest and lowest frequency features in the response. This corresponds to working in a ‘fully-rotating’ frame where the carrier ω_{IR} is referenced to zero.^{157,177,178} For the two-pulse signal, $\tau_{\text{IR}} = 0$ and the envelope is real with $\bar{N}^{(4)}(\tau_{\text{enc}}) = 2\mathcal{N}^{(4)}(\tau_{\text{enc}})$.

3.3 Pulse characteristics

We will define our pulses in the frequency domain as

$$\tilde{E}_\alpha(\omega) = A_\alpha(\omega)e^{i\Phi_\alpha(\omega)}, \quad (3.13)$$

where $A_\alpha(\omega)$ and $\Phi_\alpha(\omega)$ are real-valued functions describing the spectral amplitude and phase of pulse $\alpha = a, b$, or c , respectively. The frequency- and time-domain representations of the pulse electric fields are related by Fourier transformation

$$\tilde{E}_\alpha(\omega) = \int_{-\infty}^{\infty} E_\alpha(t)e^{i\omega t} dt, \quad (3.14a)$$

$$E_\alpha(t) = \frac{1}{2\pi} \int_{-\infty}^{\infty} \tilde{E}_\alpha(\omega)e^{-i\omega t} d\omega. \quad (3.14b)$$

The pulse spectrum is defined as the field's frequency-domain power spectrum

$$|\tilde{E}_\alpha(\omega)|^2 = A_\alpha(\omega)^2. \quad (3.15)$$

The reality of the time-domain electric field imposes the condition

$$\tilde{E}_\alpha(\omega) = \tilde{E}_\alpha^*(-\omega), \quad (3.16)$$

and for brevity in what follows we will only explicitly address the positive frequency portion. For simplicity, we will define our pulses to have Gaussian spectra with spectral bandwidth characterized by fwhm $\Delta\omega_\alpha$

$$|\tilde{E}_\alpha(\omega)|^2 = \left(A_{\alpha,0} \exp(-2 \ln(2) (\omega - \omega_\alpha)^2 / \Delta\omega_\alpha^2) \right)^2, \quad (3.17)$$

where ω_α is the center frequency and $A_{\alpha,0}$ the spectral amplitude. The spectral phase is described by the power series expansion

$$\Phi_\alpha(\omega) = \frac{\gamma_{\alpha,2}}{2!}(\omega - \omega_\alpha)^2 + \frac{\gamma_{\alpha,3}}{3!}(\omega - \omega_\alpha)^3 + \dots \quad (3.18)$$

The 2nd-order dispersion, $\gamma_{\alpha,2}$, and 3rd-order dispersion, $\gamma_{\alpha,3}$, are conventionally expressed in units of fs² and fs³, respectively. With the frequency expressed in cm⁻¹, a multiplier of $2\pi c_0$ on the frequency is required for numerical evaluation in this case. The 0th- and 1st-order terms would describe the carrier-envelope phase and a uniform temporal displacement, respectively, and are ignored.¹⁷⁹

The positive frequency component $E_\alpha^+(t)$ of the time-domain field (Eq. 3.4) is, as its name suggests, given by the one-sided Fourier transform of just the positive frequencies

$$E_\alpha^+(t) = \frac{1}{\pi} \int_0^\infty \tilde{E}_\alpha(\omega) e^{-i\omega t} d\omega. \quad (3.19)$$

Formally, $E_\alpha^+(t)$ is the complex analytic representation of the real time-domain electric field.^{133,180} Our specific decomposition of this complex field into envelope and carrier in Eq. 3.4, and repeated here for convenience,

$$E_\alpha^+(t) = \frac{1}{2} e_\alpha(t) e^{-i\omega_\alpha t} \quad (3.20)$$

uses the same center frequency ω_α as the spectrum. It is worth making some comments about this decomposition, as in general the separation of amplitude- and phase-modulation effects in an arbitrary time-dependent waveform is not unique. The temporal envelope $e_\alpha(t)$

is in general complex and can be expressed as

$$e_\alpha(t) = \mathcal{E}_\alpha(t)e^{i\phi_\alpha(t)}, \quad (3.21)$$

where $\mathcal{E}_\alpha(t)$ is a real-valued temporal amplitude function and $\phi_\alpha(t)$ is a real-valued temporal phase function. Because $\mathcal{E}_\alpha(t) = 2|E_\alpha^+(t)|$, the complex analytic representation uniquely determines the temporal amplitude. However, $\phi_\alpha(t)$ is arbitrary up to an additive factor of $\omega't$ for any shift ω' , provided the carrier phase $\omega_\alpha t$ in Eq. 3.20 is accordingly modified by $-\omega't$. This reflects the formally arbitrary assignment of the carrier frequency. However, it can be shown generally that defining ω_α as the mean of the $\omega > 0$ half of $|\tilde{E}_\alpha(\omega)|^2$ produces the slowest-varying complex analytic envelope $e_\alpha(t)$ in the mean-squared sense, and is therefore in some sense the ‘best’ choice of carrier frequency.^{133,181}

If the pulse is transform-limited, i.e. the spectral phase $\Phi_\alpha(\omega) = 0$, then the temporal phase $\phi_\alpha(t) = 0$ as well, and the envelope function is real. For our Gaussian pulse spectrum this transform-limited envelope is also a Gaussian

$$e_\alpha(t) = e_{\alpha,0} \exp(-2 \ln(2) t^2 / \tau_{p,\alpha}^2), \quad (3.22)$$

where the pulse duration $\tau_{p,\alpha}$ is defined as the fwhm of the intensity profile $|e_\alpha(t)|^2$ and $e_{\alpha,0}$ is the peak field amplitude. For non-transform-limited pulses, the temporal amplitude and phase functions each depend on both the spectrum and spectral phase in more complicated ways. In general the temporal fwhm of the intensity profile is related to the fwhm bandwidth by

$$\tau_{p,\alpha} \Delta\omega_\alpha \geq \frac{2 \ln(2)}{\pi}, \quad (3.23)$$

where the equality hold for the transform-limited Gaussian case.¹⁷⁹ Using this expression with numerical values for $\tau_{p,\alpha}$ in fs and $\Delta\omega_\alpha$ in cm^{-1} requires an additional factor of c_0 on the left-hand side.

3.4 Numerical evaluation by Monte Carlo integration

With sufficiently flexible expressions for the convolution integrals in place, all that remains is their brute-force numerical evaluation. For this purpose, we will use a Monte Carlo integration method that is straightforward to implement for our problem. The traditional deterministic approach to numerical integration divides up the entire integration region into a grid of sufficiently small bins over which the integrand can be either treated as a constant, or approximated by a more complicated quadrature rule. As the number of grid points that must be calculated scales exponentially in the dimensionality of the integral, these deterministic methods are in general difficult to apply to high dimensional problems. On the other hand, Monte Carlo integration instead operates by drawing random samples of the integrand over the integration region.¹⁸² This approach is therefore agnostic to dimensionality both in terms of scaling and practical implementation. In particular, the complicated piece-wise structure of the mixed response functions would be tricky to scan through deterministically, but are straightforward to sample randomly.

Suppose we wish to integrate the function $f(\mathbf{X})$ over some region Ω ,

$$I = \int_{\Omega} f(\mathbf{X})d\mathbf{X}, \quad (3.24)$$

where in general \mathbf{X} is a multidimensional variable and Ω is a correspondingly multidimensional region with volume $V = \int_{\Omega} d\mathbf{X}$. The basic premise of Monte Carlo integration is to

construct an estimator of this integral

$$I_N = \frac{V}{N} \sum_{i=1}^N f(\mathbf{X}_i) \quad (3.25)$$

where $\mathbf{X}_1, \dots, \mathbf{X}_N \in \Omega$ are points uniformly sampled from the integration region. According to the law of large numbers

$$I = \lim_{N \rightarrow \infty} I_N, \quad (3.26)$$

and so, in practice, with sufficiently large N the Monte Carlo estimate I_N should provide a sufficiently good value for I . Specifically, it can be shown that the error, $I - I_N$, scales as $\sim N^{-1/2}$.¹⁸² While this convergence might be somewhat slow, it is importantly independent of the dimensionality of the integral, i.e. the quality of numerical evaluation just depends on the amount of sampling. Additionally, I_N is an unbiased estimator, meaning the expectation value of I_N (for finite N) is I . This means that the error on the finitely sampled estimator is random noise without any systematic bias.

The approach codified by Eq. 3.25 is sometimes referred to as ‘naive’ Monte Carlo integration, as the integration region is being sampled uniformly. It is generally understood that the computational time required to achieve convergence for naive Monte Carlo is not lower than for typical deterministic approaches. However, using forms of enhanced sampling that preferentially address the region of the integrand that is known to be large can create considerable advantages in computational cost.¹⁸³ In this thesis we will use the ‘naive’ approach for simplicity, however we expect that improvements via enhanced sampling could be quite useful.

The integration region for the multiple convolutions we wish to evaluate in Eqs. 3.8 is

composed of infinite intervals. However, the pulse envelope functions $e_\alpha(t)$ are essentially zero beyond a few multiples of the pulse duration and therefore effectively window the integrand, so we only need to sample the integration variables within these envelopes. In particular, we use the following sampling ranges

$$t_4 \in [-L\tau_{p,c}, L\tau_{p,c}], \quad (3.27a)$$

$$\tau_c \in [0, L\tau_{p,c}], \quad (3.27b)$$

$$\tau_b \in [\max(0, -L\tau_{p,b} + \tau_{\text{enc}}), L\tau_{p,b} + \tau_{\text{enc}}], \quad (3.27c)$$

$$\tau_a \in [\max(0, -L\tau_{p,a} + \tau_{\text{enc}} + \tau_{\text{IR}}), L\tau_{p,a} + \tau_{\text{enc}} + \tau_{\text{IR}}], \quad (3.27d)$$

where $\tau_{p,\alpha}$ is the fwhm of pulse α 's temporal intensity profile $|e_\alpha(t)|^2$, and L is a multiplier that determines how far out in the profile to sample. We use the value $L = 2.5$, which was used by Jonas and co-workers in their deterministic numerical integration procedure for calculating 3rd-order signals.¹²⁹ We note that using smaller values of L produces faster convergence, as the largest regions of the integrand are being sampled more densely, however significant distortions begin to appear for $L = 1.5$ and lower. The lower range limits of the τ_α in Eq. 3.27 are constrained to be non-negative to enforce causality, and if the inter-pulse delays and pulse durations are such that any of their upper range limits become negative, the value of the integral is simply set to zero.

For every fixed combination of the inter-pulse delays τ_{enc} and τ_{IR} desired, N samples of the 4 integration variables τ_a, τ_b, τ_c , and t_4 are drawn uniformly from their respective ranges, and the Monte Carlo estimates of $\mathcal{N}_m^{(4)}(\tau_{\text{IR}}, \tau_{\text{enc}})$ for $m = \text{I}$ and II are computed via Eq. 3.25, where $f(\mathbf{X})$ represents the integrand in Eq. 3.11(b) or (c). In both cases the volume of the integration region is simply the product of the 4 sampling ranges in Eq.

3.27. Every sample of the integration variables is first categorized by its ordering (abc , bac , etc.), which determines which piece of the mixed response functions (Eq. 3.9) is used to compute the integrand. The correlation functions making up the mixed response functions are expressed analytically in the homogeneous limit (Eq. 2.103) with the RWA conjugate field phase factors directly incorporated, and are evaluated numerically for every sample of the integration variables. The pulses electric fields are specified in the frequency domain via Eq. 3.13, and their envelope functions are computed numerically via FFT. The product of the envelopes is then evaluated by lookup table for each Monte Carlo sample. Depending on the parameters in the response function, the pulse characteristics, and the resonance conditions, typically $N = 10^6$ to 5×10^7 samples are sufficient to achieve reasonable signal to noise.

3.4.1 Two-pulse signal

Figure 3.3 shows an example calculation of the two-pulse signal for the single-oscillator system discussed in Section 2.4.4 of Chapter 2 using the same molecular parameters, i.e. a lifetime-broadened mode at $\omega_{10} = 1600 \text{ cm}^{-1}$ with 1 ps lifetime. The electronic dephasing time of the encoding transition is set to $\Gamma_{e1}^{-1} = 10 \text{ fs}$. We recall that the FEIR response of this system is only composed of population pathways. The pulses are transform-limited with spectra/durations chosen to be representative of the those used in experiment. The IR pulse $E_a = E_b = E_{\text{IR}}$ is set directly on resonance with $\omega_{\text{IR}} = 1600 \text{ cm}^{-1}$ and has $\Delta\omega_{\text{IR}} = 120 \text{ cm}^{-1}$ bandwidth, which produces a transform-limited duration of $\tau_{p,\text{IR}} = 123 \text{ fs}$. The visible encoding pulse $E_c = E_{\text{vis}}$ has $\Delta\omega_{\text{vis}} = 50 \text{ cm}^{-1}$ bandwidth resulting in a 297 fs pulse duration, and is tuned such that the encoding transition is directly on resonance.

Figure 3.3a shows the contributions of the 4 allowed time-orderings abc , bac , acb , and bca overlaid on the impulsive signal, with $N = 5 \times 10^7$ samples used for every τ_{enc} point. Because $\tau_{\text{IR}} = 0$, or equivalently because both IR interactions occur within the same IR pulse profile, the abc and bac contributions are identical within noise. Neither of the misordered IR/Vis contributions acb or bca contribute any amplitude above noise ($\sim 10^{-4}$ times the maximum abc response). The relative frequency of sampling the 4 different time-orderings are shown in Figure 3.3(b), with the intensity profiles of the IR and visible pulses overlaid at $\tau_{\text{enc}} = 0$ for visual reference. We note that the τ_{enc} -dependent appearance of these relative sampling frequencies is influenced by the multiplier L , and is not indicative of the weight of the different time-orderings in the signal, but merely reflects how often they are sampled by the Monte Carlo algorithm.

The full two-pulse signal is the sum over all time-orderings, and therefore resembles the abc and bac contributions. Overall, the appearance of this finite-pulse signal is consistent with the convolution of the impulsive signal with an instrument response of duration given by the temporal cross-correlation of the IR and visible intensity profiles, $\sqrt{\tau_{p,\text{IR}}^2 + \tau_{p,\text{vis}}^2} = 321$ fs. Namely, the signal rises to roughly half its maximum by $\tau_{\text{enc}} = 0$, and is peaked at ~ 300 fs. Because the pulse cross-correlation is meaningfully shorter than the vibrational lifetime, the decay of the signal beyond the pulse-overlap region is still a good measure of the system's population relaxation kinetics.

3.4.2 Three-pulse signal and FEIR spectrum

Next we calculate the three-pulse signal and FEIR spectrum of the same system with the same pulses. The encoding delay is fixed at $\tau_{\text{enc}} = 500$ fs, which is beyond the bulk of the pulse-overlap region. As we will show in Section 3.6, spectra within the pulse-overlap region

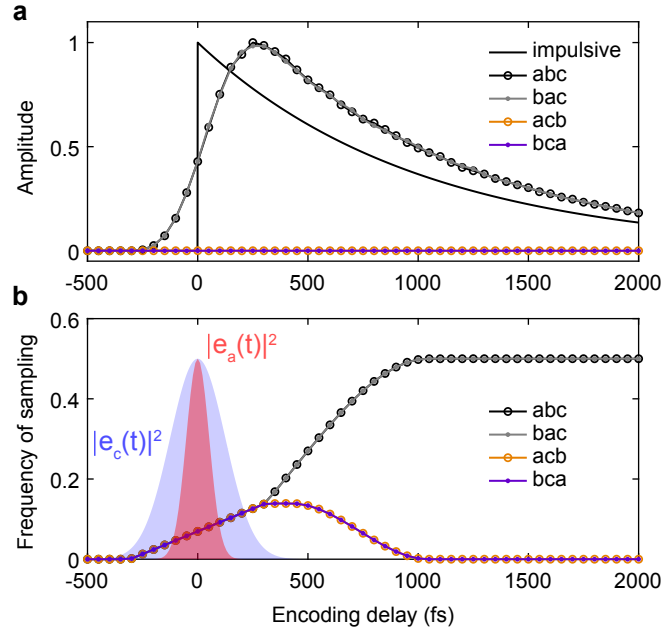


Figure 3.3: Finite-pulse calculation of the two-pulse signal for a single-oscillator system. (a) Relative amplitude of the abc , bac , acb , and bca time-ordered contributions to the total finite-pulse signal, with the impulsive limit signal shown for reference. (b) Relative frequency of sampling the abc , bac , acb , and bca time-orderings in evaluating the Monte Carlo estimate with $L = 2.5$. The intensity profiles of the IR pulse $|e_a(t)|^2 = |e_b(t)|^2$ and visible pulse $|e_c(t)|^2$ are overlaid at $\tau_{\text{enc}} = 0$.

can be subject to additional lineshape distortions. Figure 3.4(a) shows the real part of the total three-pulse envelope $\mathcal{N}^{(4)}(\tau_{\text{IR}}, \tau_{\text{enc}})$, its decomposition into the 4 time-orderings, and the impulsive signal envelope (abc ordering only). In this specific case the envelope happens to be fully real because the IR and visible fields have symmetric spectra, are transform-limited, and are exactly on resonance with the symmetric vibrational resonance. As before, the Monte Carlo sampling frequencies of each time-ordering are shown below in Figure 3.4(b). Because the vibration is lifetime-broadened, i.e. the dephasing and population relaxation rates are the same $\Gamma_{10} = \Gamma_{11}$, the abc contribution to the three-pulse envelope has a similar τ_{IR} -dependence to the τ_{enc} -dependence of the two-pulse signal. As in the two-pulse case,

neither of the mixed IR/Vis time-orderings acb or bca contribute any signal amplitude above noise. The bac contribution dominates for negative τ_{IR} but then falls off to zero when E_a starts arriving after E_c for $|\tau_{\text{IR}}| > \tau_{\text{enc}}$. However, a quickly decaying portion of the bac contribution does appear for positive τ_{IR} and will therefore play a role in the spectrum as discussed below.

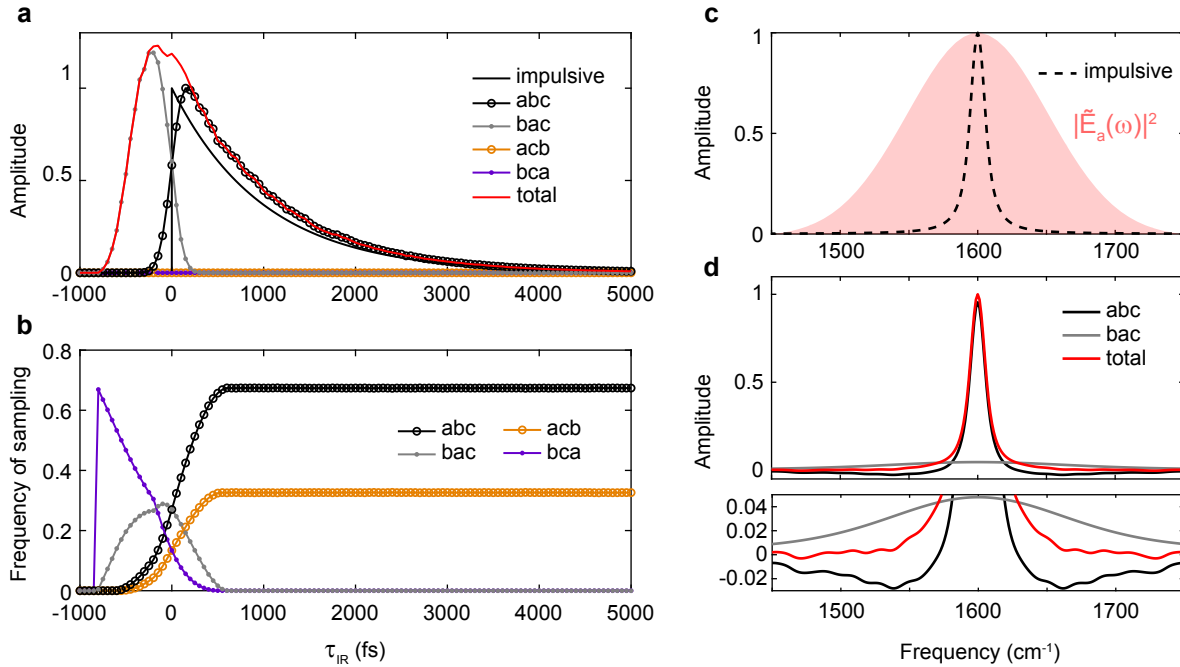


Figure 3.4: Finite-pulse calculation of the $\tau_{\text{enc}} = 500$ fs three-pulse signal and FEIR spectrum for the same single-mode system as Figure 3.3. (a) abc , bac , acb , and bca time-ordered contributions, and the total signal overlaid on the impulsive signal. (b) Relative Monte Carlo sampling frequency of the abc , bac , acb , and bca time-orderings. (c) Impulsive FEIR spectrum plotted over the IR pulse spectrum. (d) Total finite-pulse FEIR spectrum and its abc and bac contributions. The lower panel shows magnified detail around the baseline.

The spectrum of the IR pulse is shown overlaid on the impulsive FEIR spectrum in Figure 3.4c. The finite-pulse FEIR spectrum is found by Fourier transformation of the $\tau_{\text{IR}} \geq 0$ portion of the signal. Specifically, the real part of the FFT of the one-sided complex envelope $\mathcal{N}^{(4)}(\tau_{\text{IR}} \geq 0, \tau_{\text{enc}})$ is first calculated, and then shifted up to the carrier frequency

ω_{IR} . We note that in general the complex-valued nature of the time-domain envelope ensures that its frequency components can be properly assigned above or below the carrier.¹⁷⁸ Figure 3.4(d) shows the resulting FEIR spectrum as well as its decomposition into the *abc* and *bac* contributions. As the IR pulse is broadband compared to the vibrational linewidth ($\sim 11 \text{ cm}^{-1}$), the spectrum matches the impulsive limit very closely. The contribution of the *abc* ordering on its own almost entirely determines the spectrum. However, it has a small distortion in the form of shallow negative wings along the breadth of the pulse spectrum, as can be seen in a magnified view of the baseline region (lower panel of Figure 3.4(d)). This spectral distortion is caused by the delayed peak of the *abc* contribution along τ_{IR} due to the finite pulse convolutions. However, the *bac* contribution is a broad positive feature that perfectly cancels out this distortion, resulting in the proper absorptive appearance of the complete spectrum. As we will discuss in Section 3.6, in the IR/Vis pulse-overlap region the *abc* and *bac* contributions are mis-weighted and no longer add up to give an absorptive lineshape, leading to spectral distortions.

3.5 Finite-pulse effects in a two-mode system

In this section we will apply the methods described above to examine the impact of finite pulses in the FEIR spectroscopy of a system of two coupled vibrations. Since a two-mode system is the minimal case that exhibits vibrational coherence, this model system captures many of the features common to the multimode FEIR experiments discussed in this thesis. Correspondingly, we will be able to clearly demonstrate the most important finite-pulse effects, including the windowing of vibrational spectra by the finite IR bandwidth, the distortion of coherence evolution in τ_{enc} , and the resulting consequences to the interference

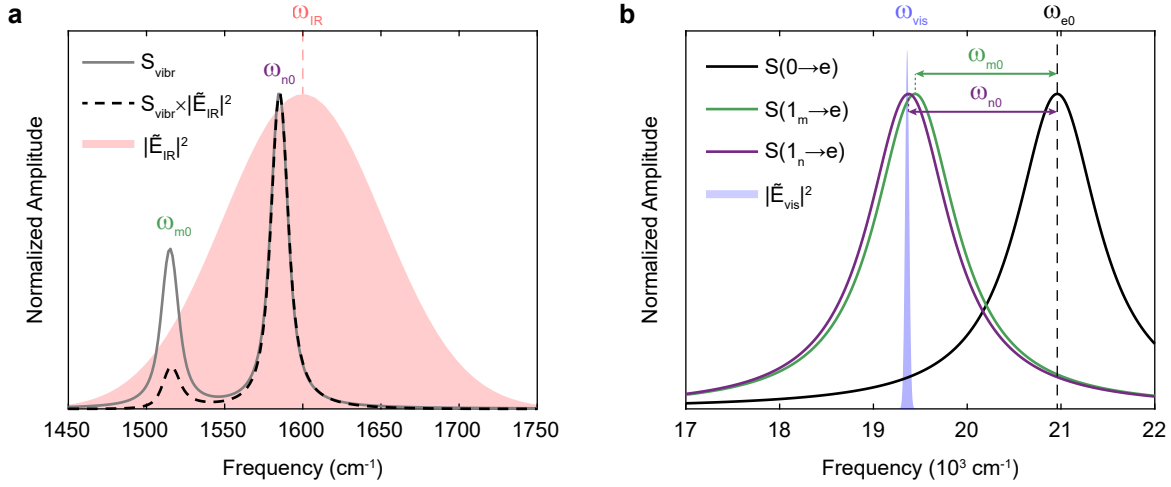


Figure 3.5: Spectral characteristics of the two-mode model system and its FEIR resonance conditions. (a) Linear IR-vibronic spectrum $S_{\text{vibr}}(\omega)$ (see text), IR pulse spectrum $|\tilde{E}_{\text{IR}}(\omega)|^2$, and their product. (b) Lineshapes of the encoding transitions $S(1_m \rightarrow e)$ and $S(1_n \rightarrow e)$ for mode m and n , respectively, and the bare 0-0 electronic transition $S(0 \rightarrow e)$. The visible pulse spectrum $|\tilde{E}_{\text{vis}}(\omega)|^2$ is overlaid.

between population and coherence contributions.

The system and its resonance conditions, depicted in Figure 3.5, are chosen to reflect a situation commonly encountered in our experiments on coumarin dyes, where modes differ both in their FEIR activity and coverage by the IR pulse spectrum. The two modes are set at $\omega_{m0} = 1515 \text{ cm}^{-1}$ and $\omega_{n0} = 1585 \text{ cm}^{-1}$, and as before we assume the homogeneous limit and lifetime broadened resonances with $\Gamma_{m0}^{-1} = \Gamma_{n0}^{-1} = \Gamma_{mm}^{-1} = \Gamma_{nn}^{-1} = 1 \text{ ps}$. We set the FEIR activity of the lower frequency mode m , i.e. the squared product of the vibrational transition moment and FC factor $|\mu_{m0} \langle 1_m^g | 0^e \rangle|^2$, to be half that of mode n . We also set the modes' FC factors $\langle 1_m^g | 0^e \rangle$ and $\langle 1_n^g | 0^e \rangle$ to have the same sign, so the resulting coherence will be positively-signed as discussed in Section 2.4.5 of Chapter 2. Figure 3.5(a) plots the IR-vibronic spectrum S_{vibr} , defined as the linear IR absorption spectrum with each vibrational resonance weighted by the square of its FC factor. This spectrum is formally equivalent to

the impulsive FEIR spectrum at $\tau_{\text{enc}} = 0$ with all coherence pathways removed, and reflects the intrinsic FEIR activity of each mode. We use the same transform-limited IR and visible pulses as before in Section 3.4. The resulting IR spectral coverage is such that the weaker mode falls in the low-frequency wing of the pulse spectrum. This difference in IR spectral intensity over each mode is evident by comparing S_{vibr} with the product $S_{\text{vibr}} \times |\tilde{E}_{\text{IR}}|^2$.

Figure 3.5(b) shows the lineshapes of the encoding transitions for each mode and that of the bare 0-0 electronic transition for reference. The visible pulse spectrum is shown superimposed, and is centered at $\omega_{\text{vis}} = 19360 \text{ cm}^{-1}$ to match that of our current experiment. The dephasing time of each of these transitions is set to $\Gamma_{em}^{-1} = \Gamma_{en}^{-1} = \Gamma_{e0}^{-1} = 10 \text{ fs}$, which results in a lorentzian fwhm of 1061 cm^{-1} that is over an order of magnitude broader than the visible pulse spectrum ($\Delta\omega_{\text{vis}} = 50 \text{ cm}^{-1}$). The resonance conditions are set with respect to the bare electronic transition so that $\omega_{e0} = \omega_{\text{IR}} + \omega_{\text{vis}}$. Given how broad the encoding transition lineshapes are, there is very little difference (indicated in Figure 3.5(b)) between their degree of resonance with the visible pulse spectrum under these conditions.

We first demonstrate the impact of the finite pulses on the system's two-pulse FEIR signal. Figure 3.6(a) shows the total signal as well as its decomposition into population and coherence contributions in the impulsive limit. The coherence dephasing time has been set at $\Gamma_{mn}^{-1} = 500 \text{ fs}$, and as mentioned above the coherence is positively-signed, leading to constructive interference with the population contribution at $\tau_{\text{enc}} = 0 \text{ fs}$. Figure 3.6(b) shows the same signal and its population and coherence components from the finite-pulse calculation. The IR/Vis temporal cross-correlation (321 fs fwhm) represents the effective instrument response function (IRF) of the measurement, and is shown for reference. The IRF and its characterization will be discussed further in Section 3.7. Perhaps the most apparent effect of the finite pulses is to reduce the amplitude of the coherence pathways

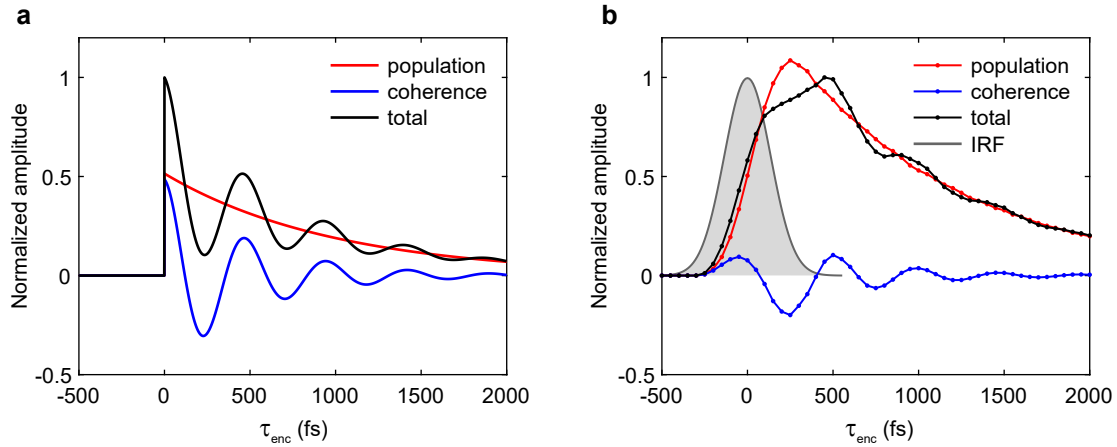


Figure 3.6: Two-pulse FEIR signals from the two-mode system in (a) the impulsive limit and (b) with finite pulses. In both cases the total signal (black) is normalized to its maximum value, while the population (red) and coherence (blue) components have not been scaled further, and add up to reproduce the total signal amplitude. The IRF is shown in (b) for reference.

relative to the population pathways, leading to a strong suppression of the beating in the total signal. This can be understood qualitatively by considering the finite duration of the IRF as a low-pass convolution filter which preferentially washes away the high-frequency variations along τ_{enc} .¹⁸⁴ This suppression is particularly strong over the first half-cycle of the coherence phase occurring during pulse overlap. The result of the interference between coherence and population pathways in this case is that the total signal peaks with the first recurrence of the coherence phase at ~ 500 fs, which is substantially beyond the decay of the IRF.

Next, we analyze the effects of the finite pulses on the FEIR spectrum, and particularly its τ_{enc} -dependence. Figure 3.7 compares the τ_{enc} -dependent FEIR spectrum in the impulsive limit with that produced by finite pulses. Starting with the impulsive limit, we note that the factor of two lower FEIR activity of mode m compared to n leads to a slightly deeper relative coherent modulation over ω_{m0} , as can be seen in Figures 3.7(a) and (g). This occurs because

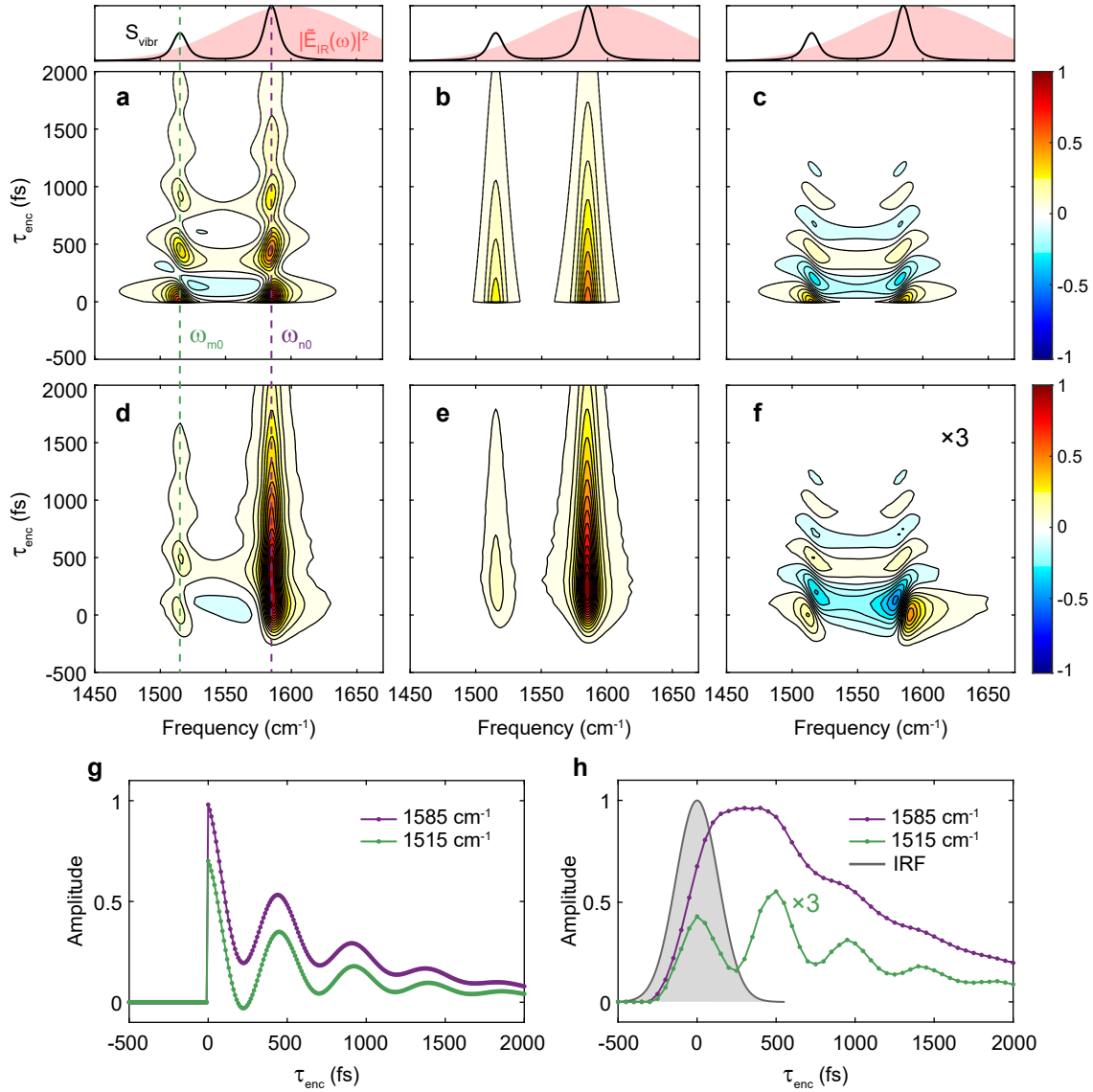


Figure 3.7: Comparison of the impulsive and finite-pulse τ_{enc} -dependent FEIR spectrum for the two-mode system. Impulsive limit (a) total spectrum, (b) population contribution, and (c) coherence contribution. The upper panels plot the IR-vibronic spectrum S_{vibr} and IR pulse spectrum for reference. (d)-(f) show the analogous quantities as (a)-(c) for the finite-pulse case. In both cases the total spectrum is normalized to its maximum value, and the components are plotted on the same scale. Contouring spacing is set at 6.7%. Panel (f) has been additionally scaled by a factor of 3 for better visualization given the small amplitude. (g) and (h) show slices through the two vibrational resonances $\omega_{m0} = 1515 \text{ cm}^{-1}$ and $\omega_{n0} = 1585 \text{ cm}^{-1}$ for the impulsive and finite-pulse τ_{enc} -dependent spectra, respectively. The IRF is included in (h), and the 1515 cm^{-1} trace has also been scaled by a factor of 3.

the population response of each mode is determined by its FEIR activity (Figure 3.7(b)), whereas the coherent response is determined by the ‘shared’ activity $\mu_{m0}\mu_{n0}\langle 1_m^g|0^e\rangle\langle 1_n^g|0^e\rangle$, and is therefore always equal over both resonances (Figure 3.7(c)). The total spectrum at ω_{m0} correspondingly has a larger fractional coherence contribution.

With finite pulses, the reduction in relative amplitude of the coherence contribution seen in the two-pulse signal is also strongly apparent in the spectra (note the additional $\times 3$ scaling in Figure 3.7(f)), as required by the projection-slice relation. However, the manner in which the coherence and population amplitudes are modified along the vibrational frequency axis are importantly different. Namely, a comparison of Figures 3.7(e) and (b) shows that the population feature from the lower-frequency mode m is suppressed relative to mode n due to the lower IR spectral intensity at its location in the wing of the pulse spectrum. However, the amplitude of the coherence pathways are still equal over both modes (i.e. comparing Figures 3.7(f) and (c) outside of the pulse overlap region). The result is that the fractional contribution of coherence to the total spectrum over the lower-frequency band at ω_{m0} is significantly amplified with respect to that over ω_{n0} . This unequal spectral weighting is evident in the much deeper coherent modulation seen in the τ_{enc} -slice along the ω_{m0} resonance at 1515 cm^{-1} compared to that along $\omega_{n0} = 1585\text{ cm}^{-1}$ (Figure 3.7(g)), when compared to the impulsive limit (Figure 3.7(h)).

The spectral filtering effect of the finite IR bandwidth is examined in more detail in Figure 3.8. The finite-pulse FEIR spectrum and its population and coherence contributions are shown at encoding delays corresponding to a coherence phase of $\phi_{mn} \sim \pi$ ($\tau_{\text{enc}} = 250\text{ fs}$, Figure 3.8(a)) and $\phi_{mn} \sim 2\pi$ ($\tau_{\text{enc}} = 500\text{ fs}$, Figure 3.8(b)). In both cases, the population response is multiplicatively windowed by the IR pulse spectrum, as can be seen by the nearly perfect overlay of the population contribution on $S_{\text{vibr}} \times |\tilde{E}_{\text{IR}}|^2$. This spectral reshaping of the

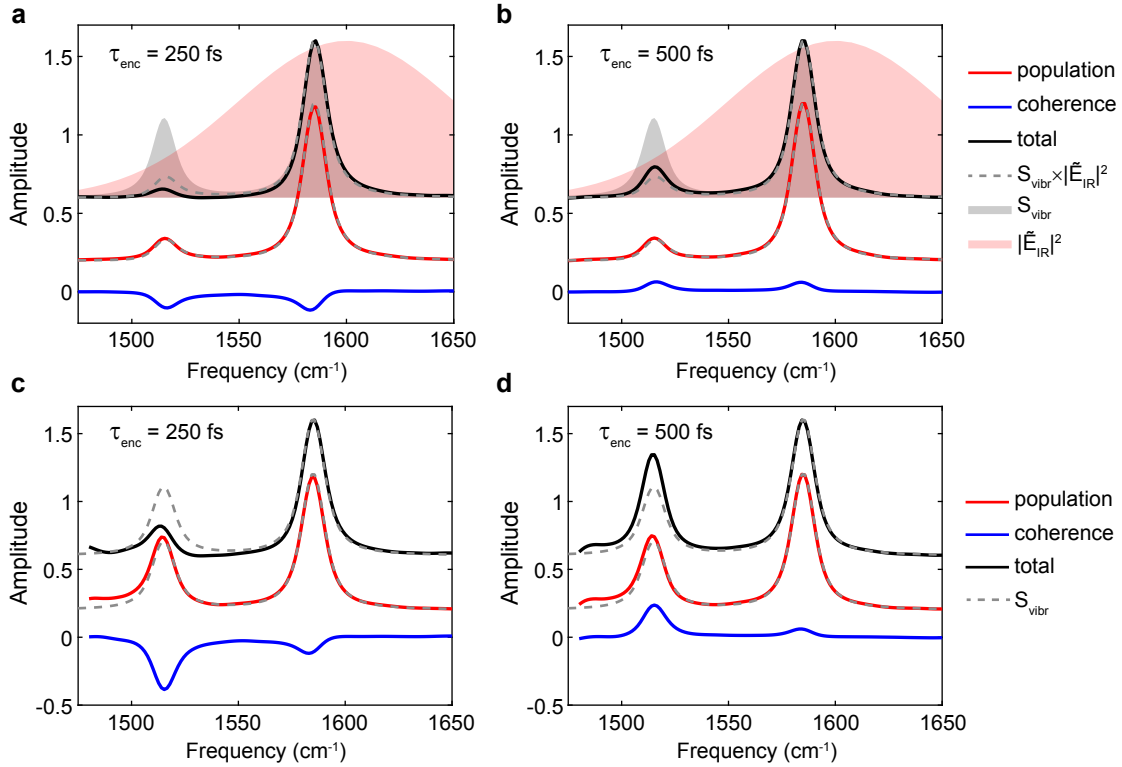


Figure 3.8: Effect of IR spectral filtering and pump-normalization on FEIR spectra of the two-mode system. Finite-pulse FEIR spectra (black) at (a) $\tau_{\text{enc}} = 250$ fs (coherence phase $\sim \pi$) and (b) $\tau_{\text{enc}} = 500$ fs (coherence phase $\sim 2\pi$) including the decomposition into population (red) and coherence (blue) contributions (offset vertically for clarity). The IR pulse spectrum $|\tilde{E}_{\text{IR}}|^2$ (red fill) and IR-vibronic spectrum S_{vibr} (gray fill) are plotted behind the total spectrum, while their product $S_{\text{vibr}} \times |\tilde{E}_{\text{IR}}|^2$ (dashed gray) is overlaid on both the total spectrum and population contribution. IR pump-normalized FEIR spectra with population and coherence components at (c) $\tau_{\text{enc}} = 250$ fs (d) $\tau_{\text{enc}} = 500$ fs. S_{vibr} (dashed gray) is plotted over the total spectrum and population component.

population features is an intuitive consequence of the one-photon IR dependence—namely, the magnitude of response at a given frequency is simply scaled by the IR intensity at that frequency. On the other hand, the excitation of vibrational coherence is non-local in frequency, in that it depends on the IR pump intensity over both resonances. As a result, the coherence amplitude remains equal and symmetric over both bands, as evident in Figures 3.7(a) and (b). In general, this state of affairs holds for any pair of vibrations with arbitrary (transform-limited) pulses.

Because the IR pulse spectrum reshapes the FEIR response in the frequency-domain, it would appear reasonable to ‘pump-normalize’ the data, i.e. divide the FEIR spectrum by the IR spectrum used in the measurement

$$S_{\text{pnorm}}(\omega_{\text{enc}}, \tau_{\text{enc}}) = \frac{S(\omega_{\text{enc}}, \tau_{\text{enc}})}{|\tilde{E}_{\text{IR}}(\omega_{\text{enc}})|^2}. \quad (3.28)$$

Figures 3.8(c) and (d) show the pump-normalized FEIR spectra and their population and coherence components corresponding to panels (a) and (b), respectively. In light of the discussion in the previous paragraph, this pump-normalization procedure correctly ‘undoes’ the spectral windowing of the population pathways, but incorrectly treats the coherence pathways. Specifically, the pump-normalized population contribution overlays onto S_{vibr} , however pump-normalizing the coherence contribution artificially inflates the amplitude over the weaker lower-frequency band from the wing of the IR spectrum. When the coherence phase is negative absorptive ($\phi_{mn} \sim \pi k$ for integer k) as in Figure 3.8(c), the result is an apparent suppression of the weaker mode’s amplitude compared to S_{vibr} . Conversely, on the positive absorptive side of the coherence cycle ($\phi_{mn} \sim 2\pi k$), the weak mode’s amplitude is exaggerated, as in Figure 3.8(d).

It is important to note that the presence of vibrational coherence will always complicate the correspondence between a multimode FEIR spectrum and the ideal FEIR activity spectrum S_{vibr} , even in the impulsive limit. However, as this analysis shows, the effect of the IR pulse spectrum can further complicate the apparent strength of a given resonance through the different way in which population and coherence pathways are affected. For example, a naive assessment of the relative FEIR activity of modes m and n based on their band intensities from the ‘pump-corrected’ spectra in Figures 3.8(c) or (d) would alternately underestimate the activity of mode m by 57%, or overestimate it by 47%, respectively.

3.6 Lineshape distortions during pulse-overlap

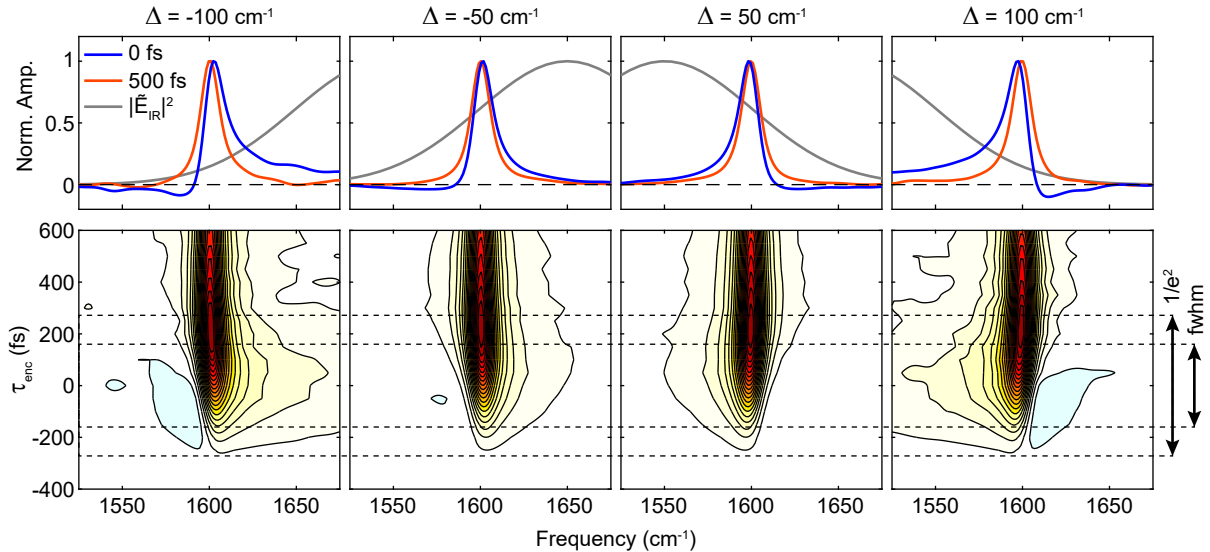


Figure 3.9: IR/Vis pulse-overlap lineshape phase distortion for a single-mode population feature, and its dependence on the IR-vibrational detuning $\Delta = \omega_{\text{IR}} - \omega_{10}$. The upper panels show the FEIR spectrum at $\tau_{\text{enc}} = 0$ fs and 500 fs overlaid on the IR pulse spectrum. Lower panels show contour plots of the full τ_{enc} -dependent FEIR spectrum, with the fwhm and $1/e^2$ full-width of the IR/Vis intensity cross-correlation indicated. Contouring spacing is set at 5%, with the same coloring as in Figure 3.7.

Our analysis of finite-pulse FEIR spectra so far has been careful to avoid early encoding delays that fall solidly within the pulse-overlap region. Here we briefly demonstrate a specific lineshape distortion to the population features that occurs within the IR/Vis pulse-overlap. Figure 3.9 shows τ_{enc} -dependent FEIR spectra of the single-mode system discussed in Section 3.4 with four different IR center frequencies, resulting in IR-vibrational detunings of $\Delta = \omega_{\text{IR}} - \omega_{10} = -100, -50, 50, \text{ and } 100 \text{ cm}^{-1}$. In each case the IR pulse remains transform-limited with $\Delta\omega_{\text{IR}} = 120 \text{ cm}^{-1}$, and the visible pulse is likewise the same as that used previously in Sections 3.4 and 3.5. At $\tau_{\text{enc}} = 0$ the vibrational lineshape exhibits a phase twist that depends on the magnitude and sign of Δ . For $\Delta = -100 \text{ cm}^{-1}$, when the vibrational resonance is deep in the red-wing of the IR pulse spectrum, this phase distortion produces a negative/positive wing on the low/high frequency side of the band, respectively. For smaller $|\Delta|$ this phase twist becomes less extreme, while it switches sign when Δ becomes positive. This lineshape distortion is contained within the pulse overlap region, whose extent is indicated by both the IR/Vis cross-correlation fwhm ($\sqrt{\tau_{p,\text{IR}}^2 + \tau_{p,\text{vis}}^2} = 321 \text{ fs}$) and $1/e^2$ full-width ($2w = \sqrt{2}\text{fwhm}/\sqrt{\ln 2} = 546 \text{ fs}$). With these pulses, the spectrum is essentially free of distortion by $\tau_{\text{enc}} = 500 \text{ fs}$.

This apparent phase distortion in the population response is likely related to the improper weighting of the *abc* and *bac* time-ordered contributions discussed in Section 3.4, although a detailed understanding of its origins requires further investigation. Coherence features are also distorted (although not in the same way) during pulse-overlap, as can be seen e.g. in Figure 3.6(f), where the amplitude near the center of the IR pulse spectrum is additionally enhanced. Overall, FEIR spectra for τ_{enc} within pulse-overlap should be approached with caution, although familiarity with the phenomenology of these artifacts should help build confidence in interpreting (or, importantly, not over-interpreting) early-time data.

3.7 IR + visible two-photon excited fluorescence

As mentioned in the overview of this chapter, vibrationally-nonresonant two-photon absorption (TPA) is a possible excitation route for generating target population, and therefore represents a potential artifactual contribution to the fluorescence signal in an FEIR experiment. Understanding how this signal artifact appears in the data is correspondingly important for interpreting early-time signals. On the other hand, the nonresonant nature of the TPA response (with respect to the IR or visible pulses individually) means that it reports in a direct way on the temporal pulse characteristics, and therefore has utility as a pulse diagnostic tool for the FEIR spectrometer. Specifically, as we will see, the TPA response directly reports on the IR/Vis intensity cross-correlation and can therefore be used to map out the experiment's IRF.

From the perspective of the molecular system, this non-degenerate two-photon process involving one IR and one visible photon is essentially instantaneous, occurring within the electronic dephasing time of some 10's of fs. In practice, TPA therefore only occurs during the temporal overlap of the IR and visible pulse electric fields. The language conventionally used is of sequential excitation mediated by a 'virtual' state. Formally, this is short-hand for describing the overall transition amplitude as a sum over two-step pathways involving all possible system states as intermediates, which is related to the system's polarizability by a Kramers-Heisenberg-Dirac expansion (i.e. the second-order version of Fermi's Golden Rule).^{81,109,185,186} In density-matrix language, the overall two-photon excitation probability (i.e. the square modulus of the overall transition amplitude) is given by the final target population, and is described to 4th-order in the incident field.¹⁸⁷ As a result, the formal structure for calculating TPA is closely related to our 4th-order response function description of FEIR excitation. In principle, it would be possible to model the TPA contribution along

the same lines as the finite-pulse response calculations developed earlier in this chapter, with the response function suitably replaced by sets of delta functions to reflect the essentially impulsive molecular polarizability response.

However, a much simpler (and formally equivalent) approach is to assume that the instantaneous excitation rate is directly proportional to the product of the IR and visible field intensities. This approach is typically adopted to describe the practical phenomenology of how multi-photon or other nonlinear parametric signals depend on the driving fields.^{179,188} The final accumulation of target population after the pulse sequence has finished interacting with the sample is then proportional to the time integral

$$\bar{N}^{\text{TPA}} \propto \int_{-\infty}^{\infty} (E_{\text{IR}}(t))^2 (E_{\text{vis}}(t))^2 dt. \quad (3.29)$$

With our FEIR pulse sequence the TPA fluorescence signal $S \propto \bar{N}^{\text{TPA}}$ is therefore

$$S(\tau_{\text{IR}}, \tau_{\text{enc}}) = \int_{-\infty}^{\infty} (E_1(t + \tau_{\text{IR}} + \tau_{\text{enc}}) + E_2(t + \tau_{\text{enc}}))^2 (E_3(t))^2 dt. \quad (3.30)$$

To evaluate this expression we break the real-valued fields into their positive and negative frequency components as before in Section 3.2. Invoking the RWA, we only keep the terms where the carrier phase oscillations between the four fields cancel,

$$\begin{aligned} S(\tau_{\text{IR}}, \tau_{\text{enc}}) &= \int_{-\infty}^{\infty} (E_1^+ E_1^- + E_2^+ E_2^- + E_1^+ E_2^- + E_1^- E_2^+) (E_3^+ E_3^-) dt \\ &= S_1(\tau_{\text{IR}} + \tau_{\text{enc}}) + S_2(\tau_{\text{enc}}) + S_{12}(\tau_{\text{IR}}, \tau_{\text{enc}}), \end{aligned} \quad (3.31a)$$

where

$$S_1(\tau_{\text{IR}} + \tau_{\text{enc}}) = \frac{1}{4} \int_{-\infty}^{\infty} \mathcal{E}_1^2(t + \tau_{\text{IR}} + \tau_{\text{enc}}) \mathcal{E}_3^2(t) dt, \quad (3.31b)$$

$$S_2(\tau_{\text{enc}}) = \frac{1}{4} \int_{-\infty}^{\infty} \mathcal{E}_2^2(t + \tau_{\text{enc}}) \mathcal{E}_3^2(t) dt, \quad (3.31c)$$

$$S_{12}(\tau_{\text{IR}}, \tau_{\text{enc}}) = \frac{1}{2} \text{Re} \left\{ e^{-i\omega_{\text{IR}}\tau_{\text{IR}}} \int_{-\infty}^{\infty} \mathcal{E}_1(t + \tau_{\text{IR}} + \tau_{\text{enc}}) \mathcal{E}_2(t + \tau_{\text{enc}}) \mathcal{E}_3^2(t) e^{i[\phi_{\text{IR}}(t+\tau_{\text{IR}}) - \phi_{\text{IR}}(t)]} dt \right\}. \quad (3.31d)$$

Here we have used the notation for temporal pulse amplitude and phase introduced in Section 3.3. Specifically, $\phi_{\text{IR}}(t)$ is the temporal phase of the IR pulse, which is assumed to be the same for both copies E_1 and E_2 . Importantly, the TPA signal is not sensitive to the phase of the visible pulse E_3 , which can be interpreted as a consequence of the bra- and ket-side pair of light-matter interactions occurring within its envelope. The subscripts labelling the different contributions in Eq. 3.31 indicate their dependence on the IR pulses in an analogous way to our notation for the different FEIR signal contributions in Section 2.4.3 of Chapter 2, i.e. S_1 depends on E_1 but not E_2 , while S_{12} depends on both. We note the clear similarity between these contributions to the TPA signal versus those for FEIR. Specifically, the ‘two-pulse’ and ‘three-pulse’ contributions are related among themselves by

$$S_{12}(\tau_{\text{IR}} = 0, \tau_{\text{enc}}) = 2S_2(\tau_{\text{enc}}) = 2S_1(\tau_{\text{enc}}), \quad (3.32)$$

as can be verified directly from the expressions in Eq. 3.31.

Figure 3.10 shows a numerical calculation of the full three-pulse-resolved TPA signal $S(\tau_{\text{IR}}, \tau_{\text{enc}})$ as well as slices along τ_{enc} and τ_{IR} , for the transform-limited Gaussian IR and visible pulses used earlier in Sections 3.4 and 3.5 (see figure caption). The three-pulse

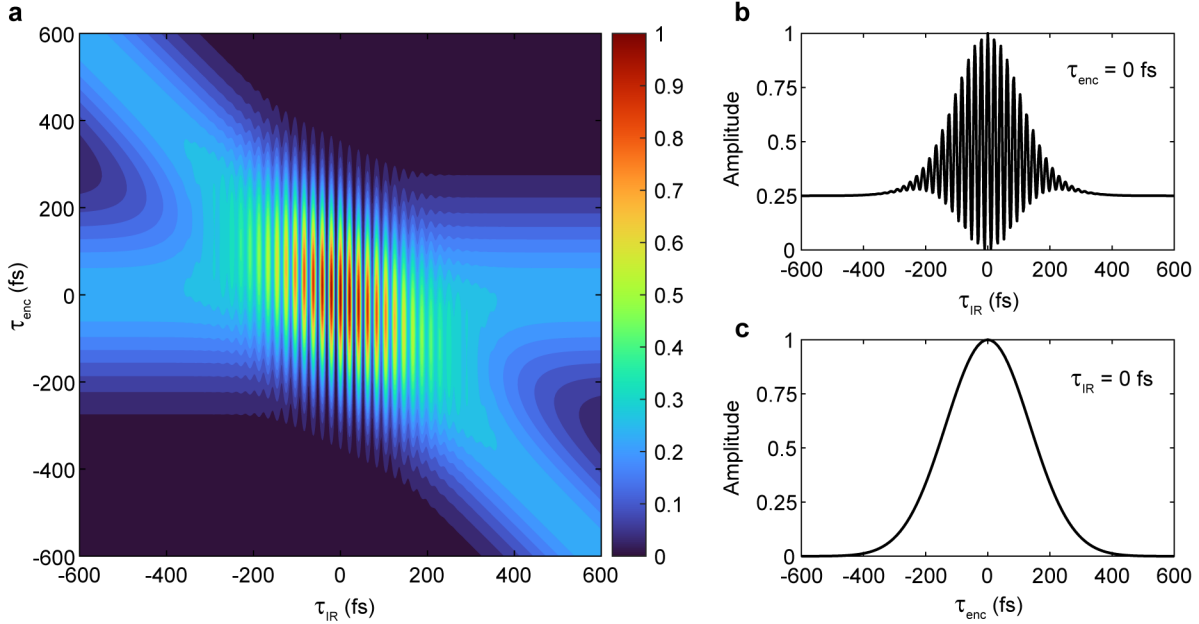


Figure 3.10: Appearance of the three-pulse-resolved TPA signal in the time-domain. The IR and visible pulses are transform-limited and Gaussian with $\Delta\omega_{\text{IR}} = 120 \text{ cm}^{-1}$ ($\tau_{p,\text{IR}} = 123 \text{ fs}$), and $\Delta\omega_{\text{vis}} = 50 \text{ cm}^{-1}$ ($\tau_{p,\text{vis}} = 297 \text{ fs}$). (a) Fully-resolved signal $S(\tau_{\text{IR}}, \tau_{\text{enc}})$, (b) the slice $S(\tau_{\text{IR}}, \tau_{\text{enc}} = 0)$, and (c) the slice $S(\tau_{\text{IR}} = 0, \tau_{\text{enc}})$.

contribution S_{12} is responsible for the interferometric oscillation along τ_{IR} , while the two-pulse contributions S_1 and S_2 form the cross-shaped pattern intersecting at the origin.

It is worth considering the similarities and differences between this three-pulse-resolved TPA signal and various types of pulse characterization techniques using parametric nonlinear sample response, e.g. interferometric autocorrelation, or the various flavors of frequency-resolved optical gating.^{179,188} The trace $S(\tau_{\text{IR}}, \tau_{\text{enc}} = 0)$ (Figure 3.10(b)) qualitatively resembles an interferometric autocorrelation, with the important differences that the intensity ratio of peak to baseline is 4:1, rather than 8:1, and the oscillating component only has frequency content around ω_{IR} , and not also at $2\omega_{\text{IR}}$. These differences arise because the TPA signal is only quadratic in E_{IR} , rather than quartic in the case of the interferometric autocorrelation. The trace $S(\tau_{\text{IR}} = 0, \tau_{\text{enc}})$ (Figure 3.10(c)) is formally the IR/Vis intensity cross-correlation,

which can also be seen explicitly in the expression Eq. 3.31(c) in conjunction with Eq. 3.32. This cross-correlation represents the IRF of an FEIR experiments, and its width is therefore a practical measure of the time-resolution. In a two-pulse FEIR measurement, the TPA signal (if present) therefore appears as a spike riding on top of the FEIR signal at $\tau_{\text{enc}} = 0$, and indicates the pulse-overlap region.

Next, we examine the behavior of the TPA signal in the frequency-domain, i.e. as it would appear when measuring FEIR spectra with the three-pulse experiment. From a pulse diagnostic standpoint, more information about the IR spectral phase can be gleaned from this frequency-domain representation of the TPA signal. The three-pulse-resolved TPA signal is processed in the same way as three-pulse FEIR data, i.e. the spectrum is the real part of the one-sided Fourier transform of $\tau_{\text{IR}} > 0$ data

$$S^{\text{TPA}}(\omega, \tau_{\text{enc}}) = \text{Re} \int_0^{\infty} S_{12}(\tau_{\text{IR}}, \tau_{\text{enc}}) e^{i\omega\tau_{\text{IR}}} d\tau_{\text{IR}}. \quad (3.33)$$

Just like the case for FEIR signals, a projection-slice relation connects the projection of the frequency-resolved TPA signal onto the encoding delay to the IR/Vis intensity cross-correlation

$$\begin{aligned} \int_{-\infty}^{\infty} S^{\text{TPA}}(\omega, \tau_{\text{enc}}) d\omega &= S_{12}(\tau_{\text{IR}} = 0, \tau_{\text{enc}}) \\ &= 2S_1(\tau_{\text{enc}}) = 2S_2(\tau_{\text{enc}}) = \frac{1}{2}S(\tau_{\text{IR}} = 0, \tau_{\text{enc}}). \end{aligned} \quad (3.34)$$

Figure 3.11 displays contour surface representations of $S^{\text{TPA}}(\omega, \tau_{\text{enc}})$ for a variety of different IR and visible pulse characteristics. Figure 3.11(a) shows the case corresponding to the time-domain data in Figure 3.10, i.e. transform-limited pulses with spectral bandwidth representative of our current experiments. The overall frequency extent of the signal follows

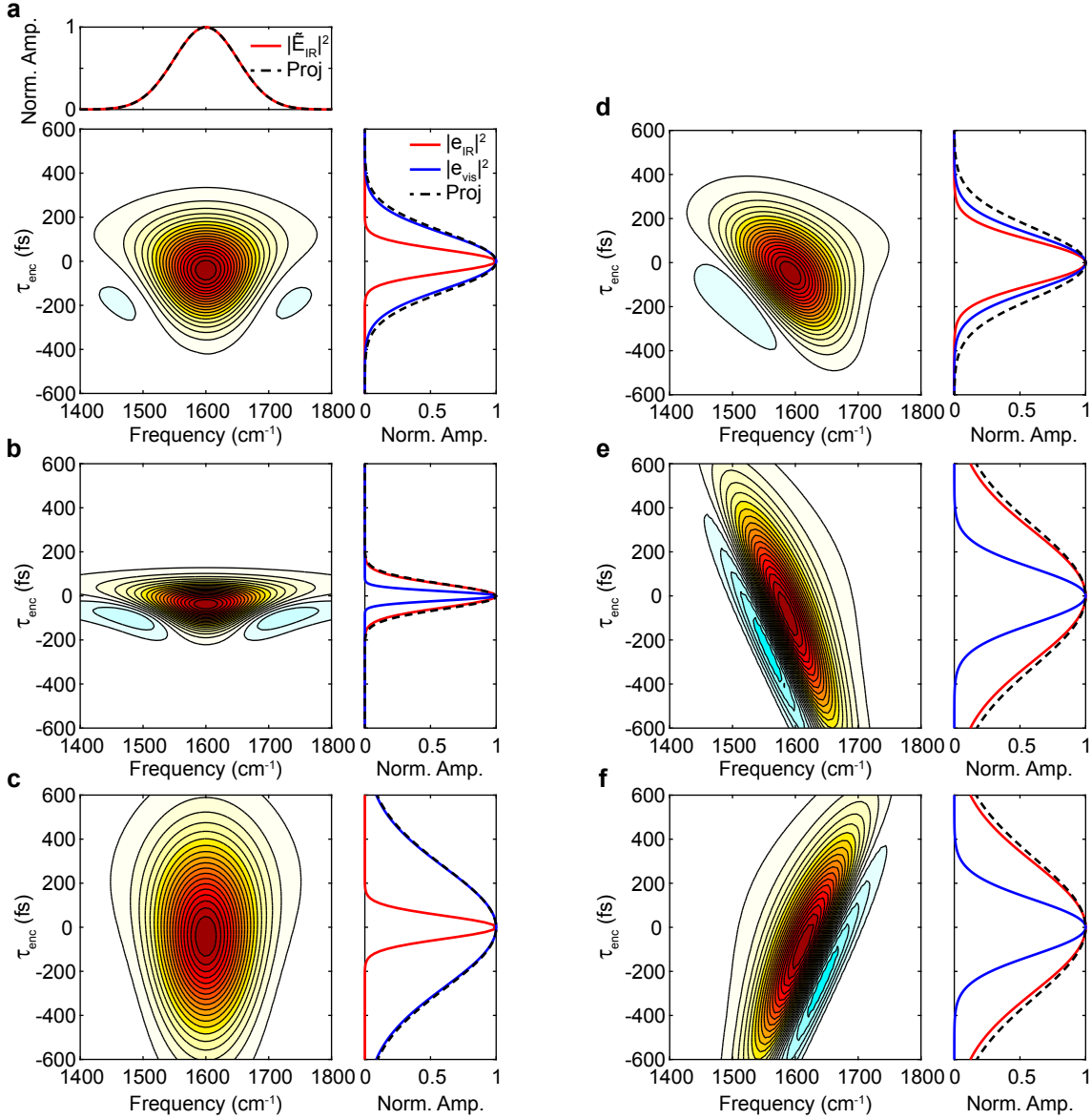


Figure 3.11: Frequency-resolved TPA signals $S^{\text{TPA}}(\omega, \tau_{\text{enc}})$ with corresponding IR and visible temporal intensity profiles and cross-correlations for a variety of relative pulse durations and values of $\gamma_{\text{IR},2}$. In all cases the IR spectrum is Gaussian with $\omega_{\text{IR}} = 1600 \text{ cm}^{-1}$ and $\Delta\omega_{\text{IR}} = 120 \text{ cm}^{-1}$. In (a)-(c) both pulses are transform-limited with $\tau_{p,\text{IR}} = 123 \text{ fs}$ and (a) $\Delta\omega_{\text{vis}} = 50 \text{ cm}^{-1}$ ($\tau_{p,\text{vis}} = 297 \text{ fs}$), (b) $\Delta\omega_{\text{vis}} = 300 \text{ cm}^{-1}$ ($\tau_{p,\text{vis}} = 49 \text{ fs}$), and (c) $\Delta\omega_{\text{vis}} = 23 \text{ cm}^{-1}$ ($\tau_{p,\text{vis}} = 640 \text{ fs}$). The top panel of (a) shows the projection of the TPA signal onto the ω -axis overlaid on the IR spectrum. (d)-(f) use the same spectra as (a), with a transform-limited visible pulse but chirped IR of (d) $\gamma_{\text{IR},2} = -8700 \text{ fs}^2$ ($\tau_{p,\text{IR}} = 232 \text{ fs}$), (e) $\gamma_{\text{IR},2} = -30,000 \text{ fs}^2$ ($\tau_{p,\text{IR}} = 689 \text{ fs}$), and (f) $\gamma_{\text{IR},2} = 30,000 \text{ fs}^2$ ($\tau_{p,\text{IR}} = 689 \text{ fs}$).

the IR pulse spectrum, and as shown in the upper panel, the projection of $S^{\text{TPA}}(\omega, \tau_{\text{enc}})$ onto the ω -axis in fact exactly reproduces the IR pulse spectrum. This equality between the ω -projection and IR spectrum holds for all the cases shown in Figure 3.11, and is therefore not shown for the other cases.

The projection onto the τ_{enc} -axis, i.e. the IR/Vis cross-correlation, is shown on the right panel superimposed on the IR and visible temporal intensity profiles. While the IR/Vis cross-correlation is symmetric in τ_{enc} , the shape of the TPA spectrum varies asymmetrically in τ_{enc} , with small negative side lobes for $\tau_{\text{enc}} < 0$, switching to exaggerated positive wings for $\tau_{\text{enc}} > 0$. Figures 3.11(b) and (c) show cases where the IR pulse is the same as in (a), but with a transform-limited visible pulse that is alternately much shorter ($\Delta\omega_{\text{vis}} = 300 \text{ cm}^{-1}$, $\tau_{p,\text{vis}} = 49 \text{ fs}$), or much longer ($\Delta\omega_{\text{vis}} = 23 \text{ cm}^{-1}$, $\tau_{p,\text{vis}} = 640 \text{ fs}$), respectively. When the visible pulse is significantly shorter than the IR (Figure 3.11(b)), the magnitude of this asymmetry is more significant (e.g. evident from the deeper negative lobes), while in the opposite scenario (Figure 3.11(c)) the asymmetry is less pronounced. This asymmetric τ_{enc} -evolution may have a physical interpretation along similar lines to that of the pulse-overlap lineshape distortion to FEIR spectra discussed previously in Section 3.6.

The effect of second-order dispersion ($\gamma_{\text{IR},2}$, Eq. 3.18), often referred to loosely as ‘chirp’, on the IR pulse is demonstrated in Figures 3.11(d)-(f). These three cases use the same IR and visible pulse spectra as in (a), and the visible remains transform-limited. Figure 3.11(d) shows the case of $\gamma_{\text{IR},2} = -8700 \text{ fs}^2$, which produces a mildly chirped pulse of 232 fs duration, and is representative of the IR pulse at the sample in our instrument as characterized by interferometric autocorrelation (discussed further in Chapter 4). The effect of this dispersion is to tilt the spectral feature in the ω - τ_{enc} plane, and roll its phase asymmetrically to one side of ω_{IR} . The direction of this tilt and asymmetry is consistent with the sign of the $\gamma_{\text{IR},2}$, in

this case a negative sign corresponding to a ‘down-chirp’ where the high frequencies precede the low frequencies within the envelope. This sensitivity to the sign of $\gamma_{\text{IR},2}$ is demonstrated in more extreme circumstances in Figures 3.11(e) and (f), where the tilt and asymmetry are flipped when switching between $\gamma_{\text{IR},2} = -30,000 \text{ fs}^2$ and $30,000 \text{ fs}^2$, respectively. In principle, evidence of higher-order IR spectral dispersion could be inferred from the frequency-resolved TPA signal, although their characteristic signatures are more complicated. For example, third-order dispersion contributes a triangular horn-shaped pattern (not shown).

Overall, we have seen how vibrationally-nonresonant TPA can manifest in FEIR measurements. Specifically, the TPA response exists within the IR/Vis pulse-overlap region, and can therefore potentially obscure the interpretation of the FEIR data at the earliest encoding delays. In two-pulse experiments, the TPA response is exactly the IR/Vis intensity cross-correlation, and appears as a spike at $\tau_{\text{enc}} = 0$. In FEIR spectra derived from three-pulse measurements, the TPA response spans the IR pulse spectrum as would be expected for a nonresonant process, although the τ_{enc} -dependence is sensitive to the pulses’ relative duration and the IR spectral phase.

Because the TPA response effectively maps out the pulse-overlap region, it can be used to characterize the temporal pulse characteristics and provides a rather direct measure of the FEIR spectrometer’s instrument response function. We will discuss this method in Chapter 4. Because the resonance conditions for FEIR excitation are automatically the same as that for IR + visible TPA, a natural question of great practical importance is under what conditions will the TPA response be present, and how large will it be relative to the proper FEIR signal? The strength of the TPA response is presumably connected to the molecular polarizability, and might correlate with the degenerate two-photon cross-section of the molecule’s electronic transition, which have often been characterized for popular fluorophores. In cases where the

FEIR activity of vibrations under investigation are small, it might be expected that the relative size of the TPA response could be significant. On the other hand, for the goal of instrument response characterization, a dye without any FEIR active vibrations resonant within the IR bandwidth is desirable.

Chapter 4

Experimental implementation of FEIR spectroscopy

4.1 Overview

This chapter describes the experimental FEIR instrumentation and data acquisition procedures used in this thesis. In general, the detection sensitivity potential of FEIR spectroscopy is facilitated by diverse and technically-mature fluorescence-based microscopy and single-molecule methodologies that may be incorporated into the experimental design. Specifically, our approach is based on adapting a confocal epifluorescence microscope configuration with single-photon counting detection. At the same time, FEIR spectroscopy requires intense, ultrashort-pulse excitation to efficiently pump and encode the weak and short-lived mid-IR vibrational resonances. Combining these disparate technologies—fluorescence microscopy and ultrafast IR spectroscopy—requires unique experimental design strategies and compromises. Here we will describe the particular path we have taken, including its drawbacks and opportunities for potential improvements.

Perhaps the single most important design feature is the choice of the instrument's pulse

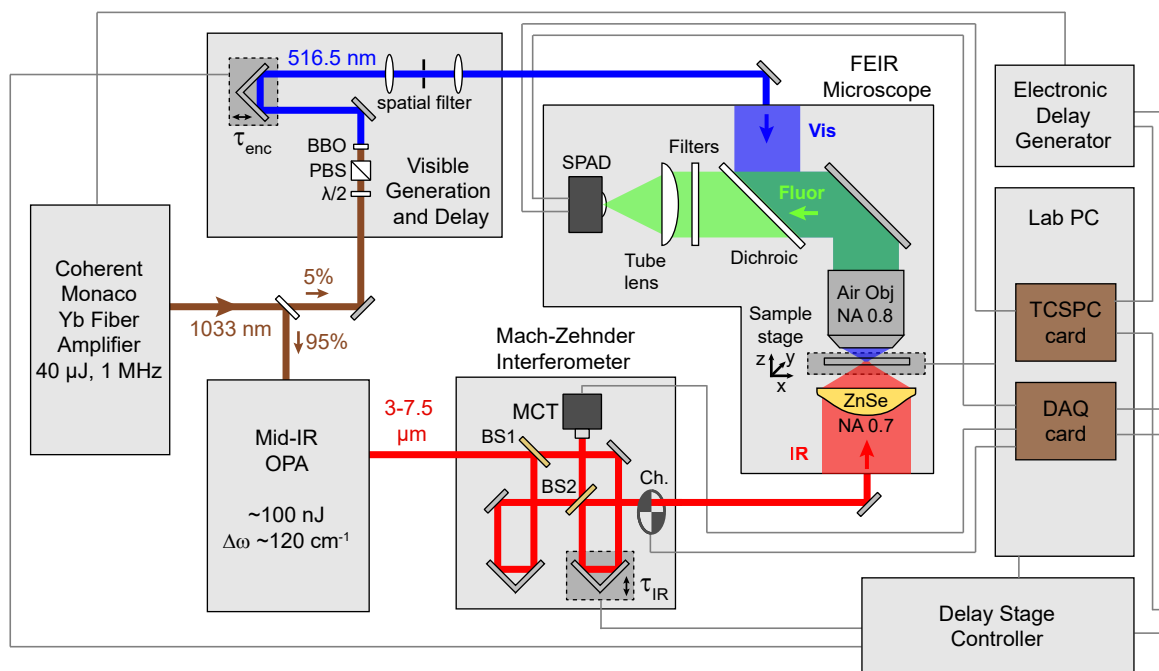


Figure 4.1: Schematic overview of the primary components of the FEIR instrument. Signal acquisition and motion control/feedback dependencies are indicated by gray wires.

repetition-rate. Specifically, photon counting detection allows at most one emitted photon to be registered in response to every repetition of the pulse sequence. Therefore, for photon counting to be efficient, the repetition-rate should be as high as possible while still allowing the system to fully relax before the next pulse sequence arrives. However, for nonlinear experiments using ultrashort pulses, especially with weak mid-IR vibrational transitions, pulse energies must also be high enough to efficiently drive population into excited states. We strike a balance between high repetition-rate and pulse energy by employing a 1 MHz repetition-rate amplified Yb fiber laser (Coherent Monaco 1035-40) to pump our experiment. Figure 4.1 shows a schematic overview of the primary components of the FEIR instrument. Femtosecond mid-IR pulses are generated by a home-built optical parametric amplifier (OPA),

which will be the subject of Section 4.2. The IR pulses are sent through a Mach-Zehnder interferometer to produce a collinear pulse-pair with controllable delay (τ_{IR}), which are then delivered to the FEIR microscope. The visible encoding pulse is generated by doubling the Yb fiber laser fundamental, passed through a delay line to set and control the encoding delay (τ_{enc}), and finally sent into the microscope. Both of these components are described briefly in Section 4.3.

Section 4.4 describes the optical design and characteristics of the FEIR microscope. To achieve intense excitation fields and a small probe volume, the IR and visible beams are focused into the sample with high numerical aperture (NA) optics in a counter-propagating geometry, with the smaller diffraction-limited visible focus centered within the larger IR focus. Fluorescence is collected with the same visible objective lens (known as the epifluorescence geometry¹⁸⁹), passed through selective bandpass filters, and imaged onto a single-photon avalanche photodiode (SPAD) with its small active area serving as a confocal aperture. This confocal aperturing reduces out of focus fluorescence, thereby restricting the experimental observation volume to a small $\sim 1 \mu\text{m}^3$ region where molecules are most efficiently excited by the focus of the visible encoding field.

Data collection during FEIR measurements and auxiliary experimental setup or characterization involves the detection of both IR and single-photon fluorescence signals, which—being analog and digital signals, respectively—use different acquisition strategies. Section 4.5 discusses the nuts and bolts of the detection electronics for the various modes of signal acquisition, as well as motion control procedures used to scan the τ_{IR} and τ_{enc} delays in experiments. With the instrumental aspects of signal acquisition covered, the specific mode of collection and processing of data in bulk FEIR measurements is then discussed in Section 4.7. Specifically, we will describe the acquisition of two- and three-pulse FEIR signals, and

the processing of the latter into Fourier transform FEIR spectra.

The tight focusing of the IR beam guarantees sufficiently high peak field intensities in the sample to drive the FEIR excitation process with reasonable efficiency. However, the correspondingly large average power densities, especially considering the high repetition-rate, can produce thermal loads in the sample. In mild and intermediate cases, these thermal loads produce artifacts in the data ranging from minor to severe, while extreme cases can render any measurement impossible by vaporizing the solvent. As the potential for these heating effects is intrinsic to FEIR spectroscopy, in particular within the current collinear IR/Vis beam geometry, we will devote some time in Section 4.8 to a thorough discussion of their phenomenology.

Finally, in Section 4.9 we will discuss the incorporation of time-resolved fluorescence detection by way of time-correlated single-photon counting (TCSPC). For typical bulk experiments, this capability does not necessarily add much insight beyond simply monitoring the fluorescence intensity, although an interesting application to using fluorescence lifetimes to disentangle the vibrational spectra of multicomponent systems will be described. However, for single-molecule or small-ensemble experiments where useful photons are limited, time-tagged and time-resolved detection is critical for making optimal use of the sparse photon stream. The major application of this TCSPC functionality is to photon correlation used in FEIR correlation spectroscopy, and background scatter suppression in small signal scenarios, both of which will be described later in Chapter 6.

4.2 Generation of femtosecond mid-IR pulses at 1 MHz repetition-rate

The material in this section is adapted from:

Penwell, S. B.; Whaley-Mayda, L.; Tokmakoff, A., Single-stage MHz mid-IR OPA using LiGaS₂ and a fiber laser pump source. *Optics Letters* **2018** *43* (6), 1363-1363.

4.2.1 Introduction

As described above, our choice of a 1 MHz repetition-rate system represents a compromise between the technical requirements of single-photon counting and ultrashort IR pulse generation. This repetition-rate is on the low end for modern photon-counting fluorescence experiments that employ pulsed excitation, where repetition-rates of 20-80 MHz are standard. On the other hand, ultrafast IR techniques are most often built on 1 kHz repetition-rate Ti:Sapphire systems, which can provide mJ-level pulses centered near 800 nm with durations well under 100 fs. Down-conversion schemes to produce μ J-level \sim 100 fs mid-IR pulses pumped by these sources have been well established, and commercial options are standard. Producing sufficiently intense femtosecond IR pulses at the much higher 1 MHz repetition-rate presents multiple new technical challenges, and in many ways represents the primary instrumental hurdle that had to be dealt with in our development of the FEIR experiment. This section describes the mid-IR optical parametric amplifier (OPA) based on a single-stage of amplification in Lithium Gallium Sulfide (LGS) developed for this purpose. Much of this material is published in Ref. [190], although improvements in performance since then, most notably higher mid-IR output power, will be noted.

The recent developments of both Yb- and fiber-based gain media in ultrafast laser technology has opened up new possibilities for high repetition-rate spectroscopy. Compared to Ti:Sapphire, Yb-doped gain media enable more efficient direct diode pumping, which allows for operation at higher repetition-rates while maintaining large pulse energies.¹⁹¹ Furthermore, fiber-based gain media readily handle higher average powers due to the increased surface-to-volume ratio's favorable thermal dissipation properties, thereby enabling further scalability into MHz repetition-rates.¹⁹² Fiber lasers are also appealing pump sources due to their lower cost, turnkey operation, reliability, and compact footprint. Among other things, the increased repetition-rate allows for high-throughput averaging, reducing the acquisition time for low signal experiments. These advantages are especially promising for IR spectroscopy, which typically suffers from low sensitivity and requires large pulse energies. Recently, an increasing number of ultrafast IR instruments operating at 100 kHz have been demonstrated using Yb:KGW or Yb fiber systems.¹⁹³⁻²⁰⁰ There are, however, limited commercial options for mid-IR generation compatible with high repetition-rate Yb laser pump sources. Furthermore, most existing commercial schemes for generating mid-IR from the 1033 nm Yb fundamental rely on multiple stages of amplification and difference frequency generation between the amplified signal and idler. The complexity of these schemes often reduces their net efficiency and results in price points comparable to or exceeding the pump laser itself. Many alternative methods for mid-IR generation have been proposed, however, most do not reduce the complexity of the design, or fail to span a sufficient portion of the mid-IR.^{193,201-214}

4.2.2 Mid-IR nonlinear crystals for Yb laser pumping

A simple, direct OPA design is appealing due to the ease of use, low cost, and potential increase in efficiency. Most materials currently used for three-wave mixing in OPA, however, are oxide crystals suitable for amplification of visible or near-IR wavelengths with 800 nm pump sources. While these materials have the high damage thresholds required for OPA pumping, they absorb in the mid-IR (typical absorption edges cutting on in the range of 3-5 μm), precluding their use for direct mid-IR generation. As such, there is currently a limited selection of materials capable of phase-matching direct OPA to generate a mid-IR idler in the range of 3-8 μm with a 1033 nm pump.²¹⁵ Of these materials, few are commercially available and many have low damage thresholds or bandgaps near/below the 2.4 eV two-photon energy of the Yb fundamental. The relatively new non-oxide Li-based materials (LGS, LSGE, LIS, and LISE) show particular promise due to their transparency across the mid-IR, high damage thresholds, and large band gaps. These materials have previously been explored for use in optical parametric oscillators (OPOs),²¹⁶ difference frequency generation (DFG) for THz generation,^{217,218} DFG for mid-IR generation,²¹⁹⁻²²¹ and there has been one report of an 800 nm pumped OPA.²²² Since the time of writing Ref. [190], these materials have seen a large increase in popularity for mid-IR generation by OPA and DFG schemes.²²³⁻²²⁸

The materials capable of Type I or II phase-matching to produce a mid-IR idler in the range of 3-8 μm with a 1033 nm pump wavelength are listed in Table 4.1. The table includes the values of the bandgap and the effective Kleinman d-coefficient for the second-order nonlinear susceptibility (d_{eff})^{139,231,232} for generation of a 5 μm idler in both Type I or II phase-matching according to the SNLO nonlinear optical code (available from A. V. Smith, AS-Photonics, Albuquerque, NM). Of this list, only AGGS, AGS, HGS, LGS, LGSE, LIS, and LISE have bandgaps larger than the two photon energy of the pump (2.4 eV). AGGS

Table 4.1: Nonlinear crystals for phase-matching 3-8 μm generation by OPA with a 1033 nm pump.

Abbreviation	Chemical Formula	Type I d_{eff} (pm/V)	Type II d_{eff} (pm/V)	E_g (eV)
AAS	Ag_3AsS_3	25	15	2.2
AGGS	AgGaGeS_4	4.9	-	3.0
AGS	AgGaS_2	12	15	2.7
ASS	Ag_3SbS_3	16	1.5	2.2
GS	GaSe	57	50	2.0 ²²⁹
HGS	HgGa_2S_4	28	32	2.79
HS	HgS	52	55	2.0 ²³⁰
LGS	LiGaS_2	-4.4	5.9	3.76
LGSE	LiGaSe_2	-7.7	9.4	3.65
LGT	LiGaTe_2	51	36	2.41
LIS	LiInS_2	-4.7	7.2	3.57
LISE	LiInSe_2	-4.8	11	2.86

Effective nonlinear susceptibility (d_{eff}) from SNLO for a 5 μm idler.
Bandgaps (E_g) taken from Petrov et al.²¹⁵ unless noted.

and AGS are common materials for DFG, but have low damage thresholds.²³³ While HGS has a large d_{eff} , it has limited transparency and is not readily commercially available due to challenges associated with the growth of sufficiently large crystals.²¹⁵

The remaining Li-based materials have large band gaps, reasonably high damage thresholds, and good transparency out to near 10 μm , but also have the lowest d_{eff} values, requiring the use of thick crystals which may limit the amplified bandwidth.²³⁴ Of these Li-based materials, LGS has the largest band gap, highest thermal conductivity, and lowest predicted spatial and temporal walk off in a collinear OPA configuration.²³⁵ Figure 4.2(a) shows the mid-IR absorption spectrum of LGS. Additionally, Type I phase-matching in LGS is predicted to produce the steepest angle-tuning curve of all the Li based materials. This tuning curve, calculated by SNLO and shown in Fig. 4.2, predicts idler generation in the range of 3-7.5 μm over a ~ 7 degree range of internal angles. Taken together, these properties

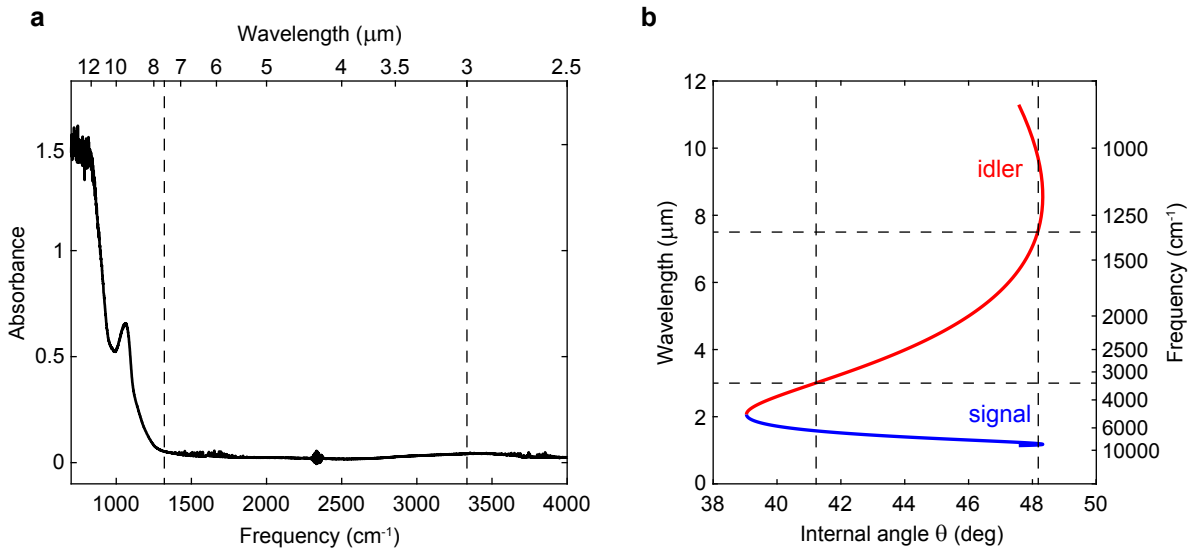


Figure 4.2: (a) LGS mid-IR absorption and (b) Type I phase-matching angles for a 1033 nm pump. (a) Absorption spectrum of a 4 mm thick LGS crystal used in the OPA (sourced from Del Mar Photonics). A baseline absorption due to clipping of the FTIR beam around the crystal’s 5×5 mm clear aperture has been subtracted. The sharp features with absorbance < 0.1 are due to imperfectly subtracted atmospheric H_2O ($\sim 1400 - 1800 \text{ cm}^{-1}$ and $\sim 3600 - 4000 \text{ cm}^{-1}$) and CO_2 ($\sim 2300 \text{ cm}^{-1}$) absorption. (b) The signal (blue) and idler (red) wavelengths are shown as a function of the crystal’s internal phase-matching angle θ . The bounds of the tuning range from 3-7.5 μm are indicated by dashed black lines in (a) and (b).

motivate our selection of LGS for mid-IR generation in an OPA configuration.

4.2.3 Design and performance of the mid-IR OPA

Here we describe the OPA’s optical design and characteristics. The final mid-IR output, tunable from 3-7.5 μm , is the idler from a single-stage of collinear amplification in LGS pumped by the 1033 nm Yb laser fundamental. The seed is provided by the near-IR (1150-1700 nm) portion of a super-continuum (SC) generated by filamentation of the fundamental in yttrium aluminum garnet (YAG). A schematic of the key components is shown in Figure 4.3. While the beam paths in Fig. 4.3 has been slightly simplified for clarity, the number of

reflections and geometries of the pump and SC seed arms are designed to match the direction of any input pointing fluctuations at the LGS crystal in order to increase stability.

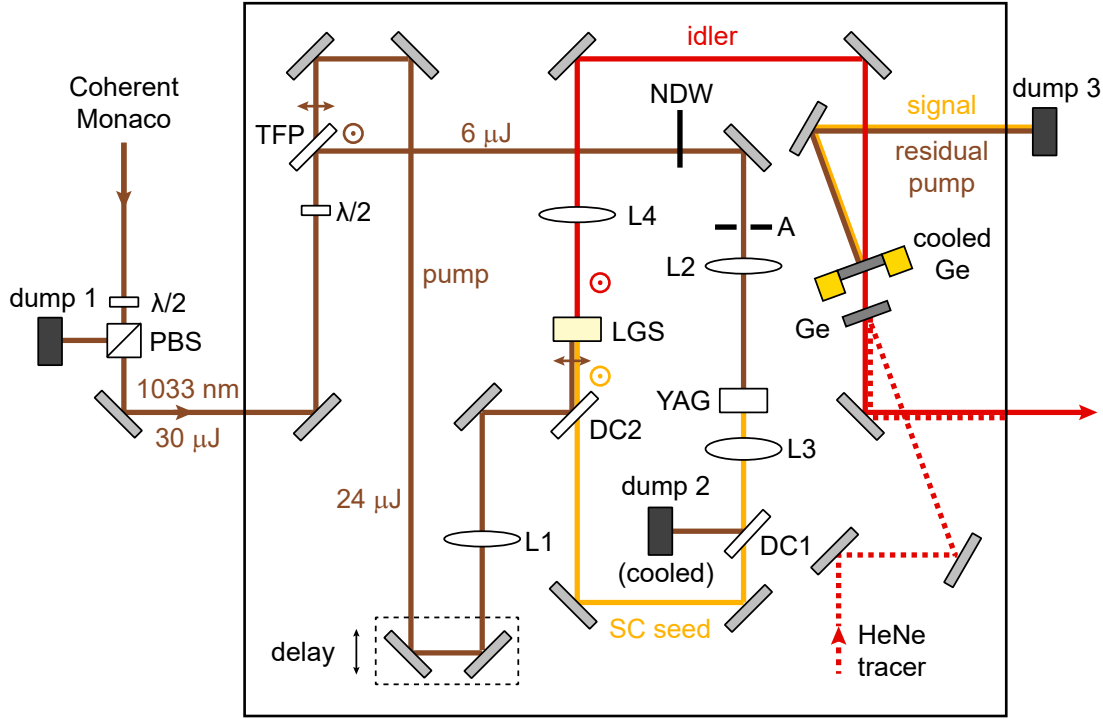


Figure 4.3: Schematic of the OPA. The pump is shown in brown, the SC seed in yellow, the mid-IR idler in red, and the HeNe tracer in dashed red. $\lambda/2$ are half-waveplates, PBS is a polarizing beamsplitter, TFP is thin film polarizer, NDW is neutral density wheel, A is an iris aperture, DC1 and DC2 are identical dichroic beamsplitters, and L1-L4 are lenses. See text for details.

The pump laser is a Coherent Monaco 1035-40, which provides a 40 W, 1 MHz repetition rate output centered at 1033 nm with $40 \mu\text{J}/\text{pulse}$, ~ 400 fs pulse durations, a ~ 3 mm $1/e^2$ beam diameter, and vertical linear polarization. 95% of its output is split toward the OPA, and a half-waveplate (Thorlabs WPH05M-1030) and high-power polarizing beam splitting cube (Thorlabs CCM1-PBS25-1064-HP) set the total input power to the OPA to 30 W, with the excess energy directed to a beam dump (dump 1). A second waveplate and

thin film polarizer (Eksma 420-1298) split the input into two components to control the balance of power for SC generation (SCG, 6 W, S-polarized) and the OPA pump (24 W, P-polarized). All mirrors in the OPA pump line and the SCG line upstream of the YAG crystal are dielectric high reflectors for the fundamental (Newport 10D20DM.10). The OPA pump line includes a manual delay stage (Newport 423) and a 250 mm lens (L1, Thorlabs LA1252-B) that focuses the pump slightly beyond a 4 mm thick LGS crystal cut for Type I phase-matching. Multiple crystals have been employed, cut with $\Phi = 0^\circ$ and either $\Theta = 45^\circ$ (phase-matching $\sim 4.5 \mu\text{m}$ at normal incidence) or $\Theta = 48^\circ$ ($\sim 7 \mu\text{m}$ at normal incidence), all of size $5 \times 5 \times 4 \text{ mm}$ (sourced from either Ascut Ltd. or Del Mar Photonics). These crystals have been either uncoated or anti-reflective (AR) coated for the pump on both faces. At the crystal, the pump beam fwhm is $\sim 250 \mu\text{m}$, and the power is 22 W due to aggregated losses through the pump line.

In the SCG line, an ND wheel (NDW, Thorlabs NDC-50C-2-B), adjustable iris aperture (A, Thorlabs SM1D12C-SM1), and 100 mm lens (L2, Thorlabs LA1509-B) determine the pump fluence and convergence into a 10 mm YAG crystal (NewLight YAG0100), where filamentation generates a SC spanning the NIR out to $\sim 1700 \text{ nm}$. This configuration for SCG was reported by Calendron et al.²³⁶. Typically, the aperture diameter is set between 2.7-3.1 mm to optimize the power and stability of the seed. A representative seed spectrum is shown in Figure 4.4(a). A 40 mm achromat (L3, Thorlabs AC254-040-C-ML) collects and refocuses the SC into the LGS crystal. One 1150 nm longpass dichroic beamsplitter (DC1, Edmund 87-043) reflects the residual SCG pump into a water-cooled beam block (dump 2) while a second (DC2) combines the OPA pump (P-polarized) and the SC (S-polarized) before the LGS crystal. A 75 mm BaF_2 lens (L4, ISP Optics BF-PX-25-75) collimates the S-polarized mid-IR idler after the crystal. An AR-coated Ge window (Edmund 83-349) in

a custom water-cooled mount reflects the residual pump and amplified signal towards a beam dump (dump 3) while transmitting the mid-IR idler. A second Ge window overlaps a reflected HeNe tracer onto the transmitted mid-IR beam to aid alignment of the output further into the downstream instrumentation. When tuned between 4 and 7 μm , a 3.6 μm long pass filter (Edmund 68-654) may be placed at the output to block a weak, P-polarized second harmonic of the idler, which can be generated incidentally in this region of the tuning curve where idler SHG is simultaneously phase-matched.²³⁷ However, this unwanted second harmonic is often not present at appreciable powers and the long pass filter is not used for the experiments in this thesis. The OPA is enclosed and purged with a dry N_2 atmosphere to protect the optics from dust and avoid idler absorption by CO_2 and water vapor.

The mid-IR output of the OPA is tunable from 3-7.5 μm , producing pulses with 85-165 cm^{-1} bandwidth and 140-540 fs duration, as summarized in Figure 4.4. The pulse energies and durations here and durations are from Ref. [190], in which a lower pump line power of 18 W was used. With the higher pump power of 24 W and small improvements in the configuration made since then, current pulse energies are in the range of 90 to 120 nJ. Tuning is achieved primarily through the LGS crystal angle, with minor adjustments to the timing, spatial overlap, and SC focusing. Representative spectra across the tuning range are shown in Figure 4.4(b). The reported spectra were collected with an Acton SpectraPro 2150i monochromator using a 150 g/mm grating blazed for 3 μm and a photovoltaic MCT detector (Boston Electronics PVM10.6). The mid-IR idler was focused at the entrance slit with a 150 mm CaF_2 lens. The entrance and exit slits were in the range of 100-400 μm . Pulse durations are determined by interferometric autocorrelation using the Mach Zehnder interferometer, which will be discussed further in Sections 4.3 and 4.6. A cooled InSb detector (InfraRed Associates IS-1.0) was used to measure the isolated second harmonic of the idler for these

measurements. The red side of the tuning range is limited by the blue edge of the dichroic used to combine the OPA pump with the SC (Figure 4.4(a)). The blue side of the tuning range is likely limited by the power in the SC.

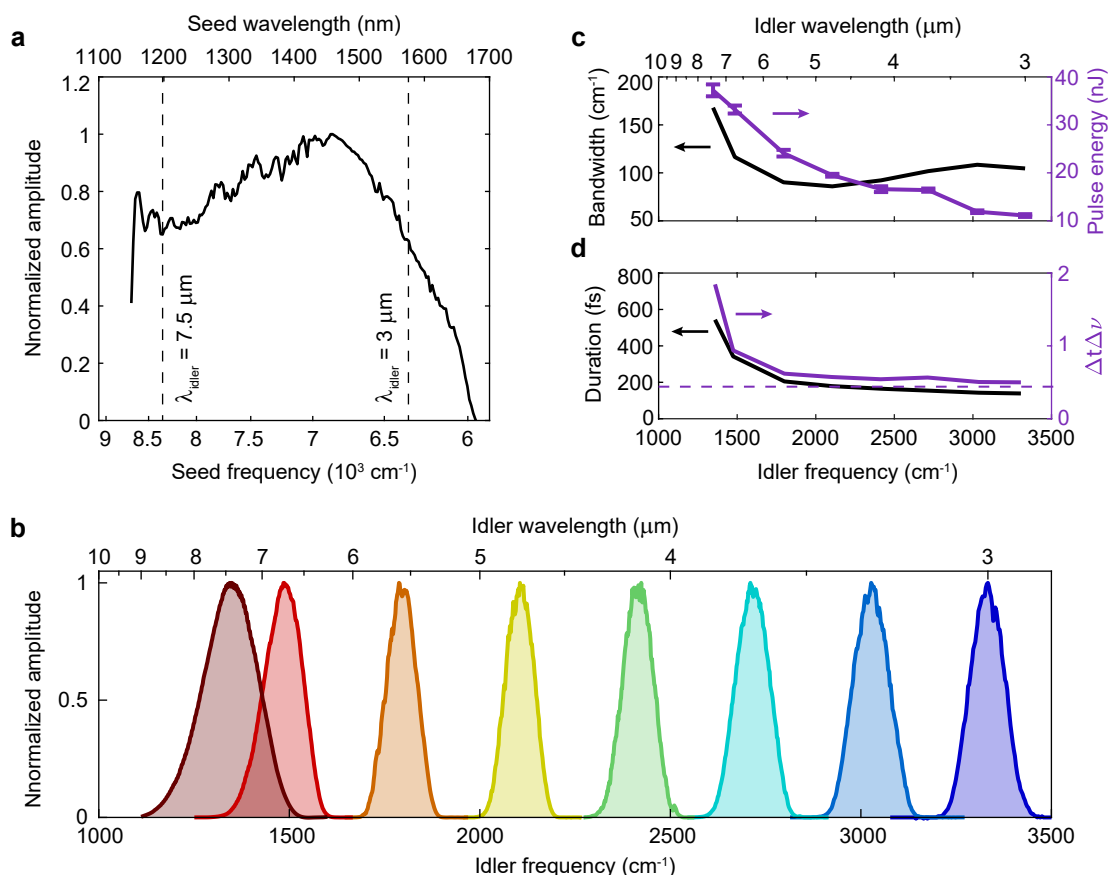


Figure 4.4: SC seed spectrum and mid-IR idler tuning range and pulse characteristics. (a) Seed spectrum as measured through a monochromator with an InGaS photodiode. The high frequency cutoff near 1150 nm is due to the dichroic beamsplitter (DC1 and 2), and the steep fall-off beyond 1600 nm reflects the red wavelength range of the InGaS detector’s sensitivity, although the seed spectrum likely does not extend appreciably further. The limits of the OPA tuning range achieved are indicated by dashed lines. (b) Example spectra of the mid-IR idler output across the tuning range. Output (c) bandwidth (black, left y axis) and pulse energy (purple, right y axis) with 2σ error-bars, and (d) pulse duration (black, left y axis) and time bandwidth product (purple, right y axis). The transform limited time-bandwidth product for a Gaussian pulse (~ 0.44) is indicated by a dashed purple line.

The mid-IR output pulse energy (at the time of writing Ref. [190]) and bandwidth are shown in Figure 4.4(c). Typical power fluctuations are $<2\%$ rms (measured over 5 min on a Coherent PS-19 power head), although $<1\%$ rms can be routinely achieved. As mentioned above, current pulse energies in the range of 4.5-6.5 μm are between 90 and 120 nJ, while the bandwidths are similar. The increase in power on the red side of the tuning curve is due to an increase in the efficiency of the process and the bandwidth of amplification. In addition, the crystal used in Ref. [190] was cut for 7 μm , so the blue side has the steepest angle of incidence. The large bandwidth on the red side of the curve can be understood from the phase-matching curve in Fig. 4.2, which approaches a vertical slope around 8.5 μm . The pulse duration and time-bandwidth product are shown in Figure 4.4(d). The time bandwidth product shows that the output is close to transform-limited except when tuned red of about 5.5 μm . This increase in pulse duration is likely due to second-order dispersion from transmissive optical elements in the IR path. In Ref. [190], a CaF_2 collimating lens was used, which exhibits a dramatic increase in nonlinear dispersion red of 6 μm (group velocity dispersion (GVD) $-1250 \text{ fs}^2/\text{mm}$ at 6.2 μm)²³⁸, and is the largest contributor to this increase in pulse duration beyond the transform limit. The material of this lens has been updated to BaF_2 , which has a slower onset of nonlinear dispersion (GVD $-591 \text{ fs}^2/\text{mm}$ at 6.2 μm), but is still significant. Section 4.6 discusses more aspects of temporal pulse characteristics and sources of dispersion downstream of the OPA. This excess second-order dispersion could potentially be compensated for by using introducing significantly more Ge into the IR line, which has an oppositely-signed GVD to BaF_2 in this frequency range (GVD $673 \text{ fs}^2/\text{mm}$ at 6.2 μm).

4.2.4 Operational details and challenges

The 1 MHz repetition rate poses unique challenges for the design, characterization, and operation of the OPA, some of which we believe will also apply more generally in the extension of ultrafast IR spectroscopy to these repetition rates. Working at a high repetition rate while maintaining pulse energies sufficient to drive nonlinear optical processes results in average beam powers higher than typically encountered with kHz systems. Controlling the resulting thermal loads on optics and mounts must be prioritized in the OPA design to avoid damaging components and ensure stable, reliable performance.

While LGS (in the absence of defects) does not absorb a significant amount of thermal energy from the pump due to its band gap being significantly above the two-photon energy, absorption of scattered pump energy has led to catastrophic damage of the crystal on two occasions. This may have been due to either an internal defect, surface damage of an AR coating, or dust particles landing and burning onto the crystal surface. As both of the crystals that failed were those sourced from Del Mar Photonics, while the crystals from Ascut Ltd. (both coated and uncoated) have not exhibited this failure mode to date, it is likely that defects introduced in the growth process played a role. In practice, burn spots appear on the exit face of the crystal after a few days or weeks of operation, at which point the crystal needs to be translated to a clean spot.

While AR coatings on the crystal could increase its susceptibility to damage in this way, they also reduce the power of unwanted back reflections and increase the input and output coupling efficiency. In Ref. [190], the LGS crystal is uncoated and the pump back reflection from the crystal face is ~ 3.6 W (from a reduced input pump power of 18 W), which is sufficient to heat optical mounts and destabilize the OPA if not controlled. This is consistent with the 12-13% Fresnel reflection at each interface, calculated from the Sellmeier

coefficients from Isaenko et al.²³⁴ Using this uncoated crystal also produced a weak ‘ghost’ IR pulse delayed by ~ 60 ps from the main idler pulse when angle-tuned near normal incidence due to internal reflections off the back and front face. AR coating both faces at the pump wavelength mitigate both of these issues.

The Ge window used to isolate the mid-IR idler from the pump and signal absorbs a portion of the pump energy and heats dramatically. Water-cooling the mount controls the heat load, but also creates a thermal lens in the Ge. Mounting configurations that maintain symmetric thermal contact with the window avoid abberating the transmitted IR mode, but also tend to distort the wavefront flatness of the Ge and thus abberate the reflected tracer beam. Therefore, a second Ge window, mounted without distortions to the Ge flatness, is required to overlap the HeNe tracer and mid-IR. An ideal solution would use a longpass dichroic mirror with a high-reflective coating over the pump and signal wavelengths, however the large idler tuning range makes finding appropriate coatings impractical. The iris aperture in the SC line also heats up substantially in regular operation (but is left uncooled), while the residual pump filtered out from the SCG is directed to a cooled beam dump to avoid heating nearby mounts.

4.3 Mach-Zehnder interferometer and visible encoding line

4.3.1 Mach-Zehnder interferometer

The Mach-Zehnder interferometer (MZI) is shown schematically in Figure 4.1 with a simplified beam path. BS1 and BS2 are matched 50:50 ZnSe beamsplitters (Rocky Mountain Instrument Co. WI1512Z) used to split the input and recombine the two arms, respectively. Both arms have protected gold retroreflectors (PLX OW-25-2G), and a precision stage (AeroTech ANT95-50L-MP) with motion controller (AeroTech A3200 Npaq) determines the relative delay of the moving and stationary arm, i.e. the τ_{IR} pulse delay. All reflective optics are protected gold. The in-phase output of the MZI (bright arm) is sent in to the FEIR microscope. The out-of-phase output (dark arm) is focused with a 25 mm CaF₂ lens onto a single-channel, room-temperature photovoltaic HgCdTe (MCT) detector (Boston Electronics PVM10.6). As described in Sections 4.5 and 4.7, this dark arm IR intensity channel is used to measure the IR pulse spectrum and act as a phase reference for three-pulse FEIR experiments. The MCT detector may alternately be placed in the FEIR microscope to measure the transmitted power of the bright arm through the sample, as described next in Section 4.4.

The MZI is enclosed and purged with dry N₂. An optical chopper (New Focus 3501 Optical Chopper using the ‘2’ wheel) is placed in the bright arm before it exits the enclosure. As described in Section 4.5, this chopper is used to isolate the total FEIR signal from any fluorescence background for experiment setup and diagnostic purposes, but is not used in regular data collection.

4.3.2 Visible encoding line

The salient components of the visible encoding pulse generation and delay line are also shown in Figure 4.1. 5% of the Monaco fundamental is split off and used for this purpose. A half-waveplate ($\lambda/2$, Thorlabs WPH05M-1030) and polarizing beam splitting cube (PBS, Thorlabs CCM1-PBS25-1064-HP) are used to set the power into a 3 mm thick BBO crystal cut for second harmonic generation of the 1033 nm P-polarized fundamental. The visible encoding pulse is the resulting S-polarized second harmonic output from the crystal (516.5 nm, spectrum shown in Figure 4.7). The first three routing mirrors after the crystal are 532 nm high reflectors that pass the residual fundamental, resulting in a sufficiently pure isolated second harmonic beam. This beam is then routed into a delay line consisting of a protected silver retroreflector mounted on an identical Aerotech ANT95-50L-MP stage. This stage sets the τ_{enc} delay, and is controlled by the same motion controller (AeroTech A3200 Npaq). The beam is then sent through a spatial filter to produce a ~ 6 mm circular mode to overfill the back aperture of the objective in the microscope. The pulse energy after the spatial filter is adjustable between ~ 10 fJ and $2.2 \mu\text{J}$ via the half-waveplate and polarizer before the doubling BBO, as measured by a Coherent LM-2 VIS power head.

4.4 The FEIR microscope

4.4.1 Microscope body and optical layout

The FEIR microscope is based on an upright epifluorescence configuration, and is constructed largely using components from the Thorlabs Cerna Series. Figure 4.5 shows photos of the microscope from the front and sides, with the IR and visible beam paths highlighted. The IR beam out of the MZI is routed into the microscope (Figure 4.5(b)) and undergoes two

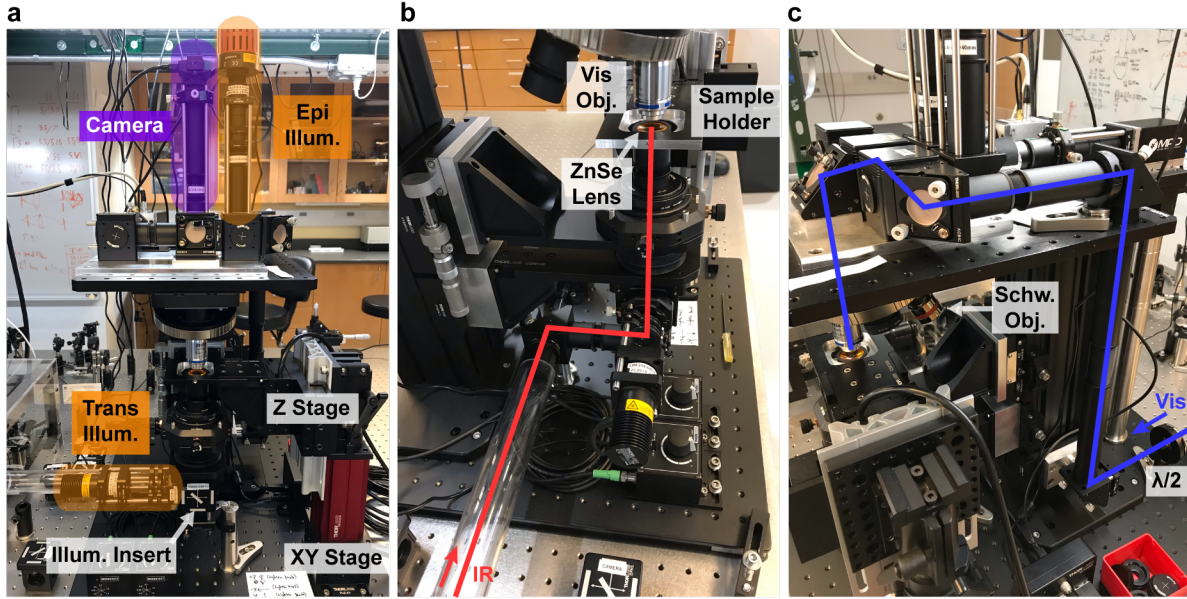


Figure 4.5: Layout of the FEIR microscope.

reflections off protected gold mirrors into an uncoated ZnSe aspheric lens (ISP Optics ASPH-ZC-25-12), which focuses the beam into the sample from below. Considering the $f = 12.7$ mm focal length and quoted 90% clear aperture of the 25.4 mm diameter, the NA of this lens is nominally

$$\text{NA} = n \sin \theta = n \sin \left[\arctan \left(\frac{D}{2f} \right) \right] \approx 0.68, \quad (4.1)$$

where D is the effective back-aperture diameter and we take the index $n = 1$ of the air gap before the sample. The size of the IR beam at the back of the lens is ~ 8 to 12 mm, and therefore does not completely fill its aperture. The ZnSe lens is mounted with X,Y and Z translation, and the IR path up to its sample-facing top surface is enclosed in beam tubes and purged with dry N_2 .

The linearly polarized visible beam is first sent through a half-waveplate (Thorlabs

WPH10M-514, $\lambda/2$ in Figure 4.5(c)) to set the polarization relative to the IR beam in the sample, then routed up to the top of the microscope, and sent downward into the objective turret. For nearly all FEIR measurements discussed in this thesis, with the important exception of polarization-dependent experiments discussed in Chapter 9, the polarization of the visible is set to be parallel with the IR. The workhorse objective for high-sensitivity FEIR measurements in this thesis is a NA 0.8 Zeiss A-Plan 63x air objective lens. The working distance of this objective, defined as the distance between the front assembly housing and the focus, is 300 μm . Alternatively, a 0.5 NA reflective Schwarzschild-type objective (Thorlabs LMM40X-P01) is used when collecting the transmitted IR beam, or when a much larger working distance (this objective having at least 7 mm) is desired, at the expense of looser focusing and lower collection efficiency. Both objectives are infinity corrected and parfocally matched, meaning their focal points occur at the same location in Z, to within a few μM .

The sample cell (discussed next in Section 4.4.2) is held in a sample holder mounted to three axes of micro-positioning (Thorlabs PLS-XY and ZFM2020) driven by a Thorlabs MCM3001 controller. The Z motion (vertically along the optical axes of the IR and visible beams) may be automatically scanned to profile the sample with ~ 1 μm repeatability, but the XY motion is not sufficiently reproducible for raster scanning, and is only used to position the sample with visual feedback e.g. from a camera (discussed below).

The routing optics and detection assembly on the top of the microscope are shown in Figure 4.6(a). To facilitate the multiple detection modalities required for experiments, alignment, and auxiliary characterization, the beam routing setup incorporates four magnetic bases (labeled Insert 1 through 4) that accept exchangeable inserts containing different optics (Thorlabs DFM1 series). For FEIR measurements, or otherwise when fluorescence from

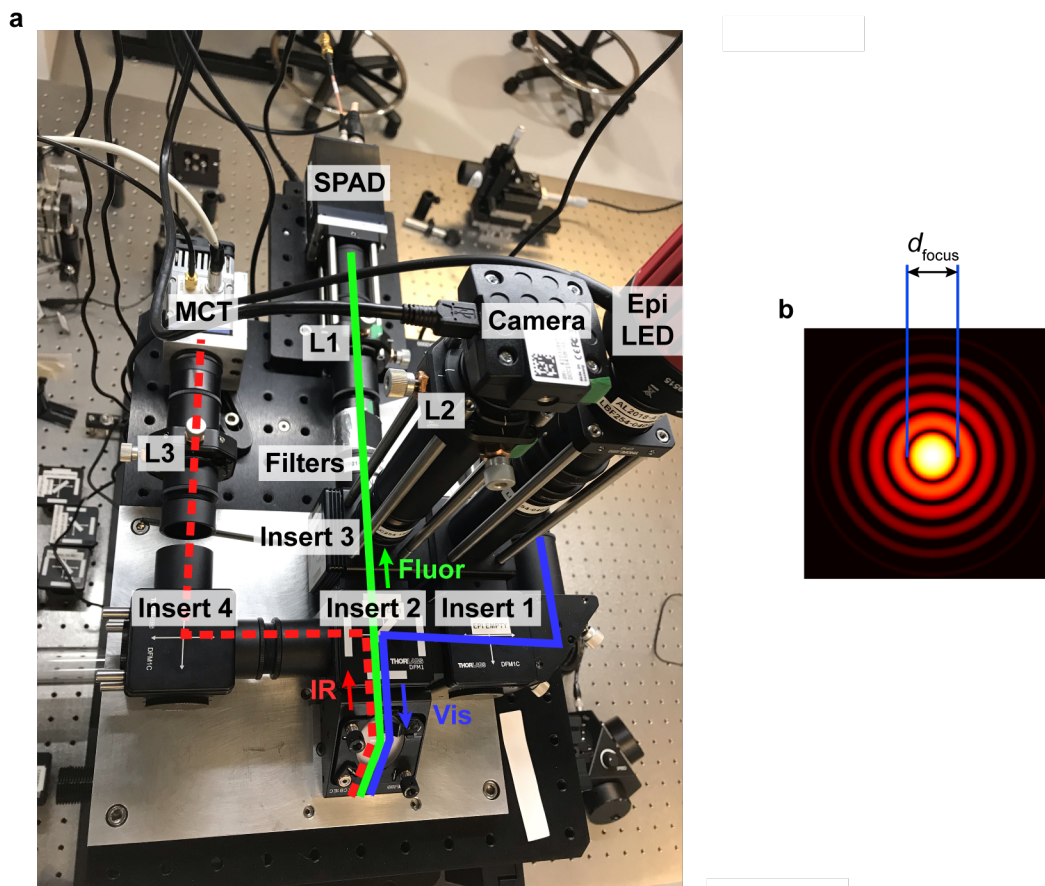


Figure 4.6: (a) Top view of the FEIR microscope detection area with principle components labelled, and (b) illustration of an Airy pattern from an idealized diffraction-limited spot in the objective's focal plane (intensity on log-scaled heat map).

the sample is being monitored, Insert 1 is empty, Insert 2 contains a dichroic mirror (Semrock FF526-Di01) which reflects the visible beam toward the objective and transmits the fluorescence, and Insert 3 is empty to pass the fluorescence towards the detector. The fluorescence is then passed through a notch (Thorlabs NF-514-17) and bandpass (Semrock FF01-550/49) filter to thoroughly remove residual scattered excitation light and spectrally restrict detection around the target molecular fluorescence spectrum. The spectral profiles of the dichroic and filter set are shown in Figure 4.7 overlaid on the visible encoding pulse

spectrum and the absorption and emission spectra of the FEIR dye coumarin 6 for reference. This dichroic/filter set collects fluorescence on the Stokes side of the visible excitation, as in a conventional fluorescence microscope. However we note that the electronic pre-resonance conditions required for FEIR in principle enable detecting emission on the anti-Stokes side, which may have advantages for dyes with small Stokes shifts.

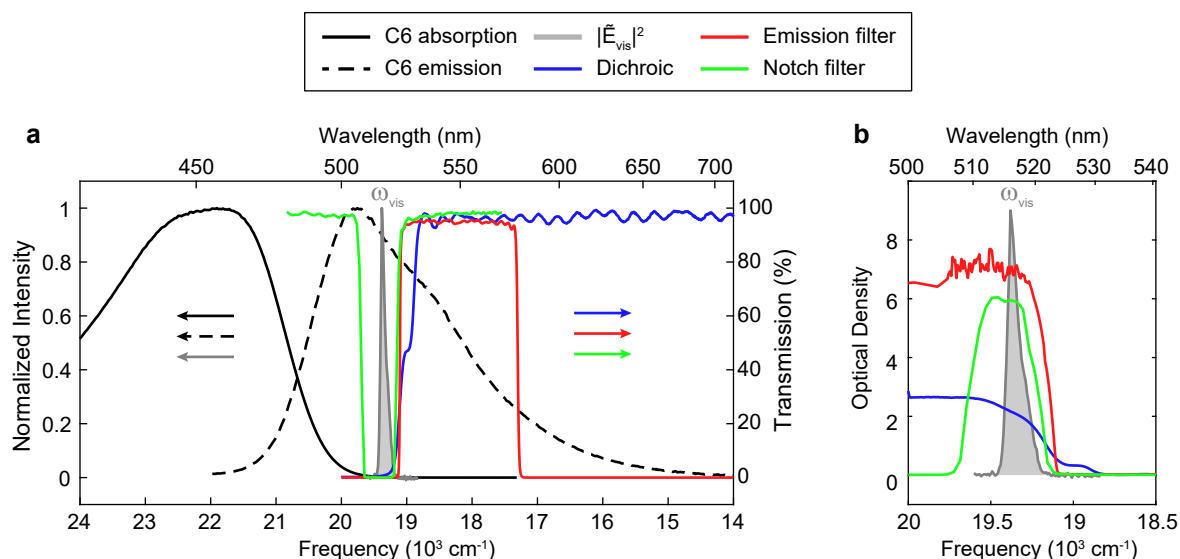


Figure 4.7: Spectral characteristics of the epifluorescence filter set. (a) Left y axis: Normalized absorption (solid black) and fluorescence (dashed black) spectra of coumarin 6 in acetonitrile and visible encoding pulse spectrum (gray). Right y axis: transmission spectra of the notch filter (green), dichroic beamsplitter (blue), and emission filter (red). (b) Transmission of the notch filter, emission filter, and dichroic beamsplitter in optical density units with the spectrum of the visible encoding pulse overlaid.

The detector is a single-photon avalanche photodiode (SPAD, MPD PDM 50) which has a $50 \mu\text{M}$ active area. To achieve confocal conditions, the focal length of the tube lens (L1 in Figure 4.6) is chosen to produce the magnification required to roughly match the image size of visible objective's point spread function with that of the active area. In this way, the active area acts as the pinhole itself, giving rise to the confocal filtering effect.²³⁹ Here

we briefly describe how this tube lens focal length is determined. An idealized diffraction-limited point spread function in the focal plane is given by an Airy pattern, shown in Figure 4.6(b).^{189,240,241} The central disk contained within the first diffraction ring has a diameter d_{focus} in the sample of

$$d_{\text{focus}} \approx \frac{1.22\lambda}{\text{NA}}, \quad (4.2)$$

where λ is the wavelength (516.5 nm for the encoding pulse). For the 0.8 NA Zeiss objective, this focal spot diameter is $d_{\text{focus}} = 0.788 \mu\text{m}$. The size of this spot imaged at the detector d_{image} is simply scaled up by the overall magnification M of the optical system

$$d_{\text{image}} = Md_{\text{focus}} = \frac{f_{\text{TL}}}{f_{\text{obj}}}d_{\text{focus}}, \quad (4.3)$$

where the magnification is in turn determined by the focal ratio of the tube lens (f_{TL}) and objective (f_{obj}). In practice, manufacturers of modern infinity-corrected objectives do not usually directly report their focal length, but rather specify a magnification which is only defined with respect to a given standard tube lens focal length. Unfortunately, each manufacturer uses their own tube lens standard (which to the detriment of the uninitiated are not always clearly indicated), some of which are summarized in Table 4.2. The 0.8 NA Zeiss objective is specified with nominal magnification of 63x, meaning its actual focal length is $f_{\text{obj}} = (165 \text{ mm})/63 = 2.62 \text{ mm}$. We therefore choose a tube lens with $f_{\text{TL}} = 150 \text{ mm}$, producing an actual magnification of $\sim 57\text{x}$ and focal spot image of $45.5 \mu\text{m}$, which is close to being matched with the detector.

To position the sample in the focus and perform other alignment procedures, a silver mirror may be placed in Insert 3, which directs the beam path upward and through a 125

Manufacturer	f_{TL} standard (mm)
Zeiss	165
Thorlabs	200
Olympus	180
Leica	200
Nikon	200
Mitutoyo	200

Table 4.2: Tube lens standards for different objective manufacturers.

mm tube lens (L2) to focus onto a CMOS camera (Thorlabs DCC1545M). To measure the transmitted IR intensity, the Schwarzschild objective is used, and Inserts 2 and 4 contain silver mirrors that instead route the beam toward a separate arm with a 25 mm CaF_2 focusing lens (L3 in Figure 4.6) onto a single-element MCT detector. This is the same detector used for the out-of-phase output of the MZI, and must be moved between these two locations.

To aid in positioning the sample, performing alignments, and other basic characterization tasks, widefield epi and transmission illumination are provided by two LEDs (Thorlabs MN-WHL4 and MCWHL1, respectively, both with LEDD1B driver), shown in Figure 4.5(a). In both cases, a relay of lens and a pair of iris apertures are used to create conditions for Köhler illumination, which essentially images perfectly out of focus light from the LEDs onto the sample to ensure uniform and homogeneous illumination.¹⁸⁹ For using epi-illumination, Insert 1 contains a mirror and some of the relay lenses, while Insert 2 has the same dichroic used for fluorescence detection. For transmission illumination, another exchangeable insert (Figure 4.5(a)) containing a mirror and relay lenses is placed in the IR beam path below the ZnSe asphere.

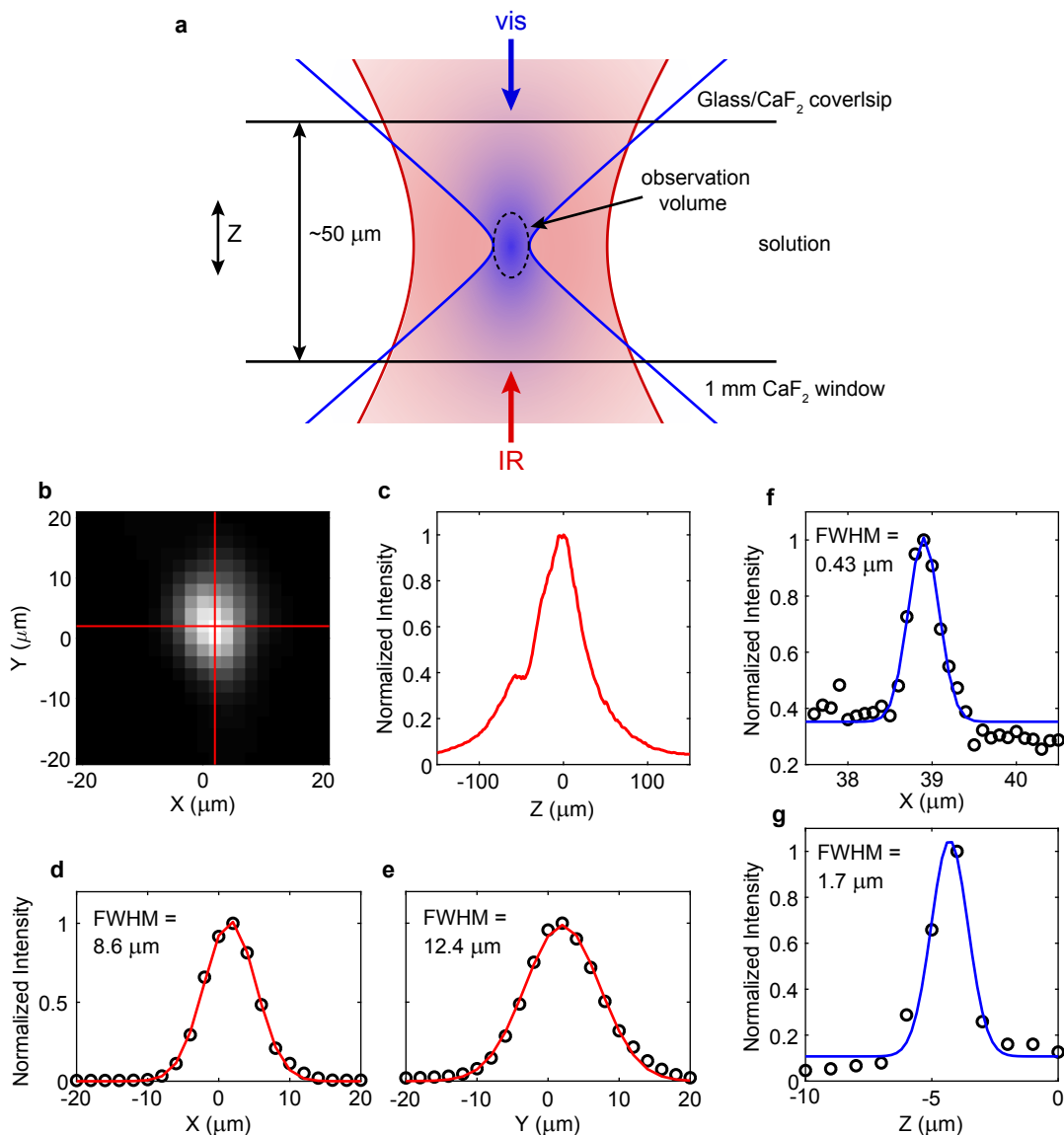


Figure 4.8: Cofocusing of the counter-propagating IR and visible beams and characterization of their focal spots. (a) Schematic representation of the focal volumes of the IR and visible beams in the sample. (b) Grayscale image of the IR intensity from a pinhole scan in the focal plane ($Z = 0$). The maximum and minimum intensities are set to white and black, respectively. Red lines indicate the slices plotted in (d-e). (c) Z scan at the maximum intensity XY position in (a). (d-e) Slices along the X and Y directions from the data in (a) (black circles) with Gaussian fits (red). (f)-(g) Visible focus characterization. (f) Bead scan across the lateral beam profile at the focus (black circles) with Gaussian fit (blue). (g) Axial scan.

4.4.2 IR and visible focal characterization and sample region

Figure 4.8(a) illustrates the FEIR microscope’s observation volume formed by the counter-propagating and cofocused IR and visible beams in solution, emphasizing the significant size mismatch in their focal volumes due to the diffraction-limit. Therefore, even though FEIR excitation depends on the intensity of both fields, the operational probe volume of the experiment is essentially determined exclusively by the visible focus and its imaging onto the detector. Sample solutions are held in a home-built aluminum cell between a coverslip (top, visible/fluorescence side) and 1 mm thick Calcium Fluoride (CaF_2) window (bottom, IR side) separated by a 50 μm thick polytetrafluoroethylene (PTFE) spacer. Both coverslip and window are 25.4 mm rounds, and the spacer is cut in an roughly 3 mm narrow annulus of similar outer diameter. For many of the experiments described in this thesis (including those in Refs. [242, 243] and some of Ref. [244]), the top coverslip is a standard 175 μm thick #1.5H glass coverslip (Marienfeld). However, as we will discuss in Section 4.8, thermal effects caused by IR absorption of these poorly transparent glass coverslips limit the signal sizes and can produce artifacts in FEIR experiments. Switching to IR-transparent CaF_2 coverslips (sourced from Crystran in either 200 or 150 μm thickness) eliminates these thermal effects, and represents a dramatic improvement in the sensitivity and quality of FEIR measurements. More details and considerations of imaging quality through these non-standard coverslips will be discussed further in Section 4.8.

The following characterization of the sizes of the IR and visible focal spots was done in an older version of the instrument (only used for the work described in Ref. [242]), which employed a modified Bruker Hyperion FTIR microscope. Unlike the less than ideal situation in the current version of the custom FEIR microscope described here, the sample stage of this commercial microscope allowed for repeatable micro-positioning in the XY plane, making

these focal profiling measurements possible. Fortunately, as the same ZnSe asphere and Zeiss objective were used in this original instrument, the following characterization should still be representative of the current experiment.

The size of the IR focus at the sample was determined by measuring the transmission through a 5 μm pinhole which is raster scanned across the beam. The pinhole was mounted between a 1 mm CaF_2 window and coverslip to mimic the sample profile. Figure 4.8(b) shows an XY scan at the IR focal plane. Cross sections with Gaussian fits are shown in Figures 4.8(d) and (e). The measured beam size represents the true beam size convoluted with the 5 μm pinhole, which is not a significant difference. For simplicity we report the spot size as the average of the measured X and Y cross-sections, yielding a 10.5 μm fwhm or 8.9 μm $1/e^2$ radius. Figure 4.8(c) shows a Z scan along the axis of the beam, where negative Z positions are above the focus.

The visible focal size with the NA 0.8 Zeiss objective was determined by measuring the emission intensity from a 100 nm fluorescent bead as it was scanned through the focus. The bead sample was prepared by drop casting a few μL of bead solution (Fluoresbrite YO Carboxylate Microspheres 0.10 μm) on a clean coverslip. Figures 4.8(f) and (g) show an X cross section at the focal plane and Z scan along the optical axis, yielding a fwhm ($1/e^2$ radius) of 0.43 μm (0.36 μm) and 1.7 μm (1.4 μm), respectively. These measurements were performed without employing a strong confocal effect by properly matching the image size of the focus on the 50 μm active area of the detector. Specifically, for this measurement a short $f = 75$ mm tube lens was used, producing a smaller 15 μm Airy disk at the detector. The resulting size should therefore only be taken as approximate, but are roughly consistent with diffraction-limited focusing with the 0.8 NA.

Refraction affects the apparent thickness of the nominally 50 μm solution layer, i.e. the

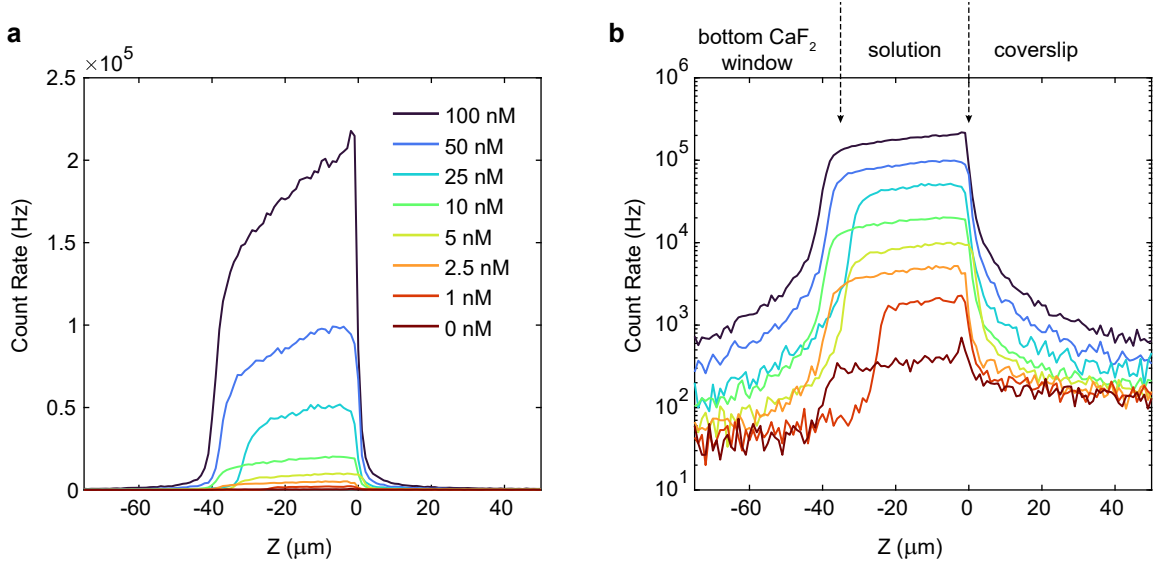


Figure 4.9: Fluorescence Z profiles of multiple samples on linear (a) and logarithmic (b) vertical scales, indicating typical variations in apparent thickness.

distance the sample needs to be translated in real space in order for the visible focus to move from the top to the bottom interface. The relation between the apparent and real thickness h and h_r , respectively, can be found from Snell's law considering the NA of focusing, and is given by

$$h = h_r \sqrt{\frac{NA^2 - n_i^2}{NA^2 - n_s^2}}, \quad (4.4)$$

where n_i is the index of the immersion medium contacting the objective (air, $n = 1$ in our case), and n_s is the index of the solution.²⁴⁵ For acetonitrile (or acetonitrile-d₃) with index of $n_s = 1.345$ at the visible excitation frequency, a 50 μm layer would appear to be ~36 μm using the Zeiss objective. Figure 4.9 shows Z profiles of the one-photon excited fluorescence from rhodamine 6G solutions in acetonitrile-d₃ of varying concentration. The width of these profiles are roughly consistent with that expected of a 50 μm layer while also giving

some indication of the sample-to-sample variations in solution layer thickness. Additionally, these profiles demonstrate the sharp $\sim 1 \mu\text{m}$ step-response in Z at the top solution interface indicative of good confocal filtering, as well as the linearity of count rate with concentration from the bulk.

FEIR measurements are typically conducted with the focus at an apparent distance (i.e. h not h_r) of $20 \mu\text{m}$ below the top interface, after first checking that the total solution layer is thick enough to accommodate this depth. The bending flexibility of the coverslip can often cause the sample to slowly decrease in thickness if the solvent evaporates over the course of the measurement, a problem that can be especially troublesome for highly volatile organic solvents. One solution is to use a spacer shape that incorporates a support structure (e.g. an arm pointing in from the one side of the annulus) near the center of the coverslip so that it cannot flex downwards.

4.5 Detection of IR and fluorescence signals

4.5.1 Data acquisition architecture

Here we describe the general approach to recording IR and single-photon fluorescence signals from the MCT detector and SPAD, respectively. For bulk FEIR measurements and routine instrument alignment, these signal acquisition tasks are handled by a multifunction data acquisition (DAQ) card (National Instruments PCIe-6361) with software written in LabVIEW. A breakout terminal block (National Instruments BNC 2090-A) is used for a front-end connection interface to the DAQ card. Time-tagged and time-resolved photon detection by TCSPC is accomplished by a separate dedicated system, and will be described in Section 4.9.

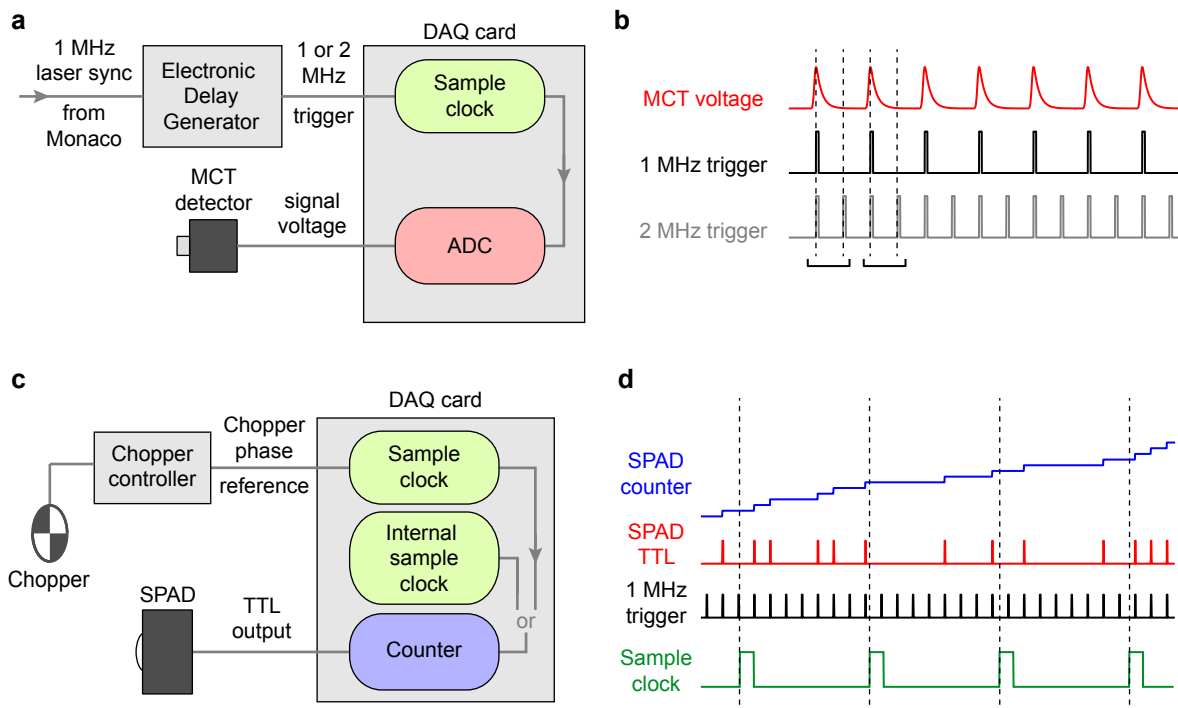


Figure 4.10: Signal acquisition architecture using the DAQ card. (a) DAQ setup for shot-to-shot detection of IR intensity from the MCT detector. A 1 or 2 MHz trigger waveform from the delay generator provides the sample clock for analog-to-digital conversion (ADC) of the signal voltage. (b) Waveforms of the MCT signal voltage and 1 and 2 MHz triggers, with sampling events indicated by vertical dashed lines. (c) DAQ setup for photon counting with the SPAD. (d) A counter enumerates incoming edges of the SPAD's digital TTL waveform, and this counter is sampled either by an internal clock, or by an external source. The case shown in (c) is of the chopper's digital phase reference waveform, which facilitates differential acquisition of the FEIR count rate above the background. The 1 MHz laser sync is shown in (d) to indicate that fluorescence photons are detected in response to the excitation pulse train, but this waveform is not used in photon counting mode.

IR detection

Shot-to-shot measurement of the mid-IR intensity at 1 MHz requires a detector bandwidth high enough to ensure that its voltage response has fully relaxed before the next pulse arrives. The photovoltaic MCT detector used has a sufficiently fast multi-nanosecond response time to satisfy this requirement. Furthermore, since boxcar integrators that can be triggered at

1 MHz are not readily available, determination of the mid-IR intensity relies on sampling the peak detector response. The DAQ architecture for synchronously recording the detector response at its peak is shown in Figures 4.10(a)-(b). A 1 MHz sync from the Monaco's amplifier (exact repetition-rate 994.7 kHz) triggers a delay generator (Stanford Research Systems DG 645), which is configured to output either a 1 or 2 MHz digital waveform with an electronic delay tuned to synchronize against the detector response profile. This waveform acts as the sample clock, triggering acquisitions of either just the peak voltage in the case of the 1 MHz trigger, or alternating peak and baseline voltages for the 2 MHz trigger (Figure 4.10(b)). In the 2 MHz mode, the digitized signal is then separated into peak and baseline values and their difference is taken for each shot. This 2 MHz detection scheme is useful for removing the constant offset voltage from the detector's preamplifier, which can drift slowly on the timescale of minutes to hours. This mode is therefore useful when the absolute magnitude of detector response is of interest, e.g. during alignment with the MCT on top of the microscope. As we will discuss below, when measuring IR interferograms from the MZI, the 1 MHz mode is used as it imposes a milder bandwidth load on the DAQ card, and the fast, continuous stage scanning procedure circumvents slow noise from this baseline drift.

Fluorescence photon counting

Unlike the case of IR detection, photon counting with the SPAD is asynchronous with respect to the laser pulse train. The acquisition scheme for photon counting is shown in Figures 4.10(c)-(d). Photon detection events registered by the SPAD are output in two separate digital channels, one using a transistor-transistor logic (TTL) waveform, and the other a Nuclear Instrument Modules (NIM) waveform. The TTL is sent to the DAQ, while the NIM, which has slightly lower timing-jitter, is used for TCSPC (Section 4.9). A counter in

the DAQ is programmed to increment on the incoming TTL edges. The value of this counter is then sampled either by an internal clock onboard the DAQ card, or by an external trigger (Figure 4.10(d)). The difference in the counter value between successive samples is the number of photons recorded in that interval, or bin. When monitoring the total fluorescence level from the sample during alignment or auxiliary characterization, an internal sample clock is used, typically with a 50 millisecond bin time (20 Hz sample clock). The number of photons per bin is converted to an intensity (count rate) by multiplying by the sampling rate.

Chopped-mode counting

One example where an external clock source is used is in ‘chopped-mode’, where the IR beam into the microscope is being chopped, and the difference in fluorescence count rate with and without the IR beam is monitored directly. This mode isolates the count rate of the FEIR signal on top of any background. The chopping rate is set at 100 Hz by the chopper controller’s internal clock, and is asynchronous with respect to the orders of magnitude higher pulse repetition-rate. Counts during successive on and off phases of the chopper cycle are separately recorded and subtracted. In practice, photon counts within adjustable portions at the beginning and end of the chopping duty cycle are ignored to avoid situations when the IR beam is only partially blocked by the blades on the chopper wheel. Chopped-mode is useful for alignment purposes when optimizing the FEIR signal magnitude, and can also be used when stepping pulse delays or sample stage positions. However, FEIR data acquisition is mostly done by fast continuous scanning of the optical delays without chopping. In this case, a position feedback waveform from the delay stage controller acts as the external sample clock, and will be described next.

4.5.2 Continuous stage ‘fastscanning’ with Position Synchronized Output (PSO)

Continuously scanning pulse delays is an attractive option for collecting time-domain data, as much of the experimental ‘dead-time’ associated with stepping delay stages, e.g. due to communication latency and mechanical settling time, can be avoided. Besides decreasing the time required to sample a given number of laser shots over a range of delay values, continuous scanning can also dramatically improve signal to noise ratios if the delays are varied faster than the slow noise fluctuations in signal due to, for example, laser power variations or mechanical drift in the spectrometer. As a result, the actual speed up in acquisition time required to achieve a given signal to noise can be quite significant. This is particularly true in our case as the 1 MHz repetition-rate is high enough to facilitate very fast scan speeds while still adequately sampling the data in real time.

Either the τ_{IR} and τ_{enc} stages in the interferometer and visible delay line, respectively, (each identical AeroTech ANT95-50L-MP) may be fastscanned. Our method for fastscanning employs the Position Synchronized Output (PSO) of the stage controller (AeroTech A3200 Npaq), which produces electronic TTL pulses synced to predefined increments of the stage’s internal encoder within a specified window of travel. The PSO waveform is used as a grid over which signal acquisition events may be referenced to in real time. How this is accomplished depends on the character of the signal channel.

The case of the IR intensity from the dark arm of the MZI is illustrated in Figure 4.11. A counter on the DAQ card enumerates incoming edges of the PSO waveform while the stage moves at constant velocity. The 1 MHz sync waveform from the delay generator is then used to simultaneously trigger samples of the MCT detector’s peak voltage and the PSO counter value. The PSO count is either then interpolated up to laser sync sampling rate to generate

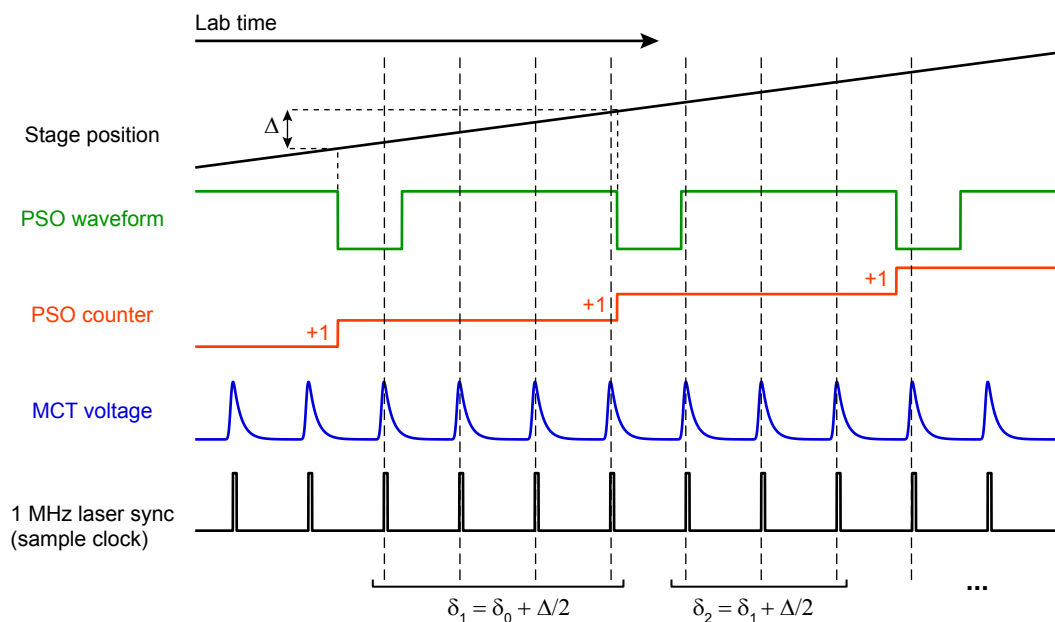


Figure 4.11: IR detection with continuous stage motion.

the position axis, or the voltages within a constant PSO count value are averaged together (shown in Figure 4.11), defining the voltage value of that position bin.

Figure 4.12 shows an example of a fastscan IR interferogram measured with the MCT detector monitoring the dark arm of the MZI. The raw data in panels (a)-(c) show the individual samples of both voltage and PSO counter at the 1 MHz sampling rate. In practice, the high 1 MHz acquisition rate produces unnecessarily dense sampling of the interferometric fringes (evident in panels (b) and (c)) even for fast scan speeds (here 2 mm/s). Therefore, data collection most often uses the binning approach described above, where after each sweep of the stage, voltages are averaged within each PSO bin (shown in panels (d)-(e)) in the LabView routine. For this data (1.8 mm scan window corresponding to $\tau_{\text{IR}} = [-2, 10]$ ps), the average duration of a forward and reverse scan cycle including turn around time and LabView processing is ~ 3.8 s. Typical PSO bin sizes for τ_{IR} -dependent signals are 300

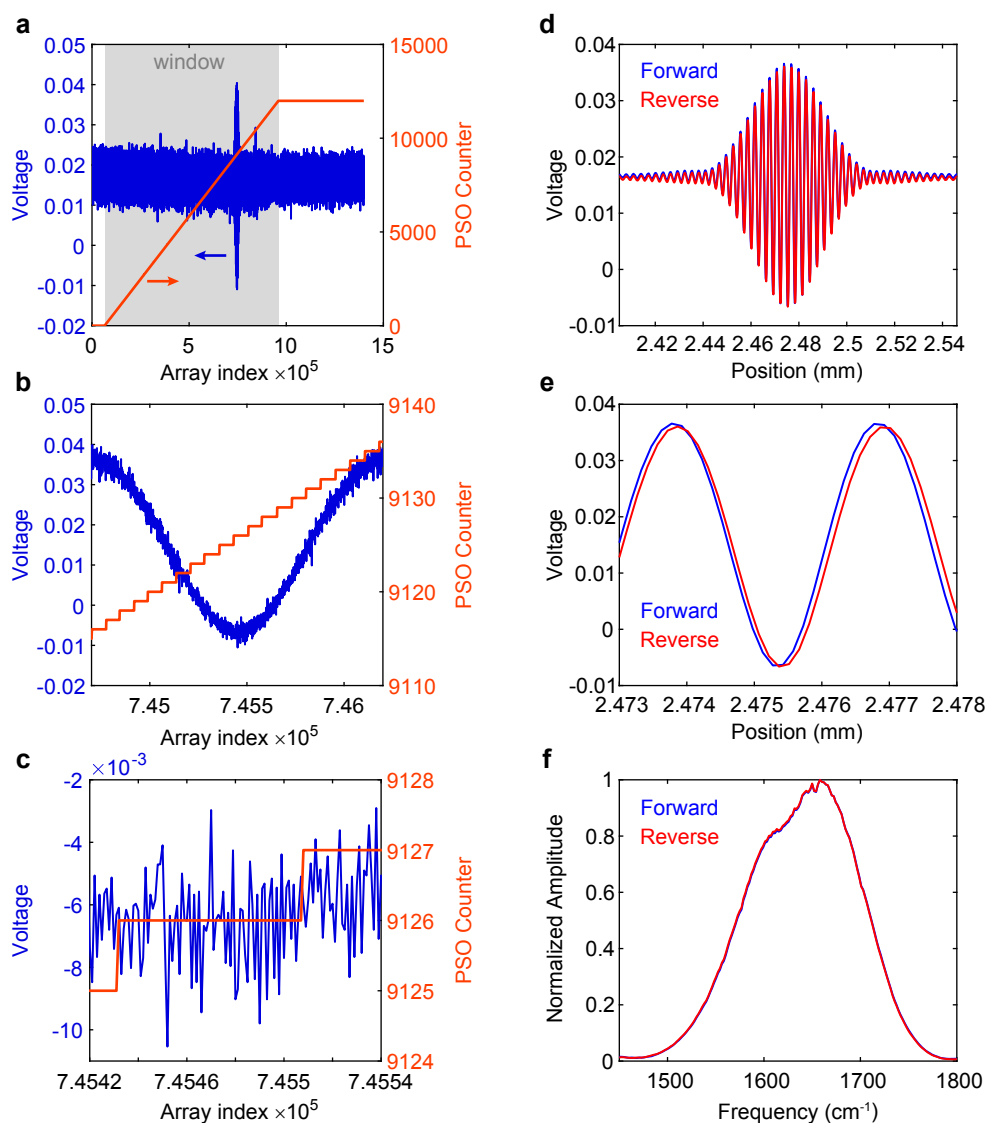


Figure 4.12: Fastscan acquisition of an IR pulse interferogram. (a)-(c) Raw MCT voltage and PSO counter acquisitions (triggered by the 1 MHz Monaco sync) for a reverse direction scan of the interferometer stage. The x axis consists of the array index in LabView that receives each sample. The grayed-out region in (a) indicates the window of delays the PSO has been programmed to monitor (here 1.8 mm of travel). (b) and (c) show successively zoomed in views of the region around the central fringe of the interferogram. The PSO increment, reflected by the width of each step of the PSO counter values, is 150 nm. (d) Interferogram in the forward (blue) and reverse (red) travel direction with the x axis binned up to 150 nm (~ 1 fs bins) and averaged over 20 scans. (e) Zoomed in view of the central fringe in (d). (f) Processed IR pulse spectra from the interferograms in (d).

nm ($\times 2/c_0 \approx 2$ fs), which is well above Nyquist sampling for the mid-IR wavelength. As the signal is being binned (i.e. averaged) within the PSO increments, rather than sampled directly at discrete positions, systematic under-sampling is not possible with this approach.

For the fluorescence channel, a second counter on the DAQ monitors the TTL output of the SPAD, i.e. counts incoming photon arrival events. The PSO counter is then used to trigger samples of the cumulative photon count. The increment in photon count between successive PSO triggers is therefore the number of photons detected within the corresponding increment of stage travel. For each repetition of the scan new photon arrivals are accumulated in their respective bins, and the data builds up as a histogram of delay bins.

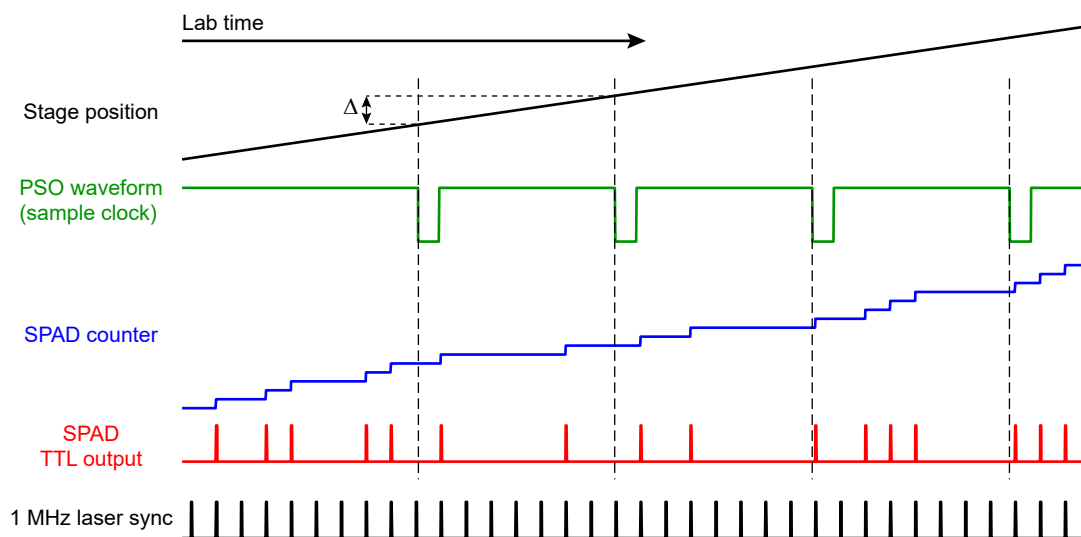


Figure 4.13: Fluorescence detection with continuous stage motion.

In either case, the accuracy of the stage's encoder in general depends on the direction and speed of travel, so care must be taken to separately process data from each direction and use the same scan speed for the three-pulse FEIR signal and IR reference data (used for processing Fourier transform spectra as described in Section 4.7). A limitation of this

acquisition procedure is that the fluorescence and IR channels cannot be detected simultaneously by the DAQ card, and must be done sequentially. In practice, an IR reference is usually taken before and after an FEIR measurement to determine if phase drift due to any instrumental pathlength change has occurred.

Fastscanning of the τ_{enc} delay is done for two-pulse FEIR measurements (Section 4.7), which can use much larger bin sizes due to the slower evolution of the FEIR signal in τ_{enc} . Typically, 40 fs bins are used, and the τ_{enc} axes in the two scan directions are sufficiently similar to be directly averaged together.

4.5.3 Fourier transform spectral artifacts from periodic stage position errors

Small periodic errors from the encoder of the τ_{IR} stage give rise to spectral artifacts that appear as satellite features in Fourier transform data, analogous to ‘Rowland ghosts’ encountered with diffraction gratings.^{246,247} For our particular stage, these satellite or ‘ghost’ peaks appear offset at spacings of $\sim n \times 250 \text{ cm}^{-1}$ for $n = \dots, -2, -1, 0, 1, 2, \dots$ with roughly 1-5% of the true band’s intensity (see e.g. Figure 4.15(c)). This behavior seems to be consistent with other Aerotech ANT95 stages of similar generation. Thankfully, these periodic position errors are reproducible from scan to scan and therefore may be corrected by calibration.

Here we describe a simple approach to this calibration using the optical phase evolution of the HeNe tracer beam extracted by the analytic signal representation of its intensity interferogram. This approach is inspired by the operation of an interferometric laser encoder. However, unlike more sophisticated strategies that directly measure in-phase and in-quadrature fringes to monitor the phase on a point-by-point basis,²⁴⁸ our approach requires measuring the entire interferogram and extracting the phase after the fact in post-processing. As such,

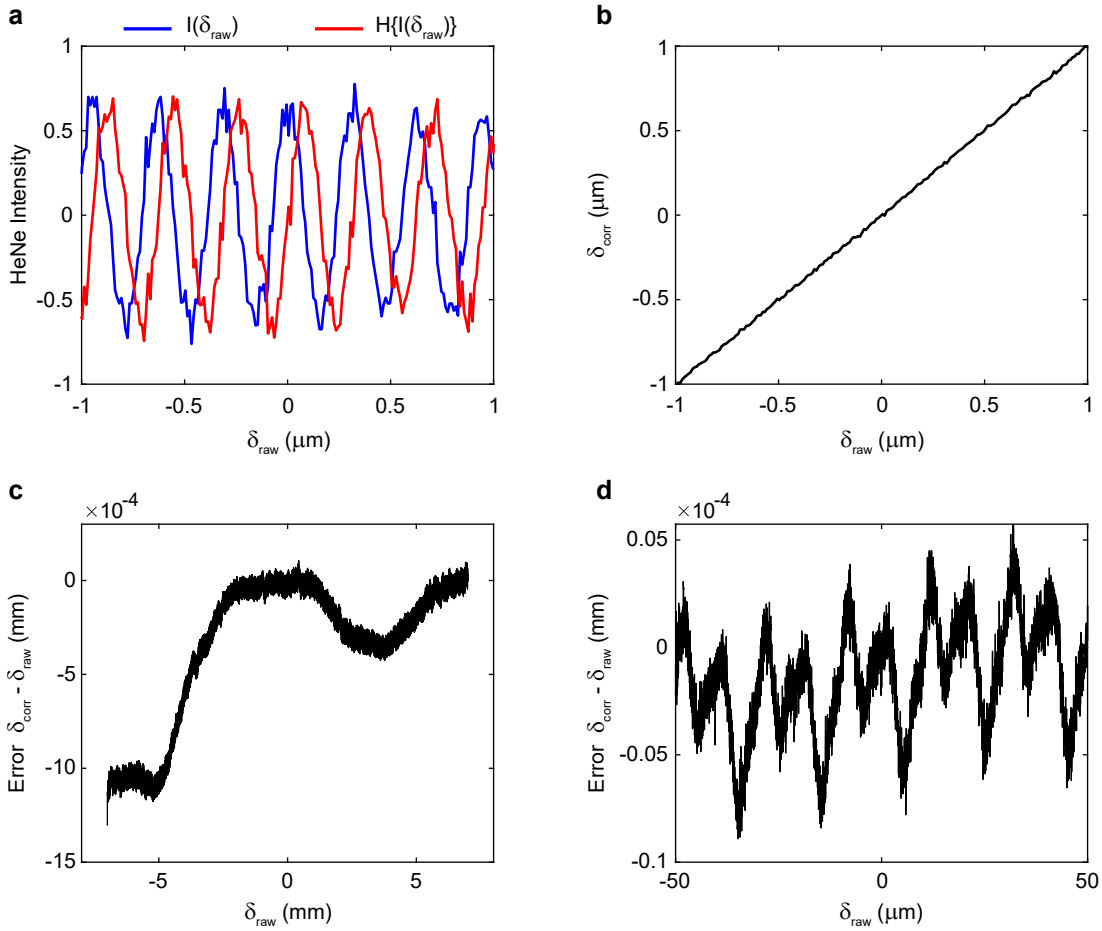


Figure 4.14: Tracking stage position errors with the HeNe tracer interferogram. (a) Detail of the raw HeNe interferogram $I(\delta_{\text{raw}})$ (blue) and its Hilbert transform (red). (b) Calibration of corrected positions δ_{corr} against raw positions δ_{raw} by Eq. 4.7 over the same range as in (a). (c) Position error $\delta_{\text{corr}} - \delta_{\text{raw}}$ over a ~ 16 mm range of stage travel. (d) Zoomed in view of the position error showing periodic structures on the $\sim 10 \mu\text{m}$ scale.

the method's success is reliant on the reproducibility of position errors over the course of the measurements being conducted. No additional optics are required, provided that the correct HeNe spot can be isolated from the multiple laterally displaced spots arising from reflections off the incorrect beamsplitter surfaces. Simply iris-ing down the beam to perform the calibration is usually sufficient.

During stage motion, the intensity of the HeNe in the dark arm of the MZI is monitored by a photodiode, and acquisitions of its voltage are sampled by the 1 MHz Monaco sync in the same way as described above for the MCT detector. In order to extract the phase evolution from the intensity fringes $I(\delta_{\text{raw}})$ (with the constant offset first subtracted), the analytic signal representation $Z(\delta_{\text{raw}})$ is calculated numerically after the fact using the Hilbert transform H ,^{133,249,250}

$$Z(\delta_{\text{raw}}) = I(\delta_{\text{raw}}) + iH\{I(\delta_{\text{raw}})\}. \quad (4.5)$$

The imaginary part of Z is referred to as the quadrature component of the signal, which is appropriate given its $\pi/2$ phase-shifted behavior evident in Figure 4.14(a). For this data the PSO increment is 50 nm, the scan speed is 2 mm/s, and the δ_{raw} of each point is the result of interpolating the PSO count up to the 1 MHz sampling rate of the HeNe intensity. In general, the fastscan parameters should be identical to those used in the measurement to be corrected. The optical phase evolution is reconstructed from the phase of $Z(\delta_{\text{raw}})$, defined with reference to an arbitrary stage position δ_{ref} such that $\varphi(\delta_{\text{ref}}) = 0$,

$$\varphi(\delta_{\text{raw}}) = \arg\{Z(\delta_{\text{raw}})\} = \tan^{-1}\left(\frac{H\{I(\delta_{\text{raw}})\}}{I(\delta_{\text{raw}})}\right). \quad (4.6)$$

The corrected stage positions are then simply given by

$$\delta_{\text{corr}} = \frac{\lambda_{\text{HeNe}}}{4\pi}\varphi(\delta_{\text{raw}}), \quad (4.7)$$

where $\lambda_{\text{HeNe}} = 632.816$ nm is the HeNe laser line wavelength in air. This relationship produces a calibration of corrected against raw stage encoder positions over a given range

of travel (shown over a small range in Figure 4.14(b)), which can be used as a lookup table to correct the position axis in a measurement. In practice, the raw positions are first converted to the corrected positions, which in general are unevenly spaced. The signal is then interpolated onto an evenly-spaced position grid. Figures 4.14(c) and (d) show the position error, $\delta_{\text{corr}} - \delta_{\text{raw}}$, as a function of raw position along a ~ 16 mm portion of the τ_{IR} stage's 50 mm range. Here we have taken $\delta_{\text{ref}} = 0$ mm. The regular periodic structure seen in panel (d) is likely the source of the spectral satellite artifacts. As in the theory of Rowland ghosts, this can be understood as the generation of side-bands by phase-modulation.

Figure 4.15 shows the effect of carrying out the calibration procedure to correct the position axis. Panels (a) and (b) show the spectrum of the HeNe derived from its interferogram before and after the correction. The inset in panel (b) demonstrates that the measured lineshape of the HeNe is exactly given by the Hann apodization window used to process the Fourier transform, i.e. the corrected HeNe interferogram is a pure cosine wave. As the same HeNe interferogram being corrected was that used to create the calibration, this is true by construction, and simply illustrates the process. Figures 4.15(c) and (d) demonstrate the correction on an independently measured IR pump interferogram. The satellite features created by the periodic position errors are successfully removed. The quality of the correction produced by a given HeNe calibration interferogram degrades within a week or so as the stage's motion and/or encoder performance drift.

In practice, the IR bandwidth used in our FEIR experiments is narrower than the spacing to the first set of satellites, and we therefore can usually leave the stage positions uncorrected. The experiments analyzed in this thesis do not employ this stage correction. However, even though these most obvious artifacts fall safely outside the IR pulse spectrum, subtle distortions may still exist within its bandwidth, and experiments requiring high precision

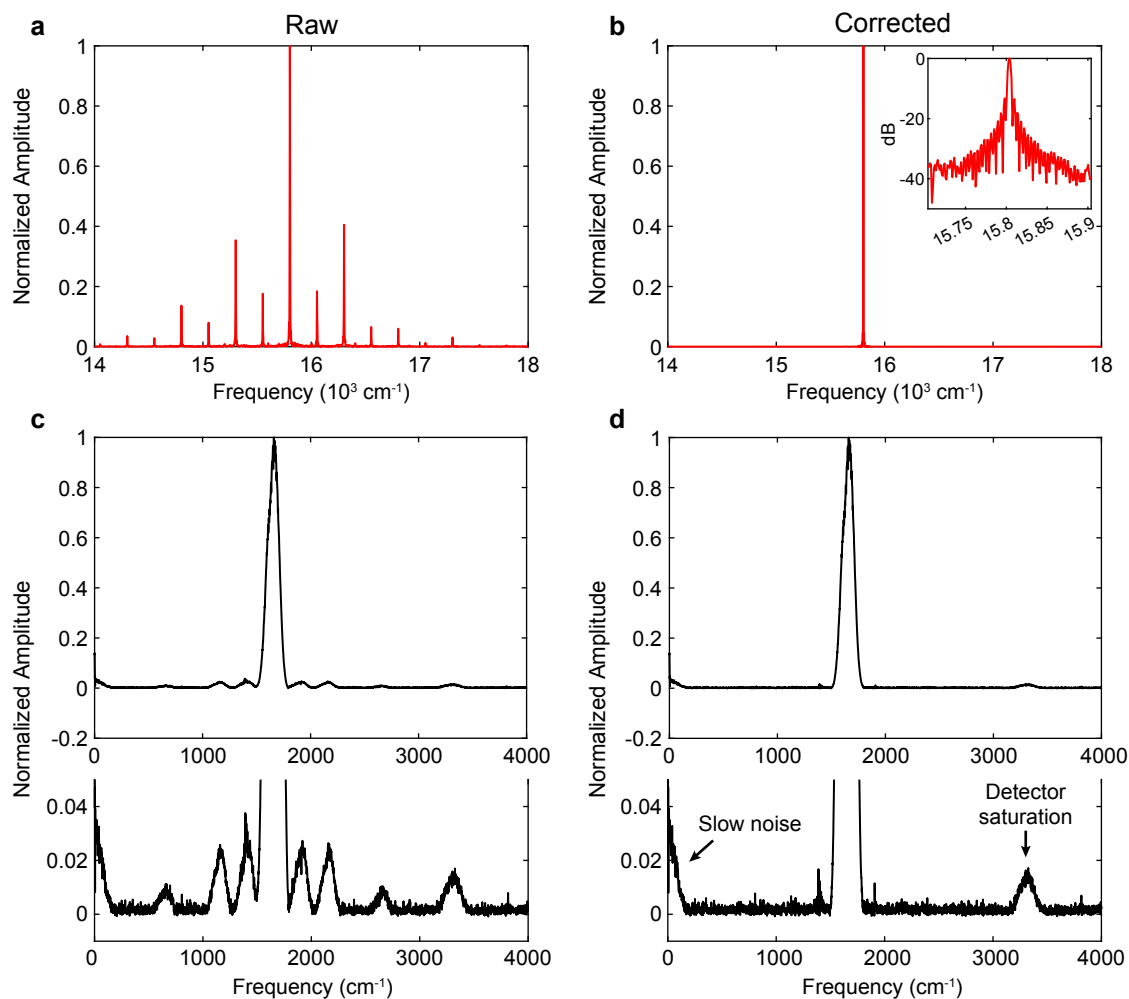


Figure 4.15: Removal of spectral satellites with the stage position correction. (a) Uncorrected HeNe spectrum calculated from its interferogram, showing multiple orders of satellites. (b) HeNe spectrum with corrected positions. The inset shows a detailed view of the laser line on a log y scale, which exhibits the characteristic side-lobe structure of the Hann window used for apodization in the Fourier transform. (c) Uncorrected IR pump spectrum. The lower panel is a zoomed-in view of the baseline, showing the satellite peaks. (d) IR pump spectrum with corrected positions. The satellites are removed, and the remaining features outside the pulse spectrum can be assigned to slow noise near zero frequency and the effect of mild detector saturation producing an apparent second-harmonic response.

lineshape analysis should be done with the correction procedure.

4.5.4 Correction to photon count rates for pile-up error

For large fluorescence intensities, single-photon counting is practically limited by the speed at which the detector can reset itself between photon arrivals, which can lead to artifacts as photons are missed. Errors of this nature are often referred to as photon pile-up.²⁵¹ Here we analyze the specific kind of pile-up error which manifests as a sub-linear response in our experimental configuration.

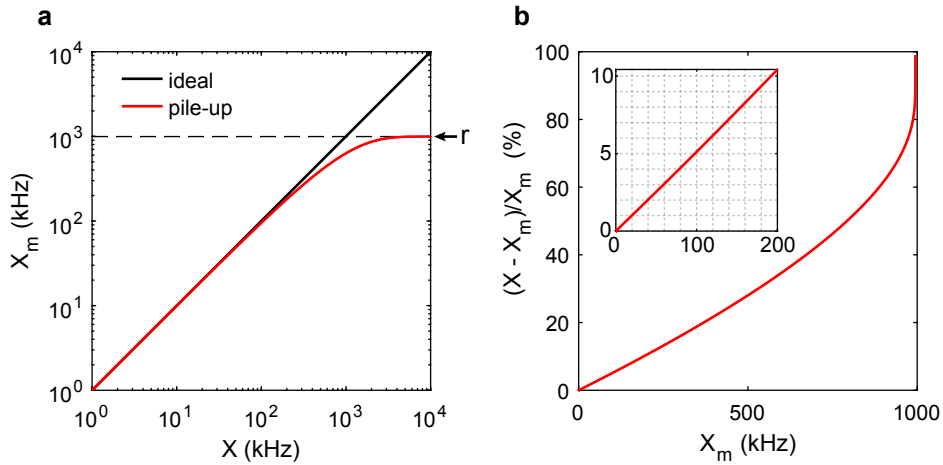


Figure 4.16: Model for pile-up error. (a) X vs X_m in the presence of pile-up (Eq. (4.11), red) compared to the ideal case where every photon is registered (black), with r indicated (dashed black). (b) Percent error in X_m , with inset showing the 0 - 200 kHz range.

The repetition-rate of our excitation pulses is fixed at $r = 994.7$ kHz, while the fluorescence lifetime of the fluorophores used is typically on the order of a few nanoseconds. Therefore, essentially all useful signal light will arrive at the detector in the few first percent of the ~ 1 μ s duty cycle. Our detector has a hardware fixed dead-time of 75 ns, so that once a photon is detected any subsequent photons reaching the detector during this dead-time interval will not be registered. In practice this means that at most one photon can be counted per excitation pulse sequence, and the measured count rate will therefore

saturate at the repetition-rate. However, even at lower count rates it is possible that multiple signal photons will arrive at the detector per excitation cycle, only the first of which will be counted. The measured count rate will therefore always be smaller than the true count rate, with the error growing as the count rate approaches saturation. It is important to note that this possibility of multiple photons per pulse sequence is only relevant for the case of an ensemble of uncorrelated emitters, e.g. from a solution at concentrations greater than a few nM. If an individual molecule is being observed then only one photon can be emitted at a time anyways, and this type of pile-up is not an issue. In practice, however, this distinction is not important in our measurements because the single-molecule count rates we encounter are far below the pile-up threshold, as shown below.

To avoid this nonlinearity, the total count rate needs to be kept below a certain level to ensure that pile-up errors are small. To determine what this level should be, we consider a simple model where the probability of n photons reaching the detector after an excitation pulse sequence follows a Poisson distribution

$$p(n, \lambda) = \frac{e^{-\lambda} \lambda^n}{n!}. \quad (4.8)$$

Here the rate parameter λ is the average photon number $\langle n \rangle$, and therefore the true count rate, i.e. without pile-up, is $X = r\lambda$ where r is the pulse repetition-rate. The measured count rate X_m is equal to the repetition-rate times the average number of photons counted per pulse sequence

$$X_m = r \langle n_c \rangle = r \sum_{n=0}^{\infty} n_c(n) p(n, \lambda), \quad (4.9)$$

where the number of counted photons is

$$n_c(n) = \begin{cases} 0 & n = 0 \\ 1 & n \geq 1. \end{cases} \quad (4.10)$$

Evaluating this expression, we get

$$X_m = r \left(0 + \sum_{n=1}^{\infty} \frac{e^{-\lambda} \lambda^n}{n!} \right) = r \left(-e^{-\lambda} + \sum_{n=0}^{\infty} \frac{e^{-\lambda} \lambda^n}{n!} \right) = r(1 - e^{-\lambda}) = r(1 - e^{-X/r}). \quad (4.11)$$

This gives the relationship between the true count rate X and measured count rate X_m , which is inverted to give the correction function cited in the main text,

$$X = -r \ln(1 - X_m/r). \quad (4.12)$$

Figure 4.16(a) shows the relationship between X and X_m for this model, while the corresponding magnitude of error in X_m is shown in Figure 4.16(b). For count rates below ~ 200 kHz, the error grows linearly in X_m with the approximate rate of 1% per 20 kHz. Beyond this range the growth rate increases and eventually diverges as saturation $X_m \sim r$ is approached.

To test how well Eq. (4.12) works to correct real data, we measured the I_{vis} -dependence of the fluorescence count rate from a 1 μM Rhodamine 6G (R6G) solution in acetonitrile-d₃. We used the same experimental configuration as an FEIR measurement (with a glass coverslip), although with the IR beam blocked. R6G is directly resonant with the visible pulse, and this concentration should be high enough to ensure we observe a large ensemble of molecules with low individual excitation probabilities to avoid photophysical saturation.

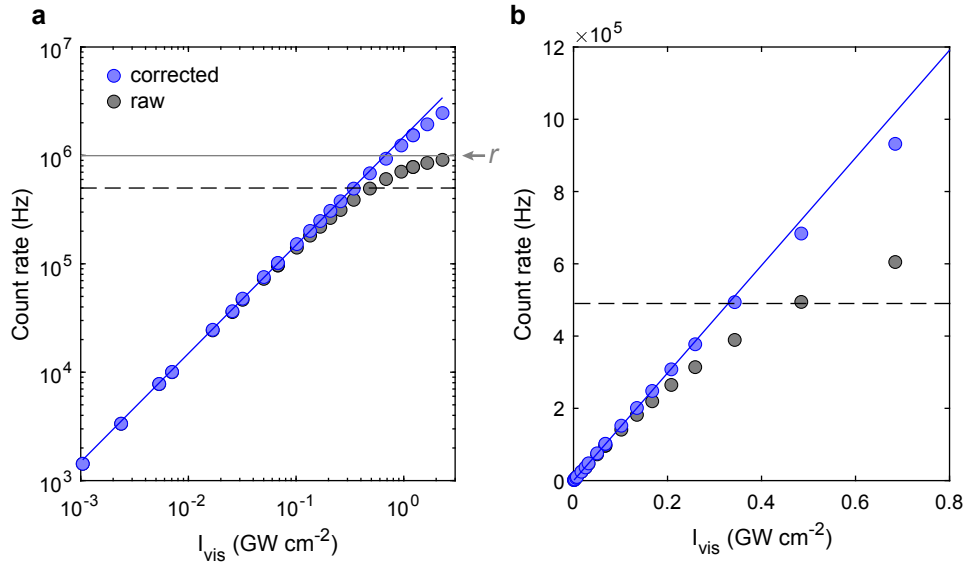


Figure 4.17: Experimental evaluation of the pile-up correction. Raw (black) and corrected (blue) count rates as a function of I_{vis} on log-log (a) and linear (b) axes (note the smaller I_{vis} range in (b)). The blue line is a linear fit to the corrected points with $I_{\text{vis}} < 0.2$ GW cm⁻². The dashed line indicates 500 kHz, which we feel is the practical limit of measured count rate that can be successfully corrected.

Ideally, the true count rate should therefore be linear in I_{vis} , and any deviations in the measured count rate reflect pile-up error. Figure 4.17 shows the raw and corrected count rates from this experiment on both log-log (panel (a)) and linear (panel (b)) axes. Applying the correction successfully restores a linear intensity dependence for measured count rates up to ~ 500 kHz (dashed line). However, beyond this point the quality of the correction evidently breaks down, as the corrected points fall below the low-intensity linear trend (blue line). In experiments where measuring the absolute count rate levels is important (as in Chapter 7), we keep the measured count rate below 200 kHz ($\sim 10\%$ error before correction), which we feel is solidly within the range that can be pile-up corrected with high fidelity by Eq. (4.12). However, for achieving higher signal to noise with more rapid acquisition times in bulk measurements (important e.g. for measuring τ_{enc} -dependent FEIR spectra), going

up to $X_m \sim 500$ kHz is reasonable with this correction.

4.6 Temporal pulse characterization and instrument response

4.6.1 IR pulse characterization by interferometric autocorrelation

The IR pulse duration is characterized by interferometric autocorrelation (IAC) in a 0.5 mm AgGaS₂ (AGS) crystal at the sample position. The resulting SHG signal is collected through the microscope as described in Section 4.4. Depending on the IR center frequency ω_{IR} , different materials are placed in front of the detector as transmission filters to block the fundamental while passing the SHG. For $\omega_{\text{IR}} \sim 3 \mu\text{m}$ clear acrylic is used, for ω_{IR} between 4 and 5 μm 10 mm of N-BK7, and for $\omega_{\text{IR}} > 5.5 \mu\text{m}$ two ~ 1 mm glass microscope slides. 1 mm of CaF₂ is included in the optical path before the AGS crystal to account for transmission into the sample cell.

Figure 4.18 shows the spectra and IACs for IR pulses produced by the OPA near 6 μm , and 4.5 μm . The IAC data is shifted and scaled so that the lowest fringe falls to zero and the long-time baseline is unity. The zero frequency band of the data is the intensity autocorrelation (IA),¹⁷⁹ which is extracted by a Fourier filter. We use the fwhm of the temporal pulse intensity profile as a definition of pulse duration, $\tau_{\text{p, IR}}$. Assuming a Gaussian profile, the pulse duration, taken as fwhm temporal intensity envelope, is related to the fwhm of the IA by $\tau_{\text{p}} = \tau_{\text{IA}}/\sqrt{2}$. We use this relation to report the pulse duration from a Gaussian fit of the recovered IA.

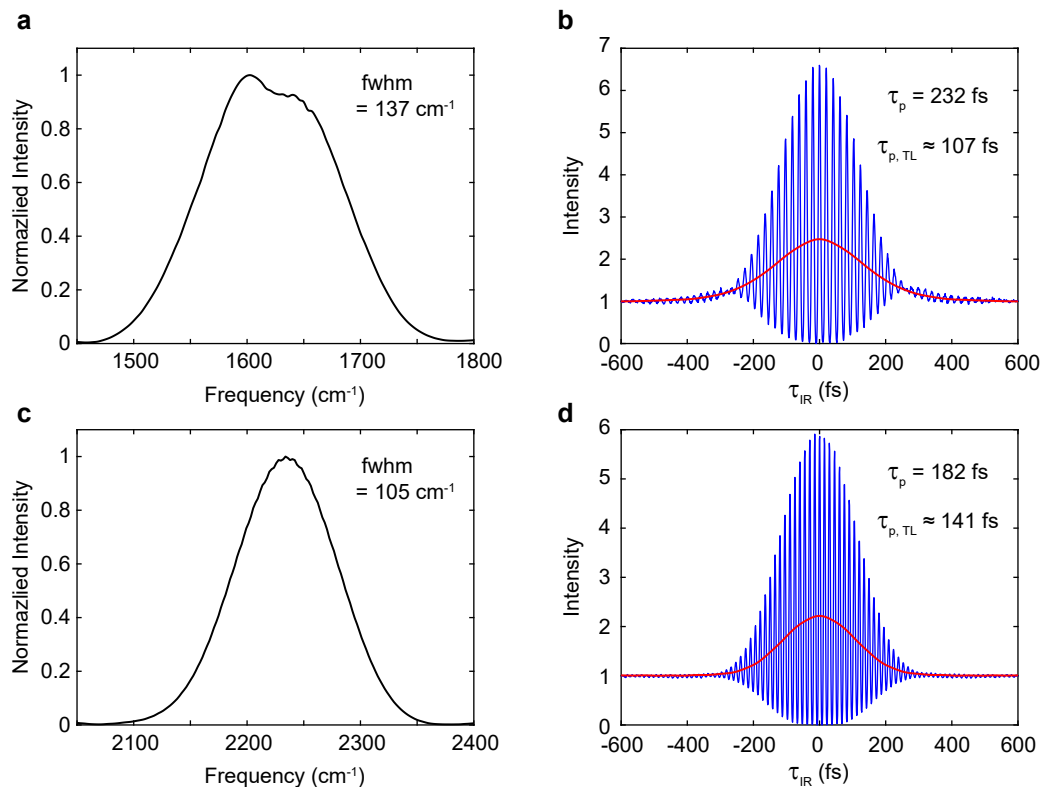


Figure 4.18: IR Pulse spectra and interferometric autocorrelations at (a)-(b) $\omega_{\text{IR}} = 1620 \text{ cm}^{-1}$ ($6.17 \mu\text{m}$) and (c)-(d) $\omega_{\text{IR}} = 2235 \text{ cm}^{-1}$ ($4.47 \mu\text{m}$). In (b) and (d) the extracted IA (red) is shown over the IAC (blue).

For the $6 \mu\text{m}$ pulse, the resulting 232 fs IR pulse duration (transform limit of 107 fs) is consistent with the dispersion that results from the summed GVD of materials in the optical path. This includes the 4 mm thick LGS OPA crystal, the BaF_2 collimating lens, two 1 mm thick Germanium windows, the ZnSe beamsplitters, ZnSe asphere, and 1 mm CaF_2 bottom sample window. The $4.5 \mu\text{m}$ pulse is closer to transform-limited, with a 182 fs duration (transform limit of 141 fs), due to the lower combined dispersion from these materials at this shorter wavelength and smaller bandwidth over which dispersion can play a role.

4.6.2 IR/Vis temporal pulse overlap characterized by two-photon-excited fluorescence

As discussed in Chapter 3, fluorescence induced by vibrationally non-resonant two-photon absorption (TPA) can be used to measure the temporal overlap of the IR and visible pulses. This method therefore characterizes the effective temporal instrument response function (IRF) of the FEIR experiment. With independent knowledge of the IR pulse characteristics, e.g. by IAC, the visible pulse duration can therefore be backed out. At minimum, a fluorophore that can be used for this purpose must exhibit IR + Vis two-photon electronic resonance, which operationally is automatically satisfied for the electronic pre-resonance condition used for FEIR. However, it must also not contain any FEIR active vibrations (or better yet, no vibrations at all) in resonance with the IR spectrum. Additionally, the molecule must have a non-vanishing two-photon cross-section. In practice, this second criterion is difficult to achieve in the 6 μm region, where most electronically-conjugated molecules have C=C ring stretching vibrations. Using TPA to characterize the IRF for 6 μm experiments therefore remains a currently unsolved problem. However, to demonstrate this method, and along the way characterize the visible pulse duration, we move the IR to 4.5 μm where many dye molecules exhibit clear windows.

Figure 4.19 shows the pure TPA signals from coumarins 6 and 343 (C343) using the 4.5 μm IR pulse characterized above in Section 4.6.1. Neither of the coumarins have any vibrations within its bandwidth, while they both exhibit good electronic resonance with the sum frequency $\omega_{\text{IR}} + \omega_{\text{vis}}$ (Figure 4.19(a)). Background-subtracted two-pulse transients for both molecules are shown in Figure 4.19(b), which are symmetric in τ_{enc} and fit well to Gaussians that decays fully to zero, indicative of a nonresonant pulse-overlap signal. The frequency-resolved version of this signal from C343 (measured via the three-pulse signal as

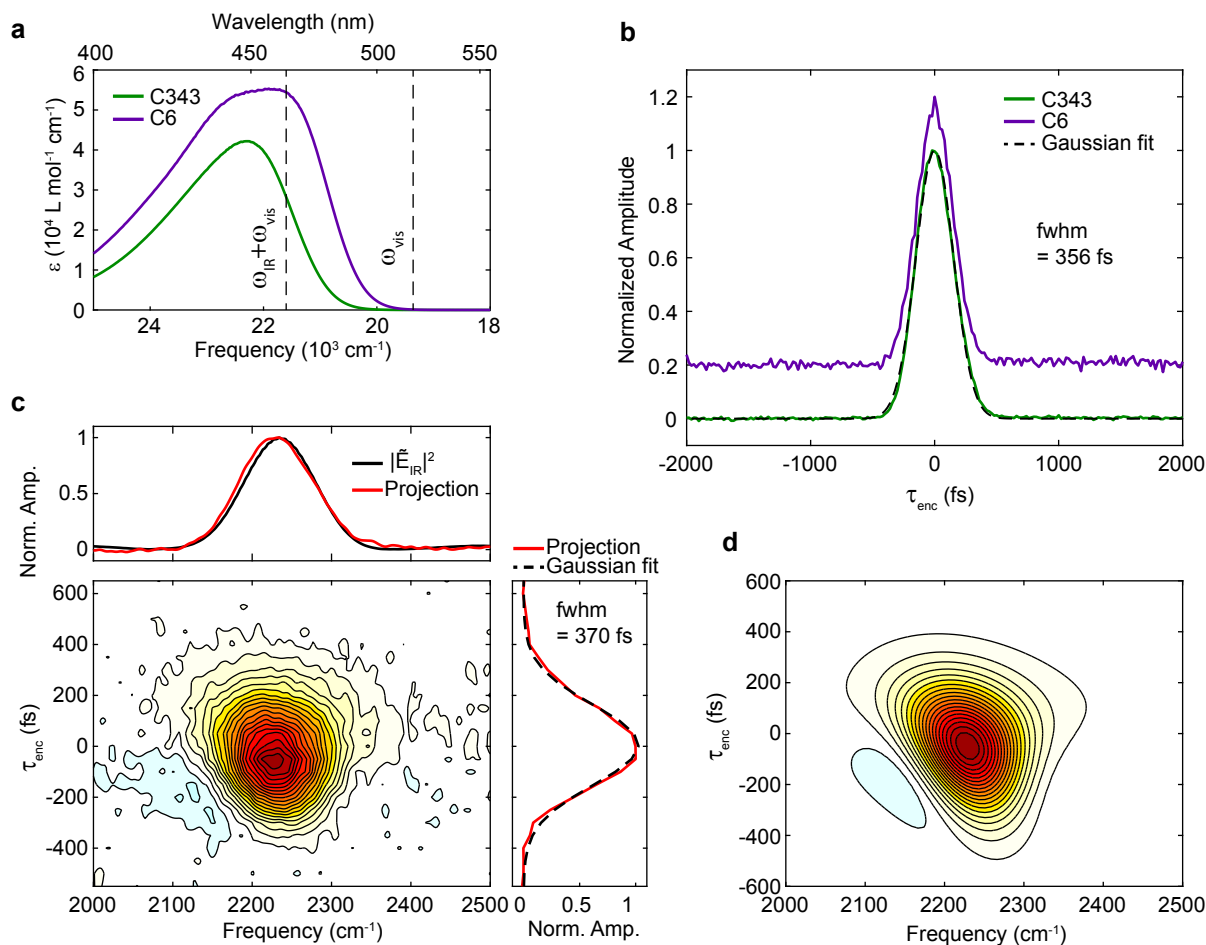


Figure 4.19: TPA signals from C343 and C6 with vibrationally off-resonant IR pumping. (a) Electronic absorption spectra for C343 and C6 indicating resonance conditions for $\omega_{\text{IR}} = 2235 \text{ cm}^{-1}$ ($4.47 \mu\text{m}$). (b) Background-subtracted, normalized two-pulse transients for C6 and C343. The two signals have been offset for clarity. A Gaussian fit yielding a fwhm of 356 fs is shown for C343. (c) Frequency-resolved TPA signal from C343. The projection of the surface onto the frequency axis is shown overlaid on the IR pulse spectrum, while the projection onto the τ_{enc} axis is shown with a Gaussian fit yielding a fwhm of 370 fs. (d) Calculation of frequency-resolved TPA signal with using a Gaussian IR pulse spectrum with second-order dispersion consistent with the experimental IAC, and a transform-limited 315 fs Gaussian visible pulse.

for an FEIR spectrum discussed in Section 4.7), is shown in Figure 4.19(c). Its projection onto the frequency axis matches well with the IR pulse spectrum, as predicted for the

frequency-resolved TPA signal in Chapter 3. Gaussian fits to the two-pulse signal and the projection of the frequency-resolved signal onto the τ_{enc} axis yield fwhm values of 356 and 370 fs, respectively. Assuming these values represent the fwhm of the IR/Vis intensity cross-correlation, and taking the IR pulse duration from the IAC, we back out the visible pulse duration of $\tau_{\text{p,vis}} = \sqrt{356^2 - 182^2} = 306$ fs or 322 fs for the longer or shorter measurements, respectively. We take the average value of 315 fs as our measure of the visible pulse duration. Figure 4.19(d) shows a calculation of the frequency-resolved TPA signal using a Gaussian IR pulse spectrum with second-order dispersion consistent with the experimental IAC, and a transform-limited 315 fs Gaussian visible pulse, yielding good agreement with features in the TPA spectrum including the shallow negative wing on the red side of the pump indicative of mild IR down-chirp.

4.6.3 Uncertainties in assigning $\tau_{\text{enc}} = 0$

The proper assignment of time zero for τ_{enc} is made difficult by the counter-propagating experimental geometry, which couples the relative timing of the IR and visible pulses to longitudinal position along the optical axis. In principle this effect could wash out the time-resolution along τ_{enc} if the signal is collected from a region with a longitudinal dimension larger than the effective pulse lengths (e.g. $\sim 30 \mu\text{m}$ for a 100 fs pulse in vacuum). In our experiment the few μm longitudinal size of the point spread function provided by the objective and confocal detection renders this effect negligible. However, another consequence is that, in order to maintain the same $\tau_{\text{enc}} = 0$ between auxiliary characterization and measurement, whatever sample or material is being used to determine $\tau_{\text{enc}} = 0$ via a TPA signal or some other nonresonant parametric response must also have the same thickness and index profile as the sample the FEIR measurement is being performed on. As mentioned

previously, we have not yet been able to independently measure $\tau_{\text{enc}} = 0$ for the $6 \mu\text{m}$ FEIR experiments studied in this thesis. Our assignment of $\tau_{\text{enc}} = 0$ for these experiments is instead based on response function calculations and is described in Chapter 8.

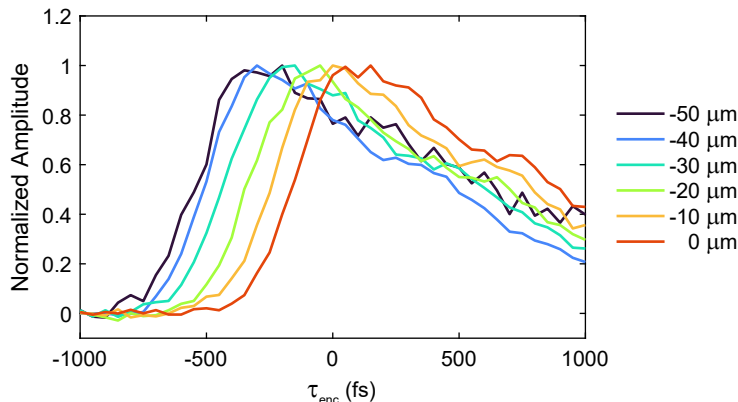


Figure 4.20: Coupling of the relative IR/Vis timing and Z position in the sample. Normalized two-pulse signals from C343 in CHCl_3 as a function of Z position (indicated in the legend).

The coupling of timing and Z position is illustrated in Figure 4.20, which shows two-pulse signals from C343 in chloroform for various Z values below the bottom of the coverslip (i.e. h in Eq. 4.4). For this solvent, there is a nearly 100 fs timing shift per $10 \mu\text{m}$ of Z travel. To achieve reproducible τ_{enc} values between measurements it is therefore important to ensure that the signal is being collected from the same Z position in the solution layer, while variations in the thickness of this layer will contribute to uncertainty in timing. This Z-dependent timing shift is less severe in acetonitrile-d₃, in which most FEIR experiments in this thesis are performed.

4.7 Acquisition and processing of bulk FEIR signals

4.7.1 Two-pulse experiments

The total photon count rate measured in any FEIR experiment is given by

$$F_{\text{tot}}(\tau_{\text{IR}}, \tau_{\text{enc}}) = F(\tau_{\text{IR}}, \tau_{\text{enc}}) + F_0 + B. \quad (4.13)$$

Here F is the desired FEIR signal, F_0 is a constant background fluorescence due to direct excitation of the target molecule by the visible pulse alone, and B encapsulates all other sources of background not arising from the target molecule, e.g. solvent Raman scattering, emission from impurities and optics, and detector dark counts. More about these latter two background components will be discussed in detail in Chapters 6 and 7. As described in the theoretical development of Chapter 2, two-pulse signals may be measured either by blocking the moving arm (\mathbf{E}_1) of the interferometer so only \mathbf{E}_2 (the stationary IR pulse) and \mathbf{E}_3 (the visible encoding pulse) are present in the sample, or by setting $\tau_{\text{IR}} = 0$, thereby superposing \mathbf{E}_1 and \mathbf{E}_2 . As shown later in Figure 4.22, this latter method produces a 4 times larger signal which can be understood by considering the effect of constructive interference between the IR pulses. Therefore, this is the preferred method for measuring two-pulse transients and is exclusively used in this thesis unless otherwise noted. Likewise, two-pulse transients are collected by fastscanning τ_{enc} at 2 mm/s with 40 fs bin size.

Figure 4.21(a) shows the raw fluorescence count rate $F_{\text{tot}}(\tau_{\text{enc}})$ from a two-pulse experiment on Coumarin 6 (C6) in acetonitrile-d₃. The coverage of the IR pulse spectrum, shown later in Figure 4.23, is centered on the high frequency coumarin ring vibrations, and represents a similar pump condition used for most of the coumarin experiments discussed in

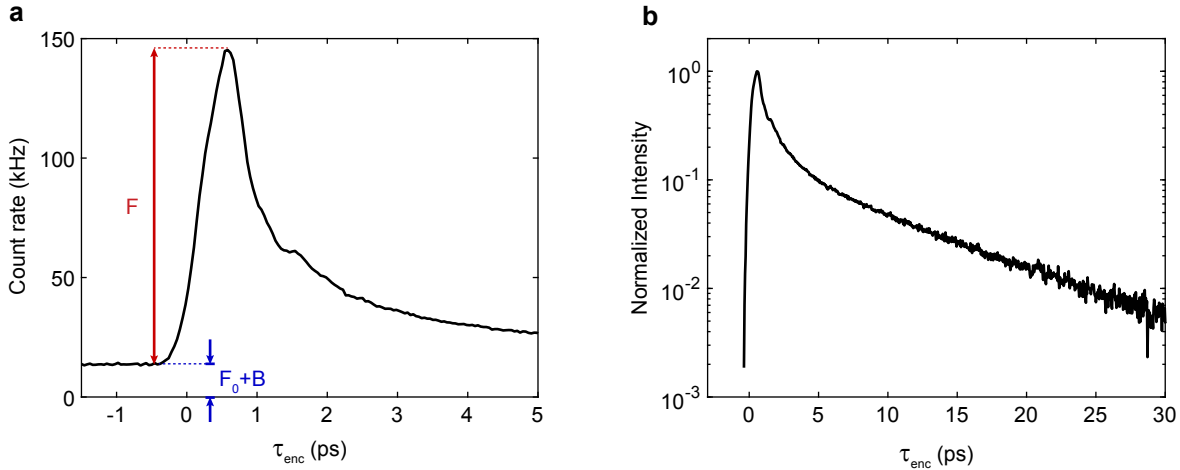


Figure 4.21: Two-pulse signal from C6 in acetonitrile-d3. (a) Raw photon count rate $F_{\text{tot}}(\tau_{\text{enc}})$ from a two-pulse measurement with the IR pulse pair at $\tau_{\text{IR}} = 0$. The maximum FEIR signal F and background $F_0 + B$ levels are indicated. (b) Same data with the background subtracted on a logarithmic y axis and showing a longer scan range.

this thesis. The signal F and background $F_0 + B$ components are labeled. Figure 4.21(b) shows the normalized F component on a logarithmic y scale, exhibiting a bimodal decay profile consisting of ~ 1 ps and ~ 10 ps decay components. This relaxation behavior will be discussed in Chapter 10, and is suggestive of intramolecular vibrational energy redistribution followed by vibrational cooling of the molecule.

4.7.2 Three-pulse Fourier transform experiments

In a three-pulse experiment, the FEIR signal has the following components

$$F(\tau_{\text{IR}}, \tau_{\text{enc}}) = F_{12}(\tau_{\text{IR}}, \tau_{\text{enc}}) + F_1(\tau_{\text{IR}} + \tau_{\text{enc}}) + F_2(\tau_{\text{enc}}). \quad (4.14)$$

Specifically, $F_1(\tau_{\text{IR}} + \tau_{\text{enc}}) = F_2(\tau_{\text{enc}})$ are two-pulse signals where both IR-vibrational interactions occur with either \mathbf{E}_1 or \mathbf{E}_2 , respectively, while $F_{12}(\tau_{\text{IR}}, \tau_{\text{enc}})$ is the three-pulse signal

due to one interaction each with \mathbf{E}_1 and \mathbf{E}_2 and two with the encoding pulse \mathbf{E}_3 .

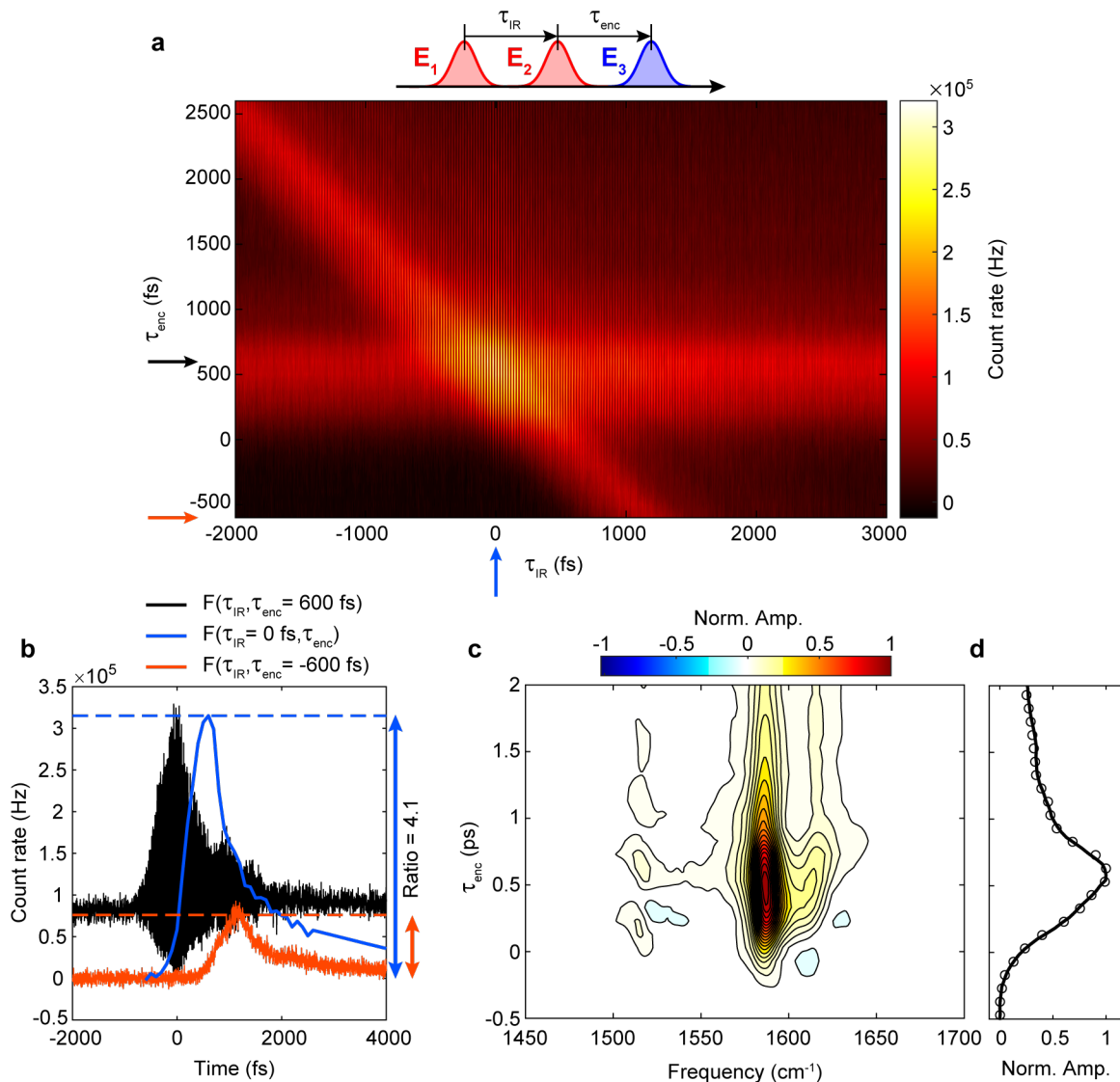


Figure 4.22: Signal contributions in a three-pulse experiment and projection slice relationship. (a) Background-subtracted FEIR signal $F(\tau_{\text{IR}}, \tau_{\text{enc}})$ from C6. (b) Various 1D slices of the FEIR signal, indicated by color-coded arrows in (a). (c) Processed FEIR spectrum and (d) projection of the spectrum onto the τ_{enc} axis (black circles). The two-pulse signal from Figure 4.21 is overlaid (solid black) to illustrate the projection-slice relationship between these quantities.

Figure 4.22(a) shows the full background-subtracted time-domain FEIR signal $F(\tau_{\text{IR}}, \tau_{\text{enc}})$

from the C6 sample. The $F_2(\tau_{\text{enc}})$ component can be seen as a horizontal stripe along $\tau_{\text{enc}} = 600$ fs, while the other two-pulse component $F_1(\tau_{\text{IR}} + \tau_{\text{enc}})$ is the stripe oriented along the anti-diagonal where $\tau_{\text{IR}} + \tau_{\text{enc}} = 600$ fs. The three-pulse signal can be made out as the rapidly oscillating component along τ_{IR} . Figure 4.22(b) shows the 1D slices $F(\tau_{\text{IR}}, \tau_{\text{enc}} = 600 \text{ fs})$, $F(\tau_{\text{IR}} = 0 \text{ fs}, \tau_{\text{enc}})$ (the two-pulse signal measured with the superposed pulse-pair), and $F(\tau_{\text{IR}}, \tau_{\text{enc}} = -600 \text{ fs})$ (only capturing the F_1 two-pulse signal). Comparing these latter two versions of the two-pulse signal shows the 4:1 amplitude ratio expected based on constructive interference (ratio of blue to orange arrow sizes in panel (b)). Figure 4.22(c) shows the FEIR spectrum processed from the three-pulse signal, as will be described next. The projection of this τ_{enc} -dependent spectrum onto the τ_{enc} axis overlays with the independently measured two-pulse signal, demonstrating the projection-slice relationship between these quantities discussed in Chapter 2.

When performing a three-pulse FEIR experiment, an IR reference (dark arm of the MZI) is collected either immediately before or after collecting the FEIR signal. The bin size, range of positions, and scan speed are kept the same to ensure identical τ_{IR} axes. Figure 4.23(a)-(c) shows an example of the time-domain three-pulse FEIR data with $\tau_{\text{enc}} = 600$ fs with the corresponding IR reference. The F_{tot} level at the far positive end of the τ_{IR} scan range is subtracted off to remove the $F_0 + B$ background and constant F_2 two-pulse signal. Next, the phase extracted from the IR reference is used to determine the absolute timing between the IR pulse-pair in a similar manner to pump-probe geometry 2D IR spectroscopy experiments.^{156,252,253} In practice, both FEIR and IR channels are Fourier transformed after having been appropriately apodized, zero-padded, and rotated to an approximate time zero bin in the τ_{IR} axis. The frequency domain FEIR data is divided by the complex phase factor from the IR reference and transformed back to the time domain, where the now correctly

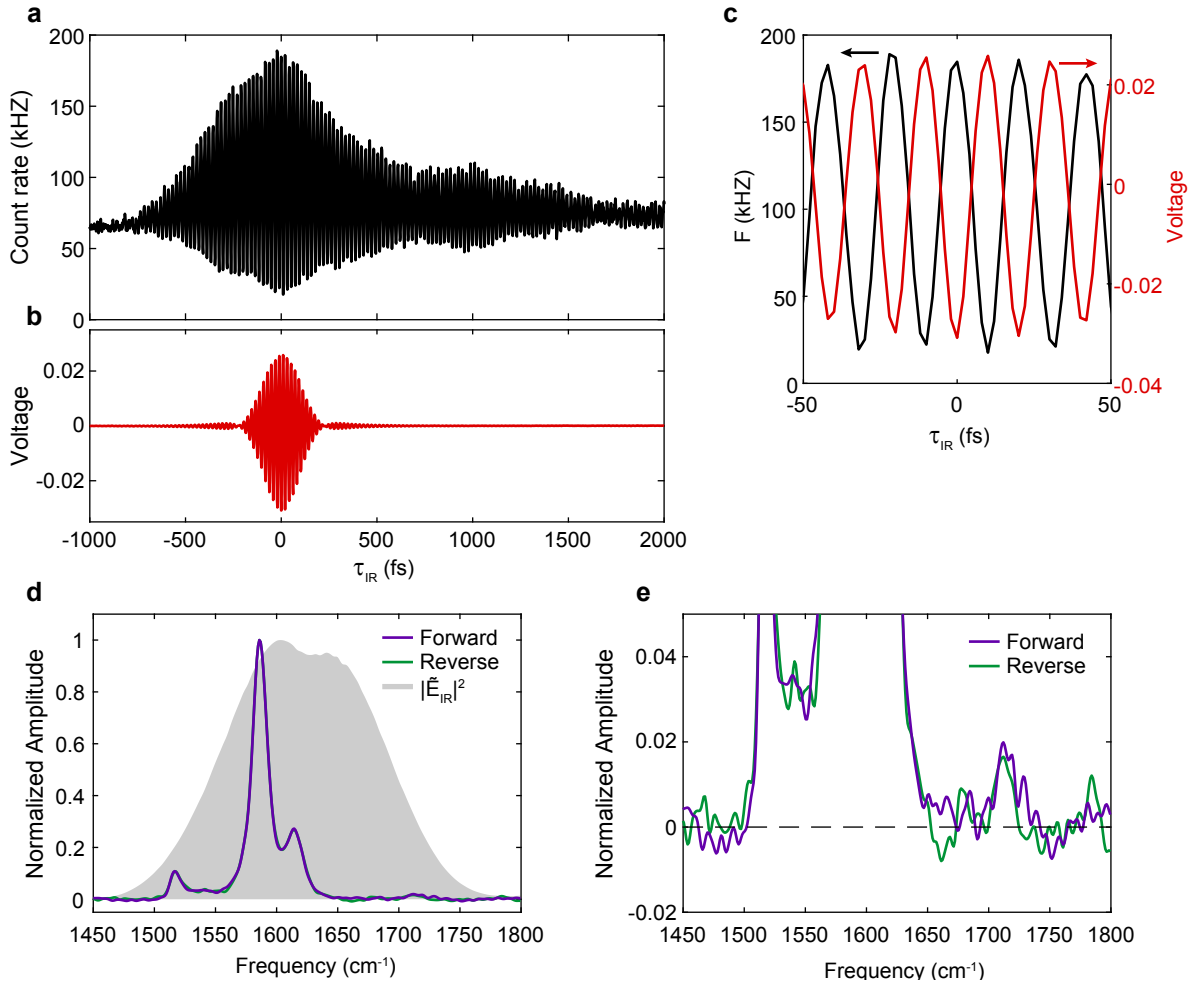


Figure 4.23: Acquisition and processing of the three-pulse signal to a spectrum. (a) Total count rate F_{tot} in a three-pulse FEIR experiment on C6 at $\tau_{\text{enc}} = 600$ fs and (b) IR reference data from the forward scan direction. A constant offset voltage in (b) has been removed, and the slight asymmetry between the amplitude of fringes above and below the zero level are caused by the onset of mild detector saturation. (c) Detail of the two signals in (a) and (b), showing the π phase-shift from the dark arm of the MZI. (d) Processed FEIR spectra from the forward scan direction (purple), reverse direction (green), and the IR pulse spectrum (gray) processed from the IR reference. (e) Detail of the baseline from the spectra in (d). The black dashed line along the baseline has been added to guide the eye.

assigned negative τ_{IR} data is removed. A final FT of the one-sided data produces the FEIR spectrum as its real part (Figure 4.23(d)), where the other two-pulse signal F_1 has been

filtered to the zero-frequency band. For τ_{enc} -dependent three-pulse experiments, this process is done for each step of τ_{enc} using the same IR reference.

Due to the direction-dependence of fastscanned position axes, this FT procedure is performed separately for the forward and reverse directions of stage travel. As shown in Figure 4.23(e), there may be small residual phase errors in the FEIR spectrum that vary between the two scan directions. In this particular measurement these errors are small enough to be inconsequential (much less than 1% of the total amplitude), however errors at the 1-3% level are also common, and are not always oppositely signed between directions. We suspect this artifact may originate from or at least be exacerbated by the fact that the IR reference is not collected simultaneously with the FEIR data, allowing for instrumental drift (e.g. in the MZI pathlength difference) between acquisitions. The character of this phase error is, however, also consistent with a thermal effect, as discussed in Section 4.8. In practice, we average the forward and reverse spectra together, which often roughly cancels this effect.

4.7.3 IR and visible power dependence

Here we show IR and visible power dependencies of the FEIR signal and background. This characterization was performed on the older version of the instrument in Ref. [242], and only investigates the lower range of effective IR intensities at the sample available in the new instrument. More extensive visible power dependence measurements, including saturation effects at much higher excitation densities than used here, are presented in Chapter 7. The measurements here are performed on 40 μm C6 in acetonitrile-d3 with the same IR spectral coverage as shown in the previous sections and using a glass coverslip. Specifically, we investigate the peak of the two-pulse signal ($\tau_{\text{enc}} = 600$ fs) while chopping the IR beam at 100 Hz, as described in Section 4.5.1. We have verified that these power dependencies do

not vary with τ_{enc} along the transient. The IR power was adjusted by a pair of wire-grid polarizers (Specac). The IR power was measured after the polarizers and scaled to the maximum power measured at the sample. The visible power was controlled by the half-waveplate and polarizer before the doubling crystal. The reported visible powers are those measured after the spatial filter but before entering the microscope, and should be scaled by ~ 0.43 to account for the overall transmission into the sample.

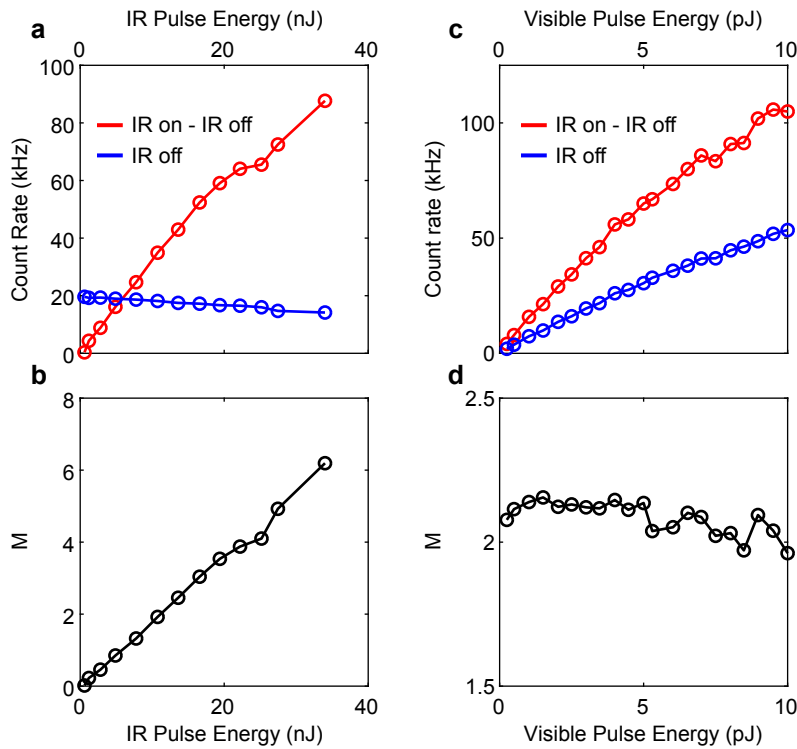


Figure 4.24: IR and visible power dependence of the FEIR signal. (a) F ($\text{IR}_{\text{on}} - \text{IR}_{\text{off}}$, red) and F_0 (IR_{off} , blue) amplitude as function of IR pulse energy. (b) The modulation ratio $M = F/F_0$ as a function of IR pulse energy. (c) F (red) and F_0 (blue) count rate as a function of visible pulse energy. (d) Modulation ratio as a function of visible pulse energy.

Figure 4.24(a) shows the IR power dependence of the F count rate ($\text{IR}_{\text{on}} - \text{IR}_{\text{off}}$), as well as the background F_0 (IR_{off} , assuming non-molecular background B is negligible). The small

decrease in the background count rate as IR power is increased is likely a thermal effect due to heating of the sample. This heating-dependent reduction in collection efficiency also affects the F amplitude, which results in a slight sub-linearity to the power dependence. However, plotting the modulation ratio $M = F/F_0$ (Figure 4.24(b)) appears to adjust for this thermal effect, resulting in a linear power dependence. This thermal effect is investigated and discussed further in Section 4.8. Figure 4.24(c) shows the visible power dependence with the IR pulse energy fixed at 9 nJ. Both the F and F_0 amplitudes grow linearly, and the modulation ratio (Figure 4.24(d)) is constant.

4.8 Bulk heating effects

4.8.1 Thermal modulation of the detected fluorescence intensity

The total fluorescence count rate in an FEIR experiment can be sensitive to the steady state heat load produced by absorption of the IR pulses in the sample and optical substrates. For example, this can be seen by comparing the IR power dependence of the C6 FEIR signal measured in solvents of varying transparency. As shown in Figure 4.25, the power dependence is roughly linear in chloroform and acetonitrile-d₃, which have good transparency in the frequency range of the IR pulse. However, in ethanol, which has substantial absorption across the entire pulse spectrum, the power dependence is markedly sub-linear. This sub-linear trend does not depend on the encoding delay τ_{enc} along the transient, that is, it is not directly related to the ultrafast or picosecond response of the sample.

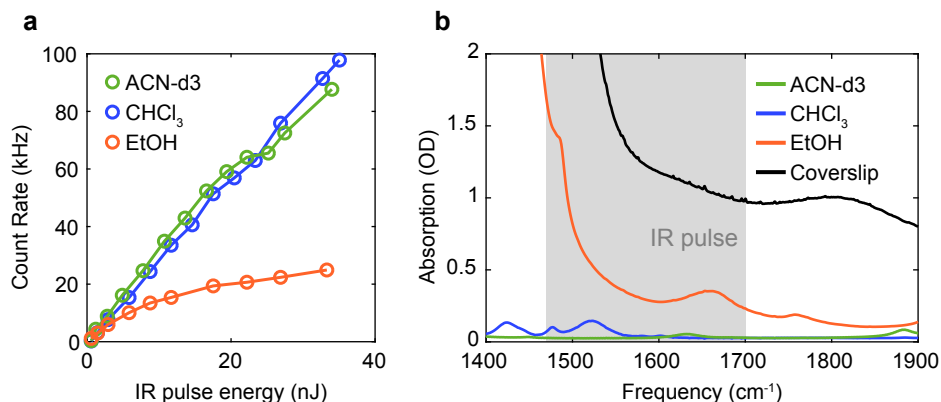


Figure 4.25: Solvent dependence of the thermal effect. (a) IR power dependence of the F signal for C6 in acetonitrile-d₃ (green), chloroform (blue), and ethanol (orange). (b) FTIR spectra of the solvents (50 μm pathlength) and the coverslip (black). The region with appreciable IR field intensity is shaded gray.

We rationalize this behavior as a decrease in overall fluorescence collection efficiency as a function of the temperature profile in the sample, likely due to thermal lensing effects. It is

important to note that the glass coverslip used for these measurements absorbs the majority of IR light incident on it (Figure 4.25(b)). However, this appears to have only a minor contribution to the thermal effect for these particular measurements, which used lower IR intensities in the older instrument of Ref. [242].

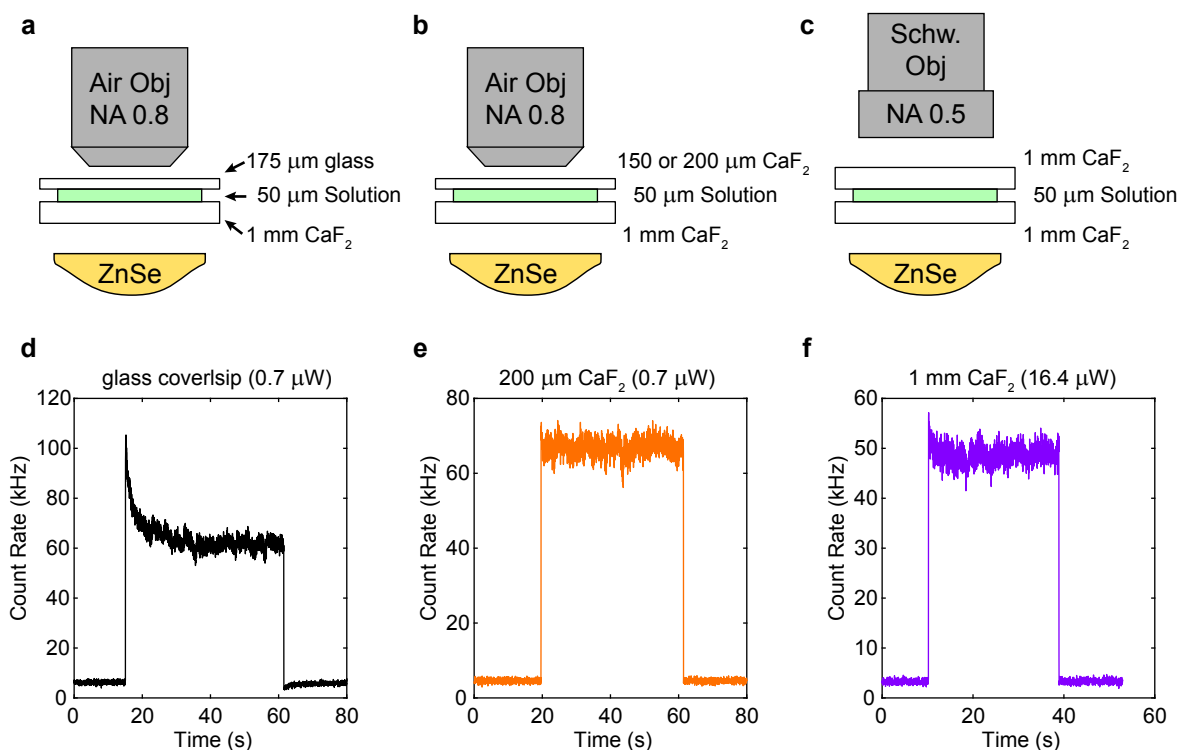


Figure 4.26: Thermal modulation with different sample configurations for a $30 \mu\text{M}$ C6 solution in acetonitrile- d_3 . (a) Glass coverslip, (b) CaF_2 coverslip, and (c) 1 mm CaF_2 window with a long working distance objective. (d)-(f) Total photon count rates measured from the sample when unblocking then re-blocking the IR beam for the corresponding configurations in (a)-(c), respectively.

As noted before and discussed later in Chapter 7, the use of glass coverslips in $6 \mu\text{m}$ experiments with the higher IR excitation densities in the updated instrument can lead to strong thermal modulation for even these highly transparent solvents. Figure 4.26 shows

three different experimental configurations and the time-dependence of the thermal modulation on the few seconds scale. In each case the same 30 μM C6 solution in acetonitrile-d₃ is used. Panel (a) shows the original configuration with a glass coverslip, while (b) replaces glass with an IR-transparent CaF_2 coverslip of either 200 or 150 μm thickness. Panel (c) shows an alternate configuration using the long working distance, but significantly lower NA, reflective Schwarzschild objective that allows for the use of a more conventional 1 mm CaF_2 window on top. Panels (d)-(f) show the real-time count rate from the sample when the IR is initially blocked (first ~ 10 -20 s), unblocked for ~ 30 s, then blocked again.

In the case of the glass coverslip (Figure 4.26(d)), a seconds-timescale relaxation of the count rate into its thermally-modulated value is clearly present. A recovery of the background level to its non-thermally-modulated value after the IR beam is blocked again is also visible. This modulation is essentially completely removed by switching to CaF_2 in both Figures 4.26(e) and (f). In (e) the IR-on count rate (with identical incident visible power) is, however, lower than the un-modulated level in (d). This reflects the degradation of the Zeiss objective's imaging performance with the excessively thick, non-standard index, coverslip. Employing a 150 μm thick CaF_2 (not shown) restores the imaging quality, and represents the best current configuration for performing sensitive FEIR measurements. This configuration is used in the concentration-dependent analysis of signal-to-background in the second part of Chapter 7.

Using the low NA reflective objective is practically convenient as the 1 mm thick windows do not flex (caused solution layer thickness issues for volatile samples as discussed in Section 4.4.2). This allows for reliable measurements over long periods of time with volatile solvents. However, as shown in Figure 4.26(f), the signal level is reduced compared to (d) and (e) even with over $20\times$ the visible power. This reduction in apparent brightness is due to the lower NA of focusing and fluorescence collection, the reduced transmission of the visible excitation

beam from the objective's central obscuration, and from not being confocally-matched to the detector. As such, this configuration is not adequate for sensitive detection, and is only useful for high concentration bulk experiments. Importantly, the lack of good confocal detection in this configuration means the Z resolution in the sample is also degraded, leading to potential time-resolution issues discussed in Section 4.6.3 as well as the possibility of collecting unwanted signals from molecules stuck to the interfaces.

4.8.2 Immersion oil heating

The highest possible NA readily achievable with an air objective is ~ 0.95 , which is expected to produce a 50% increase in collection efficiency over the current 0.8 NA. Moving to significantly higher NA is possible with immersion objectives, however the presence of an immersion medium that the IR beam will traverse after the sample could lead to thermal heating issues and must be considered. Here we show an example where such immersion medium heating destroys the possibility of performing an FEIR experiment. Specifically, Figures 4.27(a) and (b) show the IR spectra of two possible immersion media of index ~ 1.4 , silicone immersion oil (Olympus) and a fully halogenated hydrocarbon oil (Fluorolube), that could be used with a 1.35 NA silicone oil immersion objective (UPLSAPO100XS) kindly supplied by Olympus as a demo. The silicone oil has small absorption features within the IR pulse bandwidth, while the Fluorolube is exceptionally transparent as far as a molecular liquid goes (the offset could be due to reflective losses in the FTIR spectrometer). However, even with the Fluorolube, the presence of the IR beam completely destroys the imaging properties of the visible objective, as demonstrated by the reflection of the visible focus off the CaF_2 /solution interface (Figures 4.27(c) and (d)). By eye, a small distortion in the Fluorolube at the location of the IR beam, either caused by a thermal lensing effect or a

physical perturbation to the local shape of the liquid drop, is clearly visible (Figures 4.27(e) and (f))

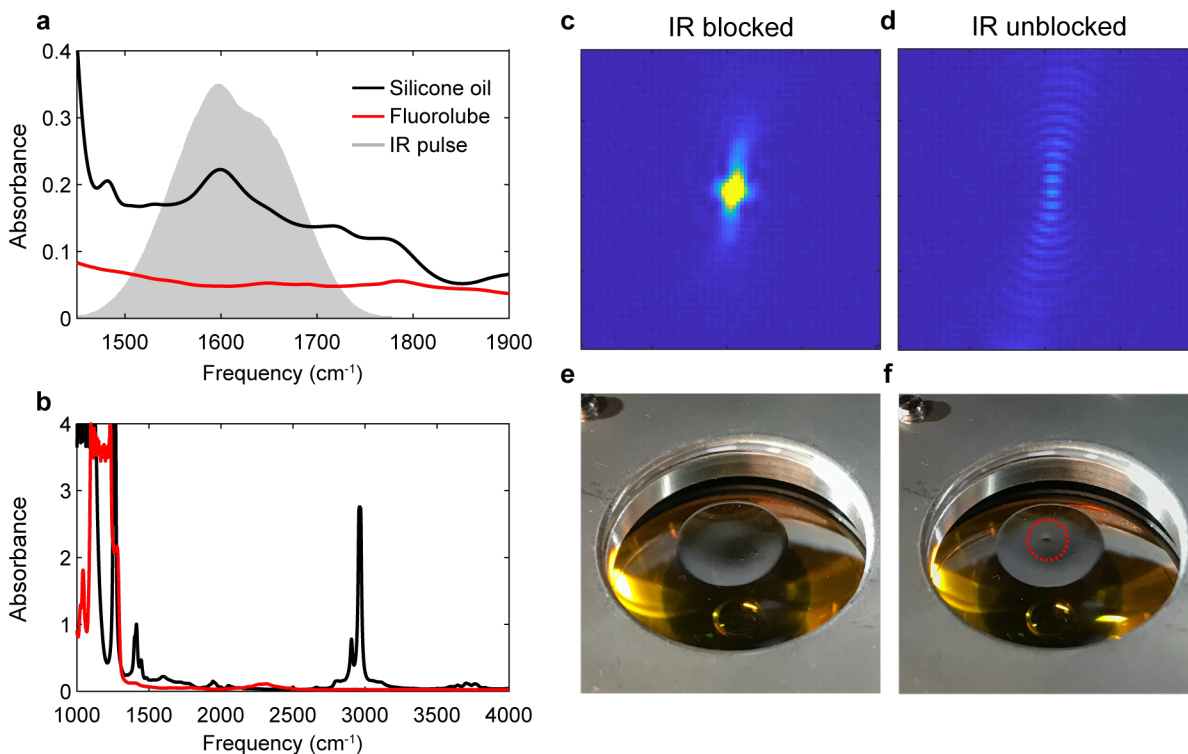


Figure 4.27: Heating effects in immersion media. (a) FTIR spectra of silicone immersion oil and Fluorolube oil ($50 \mu\text{m}$ pathlength) with the IR pulse spectrum superposed. (b) Same FTIR spectra on a much wider frequency axis. (c)-(d) Images of the reflection of the visible focus off the solution/cover slip ($\text{acetonitrile-d}_3/\text{CaF}_2$) interface on the camera with the IR blocked and unblocked, respectively, using Fluorolube as the immersion medium. (e)-(f) Photographs of the Fluorolube immersion medium corresponding to (c) and (d), respectively (visible objective rotated away). The small distortion at the location of the IR beam is circled in red. The yellow coloring below the sample cell is due to the ZnSe aspheric lens.

Even though the Fluorolube is highly transparent, it could be possible that its thermal conductivity is not sufficiently good to dissipate the small heat load, leading to the observe

phenomena. One possibility for moving to higher NA immersion objectives with the current counter-propagating IR/Vis geometry could be to use acetonitrile-d₃ as the immersion medium for a 1.2 NA water immersion objective, as the index is similar and this solvent successfully avoids thermal modulation effects in our current configuration.

4.8.3 Spectral artifacts caused by thermal modulation along τ_{IR}

As the thermal modulation of collection efficiency appears to correlate to the amount of IR optical power absorbed by the sample, Fourier transform FEIR measurements should spectrally resolve this heating response because scanning τ_{IR} will imprint the IR intensity modulation into a thermal modulation. By introducing a strong but spectrally sharp and isolated absorption into an otherwise highly transparent sample we may attempt to characterize the resulting thermal effect in a more controlled manner.

To demonstrate this effect we perform FEIR measurements on C6 in a 10:1 mixture of chloroform and acetone. The dilute acetone carbonyl stretch has a narrow, intense absorption at 1715 cm^{-1} . We tune the frequency of the IR pump to $\omega_{\text{IR}} = 1680 \text{ cm}^{-1}$, which falls in a high transparency window of chloroform, but covers the two highest frequency coumarin 6 ring modes and the acetone carbonyl stretch (shown schematically in the simulation in Figure 4.28(a)). The lactone carbonyl stretch of C6 near 1712 cm^{-1} is not sufficiently FEIR active to contribute significantly to the FEIR signal in this IR pump configuration. The optical densities of the dye ring modes are negligible compared to the acetone carbonyl (at typical μM concentrations for bulk FEIR measurements they are well below the detection sensitivity of an FTIR spectrometer). The acetone carbonyl mode should therefore act as both a thermal ‘source’ and ‘probe’.

To help interpret these measurements we will describe a minimal model for the thermal effect. We proceed by assuming that the collection efficiency modulation is a purely bulk optical effect and that the thermal load does not influence the microscopic FEIR response. That is, we may write the total measured fluorescence in a three-pulse FEIR experiment with fixed encoding delay as

$$F(\tau_{\text{IR}}) = S(\tau_{\text{IR}})T(\tau_{\text{IR}}) \quad (4.15)$$

where $S(\tau_{\text{IR}})$ is the total fluorescence of the dye (i.e. the FEIR signal and background that would be measured in the absence of any thermal effects), and $T(\tau_{\text{IR}})$ is the thermal modulation. We will also assume that the magnitude of the thermal modulation depends linearly on the average IR power absorbed by the sample, so that

$$T(\tau_{\text{IR}}) = 1 - \alpha P(\tau_{\text{IR}}) \quad (4.16)$$

where $P(\tau_{\text{IR}})$ is proportional to average IR power absorption and α is a scaling parameter that determines the strength of modulation. The thermal load most often appears to decrease the collection efficiency, so we set $\alpha > 0$. The case of $\alpha > 1$ is clearly unphysical, and for large modulations the linearity assumed in Eq. 4.16 most likely breaks down. The (normalized) IR power absorption as a function of interferometer delay τ_{IR} is given by

$$P(\tau_{\text{IR}}) = \frac{1}{2} \left(1 + I(\tau_{\text{IR}})/I_{\text{max}} \right) \quad (4.17a)$$

$$I(\tau_{\text{IR}}) = \text{FT}^{-1} \left\{ S_{\text{pump}}(\omega) S_{\text{solv}}(\omega) \right\} \quad (4.17b)$$

which is simply the interferogram of the solvent absorption spectrum $S_{\text{solv}}(\omega)$ windowed

by the IR pump spectrum $S_{\text{pump}}(\omega)$. The notation here is meant to convey that the power absorption is constant at half its maximum for large τ_{IR} (no interference), and goes to zero for perfectly destructive interference (approximately the case at the first π out-of-phase fringes).

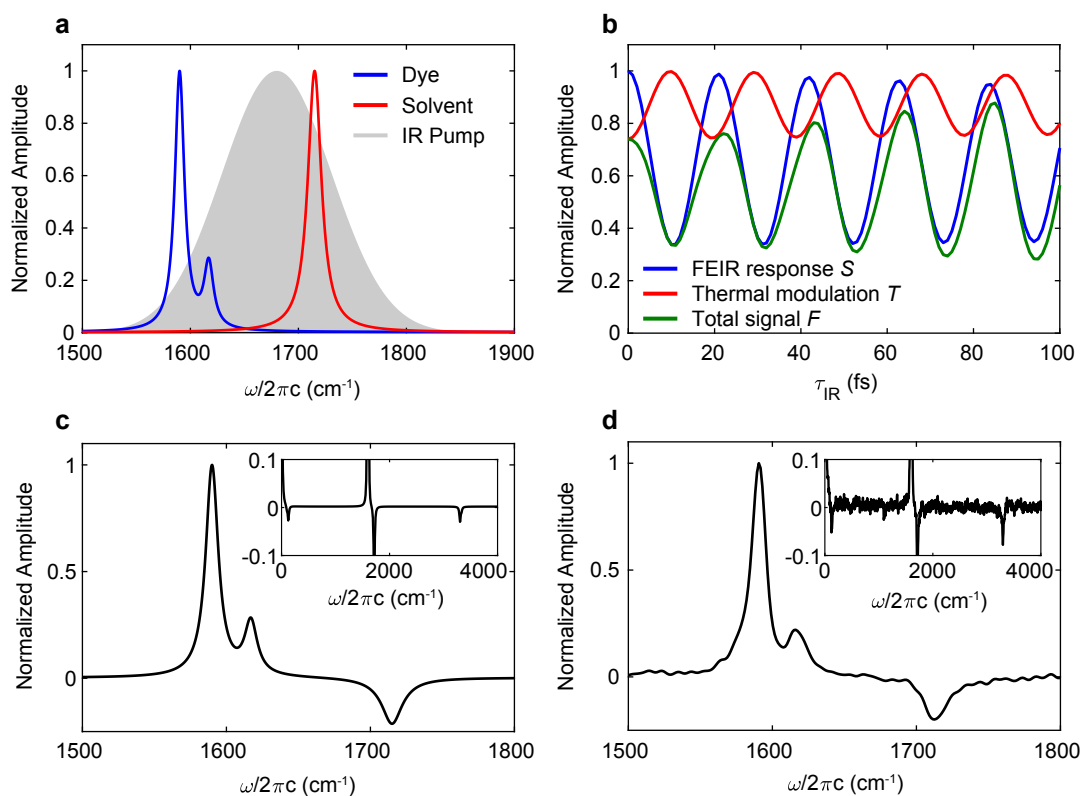


Figure 4.28: Experimental and modelled steady-state thermal signatures in an FEIR spectrum. (a) Frequency domain FEIR response of the dye ring modes (blue), absorption of the acetone carbonyl stretch in the solvent (red), and IR pulse spectrum (gray). (b) Time domain molecular response S (blue), thermal modulation T from the acetone carbonyl (red), and the resulting total detected signal F (green). (c) FEIR spectrum calculated from F . The inset displays the baseline of the same spectrum on an extended frequency axis to show the AM sidebands. (d) Measured FEIR spectrum from the dilute acetone experiment, with inset displaying the same region as in (c).

Implicit in Eq. 4.16 is the assumption that the thermal profile is at a steady state for

every interferometer delay position. This means we are considering the cumulative time-averaged effect of absorbing the 1 MHz pulse train balanced by the sample's macroscopic thermal relaxation. In our first acetone experiment we will attempt to enforce steady state conditions by stepping, rather than continuously scanning, the interferometer delay stage, which allows the sample to achieve its new steady state temperature profile before signal is collected. After discussing this steady state case, we will incorporate the effects of rapidly scanning the optical delay before the temperature profile fully relaxes.

Figure 4.28(b) shows the time domain FEIR response S , thermal modulation M , and resulting total signal F for the steady-state model. Here the molecular response is the *total* FEIR signal and background, $S(\tau_{\text{IR}}) = S_0 + S_1(\tau_{\text{IR}}) + S_2 + S_{12}(\tau_{\text{IR}})$. For simplicity the two ring modes have been given exponential dephasing times that roughly reproduce the experimental linewidths, and the relative amplitudes of the signal and background contributions are likewise set to conform to the experimental time domain data. The acetone carbonyl absorption is also given a lorentzian lineshape.

The resulting model FT FEIR spectrum is shown in Figure 4.28(c). The effect of the acetone carbonyl absorption appears as a negative feature at the same frequency (1715 cm^{-1}). This can be understood within the language of amplitude modulation (AM) in analog signal processing as being due to the 'baseband' component of the molecular response, $S_0 + S_2 + S_1$, which has been modulated up to the frequency of T .²⁵⁰ It is negative because of the π phase shift between the modulation and the three-pulse signal S_{12} (evident in the red and blue curves in Figure 4.28(b)), which physically arises because the thermal load decreases the fluorescence count rate. The modulation of S_{12} produces AM sidebands at the sum and difference frequencies between S_{12} and T , which can be seen in the FEIR spectrum near 100 cm^{-1} and 3300 cm^{-1} (inset of Figure 4.28(c)). The experimental FT FEIR spectrum (Figure

4.28(d)) shows both the negative ‘modulated baseband’ feature as well as the AM sidebands. To get qualitative similarity between the model and data, the strength of the modulation was set to $\alpha = 0.13$.

We now describe the thermal effect for the case when FEIR data is collected by continuously scanning the interferometer stage, as described in Section 4.5.2. To do this we need to consider the finite timescale of the sample’s thermal relaxation in relation to the speed at which the average power absorbed from the IR pulse-pair varies with the interferometer delay. Intuitively, one would expect that if the delay is scanned through interference fringes faster than the thermal profile can relax, then the thermal modulation will become partially washed out and lag behind the optical interference.

To capture this effect mathematically, it is convenient to describe the delay in stage displacement units, $\delta = 2c_0\tau_{\text{IR}}$, where c_0 is the speed of light. When the interferometer stage is continuously scanning, the displacement δ is a function of laboratory time t . We proceed by modifying Eq. 4.16, which is now also ultimately a function of t . Retaining the assumption of linearity, the modulation is rewritten as

$$T(t) = 1 - \alpha \int_{-\infty}^{\infty} H(t')P(t - t')dt' \quad (4.18)$$

where $H(t)$ is a response function that describes the sample’s macroscopic thermal relaxation. For simplicity we use an exponential decay with time constant τ_R

$$H(t) = \theta(t) \frac{1}{\tau_R} e^{-t/\tau_R}, \quad (4.19)$$

where the Heaviside step function $\theta(t)$ has been included to enforce causality. The other quantities in Eq. 4.18 retain their original meaning, and Eqs. 4.15 and 4.17 still hold in

their original forms after the appropriate change of variables. For example, during fast scan data acquisition the stage moves at constant velocity

$$\delta = \delta_0 + vt \tag{4.20}$$

where the velocity v has opposite signs during forward ($v > 0$) and reverse ($v < 0$) travel directions. The IR power absorption P is calculated from Eq. 4.17, transformed to lab time by $\tau_{\text{IR}} = (\delta_0 + vt)/2c_0$, and then inserted into Eq. 4.18 to calculate the resulting thermal modulation T . After transforming T back to τ_{IR} units, Eq. 4.15 is used to find the total signal F .

The important aspect of this case is that the thermal modulation now depends on the speed and direction of stage travel. As shown in Figure 4.29a, the time (or pathlength) domain thermal modulations for the forward and reverse directions have reduced amplitudes and oppositely signed phase shifts with respect to the steady state modulation. Here, the thermal time constant τ_R and the scan speed $|v|$ were chosen so that the timescale of thermal relaxation (shown by H plotted in pathlength units) is similar to the timescale of the IR optical phase evolution (shown for example by the fringes of the steady state modulation). Figure 4.29b shows the resulting effect on the calculated FEIR spectrum. The scan velocity dependent phase shift acquired by the thermal modulation manifests as a phase twist, or partially dispersive lineshape, in the negative solvent feature, while the amplitude reduction is also evident. The same effect appears in the AM sidebands (not shown).

In Figure 4.30 we compare FEIR data from the dilute acetone experiment collected alternately by stepping and fast scanning the delay. The scan direction dependent phase twist of the negative acetone feature is evident in the fast scan spectra, and is qualitatively similar to the model in Figure 4.29(b). The distinct character of the amplitude modulation

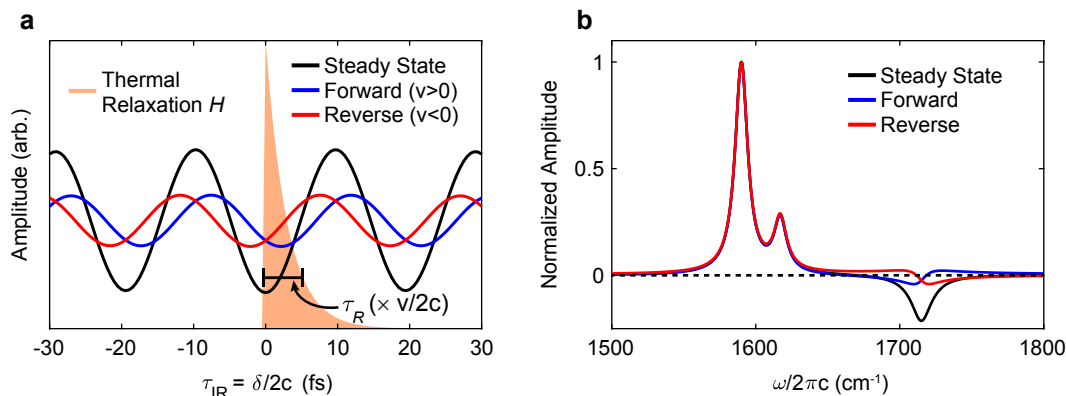


Figure 4.29: Model of thermal modulation with fastscanning of the IR delay. (a) Thermal amplitude modulation in the time or pathlength domain for fastscanning the delay in the forward (blue) and reverse (red) directions, compared to the steady state case of stepping the delay (black). The thermal response function H (orange) used to calculate the forward and reverse modulations is plotted in transformed units. (b) Effect on the FEIR spectrum. The negative solvent heating feature has reduced amplitude and acquires a phase twist with opposite signs for the forward and reverse directions.

between steady state stepping, forward scans, and reverse scans can be seen through the beating it produces in the time domain.

As the speed of stage travel is increased, the rate of IR optical phase evolution will eventually surpass the thermal relaxation timescale of the sample by enough to completely wash out the interferometric structure of the thermal modulation, and the resulting uniform scaling will have no effect on the FEIR spectrum. On the other hand, for very slow stage motion the thermal profile in the sample will keep pace with the fringes of the IR power absorption, and the steady state behavior from Eq. 4.16 will be recovered. In our model we may define an intermediate point between these regimes by considering the scan speed for which the thermal relaxation time is roughly equal to a half cycle of the interferometric

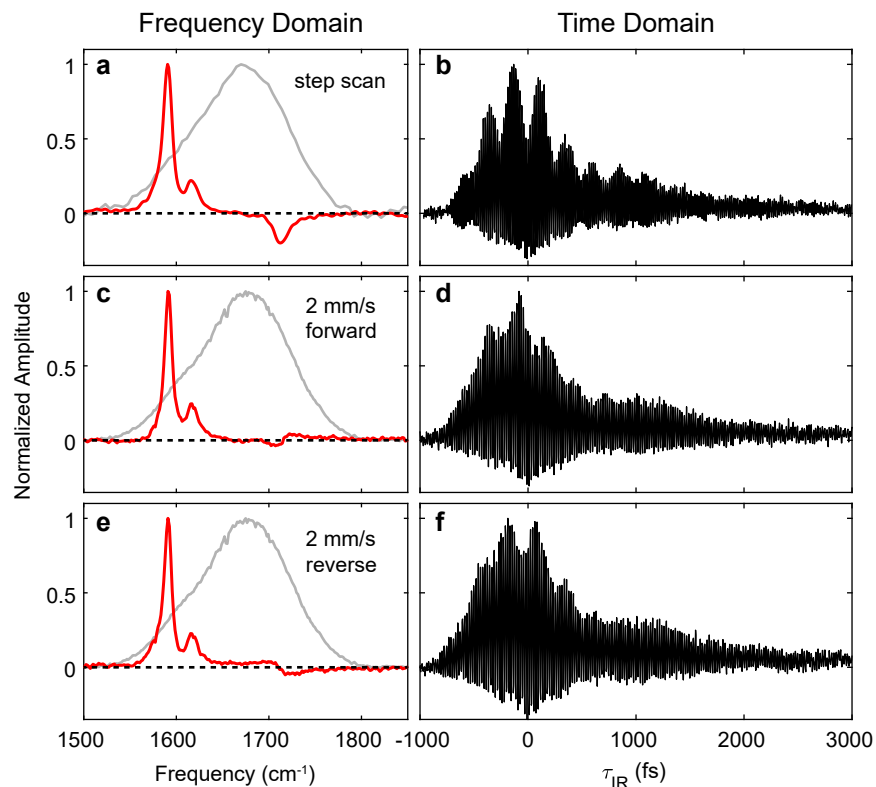


Figure 4.30: Thermal signatures in three-pulse FEIR data with stepscan and fastscan acquisition. (a) - (b) Three-pulse FEIR data in the frequency and time domain, respectively, for the dilute acetone experiment in the steady-state case of stepping the delay (same data as Figure 4.28(d)). In the frequency domain panel the IR pulse spectrum is shown in grey, and the dashed black line along the baseline is included to guide the eye. (c) - (d) FEIR data from the forward direction of a fast scan with 2 mm/s stage speed. The time domain data has been shifted to remove the constant offset ($F_0 + F_2$ contributions). (e) - (f) Reverse direction from the same fast scan experiment.

phase evolution, or

$$v_s = \frac{1}{\tilde{\nu}\tau_R} \quad (4.21)$$

where $\tilde{\nu}$ is the center frequency (in wavenumbers) of the solvent feature responsible for IR power absorption. In Figure 4.31 we show the scan speed dependence of the thermal

signature in the FEIR spectrum over roughly three orders of magnitude for the dilute acetone experiment and model. Because the frequency of the acetone carbonyl and set of scan speeds are fixed at known values from the experiment, we may estimate the thermal time constant by adjusting its value to produce the best agreement between the set of experimental spectra and a set of model spectra with the same speed ratios between scans. This results in a thermal relaxation time constant of roughly 20 ms. At the fastest experimental scan speed of 10 mm/s, the thermal signature, although much reduced in amplitude, is still visible. This speed is near the practical upper limit of our acquisition procedure, which indicates that we will not yet be able to access the ‘fast travel limit’ where artifact-free FEIR spectra could be collected even in the presence of large thermal effects.

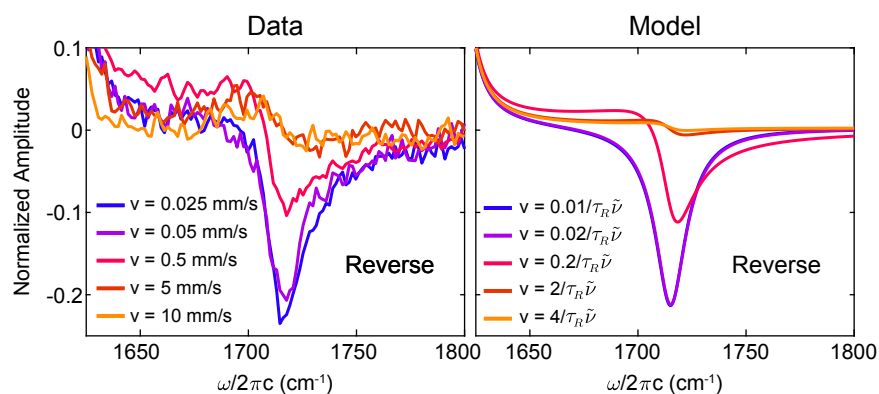


Figure 4.31: Scan speed dependence of the thermal spectral artifact. (a) Detail of the acetone thermal signature in experimental FT FEIR spectra for scan speeds between $25 \mu\text{m/s}$ and 10 mm/s in the reverse direction. (b) Model calculations with the same ratios between scan speeds. Speeds are reported in units of v_s as defined in Eq. 4.21. This set of speeds was chosen to produce the best qualitative agreement between the calculated and measured spectra, and results in the assignment of $\tau_R = 20 \text{ ms}$ when numerical values for the acetone absorption frequency and stage speeds are considered.

We conclude this section with a brief summary of our current understanding of how heating effects can influence FEIR measurements, and comment on the implications and

outlook for the application of FEIR in the future. Our observations are consistent with the presence of thermally-induced amplitude modulation of the bulk fluorescence collection efficiency. This amplitude modulation is well correlated to the average optical power the sample absorbs from the IR pulse train. As a result, if the IR absorption changes as a function of the experimentally varied optical delays, then the thermal modulation will introduce a signature, or artifact, into the measured signal. For example, τ_{IR} -dependent FEIR experiments are susceptible to this artifact while the two-pulse experiments are not, because average IR power absorption does not vary with the visible encoding delay. The timescale with which the thermal profile relaxes has been estimated by considering how the amplitude modulation is affected by stage velocity during continuous scanning data acquisition, and appears to be on the order of 20 milliseconds. This timescale corresponds to the sequential arrival of 10,000 IR pulses, which is consistent with our picture of ‘steady state’ heating due to the cumulative effect of the entire pulse train. We note this timescale is much faster than the seconds-timescale relaxation of the thermal modulation shown in Figure 4.26. These two timescales we observe are likely only partial views of a complex, multi-component process involving dissipation of the heat load from the excitation volume out to the entire sample cell configuration.

We rationalize our current experiment’s susceptibility to thermal effects by the combination of large average IR power density and sensitive high-NA optical system for fluorescence collection. Indeed, it is interesting to compare our FEIR microscope to the instrumentation used in photothermal spectroscopy and imaging experiments (see for example Li *et al*²⁵⁴). Mitigating thermal effects will be crucial for extending the application of FEIR to condensed phase systems that lack high IR transparency, most notably to aqueous solutions. Utilizing sample flow and exploring alternate IR focusing conditions, for example total internal

reflection of the IR, are possible routes forward.

4.9 Time-resolved fluorescence detection

4.9.1 Data acquisition with time-correlated single-photon counting

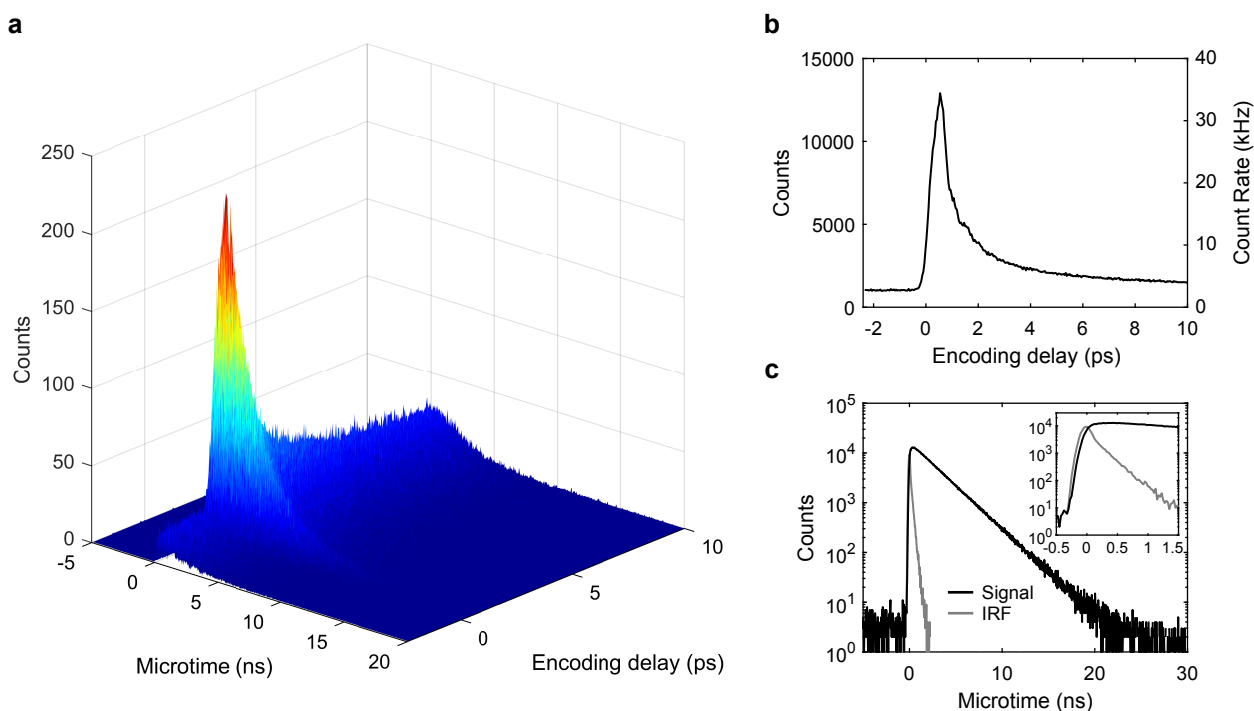


Figure 4.32: Microtime-resolved photon count data for a two-pulse FEIR measurement. (a) Raw microtime- and τ_{enc} -dependent photon data from a two-pulse experiment on $30 \mu\text{m}$ C6. (b) Projection onto the τ_{enc} axis. (c) Projection onto the microtime axis (black), and the IRF (gray). Inset shows detail of the early time data.

Time-correlated single-photon counting (TCSPC) is performed using a PicoQuant Time-Harp 260 PICO PCIe card. The sync channel is provided by the delay generator triggered off the Monaco amplifier. The photon channel is the 15dB attenuated NIM output of the SPAD. For FEIR measurements the PSO waveform from the delay stage controller during

stage fastscanning is sent to the TCSPC card and used as a marker integrated into the time-tagged time-resolved (TTTR) photon record. After every scan this raw TTTR record is processed on the fly by custom LabView code, which uses the markers to place each photon into its respective delay stage position bin. The result is two-dimensional data, where one dimension is the scanned delay (τ_{enc} or τ_{IR}), and the other is the photon arrival time relative to the sync channel (microtime) with 25 ps bins. In photon correlation measurements, like FEIR correlation spectroscopy discussed in Chapters 5 and 6, the pulse delays are fixed and the raw TTTR record is saved for analysis in post processing. The TCSPC instrument response function (IRF) is measured from visible pump light reflected from the air-coverslip interface with the spectrally-selective fluorescence filter-set replaced with appropriate neutral density filters.

Figure 4.32(a) shows the raw microtime-resolved count data from a two-pulse measurement on a 30 μm C6 solution. The τ_{enc} bin size is 40 fs. Figure 4.32(b) shows the projection of this raw data onto the τ_{enc} axis (i.e. integration over microtime). Figure 4.32(c) shows the projection onto the microtime axis, producing a TCSPC histogram. To avoid strongly distorting the microtime decay kinetics the maximum count rate (indicated on the right y-axis of Figure 4.32(b)) is kept below 5% of the repetition-rate.²⁵⁵ The IRF, shown in gray in Figure 4.32(c), has a 250 ps fwhm with a more slowly relaxing tail for positive microtimes. The zero of microtime is set at the maximum of the IRF.

4.9.2 Fluorescence lifetime-resolved FEIR spectra

Microtime-resolved three-pulse signals can be measured in the same way. Figure 4.33(a) shows a portion of the raw microtime-resolved count data from a three-pulse measurement on C6 in tetrachloroethylene (C_2Cl_4) solution. The data is processed into a spectrum along

the τ_{IR} axis by the same procedure discussed in Section 4.7, resulting in the microtime-dependent spectrum shown in Figure 4.33(b). One way to represent the emission kinetics as a function of vibrational frequency is to fit the microtime decay profile within small frequency bins. Single-exponential time-constants (i.e. fluorescence lifetimes) resulting from this process are shown overlaid on the FEIR spectrum in Figure 4.33(c). In this case, the lifetime is constant across the spectrum, as expected for a homogeneous system.

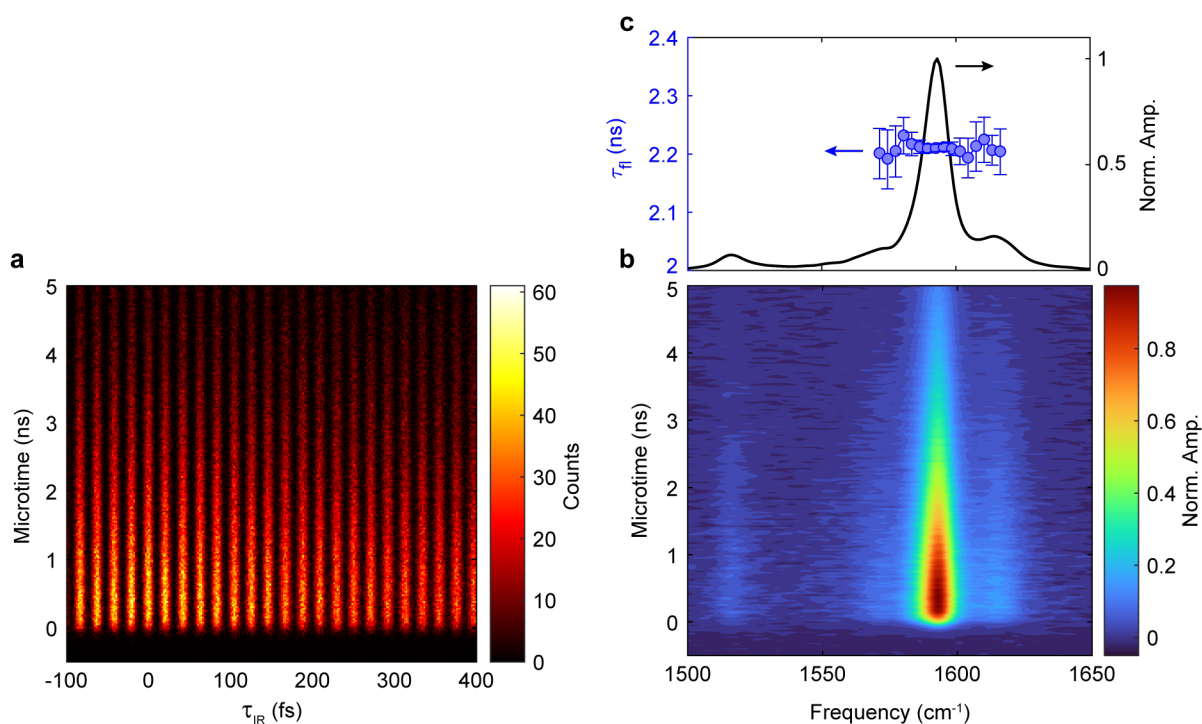


Figure 4.33: Microtime-resolved three-pulse FEIR signal and spectrum. (a) Section of the raw microtime-resolved photon count data from a three-pulse measurement on C6 in C_2Cl_4 ($\tau_{\text{enc}} = 600$ fs). (b) Microtime-resolved processed FEIR spectrum. (c) FEIR spectrum integrated over all microtimes (black), with fluorescence lifetimes (blue circles) extracted from exponential fits to the microtime decay within 3 cm^{-1} bins across the frequency axis. Error bars indicated 95% confidence intervals from the fit routine.

4.9.3 Using fluorescence lifetime-resolved FEIR spectra to disentangle multicomponent systems: hydrogen-bonded thiourea and coumarin heterodimers

In multicomponent or otherwise heterogeneous systems, the observation of multiple correlated observables can help understand the underlying distribution of species by spreading out information along multiple coordinates. Here we show a simple example where measuring fluorescence lifetime correlated to FEIR vibrational spectra can offer further insight into a bimolecular association equilibrium. Specifically, we investigate the hydrogen-bond (H-bond) facilitated dimerization of C6 with a thiourea organocatalyst, Scheiner's thiourea catalyst (STC). Thioureas are a family of organocatalysts that activate carbonyl or nitrile groups in a substrate to nucleophilic attack through the formation of strong, double H-bond interactions,^{256–258} shown schematically for our system in Figure 4.34(a). The particularly good H-bond donating ability of STC, which has been correlated to its catalytic activity, is proposed to arise in large part from the electron withdrawing bis(trifluoromethyl)phenyl groups that strongly polarize the amine N-H bonds.^{259–261}

To facilitate a strong interaction between the coumarin and thiourea, we use the non-polar solvent C_2Cl_4 . Figure 4.34(b) shows the IR spectra of C6 and a 1:1 mixture of C6 and STC. The most prominent spectral change is the presence of a new band at 1681 cm^{-1} which we assign to the C6 lactone carbonyl H-bonded to the thiourea, producing a 47 cm^{-1} red-shift from its free form. Smaller spectral shifts of the R1 and R2 ring modes are also evident. More details about the assignments of these coumarin vibrations are provided in Chapter 8. Figure 4.34(c) shows the electronic absorption spectra of C6 with and without STC. A prominent red-shift of the electronic band is induced by the interaction. As a result,

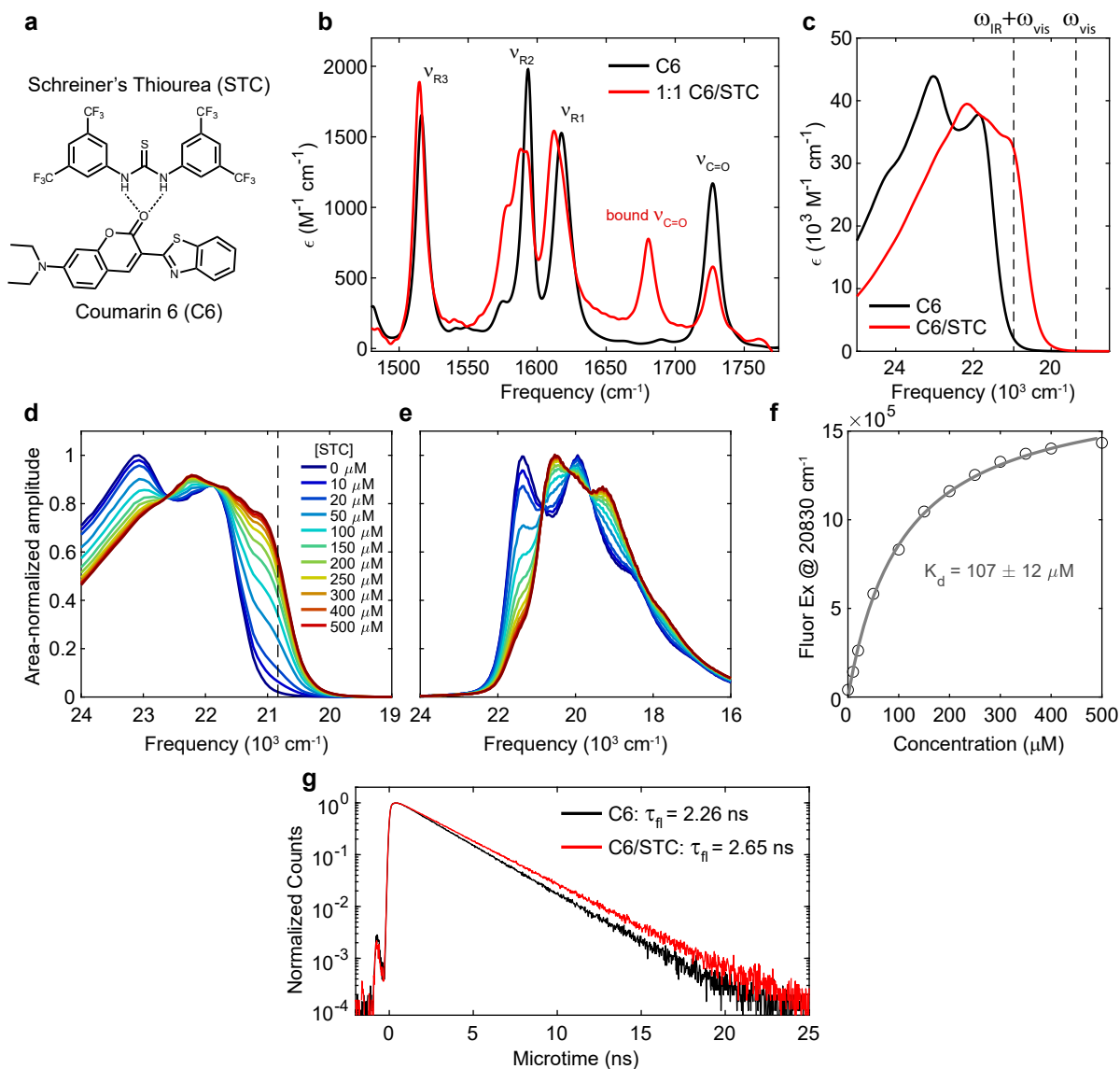


Figure 4.34: IR and electronic spectral characteristics of C6 and Schreiner's thiourea association in C_2Cl_4 . (a) Structures of C6 and STC and proposed double H-bonding configuration. (b) FTIR spectra of C6 (2 mM) and a 1:1 mixture of C6 and STC (both 0.5 mM). Both spectra are solvent subtracted, a 0.5 mM STC solution being used for subtraction in the latter case. (c) Electronic absorption spectra of C6 (20 μM) in the absence and presence of 0.5 mM STC. FEIR resonance conditions are indicated by dashed lines. (d),(e) STC concentration-dependent fluorescence excitation and emission spectra, respectively. The C6 concentration is 2 μM , and the spectra are area-normalized. (f) Integrated fluorescence intensity (counts) excited at 20830 cm^{-1} (indicted by dashed line in (d)) as a function of STC concentration, with a fit to a classic ligand-binding model. (g) TCSPC decay profile of maximum C6 FEIR signal (pumping at $\omega_{\text{IR}} = 1600 \text{ cm}^{-1}$) without (black) and with (red) 0.5 mM STC.

the bound C6 species is expected to have a much stronger FEIR resonance under the current experimental conditions. To characterize the strength of the binding equilibrium, Figures 4.34(d)-(e) show STC concentration-dependent fluorescence excitation and emission spectra. The area normalized spectra show clean isosbestic points suggestive of a two-component equilibrium. A dissociation constant K_d is extracted by fitting the concentration-dependence of the integrated fluorescence intensity excited at 20830 cm^{-1} (Figure 4.34(f)), just beyond the absorption edge of free C6, to a classic ligand-binding model (Langmiur isotherm) yielding $K_d = 107 \pm 12\ \mu\text{M}$.²⁶² Figure 4.34(g) demonstrates a change in C6 fluorescence lifetime induced by the presence of STC.

While the concentration-dependent electronic spectra are suggestive of a two-state association equilibrium between C6 and STC, it is not *a priori* clear that the change in fluorescence lifetime is explicitly linked to the formation of a specific H-bonded structure between the binding partners. Lifetime-resolved FEIR spectra provide a means to directly probe this relationship at the ensemble level. Figure 4.35 illustrates the approach. Lifetime-resolved FEIR spectra are measured with the IR pump centered near 1730 cm^{-1} to pump the weakly IR active carbonyl band, which through its large red-shift upon H-bonding provides a clear, spectrally isolated signature of the presence of an H-bonded complex. The C6 and STC concentrations are 150 and $250\ \mu\text{M}$ respectively, which ensure that both free and bound C6 are present. Figure 4.35(a) shows the resulting FEIR spectrum at $\tau_{\text{enc}} = 500\text{ fs}$, with the free and bound carbonyl bands highlighted. Figure 4.35(b) shows the microtime emission decay integrated within these two bands, which exhibit distinct fluorescence lifetimes similar to those measured from the entire ensemble in Figure 4.34(g). Figure 4.35(c) shows an alternative representation of this data introduced in Section 4.9.2, where the extracted fluorescence lifetime is plotted across the FEIR spectrum. The clear distinction in lifetime

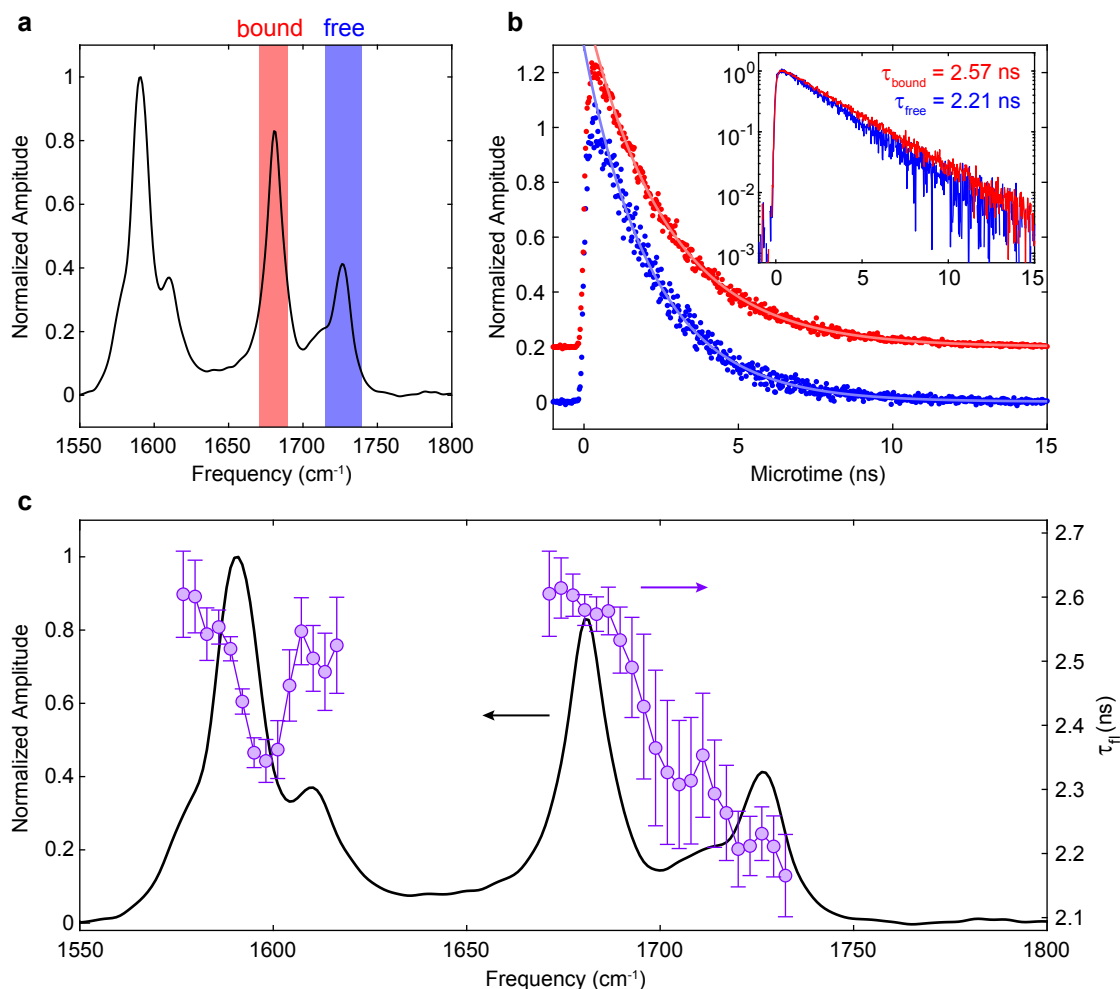


Figure 4.35: Microtime-resolved three-pulse FEIR signal and spectrum. (a) FEIR spectrum of a C6 and STC solution (150 and 250 μm , respectively) integrated over all microtimes. (b) Emission decay kinetics integrated over the free (blue) and bound (red) carbonyl bands (integration windows indicated in (a)). The inset shows the same traces on a log y scale with fluorescence lifetimes extracted from a single-exponential fit. (c) FEIR spectrum (same as in (a)) with fluorescence lifetimes extracted from 3 cm^{-1} bins across the frequency axis as in Figure 4.33(c).

between the free and bound carbonyl bands is apparent, while the lifetime is also variable in the ring-mode region, but is harder to interpret due to the spectrally overlapping bands.

The observation of a direct correlation between a H-bonded carbonyl vibration and the

change in fluorescence lifetime provides a more incisive view of the association equilibrium. Specifically, it is explicitly the formation of the H-bonded complex, rather than, e.g. a solvation effect, that changes the lifetime. The observation of this correlation also indicates that the ground-state complex persists in the electronic excited state, and provides a lower bound for the exchange timescale between the free and bound configurations. Namely, in order to produce a distinct fluorescence lifetime of ~ 2.6 ns, the H-bonded complex must, at the very least, persist for the duration of this lifetime.

Chapter 5

Principles of fluorescence and FEIR correlation spectroscopy

5.1 Overview

True single-molecule (SM) observation with FEIR spectroscopy represents the ultimate technical goal of this new method, and would enable the application of many of the strategies developed in SM fluorescence spectroscopy over the years to the investigation of chemical problems. However, short of the extended observation of individual molecules, correlative techniques that analyze the fluctuations from small ensembles of molecules—correlation spectroscopy (CS)—can offer much insight into dynamic phenomena with many of the same advantages presented by SM over bulk experiments. CS experiments, most importantly fluorescence correlation spectroscopy (FCS) and its related methods, measure the timescales of dynamical processes through the time correlation function of stochastic equilibrium fluctuations.^{263–266} Like true SM dynamics measurements, this mode of operation tracks the natural time-course of the molecular dynamics asynchronously, circumventing the need to apply a perturbation and facilitating the study of processes that are impossible to

synchronise across a macroscopic sample. As such, CS experiments rely on SM sensitivity, i.e. the ability to resolve signal changes caused by the dynamic behavior of individual molecules, and are sometimes considered as SM techniques, although they are formally ensemble measurements that record averaged kinetics. It is interesting to note that the original demonstration of FCS by Magde, Elson, and Webb involved measurements on an ensemble of $\langle N \rangle \sim 10^4$ molecules, and was therefore an impressively difficult experiment.^{263,267} Indeed, the size of the desired signal fluctuations relative to the mean scales as $\langle N \rangle^{-1/2}$, and therefore FCS is best done near SM equivalent concentrations. It was not until the early 1990's (coincidentally when SM fluorescence spectroscopy was first emerging) that Rigler and coworkers introduced the now standard methodology for performing FCS with a confocal microscope that enabled measurements with $\langle N \rangle \sim 1$,²⁶⁸⁻²⁷⁰ making the technique widely accessible.

From a technical standpoint, CS experiments are often less demanding than true SM detection in that they can take advantage of time-averaging to increase signal to noise without sacrificing time-resolution. This property is intrinsic to the acquisition of a time-correlation function, where the time *lag* between successive events, rather than their absolute sequentially, is interrogated. Beyond providing a means to increase signal-to-noise, the correlative modality of CS experiments can yield much higher time-resolution than that in the direct measurement of SM trajectories, as time-resolution is set by the shortest possible interval between photon detection events rather than the bin size for counting photons. In modern FCS experiments, the time-resolution can reach the fundamental limit of an asynchronous measurement set by the fluorescence lifetime. FCS most often operates in solution, and monitors the real-time fluorescence fluctuations from freely diffusing molecules within a small, open probe volume formed by the focal spot of a microscope. During the course of the experiment molecules are therefore continuously replaced, avoiding the most serious photo-bleaching

problems inherent to direct SM observation.

In this chapter we provide an overview of the theoretical concepts underlying CS experiments, specifically FCS, with the goal of demonstrating how FEIR spectroscopy can be implemented as a CS technique. We propose strategies for using FEIR-CS to study chemical exchange processes in solution, and comment on their relative merits. As an FEIR-CS measurement would be less technically demanding than rigorous SM observation, such experiments would serve as conceptual and practical stepping-stone towards true SM studies.

5.2 Evaluation of the correlation function for diffusion and chemical reaction

5.2.1 General method

A method of calculating the correlation function for FCS was presented by Elson and Magde in their original theoretical analysis,²⁷¹ and remains a common way of determining the functional forms produced by various dynamical models.²⁶⁴ There is a continuum framework based on a linear reaction-diffusion equation for the spatial concentration profile of each chemical species involved. Importantly, this model neglects photophysical effects, and treats the detected fluorescence intensity as a continuous classical function simply proportional to the instantaneous concentration profile integrated against the experiment's observation volume. As such, the photon correlation aspects of the measurement are ignored, and the central object of calculation is the concentration fluctuation correlation function. Likewise, all dynamical processes, such as the interconversion of species due to chemical reaction or

exchange, is handled by the time-dependence of their concentrations, and they are not assumed to be subject to any internal dynamics. Here we summarize the workings of this model in order to show how diffusion and chemical reaction phenomena may be measured by FCS, as well as providing a theoretical background for our proposed FEIR-CS experiments.

We consider a solution of multiple species, indexed by i , that exist in chemical and thermal equilibrium. The fluctuating fluorescence emission from the probed volume is expressed as

$$F(t) = \sum_i Q_i \int d^3\mathbf{r} C_i(\mathbf{r}, t) \Omega(\mathbf{r}). \quad (5.1)$$

Here $C_i(\mathbf{r}, t)$ is the concentration of the i^{th} chemical species at location \mathbf{r} and time t . $\Omega(\mathbf{r})$ is the overall optical observation function which determines the probe volume from which the signal is generated and collected from. It is shaped both by the spatial intensity profile of the excitation beam(s) as well as the imaging properties of the detection apparatus. Lastly, Q_i is the overall brightness of the i^{th} species, i.e. is proportional to the product of effective excitation cross-section and fluorescence emission probability. In analogy to conventional fluorescence brightness, we will discuss the concept of FEIR brightness in some detail in Chapter 7. Within the framework of this model, the only difference between regular FCS and FEIR-CS experiments is the dependence of this effective brightness on the external parameters of the excitation scheme. For our proposed FEIR-CS experiments, we will leverage the structural information from a molecule's vibrational spectrum by modulating the excitation resonance between the IR field and the vibrational transitions, which will be discussed in Section 5.3.

The mean value of the fluorescence signal is

$$\langle F \rangle = \sum_i Q_i \langle C_i \rangle \int d^3\mathbf{r} \Omega(\mathbf{r}), \quad (5.2)$$

where $\langle C_i \rangle$ is the average, i.e. thermodynamic, concentration of the i^{th} species. The spatial integral $\int d^3\mathbf{r} \Omega(\mathbf{r})$ may be considered as a measure of the effective volume of the observation region, in which case Eq. 5.2 has the simple interpretation as the average number of molecules of each species multiplied by their respective brightnesses. However, as we will see in Section 5.2.3, this sense of the probe region's volume is not unique, and a slightly different version more naturally comes about when considering the effective molecule number in FCS. The fluctuation about the mean is

$$\delta F(t) = F(t) - \langle F \rangle = \sum_i Q_i \int d^3\mathbf{r} \delta C_i(\mathbf{r}, t) \Omega(\mathbf{r}), \quad (5.3)$$

that is, directly reflective of the concentration fluctuations $\delta C_i(\mathbf{r}, t) = C_i(\mathbf{r}, t) - \langle C_i \rangle$. The correlation function measured in FCS is

$$G(\tau) = \frac{\langle \delta F(t) \delta F(t + \tau) \rangle}{\langle F \rangle^2} = \frac{\langle \delta F(0) \delta F(\tau) \rangle}{\langle F \rangle^2}. \quad (5.4)$$

Here τ is the lag-time, while t is laboratory time. In the second equality we have used of the stationary property, i.e. the independence from any unique origin of time, of the equilibrium fluctuations. The correlation function is often called the fluorescence autocorrelation function, although in more precise language it is the autocovariance, that is, the autocorrelation of the *fluctuations* in the fluorescence.²⁷² In these expressions, the angle brackets formally denote an ensemble average, although experimentally the correlation function is

always measured as a time average. We will always assume the system is ergodic, that is, that it samples all its possible configurations within a sufficiently long time so that these two averages are equivalent.^{273,274} As we will see later on, the denominator in Eq. 5.4 has an important role as a normalization factor, which gives FCS some useful ratiometric properties that allow—among other things—the absolute determination of local molecule number or concentration.

To proceed, the fluorescence correlation function is next decomposed into partial contributions $G_{ij}(\tau)$ connecting species i and j as

$$G(\tau) = \langle F \rangle^{-2} \langle \delta F(0) \delta F(\tau) \rangle = \langle F \rangle^{-2} \sum_{i,j} G_{ij}(\tau), \quad (5.5a)$$

where

$$G_{ij}(\tau) = Q_i Q_j \int d^3 \mathbf{r} \int d^3 \mathbf{r}' \Omega(\mathbf{r}) \Omega(\mathbf{r}') \phi_{ij}(\mathbf{r}, \mathbf{r}', \tau) \quad (5.5b)$$

and

$$\phi_{ij}(\mathbf{r}, \mathbf{r}', \tau) = \langle \delta C_i(\mathbf{r}, 0) \delta C_j(\mathbf{r}', \tau) \rangle \quad (5.6)$$

is the concentration fluctuation correlation function (CFCF). As the solution is isotropic and homogeneous on average, the CFCF can only depend on the relative displacement $|\mathbf{r} - \mathbf{r}'|$, just as it only depends on the lag-time τ . However, it will be convenient to keep both spatial variables for the sake of the ensuing calculation. The fluctuations in concentration are taken

to obey a set of linearized reaction-diffusion equations

$$\frac{\partial}{\partial t} \delta C_i(\mathbf{r}, t) = D_i \nabla^2 \delta C_i(\mathbf{r}, t) + \sum_j K_{ij} \delta C_j(\mathbf{r}, t) \quad (5.7)$$

where D_i is the diffusion constant of the i^{th} species, and K_{ij} is a matrix of first-order rate constants for inter-conversion between the different chemical species. Importantly, this assumption of a linear rate law governing the reaction essentially decouples the reaction and diffusion phenomena, leading to much simpler dynamics. Notably, nonlinear reaction-diffusion systems can be incredibly complex, giving rise to a rich diversity of unexpected behavior, and represents a large area of current investigation in physical, chemical, and biological contexts.^{275–277}

Taken at face value, Eq. 5.7, which has deterministic solutions decaying to a time-independent steady-state, may seem at odds with our physical picture of $\delta C_i(\mathbf{r}, t)$ as representing the incessant microscopic fluctuations consistent with the system equilibrated at a given temperature. More correctly, we will see below that it is really the CFCF ϕ_{ij} that obeys Eq. 5.7 (e.g. see Eq. 5.18a). The analysis can be recast to make this explicit, however, the notation is less cumbersome if we work with an equation of motion for $\delta C_i(\mathbf{r}, t)$ directly, and the result is the same. We may think of this as a statement of Onsager’s regression hypothesis, namely, that the decay of the equilibrium fluctuation correlation function follows the same rate law as the macroscopic variables.^{273,278,279} Also along these lines, the applicability of linearized rate laws for the regression of reactive fluctuations in the kinetic scheme can be seen as a consequence of being at equilibrium.²⁸⁰

The reaction-diffusion equation is more naturally handled in the spatial Fourier domain, where it takes the form of a system of linear ordinary differential equations

$$\frac{\partial}{\partial t} \delta \tilde{C}_i(\mathbf{k}, t) = \sum_j M_{ij} \delta \tilde{C}_j(\mathbf{k}, t), \quad (5.8)$$

for the spatial Fourier components of the concentration profiles

$$\delta \tilde{C}_i(\mathbf{k}, t) = \int d^3 \mathbf{r} e^{-i\mathbf{k} \cdot \mathbf{r}} \delta C_i(\mathbf{r}, t). \quad (5.9)$$

This system may be immediately solved by computing the eigenvalues and eigenvectors of the \mathbf{M} matrix which has components

$$M_{ij} = K_{ij} - D_i |\mathbf{k}|^2 \delta_{ij}, \quad (5.10)$$

where δ_{ij} is the Kronecker delta. Explicitly, this matrix is diagonalized by

$$\mathbf{\Lambda} = \mathbf{X}^{-1} \mathbf{M} \mathbf{X} \quad (5.11)$$

where $\mathbf{\Lambda}$ is a diagonal matrix of eigenvalues $\Lambda_{ij} = \lambda_i \delta_{ij}$ and the columns of \mathbf{X} are the eigenvectors. The solution of Eq. 5.8 can then be written in terms of the initial condition $\delta \tilde{C}_i(\mathbf{k}, 0)$ in the usual way

$$\delta \tilde{C}_i(\mathbf{k}, t) = \sum_k X_{ik} e^{\lambda_k t} \sum_l X_{kl}^{-1} \delta \tilde{C}_l(\mathbf{k}, 0). \quad (5.12)$$

It is convenient to rewrite this as

$$\delta\tilde{C}_i(\mathbf{k}, t) = \sum_j Z_{ij}(t, \mathbf{k}) \delta\tilde{C}_j(\mathbf{k}, 0), \quad (5.13)$$

where

$$Z_{ij}(t, \mathbf{k}) = \sum_k X_{ik} e^{\lambda_k t} X_{kj}^{-1} \quad (5.14)$$

are propagating functions that evolve the spatial Fourier components of each species' concentration profiles forward in time. It can be shown that detailed balance imposes the symmetry condition²⁷¹

$$Z_{ij}(t, \mathbf{k}) \langle C_j \rangle = Z_{ji}(t, \mathbf{k}) \langle C_i \rangle, \quad (5.15)$$

or equivalently

$$\phi_{ij}(\mathbf{r}, \mathbf{r}', t) = \phi_{ji}(\mathbf{r}, \mathbf{r}', t). \quad (5.16)$$

To proceed, we first write the CFCF as

$$\phi_{ij}(\mathbf{r}, \mathbf{r}', \tau) = \frac{1}{(2\pi)^3} \int d^3\mathbf{k} e^{i\mathbf{k}\cdot\mathbf{r}'} \langle \delta C_i(\mathbf{r}, 0) \delta\tilde{C}_j(\mathbf{k}, \tau) \rangle, \quad (5.17)$$

where we have preemptively decomposed $\delta C_j(\mathbf{r}', t)$ into its spatial Fourier components (\mathbf{k} begin conjugate to \mathbf{r}' in this case). Inserting Eq. 5.13 we get

$$\phi_{ij}(\mathbf{r}, \mathbf{r}', \tau) = \frac{1}{(2\pi)^3} \int d^3\mathbf{k} e^{i\mathbf{k}\cdot\mathbf{r}'} \sum_k Z_{jk}(\tau, \mathbf{k}) \langle \delta C_i(\mathbf{r}, 0) \delta \tilde{C}_k(\mathbf{k}, 0) \rangle \quad (5.18a)$$

$$= \frac{1}{(2\pi)^3} \int d^3\mathbf{k} \int d^3\mathbf{r}'' e^{i\mathbf{k}\cdot\mathbf{r}'} e^{-i\mathbf{k}\cdot\mathbf{r}''} \sum_k Z_{jk}(\tau, \mathbf{k}) \langle \delta C_i(\mathbf{r}, 0) \delta C_k(\mathbf{r}'', 0) \rangle, \quad (5.18b)$$

where we inserted the inverse Fourier transform of $\delta \tilde{C}_k(\mathbf{k}, 0)$. At this point we invoke the initial condition

$$\langle \delta C_i(\mathbf{r}, 0) \delta C_k(\mathbf{r}'', 0) \rangle = \langle (\delta C_i)^2 \rangle \delta_{ik} \delta(\mathbf{r} - \mathbf{r}'') = \langle C_i \rangle \delta_{ik} \delta(\mathbf{r} - \mathbf{r}''). \quad (5.19)$$

The first equality says that fluctuations of separate molecules are uncorrelated, which amounts to assuming the solution is sufficiently dilute so as to be ideal. The second equality assumes that the occupation number of molecules in a given volume obeys Poisson statistics (i.e. the variance equals the mean). Inserting this into Eq. 5.18a and performing the \mathbf{r}'' integral gives

$$\phi_{ij}(\mathbf{r}, \mathbf{r}', \tau) = \frac{1}{(2\pi)^3} \int d^3\mathbf{k} e^{i\mathbf{k}\cdot(\mathbf{r}'-\mathbf{r})} Z_{ji}(\mathbf{k}, \tau) \langle C_i \rangle. \quad (5.20)$$

The partial contribution of ϕ_{ij} to the correlation function in Eq. 5.5 is then

$$\begin{aligned} G_{ij}(\tau) &= \frac{Q_i Q_j}{(2\pi)^3} \int d^3\mathbf{r} \int d^3\mathbf{r}' \int d^3\mathbf{k} \Omega(\mathbf{r}) \Omega(\mathbf{r}') e^{i\mathbf{k}\cdot(\mathbf{r}'-\mathbf{r})} Z_{ji}(\mathbf{k}, \tau) \langle C_i \rangle \\ &= \frac{Q_i Q_j}{(2\pi)^3} \int d^3\mathbf{k} \int d^3\mathbf{r} \Omega(\mathbf{r}) e^{-i\mathbf{k}\cdot\mathbf{r}} \int d^3\mathbf{r}' \Omega(\mathbf{r}') e^{i\mathbf{k}\cdot\mathbf{r}'} Z_{ji}(\mathbf{k}, \tau) \langle C_i \rangle \end{aligned}$$

$$\begin{aligned}
 &= \frac{Q_i Q_j}{(2\pi)^3} \int d^3\mathbf{k} \tilde{\Omega}(\mathbf{k}) \tilde{\Omega}^*(\mathbf{k}) Z_{ji}(\mathbf{k}, \tau) \langle C_i \rangle \\
 &= \frac{Q_i Q_j}{(2\pi)^3} \int d^3\mathbf{k} |\tilde{\Omega}(\mathbf{k})|^2 Z_{ji}(\mathbf{k}, \tau) \langle C_i \rangle.
 \end{aligned} \tag{5.21}$$

This concludes the general method. All that needs to be done is to choose a specific kinetic model to produce a rate matrix for Eq. 5.10, assign a functional form to the optical detection function $\Omega(\mathbf{r})$, and describe each species' brightness Q_i .

5.2.2 Separation of diffusion and reaction

While Eq. 5.7 neglects direct coupling between reaction and diffusion phenomena, the propagators $Z_{ji}(\mathbf{k}, \tau)$ still describe both processes and can be complicated if the diffusion constant D_i is different for each inter-converting species. A major simplification is possible if it is assumed that each species has the same diffusion constant D . In this case Eq. 5.10 becomes

$$\mathbf{M} = \mathbf{K} - D|\mathbf{k}|^2 \mathbf{1}, \tag{5.22}$$

where $\mathbf{1}$ is the identity matrix, so that the eigenvalues of the \mathbf{M} matrix are simply those of the rate matrix \mathbf{K} minus $D|\mathbf{k}|^2$, while their eigenvectors are the same. From Eq. 5.14, the result is that the propagators factorize into a part that depends on \mathbf{k} , which reports on diffusion, and a spatially independent part Y_{ij} that reports on the reaction kinetics,

$$Z_{ji}(\mathbf{k}, \tau) = e^{-D|\mathbf{k}|^2 \tau} Y_{ji}(\tau). \tag{5.23}$$

The partial contributions G_{ij} can then also be separated as

$$G_{ij}(\tau) = \frac{Q_i Q_j}{(2\pi)^3} Y_{ji}(\tau) \langle C_i \rangle \int d^3 \mathbf{k} e^{-D|\mathbf{k}|^2 \tau} |\tilde{\Omega}(\mathbf{k})|^2. \quad (5.24)$$

The final result is that the overall correlation function factorizes into independent reaction and diffusion terms

$$G(\tau) = G_{\text{rxn}}(\tau) G_D(\tau). \quad (5.25)$$

While this simplification in the analytic form of the correlation function is very convenient, a uniform diffusion constant is often a bad assumption for many situations of practical interest. For example, in binding problems where one reactant associates with a much more massive partner, the correspondingly large change in diffusion constant is important to capture properly. These cases can be treated within the general formalism, but yield more complicated analytic forms of the correlation function.²⁸¹

5.2.3 Diffusion through a 3D Gaussian observation volume

Here we compute a widely used analytic form of the ‘diffusion only’ contribution to the correlation function $G_D(\tau)$. In the simplest case of a single species in solution, the full correlation function also reduces to $G_D(\tau)$. Specifically, an especially simple and widely used analytic form for this correlation function arises by assuming that the optical detection function is a 3D Gaussian

$$\Omega(\mathbf{r}) = \Omega_0 \exp \left[-\frac{2(x^2 + y^2)}{w_{xy}^2} - \frac{2z^2}{w_z^2} \right] \quad (5.26)$$

Here w_{xy} and w_z are the $1/e^2$ radii transverse to and along the optical axis, respectively, and Ω_0 is a constant that describes the magnitude of the excitation intensity. It is important to note that this assumption of a Gaussian probe volume is largely one of analytic convenience, and real optical geometries commonly used confocal microscope configurations can produce substantial deviations from this shape, leading to artifacts when using the resulting functional form to fit data.²⁸² The Fourier transform of the Gaussian optical detection function is

$$\tilde{\Omega}(\mathbf{k}) = \int d^3\mathbf{r} \Omega(\mathbf{r}) e^{-i\mathbf{k}\cdot\mathbf{r}} = \Omega_0 \left(\frac{\pi}{2}\right)^{3/2} w_{xy}^2 w_z \exp\left[-\frac{w_{xy}^2(q_x^2 + q_y^2)}{8} - \frac{w_z^2 q_z^2}{8}\right] \quad (5.27)$$

Assuming only a single species and therefore dropping the index i , the full correlation function given by Eqs. 5.5 and 5.24 is

$$G(\tau) = G_D(\tau) = \langle F \rangle^{-2} \frac{Q^2}{(2\pi)^3} \langle C \rangle \int d^3\mathbf{k} e^{-D|\mathbf{k}|^2\tau} |\tilde{\Omega}(\mathbf{k})|^2. \quad (5.28)$$

The mean fluorescence in Eq. 5.2 can be written as

$$\langle F \rangle = Q \langle C \rangle \int d^3\mathbf{r} \Omega(\mathbf{r}) = Q \langle C \rangle \Omega_0 \left(\frac{\pi}{2}\right)^{3/2} w_{xy}^2 w_z \quad (5.29)$$

where we have used the fact that $\int d^3\mathbf{r} \Omega(\mathbf{r}) = \tilde{\Omega}(\mathbf{k} = 0)$. Inserting Eq. 5.27 we have

$$\begin{aligned} G(\tau) &= \langle F \rangle^{-2} Q^2 \langle C \rangle \frac{w_{xy}^4 w_z^2}{2^6} \iiint dk_x dk_y dk_z \\ &\quad \times \exp\left[-\frac{(w_{xy}^2 + 4Dt)(k_x^2 + k_y^2)}{4} - \frac{(w_z^2 + 4Dt)k_z^2}{4}\right] \\ &= \langle F \rangle^{-2} Q^2 \langle C \rangle \Omega_0^2 \frac{w_{xy}^4 w_z^2}{2^6} \left(\frac{4\pi}{w_{xy}^2/4 + Dt}\right) \left(\frac{4\pi}{w_z^2/4 + Dt}\right)^{1/2} \end{aligned}$$

$$\begin{aligned}
 &= \left(Q \langle C \rangle \Omega_0 \left(\frac{\pi}{2} \right)^{3/2} w_{xy}^2 w_z \right)^{-2} Q^2 \langle C \rangle \Omega_0^2 \frac{\pi^{3/2} w_{xy}^2 w_z}{2^3} \left(1 + \frac{4Dt}{w_{xy}^2} \right)^{-1} \left(1 + \frac{4Dt}{w_z^2} \right)^{-1/2} \\
 &= \frac{1}{\langle C \rangle V} \left(1 + \frac{t}{\tau_D} \right)^{-1} \left(1 + \frac{t}{\kappa^2 \tau_D} \right)^{-1/2} \\
 &= \frac{1}{\langle N \rangle} \left(1 + \frac{t}{\tau_D} \right)^{-1} \left(1 + \frac{t}{\kappa^2 \tau_D} \right)^{-1/2}. \tag{5.30}
 \end{aligned}$$

Here

$$\tau_D = \frac{w_{xy}^2}{4D} \tag{5.31}$$

is a convenient parameter that can be seen to represent the average timescale of diffusion across the transverse profile of the optical detection region, and

$$\kappa = w_z / w_{xy} \tag{5.32}$$

is the ratio of its longitudinal to transverse profiles. In practice κ is often significantly larger than 1, and τ_D therefore marks the time-point at which G_D has approximately decayed by half. Similarly, by defining an effective volume

$$V = \pi^{3/2} w_{xy}^2 w_z, \tag{5.33}$$

the correlation function has the convenient property that

$$G_D(0) = \frac{1}{\langle N \rangle}, \tag{5.34}$$

where $\langle N \rangle = \langle C \rangle V$ is the average number of molecules in the probe volume. From the perspective of this calculation, the average molecules number is defined by the concentration and effective volume of the observation region. It is worth noting that a prolate spheroid with minor and major axes of w_{xy} and w_z , respectively, has volume

$$V = \frac{4\pi}{3} w_{xy}^2 w_z^2 \approx 4.19 w_{xy}^2 w_z^2, \quad (5.35)$$

while $\pi^{3/2} \approx 5.57$ in Eq. 5.33. With knowledge of the size and shape of the observation volume, it is in principle possible to thereby back out the concentration from a measurement. However, without assuming a known concentration or observation volume, one can treat the inverse early time amplitude $G_D(0)^{-1}$ as an independent *definition* of the average number of molecules participating in the experiment. In general, this interpretation of the early-time correlation amplitude does not even depend on the specific shape of the observation volume, and is a way of defining $\langle N \rangle$ solely based on the Poisson occupation number statistics.²⁸³ This approach only works provided that diffusion is the only dynamical process responsible for fluorescence fluctuations so that $G(\tau) = G_D(\tau)$.

5.2.4 Two-state equilibrium

To demonstrate how a chemical reaction phenomena may appears in a CS measurement, we will calculate the correlation function for the simplest case of a two-state exchange reaction



We begin by constructing the rate matrix. The forwards and backward rates are k_f and k_b , respectively, and satisfy detailed balance $k_f/k_b = K$ where K is the equilibrium constant.

In order to take advantage of the convenient factorization property in Section 5.2.2, we set the diffusion constants of each species to be equal $D_A = D_B \equiv D$. The \mathbf{M} matrix from Eq. 5.10 is

$$\mathbf{M} = \begin{pmatrix} -k_f - D|\mathbf{k}|^2 & k_b \\ k_f & -k_b - D|\mathbf{k}|^2 \end{pmatrix} \quad (5.37)$$

Its eigenvalues are

$$\lambda_1 = -D|\mathbf{k}|^2, \quad \lambda_2 = -D|\mathbf{k}|^2 - R \quad (5.38)$$

where $R = k_f + k_b$ is the kinetic relaxation rate. It is worth noting here that only one eigenvalue reports on chemical kinetics, and only through the sum of forward and backward rate constants. As in a bulk relaxation experiment, it is not possible to directly measure the forward and backward rates independently, which in this case can be considered a consequence of the ensemble-averaged nature of the correlation function.

The propagating functions Z_{ij} factorize as in Eq. 5.23, and the spatially-independent reaction propagators $Y_{ij}(\tau)$ are

$$Y_{AA}(\tau) = \frac{1 + Ke^{-R\tau}}{1 + K} \quad (5.39a)$$

$$Y_{BB}(\tau) = \frac{K + e^{-R\tau}}{1 + K} \quad (5.39b)$$

$$Y_{AB}(\tau) = \frac{K - Ke^{-R\tau}}{1 + K} \quad (5.39c)$$

$$Y_{BA}(\tau) = \frac{1 - e^{-R\tau}}{1 + K}. \quad (5.39d)$$

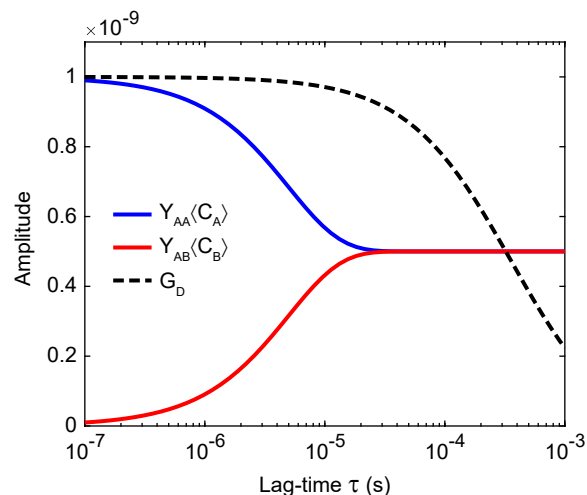


Figure 5.1: Reaction propagating functions $Y_{AA}(\tau)\langle C_A \rangle$ and $Y_{AB}(\tau)\langle C_B \rangle$ for a two-state exchange reaction. The profile of the diffusion component of the correlation function (amplitude scaled to visualization) is overlaid.

Figure 5.1 shows two of these propagating functions, the Y_{AA} ‘autocorrelation’ which dictates the persistence of A , and the Y_{AB} ‘cross-correlation’ which describes how B converts to A . In each case, the propagators are scaled by the relevant average concentration as they would appear in Eq. 5.21. In this example, the equilibrium constant is set to $K = 1$ with relaxation rate $R = k_f + f_b = 10^5 \text{ s}^{-1}$, and $\langle C_A \rangle = \langle C_B \rangle = 1 \text{ nM}$. Also shown is the decay profile of $G_D(\tau)$ for a diffusion timescale of $\tau_D = 400 \mu\text{s}$ and probe volume aspect ratio of $\kappa = 4$. In this case, the kinetics are faster than the diffusion timescale, and could therefore be measured.

The resulting reactive part of the correlation function for the two-state system is

$$G_{\text{rxn}}(\tau) = \left(1 - P + P \exp(-R\tau)\right), \quad (5.40a)$$

where

$$P = \frac{k_f k_b (Q_A - Q_B)^2}{(k_f + k_b)(k_f Q_A^2 + k_b Q_B^2)} \quad (5.41)$$

depends on the relative brightness of the two species.²⁸³ In the simplest case where B is completely dark, $Q_A = Q$ and $Q_B = 0$, this amplitude reduces to $P = k_b/(k_f + k_b)$, i.e. the fraction of B at equilibrium. In this case, the total correlation function (Eq. 5.25) is then

$$G(\tau) = \left(1 + K \exp(-R\tau)\right) \frac{1}{\langle N \rangle} \left(1 + \frac{t}{\tau_D}\right)^{-1} \left(1 + \frac{t}{\kappa^2 \tau_D}\right)^{-1/2}. \quad (5.42)$$

The inverse early-time amplitude is $G(\tau \rightarrow 0)^{-1} = \langle N \rangle / (1 - K)$, which has the simple interpretation as the average number of A molecules, i.e. the effective number of molecules that are actually visible. In general, measuring the chemical kinetics requires contrast between the states, as we can see by $P = 0$ when $Q_A = Q_B$.

5.3 FEIR correlation spectroscopy

With some of the conceptual background in place, here we describe how potential FEIR-CS experiments could be designed to track chemical phenomena in solution. The core idea is to use the changes in a molecule's vibrational spectrum sensed by the FEIR signal to create contrast between different states. This plays into the generality of the CS approach, where any dynamical process can be studied provided that it modulates the measured signal intensity. Whereas FCS methods rely on changes in electronic fluorescence observables—like spectrum, brightness, polarization, or FRET efficiency^{284–290}—FEIR-CS will act as an IR

-vibrational analogue of these methods, providing chemical bond-level information through the probing of structurally-sensitive vibrational resonances.

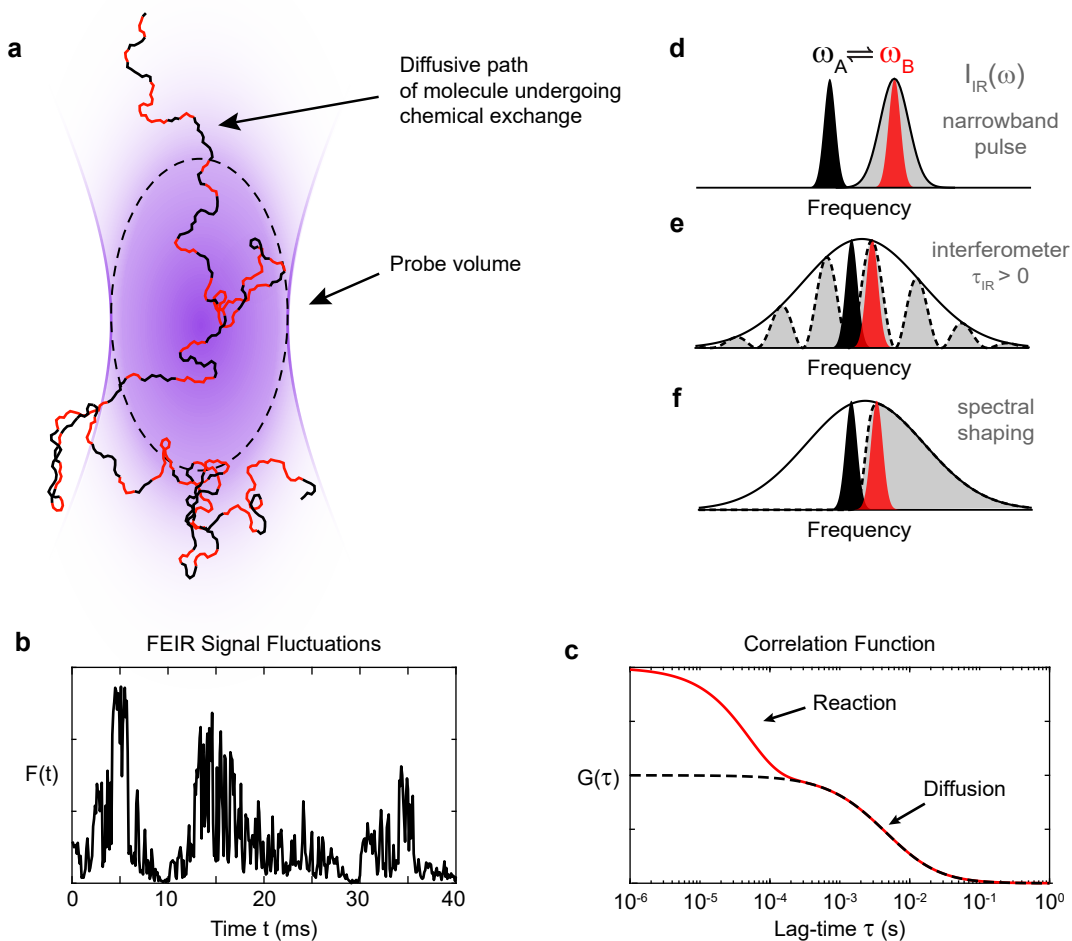


Figure 5.2: Cartoon illustrating the concept of FEIR-CS and strategies for achieving selective IR resonance for a vibration undergoing a frequency shift in response to two-state chemical exchange process. (a) Schematic trajectory of an individual molecule diffusing through the probe volume while undergoing chemical exchange between state A (black) and B (red). (b) Spontaneous fluctuations in the total detected signal. (c) Correlation function (red), showing the resolved decay components due to the exchange reaction and diffusion. also shown is the diffusion-only component (dashed black). (d)-(f) Strategies for achieving selective with the IR spectrum (gray) for a vibration undergoing a frequency shift between ω_A and ω_B . (d) Narrowband IR, (e) broadband interferometry, and (f) generalized pulse-shaping.

Figure 5.2 demonstrates the concept of a potential realization of FEIR-CS to study an idealized two-state chemical exchange process. At equilibrium, an individual molecule diffuses through the probe volume while undergoing chemical exchange events manifested by a stochastic sequence of jumps between the two states A and B (Figure 5.2(a)). Contrast between the states is achieved via spectrally-selective vibrational FEIR excitation with a controllable IR pulse spectrum. Both of these processes imprint spontaneous fluctuations onto the total FEIR signal (Figure 5.2(b)), and their average kinetic timescales are recovered from the decay profile of the resulting time correlation function (Figure 5.2(c)). The form of this correlation function is that discussed previously in Section 5.2.4, although in the current case B is made bright while A is suppressed by the excitation procedure. In this example, a large separation of timescale between exchange $R^{-1} = 10^{-5}$ s, and diffusion $\tau_D = 10^{-2}$, was chosen to clearly show how they appear in the correlation function. Additionally, this cartoon shows the schematic trajectory of one individual molecule, but in reality many molecules will contribute to the correlation signal over the course of the measurement.

The crucial factor for resolving the exchange process is therefore the spectroscopic contrast in FEIR excitation. Multiple options exist for modulating the IR spectrum experimentally, some of which are shown in Figure 5.2(d)-(f) in the context of a single vibrational band undergoing a frequency shift in response to the exchange process. The simplest option (Figure 5.2(d)) uses a narrowband IR pulse that can be tuned to selectively excite the band in one state only. Here the bandwidth must be matched to or broader than the vibrational linewidth so that the pulse duration is commensurate to or shorter than the population relaxation, ensuring efficient FEIR excitation. Such picosecond IR pulses ($> 10\text{-}20\text{ cm}^{-1}$) could be produced by the mid-IR OPA described in Chapter 4 by increasing the thickness of the nonlinear crystal to reduce the amplification phase-matching bandwidth.

With our current broadband IR pulses and interferometer, frequency selectivity can be achieved by fixing the inter-pulse delay τ_{IR} such that the resulting spectral fringes overlap with one or the other state (Figure 5.2(e)). This spectral interferometry approach will work best when the FEIR spectrum is dominated by a single vibration but has the advantage of easy switching between exciting either or both states. Being able to modulate how the various species are excited represents a means to control the way in which their reaction kinetics are manifested in the correlation function, providing additional insight for interpreting its decay components. More sophisticated methods that step through multiple interferometer delays to perform Fourier transform frequency-resolved CS, similar in concept to photon correlation Fourier spectroscopy,^{291,292} are also enabled with this approach. Finally, the most general strategy involves arbitrary control over the IR pulse spectrum (Figure 5.2(f)), for example by acousto-optic pulse-shaping or the use of custom filters. All of these strategies for converting vibrational frequency changes into FEIR intensity fluctuations could also be applied to true time-dependent SM experiments that resolve individual trajectories.

As photon emission is locked to the excitation pulse train, time resolution is set by the inverse of the repetition-rate, currently 1 μs for the instrument described in this thesis. Increasing the repetition-rate therefore represents an improvement in time-resolution, as well as general signal-to-noise by allowing more photons per molecule to be collected. The longest measurable kinetic timescales will be limited by the diffusion of molecules through the observation volume, 20-100 μs for dye molecules in common solvents, but extendable beyond the millisecond range for viscous environments.

The generic two-state exchange example shown here illustrates how potential FEIR-CS experiments could leverage changes in a molecule's vibrational spectrum to isolate the persistence of specific chemical structures or follow how reactants and products interconvert

on microsecond timescales. For example, local-mode vibrational probes could be used to address the impact of site-specific interactions like hydrogen-bonding or ion association on molecular transport in complex environments. Similarly, FEIR-CS experiments could track the formation and breaking of specific intermolecular contacts between reactive partners during the initial diffusive encounter and subsequent binding in diffusion-limited bimolecular reactions.

Chapter 6

Demonstrating single-molecule sensitivity with FEIR correlation spectroscopy

The material in this Chapter is adapted from:

Whaley-Mayda, L.; Guha, A.; Penwell, S. B.; Tokmakoff, A., Fluorescence-Encoded Infrared Vibrational Spectroscopy with Single-Molecule Sensitivity. *Journal of the American Chemical Society* **2021** *143* (8), 3060-3064.

6.1 Introduction

Up to this point we have discussed the theoretical principles of FEIR spectroscopy, the practical details of its experimental implementation, and some potential strategies for developing single-molecule (SM) applications starting with the techniques of correlation spectroscopy. In this chapter we show direct experimental evidence that FEIR spectroscopy can achieve SM sensitivity. This demonstration of sensitivity serves to establish the viability of FEIR

spectroscopy for SM investigation. From a technical perspective, it represents a major culmination of much of the work presented in this thesis so far, and validates the conception of the FEIR principle and its current experimental design. Establishing direct, quantitative proof of SM sensitivity—rather than, e.g. extrapolating signal levels from the bulk—is a critical aspect of this step.

Our method for demonstrating SM sensitivity is to perform proof-of-principle FEIR correlation spectroscopy (FEIR-CS) measurements, the basic theoretical background for which was introduced in Chapter 5. Specifically, we leverage the ability of these measurements to count the average number of molecules $\langle N \rangle$ contributing the signal at any given time, and show that experiments with $\langle N \rangle < 1$ are possible. While this establishes SM sensitivity, it is not true SM *detection*, i.e. the continuous observation of one individual molecule for an extended period. Nevertheless, this sensitivity milestone is an important step in developing SM FEIR experiments. For example, knowing how many molecules a signal is coming from allows us to benchmark the count rate per molecule and therefore overall excitation probability—quantities that are crucial for understanding the overall performance of the technique in relation to its theoretical sensitivity limits. We will explore these aspects further in Chapter 7.

Another purpose of these experiments is to demonstrate the technical feasibility of FEIR-CS. Although the FEIR-CS experiments show here only measure the diffusion of molecules through the probe volume and do not leverage vibrational spectra to track chemical exchange phenomena as proposed in Chapter 5, they indicate how such measurements could be carried out in practice and illustrate some of the technical requirements for making them work. Much of the material in the chapter can be found in Ref. [243].

6.2 FEIR resonance and signals from Coumarin 6

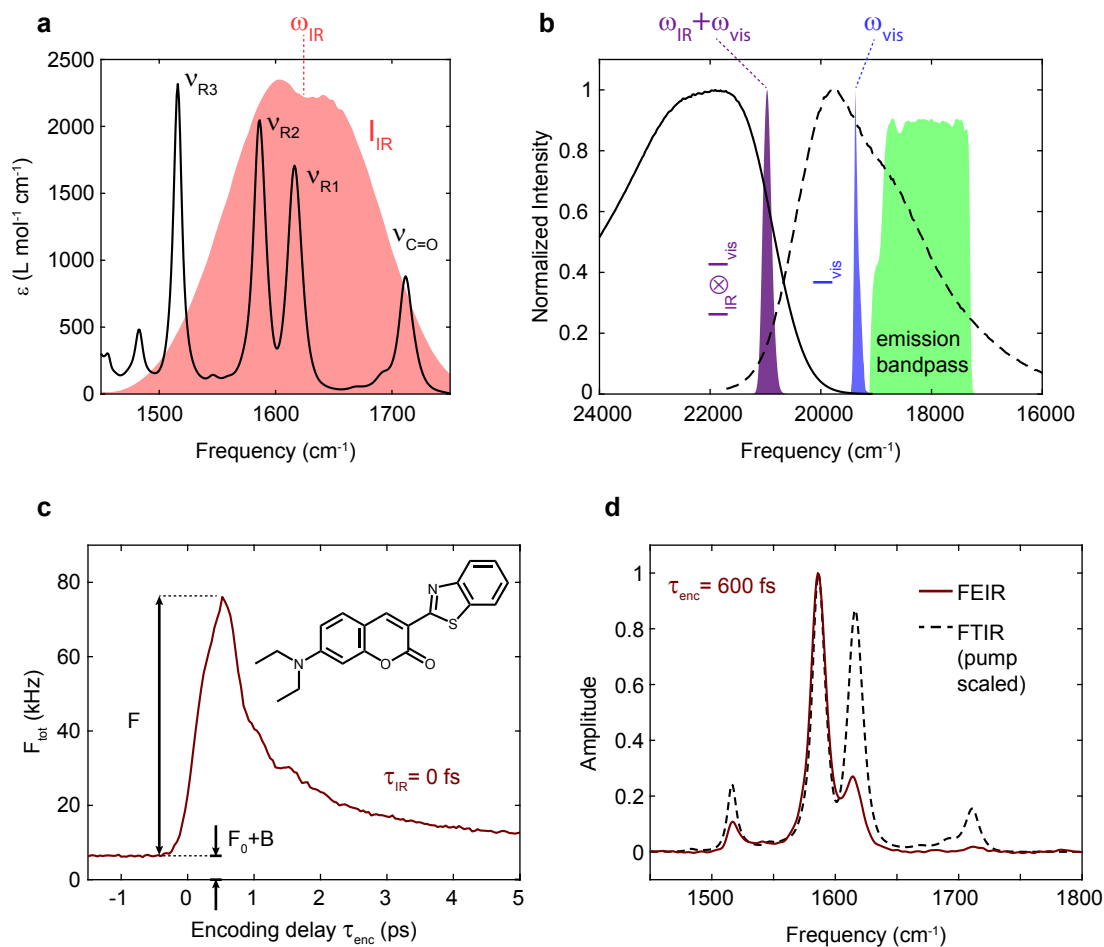


Figure 6.1: Resonance conditions and FEIR data on C6 in acetonitrile-d3. (a) FTIR spectrum of C6 in acetonitrile-d3 with IR pulse spectrum. (b) Electronic absorption (solid) and fluorescence (dashed) spectra with the visible pulse spectrum, convolution of visible and IR pulse spectra (distribution of their frequency sums), and emission bandpass. (c) Two-pulse FEIR data on a 30 μM C6 solution. Molecular structure of C6 is inset. (d) FEIR spectrum of the same sample at $\tau_{enc} = 600$ fs compared with the FTIR spectrum scaled by the IR pulse spectrum. Data acquisition times for (c) and (d) were <5 minutes

We will use coumarin 6 (C6) in acetonitrile-d3 as a model system for all FEIR experiments in this chapter. As we will see, one reason for this molecule's excellent performance as an

FEIR chromophore has to do with the resonance conditions of the experiment. Specifically, the quality of the double resonance condition plays a crucial role for achieving sensitive FEIR vibrational detection. Figure 6.1(a) shows that the tunable IR pulses have the spectral breadth to be resonant with the carbonyl ($\nu_{\text{C=O}}$) and three highest frequency C=C ring ($\nu_{\text{R1-3}}$) vibrations when centered at $\omega_{\text{IR}} = 1620 \text{ cm}^{-1}$. More detailed assignments of these vibrations will be given in Chapter 8. Figure 6.1(b) shows the electronic absorption and fluorescence spectra of C6. Maximal resonance for the encoding transition is achieved when the sum of IR and visible center frequencies ($\omega_{\text{IR}} + \omega_{\text{vis}} = 20980 \text{ cm}^{-1}$, $\lambda_{\text{sum}} = 477 \text{ nm}$) falls near the peak of the electronic absorption band. However, the visible pulse (fixed center frequency $\omega_{\text{vis}} = 19360 \text{ cm}^{-1}$, $\lambda_{\text{vis}} = 516.5 \text{ nm}$) alone directly excites the red tail of the band, creating undesirable background fluorescence. The resonance condition shown in Figure 6.1(b) is likely a nearly ideal compromise between large FEIR resonance and low one-photon background, but could be further optimized with a tunable visible pulse. The role of these resonance conditions on signal to background and overall detection sensitivity will be explored further in detail in Chapter 7.

Figure 6.1(c) shows the total fluorescence count rate from two-pulse FEIR signal measured of a $30 \mu\text{M}$ C6 solution. As discussed in Chapter 4, in practice this is done by setting $\tau_{\text{IR}} = 0$, rather than blocking the moving arm of the interferometer. The baseline apparent for $\tau_{\text{enc}} < 0$ is the sum of the aforementioned one-photon excited fluorescence F_0 and non-molecular background B , including solvent Raman scattering, impurity and optics fluorescence, and detector dark-counts. After a nearly pulse-limited rise to a maximum labeled F , the FEIR signal decays away, tracking the vibrations' population relaxation kinetics. The FEIR vibrational spectrum at $\tau_{\text{enc}} = 600 \text{ fs}$, corresponding to the signal maximum in Figure 6.1(c), is shown in Figure 6.1(d) overlaid on the FTIR linear absorption spectrum scaled by

the spectrum of the IR pulse. The FEIR spectrum is free of background due to the Fourier transform acquisition modality. Differences in relative peak amplitudes between the FEIR and conventional IR spectra are due to the contribution of vibrational-electronic coupling in the former, which controls the strength of the electronic encoding transition. Specifically, the factor of ~ 5 difference in FEIR intensity between the similarly IR-intense ν_{R2} and ν_{R1} modes at 1586 and 1616 cm^{-1} as well as the nearly absent $\nu_{C=O}$ band at 1712 cm^{-1} are well described by these vibrations' respective Huang-Rhys factors.^{74,293}

More details about the appearance of these FEIR signals with interpretation aided by simulations, including the full τ_{enc} -dependence of the spectrum, will be presented in Chapter 8. For the moment, we note that the peaking of the two-pulse signal at $\tau_{\text{enc}} = 600$ fs, notably beyond the pulse-overlap region, as well as the absorptive spectral lineshapes that match reasonably well with those of the FTIR, are influenced by a coincidental alignment of inter-mode vibrational coherence pathways—a rather fortuitous property which further adds to the ‘goodness’ of C6 as a model chromophore in these experiments.

6.3 Time-gated detection for background reduction in the small-signal regime

The ultimate detection sensitivity of an FEIR measurement hinges upon the ability to resolve the FEIR signal F against the background $F_0 + B$, quantified by the modulation ratio $M = F/(F_0 + B)$. Maximizing M therefore requires simultaneously optimizing the brightness of molecular fluorescence $F + F_0$ against B , as well as F against F_0 —a non-trivial problem strongly influenced by the double resonance condition mentioned above and subject to further analysis in Chapter 4.

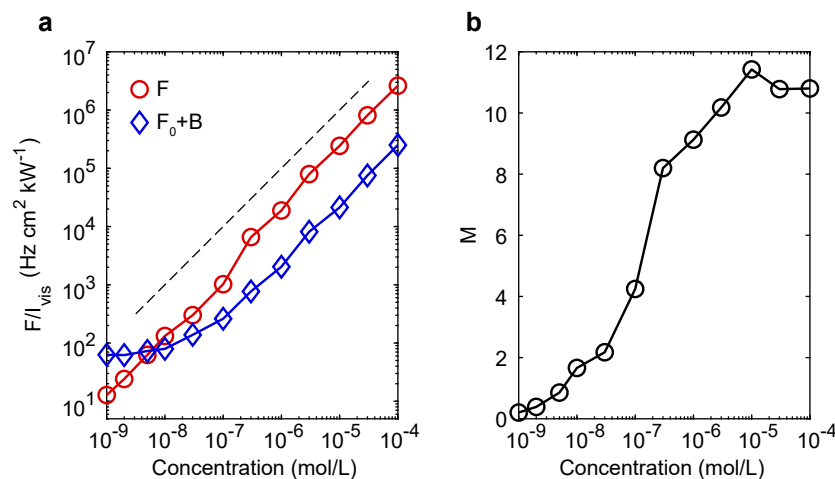


Figure 6.2: Concentration dependence of FEIR signal and background for C6. (a) C6 concentration dependence of F/I_{vis} (red circles) and $(F_0 + B)/I_{\text{vis}}$ (blue diamonds). Dashed line shows a linear dependence for reference. (b) Modulation ratios M corresponding to panel (a).

Figure 6.2a shows the concentration dependence of the maximum F signal and background level $F_0 + B$ for C6, scaled by the visible excitation intensity I_{vis} . While the FEIR signal is roughly linear in concentration across the entire range, the background levels off to a concentration-independent value in the nM regime. This constant level represents I_{vis} -dependent contributions to B , e.g. solvent Raman scattering or fluorescence from impurities and optics. Correspondingly, M (Figure 6.2b) falls by nearly two orders of magnitude from its B -free value of ~ 11 in the μM range.

One method to increase the modulation ratio in the low concentration regime where FEIR photons are scarce is to use time-gated detection to preferentially suppress contributions to B that arrive at the detector in time-windows distinct from the desired fluorescence signal. Specifically, using time-correlated single-photon counting (TCSPC) as introduced previously in Chapter 4, prompt scattering background can be suppressed by time-gating data acquisition for photon arrivals between 1-15 ns after the encoding pulse. Figure 6.3(a) shows TCSPC

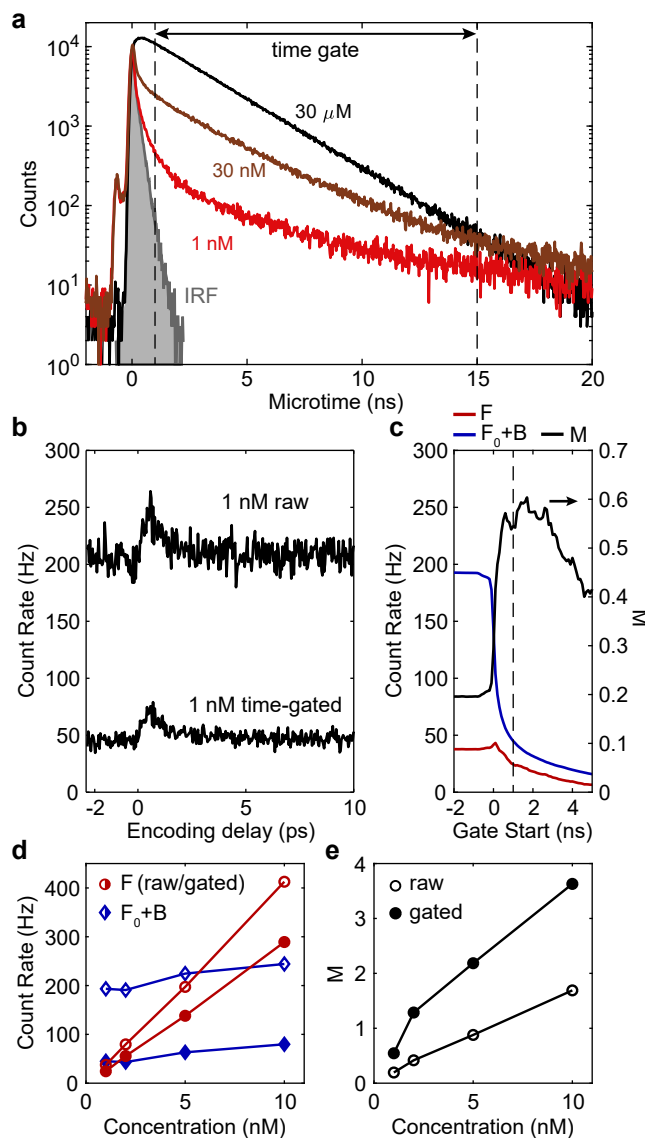


Figure 6.3: Time-gated fluorescence detection for background reduction. (a) TCSPC histograms from two-pulse FEIR measurements on C6 at 30 μM (black), 30 nM (brown), and 1 nM (red) with the IRF (gray). The time-gate (1 ns to 15 ns) used in panels (b), (d), and (e) is indicated by dashed black lines. (b) Comparison of raw and time-gated two-pulse FEIR measurements at 1 nM. (c) F (red) and $F_0 + B$ (blue) count rates (left y-axis), and M (black, right y-axis) from the data in panel (b) as a function of the starting edge of the time gate with the ending edge fixed at 15 ns. The optimal starting edge at 1 ns is indicated by a dashed black line. (d) F (red circles) and $F_0 + B$ (blue diamonds) count rates as a function of C6 concentration. Filled symbols are time-gated, open symbols are raw. (e) Modulation ratios corresponding to the count levels in panel (d). The visible pulse energy used for (b)-(e) and the 1 nM data in (a) was 12 pJ.

histograms of every photon's microtime from two-pulse FEIR measurements on C6 solutions at 30 μM , 30 nM, and 1 nM, along with the TCSPC instrument response function (IRF). At the highest concentration the emission kinetics show a clean single-exponential decay with a ~ 2.5 ns lifetime, indicating that the majority of detected photons are C6 fluorescence. At 30 nM a prompt component, most likely due to Raman scattering from the solvent, that conforms to the shape of the IRF appears, and by 1 nM dominates the distribution.

Due to the separation of timescales between the IRF duration and fluorescence lifetime, a substantial portion of this scattering component can be eliminated by only accepting photons within the time gate indicated by dashed lines in Figure 6.3(a). As shown in Figure 6.3(b), the resulting time-gated 1 nM FEIR transient has a 4-fold reduction in background and subsequently contends with less shot noise than the raw, un-gated data—at the expense of a 30% loss in FEIR signal counts. The dependence of the FEIR signal F , background $F_0 + B$, and modulation ratio $M = F/(F_0 + B)$ on the starting edge of the time gate (Figure 6.3(c)) demonstrates this tradeoff between improving signal to background and losing signal, with what we believe to be a roughly optimal compromise at a 1 ns gate starting edge indicated, improving M from 0.2 to 0.6. Figures 6.3(d) and 6.3(e) demonstrate the background-reducing effect of this time-gate on the 1-10 nM range of the C6 concentration dependence (un-gated data same as Figure 6.2). We note that time-gating offers minimal improvement for FEIR spectra, as the Fourier transform filters the background out with the DC component while its associated noise is distributed across the entire frequency axis, diluting its contribution within the IR pulse bandwidth. As we will discuss below, this background reduction procedure by time-gating also plays a critical role in FEIR-CS measurements.

6.4 SM determination by FEIR-CS

6.4.1 FEIR-CS data acquisition and processing

Before proceeding with our presentation and analysis of the FEIR-CS experiments, here we describe some of the technical details regarding the photon correlation and data processing that are involved. Raw photon time-series for FEIR-CS measurements are saved as time-tagged time-resolved (TTTR) records listing the macro- and micro-times for each detected photon. The correlation function is computed in post-processing with an algorithm described by Enderlein and coworkers,²⁹⁴ and implemented in MATLAB. This correlation algorithm is optimized for sparse photon data, and operates on the intermittency periods between successive detection events. It incorporates a so-called multi-tau binning scheme so that the lag-time axis of the correlation function has quasi-logarithmic spacing.

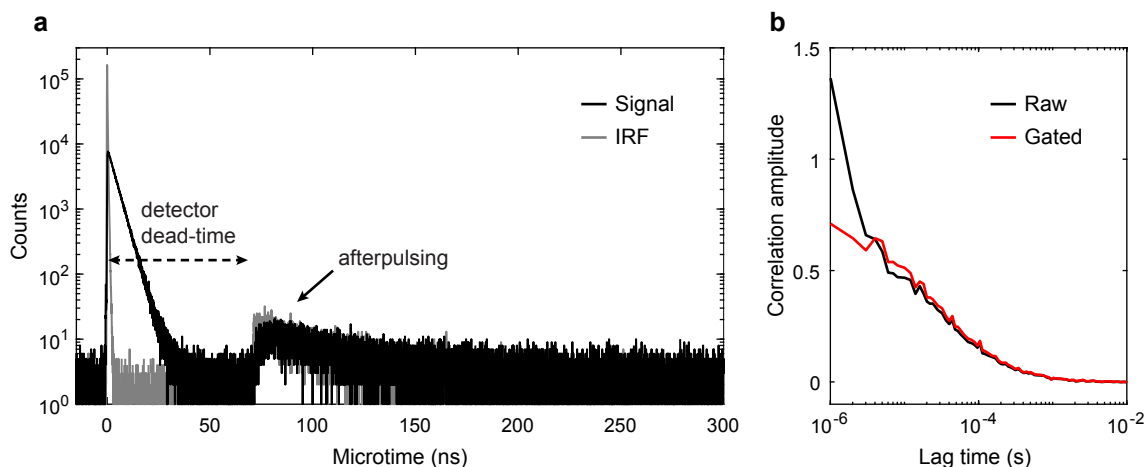


Figure 6.4: SPAD afterpulsing distribution and removal in photon correlation. (a) TCSPC histograms of R6G fluorescence and the IRF. The full microtime axis has a range of roughly 819 ns, corresponding to the TimeHarp’s 2^{15} bins of 25 ps width. (b) FCS correlation functions of the raw time series (all photons, black), and with only accepting photons with microtime < 30 ns (excluding afterpulses, red).

Time-series are recorded in 3 minute sections, and the resulting correlation functions are averaged together. Each FEIR-CS correlation function is the result of a 60 minute total acquisition time (i.e. 20 3-minute sections). Prior to autocorrelation, the time-series are time-gated by microtime, which serves the purpose of both removing the artifact caused by detector afterpulsing in a addition to reducing scattering background as discussed above. The manner in which the background affects the correlation measurement and how it is mitigated is discussed in Section 6.4.2.

Removal of detector afterpulsing

The removal of the photon correlation afterpulsing artifact is demonstrated in Figure 6.4 for a conventional FCS measurement from a 1 nM rhodamine 6G (R6G) solution in acetonitrile-d₃ as an example. The electronic transition in R6G is directly resonant with the visible encoding pulse, and the IR beam is not present. Figure 6.4(a) shows TCSPC histograms of the fluorescence signal with the IRF for reference. Afterpulses, caused by residual charge-carriers trapped after the primary photo-electron detection event, can be seen as the low-amplitude resurgence of counts after the hardware-fixed 75 ns dead-time. While rare ($< 0.2\%$ probability²⁹⁵), their high time-correlation with true photon counts leads to a prominent spike at the earliest few time points in the correlation function (Figure 6.4(b)). If the afterpulsing temporal distribution function is well characterized, this artifact may be suppressed with various filtering algorithms.²⁹⁶ However, in our case the repetition-rate (1 MHz) is low enough that the afterpulse distribution fully decays before the next excitation pulse arrives, and therefore afterpulses can be explicitly excluded by only accepting photons for correlation that have microtimes shorter than the 75 ns dead-time. As shown in Figure 6.4(b), gating photons in this way removes the afterpulsing spike, providing clean data all the way to the

1 μs time-resolution limit (inverse of the repetition-rate). We note that in this conventional FCS experiment on R6G, there is no prompt scatter background component because the visible power is much lower owing to the direct one-photon excitation resonance.

6.4.2 FEIR-CS experiments on nanomolar C6 solutions

As a demonstration of SM sensitivity, we perform FEIR-CS measurements to effectively count the average number of molecules that contribute at a given time. As introduced in Chapter 5, we measure the correlation function

$$G(t) = \langle \delta F_{\text{tot}}(0) \delta F_{\text{tot}}(t) \rangle / \langle F_{\text{tot}} \rangle^2, \quad (6.1)$$

where $F_{\text{tot}}(t)$ is the total real-time photon stream from an FEIR measurement with optical delays fixed at the maximum signal level ($\tau_{\text{enc}} = 0$ fs, $\tau_{\text{enc}} = 600$ fs). Like a conventional FCS experiment, diffusion of molecules through the probe volume produces spontaneous fluctuations in $F_{\text{tot}}(t)$, causing $G(t)$ to decay with the characteristic timescale of these transits with early-time amplitude given by the inverse of the average molecule number $G(0) = \langle N \rangle^{-1}$. In this case the coumarin vibrational resonances are uniformly covered by the IR spectrum and should not be affected by any chemical exchange processes. Therefore both the FEIR and one-photon background component, F and F_0 , contribute in the same way to the bursts of fluorescence that produce $G(t)$. However, as the intrinsic B -free modulation ratio is ~ 11 , most of this correlated signal is composed of FEIR photons.

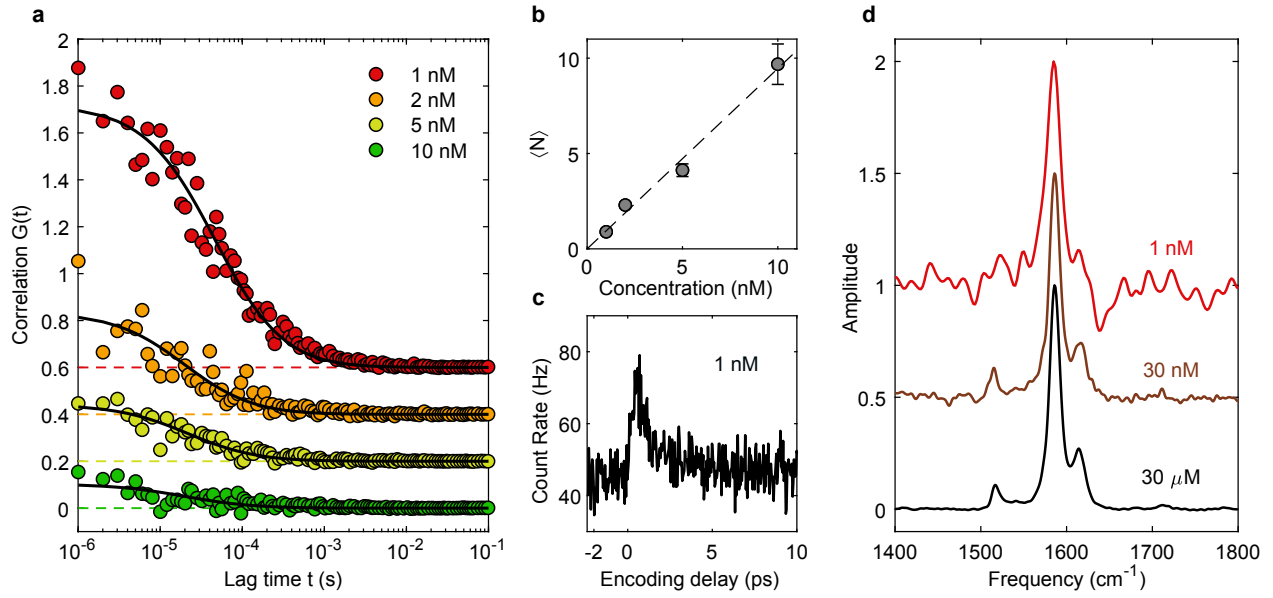


Figure 6.5: FEIR and FEIR-CS experiments at SM equivalent concentrations. (a) FEIR correlation functions from C6 solutions at 1, 2, 5, and 10 nM (offset for clarity with zero-levels indicated by dashed lines). Fits are shown by black lines. (b) $G(0) = \langle N \rangle^{-1}$ from the fits in (a) as a function of concentration, with the linear trend shown by a dashed line. (c) two-pulse FEIR transient from the 1 nM solution. (d) FEIR spectra at 1 nM, 30 nM, and 30 μM (offset for clarity). The visible pulse energy was 25 pJ for (a), (b), and the 1 nM spectrum in (d), and 12 pJ in (c). Acquisition times were 60 minutes in (a), and 30 minutes for (c) and 1 and 30 nM data in (d).

Figure 6.5(a) shows FEIR correlation functions from C6 solutions at 1, 2, 5, and 10 nM along with fits to the single-component diffusion model discussed in Chapter 5

$$G(t) = \frac{1}{\langle N \rangle} \left(1 + \frac{t}{\tau_D} \right)^{-1} \left(1 + \frac{t}{\kappa^2 \tau_D} \right)^{-1/2} \quad (6.2)$$

with $\tau_D = w_{xy}^2 / (4D)$, $\kappa = w_z / w_{xy}$, and $\langle N \rangle = C\pi^{3/2}w_{xy}^2w_z$. The average molecule number $\langle N \rangle$ and diffusion timescale τ_D are fit parameters, and the probe volume aspect ratio κ , which is rather insensitive parameter in determining the shape of the fit function, is fixed at 4—the

value estimated from the visible focal volume characterization in Chapter 4. Estimates for the individual probe volume dimensions w_{xy} and w_z can be made based on that characterization, but are not required for the determination of $\langle N \rangle$. Specifically, along the lines of the discussion in Chapter 5, we take $\langle N \rangle$ to be defined by the inverse correlation amplitude (i.e. the average occupation number consistent with the Poisson fluctuation statistics) via Eq. 6.2.

Critically, the presence of uncorrelated background can confound the measurement of $\langle N \rangle$ by the correlation amplitude. This is because uncorrelated background contributes to the denominator but not the numerator of $G(t)$ in Eq. 6.1, thereby lowering its amplitude and artificially inflating the measured value of $\langle N \rangle$.^{282,297} Reducing the background from scattering by the time-gating method described above is therefore crucial for our FEIR-CS measurements. In general, time-gating or more sophisticated filtering methods using TCSPC can be applied to FCS measurements to improve accuracy or discriminate species by lifetime.^{298,299} Here, we use the time-gating procedure introduced above in Section 6.3 to reduce the effect of this background on the correlation amplitude. Figure 6.6(a) shows the effect of varying the starting edge of the time gate on the 1 nM FEIR-CS correlation function. The starting edges relative to the TCSPC histogram are depicted in Figure 6.6(b) with the same color-coding. The ending edge of the gate is fixed at 15 ns. As shown in Figure 6.6(c), the early-time correlation amplitude $G(0)$ extracted from the fit increases dramatically as the starting edge is scanned over the prompt scattering component, and appears to reach a saturating value of 1.54 for edges > 2 ns. While other background sources with emission kinetics on the fluorescence timescale are likely still present, we take this value, corresponding to $\langle N \rangle = 0.65$ as our estimate of the average molecule number. As evident in Figure 6.6(a), the signal to noise degrades rapidly for increasingly aggressive time-gates as useful FEIR

signal is thrown away, and we choose the 1 - 15 ns gate (cyan curve) as a compromise (used for all correlation functions in main text Figure 6.5(a)).

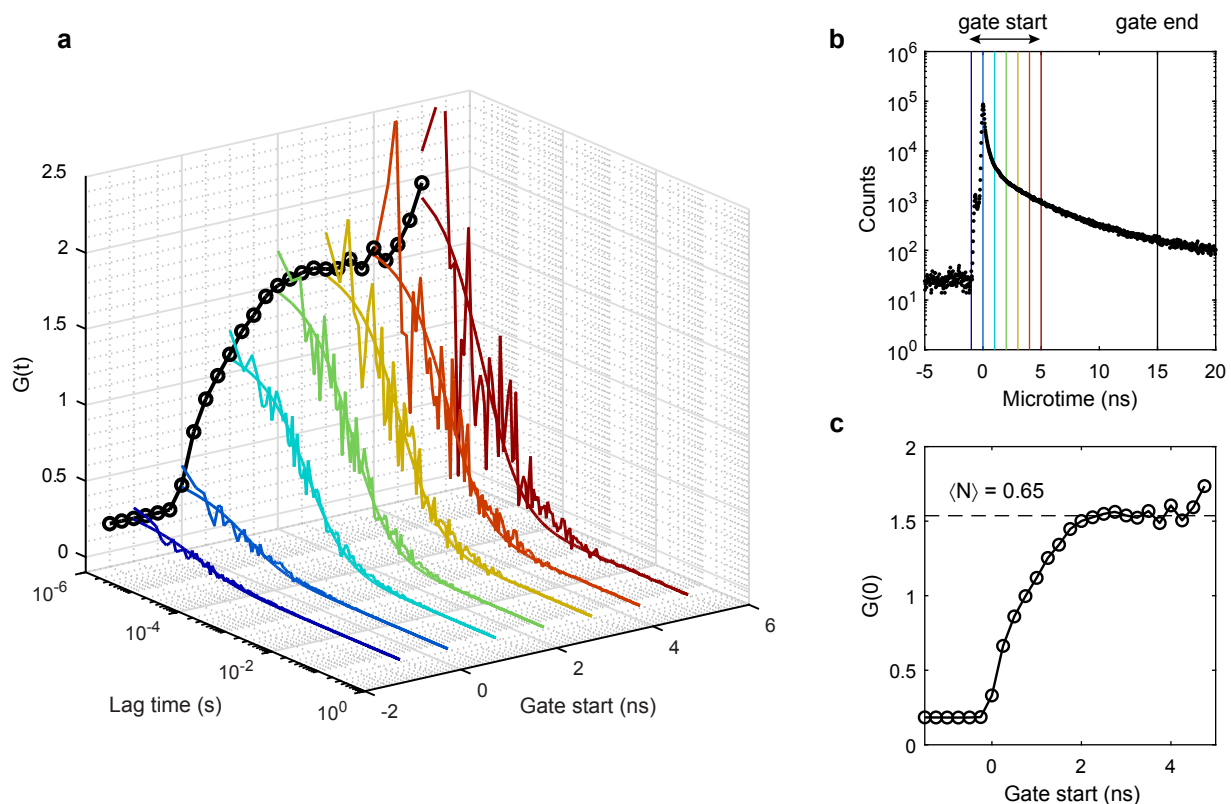


Figure 6.6: Dependence of the FEIR-CS amplitude on time-gating to remove scattering background. (a) FEIR-CS correlation functions from the 1 nM C6 solution as a function of the time gates displayed in (b). The early-time amplitude $G(0)$ is shown by black circles. (b) Time gates (color-coding matching to (a)) overlaid on the TCSPC histogram. (c) Early-time amplitude $G(0)$ as a function of the starting edge. The saturating value $G(0) = 1.54$ is indicated by a dashed line.

As demonstrated in Figure 6.5(b), $\langle N \rangle$ extracted from the fits depends linearly on concentration, which further supports the assessment of $\langle N \rangle < 1$ at 1 nM. The error bars on $\langle N \rangle$ in Figure 6.5(b) correspond to 95% confidence intervals from the fit routine. Figures 6.5(c) and (d) show the FEIR decay transient and spectrum recorded from the 1 nM solution,

demonstrating that the vibrational relaxation and frequency of the brightest ring mode ν_{R2} can still be reliably measured at this level.

The fit to the 1 nM FEIR-CS correlation function produces a diffusion time constant $\tau_D = 47 \pm 5 \mu\text{s}$, which is longer than that for the conventional FCS measurement on R6G in Figure 6.4b ($\tau_D = 32 \pm 2 \mu\text{s}$). Besides differences in molecular diffusion constant, the higher visible power used for the FEIR-CS measurement (26 pJ vs. 1.5 pJ) could result in a slightly larger effective probe volume if saturation effects are at play.³⁰⁰ In Chapter 7, we show how that the encoding transition indeed exhibits saturation behavior with an onset near the intensities used here.

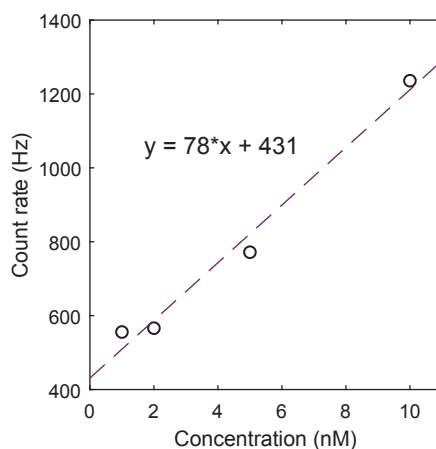


Figure 6.7: Concentration dependence of the total photon count rate for the time series underlying the FEIR-CS correlation functions (time gated to remove afterpulsing but not scattering). Linear trend shown by dashed line with equation.

In these experiments, the F count rate per molecule (un-gated) is determined to be 110 Hz by considering the concentration dependence of the total photon count rate from the time series used for the FEIR-CS measurements, shown in Figure 6.7. The offset of the linear trend measures the non-molecular background B , while the slope of 78 Hz/nM, combined with the determination that $\langle N \rangle = 0.65$ at 1 nM, leads to 120 Hz per molecule ($F + F_0$). Taking

into account the B -free modulation ratio of ~ 11 implies $F = 110$ Hz. This number is also consistent with the 40 Hz F_1 level seen in Figures 6.3(b) and (c) considering that the visible excitation intensity used there is half that for the FEIR-CS measurements (12 pJ vs. 26 pJ). To determine the overall excitation probability, the count rate per molecule is divided by the fluorescence quantum yield, instrument collection efficiency, and 1 MHz pulse-repetition rate. The instrument collection efficiency can be estimated at $\sim 1\%$, and is discussed more thoroughly in Chapter 7. Assuming a fluorescence quantum yield of 0.63 reported by Jones *et al.*,³⁰¹ this count rate per molecule corresponds to a 2% overall excitation efficiency per pulse sequence. Our recent measurement of this quantum yield is substantially higher at 0.89. Chapter 7 discusses more recent FEIR-CS measurements of this system using a sample configuration employing CaF_2 coverslips which yield significantly larger signal levels. In these updated measurements, the largest average SM count rates are 480 Hz, corresponding to a $\sim 4\%$ overall excitation probability per pulse sequence.

6.5 Discussion and Outlook

We note that the FEIR experiments shown here are fundamentally ensemble measurements, even if $\langle N \rangle < 1$. To clarify this point we highlight the distinction, commonly invoked in the context of FCS within SM fluorescence,³⁰² between SM detection—exclusively observing a particular individual for an extended period—and SM sensitivity—the ability to measure signals and resolve changes caused by individuals. Our proof-of-principle demonstration of FEIR correlation spectroscopy (FEIR-CS) establishes SM sensitivity in that it requires the observation of correlated bursts of FEIR photons from individual molecules. Furthermore, our determination that ensemble FEIR vibrational spectra and relaxation transients can be

measured ‘one molecule at a time’ is an encouraging sensitivity milestone along the path toward realizing true SM observation.

Many opportunities to optimize this technique are available, including tunable visible excitation, increasing collection efficiency, and—crucially—higher repetition-rates, and we note that the pros and cons established by comparison to the related stimulated Raman excited fluorescence spectroscopy developed by Min and co-workers—featuring tunable, frequency-domain stimulated Raman excitation—will offer important insight.^{37,38,303}

As an intermediate step toward SM spectroscopy, FEIR-CS has potential as a powerful vibrational probe of chemical processes in solution, just as FCS often plays an auxiliary role to SM fluorescence experiments. While vibrational analogues of FCS using Raman scattering have been implemented previously, to our knowledge FEIR-CS is the first to be sensitive enough for use with single molecules.^{304–306} Along the lines of the proposals in Chapter 5, changes in vibrational frequencies due to chemical interconversion or specific molecular interactions in an equilibrium state could be sensed as FEIR signal fluctuations and monitored via the correlation function.

In conclusion, we have demonstrated that FEIR vibrational spectroscopy can be performed with SM sensitivity. Careful optimization of the resonance condition is crucial for achieving sufficient signal brightness, while time-resolved photon detection can significantly reduce background levels. We demonstrated proof-of-concept FEIR-CS, which has the potential for development as a vibrational analogue of FCS for studying kinetics of chemical systems in solution with enhanced structural sensitivity. With improvements to the methods reported here, we believe true SM vibrational detection using FEIR spectroscopy is within reach.

Chapter 7

Influence of resonance conditions on detection quality and single-molecule sensitivity

The material in this Chapter is adapted from:

Whaley-Mayda, L.; Guha, A.; Tokmakoff, A., Resonance Conditions, Detection Quality, and Single-Molecule Sensitivity in Fluorescence-Encoded Infrared Vibrational Spectroscopy. *Journal of Chemical Physics* **2022** *156*, 174202.

7.1 Introduction

While our initial demonstration of SM sensitivity is encouraging, developing FEIR spectroscopy as a generally useful method will require a more thorough understanding of the optical and molecular factors involved in SM FEIR detection. Specifically, what makes a molecule a good FEIR chromophore, and given such a molecule, how is FEIR detection optimized? This first question can be initially addressed by considering the minimum requirements of a good, i.e. SM capable, FEIR chromophore from a heuristic standpoint: high

fluorescence brightness, strong IR activity of the target vibration(s), and strong vibronic coupling of this target vibration to the electronic transition, e.g. Franck-Condon activity. Next, the double-resonance condition must be met: the IR frequency ω_{IR} is tuned to cover the vibrational transition while the visible frequency ω_{vis} should “make up the difference” to bring the molecule to the electronic excited state, i.e.

$$\omega_{\text{IR}} + \omega_{\text{vis}} = \omega_{eg}, \quad (7.1)$$

where ω_{eg} is the electronic transition frequency. Practically speaking, this relation suggests that the visible pulse should be pre-resonant with the electronic absorption band by an amount commensurate with the target vibrational frequency. However, given the typically broad electronic lineshape in room-temperature solution with its interplay of intramolecular vibrational and solvation contributions, it is not *a priori* clear where this optimal resonance is located, or even to what extent the equilibrium absorption lineshape is a useful or predictive guide. Furthermore, direct excitation by the visible pulse produces an undesirable fluorescence background that degrades detection contrast and therefore must also be considered in the optimization of the resonance condition.

Motivated by these questions, in this chapter we investigate the practical experimental factors that govern FEIR signal strength and detection quality with the objective of elucidating the requirements for achieving SM sensitivity. We introduce an experimental FEIR brightness metric that accounts for instrumental parameters to isolate the intrinsic molecular factors that control signal size, and thereby facilitates comparison between different chromophores. We will focus on the particular role of the resonance condition in optimizing FEIR brightness and signal to noise. Perhaps the most direct experiment to capture the effect of electronic resonance would be to excite a single vibration at fixed ω_{IR} while tuning

ω_{vis} . However, our current instrument is limited to a fixed ω_{vis} , so here we adopt the strategy of performing measurements across a series of dyes whose electronic spectra span a range of different frequencies. Motivated by our demonstration of SM sensitivity for coumarin 6 (C6) in acetonitrile-d₃ described in Chapter 6, we use a set of structurally-similar coumarin dyes in the same solvent in order to keep the vibrational and vibronic aspects of the chromophores as similar as possible. Clearly these vibration-specific factors are crucial for sensitive FEIR detection, and we will address mode-specific considerations including normal mode character and molecular symmetry with the aid of more detailed theory and electronic structure calculations in future work.

Questions of signal strength, detection sensitivity, and ‘goodness’ of chromophore are also fundamentally coupled to the spectroscopic information content of an experiment. As a nonlinear ultrafast technique, FEIR spectroscopy can access information beyond linear vibrational spectra, including relaxation dynamics, relative orientation of the vibrational and electronic transition dipoles, and inter-mode coherence and dephasing. These phenomena are addressed to various extent in Chapters 2, 8, 9, and 10. However, our analysis here is concerned with experimental photon count rates and signal to noise at a practical level. We find that the electronic absorption spectrum can predict the dependence of FEIR brightness on the resonance condition to a reasonable degree across the full frequency range considered. For bulk measurements, signal to noise is limited by background fluorescence from direct visible excitation, and therefore detuning from resonance to decrease the overlap of ω_{vis} with the tail of the electronic band is often desirable. However, at SM equivalent concentrations background is mostly of non-molecular origin and maximal resonance should be employed. We observe saturation of the vibronic encoding transition by the visible pulse, which ultimately limits the upper range of molecular emission rates that can be achieved.

7.2 Experimental Methods

7.2.1 Steady-state spectroscopic characterization of coumarin FEIR dyes

Ten commercially available 7-aminocoumarin dyes were obtained from Sigma (C30 and C153), TCI America (C314, C337, C334, and C7), Acros Organics (C343 and C6), and Exciton-Luxottica (C525 and C545), and used as received. For each Coumarin dye, Fourier transform IR (FTIR) absorption measurements were performed in 1-5 mM acetonitrile-d₃ solution at 100-500 μm pathlength using a Bruker Tensor 27 FTIR spectrometer at 2 cm^{-1} resolution. Each FTIR spectrum was solvent-subtracted and converted to molar extinction units by dividing the measured absorbance by concentration and pathlength.

UV/Vis absorption was performed with an Agilent Technologies Cary 5000 spectrophotometer using a 4 nm excitation bandwidth with 0.5 nm steps. Dye solutions in acetonitrile at 40 μM were measured in a 1 cm pathlength quartz cuvette, resulting in maximum absorbances < 2 , which was determined to be within the linear range of the spectrometer. Each spectrum was corrected by an independently measured solvent blank and converted to molar extinction units. An exponential fit to the low-frequency absorption wing was used to extract the extinction value at ω_{vis} for all coumarins but C545 (Figure 7.A.1 in Appendix 7.A).

Fluorescence spectra were measured with a Horiba Fluorolog-3 fluorimeter using right-angle collection from 1 cm pathlength quartz cuvettes. The concentration was adjusted (typically $< 2 \mu\text{M}$) to keep the maximum absorbance below 0.1 to avoid inner filter artifacts. Excitation-emission surfaces were measured with 3 nm slit widths for both excitation and emission monochromators. The excitation spectra acquired by integrating over the

emission axis were found to match the lineshape of the UV/Vis absorption, and fluorescence emission spectra were acquired by integrating over the excitation axis. Fluorescence quantum yields were measured relative to coumarin 153 in ethanol ($\phi = 0.53$) as a standard using the procedure outlined in Ref.[307], and we estimate uncertainties of $\sim 10\%$ for these values. All solutions were air-saturated.

7.2.2 FEIR measurements

FEIR measurements were performed with the experimental apparatus described in Chapter 4. Briefly, 230 fs IR pulses (center-frequency $\omega_{\text{IR}} = 1620 \text{ cm}^{-1}$, 120 cm^{-1} fwhm bandwidth) were generated with a home-built OPA pumped by a 1 MHz repetition-rate Yb fiber laser (Coherent Monaco).¹⁹⁰ These pulses were sent through a Mach-Zehnder interferometer to create a collinear pulse-pair with controllable delay τ_{IR} , then focused into the sample from below using a ZnSe aspheric lens of numerical aperture (NA) ~ 0.7 . The visible encoding pulse (~ 330 fs, center-frequency $\omega_{\text{vis}} = 19360 \text{ cm}^{-1}$ ($= 516.5 \text{ nm}$), fwhm bandwidth $< 80 \text{ cm}^{-1}$ ($< 2 \text{ nm}$)) was generated by frequency doubling the fiber laser fundamental, delayed with respect to the stationary pulse of the IR pulse-pair by τ_{enc} , and focused into the sample from above, collinear to the IR, with a 0.8 NA air objective. The IR and visible pulses were linearly polarized with parallel orientation in the sample. Fluorescence was collected with the same objective, separated geometrically from the visible excitation beam by a long-pass dichroic, sent through both a ω_{vis} -band rejection and selective fluorescence bandpass filter, and imaged onto a single-photon counting avalanche photodiode (SPAD) using its $50 \mu\text{m}$ diameter active area as a confocal aperture to remove out of focus light. Considering the NA and magnification ($57\times$), the radius of this aperture corresponds to 4.2 optical units at ω_{vis} , or equivalently ~ 1.1 times the Airy disk radius. While slightly larger than the optimal size

for maximum signal to noise in confocal microscopy (2.4-3.3 optical units), this aperture is close to that for producing optimal signal to noise in fluorescence correlation spectroscopy (~ 4.5 optical units).^{282,308,309}

Sample solutions (30-100 μM in acetonitrile- d_3) were held between a 1 mm thick CaF_2 window (bottom, IR side) and either a 175 μm -thick glass or 150 μm -thick CaF_2 coverslip (top, visible side), separated by a 50 μm PTFE spacer, and positioned so that the visible confocal volume was ~ 20 μm below the coverslip. As discussed in Chapter 4, detrimental thermal effects due to IR absorption by the conventional glass coverslips limited the upper range of IR power that could be used and reduced signal levels.²⁴² However, switching to the CaF_2 coverslips effectively removed these artifacts, yielding FEIR signals ~ 3 times larger. In this work, both types of coverslips were used (glass for the data in Section 7.4.3, CaF_2 in Section 7.4.4), however quantitative comparisons are only made among measurements using the same type.

The IR pulse energy at the sample during total constructive interference between the pulse-pair ($\tau_{\text{IR}} = 0$) was kept constant at ~ 50 nJ, although variations of $\pm 5\%$ occurred between measurements. Considering the pulse duration and $1/e^2$ focal radius of ~ 9 μm , the corresponding peak intensity is ~ 160 GW/cm^2 , with a pulse-train average intensity of ~ 40 kW/cm^2 . The visible pulse energy was varied between 10 fJ – 100 pJ depending on the concentration and resonance condition for each sample, which considering pulse duration and 0.34 μm $1/e^2$ focal radius corresponds to peak intensities of 0.015-150 GW/cm^2 , or average intensities of 0.005-50 kW/cm^2 . In each case the visible pulse energy was chosen to keep the total fluorescence count rate from exceeding 200 kHz (20% of repetition rate) to prevent pile-up distortions—caused by the arrival of multiple photons at the detector per excitation cycle, only the first of which can be registered—from being too severe ($< 10\%$ error). As

described in Chapter 4, the raw count rates were then corrected for pile-up using the relation $x_{\text{corrected}} = -r \ln(1 - x_{\text{raw}}/r)$ where $r = 994.7$ kHz is the exact repetition-rate.

7.3 Theoretical principles of signal and background size

The total photon count rate F_{tot} (Hz) detected in an FEIR measurement consists of the following components

$$F_{\text{tot}}(\tau_{\text{IR}}, \tau_{\text{enc}}) = F(\tau_{\text{IR}}, \tau_{\text{enc}}) + F_0 + B. \quad (7.2)$$

Here F is the desired FEIR signal which depends on the pulse delays, F_0 is a constant background fluorescence due to direct excitation of the target molecule by the visible pulse alone, and B encapsulates all other sources of background not arising from the target molecule, e.g. solvent Raman scattering, emission from impurities and optics, and detector dark counts. For the sake of this analysis we will consider the IR pulse-pair delay fixed at $\tau_{\text{IR}} = 0$, i.e. two-pulse experiments (one IR and one visible pulse). In previous publications we have referred to such experiments as 1-pulse,²⁴² or 1-IR-pulse measurements,²⁴³ however here we modify our terminology to reflect the total number of pulses, in keeping with the naming convention used consistently throughout this thesis. The two-pulse amplitude $F(\tau_{\text{enc}})$ reflects the integrated response of all vibrations within the bandwidth of the IR pulse spectrum. The fractional contribution to the count rate from a distinct vibrational resonance can in principle then be calculated using the FEIR spectrum measured at that encoding delay, although we will not explore this strategy here. We will consider early, positive τ_{enc} where F is near its maximum, and suppress the time argument for brevity. In general, successful FEIR detection requires the ability to distinguish the signal F against the background $F_0 + B$, and

therefore a practical figure of merit is the modulation ratio

$$M = \frac{F}{F_0 + B}, \quad (7.3)$$

i.e. the ratio of useful FEIR photons to all other detected photons. The presence of F_0 —a fluorescence signal from the target molecule, yet contributing to the background—is an important aspect of the practical optimization of FEIR detection. As a signal to background ratio, M is a readily apparent feature of the raw data, and consequently a convenient target for optimization. However, the more fundamental descriptor of detection quality is the signal to noise ratio

$$\text{SNR} = \frac{FT}{\sqrt{F_{\text{tot}}T}} = \frac{F}{\sqrt{F + F_0 + B}}\sqrt{T} \quad (7.4)$$

defined here for the shot noise limit as the ratio of the number of FEIR photons accumulated during the integration time T relative to the Poisson noise of the total number of detected photons. Therefore, both the contrast M and the absolute magnitude of the signal F need to be considered to maximize the SNR.

7.3.1 FEIR Brightness

Since the absolute size of an FEIR signal is ultimately governed by the molecular emission rate, we seek to relate experimental count rates to the overall probability of excitation, emission, and detection per molecule. Furthermore, accounting for the instrument-specific factors that influence these probabilities should in principle isolate purely molecular metrics that describe the propensity of a given vibration to be detected via FEIR. In conventional fluorescence spectroscopy, such a metric is the fluorescence brightness, which characterizes a fluorophore's ability to emit a photon in response to optical excitation. From an external

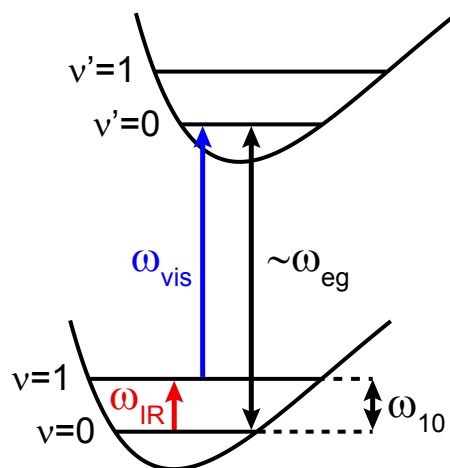


Figure 7.1: Energy-level diagram for FEIR excitation of a single vibration coupled to the electronic transition.

spectroscopic standpoint, brightness can be defined as the product of absorption cross-section (at the excitation frequency) and fluorescence quantum yield ($\sigma_{\text{el}} \times \phi$).^{307,310,311} Alternatively, fluorescence brightness has also been defined directly from experimental SM count rates, which can be related to $\sigma_{\text{el}} \times \phi$ with knowledge of the excitation beam photon flux and overall detection efficiency.³¹² This concordance of definitions is made possible by the linear nature of the fluorescence excitation process, which facilitates a straightforward separation of molecular and optical factors.

In contrast, FEIR excitation is a nonlinear process consisting of IR excitation of the vibrational $\nu = 1$ population followed sequentially by a vibronic transition to the excited electronic state (Figure 7.1). To a first approximation, these two steps may each be considered as the resonant absorption of one photon (IR, then visible), producing a linear dependence separately in the intensity of the IR and visible fields. Formally, this picture emerges from the nonlinear response function description described in Chapters 2 and 3 when assuming

non-overlapping IR and visible pulses and neglecting vibrational relaxation and inter-mode coherence. In reality, however, the overall FEIR excitation process competes with picosecond vibrational relaxation, and its efficiency is therefore sensitive to aspects of the temporal pulse profiles beyond peak or integrated photon fluxes. Additionally, inter-mode coherence excitation of pairs of vibrational fundamentals within the IR bandwidth further complicate the interplay between molecular and optical factors. While these effects can be properly treated by our theoretical response function description with finite-pulses, they are beyond the scope of our present analysis and discussion.

Given these theoretical complexities, here we take a practical route to defining FEIR brightness based on experimental count rates and a simple phenomenological model for how the signal scales with experimental parameters. We assume the overall probability P_{ex} that a molecule is electronically excited in response to a pulse sequence follows the bilinear intensity dependence

$$P_{\text{ex}} = aI_{\text{IR}}I_{\text{vis}} \quad (7.5)$$

where I_{IR} and I_{vis} are peak pulse intensities (GW cm^{-2}) and a plays the role of an FEIR cross-section and is defined by this relation. While neglecting time-dependence and pulse duration effects in general, this relation is applicable to varying the energy of pulses with fixed time-delays and temporal profiles. The measured count rate is proportional to P_{ex} , specifically

$$F = r\langle N \rangle \eta \phi a I_{\text{IR}} I_{\text{vis}}, \quad (7.6)$$

where r is the pulse repetition-rate, $\langle N \rangle$ is the average number of molecules in the probe volume, η is the overall photon detection efficiency, and ϕ the fluorescence quantum yield.

This expression neglects a negative contribution to F due to depletion of the equilibrium ground state by the IR pump which consequently reduces the amount of fluorescence from direct visible excitation. Formally, these effects arise from ground-state bleach pathways neglected in the response function description of Chapter 2, and can be seen in the negative-going FEIR signals found for the fluorescence-loss resonance condition explored with C153 in Ref. [39]. However, for the resonance conditions considered in this work, this depletion contribution is negligible compared to the proper FEIR excited contribution (i.e. described by P_{ex}), and we will not consider its effect in our analysis. As shown in Chapter 4, we have previously verified this linear I_{IR} - and I_{vis} -dependence for bulk samples where $P_{\text{ex}} \ll 1$ for any given molecule. In analogy to fluorescence brightness, the FEIR brightness in the context of this model is $a \times \phi$.

Our approach is to extract this value, or a proportional quantity, from the measured count rate by dividing out the experimental and instrument-specific parameters in Eq. (7.6). Not all of these parameters can be directly measured, although reasonable estimates can be made. For example, the detection efficiency can be approximated as

$$\eta = \eta_{\text{coll}} \int s_{\text{fl}}(\omega) T_{\text{bp}}(\omega) \eta_{\text{detector}}(\omega) d\omega. \quad (7.7)$$

Here η_{coll} is the geometric collection efficiency of the objective lens and optical path coupling the photon onto the detector, which can depend on the specific details of the experimental configuration in complicated ways and is difficult to measure absolutely. The objective's numerical aperture (NA) is the dominant factor, and for isotropic emission in a homogeneous medium of refractive index n the objective's collection efficiency is $\sin^2(\frac{1}{2} \sin^{-1}(\text{NA}/n))$, which is 10% in our experiments. The frequency integral in Eq. (7.7) is the overlap of the

molecule's area-normalized fluorescence spectrum $s_{\text{fl}}(\omega)$, transmission function of the emission filters' bandpass $T_{\text{bp}}(\omega)$, and detector quantum efficiency $\eta_{\text{detector}}(\omega)$. For our detector $\eta_{\text{detector}}(\omega)$ is $\sim 45\%$ and slowly varying over the emission frequencies considered.²⁹⁵ The factor that is significantly variable between different molecules is the fraction of the fluorescence spectrum transmitted by the bandpass filters

$$\eta_{\text{bp}} = \int s_{\text{fl}}(\omega) T_{\text{bp}}(\omega) d\omega, \quad (7.8)$$

which may be calculated directly from steady-state fluorescence and transmission measurements. Overall, using these estimates $\eta \approx 0.045 \times \eta_{\text{bp}}$, although this is likely only an upper bound due to further unknown factors in η_{coll} .

Similarly, $\langle N \rangle$ is difficult to measure in general, but can be represented up to proportionality by the solution concentration C (mol L⁻¹). As described in Chapter 6, we have previously measured $\langle N \rangle$ directly from nM solutions of C6 by performing FEIR correlation spectroscopy (FEIR-CS), finding ~ 0.65 molecules/nM, or, assuming this relation is scalable to any concentration $\langle N \rangle = 0.65 \times 10^{-9} C$.²⁴³ However, to ensure we only use parameters that are directly controlled or measured, we define FEIR brightness (mol⁻¹ L GW⁻² cm⁴) as

$$q = \frac{F}{rC\eta_{\text{bp}}I_{\text{IR}}I_{\text{vis}}} \approx 1.44 \times 10^{12} (\text{mol}^{-1}\text{L}) \phi a \quad (7.9)$$

where the second approximate equality uses the estimates stated above to isolate the fully-corrected FEIR brightness in Eq. (7.6).

7.3.2 FEIR cross-section

The FEIR cross-section a reflects the microscopic molecular factors governing the overall excitation process, shown in Figure 7.1. While a complete description that includes the effects of vibrational relaxation, pulse durations and spectra, and multimode excitation is best handled by a response function calculation, here we discuss the relevant quantities from a heuristic standpoint. For a single vibration within the Condon approximation, and assuming early encoding delays where vibrational relaxation is negligible

$$a \sim |\mu_{eg}|^2 |\langle 1_g | 0_e \rangle|^2 |\mu_{10}|^2 \cdot Y \cdot \Delta(\omega_{\text{vis}} - (\omega_{eg} - \omega_{10})). \quad (7.10)$$

Here ω_{10} and μ_{10} are the vibrational frequency and transition dipole moment, ω_{eg} and μ_{eg} are the pure electronic transition frequency and dipole moment, and $\langle 1_g | 0_e \rangle$ is the Franck-Condon factor describing the vibrational-electronic coupling. $Y = \langle [\hat{\mu}_{eg} \cdot \hat{\epsilon}_{\text{vis}}]^2 [\hat{\mu}_{10} \cdot \hat{\epsilon}_{\text{IR}}]^2 \rangle$ is an orientational factor determined by the projection of the pulse polarization vectors $\hat{\epsilon}_{\text{IR}}$ and $\hat{\epsilon}_{\text{vis}}$ onto the transition dipole directions $\hat{\mu}_{10}$ and $\hat{\mu}_{eg}$, averaged over the orientational distribution present in the experiment. Such orientational factors are common to coherent 3rd-order nonlinear techniques, the most directly analogous being 2D-VE spectroscopy,^{313,314} however in terms of overall magnitude this factor plays a minor role, and we will not discuss its contribution in detail here. Chapter 9 treats orientational effects in more detail. The final factor $\Delta(\omega_{\text{vis}} - (\omega_{eg} - \omega_{10}))$ is a normalized resonance term that accounts for the spectral overlap of the visible pulse with the encoding transition, i.e. the vibronic transition from the $\nu = 1$ state of the vibration being pumped to the excited electronic manifold. Here we have assumed that the IR pulse is spectrally broad compared to the vibrational transition and tuned to resonance $\omega_{\text{IR}} \approx \omega_{10}$, so that Δ describes the detuning from the resonance condition

in Eq. (7.1). As an effective lineshape function for the encoding transition, Δ should in principle be influenced by many of the same intramolecular vibrational and solvation coordinates that govern the lineshape of the equilibrium electronic transition.

7.3.3 Background

In analogy to Eq. (7.6), the directly excited fluorescence background F_0 can be written as

$$F_0 = r\langle N \rangle \eta \phi a_0 I_{\text{vis}}, \quad (7.11)$$

where a_0 is the coefficient relating the probability of one-photon electronic excitation to the visible peak pulse intensity. Specifically, a_0 is related to the absorption cross-section and visible pulse duration t_{vis} as $a_0 = \sigma_{\text{el}}(\omega_{\text{vis}})t_{\text{vis}}/\hbar\omega_{\text{vis}}$. Higher-order contributions in I_{vis} , e.g. two-photon absorption, can also become significant in cases when ω_{vis} is sufficiently off-resonance from the electronic absorption band. We define the direct excitation brightness ($\text{mol}^{-1} \text{ L GW}^{-1} \text{ cm}^2$) as

$$q_0 = \frac{F_0}{rC\eta_{\text{bp}}I_{\text{vis}}}. \quad (7.12)$$

When linear absorption is the dominant contribution, $q_0 \propto \phi a_0$ with the same estimated proportionality factor as Eq. (7.9), and represents the conventional fluorescence brightness excited at ω_{vis} . The nonlinearity of the FEIR excitation process spatially localizes signal generation to the product of the IR and visible intensity profiles. However, because the size of the IR focus is at least an order of magnitude larger than the visible, the spatial distribution of FEIR signal generation within the 50 μm -thick solution layer is essentially the same as the one-photon fluorescence background, which precludes the use of more aggressive confocal filtering to selectively suppress F_0 .

The sources of background not originating from the target molecule can be numerous, and naturally become increasingly prevalent in the low concentration regime of SM experiments. However, these contributions to the non-molecular background B can be decomposed by its excitation power dependence

$$B = d + bI_{\text{vis}} + \dots \quad (7.13)$$

The constant d represents the detector dark count rate (~ 40 Hz in our experiments), while the term linear in I_{vis} describes Raman scattering from the solvent as well as fluorescence from the optics or undesired impurities. In principle, higher-order terms like multiphoton-excited fluorescence could contribute but do not appear to be important under our experimental conditions. We have not observed any background signal due to excitation with the IR pulse alone.

7.4 Results and Discussion

7.4.1 Electronic absorption and fluorescence spectra

The series of 10 coumarin dyes used in this study is shown in Figure 7.2(a). Our naming convention follows the Kodak catalogue, with the exception of C525 and C545 which are Exciton catalogue names.³¹⁵ The electronic spectroscopy of the $S_0 \rightarrow S_1$ transition is influenced by the charge-transfer character of the S_1 excited state, which is modulated by the electron-donating and electron-withdrawing abilities of the amino group (shown in blue) and substituent on the lactone ring (shown in red), respectively.³¹⁶⁻³¹⁸ The variation of electron-withdrawing group and degree of alkylation of the amino group consequently tunes the absorption and fluorescence spectra (Figures 7.2(b) and (c), respectively) across a frequency range of ~ 3000

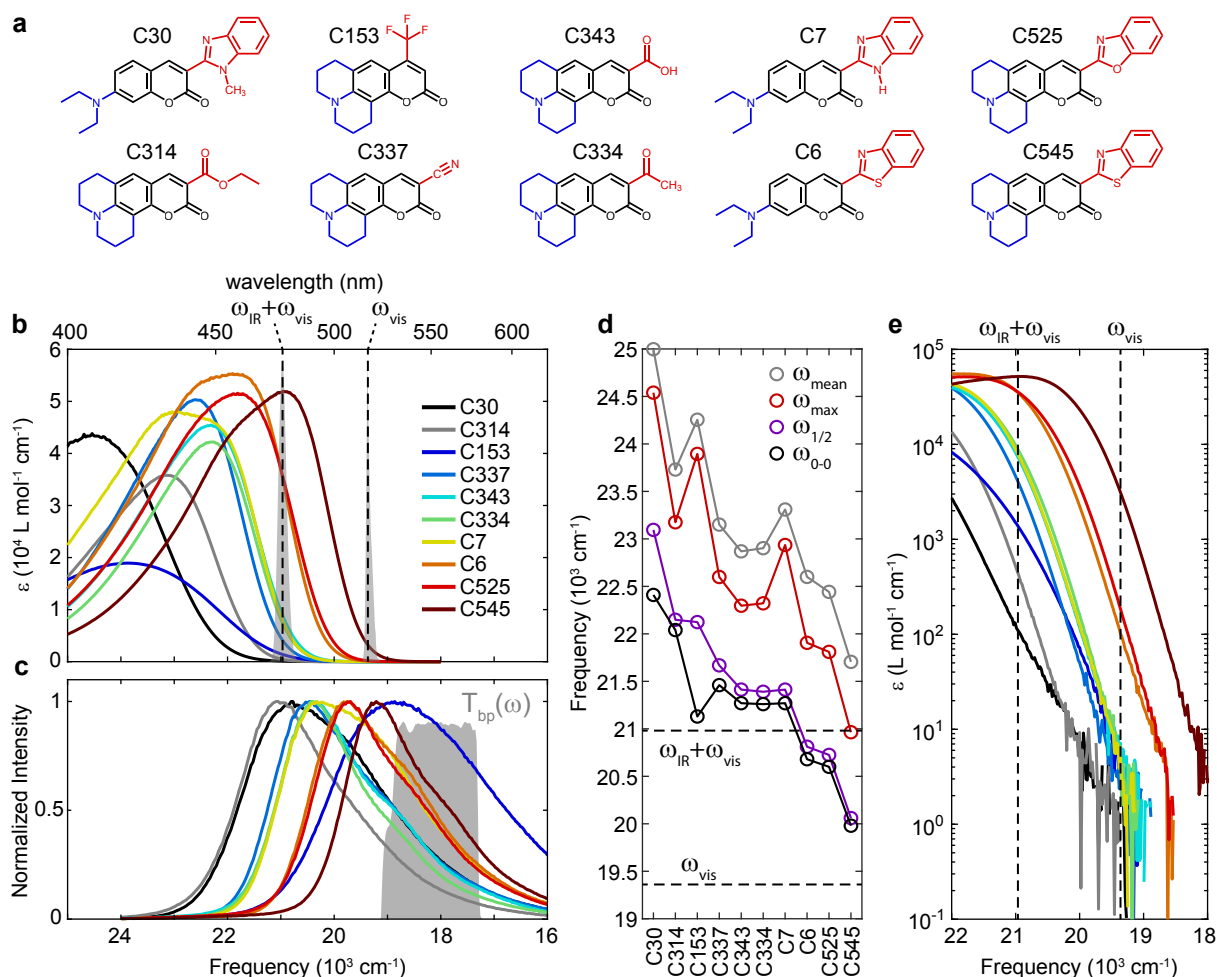


Figure 7.2: Electronic absorption and emission characteristics of the coumarin dye series in acetonitrile. (a) Structures of the coumarin dyes with their abbreviated names. (b) Electronic absorption spectra plotted as molar decadic extinction on a linear wavenumber scale (lower x-axis common with (c)) with corresponding wavelength values on the upper x-axis. Visible pulse spectrum (gray) with center frequency (dashed black) ω_{vis} indicated, and similarly for the IR/vis spectral convolution (center frequency $\omega_{\text{IR}} + \omega_{\text{vis}} = 20980 \text{ cm}^{-1} = 477 \text{ nm}$). (c) Normalized fluorescence spectra with the emission bandpass $T_{\text{bp}}(\omega)$ shown in gray. (d) First moment of the absorption spectrum (ω_{mean}), frequency of the absorption maximum (ω_{max}), half-way point up the low-frequency edge ($\omega_{1/2}$), and 0-0 transition (ω_{0-0} , see text) for each coumarin. (e) Low-frequency edges of the electronic absorption spectra in (b) plotted on a logarithmic y-axis. In (d) and (e) ω_{vis} and $\omega_{\text{IR}} + \omega_{\text{vis}}$ are indicated by dashed lines.

cm^{-1} . We illustrate the resulting span of FEIR excitation resonance conditions by overlaying the visible pulse spectrum and convolution of visible and IR pulse spectra on the absorption bands in Figure 7.2(b) (spectral distributions shown in gray, with respective center frequencies ω_{vis} and $\omega_{\text{IR}} + \omega_{\text{vis}}$ denoted by dashed lines). The IR/visible spectral convolution, formally the distribution of all IR + visible frequency sums accessible between their bandwidths, nominally indicates the breadth of double resonance around $\omega_{\text{IR}} + \omega_{\text{vis}}$ that can be supported by the pulse spectra, and has a fwhm of $\sim 140 \text{ cm}^{-1}$. Notably, both this distribution and the visible pulse spectrum are narrowband with respect to the coumarins' electronic absorption lineshapes. Figure 7.2(d) shows ω_{vis} and $\omega_{\text{IR}} + \omega_{\text{vis}}$ against various metrics characterizing the electronic absorption frequency (see also Table 7.1): ω_{mean} , first moment of the band, ω_{max} , frequency of the band maximum, $\omega_{1/2}$, frequency of the half-way point up the low-frequency edge, and ω_{0-0} , an approximation of the 0-0 transition frequency given by the crossing point of the normalized absorption and fluorescence lineshapes. The coumarins have been ordered by decreasing $\omega_{1/2}$ values. For C30, the most blue-shifted coumarin under consideration, $\omega_{\text{IR}} + \omega_{\text{vis}}$ falls $\sim 1500 \text{ cm}^{-1}$ below ω_{0-0} , while the three reddest—C6, C525, and C545—have $\omega_{\text{IR}} + \omega_{\text{vis}} > \omega_{0-0}$, notably with $\omega_{\text{IR}} + \omega_{\text{vis}} \approx \omega_{\text{max}}$ for C545.

While each of these electronic frequency metrics is influenced to some degree by the band's shape, they nevertheless cannot adequately account for the breadth of the lineshape. As a potentially more direct characterization of FEIR resonance, we will investigate $\varepsilon_{\text{el}}(\omega_{\text{IR}} + \omega_{\text{vis}})$ —the value of the extinction coefficient at the double-resonance frequency. Figure 7.2(e) shows the same absorption spectra on a logarithmic y-axis to better show the extent of the low-frequency edge, with $\omega_{\text{IR}} + \omega_{\text{vis}}$ and ω_{vis} indicated by dashed lines. From the bluest to reddest coumarins in the series, $\varepsilon_{\text{el}}(\omega_{\text{IR}} + \omega_{\text{vis}})$ spans nearly 3 orders of magnitude. In principle this metric describes both detuning, through position on the lineshape, as well

Table 7.1: $S_0 \rightarrow S_1$ spectroscopic parameters of the coumarin dye series. f is the oscillator strength, $\Delta\omega_{\text{edge}}$ is the hwhm of a Gaussian fit to the red-edge of the absorption band, and the Stokes shift is defined by the difference between the absorption and fluorescence band maxima.

Coumarin	ϵ_{max} (L mol ⁻¹ cm ⁻¹)	f	ω_{max} (cm ⁻¹)	ω_{0-0} (cm ⁻¹)	$\Delta\omega_{\text{edge}}$ (cm ⁻¹)	Stokes shift (cm ⁻¹)	ϕ	η_{bp}
30	43000	0.74	24500	22420	1240	3730	0.64	0.15
314	36000	0.47	23200	22000	900	2120	0.70	0.10
153	19000	0.36	23900	21200	1470	5030	0.65	0.35
337	50000	0.63	22600	21500	880	2130	0.76	0.18
343	42000	0.51	22300	21300	810	1960	0.63	0.18
334	45000	0.58	22300	21300	840	1920	0.89	0.16
7	48000	0.78	22900	21300	740	2600	0.86	0.23
6	55000	0.85	21900	20700	720	2150	0.89	0.29
525	51000	0.75	21800	20600	820	2120	0.75	0.28
545	52000	0.72	21000	20000	770	1750	0.71	0.39

as electronic transition strength, through the extinction magnitude. Maximum extinction values, as well as oscillator strengths f calculated from the molar decadic extinction spectra via the numerical relation $f = 4.32 \times 10^{-9} \int \varepsilon(\omega) d\omega$ with ω expressed in cm⁻¹,^{319,320} are listed in Table 7.1 and vary by a factor ~ 3 across the series. In the context of the heuristic expression for FEIR cross-section in Eq. (7.10), $\varepsilon_{\text{el}}(\omega_{\text{IR}} + \omega_{\text{vis}})$ should supply information on $|\mu_{eg}|^2$ by proportionality with f , while we would also expect similarities with the ω_{vis} -dependence of the encoding lineshape function Δ in the presence of shared line-broadening mechanisms.

Linear absorption of the visible pulse is controlled by $\varepsilon(\omega_{\text{vis}})$, which also varies dramatically by over 3 orders of magnitude across the coumarin series. Below a few percent of

the band maxima, the low-frequency absorption tails exhibit an exponential frequency dependence, apparent as linear slopes in the logarithmic scaling of Figures 7.2(e) (exponential fits shown in Figures 7.A.1 and 7.A.2 of Appendix 7.A). This so-called “Urbach tail” is a well known feature in the band-edge spectra of solid-state materials,^{321,322} but is also frequently observed for organic molecules in solution, often with a $1/k_B T$ -dependent decay constant.³²³⁻³²⁶ For molecules, this exponential tail and characteristic temperature dependence has been interpreted as the cumulative effect of hot-band transitions originating from the sparsely thermally-occupied excited levels of Franck-Condon active vibrations on the ground state. For all the coumarins, with the possible exception of C545, ω_{vis} falls within this Urbach region.

The fluorescence quantum yield ϕ and fractional spectral bandpass η_{bp} are listed in Table 7.1. The optimal location of the instrument’s emission bandpass depends on the interplay between the fluorophore’s Stokes shift, fluorescence lineshape, and the pre-resonant shift on the order of $\omega_{\text{IR}} \approx \omega_{10}$ required for FEIR resonance (i.e. Eq. (7.1)). A detection band on the Stokes side of ω_{vis} can in general only access a smaller portion of the emission spectrum than in a conventional one-photon resonant fluorescence excitation scheme due to this pre-resonant shift. For fluorophores with small Stokes shifts, placing the detection band on the anti-Stokes side of ω_{vis} could in principle allow for larger η_{bp} , with the added benefit of contending with the weaker anti-Stokes solvent Raman background. In this work we use a Stokes-side bandpass (Figure 7.2(c)) that relies on the relatively large Stokes shifts of the coumarin dyes (Table 7.1), which for the most part greatly exceed ω_{10} for the vibrations under consideration. The decrease in η_{bp} from ~ 0.4 to ~ 0.1 when moving red to blue across the coumarin series is a consequence of the increasingly off-resonant FEIR excitation with Stokes-side detection. C153 is notable by its large $\sim 5000 \text{ cm}^{-1}$ Stokes shift, which results in

the second-highest η_{bp} in the series despite its position in the blue side of the series.

7.4.2 FTIR absorption spectra

FTIR spectra of the coumarin series are shown in Figure 7.3. The IR pulse spectrum used in each FEIR measurement is superimposed to indicate the vibrations being excited. The pulse is broadband with respect to the vibrational linewidths and spans multiple modes in each case. Below 1650 cm^{-1} in the spectral range shown are C=C ring vibrations localized predominantly on the coumarin core, while the lactone carbonyl stretching band appears above 1700 cm^{-1} . In many cases this carbonyl band shows considerable structure (e.g. the splitting especially prominent for C153 and C525), which is likely due to a Fermi resonance.^{327–329} C334, C314, and C343 contain another carbonyl group in the electron-withdrawing substituent, which appears between $1650\text{--}1700\text{ cm}^{-1}$. The center of the IR pulse spectrum $\omega_{\text{IR}} = 1620\text{ cm}^{-1}$ was chosen to maximize coverage of the highest frequency ring modes, which have similar character across the coumarin series, and, as shown below, are typically the most strongly FEIR active. In contrast to the large variation in electronic resonance created by the range of absorption frequencies, here the collection of vibrational modes being pumped are fairly similar in frequency and extinction. Nevertheless, the vibrational transition strength is a critical factor for FEIR brightness via Eq. (7.10), and any differences in IR-vibrational cross-section should be reflected in the strength of the signal. To characterize these differences given the spectrally broad excitation, we compute the overlap

$$\epsilon_{\text{IR}} = \int \epsilon_{\text{vib}}(\omega) |\tilde{E}_{\text{IR}}(\omega)|^2 d\omega, \quad (7.14)$$

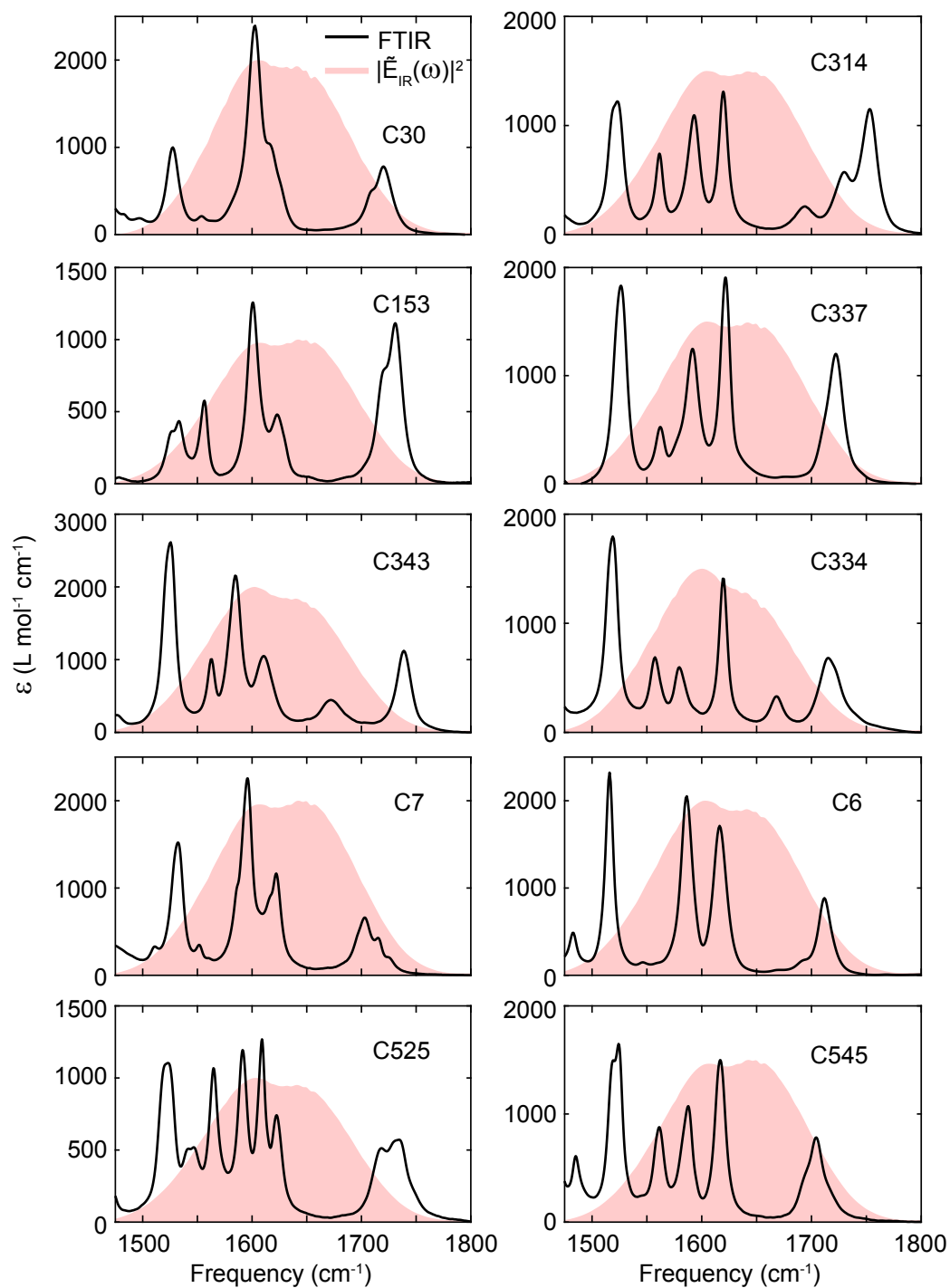


Figure 7.3: FTIR spectra of the coumarin series in acetonitrile-d₃ with the IR pulse spectrum used for each FEIR measurement overlaid.

where $\varepsilon_{\text{vib}}(\omega)$ is the vibrational extinction spectrum and $|\tilde{E}_{\text{IR}}(\omega)|^2$ is the normalized IR spectral intensity profile. As shown in Figure 7.A.8, ε_{IR} only varies by a factor of ~ 2 across the series.

7.4.3 Brightness analysis of high concentration FEIR data

Bulk FEIR measurements on 3 representative coumarins are shown in Figure 7.4 (complete series shown in Figure 7.A.3 of Appendix 7.A). High concentrations (30-100 μM) were used to keep the non-molecular background B negligibly small compared to the coumarin fluorescence. Panels (a)-(c) show the total detected photon rate F_{tot} from two-pulse measurements in brightness units, that is, divided by $rC\eta_{\text{bp}}I_{\text{vis}}$. Instead of additionally dividing the FEIR component F by I_{IR} to recover q as in Eq. 7.9, it will be convenient for our analysis to work with an effective FEIR brightness where the IR intensity dependence has not been removed

$$q_{\text{IR}} = \frac{F}{rC\eta_{\text{bp}}I_{\text{vis}}} = qI_{\text{IR}}, \quad (7.15)$$

which has the same units as q_0 , facilitating direct comparison of their respective magnitudes. Furthermore, because I_{IR} is held constant in this study, q_{IR} can still be compared between measurements on different molecules, and we will also refer to this quantity as the FEIR brightness unless further distinction is required. As B is negligible, q_0 is given by the constant offset (blue arrows) for $\tau_{\text{enc}} < 0$ where $F = 0$ by causality.

F reaches a maximum at early τ_{enc} before decaying away on a picosecond timescale due to vibrational relaxation processes. However, the details of the τ_{enc} -dependence near the maximum, notably the peak position, vary for the different coumarins. As $F(\tau_{\text{enc}})$ measures the integrated response of the multiple vibrations within the IR bandwidth, some aspects of

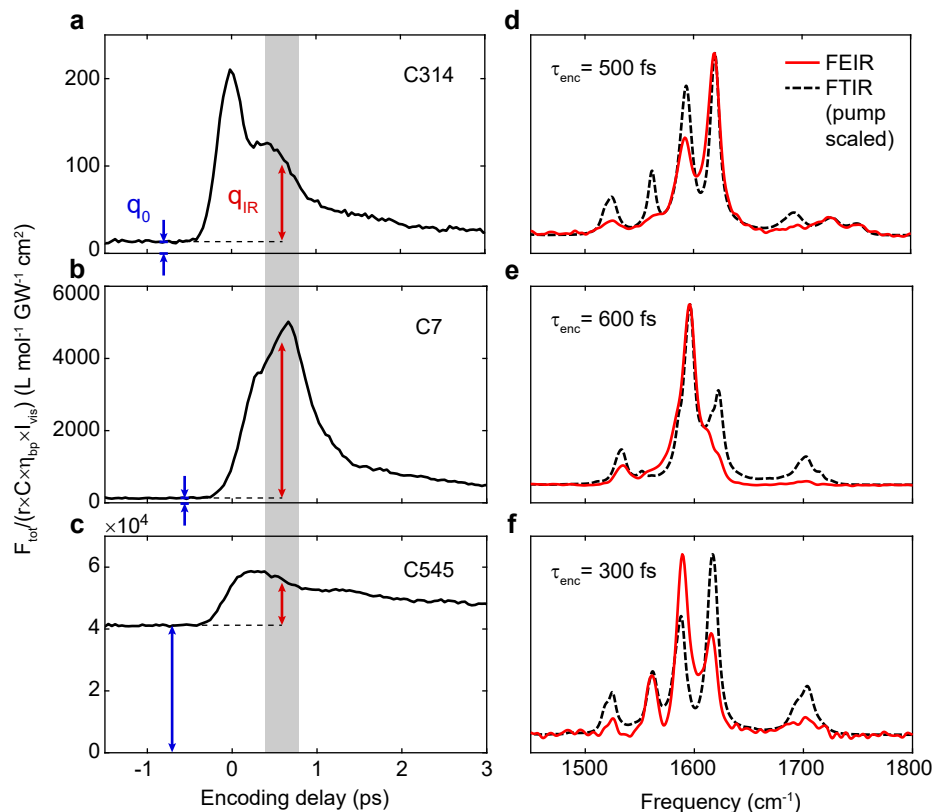


Figure 7.4: Bulk FEIR data in brightness units. (a)-(c) Total photon output F_{tot} from two-pulse FEIR experiments plotted in brightness units for C314, C7, and C545, respectively. The effective FEIR and direct excitation brightness are indicated by arrows. (d)-(f) Comparison of IR pump spectrum-scaled FTIR spectra (dashed line) with FEIR spectrum (solid line) at the encoding delay indicated for each corresponding coumarin in (a)-(c). Each spectrum is independently normalized to its largest feature.

these differences reflect the variation in frequency spread, vibronic activity, and relaxation kinetics of the modes being sampled. To show which vibrations are contributing to the response in each case, Figures 7.4(d)-(f) show the corresponding FEIR spectra at selected early encoding delays superimposed on the IR pump-scaled FTIR spectra. In all cases, the high frequency ring modes between 1570-1620 cm⁻¹ have the largest contribution to the F amplitude. Multimode coherence produces the strongly-damped oscillatory behavior

present in some two-pulse transients, which to some extent also plays a role in the location of the signal maximum. However, in the vicinity of $\tau_{\text{enc}} = 0$ the signal may also contain pulse-overlap artifacts, for example contributions from improperly ordered interactions of the IR and visible fields or vibrationally-nonresonant IR + visible two-photon absorption. We note that even in these cases the signal amplitude is still determined by the molecular response—one of the benefits of fluorescence detection which precludes non-resonant pulse-overlap contributions from the solvent or windows. Nevertheless, to avoid these potential complications, we will use the average value of $F(\tau_{\text{enc}})$ between 400 and 800 fs (gray region in Figures 7.4(a)-(c) with red arrow indicating the average) to define q_{IR} for our analysis. While this window safely avoids the pulse-overlap region, in many cases the excited vibrational population has already undergone partial relaxation which may result in artificially lower measured FEIR brightness (Section 7.A.4 compares these FEIR brightnesses with those using the maximum F values). Chapter 8 discusses the details of the FEIR signals in this early-time region using finite-pulse response function calculations.

The coumarins in Figure 7.4 were chosen to represent the full range of FEIR resonance conditions across the series; C314 being one of the bluest, C7 intermediate, and C545 the reddest. As evident from the y-axis scales of Figure 7.4(a)-(c), the brightness of the overall fluorescence ($F + F_0$) increases dramatically for the redder coumarins. However, for C545 the direct excitation background has become larger than the FEIR signal. This reduction in contrast is evident in a much smaller modulation ratio of $M = 0.35$ for C545, compared to $M = 35$ for C7 and $M = 6.8$ for C314.

In Figure 7.5 we investigate how brightness and contrast are explicitly influenced by the FEIR resonance condition discussed in Section 7.4.1. To normalize out variations in emission probability, we divide the FEIR and direct excitation brightnesses by quantum yield ϕ . The

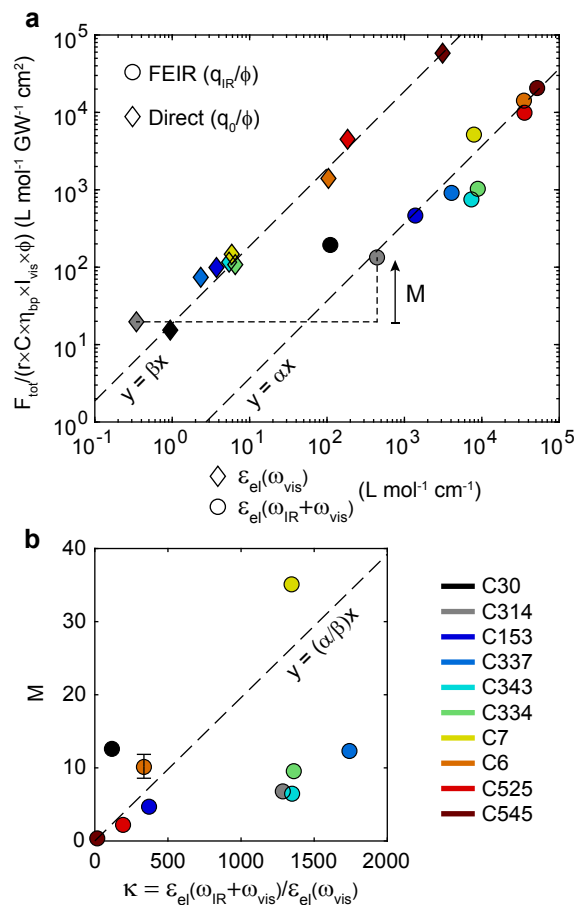


Figure 7.5: Correlations between effective FEIR and one-photon cross-sections and electronic absorption spectrum. (a) Correlation of q_{IR}/ϕ against $\epsilon(\omega_{\text{IR}} + \omega_{\text{vis}})$ (circles), and q_0/ϕ against $\epsilon(\omega_{\text{vis}})$ (diamonds) on log-log axes. Linear fits in dashed lines have a slope of $\alpha = 0.367 \text{ GW}^{-1} \text{ cm}^3$ with $R^2 = 0.943$, and $\beta = 18.7 \text{ GW}^{-1} \text{ cm}^3$ with $R^2 = 0.999$. (b) Correlation of M against κ . The dashed line has slope given by α/β , the ratio of trend lines in panel (a). This ratio is slightly larger than the regression slope of M vs. κ (not shown).

resulting quantities q_{IR}/ϕ and q_0/ϕ are proportional to aI_{IR} and a_0 , respectively, with the same proportionality constant. The quantity aI_{IR} may be interpreted as the effective cross-section seen by the visible pulse after vibrational excitation of the molecule with the IR pulse in our instrument. Figure 7.5(a) shows that these proxies for the FEIR and direct excitation cross-sections are linearly related to the electronic extinction coefficient evaluated

at $\omega_{\text{IR}} + \omega_{\text{vis}}$ and ω_{vis} , respectively, over several orders of magnitude. Logarithmic scaling is used to conveniently represent the multiple decades in each axis (same data on linear axes is shown in Figure 7.A.6 of Appendix 7.A).

The strong linear relationship between $\varepsilon_{\text{el}}(\omega_{\text{vis}})$ and q_0/ϕ indicates that linear absorption of the visible pulse is the primary contributor to the direct excitation background F_0 across the range of resonance conditions studied here, and we will consequently also refer to F_0 as the one-photon background. However, we note that for the bluest coumarins C30 and C314, the I_{vis} -dependence of F_0 becomes super-linear beyond the intensities used in Figure 7.5 (Figure 7.A.14 in Appendix 7.A), implying a cross-over to two-photon absorption being the dominant source of F_0 background for these deeply pre-resonant excitation conditions where $\varepsilon_{\text{el}}(\omega_{\text{vis}})$ is exceptionally small.

On the other hand, the linear relationship between $\varepsilon_{\text{el}}(\omega_{\text{IR}} + \omega_{\text{vis}})$ and q_{IR}/ϕ (and by proportionality a), though more diffuse, is a more striking and *a priori* less obvious result. Taken exactly, a perfect linear relationship would indicate that the effective lineshape function of the encoding transition is simply given by the equilibrium absorption lineshape red-shifted by the vibrational frequency, i.e.

$$\Delta(\omega) \sim g_{\text{el}}(\omega - \omega_{10}), \quad (7.16)$$

where $g_{\text{el}}(\omega)$ is the normalized electronic lineshape function. While intuitive and in line with the heuristic double-resonance picture evoked by Eq. (7.1), this association cannot be formally exact, as in general both the initial and final states involved in the encoding transition are different from the bare electronic transition. The equilibrium lineshape $g_{\text{el}}(\omega)$ is composed of multiple vibronic transitions involving the Franck-Condon active intramolecular coumarin vibrations—including, but importantly not limited to, the vibrations being interrogated by

FEIR—as well as being broadened by overdamped solvation coordinates. While the vibronic contribution to $\Delta(\omega)$ from the mode being pumped is certainly different because the initial state is $\nu = 1$ rather than $\nu = 0$, it is reasonable to expect a similar contribution from the solvent, as, from the solvent’s perspective, vibrational excitation on the ground-state is a small perturbation compared with electronic excitation. As the FEIR resonance conditions explored here probe the red-side of the transition where the breadth of the lineshape is likely dominated by the solvent contribution, Eq. (7.16) could therefore be a reasonable approximation. For coumarins on the blue side of the series, $\varepsilon_{\text{el}}(\omega_{\text{IR}} + \omega_{\text{vis}})$ falls within the Urbach region of the lineshape, and it is possible that initial thermal population of low-frequency modes is important. A similar correspondence between signal size and resonance condition for $\omega_{\text{vis}} < \omega_{0-0} - \omega_{\text{IR}}$ was found in some of the original experiments of Kaiser and co-workers, although the vibrations being pumped were likely combination bands.³²³ From a computational perspective, $\Delta(\omega)$ is related to the lineshape of the vibrationally pre-excited absorption spectrum introduced by Burghardt and coworkers to model the closely-related excitation process in vibrationally promoted electronic resonance (VIPER) spectroscopy.^{74,330} Although their approach only investigated the effect of the intramolecular modes and did not treat broadening from the solvation environment explicitly, their results typically show a peak red-shifted from the 0-0 transition by roughly ω_{10} due primarily to the pre-excited mode’s 1-0 vibronic transition. These computational results support the frequency shift in Eq. (7.16) as well as the simplified energy level diagram in Figure 7.1.

The scatter in the $\varepsilon_{\text{el}}(\omega_{\text{IR}} + \omega_{\text{vis}})$ vs. q_{IR}/ϕ trend is likely influenced by variations in the other terms in Eq. (7.10), i.e. the vibrational transition dipoles, Franck-Condon overlaps, and orientational factors. In fact, given that these factors are not accounted for, it is perhaps somewhat remarkable that a linear regression of this quality is even observed. This may be

explained in the following ways. First, as the a values here reflect the collective response of multiple vibrations, the differences in these unaccounted factors are potentially smoothed out between dyes, thereby isolating the electronic resonance dependence for an “average” coumarin. Second, the structural similarity between the dyes likely precludes very large variations in these factors for the dominant core ring modes, while in contrast $\epsilon_{\text{el}}(\omega_{\text{IR}} + \omega_{\text{vis}})$ varies by almost 3 orders of magnitude. As mentioned in Section 7.4.2, one way to account for the vibrational transition strength is by the factor ϵ_{IR} (Eq. (7.14)). However, using $\epsilon_{\text{IR}} \cdot \epsilon_{\text{el}}(\omega_{\text{IR}} + \omega_{\text{vis}})$ as the x-values does not substantially improve the linear relationship (Figure 7.A.8 in Appendix 7.A), perhaps because the remaining factors play the dominant role. Uncontrolled differences in the instrument’s alignment and errors in experimental parameters between measurements also contribute to uncertainty in the measured brightness values. We characterized day-to-day differences in q_{IR} and q_0 for C6, and found a coefficient of variation (standard deviation over mean) of 12% and 10%, respectively (Section 7.A.3). We expect this experimental uncertainty to be representative across the coumarin series, and it is smaller than the size of the data markers in Figure 7.5(a). Therefore, we believe that this scatter is predominantly reflective of differences in the vibrational mode-specific factors, of which the vibronic coupling is likely the most important.

Figure 7.5(b) shows the corresponding modulation ratios M (Eq. (7.3)) from the FEIR measurements in Figure 7.5(a). As B is negligible, M can be written as

$$M = (a/a_0)I_{\text{IR}}, \quad (7.17)$$

which is manifested graphically as the signed distance (in log units) between respective y-values in Figure 7.5(a), (indicated for C314). The vertical error bar for C6 shows two standard deviations for the experimental uncertainty stated above. The M values are plotted

against the extinction coefficient ratios

$$\kappa = \varepsilon_{\text{el}}(\omega_{\text{IR}} + \omega_{\text{vis}})/\varepsilon_{\text{el}}(\omega_{\text{vis}}), \quad (7.18)$$

thereby effectively combining both trends in Figure 7.5(a). The relationship between these quantities describes the extent to which the equilibrium absorption lineshape alone can predict the contrast in an FEIR experiment for given IR intensity. The resulting correlation is quite diffuse (Pearson correlation coefficient $r = 0.49$) primarily because the scatter in the q_{IR}/ϕ vs. $\varepsilon_{\text{el}}(\omega_{\text{IR}} + \omega_{\text{vis}})$ trend caused by the unaddressed vibrational and vibronic factors is magnified. Additionally, noise on the small $\varepsilon_{\text{el}}(\omega_{\text{vis}})$ values for the bluer coumarins likely amplifies the uncertainty in their κ values, although we do not estimate the corresponding error bars. While M is correlated to κ , the relationship is not sufficiently good to be widely predictive in a quantitative sense, most likely due to the importance of the vibrational mode-specific factors.

However, some general observations about how the contrast depends on the relationship between $\varepsilon_{\text{el}}(\omega)$, ω_{vis} , and ω_{10} can still be made. The order of magnitude smaller M value for C545 compared to the rest of the series is clearly due to the large one-photon background produced by ω_{vis} falling substantially higher on the absorption band tail (ω_{vis} at $\sim 6\%$ of the band maximum). Even though C545 has the highest FEIR brightness in the series—which assuming Eq. (7.16) holds corresponds to fully maximized FEIR resonance—in practice measurements on this molecule suffer from lower signal to noise caused by the large shot noise introduced by F_0 , requiring longer averaging times (Figure 7.A.4 in the Appendix 7.A). Evidently, for the frequencies of vibration under consideration the electronic absorption edge is not sufficiently steep (quantified e.g. by $\Delta\omega_{\text{edge}}$ in Table 7.1, and Figures 7.A.1 and 7.A.2 in Appendix 7.A) to allow maximal FEIR resonance without excessive one-photon background.

How much direct band overlap, i.e. $\varepsilon_{\text{el}}(\omega_{\text{vis}})/\varepsilon_{\text{el}}(\omega_{\text{max}})$, can be tolerated in practice depends on how much slower a grows with $\varepsilon_{\text{el}}(\omega_{\text{IR}} + \omega_{\text{vis}})$ than a_0 grows with $\varepsilon_{\text{el}}(\omega_{\text{vis}})$. This comparison may be quantified by the trend line slope ratio $\alpha/\beta = 2.0\%$ (dashed line in Figure 7.5(b)). Because the detuning dependence is accounted for, this value describes on average the relative efficiency of FEIR excitation vs. direct one-photon excitation for a prototypical coumarin dye with the IR pulses of our instrument. Specifically, this value suggests that FEIR vibrational detection at maximal resonance is overall ~ 50 times less efficient in these experiments than conventional fluorescence detection at maximal resonance. In terms of contrast, this implies that κ should be at least greater than ~ 50 to achieve $M > 1$.

Even if the absorption edge is too broad to support maximal FEIR resonance with low one-photon background, detuning slightly could produce a workable compromise. For example, C6 has a similarly steep absorption edge as C545, but is detuned from maximal FEIR resonance by $\sim 900 \text{ cm}^{-1}$, putting $\omega_{\text{IR}} + \omega_{\text{vis}}$ and ω_{vis} at 63% and 0.19% of the band maximum, respectively ($\kappa = 340$). The resulting FEIR cross-section is ~ 0.7 times the size of that for C545, but with a ~ 40 -fold decrease in one-photon background, leading to an excellent signal to background of $M \sim 10$.

7.4.4 Signal to background in the SM regime

The analysis in the previous section made use of high concentration measurements where essentially all of the detected light is dye fluorescence. As a per-molecule quantity, the construct of FEIR brightness is transferable to SM investigation, as is the brightness of the direct excitation background. However, in the low concentration regime where SM experiments operate, sources of background independent of the target molecule, i.e. B , will usually play the dominant role in influencing contrast and signal to noise. To investigate

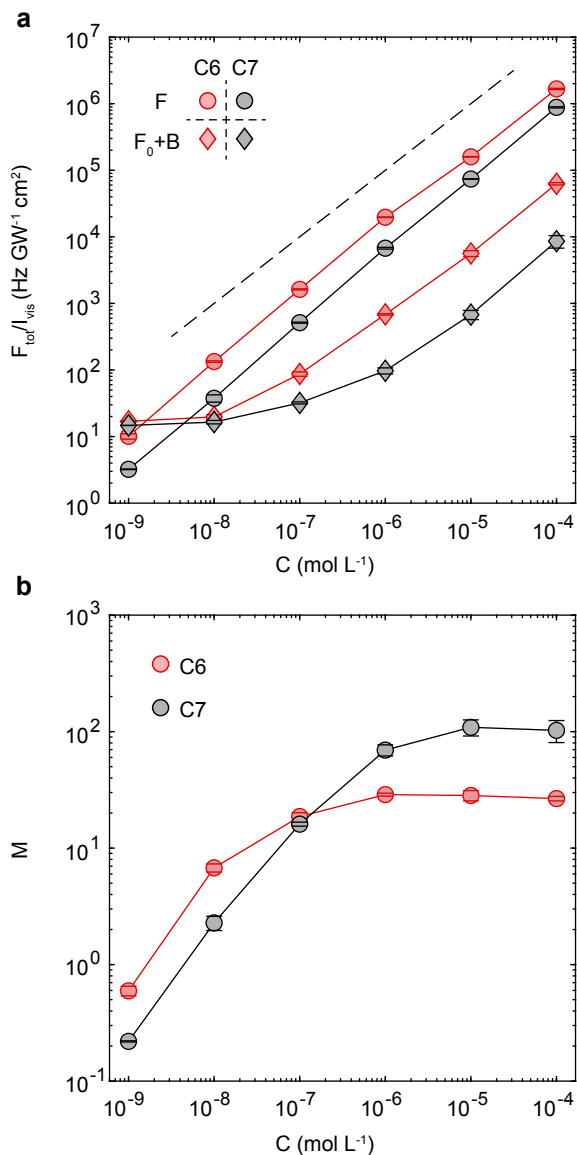


Figure 7.6: Concentration dependence of the FEIR signal and background for C6 and C7. (a) Concentration dependence of F/I_{vis} (circles) and $(F_0 + B)/I_{\text{vis}}$ (diamonds) for C6 (red) and C7 (black). The dashed line indicates a linear relationship between the log-scaled x- and y-axes to guide the eye. (b) M values corresponding to panel (a).

the impact of B and how the practical considerations for contrast and signal to noise differ in the SM limit, we perform concentration-dependent measurements for two members of the

coumarin series: C6 and C7. These molecules have similar FEIR spectra that are dominated by a single ring mode just below 1600 cm^{-1} , and likewise show similarly-shaped two-pulse transients (Figure 7.A.3 in Appendix 7.A). C6 was previously used to demonstrate SM sensitivity in Chapter 6, and produces the second-brightest FEIR signal in the series. With the fixed resonance conditions of our instrument, C7 is $\sim 1/3$ as FEIR bright as C6, but displays an ~ 3 -fold higher B -free modulation ratio. As such, at high concentrations where I_{vis} can be varied to set the total fluorescence output at will, C7 is technically the better FEIR chromophore in terms of detection quality, although M is sufficiently high for both to be excellent. As mentioned in Section 7.2.2, the CaF_2 coverslips employed for the measurements in this section allowed for a ~ 3 -fold increase in FEIR brightness relative to the experiments in the previous section and Chapter 6, while maintaining a similar background size (cf. high-concentration M values in Figure 7.6 and Figure 7.5).

Figure 7.6(a) shows the concentration-dependence of the FEIR signal size F/I_{vis} and background $(F_0 + B)/I_{\text{vis}}$ from $100\text{ }\mu\text{M}$ to 1 nM for both molecules (complete FEIR data is provided in Section 7.A.5). In this representation, the effect of increasing I_{vis} to achieve reasonable count rates as C is lowered is normalized out to isolate the C -dependence across 5 orders of magnitude. For both dyes the FEIR component decreases roughly linearly with C . The lowest concentration points fall slightly below a linear dependence, which may be due to a saturation effect as discussed below, or could be caused by systematic error in the concentration from the serial dilution procedure. On the other hand, the background is linear in C at high concentrations, but in the low- C limit approaches a C -independent value which is the same for both coumarins: $\sim 15\text{ Hz GW}^{-1}\text{ cm}^2$, which can be assigned as the b coefficient in Eq. 7.13. This reflects the change from the background being dominated by F_0 at high C to being almost entirely composed of B in the nM range. As shown in Chapter

6, the distribution of photon arrival times for measurements in the nM range is dominated by a prompt component absent at high C , which suggests that solvent Raman scattering is likely the major contributor to B . As shown in that work, time-gating photon detection to exclude this prompt component can therefore increase M and the SNR, however we will not discuss this approach further here.

The C -dependence of the corresponding modulation ratios is shown in Figure 7.6(b). At high concentrations M is C -independent because $F_0 \gg B$ (i.e. Eq. (7.17) holds) and the empirical contrast guidelines discussed in Section 7.4.3 apply. However, below a certain concentration M begins to fall as the dye's fluorescence must compete with the C -independent B background, and at SM equivalent concentrations (~ 1 nM, see below) M is 1-3 orders of magnitude lower than its high- C limit. The threshold concentration below which M decreases is notably lower for C6 than C7, and results in a crossing of their M vs. C curves at ~ 100 nM. As a result C6 is distinctly the better SM FEIR chromophore under these resonance conditions, although C7 can still be detected at SM equivalent concentrations due to the ~ 3 -fold increase in FEIR signal facilitated by the updated sample configuration. This difference in bulk versus SM signal to background reflects a crossover from prioritizing a large F vs. F_0 contrast to prioritizing the brightness of overall fluorescence $F + F_0$ against B . As long as the high- C limit of the modulation ratio is sufficiently large, say $M > 1$, we can define a limiting concentration C_{lim} where the F and B rates are predicted to be equal based on FEIR brightness, and below which FEIR detection becomes increasingly impractical,

$$C_{\text{lim}} = \frac{b/r}{q_{\text{IR}}\eta_{\text{bp}}}. \quad (7.19)$$

The potential for SM detectability of an FEIR chromophore can then be simply assessed from a high concentration measurement by how close the calculated C_{lim} is to the SM-equivalent

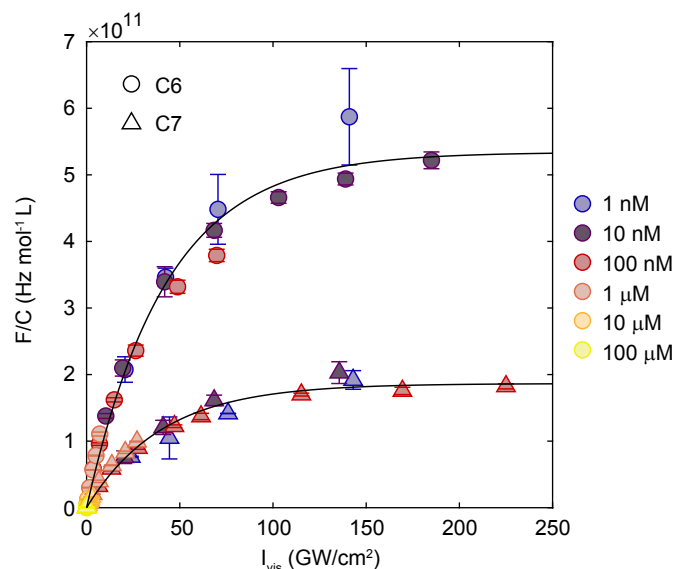


Figure 7.7: Saturation of the encoding transition. F/C as a function of I_{vis} for C6 (circles) and C7 (triangles). C is indicated by color, and black lines are fits to the exponential model described in the text.

concentration (Figure 7.A.12 in Appendix 7.A). For example, we predict that C525 and C545 would also be possible SM FEIR candidates under the current resonance conditions, as at high- C we expect an increase to $M \sim 1$ for C545 with the new sample configuration.

In the range where F , F_0 , and B each grow linearly with visible intensity, the signal to noise of a measurement may be improved by increasing I_{vis} while M remains constant, e.g. Eq. (7.4) predicts improvement by $\sim \sqrt{I_{\text{vis}}}$. In practice, however, saturation effects in the encoding transition set a limit on how large I_{vis} can usefully be made while still increasing the SNR. Figure 7.7 shows the I_{vis} -dependence of the FEIR signal size, here represented as F/C , for C6 and C7. Data from the entire concentration range in Figure 7.6 has been used in order to access both very low and high I_{vis} while keeping F_{tot} within the linear range of photon counting, and dividing F by C collapses the points onto a common saturation curve for each coumarin (log-scale plot in Figure 7.A.13). Figure 7.6 uses the lowest I_{vis} point for

Dye	c (Hz mol ⁻¹ L)	I_S (GW cm ⁻²)
C6	$5.3 \times 10^{11} \pm 0.3 \times 10^{11}$	42 ± 6
C7	$1.9 \times 10^{11} \pm 0.1 \times 10^{11}$	40 ± 5

Table 7.2: Saturation curve fit parameters for the exponential model $c(1 - \exp(-I_{\text{vis}}/I_S))$ including 95% confidence intervals from the fitting routine.

each concentration, which at the lowest concentrations nevertheless lies near the onset of saturation, which may partially explain the deviation from a linear F/I_{vis} vs. C relationship in Figure 7.6(a) mentioned above.

In general, the intensity-dependent form of saturation is influenced by the temporal characteristics of excitation. For a two-level system with cw pumping, the steady-state upper level population, and hence the emission rate, saturates with the hyperbolic form

$$p_{ss} = \frac{\sigma I_{\text{vis}}/\hbar\omega_{\text{vis}}}{1 + I_{\text{vis}}/I_S}, \quad (7.20)$$

where the saturation intensity is $I_S = \hbar\omega_{\text{vis}}/(2\sigma\tau_{\text{fl}})$, τ_{fl} is the fluorescence lifetime, and σ the absorption cross-section.³⁰² However, for pulsed excitation where the pulse duration t_{vis} is much shorter than τ_{fl} while the repetition period τ_{rep} is simultaneously much longer than τ_{fl} , the excited population immediately after each pulse is

$$p_{max} = \frac{1}{2} \left(1 - \exp(-I_{\text{vis}}/I_S) \right), \quad (7.21)$$

where $I_S = \hbar\omega_{\text{vis}}/(2\sigma t_{\text{vis}})$.^{77,331} The lower level population fully recovers before the next pulse arrives, and the average fluorescence output is therefore proportional to p_{max} . Our experiments operate in this short pulse limit ($t_{\text{vis}} \approx 300$ fs, $\tau_{\text{fl}} \approx 1$ ns, $\tau_{\text{rep}} \approx 1$ μ s) and fits to the measured saturation curves using this exponential model are shown in Figure 7.7 with fit

parameters listed in Table 7.2. In line with their relative FEIR brightnesses, F saturates at ~ 3 times higher count rates for C6 than C7. However, the threshold intensities I_S extracted from the fits are the same within error, which is surprising given that I_S should be inversely proportional to the cross-section of the transition, and aI_{IR} is ~ 3 times smaller for C7 compared to C6. Other photophysical mechanisms that sequester population, like intersystem crossing to triplet states, could also be playing a role in the saturation threshold.³³² Perhaps more importantly, treating the initial and final states of the encoding transition as a simple two-level system is likely not a reasonable assumption to describe the observed saturation behavior. So far we have not observed a similar saturation behavior in I_{IR} , although a more careful investigation is needed.

The background continues to grow roughly linearly in I_{vis} over the same range of intensities (Figure 7.A.13 in Appendix 7.A). Therefore, the contrast degrades as I_{vis} is increased into the saturating regime, leading to an eventual decrease in SNR. We find that a practical compromise is to operate near the saturation threshold I_S . Regardless of the mechanism, saturation leads to an increase in the effective size of the visible probe volume because the spatial distribution of excitation efficiency flattens out near the center of the focus but continues to increase in the wings.³³³ At a given concentration the average number of molecules $\langle N \rangle$ in the probe volume therefore increases with I_{vis} , and determination of $\langle N \rangle$ by FEIR-CS is intensity-dependent. We measure $\langle N \rangle = 0.7$ for 1 nM C6 via FEIR-CS at the saturation threshold $I_{\text{vis}} = 42 \text{ GW cm}^{-2}$, which from the two-pulse transient at the same intensity yields an F count rate per molecule of 480 Hz (see Figures 7.A.15 and 7.A.9 in Appendix 7.A, respectively). While FEIR-CS was not performed on the 1 nM C7 solution, assuming equivalent $\langle N \rangle$ at the same I_{vis} gives a lower count rate per molecule of 150 Hz, and the signal to noise of the two-pulse signal is also correspondingly lower (cf. Figures 7.A.9 and

7.A.10 in Appendix 7.A). To facilitate comparison with existing SM optical methods it is useful to estimate the overall excitation probability P_{ex} . Considering our estimate for the total detection efficiency of fluorescence from C6 ($\eta \approx 1.3\%$), its quantum yield ($\phi = 0.89$), and the repetition-rate (994.7 kHz), this measured count rate per molecule corresponds to $P_{ex} \approx 4.2\%$. If this is indeed at the saturation threshold for the encoding transition (i.e. at $(1 - 1/e)$ of the saturated transition probability of 50%), this P_{ex} value implies a 13% IR-vibrational excitation probability. In this case we would expect that meaningful improvements to the overall excitation efficiency can still be made with larger IR fields.

7.5 Conclusions

In this work, we have examined some of the practical spectroscopic aspects of optimizing an FEIR experiment for bulk and SM vibrational detection. For a given molecule and vibration, the FEIR resonance condition is the most important aspect of experimental optimization. As ω_{IR} must always be tuned to cover the vibrational transition, this resonance condition amounts to a selection of ω_{vis} that efficiently brings the vibrationally-excited molecule to the electronic excited state. Our experimental results indicate that the electronic absorption spectrum is a useful guide for this selection, specifically that the brightness of the FEIR signal scales linearly with $\varepsilon_{el}(\omega_{IR} + \omega_{vis})$ on the low-frequency side of the band. However, optimizing the resonance condition is also constrained by the background fluorescence from direct visible excitation, which for all but the most deeply pre-resonant cases is caused by linear absorption and hence proportional to $\varepsilon_{el}(\omega_{vis})$. For bulk measurements, keeping this fluorescence background small compared to the FEIR signal is the primary consideration for high signal to noise data acquisition. To this end, depending on the shape of the electronic

absorption edge and particularly the fall-off of its red wing, bulk FEIR detection can be improved by detuning the resonance condition. In the SM regime, however, background is dominated by sources independent of the target molecule and signal photons are scarce, so the resonance condition should be adjusted to increase the absolute brightness of the FEIR signal at the expense of more one-photon background. Saturation of the encoding transition in the visible intensity limits the maximum photon count rates that can be achieved, although further improvements to the IR-vibrational excitation efficiency are likely still available.

Although the experiments presented here utilized a series of dyes with variable electronic spectra against a fixed ω_{vis} , we have framed the discussion of resonance conditions from the perspective of a tunable ω_{vis} . Indeed, our results indicate that being able to freely adjust ω_{vis} to carefully optimize resonance for the chromophore at hand will significantly improve the versatility of FEIR spectroscopy, and represents an important technical step towards its application to more general SM vibrational investigation. Additionally, a wide tuning range will facilitate the selection of fluorophores across the entire visible spectrum as potential FEIR candidates. While the equilibrium electronic spectrum can be used to predict the effect of resonance, our results also show that it alone is not sufficient to predict FEIR brightness and that substantial variations occur even for similar-character vibrations of the structurally-related coumarin dyes we studied. Therefore, a more detailed understanding of vibrational mode-specific factors will be crucial for predicting which vibrations on different families of fluorophores can be used as FEIR probes. In particular, we are interested in understanding the symmetry and structural properties required of a fluorophore to exhibit FEIR bright vibrations, and to what extent various spectroscopically useful probe vibrations, e.g. local carbonyl stretching modes, can be made sufficiently FEIR active to yield SM sensitivity.

The largest SM signal count rates (480 Hz) achieved with our current implementation of

FEIR spectroscopy are still low compared with the few to hundreds of kHz rates commonly encountered in modern solution-phase SM fluorescence experiments.^{14,334–336} From the perspective of photon budget, further improvement beyond this level would likely be required to successfully implement SM dynamics measurements based on the direct analysis of signal intensity trajectories. With our current signal levels, however, one route towards accessing kinetic information from real-time SM fluctuations is through correlation spectroscopy (CS) methods analogous to fluorescence correlation spectroscopy and related techniques.^{264,266} These methods measure ensemble-averaged kinetic timescales via time-correlation functions of signal fluctuations that arise from the dynamics of individual molecules transiently occupying the probe volume. Because the time-resolution of a correlation function is not degraded by time-averaging, CS methods can use longer data acquisition times when signal levels are small, and are also less susceptible to photobleaching as diffusion replenishes the probe volume with new molecules. The FEIR-CS measurements used here and in Ref. [243] to characterize SM sensitivity demonstrate the basic feasibility of this approach.

Multiple routes exist for increasing SM FEIR signal sizes. Increasing the pulse repetition-rate beyond the current 1 MHz would have the greatest impact on accessing higher count rates. While the repetition-rate scalability of generating nJ-level sub-ps mid-IR pulses has technical challenges, increases by a factor of ~ 10 with reduced pulse energy and bandwidth are feasible. When coupled with higher NA focusing of the IR, sufficiently large IR-vibrational excitation rates should still be accessible. Important gains in detection efficiency are also expected through increasing the NA of fluorescence collection, which at 0.8 is currently low compared to typical SM fluorescence experiments. With these improvements, we believe more useful kHz-level SM FEIR count rates should be accessible.

7.A Appendix: Supplementary material

7.A.1 Low-frequency electronic absorption tails

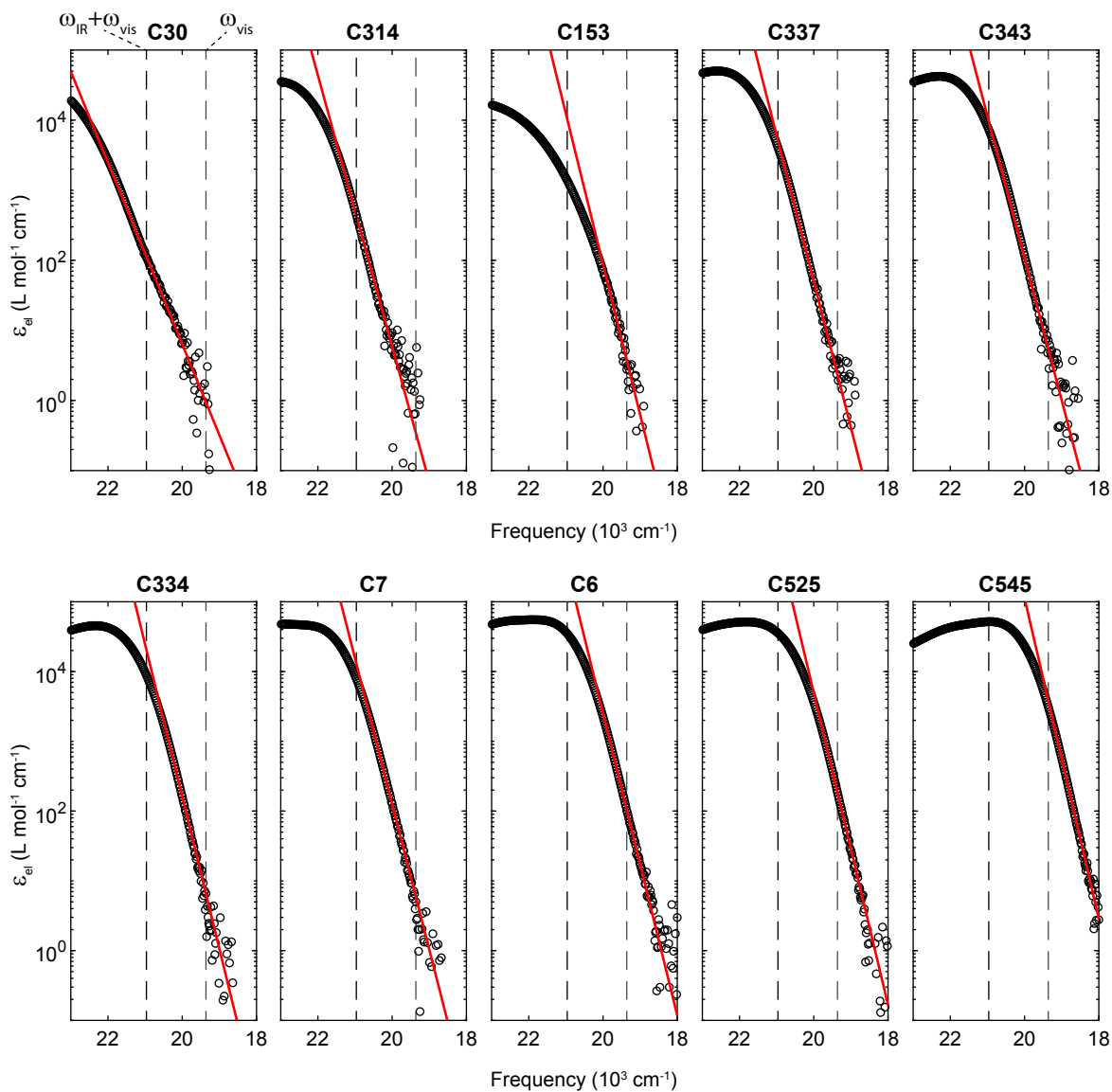


Figure 7.A.1: Low-frequency electronic extinction spectra (black circles) for each coumarin on a log y-scale, with fits of the Urbach region to an exponential (red). ω_{vis} and $\omega_{\text{IR}} + \omega_{\text{vis}}$ are indicated by dotted lines.

As shown in Figure 7.A.1, for all but the reddest 3 coumarins in the series (C6, C525, C545) the extinction spectrum at ω_{vis} is just above or within the noise floor of the absorption measurement. To extract the value of $\varepsilon(\omega_{\text{vis}})$, we fit the band tail to an exponential $a \exp(k_{\text{edge}}\omega)$, which describes the band shape in the low-frequency Urbach region, as described in Section 7.4.1. In the case of C30 and C314, this fit essentially provides an extrapolation as $\varepsilon(\omega_{\text{vis}})$ is solidly in the noise floor. The fitted decay constants k_{edge} are plotted in Figure 7.A.2.

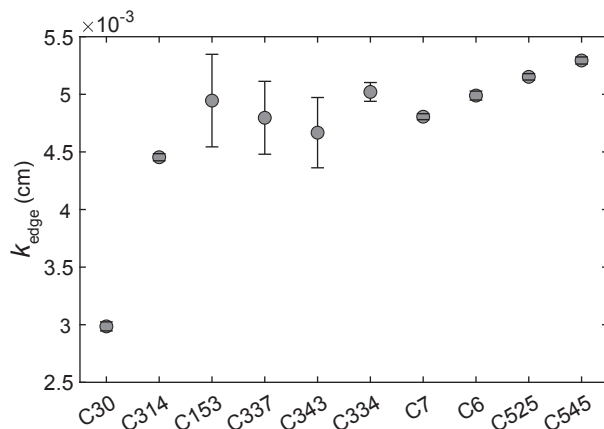


Figure 7.A.2: Exponential decay parameter k_{edge} from the fits to the low-frequency absorption edge in Figure 7.A.1. Error bars represent 95% confidence intervals from the fit routine.

7.A.2 Complete coumarin series high concentration FEIR data and acquisition details

The two-pulse transients were recorded with 40 fs τ_{enc} bins from roughly -3 to 10 ps (323 total bins), while the τ_{IR} scan range used for the FT spectra (raw data not shown) was from -2 to 8 ps with 2 fs bins (4995 total bins). The fastscanning procedure used to sweep these delays as well as the processing steps for FT spectra are described in Chapter 4. In both cases, the scan speed of the delay stage was 2 mm/s (scan rates of ~ 3 and ~ 0.15 ms per bin,

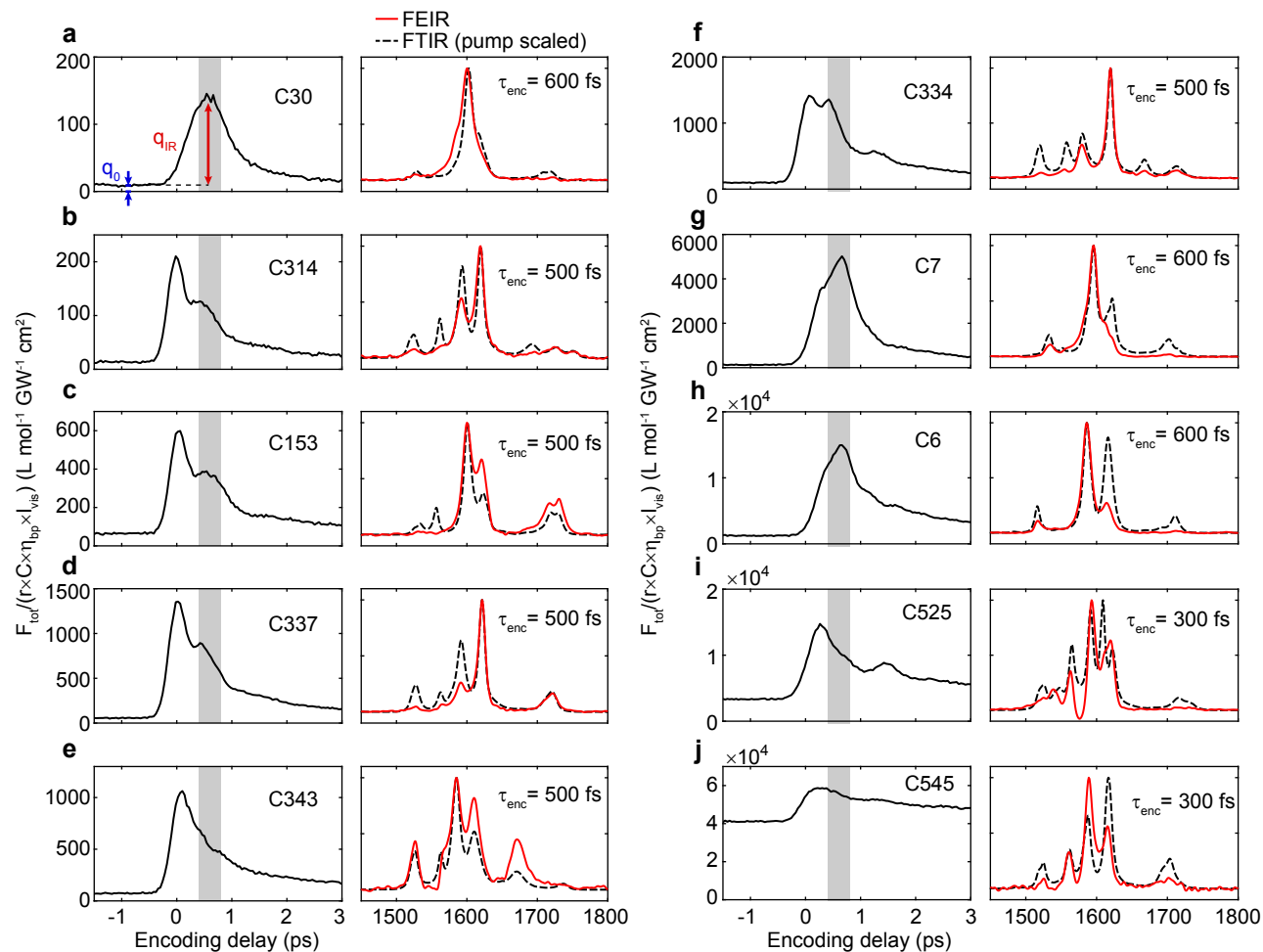


Figure 7.A.3: Complete coumarin series data in brightness units. (a-j) Left panels: Total photon output F_{tot} from two-pulse experiments on each coumarin plotted in brightness units. The effective FEIR (q_{IR}) and direct excitation (q_0) brightness are indicated by arrows in (a) and are found analogously for the remaining data. Right panels: Comparison of IR pump spectrum-scaled FTIR spectra (dashed line) with FEIR spectrum (solid line) at the encoding delay indicated.

respectively), and photon counts were accumulated over many scans. To represent the data acquisition time in these measurements, Figure 7.A.4 shows the effective integration time per bin (T_{bin}), i.e. number of scans times scan rate per bin, for each measurement in Figure 7.A.3. The total data acquisition time of a measurement (T_{total}) is found by multiplying T_{bin}

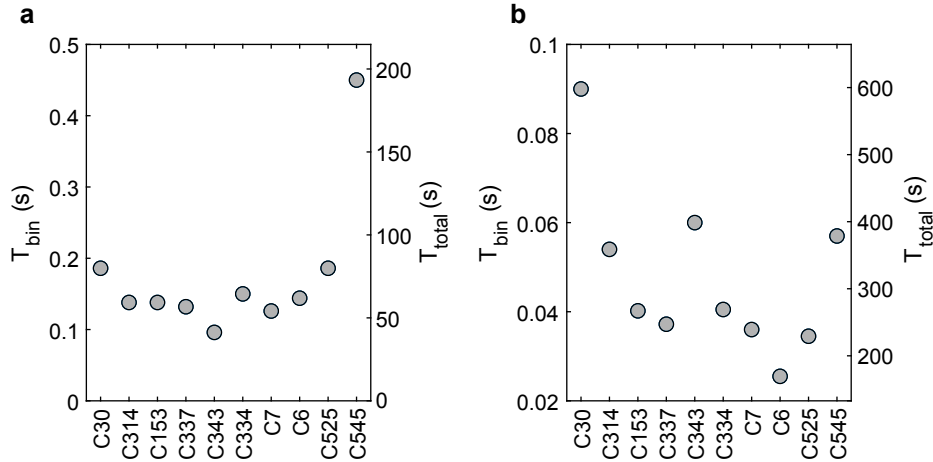


Figure 7.A.4: Integration time per bin (T_{bin} , left axis) and total experimental acquisition time (T_{total} , right axis) for (a) the two-pulse transients and (b) spectra shown in Figure 7.A.3.

by the total bin number and constant factor of ~ 1.33 which accounts for dead-time during stage turnaround and software latency.

7.A.3 Instrument-dependent uncertainty in brightness values

Estimating the error in the experimental FEIR and one-photon brightnesses is difficult due to the many parameters used in their determination, as well as factors beyond direct control. Here we investigate the contribution from the most important of this latter category—day-to-day variations in IR intensity and the overall alignment of the instrument. Figure 7.A.5(a) shows the q_{IR} and q_0 values from 12 independent measurements on C6 each taken on separate days during the period when the data was collected. These measurements shared the same nominal experimental configuration including the use of glass coverslips. The vertical and horizontal bars indicate intervals of 2 standard deviations around the mean in q_{IR} and q_0 , respectively. Notably, the variation in these values are highly correlated to each other as evident from the clustering along the diagonal. Figure 7.A.5(b) shows the corresponding

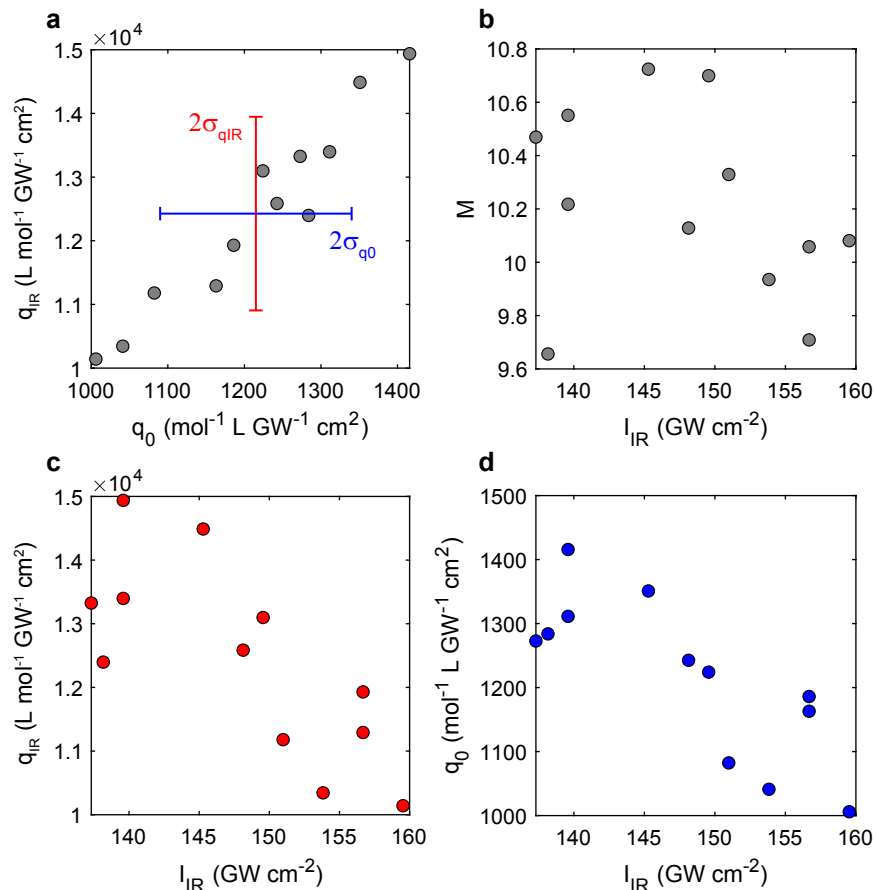


Figure 7.A.5: Experimental uncertainty in brightness values. (a) q_{IR} vs. q_0 from repeat measurements on C6 ($\mu_{q_{\text{IR}}} = 1.24 \times 10^4$ L mol $^{-1}$ GW $^{-1}$ cm $^{-2}$, $\sigma_{q_{\text{IR}}} = 0.15 \times 10^4$ L mol $^{-1}$ GW $^{-1}$ cm $^{-2}$, $\mu_{q_0} = 1.22 \times 10^3$ L mol $^{-1}$ GW $^{-1}$ cm $^{-2}$, $\sigma_{q_0} = 0.13 \times 10^3$ L mol $^{-1}$ GW $^{-1}$ cm $^{-2}$). (b) M , (c) q_{IR} , and (d) q_0 vs. I_{IR} from the same set of measurements.

modulation ratios against I_{IR} (calculated from the measured average IR power out of the OPA assuming a constant pulse duration, spot size, and transmission factor), which shows day-to-day variations with mean $\mu = 148$ GW cm $^{-2}$ and standard deviation $\sigma = 8$ GW cm $^{-2}$. M does not appear to be correlated to I_{IR} over this range, which is at odds with the linear power dependence assumed in our model. As shown in Figures 7.A.5(c) and (d), both q_{IR} and q_0 are anti-correlated with I_{IR} over this range, which explains part of the spread and

correlation in panel (a). As noted in Section 7.2.2, these IR intensities are near the upper limit that can be tolerated before thermal effects become severe, leading to more significant decreases in overall fluorescence collection efficiency and eventually bubble formation in the solvent. The negative trend in q_{IR} and q_0 in panels (c) and (d) is most likely a result of such a thermal effect, although of manageable severity. Because of this thermal effect, we will use the average value of I_{IR} when converting between q_{IR} and q . The remaining variation in q_{IR} and q_0 is likely due to the overall microscope alignment. Systematic errors in sample concentration were not characterized.

7.A.4 Brightness vs. extinction on linear axes, FEIR brightness at signal maximum, and correlation incorporating ε_{IR}

Table 7.3: FEIR and one-photon background brightnesses

Coumarin	q (L mol ⁻¹ GW ² cm ⁻⁴)	q_{IR} (L mol ⁻¹ GW cm ⁻²)	$q_{\text{IR}}^{\text{max}}$ (L mol ⁻¹ GW cm ⁻²)	q_0 (L mol ⁻¹ GW cm ⁻²)
30	7.79×10^{-1}	1.24×10^2	1.36×10^2	9.80
314	5.89×10^{-1}	9.33×10^1	1.97×10^2	1.38×10^1
153	1.90	3.01×10^2	5.35×10^2	6.43×10^1
337	4.35	6.90×10^2	1.30×10^3	5.61×10^1
343	3.00	4.75×10^2	9.89×10^2	7.35×10^1
334	5.81	9.21×10^2	1.32×10^3	9.65×10^1
7	2.79×10^1	4.41×10^3	4.89×10^3	1.26×10^2
6	7.94×10^1	1.24×10^4	1.37×10^4	1.24×10^3
525	4.66×10^1	7.39×10^3	1.14×10^4	3.36×10^3
545	9.20×10^1	1.46×10^4	1.75×10^4	4.11×10^4

Table 7.3 lists the numerical values for three versions of the FEIR brightness (q , q_{IR} , and $q_{\text{IR}}^{\text{max}}$) and the one-photon background brightness q_0 . As mentioned in the previous section,

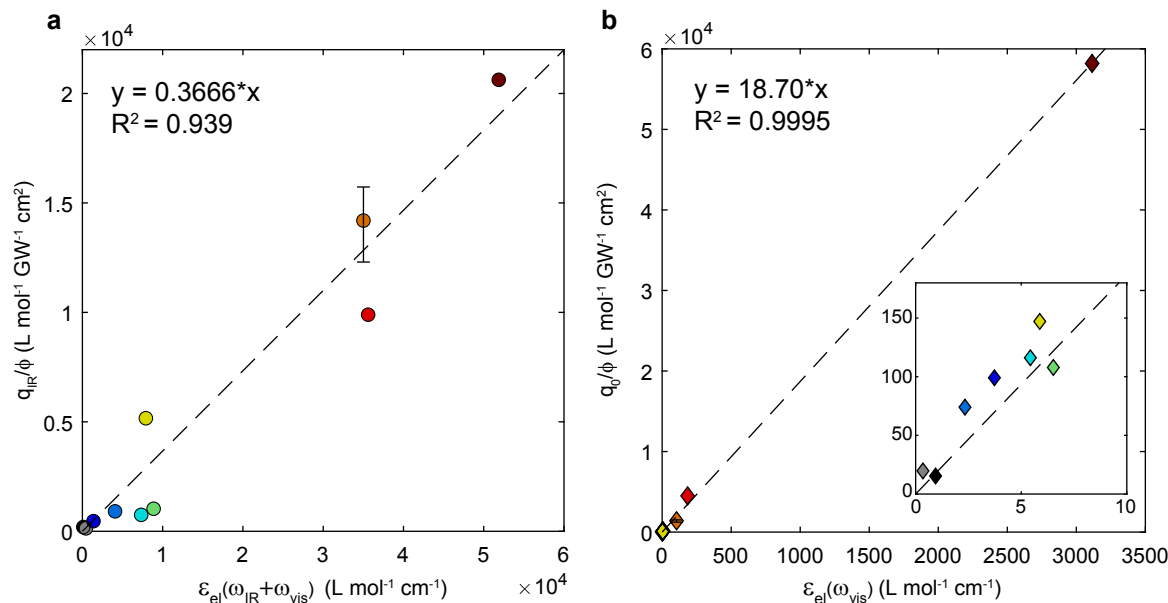


Figure 7.A.6: Brightness and electronic extinction correlations on linear axes. (a) q_{IR} vs. $\epsilon_{\text{el}}(\omega_{\text{IR}} + \omega_{\text{vis}})$ and (b) q_0 vs. $\epsilon_{\text{el}}(\omega_{\text{vis}})$ on linear axes. These data and the linear regressions (dashed lines) are the same as shown Figure 7.5(a). The vertical error bars for C6 indicate a range of 2 standard deviations from experimental uncertainty referred to in Section 7.4.3 and described in Section 7.A.3. The inset in (b) shows a blown up view of the points near the origin.

q is derived from q_{IR} by dividing out the average value of I_{IR} over all measurements in order to avoid including spurious variations due to thermal effects (present with glass coverslips). $q_{\text{IR}}^{\text{max}}$ is analogous to q_{IR} but uses the maximum value of F , regardless of the encoding delay at which it occurs. Figure 7.A.6 shows the same data as Figure 7.5(a), but on linear axes with q_{IR} vs. $\epsilon_{\text{el}}(\omega_{\text{IR}} + \omega_{\text{vis}})$ and q_0 vs. $\epsilon_{\text{el}}(\omega_{\text{vis}})$ displayed on separate plots. The linear regressions were performed on this unmodified data, and the logarithmic scaling in Figure 7.5(a) is merely to show the many decades in each axis.

Figure 7.A.7 compares the correlation between effective FEIR cross-section and $\epsilon_{\text{el}}(\omega_{\text{IR}} + \omega_{\text{vis}})$ using q as defined in Section 7.4.3 (averaging over $400 < \tau_{\text{enc}} < 800$ fs) and alternately using the maximum signal, i.e. $q_{\text{IR}}^{\text{max}}/I_{\text{IR}}$. Using the signal maximum produces a higher R^2

value and slightly higher slope. The inset in panel (b) shows the ratios of FEIR brightnesses calculated using the two methods. Panel (c) shows the M values using the maximum signal against κ (cf. Figure 7.5). The resulting correlation (correlation coefficient 0.69) is better than the case shown in Section 7.4.3, but still diffuse.

Figure 7.A.8 shows the correlation between q/ϕ and the product of $\varepsilon_{\text{el}}(\omega_{\text{IR}} + \omega_{\text{vis}})$ and ε_{IR} as defined by Eq. 7.14 and displayed for each coumarin in the inset to panel (a).

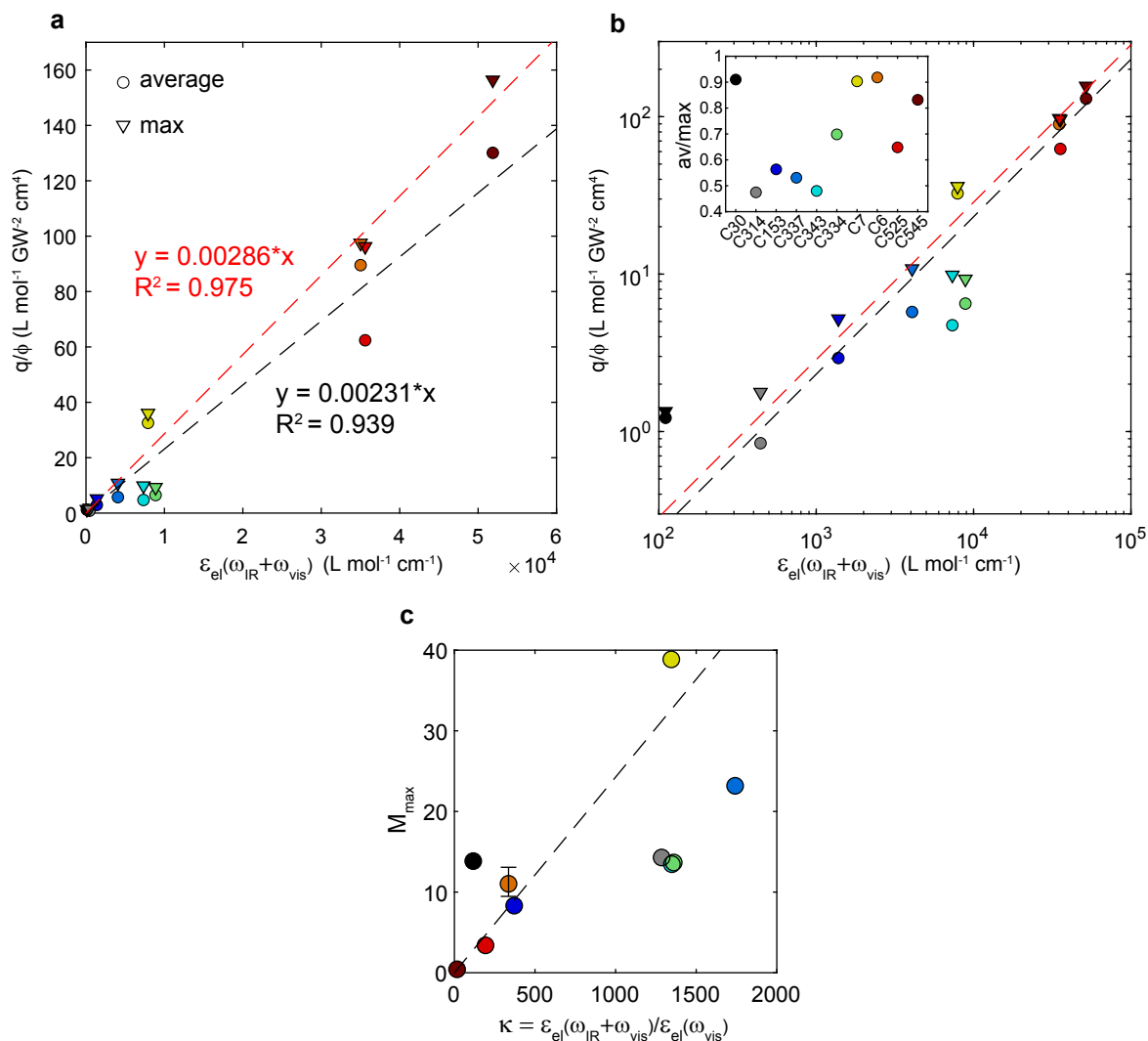


Figure 7.A.7: Effect on the q/ϕ vs. $\epsilon_{el}(\omega_{IR} + \omega_{vis})$ correlation when alternately using the signal maximum (triangles, regression line in red) instead of the averaged signal as in Section 7.4.3 (circles, regression line in black). (a) linear axes and (b) log-log axes. Ratios of FEIR brightness from the averaged signal to max signal (insert). (c) M using the signal maxima vs. κ , with dashed line showing the quotient of the (red) linear regression slope with the q_0 vs. $\epsilon_{el}(\omega_{vis})$ slope.

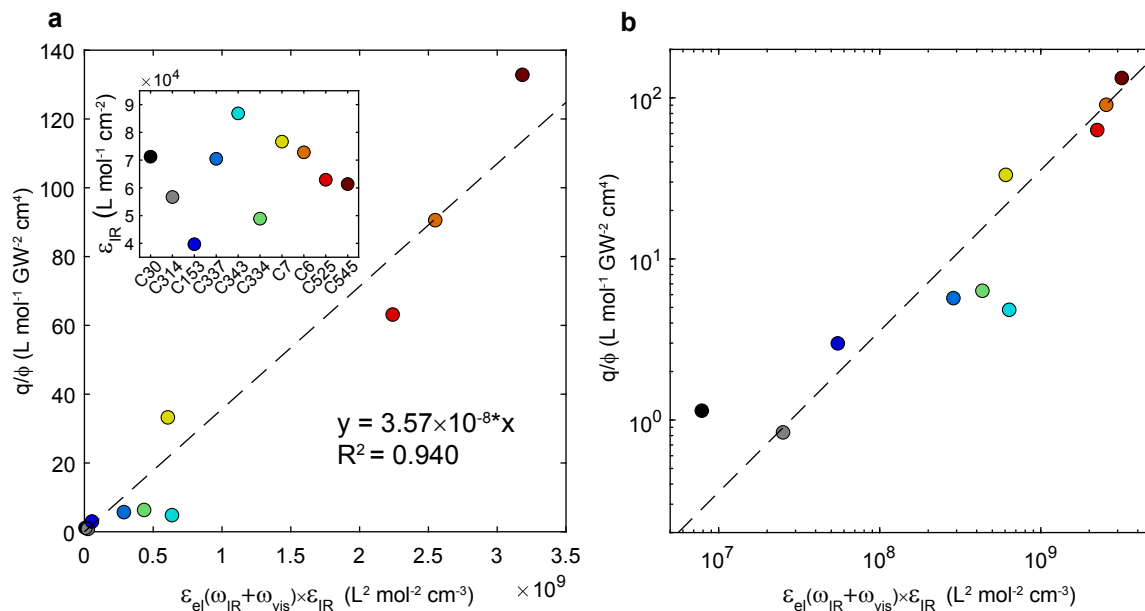


Figure 7.A.8: q/ϕ vs. $\epsilon_{\text{IR}} \times \epsilon_{\text{el}}(\omega_{\text{IR}} + \omega_{\text{vis}})$ on (a) linear and (b) log-log axes. Linear regressions indicated by dashed lines. The inset in (a) shows the ϵ_{IR} value for each coumarin.

7.A.5 C6 and C7 concentration and visible intensity dependent data

Figures 7.A.9 and 7.A.10 show the full concentration and I_{vis} dependent FEIR data used in Section 7.4.4. The raw count rate F_{tot} , background subtracted F count rate, and normalized F signal are shown for each concentration and intensity. The IR intensity is nominally constant, but varies day-to-day with a similar spread as discussed in Section 7.A.3. These measurements used CaF₂ coverslips. For all but 1 nM C7, two repeated measurements for each concentration and I_{vis} point were made and both are shown. The F count rate used in Figures 7.6 and 7.7 is the mean over $400 < \tau_{\text{enc}} < 800$ fs averaged over the repeat measurements, while the background $F_0 + B$ is determined from the mean over $-3 < \tau_{\text{enc}} < -1$ ps. In each case the error bars represent 2 standard deviations. For the measurements

that exhibit saturation in I_{vis} , there is a small change in the shape of the decay transient (most apparent in the normalized signals) consistent with the suppression of the maximum, however the effect is subtle. The integration time per bin and total experimental acquisition times are summarized in Figure 7.A.11.

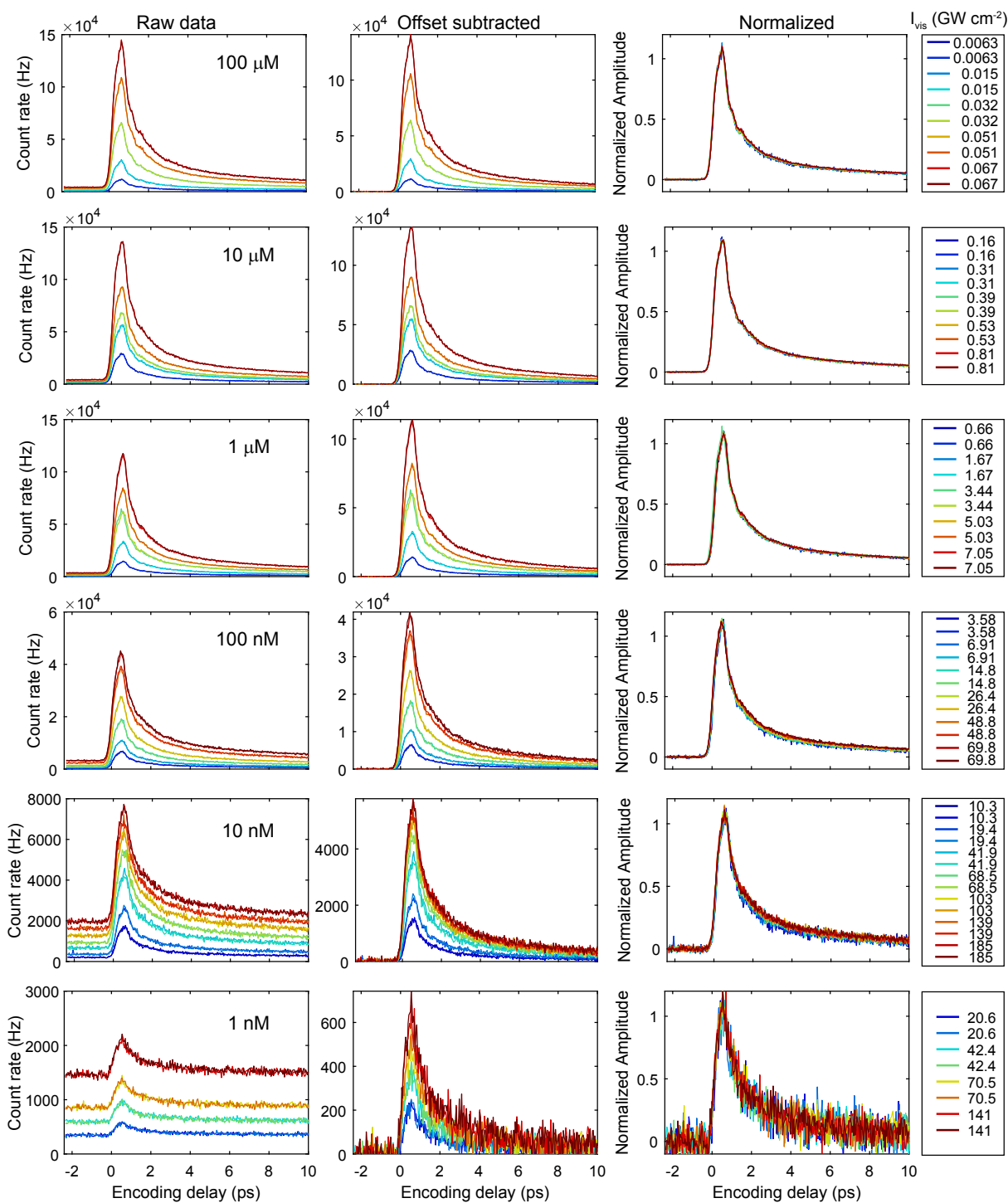


Figure 7.A.9: C6 concentration and I_{vis} dependent two-pulse FEIR data.

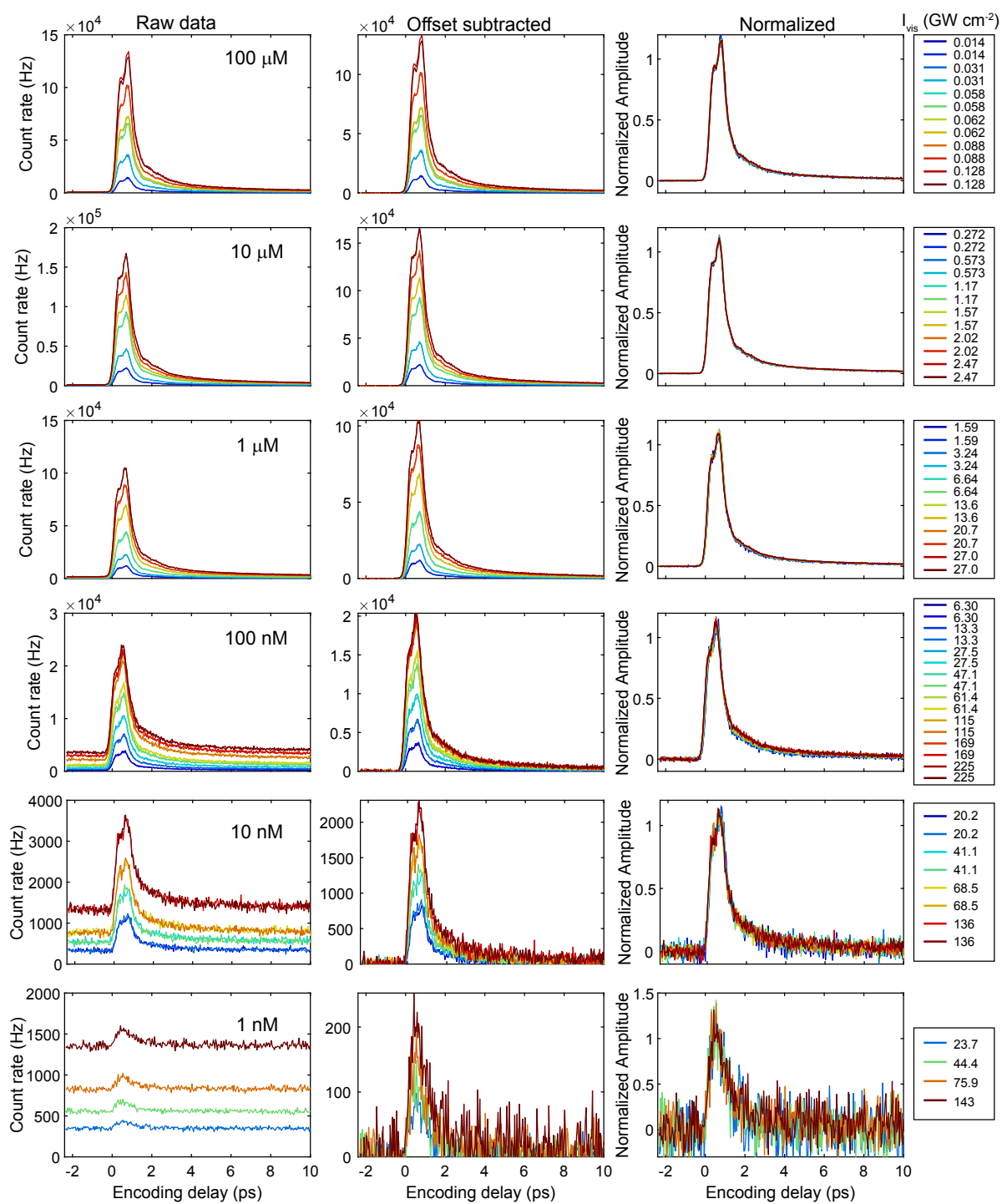


Figure 7.A.10: C7 concentration and I_{vis} dependent two-pulse FEIR data.

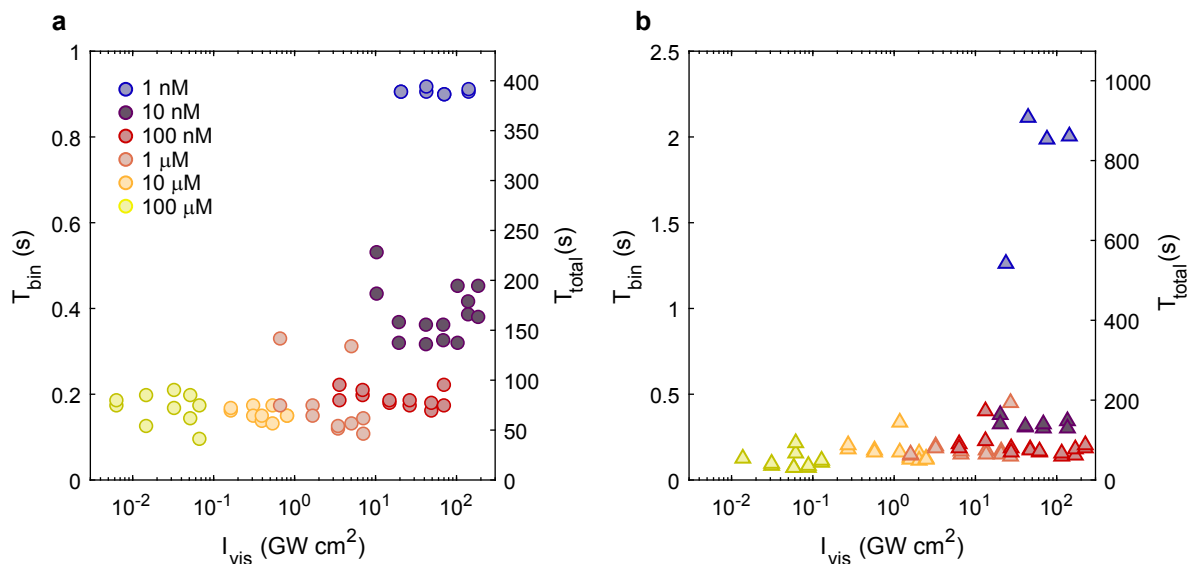


Figure 7.A.11: Integration time per bin (T_{bin} , left y axis) and total experimental acquisition time (T_{total} , right y axis) for the measurements on (a) C6 and (b) C7.

7.A.6 Limiting concentrations of the coumarin series

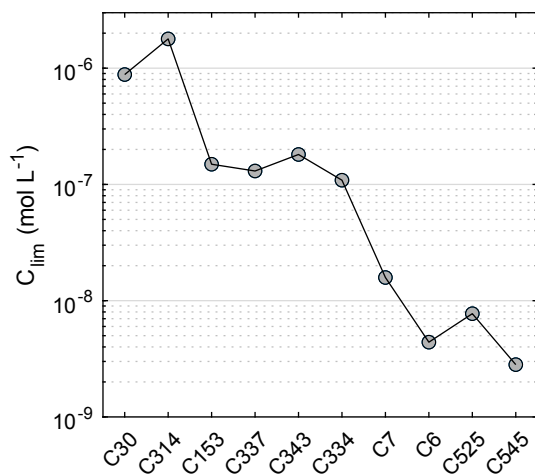


Figure 7.A.12: C_{lim} (Eq. 7.19) for the coumarin series, using the q_{IR} values measured with glass coverslips (Table 7.3). The C_{lim} values for the newer sample configuration using CaF_2 coverslips are ~ 3 times lower.

7.A.7 Details of encoding transition saturation behavior

The saturation curves for C6 and C7 shown in Figure 7.7 are reproduced here in Figure 7.A.13(a) and shown on log-log axes in Figure 7.A.13(b). We have also included a fit to the hyperbolic model (Eq. 7.20) which qualitatively follows the shape of the saturation curves slightly better than the exponential model. In the short pulse limit, saturation due to trapping in μ s-lifetime triplet states is predicted to produce a hyperbolic shape to the saturation curve.³³² The I_{vis} dependence of the background level is shown in Figure 7.A.13(c) and (d) for C6 and C7, respectively. The constant dark count level $d = 43$ Hz has been subtracted off. Due to the concentration-independent B contribution, dividing the count rates by concentration as in panels (a) and (b) would not collapse the data onto a single trend (this is evident by the diminishing vertical offsets between the trends for each concentration as the concentration decreases). Data for each concentration is fit to a power law, and the resulting exponents are shown in Figure 7.A.13(e) and (f). These exponents are close enough to 1 to indicate an approximately linear intensity-dependence, although there is a slight decrease in exponent for the lowest concentrations where the highest I_{vis} are used.

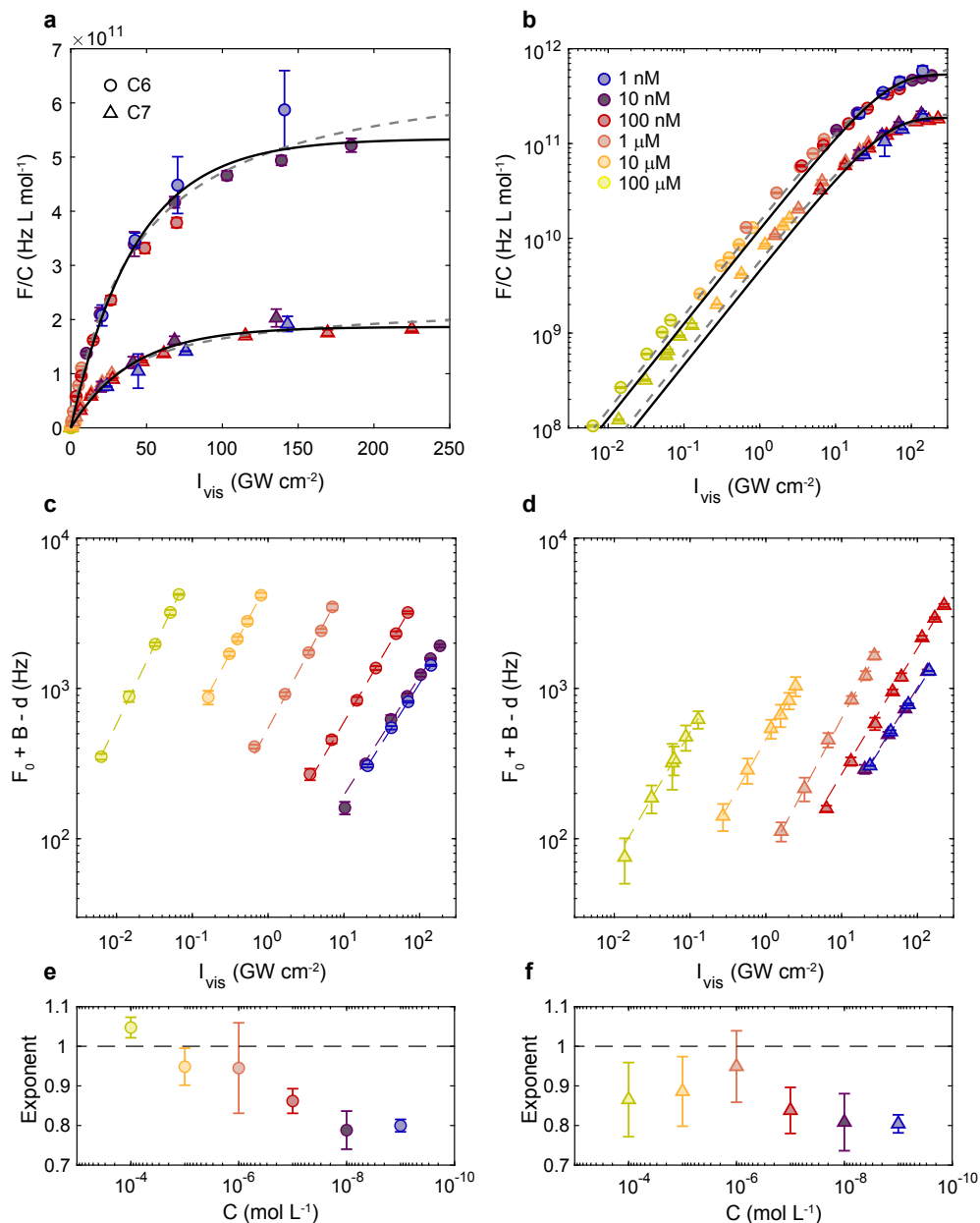


Figure 7.A.13: Details of the encoding transition saturation behavior. (a) F saturation curves for C6 (circles) and C7 (triangles). (b) same data as (a) on log-log axes. Fits to the exponential and hyperbolic models are shown by solid black and dashed gray lines, respectively. (c-d) Dark count subtracted background level vs. I_{vis} for C6 and C7, respectively. The color coding for concentration is the same as in (a) and (b). Power law fits for each concentration are shown by dashed lines. (e-f) Power law exponents from the fits in (c) and (d), respectively, with error bars indicating 95% confidence intervals.

7.A.8 Visible intensity dependence for C30 and C314

Figure 7.A.14 summarizes the I_{vis} dependence for the two most pre-resonant coumarins in the series: C30 and C314. As mentioned in Section 7.4.3, the background level is super-linear above a certain range, where it follows a quadratic I_{vis} dependence. The I_{vis} used for the brightness analysis are indicated by arrows in panels (b) and (e), and fall below the onset of this quadratic behavior. The F count rate also shows an apparent saturation behavior in I_{vis} , and the saturation thresholds I_S extracted from fits to the exponential model in discussed in Section 7.4.4 are listed. However, as the concentration is high (100 μM for both), the measured count rates correspond to very small overall excitation probabilities, so this mechanism for the observed saturation is unlikely. Given the deeply pre-resonant excitation conditions and the corresponding cross-over to multiphoton background excitation, a different explanation beyond our current treatment of the FEIR excitation process is likely needed to explain this effect.

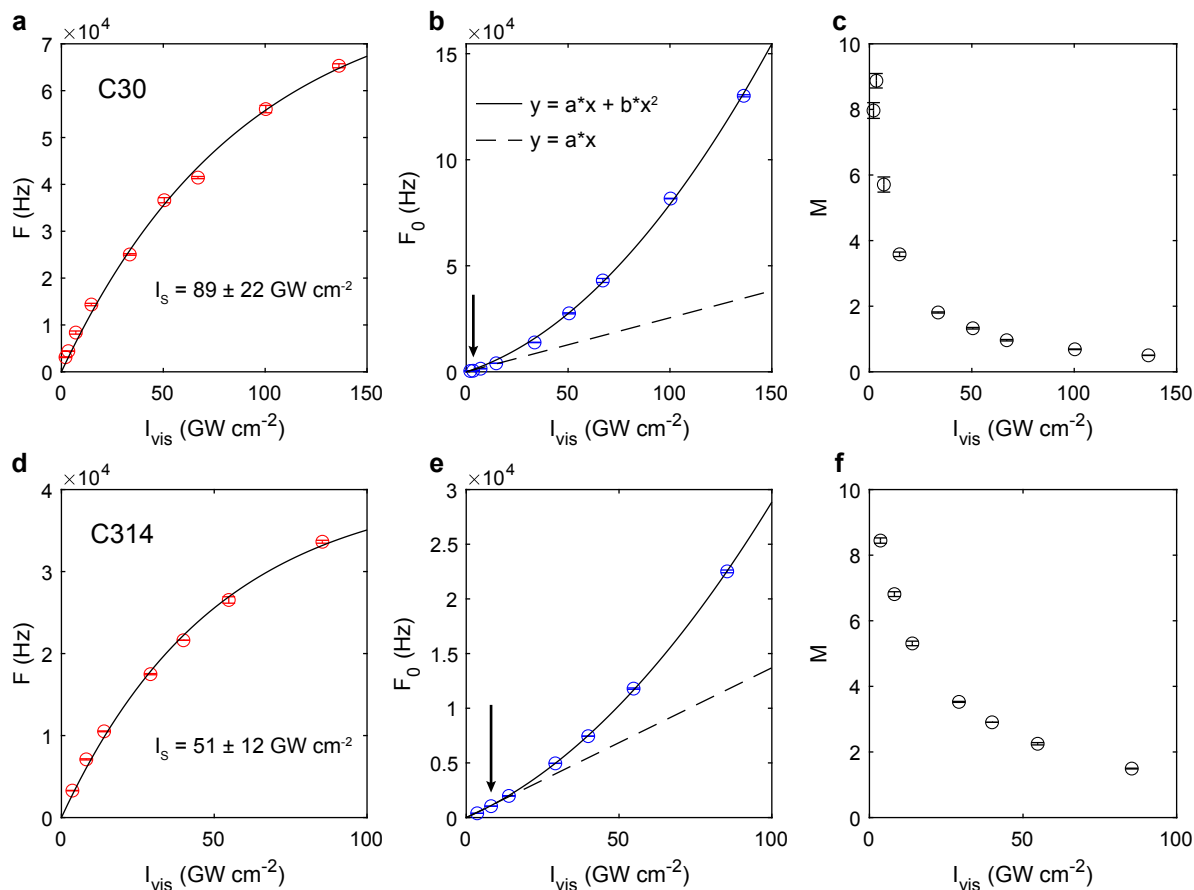


Figure 7.A.14: Super-linear visible intensity dependence for C30 and C314. I_{vis} -dependence of (a) F , (b) F_0 , and (c) M for C30. Panels (d-f) show the analogous information for C314. Fits to the exponential saturation model are shown as black lines in (a) and (d) with corresponding I_s listed. (b) and (e) include fits to a quadratic polynomial (solid line) and linear dependence of the first 3 points (dashed line), while the black arrows indicate the I_{vis} used in the brightness analysis.

7.A.9 FEIR-CS on 1 nM C6 solution

The FEIR-CS measurement used to determine $\langle N \rangle$ for the 1 nM C6 solution is shown in Figure 7.A.15. A CaF_2 coverslip was used. Details on the method and procedure are found in Chapter 6. $\langle N \rangle$ is given by the inverse of the early-time amplitude $G(0)$ of the correlation function, which is extracted from a fit to the data using a standard model assuming diffusion

through a Gaussian probe volume.

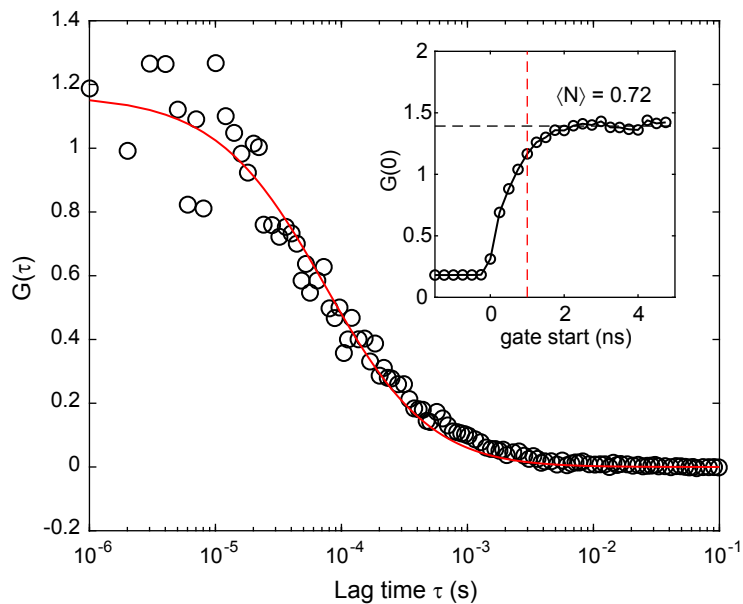


Figure 7.A.15: 1 nM C6 FEIR-CS measurement with updated sample configuration. FEIR-CS data at $I_{\text{vis}} = 42 \text{ GW cm}^{-2}$ (black circles) with fit to a standard diffusion model (red). The inset shows the dependence on the early time amplitude $G(0)$ extracted from the fit on the starting edge of the time-gate used to filter the photon stream, with the limiting value of 1.39 (corresponding to $\langle N \rangle = 0.72$) indicated. The red dashed line indicates the 1 ns starting edge of the time-gate used for the data in the main plot.

Chapter 8

Interpreting early encoding-delay FEIR signals

8.1 Overview

This chapter deals with the practical phenomenology of multimode FEIR signals at early encoding delays. Specifically, the ‘early-time’ region may refer to the range of encoding delays in which intermode vibrational coherence has not dephased, the IR/vis pulse-overlap region and its near vicinity, or both. As we have discussed previously in Chapters 2 and 3, vibrational coherence can lead to strange lineshapes and non-intuitive band intensity patterns in FEIR spectra, while the effect of the finite pulse durations and spectra can introduce further distortions that are most strongly apparent in the early-time region. At the same time, the FEIR signal size is invariably largest at early times, which compels us to work in this region for single-molecule or otherwise high-sensitivity applications. This state of affairs suggests that we had better get properly acquainted with the various quirks of early-time FEIR data.

With this in mind, our primary goal in this chapter is to develop some practical insight

into the ins and outs of early-time FEIR signals through a comparison of experimental data with finite-pulse response function calculations developed in Chapter 3. We will adopt a descriptive approach, and try to catalogue some of the early-time behavior at a qualitative level. Specifically, the calculations in this chapter are intended to be demonstrative, rather than to facilitate proper fits to the measured data (a much more serious undertaking). That is, instead of trying to rigorously extract molecular parameters from FEIR measurements, we will attempt to show how various features in the data can be seen to arise from minimal models of the molecular response and pulse sequence with a reasonable choice of parameters. We will not treat orientational effects in these calculations.

The experimental data examined here are from FEIR measurements on coumarin dyes, with the IR pulse tuned to cover the highest-frequency coumarin ring modes and lactone carbonyl stretch. The full data set of measurements on 10 coumarins is used in Chapter 7 to explore the impact of experimental resonance conditions on practical aspects of detection sensitivity. All measurements were performed in acetonitrile-d₃ solution at high concentrations (30 - 100 μ M). Our focus here is on the τ_{enc} -dependent behavior of these signals, and we refer the reader to Chapter 7 for more details regarding the FEIR experiments and further characteristics of the coumarins.

Figure 8.1 shows two-pulse FEIR transients from the full series of coumarins. Overall, there are distinct variations in the shape of the signals, including steepness of the rising edge, location of the signal maximum, and character of beating (or lack thereof). For example, in some cases the signal peaks notably beyond the extent of the pulse-overlap region, while in others the peak occurs near $\tau_{\text{enc}} = 0$ ps. We will specifically treat coumarin 6 (C6) and coumarin 153 (C153) as case studies, which are for the most part representative of these two types of τ_{enc} -dependent behavior, respectively. Additionally, C6 in this pump configuration is

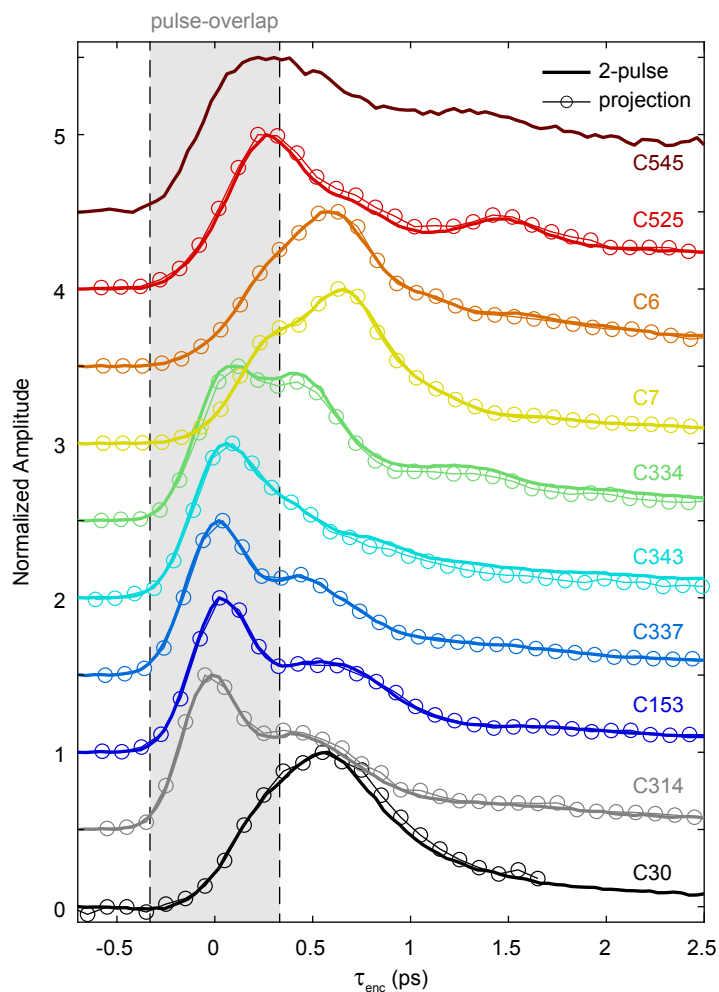


Figure 8.1: Early-time two-pulse FEIR signals measured for 10 coumarin dyes with $\omega_{\text{IR}} = 1620 \text{ cm}^{-1}$ (same data as in Chapter 7). The projection of the τ_{enc} -dependent FEIR spectrum onto the τ_{enc} -axis is overlaid to demonstrate the projection-slice relationship. The full τ_{enc} -dependent spectrum was not measured for C545. The $1/e^2$ full-width of the pulse-overlap region is indicated by the grayed-out box. Traces are normalized to their respective maxima and offset vertically by increments of 0.5 for clarity.

the model system we have used for demonstrating single-molecule sensitivity by FEIR-CS in Chapter 6, and therefore has obvious importance to the development of FEIR spectroscopy presented in this thesis. For good measure, we include τ_{enc} -dependent FEIR data for the full series of coumarins in Appendix 8.A.

The width of the pulse-overlap region indicated in Figure 8.1 is the more generous 663 fs $1/e^2$ full-width (e.g. as compared to the 390 fs fwhm) of the IR/vis cross-correlation, calculated assuming Gaussian IR and visible pulse durations of 230 and 315 fs, respectively. As discussed in Chapter 4, identifying the absolute origin of time along the τ_{enc} axis is currently difficult in this IR frequency range, and in fact our assignment of $\tau_{\text{enc}} = 0$ here is an educated guess. Therefore, another goal of this chapter is to show why this guess is reasonable through comparison against finite-pulse calculations. While the assignment of $\tau_{\text{enc}} = 0$ was thus done after the fact, the relative timing of the transients for the different coumarins is correct up to an uncertainty of ~ 100 fs.

8.2 Coumarin 6

Figure 8.2 shows the FTIR linear absorption spectrum of C6 with ground-state normal mode frequencies and intensities calculated by density functional theory (DFT) overlaid. The DFT calculation employed the B3LYP functional with 6-31G(d,p) basis set, and were carried out in the Gaussian09 package using a polarizable continuum model to account for the acetonitrile solvent. As we will see, the FEIR data can be adequately described by considering the three most intense bands, labelled in order of descending frequency as ν_{R1} (experimental frequency 1616 cm^{-1}), ν_{R2} (1586 cm^{-1}), and ν_{R3} (1515 cm^{-1}). With the help of the DFT calculation, we assign these three bands to various high-frequency ring vibrations of

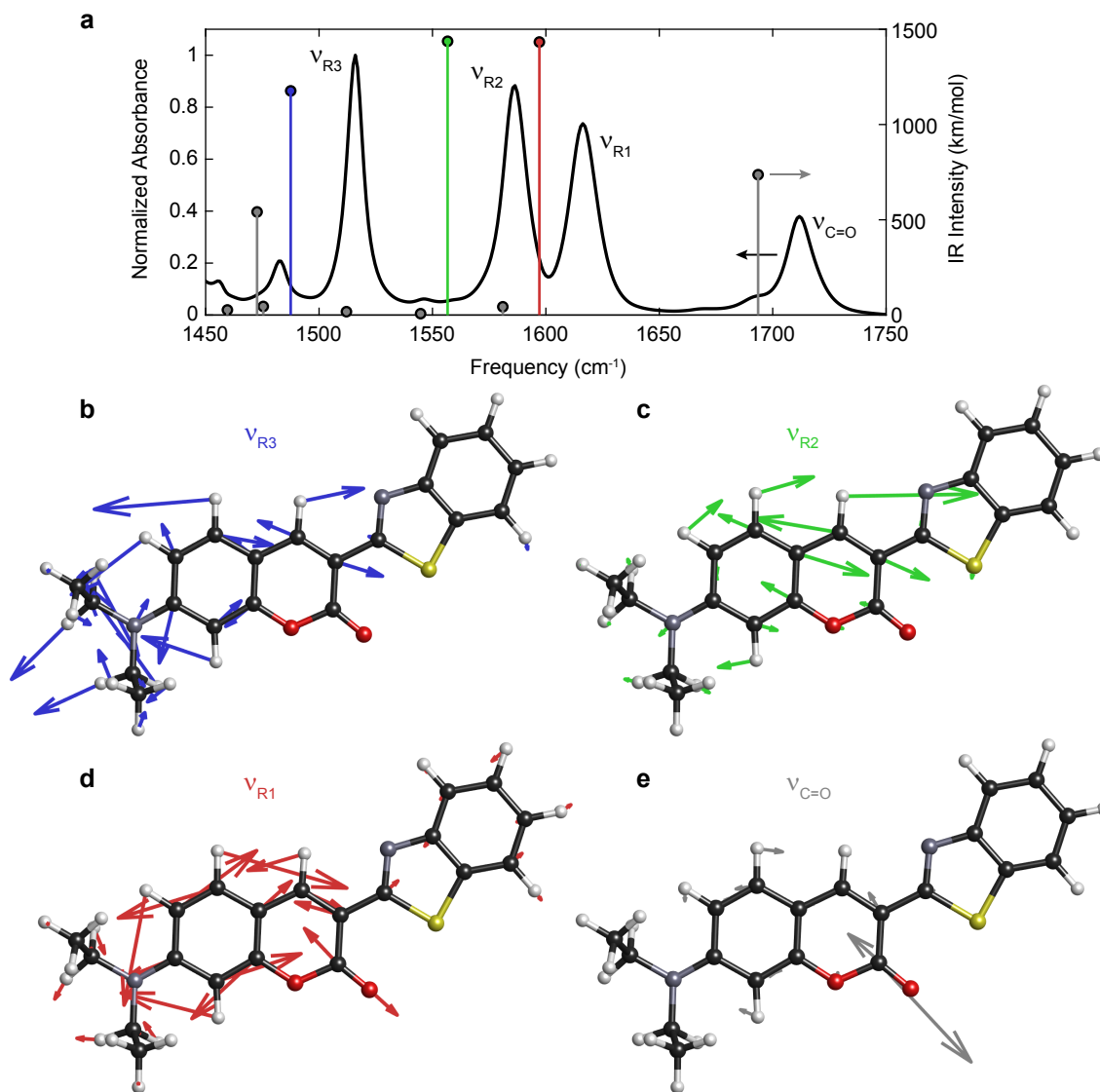


Figure 8.2: C6 experimental FTIR absorption spectrum and normal modes calculated by DFT. (a) Solvent-subtracted and normalized FTIR absorption (left y axis) with frequencies and intensities of DFT-calculated normal modes (right y axis) overlaid. The calculated frequencies have been scaled by the factor 0.961.³³⁷ The three normal modes involved in the FEIR calculation ν_{R3} , ν_{R2} , ν_{R1} , as well as the carbonyl stretch $\nu_{C=O}$, are assigned in (a), and their atomic displacements are shown with the same color-coding in (b)-(e), respectively. In each case, the displacement vectors are normalized to the largest in the normal mode.

the coumarin core, for which normal mode atomic displacement vectors are shown in Figures 8.2(b)-(d). The mode ν_{R3} also has substantial contributions from bending motions of the diethylamino substituent. The band at 1712 cm^{-1} in experiment corresponds to the lactone carbonyl stretch $\nu_{C=O}$ (Figures 8.2(e)), but is not sufficiently FEIR active to contribute to the measurement with the IR pump spectrum used, and will not be included in the present calculation.

Mode	ω_{10} (cm^{-1})	μ_{10}	$\langle 0^e 1^g \rangle$	Γ_{10}^{-1} (fs)	Γ_{11}^{-1} (fs)	Γ_{e1}^{-1} (fs)
ν_{R1}	1616	0.9	-0.11	1200	1200	10
ν_{R2}	1586	1	0.27	1000	1000	10
ν_{R3}	1515	1.12	0.12	1000	1000	10

Table 8.1: Response function parameters for C6. The intermode coherence dephasing between each pair of fundamentals is set to $\Gamma_{nm}^{-1} = 400$ fs.

To model the FEIR spectroscopy of this molecule, we construct a minimal system consisting of these three vibrational modes. Along the lines of the theory discussed in Chapter 2, this results in a 5-level system consisting of the global ground state, the three singly-excited vibrational states, and the zero-quantum level of the electronic excited state which is the target state. We employ the homogeneous limit, and the relevant parameters for the response function are listed in Table 8.1. The frequencies ω_{10} are taken from experiment, and we similarly choose the vibrational transition moments μ_{10} and dephasings Γ_{10}^{-1} so that the resulting Lorentzian lines that roughly match the intensities and linewidths from the FTIR spectrum. Vibrational population relaxation is set by assuming lifetime broadening. We note that only the relative sizes of the modes' transition matrix elements are meaningful in the calculation. The magnitude and relative sign of the FC factors $\langle 0^e | 1^g \rangle$ are chosen to produce qualitative agreement with the FEIR measurement, although we note that the

resulting values in Table 8.1 also agree reasonably well with those calculated from optimized ground- and excited-state electronic structure calculations,²⁹³ and their arbitrary common scaling factor was chosen to highlight this correspondence. There are three pairs of intermode vibrational coherences, and we set the dephasing time for each of these to 400 fs.

The overall comparison of the experimental and calculated τ_{enc} -dependent FEIR spectroscopy of this system is shown in Figures 8.3 and 8.4. Panels (a) and (d) of Figure 8.3 compare the coverage of the IR pulse spectrum with the vibrational resonances in experiment and the calculation, respectively. For the calculation, the IR pulse is taken to be a transform-limited Gaussian centered at $\omega_{\text{IR}} = 1600 \text{ cm}^{-1}$ with $\Delta\omega_{\text{IR}} = 120 \text{ cm}^{-1}$ bandwidth, which results in a duration of $\tau_{p,\text{IR}} = 123 \text{ fs}$. This pulse spectrum is slightly narrower than that in the experiment ($\omega_{\text{IR}} = 1620 \text{ cm}^{-1}$ with $\Delta\omega_{\text{IR}} \sim 140 \text{ cm}^{-1}$), but is closely matched in profile on the red-side where the vibrational resonances are located. Residual 2nd-order dispersion in the experiment leads to a somewhat chirped IR pulse duration of $\sim 230 \text{ fs}$. Panel (d) shows both the model's linear IR absorption spectrum S_{IR} as well as the IR-vibronic spectrum S_{vibr} introduced in Chapter 3 to represent the FEIR activity of each mode. The visible encoding pulse is taken to be transform-limited with $\Delta\omega_{\text{vis}} = 50 \text{ cm}^{-1}$ bandwidth resulting in a 297 fs pulse duration. As in Chapter 3, the visible pulse is tuned so that $\omega_{e0} = \omega_{\text{IR}} + \omega_{\text{vis}}$. Similarly, the dephasing time of the encoding transitions are all set to $\Gamma_{e1}^{-1} = 10 \text{ fs}$, which produces lineshapes sufficiently broad to not cause variations in resonance with the encoding pulse.

We start by identifying some of the most salient features of the experimental signals. Figure 8.3(b) shows the full τ_{enc} -dependent FEIR spectrum, while slices taken along the frequencies of the three bands are plotted in Figure 8.3(c). Overall, the response is dominated the $\nu_{\text{R}2}$ mode. Coherent amplitude modulation is strongly apparent over the $\nu_{\text{R}3}$ band, but

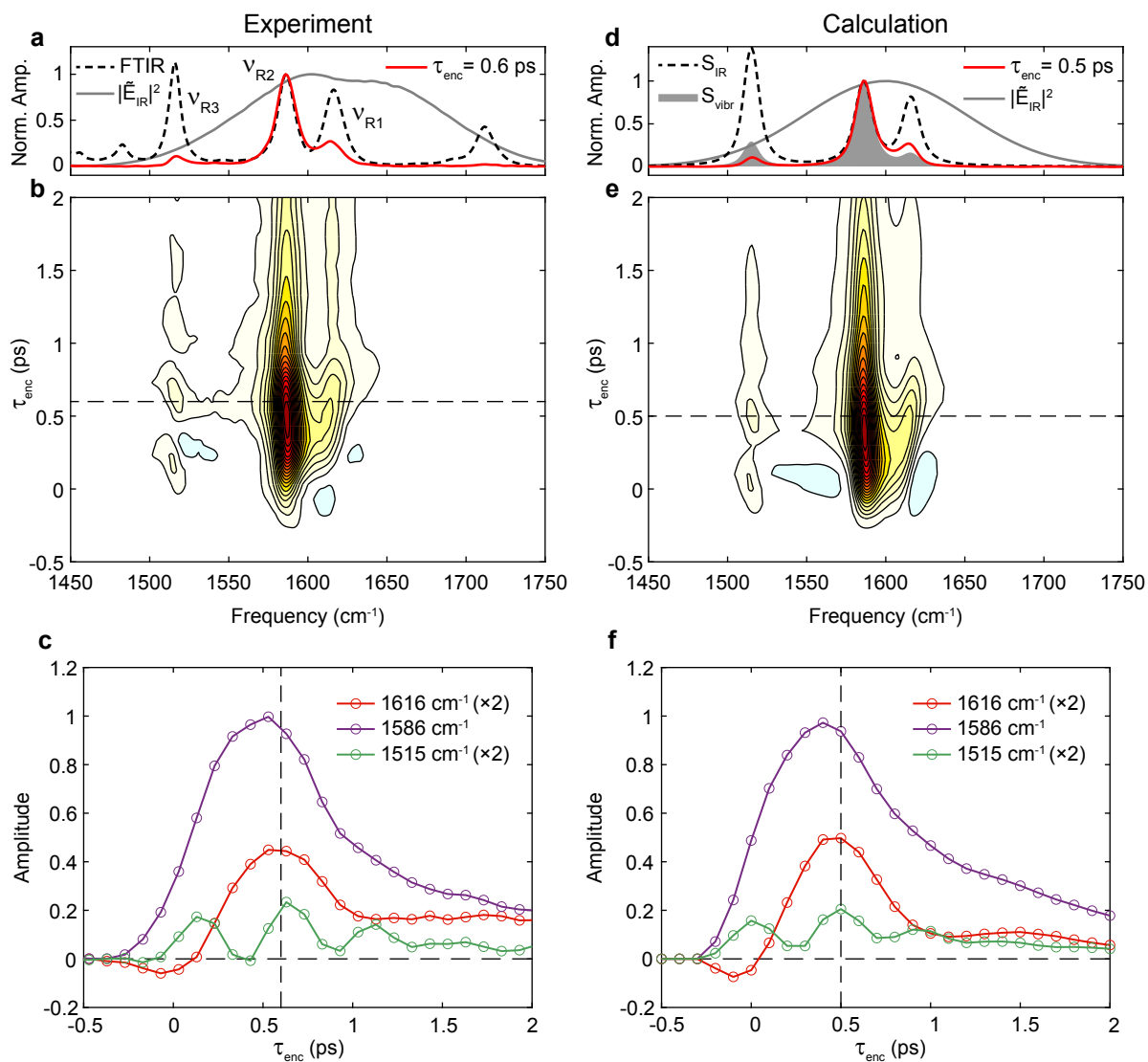


Figure 8.3: Comparison of (a)-(c) experimental and (d)-(f) calculated τ_{enc} -dependent FEIR spectra of C6. (a) Experimental FTIR spectrum (dashed black), IR pulse spectrum (gray), and FEIR spectrum at $\tau_{\text{enc}} = 600$ fs (red). (b) Experimental τ_{enc} -dependent FEIR spectrum. (c) Slices along the three vibrational mode frequencies ν_{R1} (1616 cm^{-1}), ν_{R2} (1586 cm^{-1}), and ν_{R3} (1515 cm^{-1}). Dashed lines in (b) and (c) indicate $\tau_{\text{enc}} = 600$ fs. Panels (d)-(f) show the calculated signals analogous to those in (a)-(c), where $\tau_{\text{enc}} = 500$ fs has been used instead. Contouring spacing for both surfaces (b) and (e) is set at 5%. In (c) and (f) the ν_{R1} and ν_{R3} traces have been scaled up by a factor of 2 for more convenient visualization.

much less obvious on the other two resonances. Figure 8.4(a) shows the experimental two-pulse signal. The τ_{enc} -projection of the surface in Figure 8.3(b) has been superimposed to demonstrate the projection-slice relationship between these two measurements. The two-pulse signal correspondingly exhibits very little obvious beating, although subtle features in its τ_{enc} -dependent shape are visible. Notably, this signal is peaked at ~ 600 fs—safely beyond the pulse-overlap region as shown in Figure 8.1. At this encoding delay, the bands in the FEIR spectrum (Figure 8.3(a)) have essentially absorptive lineshapes that closely match those in the FTIR spectrum, although their relative amplitudes are reweighed by the differing vibronic activities. Taken together, these characteristics (i.e. intuitive spectrum at maximum signal strength) make this system an ideal example case for demonstrating high sensitivity FEIR vibrational detection, hence its use in Chapters 4 and 6 and Refs. [242–244].

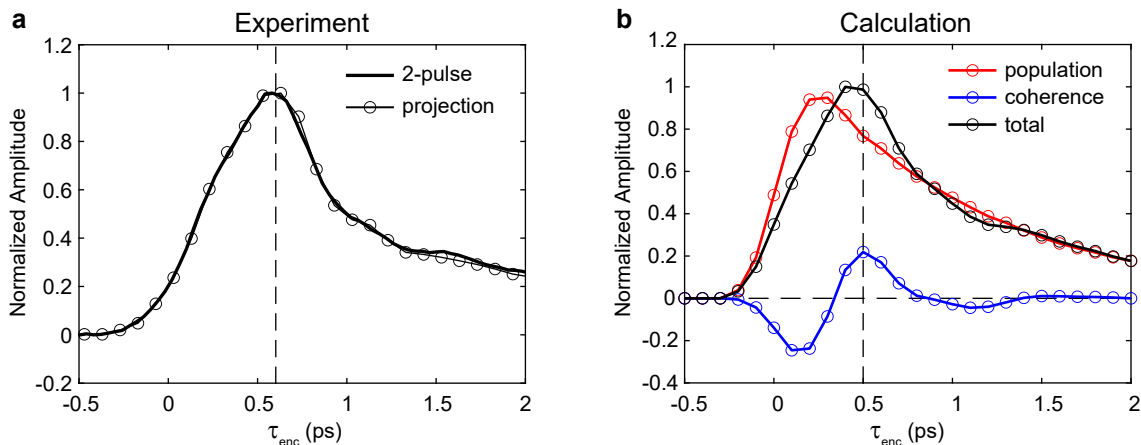


Figure 8.4: Comparison of experimental and calculated two-pulse signals from C6. (a) Experimental two-pulse signal (solid) and τ_{enc} -projection of the spectrum (circles). (b) Calculated two-pulse signal (black) and its decomposition into population (red) and coherence (blue) contributions. Vertical dashed lines indicate $\tau_{\text{enc}} = 600$ and 500 fs in (a) and (b), respectively.

To gain insight into the origin of these features we turn to the calculation. The calculated signals are shown in Figures 8.3(d)–(f) and Figure 8.4(b). The three-mode model with

finite pulses succeeds in qualitatively capturing the τ_{enc} -dependence of the spectrum and corresponding two-pulse transient across the entire early-time region. Overall, the observed behavior can be seen to originate from the dominant FEIR activity of the ν_{R2} mode (modelled activities appearing in ratio of 0.24:1:0.13 for $\nu_{\text{R1}}:\nu_{\text{R2}}:\nu_{\text{R3}}$), the signs of the coherences between pairs of modes, and the coverage by the IR pulse spectrum. The much larger activity of ν_{R2} causes the amplitude of the coherences to be significant relative to population response over the ν_{R3} and ν_{R1} bands, while being only a minor relative contribution over ν_{R2} . The relative signs of the FC factors, $(-, +, +)$ for $(\nu_{\text{R1}}, \nu_{\text{R2}}, \nu_{\text{R3}})$, are such that the $\nu_{\text{R2}}-\nu_{\text{R3}}$ coherence is positively signed (in the sense defined in Section 2.4.5 of Chapter 2), while the $\nu_{\text{R2}}-\nu_{\text{R1}}$ coherence is negatively signed. The $\nu_{\text{R1}}-\nu_{\text{R3}}$ coherence is negligible due to the small FEIR activities of the modes involved, as well as being more strongly suppressed by the finite pulses' convolution filter effect owing to its higher τ_{enc} evolution frequency. The signature of the positive $\nu_{\text{R2}}-\nu_{\text{R3}}$ coherence is seen in the appearance near $\tau_{\text{enc}} = 0$ fs of the first oscillatory peak of the ν_{R3} band (Figures 8.3(e)-(f)). On the contrary, the negative $\nu_{\text{R2}}-\nu_{\text{R1}}$ coherence results in a shallow negative dip along the ν_{R2} mode near $\tau_{\text{enc}} = 0$ fs, followed by a first maximum near $\tau_{\text{enc}} = 500$ fs.

A more detailed view of these interference effects, as well as the role of the pulses, is revealed in Figure 8.5, which shows the decomposition of the calculated τ_{enc} -dependent spectrum into population and coherence contributions in both the impulsive and finite-pulse cases. The frequency differences between the modes, $\omega_{\text{R2}} - \omega_{\text{R3}} = 71 \text{ cm}^{-1}$ and $\omega_{\text{R1}} - \omega_{\text{R2}} = 30 \text{ cm}^{-1}$, are such that $\omega_{\text{R2}} - \omega_{\text{R3}} \approx 2(\omega_{\text{R1}} - \omega_{\text{R2}})$. This difference-frequency relation between the mode pairs, together with their oppositely signed coherences, produces a striking coincidental alignment of their coherence phases. Specifically, the location of the negative $\nu_{\text{R2}}-\nu_{\text{R1}}$ coherence's first peak near $\tau_{\text{enc}} = 500$ fs (coherence phase $\phi_{nm} \sim \pi$) roughly coincides

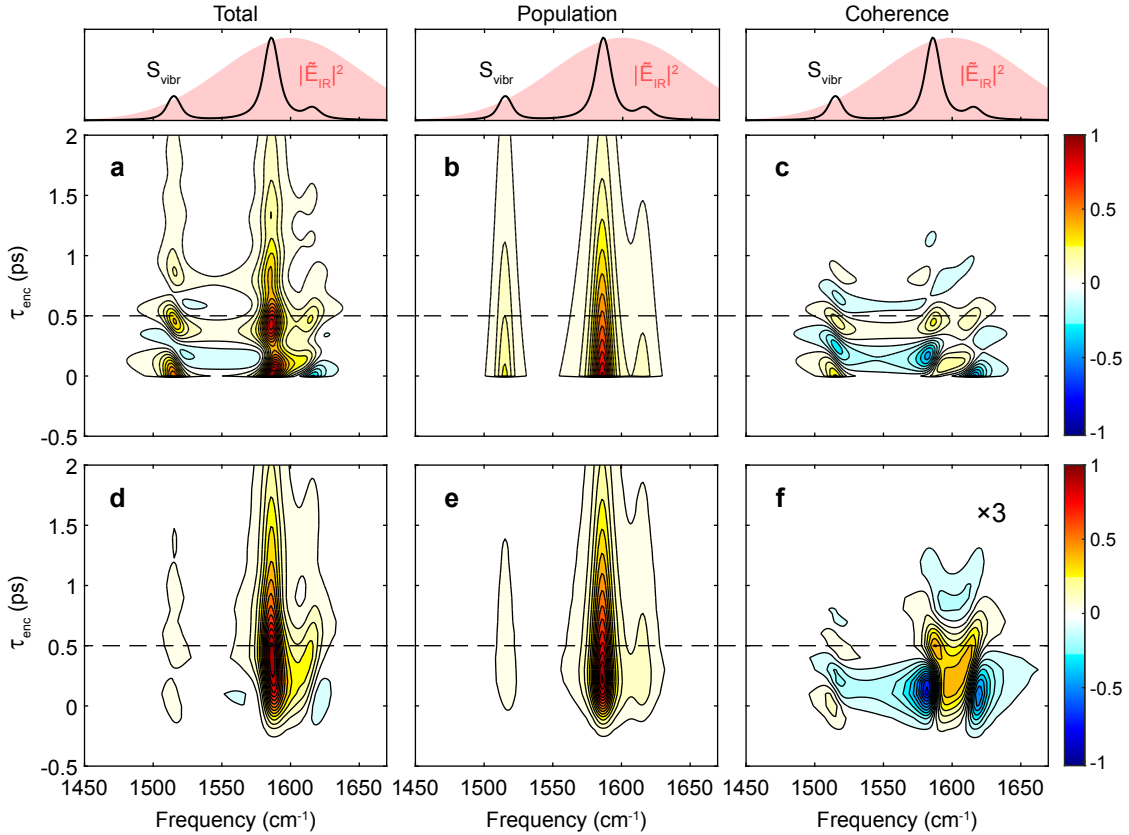


Figure 8.5: Comparison of impulsive and finite-pulse calculations for the C6 model system. Impulsive limit (a) total spectrum, (b) population contribution, and (c) coherence contribution. The upper panels plot the IR pulse spectrum overlaid on the IR-vibronic spectrum S_{vibr} . (d)-(f) show the analogous quantities as (a)-(c) for the finite-pulse case. In both cases the total spectrum is normalized to its maximum value, and the components are plotted on the same scale. In all cases the contour spacing is set at 6.7%. Panel (f) has been additionally scaled by a factor of 3 for better visualization given the small amplitude.

with the positive $\nu_{R2}-\nu_{R3}$ coherence's first recurrence ($\phi_{nm} \sim 2\pi$). As a result, the total coherence lineshape is essentially absorptive across all modes at this encoding delay, which can be seen in Figure 8.5(c). Then, as evident in Figure 8.5(f), the amplitude of the $\nu_{R2}-\nu_{R3}$ coherence is greatly reduced relative to that of $\nu_{R2}-\nu_{R1}$ through both spectral windowing by the IR pulse as well as the time-domain convolution filter effect.

The overall effect of the interference between these coherences and the population response are therefore seen to give rise to the convenient features of the C6 response mentioned above. Namely, the peaking of the ν_{R1} and ν_{R2} bands near $\tau_{\text{enc}} = 400\text{-}500$ fs in the calculation is due to alternating destructive and constructive interference of their negatively-signed coherence's $\phi_{nm} = 0$ minimum ($\tau_{\text{enc}} \sim 0$ fs) and $\phi_{nm} = \pi$ maximum ($\tau_{\text{enc}} \sim 500$ fs) with the population response, respectively. As these two bands together make up the majority of the overall response under these IR pump conditions, the two-pulse signal is correspondingly peaked near $\tau_{\text{enc}} = 500$ fs as well. In fact, as shown in Figure 8.4(b), roughly 20% of the total FEIR signal at maximum is due to coherence. The fact the all three modes then exhibit absorptive lineshapes at this encoding delay is due to the approximate alignment of coherence phases resulting from the chance difference-frequency relationship $\omega_{R2} - \omega_{R3} \approx 2(\omega_{R1} - \omega_{R2})$.

Overall, the good qualitative agreement between the signals' τ_{enc} -evolution in experiment and the calculation supports our assignment of $\tau_{\text{enc}} = 0$ in experiment. However, a more careful comparison reveals a discrepancy of $\sim 100\text{-}150$ fs in timing between the calculation and experiment, e.g. evident by the relative offset between the maxima of two-pulse signals in Figures 8.4(a) and (b). One possible contribution on the side of the calculation is our use of transform-limited Gaussian pulses, of which the IR is notably shorter than the chirped (and spectrally non-Gaussian) IR pulse in experiment. Similarly, our homogeneous three-mode model system is highly idealized, and we have not chosen its parameters by any rigorous optimization procedure. On the other hand, this timing discrepancy is also on the scale of the instrumental uncertainty in τ_{enc} from sample to sample (without a reliable auxiliary procedure for setting timing), and could therefore represent a legitimate error in our experimental $\tau_{\text{enc}} = 0$ assignment.

8.3 Coumarin 153

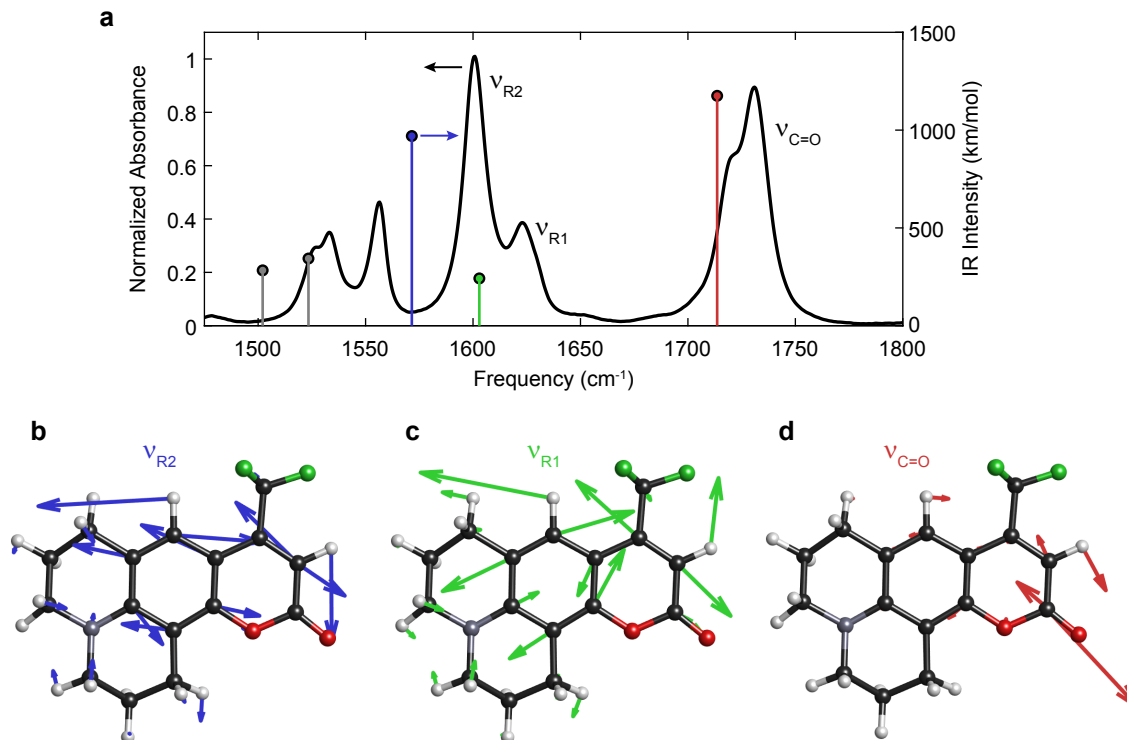


Figure 8.6: C153 experimental IR absorption spectrum and relevant normal modes calculated by DFT. Panels (a)-(d) are analogous to those in Figure 8.2.

In this section we present an analogous analysis of the FEIR signals of C153. As mentioned previously and demonstrated in Figure 8.1, our measurements on C153 exhibit a prominent signal peak near $\tau_{\text{enc}} = 0$, which is also observed in four other coumarins. Figure 8.6 shows the FTIR spectrum of C153 and its DFT-calculated normal modes, using the same level of theory as before in Section 8.2. Unlike in C6, the lactone carbonyl stretch $\nu_{\text{C=O}}$ of C153 (experimental peak frequency 1731 cm^{-1} , Figure 8.6(d)) is strongly FEIR active, which as we will see below has important consequences to the appearance of early-time signals. The band exhibits a broad linewidth with substructure consistent with the presence of two

split resonances. Similar behavior is often observed in unsaturated lactone carbonyl bands, and is likely due to a Fermi resonance.^{327–329} Indeed, many of the coumarin lactone carbonyls show similar complicated substructure (see e.g. Appendix 8.A or Chapter 7). However, for the FEIR calculation we will model the carbonyl as a single Lorentzian line. We will additionally include the two highest frequency ring vibrations ν_{R1} (1620 cm^{-1}) and ν_{R2} (1600 cm^{-1}), shown from the DFT calculation in Figures 8.6(c) and (b)), respectively. The lower frequency modes present in the spectrum are also of coumarin ring character, but do not contribute significantly to the FEIR response with the IR pump spectrum used and will not be considered.

Mode	ω_{10} (cm^{-1})	μ_{10}	$\langle 0^e 1^g \rangle$	Γ_{10}^{-1} (fs)	Γ_{11}^{-1} (fs)	Γ_{e1}^{-1} (fs)
$\nu_{C=O}$	1725	1.5	-0.31	400	600	10
ν_{R1}	1620	0.5	0.10	1000	1000	10
ν_{R2}	1600	1	-0.13	1000	1000	10

Table 8.2: Response function parameters for C153. The intermode coherence dephasing between each pair of modes is set to $\Gamma_{nm}^{-1} = 400$ fs.

We employ the same homogeneous 5-level model for the response function calculation, for which the system parameters are shown in Table 8.2. To account for the broader carbonyl lineshape, its dephasing is taken to be slightly faster than its population relaxation. The other parameters were chosen in similar fashion as in the case of C6 above, and all intermode coherence dephasings are set to 400 fs. We use the same pulse characteristics as in the C6 calculation, with the exception of setting the IR center frequency to $\omega_{IR} = 1620 \text{ cm}^{-1}$ to achieve more representative coverage of $\nu_{C=O}$.

The experimental and calculated FEIR signals are compared in Figure 8.7. Panels 8.7(a)-(c) shows the experimental IR spectral coverage of the vibrational bands, the τ_{enc} -dependent

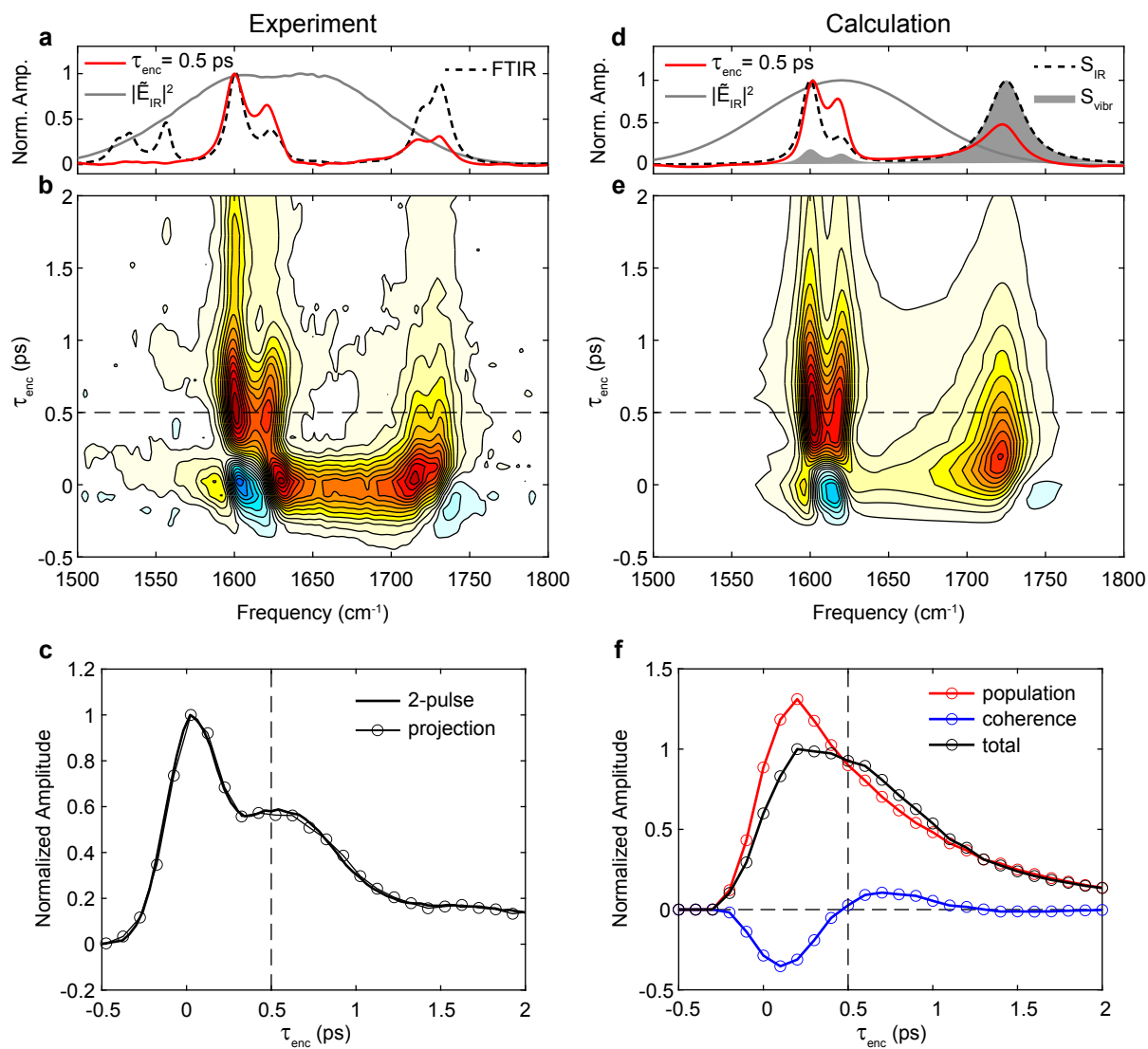


Figure 8.7: Comparison of (a)-(c) experimental and (d)-(f) calculated τ_{enc} -dependent FEIR signals of C153. (a) Experimental FTIR spectrum (dashed black), IR pulse spectrum (gray), and FEIR spectrum at $\tau_{\text{enc}} = 500$ fs (red). (b) Experimental τ_{enc} -dependent FEIR spectrum. (c) Experimental two-pulse signal (solid) and τ_{enc} -projection of the spectrum (circles). Panels (d)-(f) show the calculated signals analogous to those in (a)-(c). Panel (f) also shows the decomposition of the two-pulse signal (black) into population (red) and coherence (blue) contributions. Contour spacing in (c) and (e) is set at 6.7%. Dashed lines in (b)-(c) and (e)-(f) indicate $\tau_{\text{enc}} = 500$ fs.

spectrum, and the two-pulse signal. Comparing panels (b) and (c), we see that the peak in the two-pulse signal at $\tau_{\text{enc}} = 0$ ps corresponds to a broad ridge-like feature connecting the carbonyl resonance to that of the ring modes. The τ_{enc} -extent of this ridge (fwhm ~ 350 fs) is similar to the estimated duration of the IR/vis cross-correlation (fwhm ~ 390 fs). In addition to this ridge feature, the lineshapes of all three modes appear strongly phase-distorted in the vicinity of $\tau_{\text{enc}} = 0$ ps, evident e.g. in the substantial negative features near 1610 and 1740 cm^{-1} . Figures 8.7(d)-(f) show the analogous quantities from the calculation. Overall, the calculation captures much of the τ_{enc} -dependent shape of the spectral features, including the ridge and pattern of lineshape distortions near $\tau_{\text{enc}} = 0$ ps. However, the magnitude of the ridge feature is significantly smaller than in experiment, and as a result the calculation does not reproduce the spike in the two-pulse signal at $\tau_{\text{enc}} \sim 0$ ps.

As before, more insight into the τ_{enc} -dependence can be found by decomposing the calculated signals into population and coherence contributions, as well as comparing the finite-pulse and impulsive versions. Figure 8.8 shows this decomposition in both cases. Due to the large FEIR activity of $\nu_{\text{C=O}}$, the impulsive FEIR signals are strongly modulated by the $\nu_{\text{C=O}}-\nu_{\text{R1}}$ and $\nu_{\text{C=O}}-\nu_{\text{R2}}$ coherences, which evolve rapidly in τ_{enc} on account of the large >100 cm^{-1} difference-frequency between pairs of modes (Figures 8.8(a) and (c)). However, this high-frequency τ_{enc} -modulation is consequently strongly suppressed by the low-pass convolution filtering action of the finite pulses, and is essentially completely washed out. The only remaining coherent contribution is therefore from the negatively-signed $\nu_{\text{R1}}-\nu_{\text{R2}}$ coherence (Figure 8.8(f)). In the vicinity of $\tau_{\text{enc}} = 0$ ps this inter-ring-mode coherence interferes destructively with the population response, contributing to the distorted lineshape. The overall amplitude over the ring modes peaks near $\tau_{\text{enc}} = 500$ fs due to the overlap of the coherence maximum (at $\phi_{nm} < \pi$ because the dephasing is substantially faster than the oscillation

period) with the population features. At this location the resulting ν_{R1} and ν_{R2} lineshapes are therefore roughly absorptive (although their inter-peak spacing is reduced by $\sim 4 \text{ cm}^{-1}$), while $\nu_{C=O}$ is similarly absorptive due to the complete suppression of its coherences.

The distortion of the $\nu_{C=O}$ band near $\tau_{\text{enc}} = 0$ ps is necessarily unrelated to vibrational coherence. As shown in Figure 8.8(e), this distortion is present in the population response and is a result of the pulse-overlap-induced phase distortion discussed in Section 3.6 of Chapter 3. The coverage of the $\nu_{C=O}$ band by the extreme blue wing of the IR pulse spectrum gives rise to the notable severity of this phase distortion as well as its sign (positive/negative wings on the low/high frequency side of the band). In fact, the low-frequency wing of this phase-twisted lineshape itself is seen to constitute the ridge feature, which is so dominant due to the broad linewidth of the $\nu_{C=O}$ band.

Overall, much of the phenomenology of the early-time region can therefore be explained by the influence of the finite pulses on interfering population and coherence contributions, as well as additional pulse-overlap-induced lineshape distortions. However, the full amplitude of the $\tau_{\text{enc}} = 0$ ridge in the experimental spectrum, or corresponding spike in the two-pulse signal, is critically not accounted for. One possible conclusion is that a substantial portion of the amplitude of this ridge/spike does not originate from the vibrations' FEIR response, but rather arises from vibrationally-nonresonant IR + visible two-photon absorption (TPA). Indeed, this feature has many of the characteristics of the TPA response analyzed in Chapter 3, including being restricted to the IR/vis temporal overlap, and being spectrally-extended along much of the IR pulse spectrum. If this feature is indeed due at least partially to TPA, its center can be used to set $\tau_{\text{enc}} = 0$, which would further support our current timing assignment for the coumarin experiments.

C153 exhibits the most extreme case of this ridge/spike feature, which, as shown in

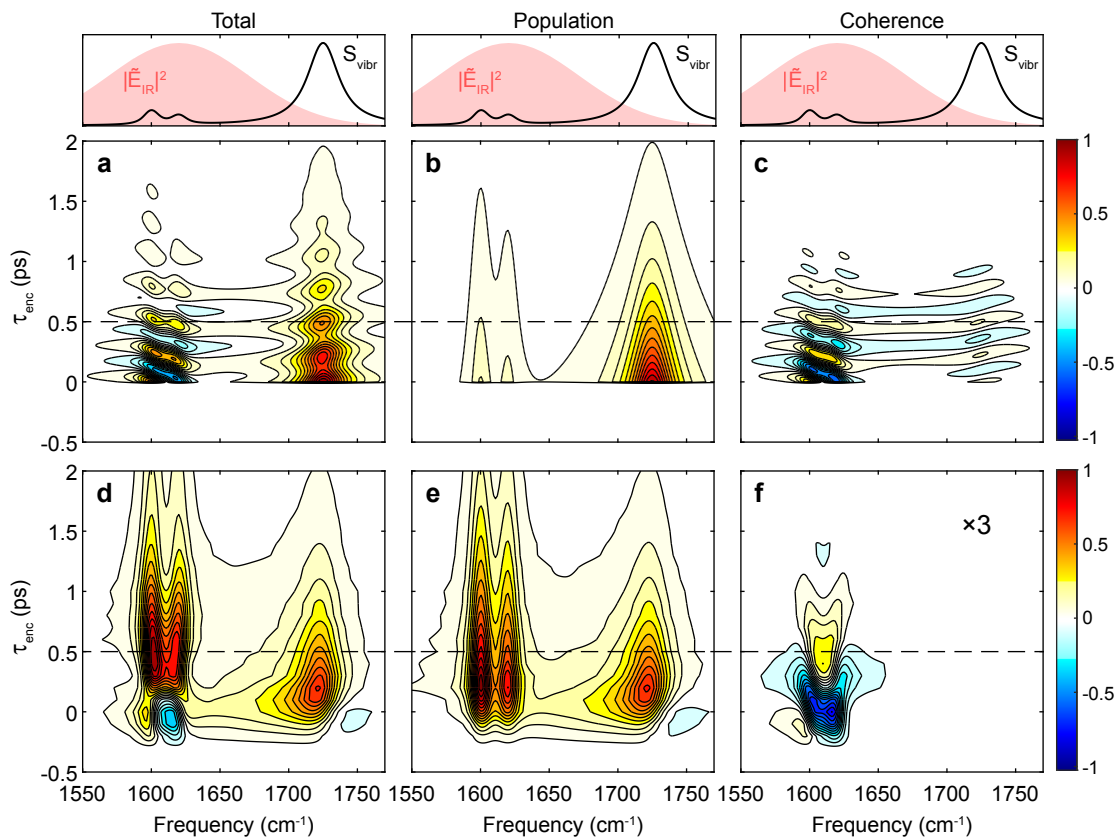


Figure 8.8: Comparison of impulsive and finite-pulse calculations for the C153 model system. All panels are analogous to those in Figure 8.5. Contour spacing is set to 6.7%

Appendix 8.A, can also be found in the measurements on C314, C337, C343, and C334 (and perhaps in C525 at very low amplitude). We may speculate on two possible reasons for why this subset of the coumarins studied show this feature. First, these coumarins are those which show some degree of response from their carbonyl modes under these pump conditions. As the carbonyl bands fall under the blue-wing of the IR pulse spectrum, the ridge feature could be at least partially caused by the pulse-overlap lineshape phase distortion in a similar manner as in the C153 calculation above. Second, these coumarins are also those whose overall experimental FEIR cross-section falls below the electronic resonance trend line

discussed in Chapter 7, and therefore can be considered to have intrinsically weaker FEIR response than the others. As such, the balance in strength between FEIR excitation and TPA could be shifted more toward TPA for these dyes, resulting in the relative prominence of a ridge/spike feature. A much more extreme example of the dominance of TPA over FEIR response can be found in the experiments on the C337 nitrile mode in Chapter 9.

8.A Appendix: Coumarin series τ_{enc} -dependent FEIR data with $\omega_{\text{IR}} = 1620 \text{ cm}^{-1}$

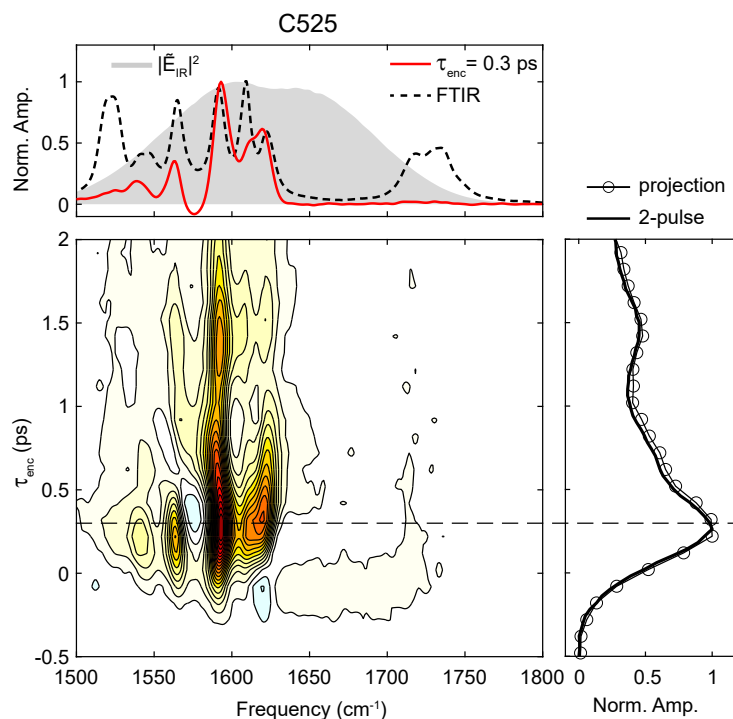


Figure 8.A.1: Coumarin 525 τ_{enc} -dependent FEIR data. Top panel: FTIR spectrum (dashed black), IR pulse spectrum (gray), and FEIR spectrum at the indicated encoding delay. Center panel: τ_{enc} -dependent FEIR spectrum. Contour spacing is set at 5%. Right panel: Experimental two-pulse signal (solid) and τ_{enc} -projection of the spectrum (circles). The encoding delay used for the FEIR spectrum in the top panel is indicated by a dashed line across the central and right panels.

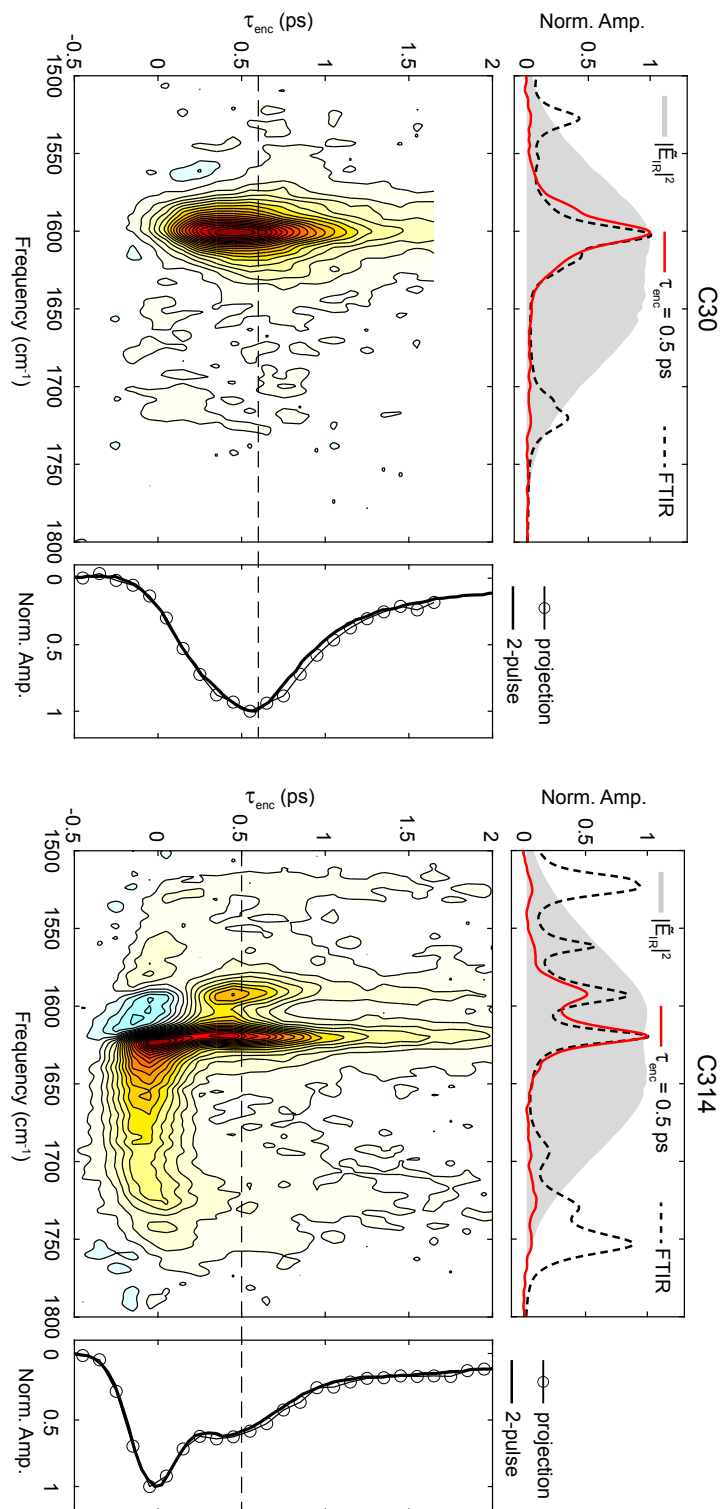


Figure 8.A.2: Coumarin 30 and 314 experimental τ_{enc} -dependent FEIR data. All panels are analogous to Figure 8.A.1.

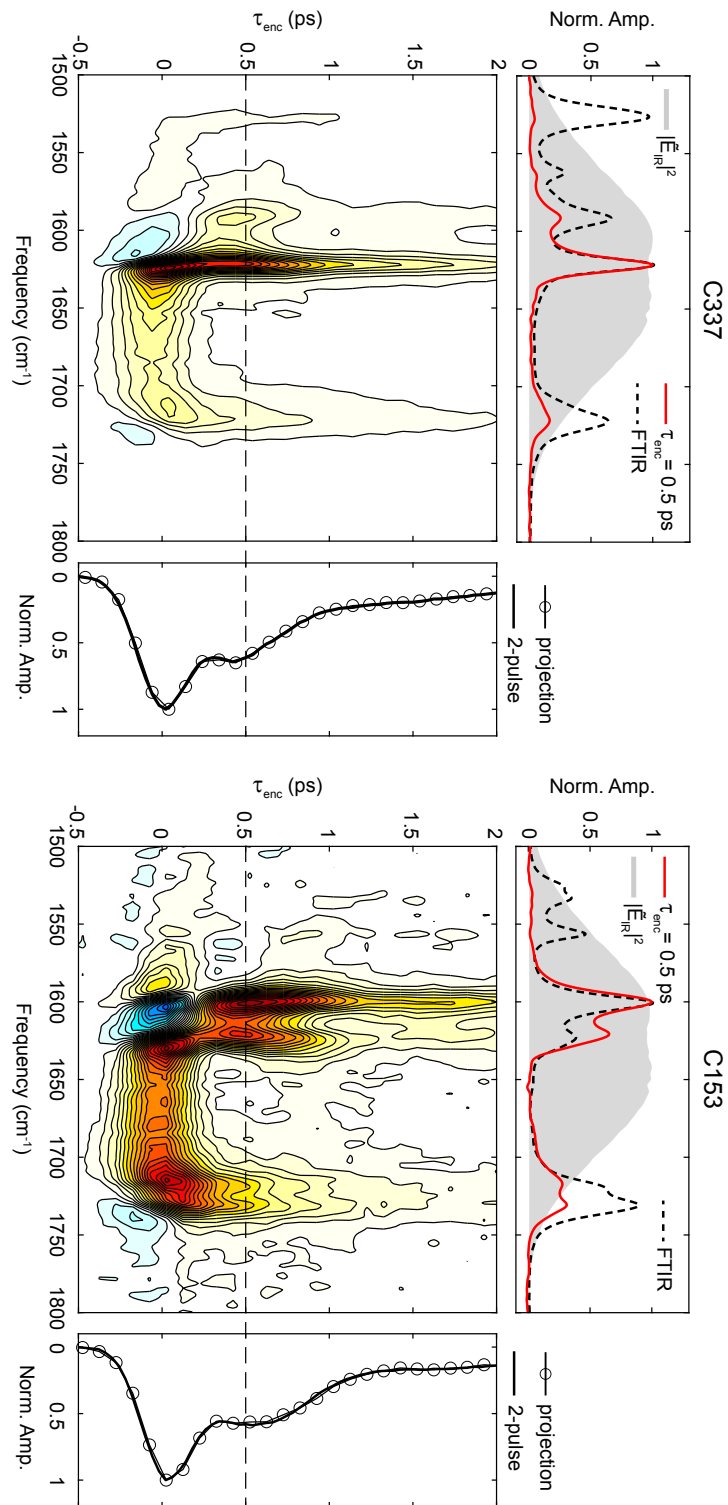


Figure 8.A.3: Coumarin 153 and 337 experimental τ_{enc} -dependent FEIR data. All panels are analogous to Figure 8.A.1.

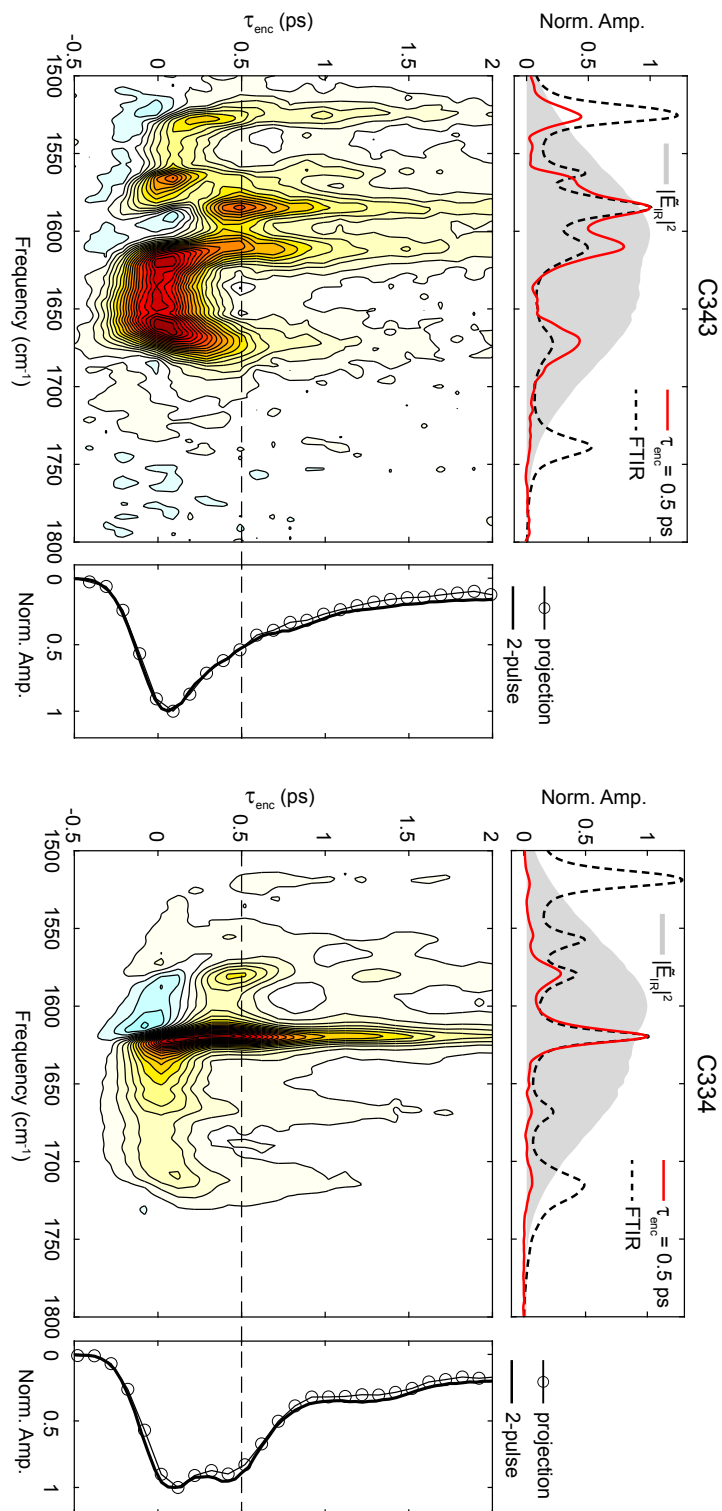


Figure 8.A.4: Coumarin 343 and 334 experimental τ_{enc} -dependent FEIR data. All panels are analogous to Figure 8.A.1.

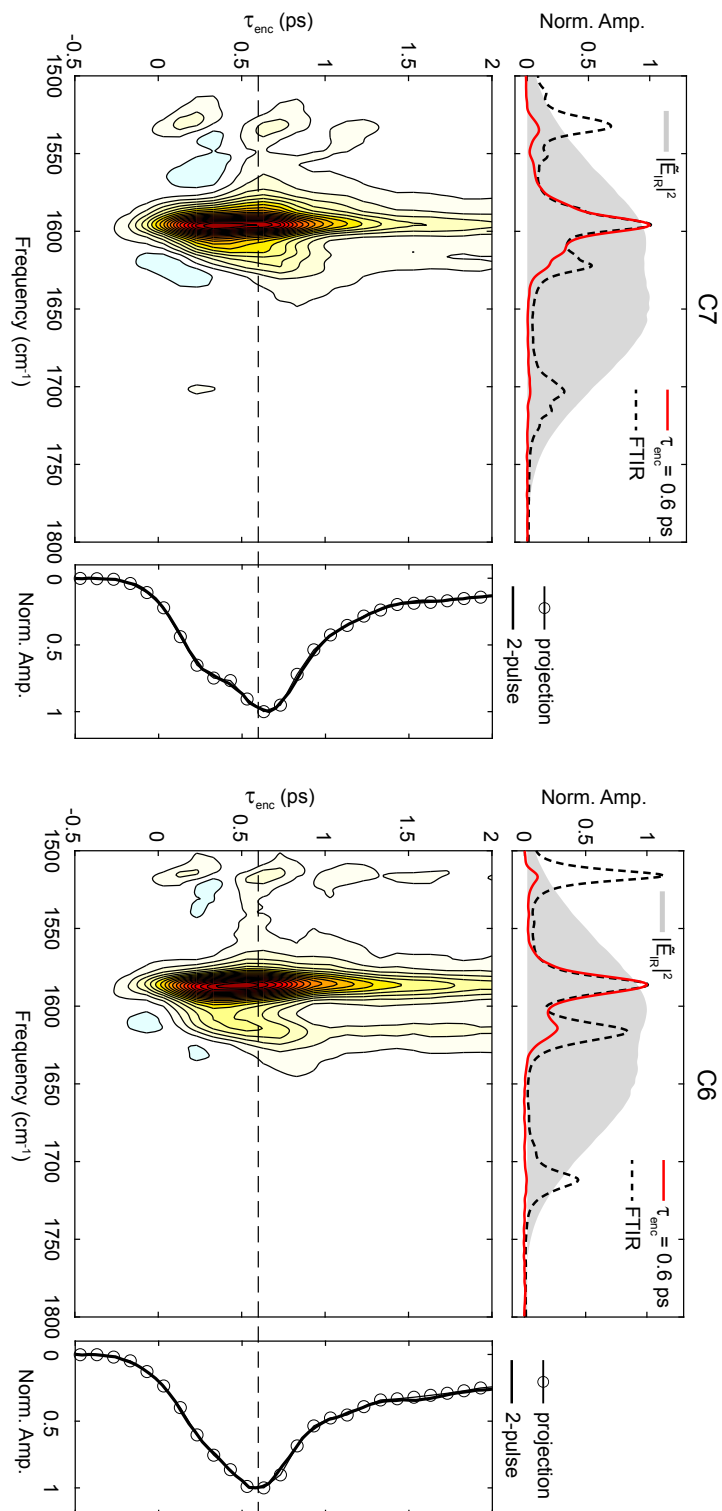


Figure 8.A.5: Coumarin 7 and 6 experimental τ_{enc} -dependent FEIR data. All panels are analogous to Figure 8.A.1.

Chapter 9

Polarization-dependent FEIR

spectroscopy

9.1 Overview

As a nonlinear technique that successively excites a molecule's vibrational and electronic transitions, FEIR spectroscopy is sensitive to the relative orientation of their dipole moments. From the standpoint of spectroscopic information content, this sensitivity can reveal more structural detail in a number of ways. Knowing the orientation of various transition dipoles within a molecule represents yet another view of its structure. As a practical matter, being able to access this information can help in assigning the features of complicated spectra. Furthermore, as specific intermolecular interactions or rotational dynamics can change these orientations, their observation provides probes into many condensed phase phenomena, thereby augmenting the spectroscopic tool-kit of FEIR. From a detection sensitivity perspective, the signal's dependence on transition orientation represents an important factor that must be understood and handled to optimize absolute brightness for single-molecule applications. Additionally, orientational effects could be leveraged to preferentially enhance

or suppress signals from certain vibrations to improve a measurement's sensitivity to the desired coordinates.

Orientalional information manifests in the polarization-dependence of spectroscopic signals. In the dipole approximation (Chapter 2), the strength of the light-matter interaction V between a molecular transition μ_{ba} and the electric field \mathbf{E} driving it depends on the angle θ between the transition's dipole moment unit vector and the field's polarization vector as

$$V = -\mu_{ba}E \cos \theta. \quad (9.1)$$

With linear techniques like conventional absorption spectroscopy, this dependence can only be seen when interrogating an individual molecule with fixed orientation, or otherwise an ensemble of similarly oriented molecules. For measurements in solution, the incessant rotational motion of molecules and the randomized distribution thereof washes out this dependence. Nonlinear techniques, on the other hand, follow a sequence of multiple transitions, ensuring that some information on their relative orientation can still be recovered even from an isotropic distribution of molecules.

In this chapter, we describe the orientational component of the FEIR response, and how orientational information can be extracted from polarization-dependent experiments. The theoretical description of orientational effects is contained within the response function framework for FEIR spectroscopy laid out in Chapter 2. Specifically, the relative orientation of the multiple transition dipoles probed in a nonlinear experiment with polarized excitation fields are encoded in the orientational correlation functions. Due to the formal correspondence between n^{th} -order coherent and $(n + 1)^{\text{th}}$ -order action response functions analyzed in Section 2.3, the orientational correlation functions for 4th-order FEIR experiments have the same form as those for 3rd-order coherent spectroscopies, and therefore—to our great

convenience—can be developed with the same existing methods and notation. Here we give an overview of the approach and develop the expressions that will allow us to calculate the cases relevant for FEIR spectroscopy. We then show some experimental examples of polarization-dependent measurements, and discuss their potential application.

9.2 Orientational response

9.2.1 Orientational averaging

Calculating the orientational response functions for a given system requires knowledge of the molecular-frame orientation of the transition dipoles participating in the material pathway, the dynamics that rotate the molecular frame during the pulse sequence, and the distribution of all possible initial orientations of the molecular frame that must be averaged over. As introduced in Chapter 2, this is accomplished by the orientational averaging tensor $\tilde{Y}_{IJKL}^{ijkl}(\tau_3, \tau_2, \tau_1)$, which transforms the molecular-frame to the lab-frame coordinates, thereby taking into account all relative orientations of these two coordinate systems consistent with the experimental configuration. For the solution-phase ensemble measurements mostly analyzed in this thesis, we will use the well-known orientational averages for isotropic distributions. However, it is worth noting that in some potential application of single-molecule measurements, the molecular frame can be fixed relative to the lab frame over the course of the experiment, and this averaging may not always be needed.

In the simplest case, evolution of the relative orientation of the vibrational and electronic transitions during the experimental inter-pulse delays occurs due to the body-fixed rotation of the entire molecule, which given the relatively large size of a typical fluorophore used in FEIR occurs on the timescale of tens to hundreds of picoseconds or longer in solution.³³⁸ In what

follows, we will largely assume these orientational dynamics are slow relative to the vibronic dynamics in the scalar part of the response function so that they may be neglected. Doing so lets us replace the time-dependent orientational averaging tensor $\tilde{Y}_{IJKL}^{ijkl}(\tau_3, \tau_2, \tau_1)$ with its constant $\tau_i = 0$ value. However, we will briefly describe the appearance of orientational relaxation in long-time τ_{enc} -dependent measurements in Section 9.2.3.

To see how this transformation is accomplished, let $\boldsymbol{\mu}$ be a vector in the molecular frame and \mathbf{m} represent the same vector in the lab frame. As in Chapter 2, we use upper case letters I, J, K, L and lower case letters i, j, k, l to index the Cartesian coordinates in the lab-frame (X, Y, Z) and molecular-frame (x, y, z) , respectively. For one particular realization of the two frame's relative orientation, these two vectors are related by a rotational transformation \mathbf{S}

$$\mathbf{m} = \mathbf{S}(\Omega)\boldsymbol{\mu}, \quad (9.2)$$

parameterized by a set of angles Ω . For example, the Euler angles $\Omega = (\alpha, \beta, \gamma)$ can be used to conveniently represent this transformation. Many definitions of the Euler angles and the construction of the rotation matrix are possible, and we use the following representation favored by Arfken⁶³

$$\mathbf{S} = \begin{pmatrix} c_\gamma c_\beta c_\alpha - s_\gamma s_\alpha & c_\gamma c_\beta s_\alpha + c_\gamma c_\alpha & -c_\gamma s_\beta \\ -s_\gamma c_\beta c_\alpha - c_\gamma s_\alpha & -s_\gamma c_\beta s_\alpha - c_\gamma c_\alpha & s_\alpha s_\beta \\ s_\beta c_\alpha & s_\beta s_\alpha & c_\beta \end{pmatrix}. \quad (9.3)$$

Here, $c_\alpha = \cos \alpha$ and $s_\alpha = \sin \alpha$ and similarly for the other angles. The angles are defined over $0 \leq \alpha < 2\pi$, $0 \leq \beta \leq \pi$, $0 \leq \gamma \leq 2\pi$, and integration over their full range is given by

$$\int d\Omega = \int_0^{2\pi} d\alpha \int_0^\pi \sin \beta d\beta \int_0^{2\pi} d\gamma = \frac{1}{8\pi^2}. \quad (9.4)$$

The probability density of orientations representing isotropic solution is therefore the uniform distribution $P_0(\Omega) = 1/8\pi^2$.

The product of four molecular-frame dipole unit vectors appearing in a given pathway, denoted generically by $\boldsymbol{\mu}$, $\boldsymbol{\nu}$, $\boldsymbol{\rho}$, and $\boldsymbol{\sigma}$, is formally a fourth-rank tensor that is transformed by four successive applications of $\mathbf{S}(\Omega)$. Explicitly, the tensor components of the corresponding lab-frame dipole product, denoted respectively by Roman letters, are

$$s_I r_J n_K m_L = \sum_{ijkl} S_{Ii}(\Omega) S_{Jj}(\Omega) S_{Kk}(\Omega) S_{Ll}(\Omega) \sigma_i \rho_j \nu_k \mu_l \quad (9.5)$$

Averaging this expression over the orientational distribution $P_0(\Omega)$ produces the desired orientational tensor element

$$Y_{IJKL}^{\sigma\rho\nu\mu} \equiv \langle s_I r_J n_K m_L \rangle_{P_0} = \sum_{ijkl} \tilde{Y}_{IJKL}^{ijkl} \sigma_i \rho_j \nu_k \mu_l, \quad (9.6)$$

where the orientational averaging tensor is

$$\tilde{Y}_{IJKL}^{ijkl} = \int S_{Ii}(\Omega) S_{Jj}(\Omega) S_{Kk}(\Omega) S_{Ll}(\Omega) P_0(\Omega) d\Omega. \quad (9.7)$$

The notation for a general orientational tensor element lists the molecular-frame transition dipoles as superscripts from right to left in order of interaction, for example, $Y_{IJKL}^{\sigma\rho\nu\mu}$ represents

$(Y_1)_{IJKL}^{a,b,c,d}$ in Eq. 2.93 in Chapter 2 when $\boldsymbol{\mu} = \hat{\boldsymbol{\mu}}_{ba}$, $\boldsymbol{\nu} = \hat{\boldsymbol{\mu}}_{ad}$, $\boldsymbol{\rho} = \hat{\boldsymbol{\mu}}_{cb}$, and $\boldsymbol{\sigma} = \hat{\boldsymbol{\mu}}_{dc}$. Alternatively, these superscripts will be suppressed when discussing properties of the orientational tensor common to any set of dipoles.

The spatial symmetries of isotropic media put substantial constraints on what the orientational tensor elements can be. The inversion symmetry rules for even and odd-order response functions discussed previously in Chapter 2 are a powerful example. That analysis showed that odd-rank tensors vanish because each element must simultaneously change sign and remain the same upon inversion of all coordinates. Beyond centrosymmetry, isotropic media are additionally invariant to all reflections and rotations—in short, any orthogonal transformation (as defined by Eq. 2.73 in Chapter 2). Applying a similar line of reasoning to the reflections across the principle YZ , ZX , or XY lab-frame planes

$$\mathbf{T}(YZ) = \begin{pmatrix} -1 & 0 & 0 \\ 0 & 1 & 0 \\ 0 & 0 & 1 \end{pmatrix}, \quad \mathbf{T}(ZX) = \begin{pmatrix} 1 & 0 & 0 \\ 0 & -1 & 0 \\ 0 & 0 & 1 \end{pmatrix}, \quad \mathbf{T}(XY) = \begin{pmatrix} 1 & 0 & 0 \\ 0 & 1 & 0 \\ 0 & 0 & -1 \end{pmatrix}, \quad (9.8)$$

we find that tensor components with an odd number of any given index must vanish. For example, invariance under $\mathbf{T}(ZX)$ requires $Y_{ZZZY} = -Y_{ZZZY} = 0$, while Y_{ZZYY} is unaffected as the pair of negative signs cancel. For the fourth-rank orientational tensor components this means indices must appear in pairs or all be the same, reducing the total number of non-zero terms from $3^4 = 81$ to $3 + 3 \times 3 \times 2 = 21$. This condition applies independently to both the upper and lower indices of the orientational averaging tensors \tilde{Y}_{IJKL}^{ijkl} . Applying

this result greatly simplifies the terms that need to be summed over in Eq. 9.6, namely

$$\begin{aligned}
 Y_{IJKL}^{\sigma\rho\nu\mu} &= \sum_{ijkl} \tilde{Y}_{IJKL}^{ijkl} \sigma_i \rho_j \nu_k \mu_l \\
 &= \sum_{i \neq j} \left[\tilde{Y}_{IJKL}^{iiii} \sigma_i \rho_i \nu_i \mu_i + \tilde{Y}_{IJKL}^{iijj} \sigma_i \rho_i \nu_j \mu_j \right. \\
 &\quad \left. + \tilde{Y}_{IJKL}^{ijij} \sigma_i \rho_j \nu_i \mu_j + \tilde{Y}_{IJKL}^{ijji} \sigma_i \rho_j \nu_j \mu_i \right].
 \end{aligned} \tag{9.9}$$

Finally, using similar arguments it can be shown that invariance to rotations equates tensor components in which the identity of X, Y , or Z are freely interchanged among all the indices, i.e. $Y_{ZZZZ} = Y_{YYYY} = Y_{XXXX}$, $Y_{ZZYY} = Y_{ZZXX} = Y_{YYXX} = \dots$, and so on.¹²¹ In fact, only three independent components are needed to build up all 21 non-zero terms in an isotropic fourth-rank tensor using these symmetry properties and the following relation

$$Y_{ZZZZ} = Y_{ZZYY} + Y_{ZYZY} + Y_{ZYYZ}. \tag{9.10}$$

Again, this relation holds independently for both the upper and lower indices of the orientational averaging tensor.

Tensor element	Value
Y_{ZZZZ}^{zzzz}	1/5
$Y_{ZZZZ}^{zzyy} = Y_{ZZZY}^{zzzz}$	1/15
$Y_{ZZZZ}^{zyyz} = Y_{ZZZZ}^{zyzy}$	1/15
Y_{ZZZY}^{zzyy}	2/15
$Y_{ZZZY}^{zyyz} = Y_{ZZZY}^{zyzy}$	-1/30

Table 9.1: Elements of the orientational averaging tensor for isotropic media.

For illustration purposes, we calculate some of the elements of the orientational averaging tensor using Eqs. 9.3 and 9.7,

$$\begin{aligned} Y_{ZZZZ}^{zzzz} &= \int S_{Zz}(\Omega)^4 P_0(\Omega) d\Omega \\ &= \frac{1}{8\pi^2} \int_0^{2\pi} d\alpha \int_0^\pi \cos^4 \beta \sin \beta d\beta \int_0^{2\pi} d\gamma = \frac{1}{5}, \end{aligned} \quad (9.11)$$

$$\begin{aligned} Y_{ZZZZ}^{zzyy} &= Y_{ZZZZ}^{zyyz} = Y_{ZZZZ}^{zyzy} = \int S_{Zz}(\Omega)^2 S_{Zy}(\Omega)^2 P_0(\Omega) d\Omega \\ &= \frac{1}{8\pi^2} \int_0^{2\pi} \sin^2 \alpha d\alpha \int_0^\pi \cos^2 \beta \sin^3 \beta d\beta \int_0^{2\pi} d\gamma = \frac{1}{15}. \end{aligned} \quad (9.12)$$

A minimal number of elements, some of which involve a more tedious calculation than those above, are listed in Table 9.1. Employing the symmetries discussed above allows for the construction of the entire orientational averaging tensor from these elements.

9.2.2 FEIR orientational response for population and coherence pathways

As we saw in Chapter 2, in FEIR spectroscopy the number of unique transitions appearing in any pathway can either be two (for population pathways), or four (for coherence pathways). Population pathways involve one vibrational fundamental, $\boldsymbol{\mu} = \boldsymbol{\nu}$, and one vibronic transition $\boldsymbol{\rho} = \boldsymbol{\sigma}$. In this case the orientational response depends only on the projection angle of one dipole onto the other. This case is common to the 2D spectroscopy of coupled transitions, e.g. the orientational dependence of a cross-peak.³³⁹ On the other hand, multimode coherence pathways involve four different transition dipoles, which in the most general case could each have unique orientations in the molecular-frame. However, as discussed in Chapter 2, we will take the Condon approximation where the vibronic transitions are all parallel to the

bare electronic transition. In this case the number of unique transition dipole unit vectors in a coherence pathway reduces to three—the electronic transition dipole $\rho = \sigma$, and two ground state vibrational transition dipoles μ , and ν .

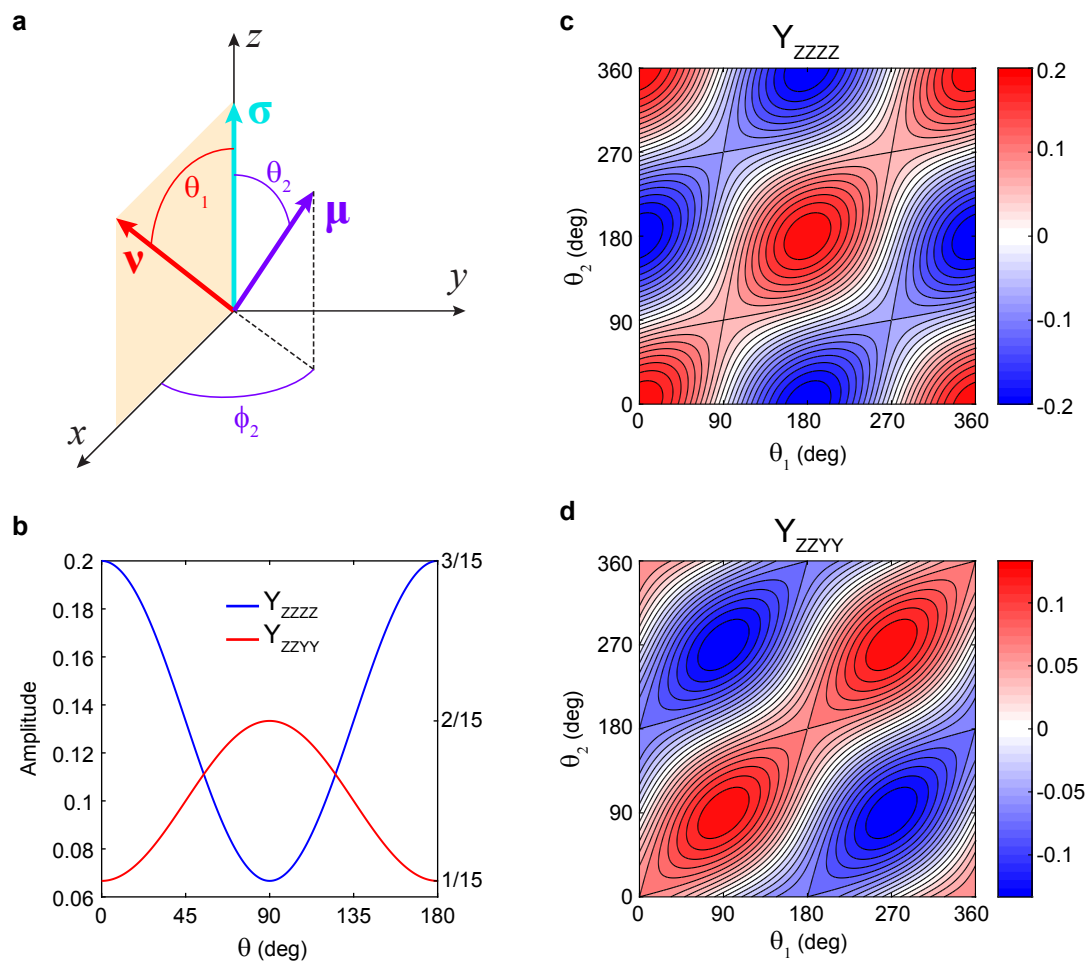


Figure 9.1: Orientational correlation functions for two and three independent transition dipoles. (a) Angles describing three arbitrarily oriented dipole unit vectors in the molecular frame. (b) Orientational correlation functions Y_{ZZZZ} (blue) and Y_{ZZYY} (red) in the two-dipole case when $\mu = \nu$ with $\theta_1 = \theta_2 \equiv \theta$ and $\phi_2 = 0$. (c) Y_{ZZZZ} and (d) Y_{ZZYY} in the case of three co-planar dipoles (Eqs. 9.15 and b).

Here we explicitly calculate the orientational tensor elements for these two-dipole (population) and three-dipole (coherence) pathways in the $ZZZZ$ and $ZZYY$ polarization schemes.

The two-dipole expressions are found as a special case of the three-dipole expression when $\boldsymbol{\mu} = \boldsymbol{\nu}$, so we only need to calculate the three-dipole case. Figure 9.1(a) shows the arrangement of the three unit dipoles in the molecular frame. We take the electronic unit dipole $\boldsymbol{\sigma}$ to be aligned along the z axis. Then without loss of generality, one of the vibrational unit dipoles $\boldsymbol{\nu}$ can be taken to lie in the xz plane with polar angle θ_1 , while the other vibrational unit dipole $\boldsymbol{\mu}$ is described by the polar and azimuthal angles θ_2 and ϕ_2 , respectively. Explicitly, the molecular-frame components of each unit dipole are

$$\boldsymbol{\sigma} = \begin{bmatrix} \sigma_x \\ \sigma_y \\ \sigma_z \end{bmatrix} = \begin{bmatrix} 0 \\ 0 \\ 1 \end{bmatrix}, \quad \boldsymbol{\nu} = \begin{bmatrix} \sin \theta_1 \\ 0 \\ \cos \theta_1 \end{bmatrix}, \quad \boldsymbol{\mu} = \begin{bmatrix} \cos \phi_2 \sin \theta_2 \\ \sin \phi_2 \sin \theta_2 \\ \cos \theta_2 \end{bmatrix}. \quad (9.13)$$

Starting with the all parallel polarization scheme, we find only two non-vanishing terms in Eq. 9.9

$$\begin{aligned} Y_{ZZZZ}^{\boldsymbol{\sigma}\boldsymbol{\sigma}\boldsymbol{\nu}\boldsymbol{\mu}} &= \tilde{Y}_{ZZZZ}^{zzzz}(\sigma_z)^2\nu_z\mu_z + \tilde{Y}_{ZZZZ}^{zzxx}(\sigma_z)^2\nu_x\mu_x \\ &= \frac{1}{5} \cos \theta_1 \cos \theta_2 + \frac{1}{15} \cos \phi_2 \sin \theta_1 \sin \theta_2. \end{aligned} \quad (9.14a)$$

Similarly, for perpendicular IR/vis polarizations, we have

$$\begin{aligned} Y_{ZZYY}^{\boldsymbol{\sigma}\boldsymbol{\sigma}\boldsymbol{\nu}\boldsymbol{\mu}} &= \tilde{Y}_{ZZYY}^{zzzz}(\sigma_z)^2\nu_z\mu_z + \tilde{Y}_{ZZYY}^{zzxx}(\sigma_z)^2\nu_x\mu_x \\ &= \frac{1}{15} \cos \theta_1 \cos \theta_2 + \frac{2}{15} \cos \phi_2 \sin \theta_1 \sin \theta_2. \end{aligned} \quad (9.14b)$$

The fluorophores used in FEIR experiments are typically planar, electronically-conjugated molecules, in which the electronic transition dipole is contained in the plane of the conjugated

core. The mid-IR vibrations being interrogated most often involve the in-plane motion of nuclei, and therefore also have transition dipoles in this same plane. In this case, all transition dipoles are coplanar, and ϕ_2 can be set to zero. The resulting orientational correlation functions in this fully-coplanar limit are

$$\begin{aligned} Y_{ZZZZ}^{\sigma\sigma\nu\mu} &= \frac{1}{5} \cos \theta_1 \cos \theta_2 + \frac{1}{15} \sin \theta_1 \sin \theta_2 \\ &= \frac{1}{15} \left(2 \cos(\theta_1 - \theta_2) + \cos(\theta_1 + \theta_2) \right), \end{aligned} \quad (9.15a)$$

$$\begin{aligned} Y_{ZZYY}^{\sigma\sigma\nu\mu} &= \frac{1}{15} \cos \theta_1 \cos \theta_2 + \frac{2}{15} \sin \theta_1 \sin \theta_2 \\ &= \frac{1}{30} \left(3 \cos(\theta_1 - \theta_2) - \cos(\theta_1 + \theta_2) \right). \end{aligned} \quad (9.15b)$$

These functions are plotted in Figure 9.1(c) and (d). When $\boldsymbol{\mu} = \boldsymbol{\nu}$, only a single projection angle $\theta = \theta_1 = \theta_2$ is at play, and these expressions reduce to the two-dipole orientational correlation functions

$$Y_{ZZZZ}^{\sigma\sigma\nu\nu} = \frac{1}{15} \left(2 \cos^2 \theta + 1 \right), \quad (9.16a)$$

$$Y_{ZZYY}^{\sigma\sigma\nu\nu} = \frac{1}{15} \left(2 - 2 \cos^2 \theta \right), \quad (9.16b)$$

which are plotted in Figure 9.1(b).

9.2.3 Polarization-dependence of signals and the FEIR anisotropy.

In the FEIR experiment, both IR pulses \mathbf{E}_1 and \mathbf{E}_2 have the same linear polarization, which may be varied with respect to the linear polarization of \mathbf{E}_3 (Figure 9.2). Each pulse's electric field polarization unit vector is denoted by $\hat{\mathbf{e}}_\alpha$ with $\alpha = 1, 2$, or 3, and Θ is the angle

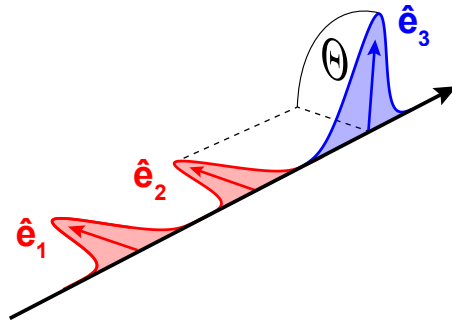


Figure 9.2: Polarized FEIR pulse sequence.

between \hat{e}_1 or \hat{e}_2 and \hat{e}_3 . To be consistent with the typical convention in 3rd-order coherent spectroscopies, we assign the beams' direction of propagation to be along the lab-frame X axis, and take \hat{e}_3 to lie along the Z axis. We note this convention breaks with our notation for the lab frame coordinates when discussing the sample region in the microscope in Chapter 4, however, having the directly analogous terminology for polarization configurations is useful. Then each polarization unit vector is expressed as

$$\hat{e}_1 = \begin{bmatrix} (\hat{e}_1)_X \\ (\hat{e}_1)_Y \\ (\hat{e}_1)_Z \end{bmatrix} = \begin{bmatrix} 0 \\ \sin \Theta \\ \cos \Theta \end{bmatrix}, \quad \hat{e}_2 = \begin{bmatrix} 0 \\ \sin \Theta \\ \cos \Theta \end{bmatrix}, \quad \hat{e}_3 = \begin{bmatrix} 0 \\ 0 \\ 1 \end{bmatrix}. \quad (9.17)$$

The polarization-dependence of an individual pathway depending on the arbitrary transition dipoles σ , ρ , ν , and μ in either the two- or three-pulse signal can then be expressed as the linear combination of the parallel ($ZZZZ$) and perpendicular ($ZZYY$) orientational

response function components

$$\begin{aligned}
 S_{\text{pol}}(\Theta) &= \sum_{IJKL} Y_{IJKL}^{\sigma\rho\nu\mu}(\hat{e}_3)_I(\hat{e}_3)_J(\hat{e}_2)_K(\hat{e}_1)_L \\
 &= Y_{ZZZZ}^{\sigma\rho\nu\mu} \cos(\Theta)^2 + Y_{ZZYY}^{\sigma\rho\nu\mu} \sin(\Theta)^2 = (Y_{ZZZZ}^{\sigma\rho\nu\mu} - Y_{ZZYY}^{\sigma\rho\nu\mu}) \cos(\Theta)^2 + Y_{ZZYY}^{\sigma\rho\nu\mu}. \quad (9.18)
 \end{aligned}$$

The parallel and perpendicular response components are recovered when $\Theta = 0^\circ$ or 90° , respectively.

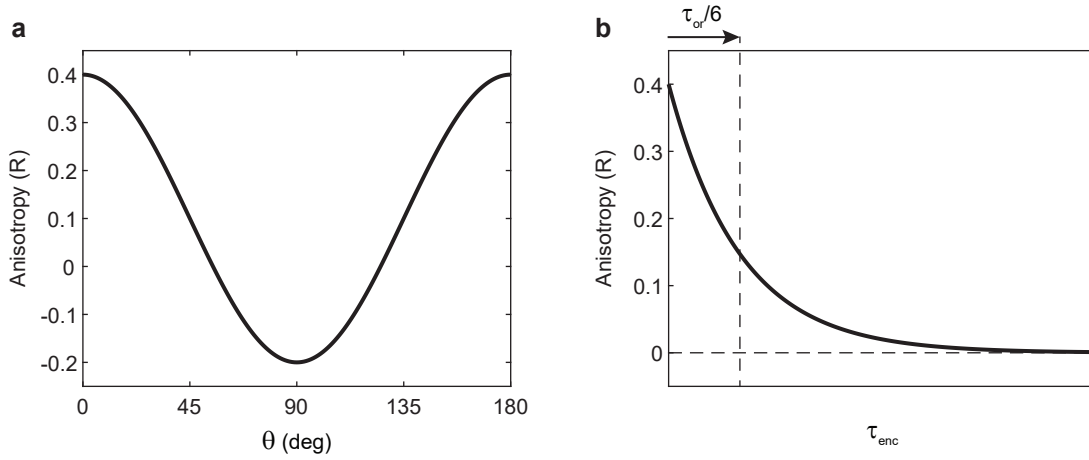


Figure 9.3: (a) Anisotropy (R) of the single-mode population response as a function the relative angle θ between vibrational and electronic transition dipoles. (b) Anisotropy decay for the case of parallel transition dipoles due to orientational diffusion of the chromophore modelled as a spherical rotor.

A particularly useful quantity is the polarization anisotropy R , defined as

$$R = \frac{F_{ZZZZ} - F_{ZZYY}}{F_{ZZZZ} + 2F_{ZZYY}}, \quad (9.19)$$

where F_{ZZZZ} and F_{ZZYY} are the FEIR signals measured in the all parallel ($\Theta = 0^\circ$) or perpendicular ($\Theta = 90^\circ$) polarization configurations. The anisotropy defined in this way is

a well-known experimental observable in 3rd-order coherent techniques,^{111,132,340–343} and also has analogies in linear fluorescence and Raman spectroscopies.^{255,280} In FEIR, the anisotropy is especially useful when the isolated population response can be measured, either in a two-pulse experiment of a single-mode system, or in the FEIR spectrum where coherence contributions have dephased or are otherwise absent. In a single-mode system (described in Section 2.4.4) without any orientational dynamics, the anisotropy can be computed using Eq. 9.16

$$R = \frac{1}{5} \left(3 \cos^2 \theta - 1 \right), \quad (9.20)$$

where θ is the angle between the vibrational and electronic transition dipole unit vectors. This expression is plotted in Figure 9.3(a), where its symmetry and extreme values of $2/5$ at $\theta = 0^\circ$ and $-1/5$ at $\theta = 90^\circ$ can be seen. As coherence pathways have more complicated orientational dependencies described by Eqs. 9.14 or 9.15, their contribution to the anisotropy is similarly much more complex and likely of limited experimental utility.

Rotational diffusion of the entire chromophore on the timescale of the pulse sequence will cause the orientational correlation functions to decay, and can be treated by calculating the full time-dependence of the orientational averaging tensors $\tilde{Y}_{IJKL}^{ijkl}(\tau_3, \tau_2, \tau_1)$.³⁴⁴ Here we briefly cite the result, illustrated in Figure 9.3(b), for how the anisotropy of the population response decays along the encoding delay assuming a simple model for rotational diffusion based on a classical small-angle orientational diffusion equation of a spherical rotor.^{280,339} Specifically,

$$R(\tau_{enc}) = R(\tau_{enc} = 0) \exp(-6\tau_{enc}/\tau_{or}). \quad (9.21)$$

Here $R(\tau_{enc} = 0)$ is the initial value of the anisotropy (i.e. Eq. 9.20, τ_{or} is the orientational correlation time characterizing the diffusion process, and we have assumed the impulsive limit. This expression could refer to anisotropy of the two-pulse signal from a single-mode system, or the decay of a particular band in a multimode FEIR spectrum in the absence of coherence.

In this rather simple situation, the anisotropy decay is independent of an population dynamics and therefore is a useful measure of orientational relaxation. The opposite effect, i.e. removing the orientational contribution to the signal, may be accomplished by recording the isotropic component

$$F_{\text{iso}} = F_{ZZZZ} + 2F_{ZZYY}, \quad (9.22)$$

i.e. the denominator in Eq. 9.20. The isotropic two-pulse signal will be considered in Chapter 10 to investigate population relaxation phenomena in FEIR measurements.

9.3 Polarization-dependent FEIR experiments

9.3.1 Polarization-dependence and anisotropy decay of a single-mode system: coumarin 337 nitrile stretch

To demonstrate some of the basic orientational effects in FEIR spectroscopy, and correspondingly test our theoretical description, we perform polarization-dependent experiments on the simplest case of a single-mode system. The nitrile stretch vibration of coumarin 337 (C337), shown in Figure 9.4(a), is a convenient choice of model system, as this vibrational resonance is spectrally isolated as well as being a local mode that has an intuitive transition dipole

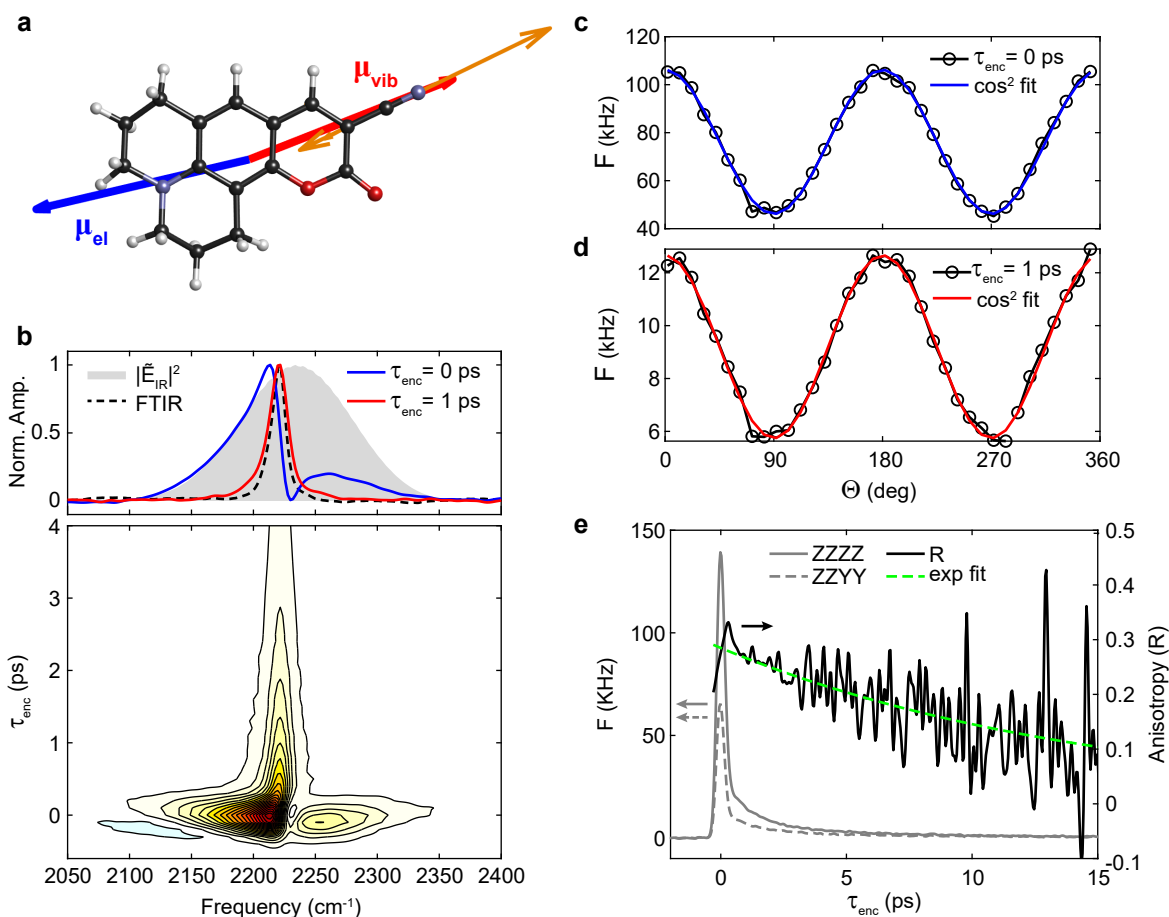


Figure 9.4: Polarization-dependent FEIR signals from the coumarin 337 nitrile stretch. (a) Optimized ground-state structure of coumarin 337 calculated by DFT, showing the atomic displacement vectors associated with the nitrile stretching band (orange), its transition dipole unit vector (red), and the $S_0 \rightarrow S_1$ electronic transition dipole unit vector (blue). (c) Top panel: FEIR spectra at $\tau_{\text{enc}} = 0$ ps (blue), $\tau_{\text{enc}} = 1$ ps (red), and pump-scaled FTIR spectrum (dashed black) of the nitrile mode in dimethylformamide (DMF). The IR pump spectrum is overlaid in grey. Bottom panel: full τ_{enc} -dependent FEIR spectrum. Polarization-dependence of the background-subtracted two-pulse FEIR count rate at (c) $\tau_{\text{enc}} = 0$ ps and (d) $\tau_{\text{enc}} = 1$ ps. Fits to the model $a \cos^2 \Theta + b$ are superimposed. (e) Left y axis: two-pulse FEIR signals in ZZZZ (solid gray) and ZZYY (dashed gray). Right y axis: anisotropy (R) (solid black) calculated from the two-pulse signals, with an exponential fit with no offset parameter (dashed green). The two-pulse measurements in (e) use a slightly higher visible intensity than those in (c)-(d), resulting in the slightly higher count rates.

direction within the molecule. FEIR measurements are performed in dimethylformamide (DMF) solution at 100 μM concentration. As calculated by DFT (using the same methods described in Chapter 8), the nitrile's transition dipole is oriented nearly anti-parallel to the $S_0 \rightarrow S_1$ electronic transition dipole, forming an angle of $\theta = 172^\circ$. The electronic transition dipole falls roughly along a line connecting the electron-donating amino substituent with the electron-withdrawing nitrile, consistent with the charge-transfer character of the transition.^{150,316} This orientation of the electronic transition is roughly conserved in DFT calculations across the series of coumarin dyes studied in this thesis.

Figure 9.4(b) shows the nitrile's IR absorption spectrum and τ_{enc} -dependent FEIR spectra for $ZZZZ$ polarization. During pulse-overlap, the FEIR signal is contaminated with the vibrationally-nonresonant two-photon absorption (TPA) signal discussed in Chapters 3, 4, and 8. Interestingly, within the expected TPA signal extended along the breadth of the IR pulse spectrum, the nitrile feature appears as a fully dispersive resonance ($\tau_{\text{enc}} = 0$ ps in the top panel Figure 9.4(b)) resembling a Fano lineshape.³⁴⁵ This phase-distortion is importantly not accounted for by the pulse-overlap induced phase artifact discussed in Chapter 3, which would have the opposite sign. A possible explanation might involve coupling of the IR-vibrational resonance to the molecule's polarizability. Regardless of its origin, this dispersive feature fully decays with the pulse cross-correlation, and at $\tau_{\text{enc}} > 0.5$ ps an intuitive absorptive lineshape matching that of the FTIR spectrum is present, indicative of a simple population feature.

The experimental polarization-dependence of the total FEIR signal at $\tau_{\text{enc}} = 0$ ps and $\tau_{\text{enc}} = 1$ ps are shown in Figure 9.4(c) and (d), respectively. In both cases, the signals are well-fit to an $a \cos^2 \Theta + b$ dependence as predicted by Eq. 9.18. As shown in Table 9.2, the anisotropy value from the polarization dependence of the $\tau_{\text{enc}} = 1$ ps signal is somewhat

	R	θ (deg)
Experiment	0.29	154
Calculation	0.39	172

Table 9.2: Experimental ($\tau_{\text{enc}} = 1$ ps) and calculated C337 nitrile FEIR anisotropy and relative transition dipole angle.

lower than that predicted by Eq. 9.20 using the transition dipoles calculated by DFT. One possible explanation for this discrepancy on the experimental side is the effect of the non-ideal polarization purity of the IR and visible beams resulting from the high numerical aperture focusing in the FEIR microscope. Further characterization and modelling of this effect would be necessary to ensure accurate anisotropies can be reliably measured. The anisotropy at $\tau_{\text{enc}} = 0$ ps is slightly higher at $R = 0.31$, but still lower than the predicted value, while also complicated by the pulse-overlap signal.

The two-pulse signals in $ZZZZ$ and $ZZYY$ polarization and resulting anisotropy decay are shown in Figure 9.4(e). The pulse-overlap signal produces the large spikes at $\tau_{\text{enc}} = 0$ ps in both polarizations, and the amplitude of the ensuing true FEIR population response is significantly smaller. The anisotropy decay is fit to a single exponential with decay constant of 15 ± 3 ps, where the high uncertainty is due to both the noisy signal and consequently limited scan range. Assuming the simple spherical rotor model leading to Eq. 9.21, the resulting orientational correlation time is on the order of $\tau_{\text{or}} = 90 \pm 20$ ps, which is consistent with previous studies on coumarin rotational dynamics by fluorescence up-conversion and anisotropy.³³⁸

9.3.2 Anisotropy in a multimode system: coumarin 334 carbonyl and ring vibrations

Another potentially useful application of polarization-dependent FEIR measurements is to measure the relative orientation among multiple vibrational modes to aid in their assignment, or eventually provide more detail into the kind of structures formed during intermolecular association events. To investigate how well FEIR anisotropy measurements can distinguish relative orientation in a multimode system, we examine the polarization-dependent FEIR spectroscopy of coumarin 334 (C334) in acetonitrile-d₃. These FEIR measurements belong to the larger data set investigated in Chapter 7, where only the *ZZZZ* signals were used. As shown in Figures 9.5(a)-(d), C334 has two carbonyl local modes, ν_{lactone} and ν_{actyl} , in addition to a ring mode ν_{R1} , that are each expected to have distinct orientations based on DFT calculation. These three vibrational transition dipoles are essentially co-planar with the electronic transition. Each mode is assigned in the FTIR spectrum in 9.5(e).

Figure 9.5(f) shows the FEIR spectra at $\tau_{\text{enc}} = 0.5$ ps in both *ZZZZ* and *ZZYY* polarizations, along with the resulting anisotropy spectrum. The anisotropy exhibits distinct values at the locations of the three bands. The presence of coherence pathways, which could lead to more complicated orientational dependence in the anisotropy, are likely at play to some extent in these spectra, which can be appreciated in the full *ZZZZ* τ_{enc} -dependent spectrum shown in Figure 8.A.4 in Chapter 8. However, here we will attempt to see how well the different vibrations' anisotropies as measured by integrating along their respective bands (indicated by the grayed out regions in Figure 9.5(f)) can be used to extract relative angles by Eq. 9.20.

The resulting anisotropies and angles are summarized in Table 9.3 along with the predictions from the DFT calculation. Qualitatively, these anisotropies and extracted angles

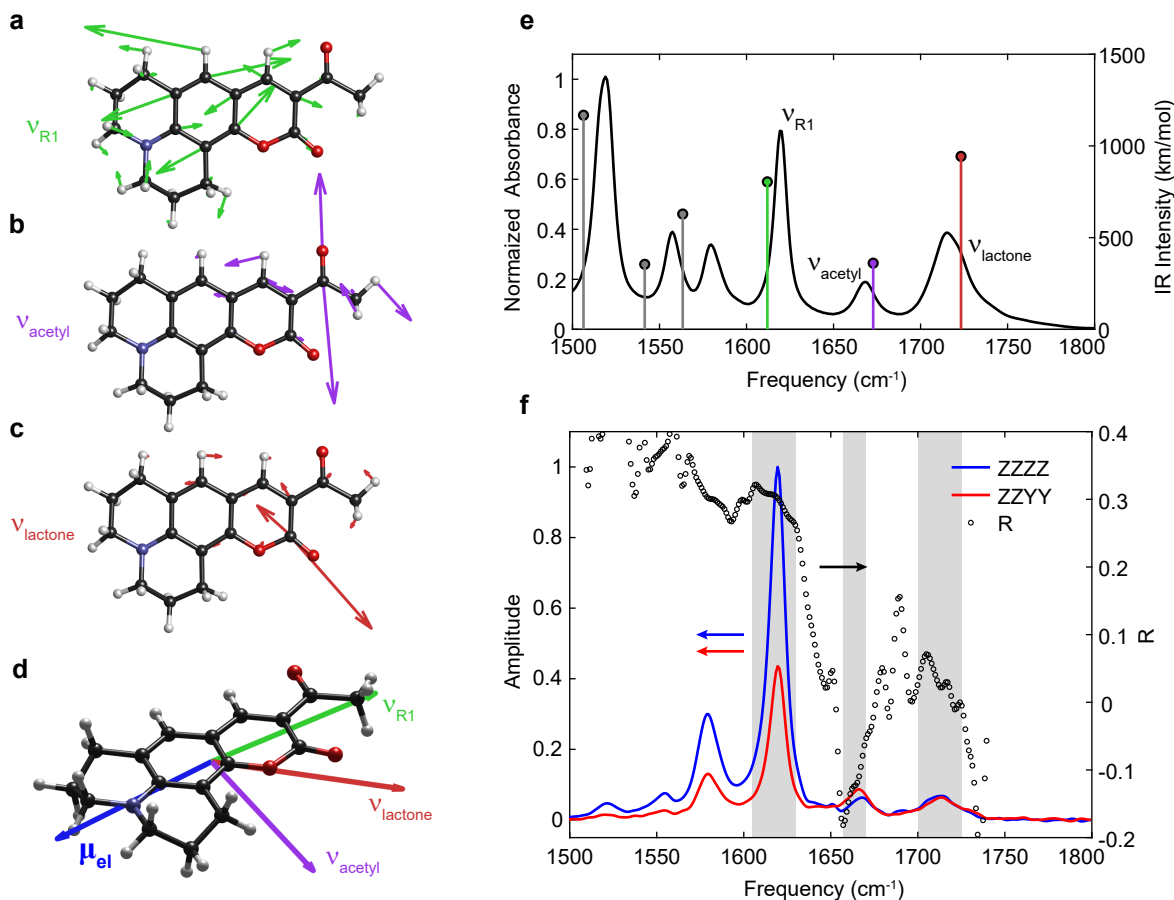


Figure 9.5: C334 FEIR spectrum anisotropy. (a)-(c) DFT-calculated normal mode atomic displacement vectors for ν_{R1} , ν_{actyl} , and $\nu_{lactone}$, respectively, and (d) their normalized transition dipole unit vectors along with that of the electronic transition. (e) FTIR spectrum (left y axis) of C334 in acetonitrile-d₃, with the DFT calculated normal modes superimposed. (f) Left y axis: $\tau_{enc} = 0.5$ ps FEIR spectra in ZZZZ (blue) and ZZYY (red) polarizations. Both spectra are commonly normalized to the brightest feature in the ZZZZ spectrum. Right y axis: Anisotropy spectrum. The gray bands indicate the regions the anisotropy is averaged over to produce the values in Table 9.3.

show reasonable agreement with the calculation, although, as in Section 9.3.1, the experimental values do not seem to reach the extreme high and low values predicted for ν_{R1} and ν_{actyl} , respectively. This behavior is consistent with impure polarization, which by averaging around a spread in experimental polarization angles Θ would in effect alternately lower and

	R (exp)	R (calc)	θ (exp)	θ (calc)
ν_{R1}	0.31	0.40	157°	175°
ν_{actyl}	-0.10	-0.19	114°	96°
ν_{lactone}	0.02	0.05	127°	130°

Table 9.3: Experimental ($\tau_{\text{enc}} = 0.5$ ps) and calculated FEIR anisotropy and relative transition dipole angles for selected modes in C334.

raise the extreme values for parallel or perpendicular transition dipoles, respectively. Overall, these spectral anisotropy measurements provide useful qualitative insight. In particular, if the frequency ordering of the two carbonyls ν_{actyl} and ν_{lactone} was not known ahead of time by DFT calculation, the difference in their measured anisotropies combined with chemical intuition about how the C=O bonds should be oriented against the electronic transition in the molecule would lead us to correctly assign ν_{actyl} as the lower frequency of the two bands.

Chapter 10

Vibrational relaxation through the lens of FEIR spectroscopy

10.1 Overview

Over the course of this thesis we have largely demonstrated the principles of FEIR spectroscopy and investigated its information content at early encoding delays, where vibrational relaxation has not substantially depleted the initially excited populations. From a practical standpoint, this early-time region is the natural arena for single-molecule applications of FEIR spectroscopy, as the signals are largest. Indeed, using short pulses in order to access the early-time region for high overall excitation efficiency is one of the central experimental design principles for FEIR spectroscopy. However, further insight into the FEIR process, and specifically a deeper understanding of how the encoding step samples the vibrational resonances, can be gained from analyzing the full encoding delay dependence of the signal. In this chapter we explore some of the longer timescale relaxation phenomena observed in FEIR spectroscopy. Specifically, we will focus on the region of encoding delays after intermode vibrational coherence has fully dephased—in some senses the opposite limit of the

early-time region that was the subject of Chapter 8.

From a time-resolved spectroscopy perspective, such encoding-delay dependent FEIR experiments provide a means to study vibrational relaxation processes. Indeed, the historical origins of FEIR spectroscopy in the 1970's represented just such a method to study vibrational relaxation dynamics using the newly available picosecond IR laser pulses.^{31,32} Since then, much has been learned about the complexities of these phenomena from time-resolved IR and Raman methods as well as theoretical approaches, and the study of vibrational relaxation in the condensed phase is by now in many ways a mature field.³⁴⁶⁻³⁵¹ In large molecules like the fluorophores used for FEIR, the general picture that has emerged is one dominated by fast depopulation of the initially excited level by intramolecular vibrational energy redistribution (IVR),³⁵²⁻³⁵⁴ followed by a slower dissipation of the excess energy into the solvent.³² For fundamentals in the mid-IR range, this initial depopulation step often occurs on the timescale of a few picosecond or even hundreds of femtoseconds, due to the ubiquitous anharmonic coupling among intramolecular vibrations and the high density of states that are in resonance arising from the dense vibrational ladders of low-frequency modes.

Here we will discuss two main observations about the nature of FEIR signals in the late-time region. First, that the character of the observed decay kinetics depends on the electronic resonance conditions in the experiment. We demonstrate this phenomenon by analyzing the same FEIR measurements on the coumarin series used previously in Chapter 7 to explore how resonance influences signal size at early times. Second, while in the early-time region the FEIR activity of each mode is influenced by its vibronic coupling to the electronic transition, at late-times the relative amplitudes of vibrational bands are effectively reshaped to more closely resemble those in the conventional IR absorption spectrum. We interpret both of these observations in terms of a rapid statistical IVR process that redistributes the initial

population into a ‘hot’ ground state with a quasi-thermal distribution of excitation in the molecule’s low-frequency modes, which subsequently cools by dissipation into the solvent. In this case, the encoding transitions originate from the sub-ensemble of levels from modes with some degree of Franck-Condon activity. The apparent resonance dependence of the signals’ decay kinetics are then seen to reflect how this distribution is sampled by the encoding process, while the reshaping of the relative band intensities indicates how the encoding step no longer involves the specific vibronic transitions originating from each mode’s excited state, but rather depends only on the IR energy initially absorbed.

10.2 Encoding-resonance dependent long-time relaxation behavior in coumarins

As in Chapter 7, studying a series of structurally-similar coumarin dyes with variable electronic transition frequencies allows us to investigate effects related to the experimental resonance conditions in lieu of a tunable visible encoding pulse. Here we analyze the two-pulse decay transients of the coumarin series under the same experimental condition as in Chapters 7 and 8, i.e. in 30-100 μM acetonitrile-d₃ solution with the IR pulse tuned to cover the high-frequency coumarin ring vibrations. This FEIR data uses slightly higher visible excitation intensities to produce larger signals for better signal to noise acquisition of the small late-time amplitude, but otherwise follows the same methods described in Section 7.2.2.

Figure 10.1 shows the long-time behavior of the coumarin series’ two-pulse transients, and demonstrates how they depend on the extent of FEIR resonance as characterized by the detuning between the frequency of the electronic 0-0 transition, defined by the crossing-point of the normalized absorption and fluorescence lineshapes, and the encoding pulse, $\Delta = \omega_{0-0} -$

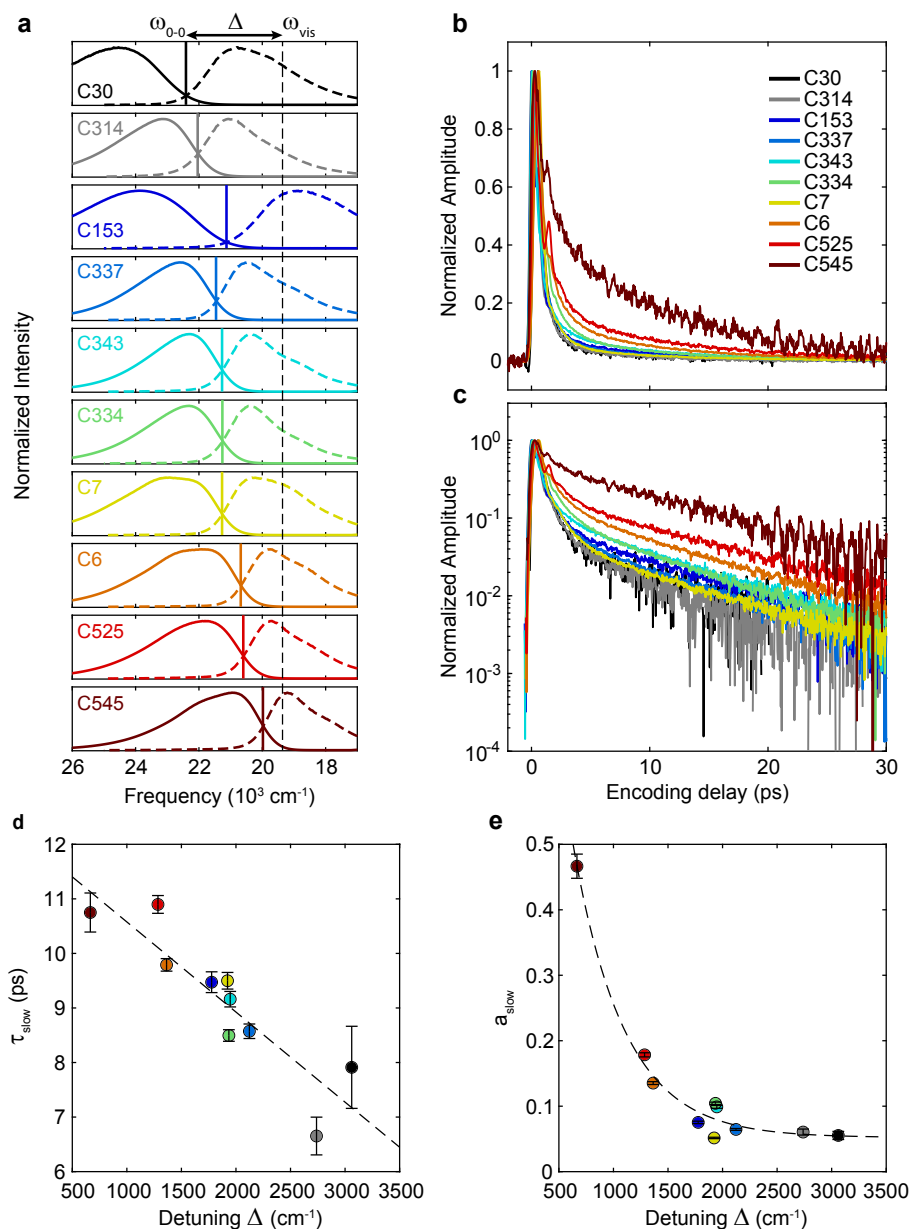


Figure 10.1: Dependence of the two-pulse slow decay component on detuning between the electronic energy gap and encoding frequency. (a) Normalized electronic absorption (solid lines) and fluorescence (dashed lines) spectra for the coumarin series, with ω_{0-0} and the detuning $\Delta = \omega_{0-0} - \omega_{\text{vis}}$ indicated. (b) Normalized isotropic two-pulse signals on a linear and (c) logarithmic vertical scale. Extracted (d) time-constant τ_{slow} and (e) amplitude a_{slow} of the slow component from bi-exponential fits to each two-pulse transients as a function of detuning Δ . Error bars represent 95% confidence intervals from the fit routine. The dashed line in (a) shows a linear regression and in (b) an exponential fit. The same color coding for the coumarins is used throughout each panel.

ω_{vis} . Figure 10.1(a) plots each coumarin’s electronic absorption and fluorescence lineshapes, showing the resulting spread in detunings Δ from ~ 3000 to ~ 500 cm^{-1} . Figures 10.1(b) and (c) show the background-subtracted, normalized isotropic component of the two-pulse FEIR signals for each coumarin on linear and logarithmic vertical scales, respectively. As discussed in Chapter 9, the isotropic signal is used to avoid any dependence of orientational dynamics in the decay kinetics, although we note that the all parallel FEIR signals show essentially the same behavior. A persistent small amplitude oscillatory component evident in the C545 signal is a noise artifact, and is especially evident for this measurement due to its large one-photon background.

All of the coumarin two-pulse signals exhibit a similar bimodal decay profile. The early-time region is characterized by a roughly picosecond decay accompanied in some cases by strongly damped oscillations due to inter-mode vibrational coherences, as discussed in Chapter 8. After this fast component has relaxed, a second slower decay is evident, which may be seen more clearly in the logarithmic scaling of Figure 10.1(c). Strikingly, the relative amplitude of this slow relaxation component is much higher for the redder coumarins with smaller Δ .

To extract the characteristics of this slow relaxation component, we fit the two-pulse transients to a bi-exponential model

$$a_{\text{fast}} \exp(-\tau_{\text{enc}}/\tau_{\text{fast}}) + a_{\text{slow}} \exp(-\tau_{\text{enc}}/\tau_{\text{slow}}) \quad (10.1)$$

shown in Figure 10.A.1 of Appendix 10.A. As only the slow component is of interest, we restrict the fitting procedure to data with $\tau_{\text{enc}} > 2$ ps, with the fast component in the model used solely to provide sufficient flexibility in fitting the late-time behavior. The resulting fits adequately capture the decay profile out to the full 30 ps range scanned. The relationship

between detuning Δ and the slow component's time-constant and amplitude is shown in Figures 10.1(d) and (e), respectively. The time-constants τ_{slow} exhibit a mild slowdown as the detuning is decreased, varying by a factor of roughly 2 from the bluest to reddest energy gaps. This slowdown appears to be roughly linear in Δ , and is fit to a trend line of

$$\tau_{\text{slow}} = p_1 \Delta + p_0, \quad (10.2)$$

with $p_1 = 1.65 \times 10^{-3} \pm 0.7 \times 10^{-3}$ ps/cm⁻¹ and $p_0 = 12.2 \pm 1.3$ ps in Figure 10.1(d). The amplitude exhibits a much stronger dependence on Δ , which can be fit to an exponential model

$$a_{\text{slow}} = a \exp(-\Delta/b) + c, \quad (10.3)$$

with $a = 1.8 \pm 0.8$, $b = 450 \pm 140$ cm⁻¹, and $c = 0.051 \pm 0.028$, as shown in Figure 10.1(e).

In order to interpret these trends in the slow relaxation behavior, we must first assume that the mechanism of vibrational relaxation is qualitatively the same in each coumarin. Indeed, while small differences in behavior owing to the varying chemical substitution of the coumarin core may certainly exist, it is highly improbable that these differences should happen to conspire in such a way to produce the trends in Figures 10.1(d) and (e). Under this assumption, because the way in which the measurement is conducted cannot affect the underlying vibrational relaxation dynamics, the observed trends must reflect the differing way in which the FEIR signal reports on the molecules' time-evolving state. Figure 10.2 shows a cartoon picture indicating our proposed model for the detuning-dependence of the encoding process. As the detuning increases, the set of vibrational energy levels from which transitions to the electronic excited state are in resonance is restricted to increasingly higher energies. In

a statistical IVR process where the initially excited fundamentals have depopulated to create a distribution of population in the molecule's many lower frequency modes, the encoding process therefore samples the increasingly high energy tail of this distribution for the larger detunings.

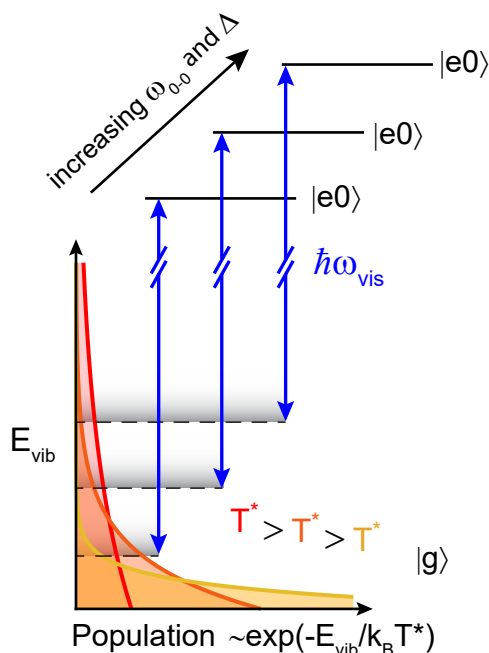


Figure 10.2: Schematic representation of vibrational cooling and how the FEIR resonance condition influences the sampling of the resulting quasi-thermal distribution.

The faster observed relaxation for these large detunings can be explained by considering a Boltzmann distribution of vibrational energy with a time-dependent temperature T^* (Figure 10.2), in which case cooling more rapidly depletes the higher energy portion of the distribution. A similar probe frequency-dependence to vibrational relaxation rates was observed in transient IR-pump visible-probe spectroscopy on small molecules in solution by Crim and coworkers.^{326,355} Within this picture of a cooling, quasi-thermal vibrational distribution, the

exponential detuning-dependence of the slow component's amplitude then follows as a natural consequence of the varying amount of population that is within encoding resonance and therefore can be sampled. Specifically, as the detuning is decreased, an increasingly larger fraction of the vibrational distribution is accessible, resulting in a larger amplitude late-time signal. The observed exponential dependence, suggesting Boltzmann statistics, is a compelling indicator of an internally relaxed, thermal distribution. In fact, directly interpreting the exponential fit parameter b in Eq. 10.3 as a thermal energy via $b = k_B T^*$ yields a value of $T^* = 650 \pm 200$ K. The original picosecond FEIR experiments by Kaiser and coworkers observed a similar exponential encoding frequency dependence of the late-time amplitude for coumarin 7 when pumping N-H and combination bands near $3 \mu\text{m}$, which suggested an internal temperature of $T^* = 400$ K.^{32,323}

10.3 Reshaping of the FEIR spectrum at late encoding delays

Resolving the relaxation kinetics in a mode-specific manner by measuring τ_{enc} -dependent FEIR spectra suggests the possibility of following the fate of each vibrational excitation through the relaxation process. However, within the statistical IVR picture suggested by the detuning-dependence, these initially prepared excited populations are essentially fully depopulated after a picosecond or so, and the surviving FEIR spectrum must be interpreted in terms of encoding the hot thermal distribution that results. Specifically, at late times the vibrational bands in the spectrum no longer reflect the population and coherence pathways involving the IR resonant fundamental transitions as laid out in the response function

framework of Chapter 2, but rather simply indicate the frequencies at which the molecule initially absorbed vibrational energy.

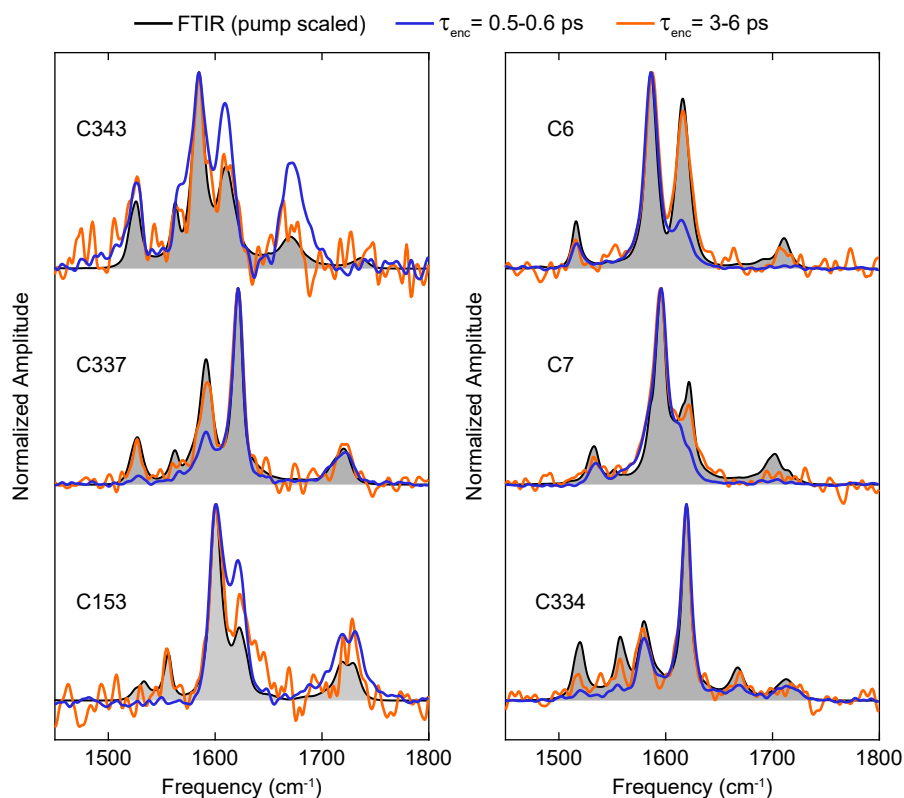


Figure 10.3: Comparison of FEIR spectra at early and late encoding delays with the IR pump-scaled FTIR spectrum for selected coumarins. The early-time spectra (blue) are the same as those shown in Chapters 7 and 8 and are either at $\tau_{\text{enc}} = 500$ or 600 fs. The late-time spectra (orange) are the result of averaging together spectra at 3, 4, 5, and 6 ps from the τ_{enc} -dependent data sets shown in Chapter 8 in order to recover somewhat higher signal to noise. The data sets on the four remaining coumarins (C30, C314, C525, C545) not shown here did not have sufficiently high signal to noise in this τ_{enc} range.

This picture is supported by comparing the early-time FEIR, late-time FEIR, and IR pump-scaled FTIR absorption spectra for various coumarins in Figure 10.3. The pump-scaled FTIR spectrum represents the frequency spectrum of absolute IR energy absorption by the molecule in the FEIR experiment. In this thesis we have discussed the various ways in

which the early-time FEIR spectra differ from conventional IR absorption, most importantly through the vibronic coupling strength that determines FEIR activity but also through the presence of vibrational coherences as well as possible finite-pulse effects. However, the late-time spectra more closely track the profile of the pump-scaled IR absorption spectra, within their more limited signal to noise. For example, the 1616 cm^{-1} ν_{R1} mode in C6 has become substantially more intense in the late-time spectrum to essentially match with its relative level in the FTIR. A similar reshaping of vibrational bands in response to relaxation has been observed in ion-detected transient IR action spectroscopy in the gas phase.³⁵⁶

10.4 Discussion and outlook

Taken together, the encoding resonance-dependence of the slow relaxation component and the reshaping of the spectra to resemble direct IR absorption suggest a rapid depletion of the initially created vibrational populations into a quasi-thermal distribution throughout the molecule's low-frequency modes, which then cools through vibrational energy transfer into the solvent. As in Chapter 7, where the effect of resonance was tuned by varying the molecular system rather than the encoding pulse, a more ideal investigation of this behavior could be achieved by way of a tunable encoding pulse. While our study here was restricted to coumarins, we have observed similar bimodal two-pulse decay kinetics in acridine and flavin dyes. It would be interesting to see under which conditions deviations from this vibrational relaxation behavior may exist in FEIR measurements.

The vibrational relaxation phenomena discussed here have some important implications for the interpretation of FEIR experiments and their possible applications. From a practical

standpoint, using relaxation transients from τ_{enc} -dependent FEIR measurements to investigate a molecule's interactions with its environment must be approached with caution to avoid convolving resonance effects with real differences in vibrational dynamics. For example, while the vibrational cooling process is undoubtedly sensitive to changing the solvent, or otherwise introducing the chromophore into a different environment, any accompanying electronic solvatochromism will also influence the observed relaxation kinetics through its modulation of the encoding resonance. Being able to separate these effects will be critical for recovering the true changes in vibrational dynamics that are of interest. Similarly, as a consequence of the spectral reshaping, the τ_{enc} -dependence of individual bands can show different relaxation kinetics. Such differences do not necessarily reflect the variations in true population lifetimes, as they are influenced by the mismatch in FEIR and IR activity of the modes in question. Another interpretation of the reshaping of band intensities is through direct energy transfer between the fundamentals. However, this interpretation is at odds with the present quasi-thermal model for the observed detuning dependence, in which the the fundamental $\nu = 1$ levels are essentially fully depopulated at these late encoding delays.

The way in which vibrational relaxation manifests in FEIR spectroscopy suggests interesting possibilities for the generation of useful FEIR signals through vibrational energy transfer. Indeed, one potential application of the spectral reshaping phenomenon is as a method for interrogating vibrations that are IR active but not vibronically coupled, and therefore appear dark in early-time spectra. While the overall signal brightness is drastically reduced for the late-time spectra of the coumarins shown here, under appropriate resonance conditions or in cases of much slower vibrational cooling these relaxation-induced FEIR bands could be used as highly sensitive or even single-molecule vibrational probes. Besides extending the set of vibrations on the fluorophore that may be used, there is the intriguing possibility of

using energy transfer to measure FEIR signals from vibrations on other molecules in contact with the fluorophore. For example, a binding partner whose intermolecular contacts induce strong anharmonic coupling of its vibrations with those of the FEIR chromophore may conceivably transfer enough vibrational energy on a picosecond timescale to yield an FEIR signal. Being able to measure the vibrational spectra of molecules in the fluorophore's immediate environment would dramatically expand the scope of investigations possible with FEIR spectroscopy.

10.A Appendix: Fitting of two-pulse transients

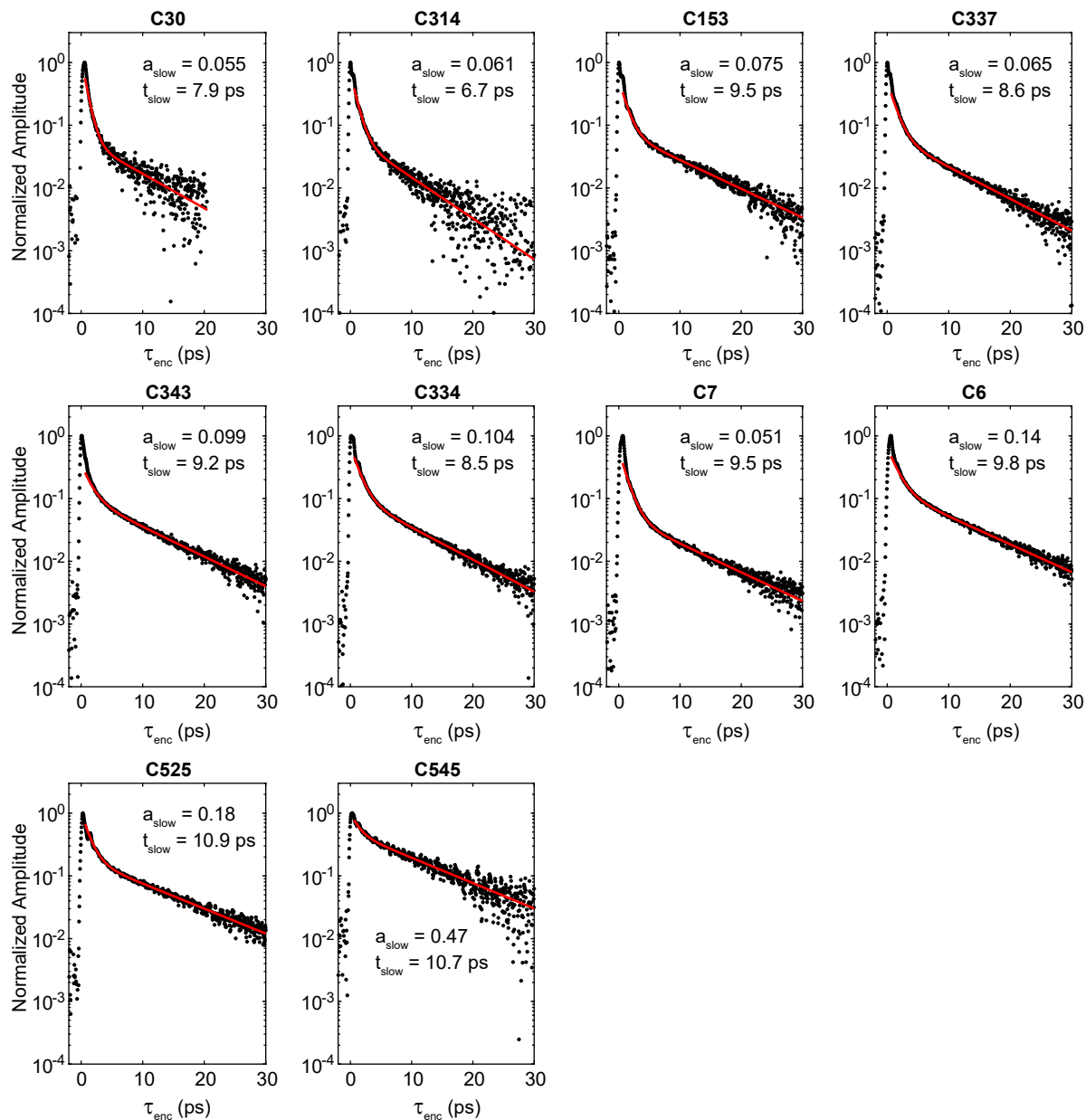


Figure 10.A.1: Bi-exponential fitting of the late-time two-pulse decay transients.

Bibliography

- (1) Moerner, W. E.; Kador, L. Optical detection and spectroscopy of single molecules in a solid. *Phys. Rev. Lett.* **1989**, *62*, 2535–2538, DOI: 10.1103/PhysRevLett.62.2535.
- (2) Orrit, M.; Bernard, J. Single pentacene molecules detected by fluorescence excitation in a p-terphenyl crystal. *Phys. Rev. Lett.* **1990**, *65*, 2716–2719, DOI: 10.1103/PhysRevLett.65.2716.
- (3) Moerner, W. E.; Orrit, M. Illuminating Single Molecules in Condensed Matter. *Science* **1999**, *283*, 1670–1676, DOI: 10.1126/science.283.5408.1670.
- (4) Moerner, W. E.; Shechtman, Y.; Wang, Q. Single-molecule spectroscopy and imaging over the decades. *Faraday Discuss.* **2015**, *184*, 9–36, DOI: 10.1039/C5FD00149H.
- (5) Brooks Shera, E.; Seitzinger, N. K.; Davis, L. M.; Keller, R. A.; Soper, S. A. Detection of single fluorescent molecules. *Chem. Phys. Lett.* **1990**, *174*, 553–557, DOI: [https://doi.org/10.1016/0009-2614\(90\)85485-U](https://doi.org/10.1016/0009-2614(90)85485-U).
- (6) Betzig, E.; Chichester, R. J. Single Molecules Observed by Near-Field Scanning Optical Microscopy. *Science* **1993**, *262*, 1422–1425, DOI: 10.1126/science.262.5138.1422.
- (7) Xie, X. S.; Dunn, R. C. Probing Single Molecule Dynamics. *Science* **1994**, *265*, 361–364, DOI: 10.1126/science.265.5170.361.
- (8) Ambrose, W. P.; Goodwin, P. M.; Keller, R. A.; Martin, J. C. Alterations of single molecule fluorescence lifetimes in near-field optical microscopy. *Science* **1994**, *265*, 364–367.
- (9) Macklin, J. J.; Trautman, J. K.; Harris, T. D.; Brus, L. E. Imaging and Time-Resolved Spectroscopy of Single Molecules at an Interface. *Science* **1996**, *272*, 255–258, DOI: 10.1126/science.272.5259.255.

- (10) Funatsu, T.; Harada, Y.; Tokunaga, M.; Saito, K.; Yanagida, T. Imaging of single fluorescent molecules and individual ATP turnovers by single myosin molecules in aqueous solution. *Nature* **1995**, *374*, 555–559, DOI: 10.1038/374555a0.
- (11) Deniz, A. A.; Mukhopadhyay, S.; Lemke, E. A. Single-molecule biophysics: at the interface of biology, physics and chemistry. *J. R. Soc. Interface* **2007**, *5*, 15–45, DOI: 10.1098/rsif.2007.1021.
- (12) Sauer, M.; Hofkens, J.; Enderlein, J., *Handbook of Fluorescence Spectroscopy and Imaging: From Ensemble to Single Molecules*; Wiley: 2010.
- (13) Shashkova, S.; Leake, M. C. Single-molecule fluorescence microscopy review: shedding new light on old problems. *Biosci. Rep.* **2017**, *37*, DOI: 10.1042/bsr20170031.
- (14) Ha, T.; Tinnefeld, P. Photophysics of Fluorescent Probes for Single-Molecule Biophysics and Super-Resolution Imaging. *Annu. Rev. Phys. Chem.* **2012**, *63*, 595–617, DOI: 10.1146/annurev-physchem-032210-103340.
- (15) English, B. P.; Min, W.; van Oijen, A. M.; Lee, K. T.; Luo, G.; Sun, H.; Cherayil, B. J.; Kou, S. C.; Xie, X. S. Ever-fluctuating single enzyme molecules: Michaelis-Menten equation revisited. *Nat. Chem. Biol* **2005**, *2*, 87–94, DOI: 10.1038/nchembio759.
- (16) Eggeling, C.; Fries, J. R.; Brand, L.; Günther, R.; Seidel, C. A. M. Monitoring conformational dynamics of a single molecule by selective fluorescence spectroscopy. *Proc. Natl. Acad. Sci. U.S.A* **1998**, *95*, 1556–1561, DOI: 10.1073/pnas.95.4.1556.
- (17) Ha, T.; Laurence, T. A.; Chemla, D. S.; Weiss, S. Polarization Spectroscopy of Single Fluorescent Molecules. *J. Phys. Chem. B* **1999**, *103*, 6839–6850, DOI: 10.1021/jp990948j.
- (18) Roy, R.; Hohng, S.; Ha, T. A practical guide to single-molecule FRET. *Nat. Methods* **2008**, *5*, 507–516, DOI: 10.1038/nmeth.1208.
- (19) Schuler, B.; Eaton, W. A. Protein folding studied by single-molecule FRET. *Curr. Opin. Struct. Biol.* **2008**, *18*, 16–26, DOI: <https://doi.org/10.1016/j.sbi.2007.12.003>.
- (20) Lerner, E.; Cordes, T.; Ingargiola, A.; Alhadid, Y.; Chung, S.; Michalet, X.; Weiss, S. Toward dynamic structural biology: Two decades of single-molecule Förster resonance energy transfer. *Science* **2018**, *359*, DOI: 10.1126/science.aan1133.

- (21) Lerner, E. et al. FRET-based dynamic structural biology: Challenges, perspectives and an appeal for open-science practices. *eLife* **2021**, *10*, ed. by Boudker, O., e60416, DOI: 10.7554/eLife.60416.
- (22) Nie, S.; Emory, S. R. Probing Single Molecules and Single Nanoparticles by Surface-Enhanced Raman Scattering. *Science* **1997**, *275*, 1102–1106, DOI: 10.1126/science.275.5303.1102.
- (23) Kneipp, K.; Wang, Y.; Kneipp, H.; Perelman, L. T.; Itzkan, I.; Dasari, R. R.; Feld, M. S. Single Molecule Detection Using Surface-Enhanced Raman Scattering (SERS). *Phys. Rev. Lett.* **1997**, *78*, 1667–1670, DOI: 10.1103/PhysRevLett.78.1667.
- (24) Le Ru, E. C.; Etchegoin, P. G. Single-Molecule Surface-Enhanced Raman Spectroscopy. *Annu. Rev. Phys. Chem.* **2012**, *63*, 65–87, DOI: 10.1146/annurev-physchem-032511-143757.
- (25) Sonntag, M. D.; Pozzi, E. A.; Jiang, N.; Hersam, M. C.; Van Duyne, R. P. Recent Advances in Tip-Enhanced Raman Spectroscopy. *J. Phys. Chem. Lett.* **2014**, *5*, 3125–3130, DOI: 10.1021/jz5015746.
- (26) Yu, Y.; Xiao, T.-H.; Wu, Y.; Li, W.; Zeng, Q.-G.; Long, L.; Li, Z.-Y. Roadmap for single-molecule surface-enhanced Raman spectroscopy. *Adv. Photonics* **2020**, *2*, 1–20, DOI: 10.1117/1.AP.2.1.014002.
- (27) Xu, X. G.; Rang, M.; Craig, I. M.; Raschke, M. B. Pushing the Sample-Size Limit of Infrared Vibrational Nanospectroscopy: From Monolayer toward Single Molecule Sensitivity. *J. Phys. Chem. Lett.* **2012**, *3*, 1836–1841, DOI: 10.1021/jz300463d.
- (28) Tanaka, T.; Yano, T.; Kato, R. Nanostructure-enhanced infrared spectroscopy. *Nanophotonics* **2021**.
- (29) Ruggeri, F. S.; Mannini, B.; Schmid, R.; Vendruscolo, M.; Knowles, T. P. J. Single molecule secondary structure determination of proteins through infrared absorption nanospectroscopy. *Nat. Commun.* **2020**, *11*, 1–9, DOI: 10.1038/s41467-020-16728-1.
- (30) Ho, W. Single-molecule chemistry. *J. Chem. Phys.* **2002**, *117*, 11033–11061, DOI: 10.1063/1.1521153.

- (31) Laubereau, A.; Seilmeier, A.; Kaiser, W. A new technique to measure ultrashort vibrational relaxation times in liquid systems. *Chem. Phys. Lett.* **1975**, *36*, 232–237, DOI: [https://doi.org/10.1016/0009-2614\(75\)87023-0](https://doi.org/10.1016/0009-2614(75)87023-0).
- (32) Seilmeier, A.; Kaiser, W., Ultrashort intramolecular and intermolecular vibrational energy transfer of polyatomic molecules in liquids In *Ultrashort Laser Pulses: Generation and Applications*, Kaiser, W., Ed.; Springer Berlin Heidelberg: Berlin, Heidelberg, 1993, pp 279–317, DOI: 10.1007/BFb0070984.
- (33) Hübner, H.-J.; Wörner, M.; Kaiser, W.; Seilmeier, A. Subpicosecond vibrational relaxation of skeletal modes in polyatomic molecules. *Chem. Phys. Lett.* **1991**, *182*, 315–320, DOI: 10.1016/0009-2614(91)80221-I.
- (34) Dahinten, T.; Baier, J.; Seilmeier, A. Vibrational energy transfer processes in dye molecules after ultrafast excitation of skeletal modes. *Chem. Phys.* **1998**, *232*, 239–245, DOI: 10.1016/S0301-0104(98)00072-X.
- (35) Wright, J. C. Double Resonance Excitation of Fluorescence in the Condensed Phase—An Alternative to Infrared, Raman, and Fluorescence Spectroscopy. *Appl. Spectrosc.* **1980**, *34*, 151–157.
- (36) Winterhalder, M. J.; Zumbusch, A.; Lippitz, M.; Orrit, M. Toward Far-field Vibrational Spectroscopy of Single Molecules at Room Temperature. *J. Phys. Chem. B* **2011**, *115*, 5425–5430, DOI: 10.1021/jp109652s.
- (37) Xiong, H.; Shi, L.; Wei, L.; Shen, Y.; Long, R.; Zhao, Z.; Min, W. Stimulated Raman excited fluorescence spectroscopy and imaging. *Nat. Photonics* **2019**, *13*, 412–417, DOI: 10.1038/s41566-019-0396-4.
- (38) Xiong, H.; Min, W. Combining the best of two worlds: Stimulated Raman excited fluorescence. *J. Chem. Phys.* **2020**, *153*, 210901, DOI: 10.1063/5.0030204.
- (39) Mastron, J. N.; Tokmakoff, A. Two-Photon-Excited Fluorescence-Encoded Infrared Spectroscopy. *J. Phys. Chem. A* **2016**, *120*, 9178–9187, DOI: 10.1021/acs.jpca.6b09158.
- (40) Mastron, J. N.; Tokmakoff, A. Fourier Transform Fluorescence-Encoded Infrared Spectroscopy. *J. Phys. Chem. A* **2018**, *122*, 554–562, DOI: 10.1021/acs.jpca.7b10305.

- (41) Courtney, T. L.; Fox, Z. W.; Slenkamp, K. M.; Khalil, M. Two-dimensional vibrational-electronic spectroscopy. *J. Chem. Phys.* **2015**, *143*, 154201, DOI: 10.1063/1.4932983.
- (42) Courtney, T. L.; Fox, Z. W.; Estergreen, L.; Khalil, M. Measuring Coherently Coupled Intramolecular Vibrational and Charge-Transfer Dynamics with Two-Dimensional Vibrational–Electronic Spectroscopy. *J. Phys. Chem. Lett.* **2015**, *6*, 1286–1292, DOI: 10.1021/acs.jpcllett.5b00356.
- (43) Gaynor, J. D.; Khalil, M. Signatures of vibronic coupling in two-dimensional electronic-vibrational and vibrational-electronic spectroscopies. *J. Chem. Phys.* **2017**, *147*, 094202, DOI: 10.1063/1.4991745.
- (44) Azumi, T.; Matsuzaki, K. What Does the Term “Vibronic Coupling” Mean? *Photochem. Photobiol.* **1977**, *25*, 315–326, DOI: <https://doi.org/10.1111/j.1751-1097.1977.tb06918.x>.
- (45) Domcke, W.; Yarkony, D. R.; Köppel, H., *Conical Intersections*; WORLD SCIENTIFIC: 2004, DOI: 10.1142/5406.
- (46) Heller, E. J. The semiclassical way to molecular spectroscopy. *Acc. Chem. Res.* **1981**, *14*, 368–375, DOI: 10.1021/ar00072a002.
- (47) Tannor, D., *Introduction to Quantum Mechanics: A Time-Dependent Perspective*; University Science Books: Sausalito, CA, 2007.
- (48) Mukamel, S., *Principles of Nonlinear Optical Spectroscopy*; Oxford University Press: New York, 1995.
- (49) Wilson, E. B.; Decius, J. C.; Cross, P. C., *Molecular vibrations: the theory of infrared and Raman vibrational spectra*; Courier Corporation: 1980.
- (50) Tokmakoff, A. Time-dependent quantum mechanics and spectroscopy, 2014.
- (51) Duschinsky, F. The importance of the electron spectrum in multi atomic molecules. Concerning the Franck-Condon principle. *Acta Physicochim. URSS* **1937**, *7*, 551–566.
- (52) Olbrich, G.; Kupka, H. The Duschinsky Effect and Optical Spectra. *Zeitschrift für Naturforschung A* **1983**, *38*, 937–946, DOI: [doi:10.1515/zna-1983-0819](https://doi.org/10.1515/zna-1983-0819).

- (53) Sharp, T. E.; Rosenstock, H. M. Franck—Condon Factors for Polyatomic Molecules. *J. Chem. Phys.* **1964**, *41*, 3453–3463, DOI: 10.1063/1.1725748.
- (54) Yan, Y. J.; Mukamel, S. Eigenstate-free, Green function, calculation of molecular absorption and fluorescence line shapes. *J. Chem. Phys.* **1986**, *85*, 5908–5923, DOI: 10.1063/1.451502.
- (55) Kundu, S.; Roy, P. P.; Fleming, G. R.; Makri, N. Franck–Condon and Herzberg–Teller Signatures in Molecular Absorption and Emission Spectra. *J. Phys. Chem. B* **2022**, *126*, 2899–2911, DOI: 10.1021/acs.jpcc.2c00846.
- (56) Orlandi, G.; Siebrand, W. Theory of vibronic intensity borrowing. Comparison of Herzberg-Teller and Born-Oppenheimer coupling. *J. Chem. Phys.* **1973**, *58*, 4513–4523, DOI: 10.1063/1.1679014.
- (57) Struve, W. S., *Fundamentals of Molecular Spectroscopy*; Wiley New York: 1989.
- (58) Kong, F.-F.; Tian, X.-J.; Zhang, Y.; Yu, Y.-J.; Jing, S.-H.; Zhang, Y.; Tian, G.-J.; Luo, Y.; Yang, J.-L.; Dong, Z.-C., et al. Probing intramolecular vibronic coupling through vibronic-state imaging. *Nat. Commun.* **2021**, *12*, 1–8.
- (59) Merzbacher, E., *Quantum Mechanics*, 3rd; Wiley: 1998.
- (60) Cohen-Tannoudji, C.; Diu, B.; Laloë, F., *Quantum mechanics*; WILEY-VCH Verlag GmbH: 2005; Vol. 1.
- (61) Kupka, H.; Cribb, P. H. Multidimensional Franck–Condon integrals and Duschinsky mixing effects. *J. Chem. Phys.* **1986**, *85*, 1303–1315, DOI: 10.1063/1.451216.
- (62) Palma, A.; Morales, J. Franck-CONDON factors and ladder operators. I. harmonic oscillator. *Int. J. Quantum Chem.* **2009**, *24*, 393–400, DOI: 10.1002/qua.560240843.
- (63) Arfken, G. B.; Weber, H. J.; Harris, F. E., *Mathematical Methods for Physicists*, 7th; Elsevier: 2013.
- (64) Ohta, K.; Larsen, D. S.; Yang, M.; Fleming, G. R. Influence of intramolecular vibrations in third-order, time-domain resonant spectroscopies. II. Numerical calculations. *J. Chem. Phys.* **2001**, *114*, 8020–8039.
- (65) Shim, S.; Stuart, C. M.; Mathies, R. A. Resonance Raman Cross-Sections and Vibronic Analysis of Rhodamine 6G from Broadband Stimulated Raman Spectroscopy.

- ChemPhysChem* **2008**, *9*, 697–699, DOI: <https://doi.org/10.1002/cphc.200700856>.
- (66) Lee, G.; Kim, J.; Kim, S. Y.; Kim, D. E.; Joo, T. Vibrational Spectrum of an Excited State and Huang–Rhys Factors by Coherent Wave Packets in Time-Resolved Fluorescence Spectroscopy. *ChemPhysChem* **2017**, *18*, 670–676, DOI: <https://doi.org/10.1002/cphc.201601295>.
- (67) Doktorov, E.; Malkin, I.; Man'ko, V. Dynamical symmetry of vibronic transitions in polyatomic molecules and the Franck–Condon principle. *JJ. Mol. Spectrosc.* **1975**, *56*, 1–20, DOI: [https://doi.org/10.1016/0022-2852\(75\)90199-X](https://doi.org/10.1016/0022-2852(75)90199-X).
- (68) Doktorov, E.; Malkin, I.; Man'ko, V. Dynamical symmetry of vibronic transitions in polyatomic molecules and the Franck–Condon principle. *JJ. Mol. Spectrosc.* **1977**, *64*, 302–326, DOI: [https://doi.org/10.1016/0022-2852\(77\)90269-7](https://doi.org/10.1016/0022-2852(77)90269-7).
- (69) Lermé, J. Iterative methods to compute one- and two-dimensional Franck–Condon factors. Tests of accuracy and application to study indirect molecular transitions. *Chem. Phys.* **1990**, *145*, 67–88, DOI: [https://doi.org/10.1016/0301-0104\(90\)80119-I](https://doi.org/10.1016/0301-0104(90)80119-I).
- (70) Ruhoff, P. T.; Ratner, M. A. Algorithms for computing Franck–Condon overlap integrals. *Int. J. Quantum Chem.* **2000**, *77*, 383–392, DOI: [https://doi.org/10.1002/\(SICI\)1097-461X\(2000\)77:1<383::AID-QUA38>3.0.CO;2-0](https://doi.org/10.1002/(SICI)1097-461X(2000)77:1<383::AID-QUA38>3.0.CO;2-0).
- (71) Liang, J.; Zheng, H.; Zhang, X.; Li, R.; Cui, Z. Exact evaluation of the multidimensional Franck–Condon integrals based on the contour integral method. *Mol. Phys.* **2007**, *105*, 1903–1907, DOI: [10.1080/00268970701463276](https://doi.org/10.1080/00268970701463276).
- (72) Lee, C.-L.; Yang, S.-H.; Kuo, S.-Y.; Chang, J.-L. A general formula of two-dimensional Franck–Condon integral and the photoelectron spectroscopy of sulfur dioxide. *JJ. Mol. Spectrosc.* **2009**, *256*, 279–286, DOI: <https://doi.org/10.1016/j.jms.2009.05.006>.
- (73) Fu, Z.; Zheng, X.; Liang, J. A general analytical expression for evaluation of an arbitrary n-dimensional Franck–Condon overlap integral including the Duschinsky effect. *Comput. Theor. Chem* **2022**, *1207*, 113501, DOI: <https://doi.org/10.1016/j.comptc.2021.113501>.
- (74) Von Cosel, J.; Cerezo, J.; Kern-Michler, D.; Neumann, C.; van Wilderen, L. J. G. W.; Bredenbeck, J.; Santoro, F.; Burghardt, I. Vibrationally resolved electronic spectra

- including vibrational pre-excitation: Theory and application to VIPER spectroscopy. *J. Chem. Phys.* **2017**, *147*, 164116, DOI: 10.1063/1.4999455.
- (75) Santoro, F.; Lami, A.; Improta, R.; Barone, V. Effective method to compute vibrationally resolved optical spectra of large molecules at finite temperature in the gas phase and in solution. *J. Chem. Phys.* **2007**, *126*, 184102, DOI: 10.1063/1.2721539.
- (76) Milonni, P. W. Why Spontaneous Emission? *Am. J. Phys.* **1984**, *52*, 340–343.
- (77) Loudon, R., *The Quantum Theory of Light*, 3rd; Oxford University Press: Oxford, 2000.
- (78) Cohen-Tannoudji, C.; Dupont-Roc, J.; Grynberg, G., *Photons and Atoms*; Wiley: 1997, DOI: 10.1002/9783527618422.
- (79) Lamb, W. E. Anti-photon. *Appl. Phys. B* **1995**, *60*, 77–84, DOI: 10.1007/bf01135846.
- (80) Cohen-Tannoudji, C.; Dupont-Roc, J.; Grynberg, G., *Atom—Photon Interactions*; Wiley: 1998, DOI: 10.1002/9783527617197.
- (81) Craig, D. P.; Thirunamachandran, T., *Molecular Quantum Electrodynamics: an Introduction to Radiation-Molecule Interactions*; Courier Corporation: 1998.
- (82) Scully, M. O.; Zubairy, M. S., *Quantum Optics*; Cambridge University Press: 1997, DOI: 10.1017/CB09780511813993.
- (83) Setlow, R., Action Spectroscopy In *Advances in Biological and Medical Physics*, Vol. 5; Elsevier: 1957, pp 37–74, DOI: <https://doi.org/10.1016/B978-1-4832-3111-2.50005-5>.
- (84) Schäfer, E.; Fukshansky, L.; Shropshire, W., Action Spectroscopy of Photoreversible Pigment Systems In *Photomorphogenesis*, Shropshire, W., Mohr, H., Eds.; Springer Berlin Heidelberg: Berlin, Heidelberg, 1983, pp 39–68, DOI: 10.1007/978-3-642-68918-5_4.
- (85) Engelmann, T. W. Farbe und assimilation. *Botanische Zeitung* **1883**, *41*, 17–29.
- (86) Hintz, N. H. Highlighting Theodor W. Engelmann’s “Farbe und Assimilation” [Color and Assimilation]. *Limnol Oceanogr Bull* **2021**, *30*, 121–126, DOI: <https://doi.org/10.1002/lob.10470>.

- (87) Baer, T.; Dunbar, R. C. Ion spectroscopy: Where did it come from; where is it now; and where is it going? *Journal of the American Society for Mass Spectrometry* **2010**, *21*, 681–693, DOI: 10.1016/j.jasms.2010.01.028.
- (88) Scherer, N. F.; Ruggiero, A. J.; Du, M.; Fleming, G. R. Time resolved dynamics of isolated molecular systems studied with phase-locked femtosecond pulse pairs. *J. Chem. Phys.* **1990**, *93*, 856–857, DOI: 10.1063/1.459456.
- (89) Scherer, N. F.; Carlson, R. J.; Matro, A.; Du, M.; Ruggiero, A. J.; Romero-Rochin, V.; Cina, J. A.; Fleming, G. R.; Rice, S. A. Fluorescence-detected wave packet interferometry: Time resolved molecular spectroscopy with sequences of femtosecond phase-locked pulses. *J. Chem. Phys.* **1991**, *95*, 1487–1511, DOI: 10.1063/1.461064.
- (90) Tekavec, P. F.; Dyke, T. R.; Marcus, A. H. Wave packet interferometry and quantum state reconstruction by acousto-optic phase modulation. *J. Chem. Phys.* **2006**, *125*, 194303, DOI: 10.1063/1.2386159.
- (91) Wagner, W.; Li, C.; Semmlow, J.; Warren, W. S. Rapid phase-cycled two-dimensional optical spectroscopy in fluorescence and transmission mode. *Opt. Express* **2005**, *13*, 3697–3706, DOI: 10.1364/OPEX.13.003697.
- (92) Tekavec, P. F.; Lott, G. A.; Marcus, A. H. Fluorescence-detected two-dimensional electronic coherence spectroscopy by acousto-optic phase modulation. *J. Chem. Phys.* **2007**, *127*, 214307, DOI: 10.1063/1.2800560.
- (93) Perdomo-Ortiz, A.; Widom, J. R.; Lott, G. A.; Aspuru-Guzik, A.; Marcus, A. H. Conformation and Electronic Population Transfer in Membrane-Supported Self-Assembled Porphyrin Dimers by 2D Fluorescence Spectroscopy. *J. Phys. Chem. B* **2012**, *116*, 10757–10770, DOI: 10.1021/jp305916x.
- (94) Kühn, O.; Mančal, T.; Pullerits, T. Interpreting Fluorescence Detected Two-Dimensional Electronic Spectroscopy. *J. Phys. Chem. Lett.* **2020**, *11*, 838–842, DOI: 10.1021/acs.jpcllett.9b03851.
- (95) Nardin, G.; Autry, T. M.; Silverman, K. L.; Cundiff, S. T. Multidimensional coherent photocurrent spectroscopy of a semiconductor nanostructure. *Opt. Express* **2013**, *21*, 28617–28627, DOI: 10.1364/OE.21.028617.
- (96) Karki, K. J.; Widom, J. R.; Seibt, J.; Moody, I.; Lonergan, M. C.; Pullerits, T.; Marcus, A. H. Coherent two-dimensional photocurrent spectroscopy in a PbS quantum dot photocell. *Nat. Commun.* **2014**, *5*, DOI: 10.1038/ncomms6869.

- (97) Bakulin, A. A.; Silva, C.; Vella, E. Ultrafast Spectroscopy with Photocurrent Detection: Watching Excitonic Optoelectronic Systems at Work. *J. Phys. Chem. Lett.* **2016**, *7*, 250–258, DOI: 10.1021/acs.jpcllett.5b01955.
- (98) Grégoire, P.; Srimath Kandada, A. R.; Vella, E.; Tao, C.; Leonelli, R.; Silva, C. Incoherent population mixing contributions to phase-modulation two-dimensional coherent excitation spectra. *J. Chem. Phys.* **2017**, *147*, 114201, DOI: 10.1063/1.4994987.
- (99) Ouyang, Z.; Zhou, N.; Hu, J.; Williams, O. F.; Yan, L.; You, W.; Moran, A. M. Nonlinear fluorescence spectroscopy of layered perovskite quantum wells. *J. Chem. Phys.* **2020**, *153*, 134202, DOI: 10.1063/5.0021759.
- (100) Zhou, N.; Ouyang, Z.; Hu, J.; Williams, O. F.; Yan, L.; You, W.; Moran, A. M. Distinguishing Energy- and Charge-Transfer Processes in Layered Perovskite Quantum Wells with Two-Dimensional Action Spectroscopies. *J. Phys. Chem. Lett.* **2020**, *11*, 4570–4577, DOI: 10.1021/acs.jpcllett.0c00844.
- (101) Bolzonello, L.; Bernal-Texca, F.; Gerling, L. G.; Ockova, J.; Collini, E.; Martorell, J.; van Hulst, N. F. Photocurrent-Detected 2D Electronic Spectroscopy Reveals Ultrafast Hole Transfer in Operating PM6/Y6 Organic Solar Cells. *J. Phys. Chem. Lett.* **2021**, *12*, 3983–3988, DOI: 10.1021/acs.jpcllett.1c00822.
- (102) Aeschlimann, M.; Brixner, T.; Fischer, A.; Kramer, C.; Melchior, P.; Pfeiffer, W.; Schneider, C.; Strüber, C.; Tuchscherer, P.; Voronine, D. V. Coherent Two-Dimensional Nanoscopy. *Science* **2011**, *333*, 1723–1726, DOI: 10.1126/science.1209206.
- (103) Roeding, S.; Brixner, T. Coherent two-dimensional electronic mass spectrometry. *Nat. Commun.* **2018**, *9*, DOI: 10.1038/s41467-018-04927-w.
- (104) Bruder, L.; Bangert, U.; Binz, M.; Uhl, D.; Vexiau, R.; Bouloufa-Maafa, N.; Dulieu, O.; Stienkemeier, F. Coherent multidimensional spectroscopy of dilute gas-phase nanosystems. *Nat. Commun.* **2018**, *9*, DOI: 10.1038/s41467-018-07292-w.
- (105) Bruder, L.; Bangert, U.; Binz, M.; Uhl, D.; Stienkemeier, F. Coherent multidimensional spectroscopy in the gas phase. *J. Phys. B: At. Mol. Opt. Phys.* **2019**, *52*, 183501, DOI: 10.1088/1361-6455/ab319f.

- (106) Chen, L.; Dean, J. L. S.; Fournier, J. A. Time-Domain Vibrational Action Spectroscopy of Cryogenically Cooled, Messenger-Tagged Ions Using Ultrafast IR Pulses. *J. Phys. Chem. A* **2021**, *125*, 10235–10244, DOI: 10.1021/acs.jpca.1c01996.
- (107) Kubo, R. Statistical-Mechanical Theory of Irreversible Processes. I. General Theory and Simple Applications to Magnetic and Conduction Problems. *J. Phys. Soc. Japan* **1957**, *12*, 570–586, DOI: 10.1143/JPSJ.12.570.
- (108) Sakurai, J. J., *Modern Quantum Mechanics; rev. ed.* Addison-Wesley: Reading, MA, 1994.
- (109) Schatz, G. C.; Ratner, M. A., *Quantum Mechanics in Chemistry*; Courier Corporation: 2002.
- (110) Power, E. A.; Thirunamachandran, T. On the Nature of the Hamiltonian for the Interaction of Radiation with Atoms and Molecules: $(e/mc)p \cdot A$, $-\mu \cdot E$, and All That. *Am. J. Phys.* **1978**, *46*, 370–378, DOI: 10.1119/1.11313.
- (111) Cho, M., *Two-Dimensional Optical Spectroscopy*; CRC Press: 2009, DOI: 10.1201/9781420084306.
- (112) Mukamel, S. Nonimpact unified theory of four-wave mixing and two-photon processes. *Phys. Rev. A* **1983**, *28*, 3480–3492, DOI: 10.1103/PhysRevA.28.3480.
- (113) Mukamel, S., Solvation Effects in Four-Wave Mixing and Spontaneous Raman and Fluorescence Lineshapes of Polyatomic Molecules In *Advances in Chem. Phys.* John Wiley & Sons, Ltd: 1988, pp 165–230, DOI: <https://doi.org/10.1002/9780470141199.ch6>.
- (114) Cho, M.; Scherer, N. F.; Fleming, G. R.; Mukamel, S. Photon echoes and related four-wave-mixing spectroscopies using phase-locked pulses. *J. Chem. Phys.* **1992**, *96*, 5618–5629, DOI: 10.1063/1.462686.
- (115) Khalil, M.; Demirdöven, N.; Tokmakoff, A. Coherent 2D IR Spectroscopy: Molecular Structure and Dynamics in Solution. *J. Phys. Chem. A* **2003**, *107*, 5258–5279, DOI: 10.1021/jp0219247.
- (116) Tan, H.-S. Theory and phase-cycling scheme selection principles of collinear phase coherent multi-dimensional optical spectroscopy. *J. Chem. Phys.* **2008**, *129*, 124501, DOI: 10.1063/1.2978381.

- (117) Schröter, M.; Pullerits, T.; Kühn, O. Using fluorescence detected two-dimensional spectroscopy to investigate initial exciton delocalization between coupled chromophores. *J. Chem. Phys.* **2018**, *149*, 114107, DOI: 10.1063/1.5046645.
- (118) Karki, K. J.; Chen, J.; Sakurai, A.; Shi, Q.; Gardiner, A. T.; Kühn, O.; Cogdell, R. J.; Pullerits, T. Before Förster. Initial excitation in photosynthetic light harvesting. *Chem. Sci.* **2019**, *10*, 7923–7928, DOI: 10.1039/C9SC01888C.
- (119) Malý, P.; Mančal, T. Signatures of Exciton Delocalization and Exciton–Exciton Annihilation in Fluorescence-Detected Two-Dimensional Coherent Spectroscopy. *J. Phys. Chem. Lett.* **2018**, *9*, 5654–5659, DOI: 10.1021/acs.jpcllett.8b02271.
- (120) Ippen, E. P. Nonlinear Optics, Lecture notes, MIT, 2012.
- (121) Butcher, P. N.; Cotter, D., *The Elements of Nonlinear Optics*; 9; Cambridge university press: 1990.
- (122) De, A. K.; Monahan, D.; Dawlaty, J. M.; Fleming, G. R. Two-dimensional fluorescence-detected coherent spectroscopy with absolute phasing by confocal imaging of a dynamic grating and 27-step phase-cycling. *J. Chem. Phys.* **2014**, *140*, 194201, DOI: 10.1063/1.4874697.
- (123) Sung, J.; Silbey, R. J. Four wave mixing spectroscopy for a multilevel system. *J. Chem. Phys.* **2001**, *115*, 9266–9287, DOI: 10.1063/1.1413979.
- (124) Mukamel, S. Collisional broadening of spectral line shapes in two-photon and multiphoton processes. *Phys. Rep.* **1982**, *93*, 1–60, DOI: [https://doi.org/10.1016/0370-1573\(82\)90064-3](https://doi.org/10.1016/0370-1573(82)90064-3).
- (125) Allen, L.; Eberly, J. H., *Optical resonance and two-level atoms*; Courier Corporation: 1987; Vol. 28.
- (126) Bloch, F. Nuclear Induction. *Phys. Rev.* **1946**, *70*, 460–474, DOI: 10.1103/PhysRev.70.460.
- (127) Jean, J. M.; Fleming, G. R. Competition between energy and phase relaxation in electronic curve crossing processes. *J. Chem. Phys.* **1995**, *103*, 2092–2101, DOI: 10.1063/1.469684.
- (128) Fiete, G. A.; Heller, E. J. Semiclassical theory of coherence and decoherence. *Phys. Rev. A* **2003**, *68*, 022112, DOI: 10.1103/PhysRevA.68.022112.

- (129) Gallagher Faeder, S. M.; Jonas, D. M. Phase-resolved time-domain nonlinear optical signals. *Phys. Rev. A* **2000**, *62*, 033820, DOI: 10.1103/PhysRevA.62.033820.
- (130) Cho, M.; Fleming, G. R.; Mukamel, S. Nonlinear response functions for birefringence and dichroism measurements in condensed phases. *J. Chem. Phys.* **1993**, *98*, 5314–5326, DOI: 10.1063/1.464931.
- (131) Lee, D.; Albrecht, A. C. A unified view of Raman, resonance Raman, and fluorescence spectroscopy (and their analogues in two-photon absorption). *Advances in infrared and Raman Spectroscopy* **1985**, *12*, 179–213.
- (132) Hamm, P.; Zanni, M., *Concepts and Methods of 2D Infrared Spectroscopy*; Cambridge University Press: 2011, DOI: 10.1017/CB09780511675935.
- (133) Mandel, L.; Wolf, E., *Optical Coherence and Quantum Optics*; Cambridge university press: 1995.
- (134) Shen, Y.-R., *Principles of Nonlinear Optics*; Wiley-Interscience, New York, NY, USA: 1984.
- (135) Jonas, D. M. Two-Dimensional Femtosecond Spectroscopy. *Annu. Rev. Phys. Chem.* **2003**, *54*, 425–463, DOI: 10.1146/annurev.physchem.54.011002.103907.
- (136) Kunsel, T.; Tiwari, V.; Matutes, Y. A.; Gardiner, A. T.; Cogdell, R. J.; Ogilvie, J. P.; Jansen, T. L. C. Simulating Fluorescence-Detected Two-Dimensional Electronic Spectroscopy of Multichromophoric Systems. *J. Phys. Chem. B* **2019**, *123*, 394–406, DOI: 10.1021/acs.jpcc.8b10176.
- (137) Malý, P.; Lüttig, J.; Mueller, S.; Schreck, M. H.; Lambert, C.; Brixner, T. Coherently and fluorescence-detected two-dimensional electronic spectroscopy: direct comparison on squaraine dimers. *Phys. Chem. Chem. Phys.* **2020**, *22*, 21222–21237, DOI: 10.1039/D0CP03218B.
- (138) Damtie, F. A.; Wacker, A.; Pullerits, T.; Karki, K. J. Two-dimensional action spectroscopy of excitonic systems: Explicit simulation using a phase-modulation technique. *Phys. Rev. A* **2017**, *96*, 053830, DOI: 10.1103/PhysRevA.96.053830.
- (139) Boyd, R. W., *Nonlinear Optics*; Academic press: 2020.
- (140) Hybl, J. D.; Albrecht Ferro, A.; Jonas, D. M. Two-dimensional Fourier transform electronic spectroscopy. *J. Chem. Phys.* **2001**, *115*, 6606–6622, DOI: 10.1063/1.1398579.

- (141) Gallagher Faeder, S. M.; Jonas, D. M. Two-Dimensional Electronic Correlation and Relaxation Spectra: Theory and Model Calculations. *J. Phys. Chem. A* **1999**, *103*, 10489–10505, DOI: 10.1021/jp9925738.
- (142) Malý, P.; Brixner, T. Fluorescence-Detected Pump–Probe Spectroscopy. *Angew. Chem. Int. Ed.* **2021**, *60*, 18867–18875, DOI: <https://doi.org/10.1002/anie.202102901>.
- (143) Brinks, D.; Stefani, F. D.; Kulzer, F.; Hildner, R.; Taminiau, T. H.; Avlasevich, Y.; Müllen, K.; van Hulst, N. F. Visualizing and controlling vibrational wave packets of single molecules. *Nature* **2010**, *465*, 905–908, DOI: 10.1038/nature09110.
- (144) Hildner, R.; Brinks, D.; Nieder, J. B.; Cogdell, R. J.; van Hulst, N. F. Quantum Coherent Energy Transfer over Varying Pathways in Single Light-Harvesting Complexes. *Science* **2013**, *340*, 1448–1451, DOI: 10.1126/science.1235820.
- (145) Weigel, A.; Sebesta, A.; Kukura, P. Shaped and Feedback-Controlled Excitation of Single Molecules in the Weak-Field Limit. *J. Phys. Chem. Lett.* **2015**, *6*, 4032–4037, DOI: 10.1021/acs.jpcllett.5b01748.
- (146) Piatkowski, L.; Gellings, E.; van Hulst, N. F. Broadband single-molecule excitation spectroscopy. *Nat. Commun.* **2016**, *7*, DOI: 10.1038/ncomms10411.
- (147) Liebel, M.; Toninelli, C.; van Hulst, N. F. Room-temperature ultrafast nonlinear spectroscopy of a single molecule. *Nature Photonics* **2017**, *12*, 45–49, DOI: 10.1038/s41566-017-0056-5.
- (148) Moya, R.; Kondo, T.; Norris, A. C.; Schlau-Cohen, G. S. Spectrally-tunable femtosecond single-molecule pump-probe spectroscopy. *Opt. Express* **2021**, *29*, 28246–28256, DOI: 10.1364/OE.432995.
- (149) Moya, R.; Norris, A. C.; Kondo, T.; Schlau-Cohen, G. S. Observation of robust energy transfer in the photosynthetic protein allophycocyanin using single-molecule pump–probe spectroscopy. *Nature Chemistry* **2022**, *14*, 153–159, DOI: 10.1038/s41557-021-00841-9.
- (150) Monmayrant, A.; Weber, S.; Chatel, B. A newcomer’s guide to ultrashort pulse shaping and characterization. *J. Phys. B: At. Mol. Opt. Phys.* **2010**, *43*, 103001, DOI: 10.1088/0953-4075/43/10/103001.

- (151) Gundogdu, K.; Stone, K. W.; Turner, D. B.; Nelson, K. A. Multidimensional coherent spectroscopy made easy. *Chem. Phys.* **2007**, *341*, 89–94, DOI: <https://doi.org/10.1016/j.chemphys.2007.06.027>.
- (152) Draeger, S.; Roeding, S.; Brixner, T. Rapid-scan coherent 2D fluorescence spectroscopy. *Opt. Express* **2017**, *25*, 3259–3267, DOI: [10.1364/OE.25.003259](https://doi.org/10.1364/OE.25.003259).
- (153) Tiwari, V.; Matutes, Y. A.; Konar, A.; Yu, Z.; Ptaszek, M.; Bocian, D. F.; Holten, D.; Kirmaier, C.; Ogilvie, J. P. Strongly coupled bacteriochlorin dyad studied using phase-modulated fluorescence-detected two-dimensional electronic spectroscopy. *Opt. Express* **2018**, *26*, 22327–22341, DOI: [10.1364/OE.26.022327](https://doi.org/10.1364/OE.26.022327).
- (154) Agathangelou, D.; Javed, A.; Sessa, F.; Solinas, X.; Joffre, M.; Ogilvie, J. P. Phase-modulated rapid-scanning fluorescence-detected two-dimensional electronic spectroscopy. *J. Chem. Phys.* **2021**, *155*, 094201, DOI: [10.1063/5.0057649](https://doi.org/10.1063/5.0057649).
- (155) Karki, K. J.; Ciappina, M. F. Advances in nonlinear spectroscopy using phase modulated light fields: prospective applications in perturbative and non-perturbative regimes. *Adv. Phys.: X* **2022**, *7*, 2090856, DOI: [10.1080/23746149.2022.2090856](https://doi.org/10.1080/23746149.2022.2090856).
- (156) DeFlores, L. P.; Nicodemus, R. A.; Tokmakoff, A. Two-dimensional Fourier transform spectroscopy in the pump-probe geometry. *Optics Letters* **2007**, *32*, 2966–2968, DOI: [10.1364/OL.32.002966](https://doi.org/10.1364/OL.32.002966).
- (157) Shim, S.-H.; Zanni, M. T. How to turn your pump-probe instrument into a multidimensional spectrometer: 2D IR and Vis spectroscopies via pulse shaping. *Phys. Chem. Chem. Phys.* **2009**, *11*, 748–761, DOI: [10.1039/B813817F](https://doi.org/10.1039/B813817F).
- (158) Dong, H.; Lewis, N. H. C.; Oliver, T. A. A.; Fleming, G. R. Determining the static electronic and vibrational energy correlations via two-dimensional electronic-vibrational spectroscopy. *J. Chem. Phys.* **2015**, *142*, 174201, DOI: [10.1063/1.4919684](https://doi.org/10.1063/1.4919684).
- (159) De A. Camargo, F. V.; Grimmelsmann, L.; Anderson, H. L.; Meech, S. R.; Heisler, I. A. Resolving Vibrational from Electronic Coherences in Two-Dimensional Electronic Spectroscopy: The Role of the Laser Spectrum. *Phys. Rev. Lett.* **2017**, *118*, 033001, DOI: [10.1103/PhysRevLett.118.033001](https://doi.org/10.1103/PhysRevLett.118.033001).
- (160) Perlík, V.; Hauer, J.; Šanda, F. Finite pulse effects in single and double quantum spectroscopies. *J. Opt. Soc. Am. B* **2017**, *34*, 430–439, DOI: [10.1364/JOSAB.34.000430](https://doi.org/10.1364/JOSAB.34.000430).

- (161) Joo, T.; Jia, Y.; Yu, J.-Y.; Lang, M. J.; Fleming, G. R. Third-order nonlinear time domain probes of solvation dynamics. *J. Chem. Phys.* **1996**, *104*, 6089–6108, DOI: 10.1063/1.471276.
- (162) Farrow, D. A.; Yu, A.; Jonas, D. M. Spectral relaxation in pump–probe transients. *J. Chem. Phys.* **2003**, *118*, 9348–9356, DOI: 10.1063/1.1564058.
- (163) Yang, M. Effect of finite pulse duration in three pulse photon echo experiments: Numerical comparison of 3PEPS and S3PE. *Chem. Phys. Lett.* **2009**, *467*, 304–308, DOI: <https://doi.org/10.1016/j.cplett.2008.11.051>.
- (164) Tekavec, P. F.; Myers, J. A.; Lewis, K. L. M.; Fuller, F. D.; Ogilvie, J. P. Effects of chirp on two-dimensional Fourier transform electronic spectra. *Opt. Express* **2010**, *18*, 11015–11024, DOI: 10.1364/OE.18.011015.
- (165) Polli, D.; Brida, D.; Mukamel, S.; Lanzani, G.; Cerullo, G. Effective temporal resolution in pump-probe spectroscopy with strongly chirped pulses. *Phys. Rev. A* **2010**, *82*, 053809, DOI: 10.1103/PhysRevA.82.053809.
- (166) Smallwood, C. L.; Autry, T. M.; Cundiff, S. T. Analytical solutions to the finite-pulse Bloch model for multidimensional coherent spectroscopy. *J. Opt. Soc. Am. B* **2017**, *34*, 419–429, DOI: 10.1364/JOSAB.34.000419.
- (167) Hamm, P. Coherent effects in femtosecond infrared spectroscopy. *Chem. Phys.* **1995**, *200*, 415–429, DOI: [https://doi.org/10.1016/0301-0104\(95\)00262-6](https://doi.org/10.1016/0301-0104(95)00262-6).
- (168) Yan, S.; Seidel, M. T.; Tan, H.-S. Perturbed free induction decay in ultrafast mid-IR pump–probe spectroscopy. *Chem. Phys. Lett.* **2011**, *517*, 36–40, DOI: <https://doi.org/10.1016/j.cplett.2011.10.013>.
- (169) Dobryakov, A. L.; Kovalenko, S. A.; Ernsting, N. P. Coherent and sequential contributions to femtosecond transient absorption spectra of a rhodamine dye in solution. *J. Chem. Phys.* **2005**, *123*, 044502, DOI: 10.1063/1.1948383.
- (170) Hybl, J. D.; Christophe, Y.; Jonas, D. M. Peak shapes in femtosecond 2D correlation spectroscopy. *Chem. Phys.* **2001**, *266*, 295–309, DOI: [https://doi.org/10.1016/S0301-0104\(01\)00233-6](https://doi.org/10.1016/S0301-0104(01)00233-6).
- (171) Paleček, D.; Edlund, P.; Gustavsson, E.; Westenhoff, S.; Zigmantas, D. Potential pitfalls of the early-time dynamics in two-dimensional electronic spectroscopy. *J. Chem. Phys.* **2019**, *151*, 024201, DOI: 10.1063/1.5079817.

- (172) Rose, P. A.; Krich, J. J. Automatic Feynman diagram generation for nonlinear optical spectroscopies and application to fifth-order spectroscopy with pulse overlaps. *J. Chem. Phys.* **2021**, *154*, 034109, DOI: 10.1063/5.0024105.
- (173) Ekvall, K.; van der Meulen, P.; Dhollande, C.; Berg, L.-E.; Pommeret, S.; Naskrecki, R.; Mialocq, J.-C. Cross phase modulation artifact in liquid phase transient absorption spectroscopy. *J. Appl. Phys.* **2000**, *87*, 2340–2352, DOI: 10.1063/1.372185.
- (174) Lorenc, M.; Ziolk, M.; Naskrecki, R.; Karolczak, J.; Kubicki, J.; Maciejewski, A. Artifacts in femtosecond transient absorption spectroscopy. *Appl. Phys. B: Lasers and Optics* **2002**, *74*, 19–27, DOI: 10.1007/s003400100750.
- (175) Gdor, I.; Ghosh, T.; Lioubashevski, O.; Ruhman, S. Nonresonant Raman Effects on Femtosecond Pump–Probe with Chirped White Light: Challenges and Opportunities. *J. Phys. Chem. Lett.* **2017**, *8*, 1920–1924, DOI: 10.1021/acs.jpcllett.7b00559.
- (176) Mueller, S.; Draeger, S.; Ma, X.; Hensen, M.; Kenneweg, T.; Pfeiffer, W.; Brixner, T. Fluorescence-Detected Two-Quantum and One-Quantum–Two-Quantum 2D Electronic Spectroscopy. *J. Phys. Chem. Lett.* **2018**, *9*, 1964–1969, DOI: 10.1021/acs.jpcllett.8b00541.
- (177) Marshall, A. G.; Verdun, F. R., *Fourier transforms in NMR, optical, and mass spectrometry: a user's handbook*; Elsevier: 1990.
- (178) Albrecht, A. W.; Hybl, J. D.; Gallagher Faeder, S. M.; Jonas, D. M. Experimental distinction between phase shifts and time delays: Implications for femtosecond spectroscopy and coherent control of chemical reactions. *J. Chem. Phys.* **1999**, *111*, 10934–10956, DOI: 10.1063/1.480457.
- (179) Diels, J.-C.; Rudolph, W., *Ultrashort Laser Pulse Phenomena*; Elsevier: 2006.
- (180) Boashash, B. Estimating and interpreting the instantaneous frequency of a signal. I. Fundamentals. *Proc. IEEE* **1992**, *80*, 520–538, DOI: 10.1109/5.135376.
- (181) Mandel, L. Complex Representation of Optical Fields in Coherence Theory. *J. Opt. Soc. Am.* **1967**, *57*, 613–617, DOI: 10.1364/JOSA.57.000613.
- (182) Caffisch, R. E. Monte carlo and quasi-monte carlo methods. *Acta numerica* **1998**, *7*, 1–49.
- (183) Robert, C. P.; Casella, G.; Casella, G., *Monte Carlo statistical methods*; Springer: 1999; Vol. 2.

- (184) McMorro, D.; Lotshaw, W. T. The frequency response of condensed-phase media to femtosecond optical pulses: spectral-filter effects. *Chem. Phys. Lett.* **1990**, *174*, 85–94, DOI: [https://doi.org/10.1016/0009-2614\(90\)85331-6](https://doi.org/10.1016/0009-2614(90)85331-6).
- (185) Göppert-Mayer, M. Über Elementarakte mit zwei Quantensprüngen. *Annalen der Physik* **1931**, *401*, 273–294, DOI: <https://doi.org/10.1002/andp.19314010303>.
- (186) Peticolas, W. L. Multiphoton Spectroscopy. *Annu. Rev. Phys. Chem.* **1967**, *18*, 233–260, DOI: [10.1146/annurev.pc.18.100167.001313](https://doi.org/10.1146/annurev.pc.18.100167.001313).
- (187) Raymer, M. G.; Landes, T.; Marcus, A. H. Entangled two-photon absorption by atoms and molecules: A quantum optics tutorial. *J. Chem. Phys.* **2021**, *155*, 081501, DOI: [10.1063/5.0049338](https://doi.org/10.1063/5.0049338).
- (188) Weiner, A., *Ultrafast Optics*; Wiley Series in Pure and Applied Optics; Wiley: 2011.
- (189) Murphy, D. B.; Davidson, M. W., *Fundamentals of light microscopy and electronic imaging*, 2nd ed.; Wiley-Blackwell: Chichester, England, 2011.
- (190) Penwell, S. B.; Whaley-Mayda, L.; Tokmakoff, A. Single-stage MHz mid-IR OPA using LiGaS₂ and a fiber laser pump source. *Opt. Lett.* **2018**, *43*, 1363, DOI: [10.1364/OL.43.001363](https://doi.org/10.1364/OL.43.001363).
- (191) Limpert, J.; Schreiber, T.; Clausnitzer, T.; Zöllner, K.; Fuchs, H.-J.; Kley, E.-B.; Zellmer, H.; Tünnermann, A. High-power femtosecond Yb-doped fiber amplifier. *Opt. Express* **2002**, *10*, 628–638, DOI: [10.1364/OE.10.000628](https://doi.org/10.1364/OE.10.000628).
- (192) Li, X.; Reber, M. A. R.; Corder, C.; Chen, Y.; Zhao, P.; Allison, T. K. High-power ultrafast Yb: fiber laser frequency combs using commercially available components and basic fiber tools. *Rev. Sci. Instrum.* **2016**, *87*, 093114, DOI: [10.1063/1.4962867](https://doi.org/10.1063/1.4962867).
- (193) Luther, B. M.; Tracy, K. M.; Gerrity, M.; Brown, S.; Krummel, A. T. 2D IR spectroscopy at 100 kHz utilizing a Mid-IR OPCPA laser source. *Opt. Express* **2016**, *24*, 4117–4127, DOI: [10.1364/OE.24.004117](https://doi.org/10.1364/OE.24.004117).
- (194) Heiner, Z.; Petrov, V.; Mero, M. Compact, high-repetition-rate source for broadband sum-frequency generation spectroscopy. *APL Photonics* **2017**, *2*, 066102, DOI: [10.1063/1.4983691](https://doi.org/10.1063/1.4983691).
- (195) Grupp, A.; Budweg, A.; Fischer, M. P.; Allerbeck, J.; Soavi, G.; Alfred Leitenstorfer; Brida, D. Broadly tunable ultrafast pump-probe system operating at multi-kHz repetition rate. *J. Opt.* **2018**, *20*, 014005, DOI: [10.1088/2040-8986/aa9b07](https://doi.org/10.1088/2040-8986/aa9b07).

- (196) Donaldson, P.; Greetham, G.; Shaw, D.; Parker, A.; Towrie, M. A 100 kHz Pulse Shaping 2D-IR Spectrometer Based on Dual Yb:KGW Amplifiers. *J. Phys. Chem. A* **2017**, DOI: 10.1021/acs.jpca.7b10259.
- (197) Donaldson, P.; Greetham, G.; Shaw, D.; Parker, A.; Towrie, M. A 100 kHz Pulse Shaping 2D-IR Spectrometer Based on Dual Yb:KGW Amplifiers. *J. Phys. Chem. A* **2018**, *122*, 780–787, DOI: 10.1021/acs.jpca.7b10259.
- (198) Heiner, Z.; Wang, L.; Petrov, V.; Mero, M. Broadband vibrational sum-frequency generation spectrometer at 100 kHz in the 950–1750 cm^{-1} spectral range utilizing a LiGaS₂ optical parametric amplifier. *Opt. Express* **2019**, *27*, 15289–15297, DOI: 10.1364/OE.27.015289.
- (199) Farrell, K. M.; Ostrander, J. S.; Jones, A. C.; Yakami, B. R.; Dicke, S. S.; Middleton, C. T.; Hamm, P.; Zanni, M. T. Shot-to-shot 2D IR spectroscopy at 100 kHz using a Yb laser and custom-designed electronics. *Opt. Express* **2020**, *28*, 33584–33602, DOI: 10.1364/OE.409360.
- (200) Hamm, P. Transient 2D IR spectroscopy from micro- to milliseconds. *J. Chem. Phys.* **2021**, *154*, 104201, DOI: 10.1063/5.0045294.
- (201) Erny, C.; Moutzouris, K.; Biegert, J.; Kühlke, D.; Adler, F.; Leitenstorfer, A.; Keller, U. Mid-infrared difference-frequency generation of ultrashort pulses tunable between 3.2 and 4.8 μm from a compact fiber source. *Opt. Lett.* **2007**, *32*, 1138–1140, DOI: 10.1364/OL.32.001138.
- (202) Pires, H.; Baudisch, M.; Sanchez, D.; Hemmer, M.; Biegert, J. Ultrashort pulse generation in the mid-IR. *Prog. Quantum. Electron.* **2015**, *43*, 1–30, DOI: 10.1016/j.pquantelec.2015.07.001.
- (203) Brida, D.; Marangoni, M.; Manzoni, C.; Silvestri, S. D.; Cerullo, G. Two-optical-cycle pulses in the mid-infrared from an optical parametric amplifier. *Opt. Lett.* **2008**, *33*, 2901–2903, DOI: 10.1364/OL.33.002901.
- (204) Huang, J.; Parobek, A.; Ganim, Z. Octave-spanning mid-infrared pulses by plasma generation in air pumped with an Yb:KGW source. *Opt. Lett.* **2016**, *41*, 4855–4858, DOI: 10.1364/OL.41.004855.
- (205) Krauth, J.; Steinmann, A.; Hegenbarth, R.; Conforti, M.; Giessen, H. Broadly tunable femtosecond near- and mid-IR source by direct pumping of an OPA with a 41.7 MHz

- Yb:KGW oscillator. *Opt. Express* **2013**, *21*, 11516–11522, DOI: 10.1364/OE.21.011516.
- (206) Mayer, B. W.; Phillips, C. R.; Gallmann, L.; Keller, U. Mid-infrared pulse generation via achromatic quasi-phase-matched OPCPA. *Opt. Express* **2014**, *22*, 20798–20808, DOI: 10.1364/OE.22.020798.
- (207) Rigaud, P.; Walle, A. V. d.; Hanna, M.; Forget, N.; Guichard, F.; Zaouter, Y.; Guesmi, K.; Druon, F.; Georges, P. Supercontinuum-seeded few-cycle mid-infrared OPCPA system. *Opt. Express* **2016**, *24*, 26494–26502, DOI: 10.1364/OE.24.026494.
- (208) Kaindl, R. A.; Smith, D. C.; Joschko, M.; Hasselbeck, M. P.; Woerner, M.; Elsaesser, T. Femtosecond infrared pulses tunable from 9 to 18 μm at an 88-MHz repetition rate. *Opt. Lett.* **1998**, *23*, 861–863, DOI: 10.1364/OL.23.000861.
- (209) Steinle, T.; Mörz, F.; Steinmann, A.; Giessen, H. Ultra-stable high average power femtosecond laser system tunable from 1.33 to 20 μm . *Opt. Lett.* **2016**, *41*, 4863–4866, DOI: 10.1364/OL.41.004863.
- (210) Grisard, A.; Lallier, E.; Gérard, B. Quasi-phase-matched gallium arsenide for versatile mid-infrared frequency conversion. *Opt. Mater. Express* **2012**, *2*, 1020–1025, DOI: 10.1364/OME.2.001020.
- (211) Isaienko, O.; Borguet, E. Ultrabroadband few-cycle infrared pulse generation from a noncollinear optical parametric amplifier based on bulk niobate crystals. *J. Opt. Soc. Am. B* **2013**, *30*, 2075–2080, DOI: 10.1364/JOSAB.30.002075.
- (212) Liang, H.; Krogen, P.; Wang, Z.; Park, H.; Kroh, T.; Zawilski, K.; Schunemann, P.; Moses, J.; DiMauro, L. F.; Kärtner, F. X.; Hong, K.-H. High-energy mid-infrared sub-cycle pulse synthesis from a parametric amplifier. *Nat. Commun.* **2017**, *8*, 141, DOI: 10.1038/s41467-017-00193-4.
- (213) Thiré, N.; Maksimenka, R.; Kiss, B.; Ferchaud, C.; Bizouard, P.; Cormier, E.; Os-vay, K.; Forget, N. 4-W, 100-kHz, few-cycle mid-infrared source with sub-100-mrad carrier-envelope phase noise. *Opt. Express* **2017**, *25*, 1505–1514, DOI: 10.1364/OE.25.001505.
- (214) Yodh, A. G.; Tom, H. W. K.; Aumiller, G. D.; Miranda, R. S. Generation of tunable mid-infrared picosecond pulses at 76 MHz. *J. Opt. Soc. Am. B* **1991**, *8*, 1663–1667, DOI: 10.1364/JOSAB.8.001663.

- (215) Petrov, V. Frequency down-conversion of solid-state laser sources to the mid-infrared spectral range using non-oxide nonlinear crystals. *Prog. Quantum. Electron.* **2015**, *42*, 1–106, DOI: 10.1016/j.pquantelec.2015.04.001.
- (216) Tyazhev, A.; Vedenyapin, V.; Marchev, G.; Isaenko, L.; Kolker, D.; Lobanov, S.; Petrov, V.; Yelisseyev, A.; Starikova, M.; Zondy, J.-J. Singly-resonant optical parametric oscillation based on the wide band-gap mid-IR nonlinear optical crystal LiGaS₂. *Opt. Mater.* **2013**, *35*, 1612–1615, DOI: 10.1016/j.optmat.2013.03.016.
- (217) Knorr, M.; Raab, J.; Tauer, M.; Merkl, P.; Peller, D.; Wittmann, E.; Riedle, E.; Lange, C.; Huber, R. Phase-locked multi-terahertz electric fields exceeding 13 MV/cm at a 190 kHz repetition rate. *Opt. Lett.* **2017**, *42*, 4367–4370, DOI: 10.1364/OL.42.004367.
- (218) Fu, Y.; Takahashi, E. J.; Midorikawa, K. Energy Scaling of Infrared Femtosecond Pulses by Dual-Chirped Optical Parametric Amplification. *IEEE Photonics J.* **2017**, *9*, 1–8, DOI: 10.1109/JPHOT.2017.2704096.
- (219) Kaneshima, K.; Ishii, N.; Takeuchi, K.; Itatani, J. Generation of carrier-envelope phase-stable mid-infrared pulses via dual-wavelength optical parametric amplification. *Opt. Express* **2016**, *24*, 8660–8665, DOI: 10.1364/OE.24.008660.
- (220) Pupeza, I. et al. High-power sub-two-cycle mid-infrared pulses at 100 MHz repetition rate. *Nature Photonics* **2015**, *9*, 721, DOI: 10.1038/nphoton.2015.179.
- (221) Morimoto, T.; Sono, N.; Miyamoto, T.; Kida, N.; Okamoto, H. Generation of a carrier-envelope-phase-stable femtosecond pulse at 10 μm by direct down-conversion from a Ti:sapphire laser pulse. *Appl. Phys. Express* **2017**, *10*, 122701, DOI: 10.7567/APEX.10.122701.
- (222) Petrov, V.; Yelisseyev, A.; Isaenko, L.; Lobanov, S.; Titov, A.; Zondy, J.-J. Second harmonic generation and optical parametric amplification in the mid-IR with orthorhombic biaxial crystals LiGaS₂ and LiGaSe₂. *Appl. Phys. B* **2004**, *78*, 543–546, DOI: 10.1007/s00340-004-1463-0.
- (223) Chen, B.-H.; Wittmann, E.; Morimoto, Y.; Baum, P.; Riedle, E. Octave-spanning single-cycle middle-infrared generation through optical parametric amplification in LiGaS₂. *Opt. Express* **2019**, *27*, 21306–21318, DOI: 10.1364/OE.27.021306.

- (224) Qu, S.; Liang, H.; Liu, K.; Zou, X.; Li, W.; Wang, Q. J.; Zhang, Y. 9 μm few-cycle optical parametric chirped-pulse amplifier based on LiGaS₂. *Opt. Lett.* **2019**, *44*, 2422–2425, DOI: 10.1364/OL.44.002422.
- (225) Villa, A.; Ross, A. M.; Gotti, R.; Lamperti, M.; Scotognella, F.; Cerullo, G.; Marangoni, M. Broadly tunable mid-infrared femtosecond pulses directly generated by an optical parametric amplifier. *OSA Continuum* **2021**, *4*, 2837–2844, DOI: 10.1364/OSAC.439298.
- (226) Zhou, L.; Novák, O.; Smrž, M.; Mocek, T. Analysis of broadband mid-infrared optical parametric amplification based on LiGaS₂, LiGaSe₂, LiInS₂, and LiInSe₂ crystals. *J. Opt. Soc. Am. B* **2022**, *39*, 1174–1185, DOI: 10.1364/JOSAB.454372.
- (227) Bournet, Q.; Jonusas, M.; Zheng, A.; Guichard, F.; Natile, M.; Zaouter, Y.; Joffre, M.; Bonvalet, A.; Druon, F.; Hanna, M.; Georges, P. Inline amplification of mid-infrared intrapulse difference frequency generation. *Opt. Lett.* **2022**, *47*, 4885–4888, DOI: 10.1364/OL.467792.
- (228) Heiner, Z.; Petrov, V.; Panyutin, V. L.; Badikov, V. V.; Kato, K.; Miyata, K.; Mero, M. Efficient generation of few-cycle pulses beyond 10 μm from an optical parametric amplifier pumped by a 1- μm laser system. *Sci. Rep.* **2022**, *12*, DOI: 10.1038/s41598-022-08964-w.
- (229) Adduci, F.; Catalano, I. M.; Cingolani, A.; Minafra, A. Direct and indirect two-photon processes in layered semiconductors. *Phys. Rev. B* **1977**, *15*, 926–931, DOI: 10.1103/PhysRevB.15.926.
- (230) Boldish, S. I.; White, W. B. Optical band gaps of selected ternary sulfide minerals. *American Mineralogist* **1998**, *83*, 865–871, DOI: 10.2138/am-1998-7-818.
- (231) Zernike, F.; Midwinter, J., *Applied Nonlinear Optics*; Dover books on physics; Dover Publications: 2006.
- (232) Powers, P., *Fundamentals of Nonlinear Optics*; Taylor & Francis: 2011.
- (233) Petrov, V.; Badikov, V.; Shevyrdyaeva, G.; Panyutin, V.; Chizhikov, V. Phase-matching properties and optical parametric amplification in single crystals of AgGaGeS₄. *Opt. Mater.* **2004**, *26*, 217–222, DOI: 10.1016/j.optmat.2004.04.007.
- (234) Isaenko, L.; Yelissejev, A.; Lobanov, S.; Titov, A.; Petrov, V.; Zondy, J.-J.; Krinitsin, P.; Merkulov, A.; Vedenyapin, V.; Smirnova, J. Growth and properties of LiGaX₂ (X

- = S, Se, Te) single crystals for nonlinear optical applications in the mid-IR. *Cryst. Res. Technol.* **2003**, *38*, 379–387, DOI: 10.1002/crat.200310047.
- (235) Isaenko, L.; Yelisseyev, A.; Lobanov, S.; Krinitsin, P.; Petrov, V.; Zondy, J. -. Ternary chalcogenides LiBC₂ (B=In,Ga; C=S,Se,Te) for mid-IR nonlinear optics. *J. Non-Cryst. Solids* **2006**, *352*, 2439–2443, DOI: 10.1016/j.jnoncrysol.2006.03.045.
- (236) Calendron, A.-L.; Çankaya, H.; Cirimi, G.; Kärtner, F. X. White-light generation with sub-ps pulses. *Opt. Express* **2015**, *23*, 13866–13879, DOI: 10.1364/OE.23.013866.
- (237) Kato, K.; Miyata, K.; Isaenko, L.; Lobanov, S.; Vedenyapin, V.; Petrov, V. Phase-matching properties of LiGaS₂ in the 1.025–10.5910 μm spectral range. *Opt. Lett.* **2017**, *42*, 4363–4366, DOI: 10.1364/OL.42.004363.
- (238) Polyanskiy, M. N. Refractive index database, <https://refractiveindex.info>.
- (239) Mertz, J., *Introduction to Optical Microscopy*; W. H. Freeman: 2009.
- (240) Pluta, M., *Advanced Light Microscopy: Principles and basic properties*; Advanced Light Microscopy; Elsevier: 1988.
- (241) Goodman, J., *Introduction to Fourier Optics*, 4th ed.; W. H. Freeman: 2017.
- (242) Whaley-Mayda, L.; Penwell, S. B.; Tokmakoff, A. Fluorescence-Encoded Infrared Spectroscopy: Ultrafast Vibrational Spectroscopy on Small Ensembles of Molecules in Solution. *J. Phys. Chem. Lett.* **2019**, *10*, 1967–1972, DOI: 10.1021/acs.jpcllett.9b00748.
- (243) Whaley-Mayda, L.; Guha, A.; Penwell, S. B.; Tokmakoff, A. Fluorescence-Encoded Infrared Vibrational Spectroscopy with Single-Molecule Sensitivity. *J. Am. Chem. Soc.* **2021**, *143*, 56, DOI: 10.1021/jacs.1c00542.
- (244) Whaley-Mayda, L.; Guha, A.; Tokmakoff, A. Resonance conditions, detection quality, and single-molecule sensitivity in fluorescence-encoded infrared vibrational spectroscopy. *J. Chem. Phys.* **2022**, *156*, 174202, DOI: 10.1063/5.0088435.
- (245) Banachowicz, E.; Patkowski, A.; Meier, G.; Klamecka, K.; Gapiński, J. Successful FCS Experiment in Nonstandard Conditions. *Langmuir* **2014**, *30*, 8945–8955, DOI: 10.1021/la5015708.
- (246) Gale, H. Rowland Ghosts. *Astrophys. J.* **1937**, *85*, 49–61, DOI: 10.1086/143800.

- (247) Jenkins, F.; White, H., *Fundamentals of Optics*, 4th ed.; McGraw-Hill: 1976.
- (248) Roberts, S. T.; Loparo, J. J.; Ramasesha, K.; Tokmakoff, A. A fast-scanning Fourier transform 2D IR interferometer. *Opt. Commun.* **2011**, *284*, 1062–1066.
- (249) Bracewell, R., *The Fourier Transform and Its Applications*; Electrical engineering series; McGraw Hill: 2000.
- (250) Hobbs, P. C. D., *Building Electro-Optical Systems*, 2nd ed.; Wiley Series in Pure and Applied Optics; John Wiley & Sons: Nashville, TN, 2011.
- (251) Arlt, J.; Tyndall, D.; Rae, B. R.; Li, D. D.-U.; Richardson, J. A.; Henderson, R. K. A study of pile-up in integrated time-correlated single photon counting systems. *Rev. Sci. Instr.* **2013**, *84*, 103105, DOI: 10.1063/1.4824196.
- (252) Helbing, J.; Hamm, P. Compact Implementation of Fourier Transform Two-Dimensional IR Spectroscopy without Phase Ambiguity. *J. Opt. Soc. Am. B* **2011**, *28*, 171–178, DOI: 10.1364/JOSAB.28.000171.
- (253) De Marco, L. The molecular dynamics of hydrogen-bonding explored with broadband two dimensional infrared spectroscopy, Ph.D. Thesis, MIT, 2016.
- (254) Li, Z.; Aleshire, K.; Kuno, M.; Hartland, G. Super-Resolution Far-Field Infrared Imaging by Photothermal Heterodyne Imaging. *J. Phys. Chem. B* **2017**, *121*, 8838–8846, DOI: 10.1021/acs.jpccb.7b06065.
- (255) Lakowicz, J., *Principles of Fluorescence Spectroscopy*, 3rd ed.; Springer US: 2006.
- (256) Doyle, A. G.; Jacobsen, E. N. Small-Molecule H-Bond Donors in Asymmetric Catalysis. *Chem. Rev.* **2007**, *107*, 5713–5743, DOI: 10.1021/cr068373r.
- (257) Knowles, R. R.; Jacobsen, E. N. Attractive noncovalent interactions in asymmetric catalysis: Links between enzymes and small molecule catalysts. *Proc. Natl. Acad. Sci. U.S.A* **2010**, *107*, 20678–20685, DOI: 10.1073/pnas.1006402107.
- (258) Žabka, M.; Šebesta, R. Experimental and Theoretical Studies in Hydrogen-Bonding Organocatalysis. *Molecules* **2015**, *20*, 15500–15524, DOI: 10.3390/molecules200915500.

- (259) Lippert, K. M.; Hof, K.; Gerbig, D.; Ley, D.; Hausmann, H.; Guenther, S.; Schreiner, P. R. Hydrogen-Bonding Thiourea Organocatalysts: The Privileged 3,5-Bis(trifluoromethyl)phenyl Group. *Eur. J. Org. Chem.* **2012**, *2012*, 5919–5927, DOI: <https://doi.org/10.1002/ejoc.201200739>.
- (260) Nödling, A. R.; Jakab, G.; Schreiner, P. R.; Hilt, G. ³¹P NMR Spectroscopically Quantified Hydrogen-Bonding Strength of Thioureas and Their Catalytic Activity in Diels–Alder Reactions. *Eur. J. Org. Chem.* **2014**, *2014*, 6394–6398, DOI: <https://doi.org/10.1002/ejoc.201402871>.
- (261) Ehrhard, A. A.; Jäger, S.; Malm, C.; Basaran, S.; Hunger, J. CF₃-groups critically enhance the binding of thiourea catalysts to ketones – a NMR and FT-IR study. *J. Mol. Liq.* **2019**, *296*, 111829, DOI: <https://doi.org/10.1016/j.molliq.2019.111829>.
- (262) Cantor, C. R.; Schimmel, P. R., *Biophysical chemistry: Part III: the behavior of biological macromolecules*; Macmillan: 1980.
- (263) Magde, D.; Elson, E.; Webb, W. W. Thermodynamic Fluctuations in a Reacting System—Measurement by Fluorescence Correlation Spectroscopy. *Phys. Rev. Lett.* **1972**, *29*, 705–708, DOI: [10.1103/PhysRevLett.29.705](https://doi.org/10.1103/PhysRevLett.29.705).
- (264) Krichevsky, O.; Bonnet, G. Fluorescence correlation spectroscopy: the technique and its applications. *Rep. Prog. Phys.* **2002**, *65*, 251.
- (265) Hess, S. T.; Huang, S.; Heikal, A. A.; Webb, W. W. Biological and Chemical Applications of Fluorescence Correlation Spectroscopy: A Review. *Biochemistry* **2002**, *41*, 697–705, DOI: [10.1021/bi0118512](https://doi.org/10.1021/bi0118512).
- (266) Elson, E. L. Fluorescence Correlation Spectroscopy: Past, Present, Future. *Biophys. J.* **2011**, *101*, 2855–2870, DOI: [10.1016/j.bpj.2011.11.012](https://doi.org/10.1016/j.bpj.2011.11.012).
- (267) Magde, D.; Elson, E. L.; Webb, W. W. Fluorescence correlation spectroscopy. II. An experimental realization. *Biopolymers: Original Research on Biomolecules* **1974**, *13*, 29–61.
- (268) Rigler, R. Ultrasensitive detection of single molecules by fluorescence correlation spectroscopy. *Bioscience* **1990**, 180–183.

- (269) Rigler, R.; Mets, Ü.; Widengren, J.; Kask, P. Fluorescence correlation spectroscopy with high count rate and low background: analysis of translational diffusion. *European Biophysics Journal* **1993**, *22*, DOI: 10.1007/bf00185777.
- (270) Rigler, R. Fluorescence correlations, single molecule detection and large number screening Applications in biotechnology. *J. Biotechnol.* **1995**, *41*, Genome Research/Molecular Biotechnology, Part II, 177–186, DOI: [https://doi.org/10.1016/0168-1656\(95\)00054-T](https://doi.org/10.1016/0168-1656(95)00054-T).
- (271) Elson, E. L.; Magde, D. Fluorescence correlation spectroscopy. I. Conceptual basis and theory. *Biopolymers* **1974**, *13*, 1–27, DOI: 10.1002/bip.1974.360130102.
- (272) Gillespie, D. T., *Markov processes: an introduction for physical scientists*; Elsevier: 1991.
- (273) Chandler, D. Introduction to modern statistical. *Mechanics. Oxford University Press, Oxford, UK* **1987**, *5*, 449.
- (274) McQuarrie, D. A., *Statistical Mechanics*, 2nd ed.; University Science Books: Sausalito, CA, 2000.
- (275) Turing, A. M. The Chemical Basis of Morphogenesis. *Philos. Trans. R. Soc. B: Biol. Sci* **1952**, *237*, 37–72.
- (276) Érdi, P.; Tóth, J., *Mathematical Models of Chemical Reactions: Theory and Applications of Deterministic and Stochastic Models*; Nonlinear science : theory and applications; Manchester University Press: 1989.
- (277) Kondo, S.; Miura, T. Reaction-Diffusion Model as a Framework for Understanding Biological Pattern Formation. *Science* **2010**, *329*, 1616–1620, DOI: 10.1126/science.1179047.
- (278) Onsager, L. Reciprocal relations in irreversible processes. II. *Physical review* **1931**, *38*, 2265.
- (279) Landau, L. D.; Lifshitz, E. M., *Statistical Physics: Volume 5*; Elsevier: 2013; Vol. 5.
- (280) Berne, B. J.; Pecora, R., *Dynamic light scattering: with applications to chemistry, biology, and physics*; Courier Corporation: 2000.

- (281) Holyst, R.; Poniewierski, A.; Zhang, X. Analytical form of the autocorrelation function for the fluorescence correlation spectroscopy. *Soft Matter* **2017**, *13*, 1267–1275, DOI: 10.1039/C6SM02643E.
- (282) Hess, S. T.; Webb, W. W. Focal Volume Optics and Experimental Artifacts in Confocal Fluorescence Correlation Spectroscopy. *Biophys. J.* **2002**, *83*, 2300–2317, DOI: [https://doi.org/10.1016/S0006-3495\(02\)73990-8](https://doi.org/10.1016/S0006-3495(02)73990-8).
- (283) Widengren, J.; Mets, Ü., Conceptual Basis of Fluorescence Correlation Spectroscopy and Related Techniques as Tools in Bioscience In *Single Molecule Detection in Solution*, Zander, C., Jorg, E., Keller, R. A., Eds.; Wiley-VCH Verlag GmbH & Co. KGaA: 2003; Chapter 3, pp 69–120.
- (284) Schwille, P.; Meyer-Almes, F.-J.; Rigler, R. Dual-color fluorescence cross-correlation spectroscopy for multicomponent diffusional analysis in solution. *Biophys. J.* **1997**, *72*, 1878–1886.
- (285) Kettling, U.; Koltermann, A.; Schwille, P.; Eigen, M. Real-time enzyme kinetics monitored by dual-color fluorescence cross-correlation spectroscopy. *Proc. Natl. Acad. Sci. U.S.A* **1998**, *95*, 1416–1420.
- (286) Kapusta, P.; Macháň, R.; Benda, A.; Hof, M. Fluorescence lifetime correlation spectroscopy (FLCS): concepts, applications and outlook. *Int. J. Mol. Sci.* **2012**, *13*, 12890–12910.
- (287) Otsu, T.; Ishii, K.; Tahara, T. Microsecond protein dynamics observed at the single-molecule level. *Nat. Commun.* **2015**, *6*, 1–9.
- (288) Oura, M.; Yamamoto, J.; Ishikawa, H.; Mikuni, S.; Fukushima, R.; Kinjo, M. Polarization-dependent fluorescence correlation spectroscopy for studying structural properties of proteins in living cell. *Sci. Rep.* **2016**, *6*, 1–7.
- (289) Wallace, M. I.; Ying, L.; Balasubramanian, S.; Klenerman, D. FRET fluctuation spectroscopy: exploring the conformational dynamics of a DNA hairpin loop. *J. Phys. Chem. B* **2000**, *104*, 11551–11555.
- (290) Torres, T.; Levitus, M. Measuring conformational dynamics: a new FCS-FRET approach. *J. Phys. Chem. B* **2007**, *111*, 7392–7400.
- (291) Brokmann, X.; Bawendi, M.; Coolen, L.; Hermier, J.-P. Photon-correlation Fourier spectroscopy. *Opt. Express* **2006**, *14*, 6333–6341.

- (292) Marshall, L. F.; Cui, J.; Brokmann, X.; Bawendi, M. G. Extracting spectral dynamics from single chromophores in solution. *Phys. Rev. Lett.* **2010**, *105*, 053005.
- (293) Guha, A.; Whaley-Mayda, L.; Lee, S. Y.; Tokmakoff, A., 2022, in preparation.
- (294) Wahl, M.; Gregor, I.; Patting, M.; Enderlein, J. Fast calculation of fluorescence correlation data with asynchronous time-correlated single-photon counting. *Opt. Express* **2003**, *11*, 3583–3591, DOI: 10.1364/OE.11.003583.
- (295) Giudice, A.; Ghioni, M.; Biasi, R.; Zappa, F.; Cova, S.; Maccagnani, P.; Gulinatti, A. High-rate photon counting and picosecond timing with silicon-SPAD based compact detector modules. *Journal of Modern Optics* **2007**, *54*, 225–237, DOI: 10.1080/09500340600763698.
- (296) Enderlein, J.; Gregor, I. Using fluorescence lifetime for discriminating detector afterpulsing in fluorescence-correlation spectroscopy. *Rev. Sci. Instrum.* **2005**, *76*, 033102, DOI: 10.1063/1.1863399.
- (297) Koppel, D. E. Statistical accuracy in fluorescence correlation spectroscopy. *Phys. Rev. A* **1974**, *10*, 1938–1945, DOI: 10.1103/PhysRevA.10.1938.
- (298) Lamb, D. C.; Schenk, A.; Röcker, C.; Scalfi-Happ, C.; Nienhaus, G. U. Sensitivity Enhancement in Fluorescence Correlation Spectroscopy of Multiple Species Using Time-Gated Detection. *Biophys. J.* **2000**, *79*, 1129–1138, DOI: [https://doi.org/10.1016/S0006-3495\(00\)76366-1](https://doi.org/10.1016/S0006-3495(00)76366-1).
- (299) Ghosh, A.; Karedla, N.; Thiele, J. C.; Gregor, I.; Enderlein, J. Fluorescence lifetime correlation spectroscopy: Basics and applications. *Methods* **2018**, *140-141*, Developments in Fluorescence Correlation Spectroscopy and related techniques, 32–39, DOI: <https://doi.org/10.1016/j.ymeth.2018.02.009>.
- (300) Enderlein, J.; Gregor, I.; Patra, D.; Dertinger, T.; Kaupp, U. B. Performance of Fluorescence Correlation Spectroscopy for Measuring Diffusion and Concentration. *ChemPhysChem* **2005**, *6*, 2324–2336, DOI: <https://doi.org/10.1002/cphc.200500414>.
- (301) Jones, G.; Jackson, W. R.; Choi, C. Y.; Bergmark, W. R. Solvent effects on emission yield and lifetime for coumarin laser dyes. Requirements for a rotatory decay mechanism. *J. Phys. Chem.* **1985**, *89*, 294–300, DOI: 10.1021/j100248a024.

- (302) Moerner, W. E.; Fromm, D. P. Methods of single-molecule fluorescence spectroscopy and microscopy. *Rev. Sci. Instrum.* **2003**, *74*, 3597–3619, DOI: 10.1063/1.1589587.
- (303) Xiong, H.; Qian, N.; Miao, Y.; Zhao, Z.; Min, W. Stimulated Raman Excited Fluorescence Spectroscopy of Visible Dyes. *J. Phys. Chem. Lett.* **2019**, *10*, 3563–3570, DOI: 10.1021/acs.jpcllett.9b01289.
- (304) Schrof, W.; Klingler, J. F.; Rozouvan, S.; Horn, D. Raman correlation spectroscopy: A method for studying chemical composition and dynamics of disperse systems. *Phys. Rev. E* **1998**, *57*, R2523–R2526, DOI: 10.1103/PhysRevE.57.R2523.
- (305) Cheng, J.-x.; Potma, E. O.; Xie, S. X. Coherent Anti-Stokes Raman Scattering Correlation Spectroscopy: Probing Dynamical Processes with Chemical Selectivity. *J. Phys. Chem. A* **2002**, *106*, 8561–8568, DOI: 10.1021/jp025774b.
- (306) Barbara, A.; Dubois, F.; Quémerais, P.; Eng, L. Non-resonant and non-enhanced Raman Correlation Spectroscopy. *Opt. Express* **2013**, *21*, 15418–15429, DOI: 10.1364/OE.21.015418.
- (307) Würth, C.; Grabolle, M.; Pauli, J.; Spieles, M.; Resch-Genger, U. Relative and absolute determination of fluorescence quantum yields of transparent samples. *Nat. Protoc.* **2013**, *8*, 1535–1550, DOI: 10.1038/nprot.2013.087.
- (308) Sandison, D. R.; Webb, W. W. Background rejection and signal-to-noise optimization in confocal and alternative fluorescence microscopes. *Appl. Opt.* **1994**, *33*, 603–615, DOI: 10.1364/AO.33.000603.
- (309) Sandison, D. R.; Piston, D. W.; Williams, R. M.; Webb, W. W. Quantitative comparison of background rejection, signal-to-noise ratio, and resolution in confocal and full-field laser scanning microscopes. *Appl. Opt.* **1995**, *34*, 3576–3588, DOI: 10.1364/AO.34.003576.
- (310) Lavis, L. D.; Raines, R. T. Bright Ideas for Chemical Biology. *ACS Chem. Biol.* **2008**, *3*, 142–155, DOI: 10.1021/cb700248m.
- (311) Lavis, L. D.; Raines, R. T. Bright Building Blocks for Chemical Biology. *ACS Chem. Biol.* **2014**, *9*, 855–866, DOI: 10.1021/cb500078u.
- (312) Tian, Y.; Halle, J.; Wojdyr, M.; Sahoo, D.; Scheblykin, I. G. Quantitative measurement of fluorescence brightness of single molecules. *Methods Appl. Fluoresc.* **2014**, *2*, 035003, DOI: 10.1088/2050-6120/2/3/035003.

- (313) Fox, Z. W.; Blair, T. J.; Khalil, M. Determining the Orientation and Vibronic Couplings between Electronic and Vibrational Coordinates with Polarization-Selective Two-Dimensional Vibrational-Electronic Spectroscopy. *J. Phys. Chem. Lett.* **2020**, 1558–1563, DOI: 10.1021/acs.jpcllett.9b03752.
- (314) Gaynor, J. D.; Weakly, R. B.; Khalil, M. Multimode two-dimensional vibronic spectroscopy. I. Orientational response and polarization-selectivity. *J. Chem. Phys.* **2021**, 154, 184201, DOI: 10.1063/5.0047724.
- (315) Kauffman, J. M. Laser dye structures and synonyms. *Appl. Opt.* **1980**, 19, 3431–3435, DOI: 10.1364/AO.19.003431.
- (316) Drexhage, K. H., Structure and Properties of Laser Dyes In *Dye Lasers*, Schäfer, F. P., Ed.; Springer Berlin Heidelberg: Berlin, Heidelberg, 1973, pp 144–193, DOI: 10.1007/978-3-662-11579-4_4.
- (317) Reynolds, G.; Drexhage, K. New coumarin dyes with rigidized structure for flashlamp-pumped dye lasers. *Opt. Commun.* **1975**, 13, 222–225, DOI: [https://doi.org/10.1016/0030-4018\(75\)90085-1](https://doi.org/10.1016/0030-4018(75)90085-1).
- (318) Liu, X.; Cole, J. M.; Waddell, P. G.; Lin, T.-C.; Radia, J.; Zeidler, A. Molecular Origins of Optoelectronic Properties in Coumarin Dyes: Toward Designer Solar Cell and Laser Applications. *J. Phys. Chem. A* **2012**, 116, 727–737, DOI: 10.1021/jp209925y.
- (319) Birks, J. B., *Photophysics of Aromatic Molecules*; Wiley-Interscience: London, 1973.
- (320) Tarleton, A. S.; Garcia-Alvarez, J. C.; Wynn, A.; Awbrey, C. M.; Roberts, T. P.; Gozem, S. OS100: A Benchmark Set of 100 Digitized UV–Visible Spectra and Derived Experimental Oscillator Strengths. *J. Phys. Chem. A* **2022**, 126, 435–443, DOI: 10.1021/acs.jpca.1c08988.
- (321) Urbach, F. The Long-Wavelength Edge of Photographic Sensitivity and of the Electronic Absorption of Solids. *Phys. Rev.* **1953**, 92, 1324–1324, DOI: 10.1103/PhysRev.92.1324.
- (322) Dow, J. D.; Redfield, D. Toward a Unified Theory of Urbach’s Rule and Exponential Absorption Edges. *Phys. Rev. B* **1972**, 5, 594–610, DOI: 10.1103/PhysRevB.5.594.

- (323) Wondrazek, F.; Seilmeier, A.; Kaiser, W. Ultrafast intramolecular redistribution and intermolecular relaxation of vibrational energy in large molecules. *Chem. Phys. Lett.* **1984**, *104*, 121–128, DOI: [https://doi.org/10.1016/0009-2614\(84\)80181-5](https://doi.org/10.1016/0009-2614(84)80181-5).
- (324) Scherer, P. O. J.; Seilmeier, A.; Kaiser, W. Ultrafast intra- and intermolecular energy transfer in solutions after selective infrared excitation. *J. Chem. Phys.* **1985**, *83*, 3948–3957, DOI: [10.1063/1.449107](https://doi.org/10.1063/1.449107).
- (325) Kinoshita, S.; Nishi, N.; Saitoh, A.; Kushida, T. Urbach Tail of Organic Dyes in Solution. *J. Phys. Soc. Japan* **1987**, *56*, 4162–4175, DOI: [10.1143/JPSJ.56.4162](https://doi.org/10.1143/JPSJ.56.4162).
- (326) Bingemann, D.; King, A. M.; Crim, F. F. Transient electronic absorption of vibrationally excited CH₂I₂: Watching energy flow in solution. *J. Chem. Phys.* **2000**, *113*, 5018–5025, DOI: [10.1063/1.1289532](https://doi.org/10.1063/1.1289532).
- (327) Jones, R. N.; Angell, C. L.; Ito, T.; Smith, R. J. D. The Carbonyl Stretching Bands in the Infrared Spectra of Unsaturated Lactones. *Can. J. Chem.* **1959**, *37*, 2007–2022, DOI: [10.1139/v59-293](https://doi.org/10.1139/v59-293).
- (328) Nyquist, R. A.; Settineri, S. E. Infrared Study of Coumarin in Different Solvent Systems. *Applied Spectroscopy* **1990**, *44*, 791–796, DOI: [10.1366/0003702904087055](https://doi.org/10.1366/0003702904087055).
- (329) Chudoba, C.; Nibbering, E. T. J.; Elsaesser, T. Site-Specific Excited-State Solute-Solvent Interactions Probed by Femtosecond Vibrational Spectroscopy. *Phys. Rev. Lett.* **1998**, *81*, 3010–3013, DOI: [10.1103/PhysRevLett.81.3010](https://doi.org/10.1103/PhysRevLett.81.3010).
- (330) Van Wilderen, L. J. G. W.; Messmer, A. T.; Bredenbeck, J. Mixed IR/Vis Two-Dimensional Spectroscopy: Chemical Exchange beyond the Vibrational Lifetime and Sub-ensemble Selective Photochemistry. *Angew. Chem. Int. Ed.* **2014**, *53*, 2667–2672, DOI: <https://doi.org/10.1002/anie.201305950>.
- (331) Ghauharali, R. I.; Müller, M.; Buist, A. H.; Sosnowski, T. S.; Norris, T. B.; Squier, J.; Brakenhoff, G. J. Optical saturation measurements of fluorophores in solution with pulsed femtosecond excitation and two-dimensional CCD camera detection. *Appl. Opt.* **1997**, *36*, 4320–4328, DOI: [10.1364/AO.36.004320](https://doi.org/10.1364/AO.36.004320).
- (332) Humpolíčková, J.; Benda, A.; Enderlein, J. Optical Saturation as a Versatile Tool to Enhance Resolution in Confocal Microscopy. *Biophys. J.* **2009**, *97*, 2623–2629, DOI: <https://doi.org/10.1016/j.bpj.2009.08.002>.

- (333) Gregor, I.; Patra, D.; Enderlein, J. Optical Saturation in Fluorescence Correlation Spectroscopy under Continuous-Wave and Pulsed Excitation. *ChemPhysChem* **2005**, *6*, 164–170, DOI: <https://doi.org/10.1002/cphc.200400319>.
- (334) Wang, Q.; Moerner, W. E. Lifetime and Spectrally Resolved Characterization of the Photodynamics of Single Fluorophores in Solution Using the Anti-Brownian Electrokinetic Trap. *J. Phys. Chem. B* **2013**, *117*, 4641–4648, DOI: [10.1021/jp308949d](https://doi.org/10.1021/jp308949d).
- (335) Kim, J.-Y.; Chung, H. S. Disordered proteins follow diverse transition paths as they fold and bind to a partner. *Science* **2020**, *368*, 1253–1257, DOI: [10.1126/science.aba3854](https://doi.org/10.1126/science.aba3854).
- (336) Hou, S.; Exell, J.; Welsher, K. Real-time 3D single molecule tracking. *Nat. Commun.* **2020**, *11*, 1–10.
- (337) Merrick, J. P.; Moran, D.; Radom, L. An Evaluation of Harmonic Vibrational Frequency Scale Factors. *J. Phys. Chem. A* **2007**, *111*, 11683–11700, DOI: [10.1021/jp073974n](https://doi.org/10.1021/jp073974n).
- (338) Dutt, G. B.; Raman, S. Rotational dynamics of coumarins: An experimental test of dielectric friction theories. *J. Chem. Phys.* **2001**, *114*, 6702–6713, DOI: [10.1063/1.1357797](https://doi.org/10.1063/1.1357797).
- (339) Golonzka, O.; Tokmakoff, A. Polarization-selective third-order spectroscopy of coupled vibronic states. *J. Chem. Phys.* **2001**, *115*, 297–309, DOI: [10.1063/1.1376144](https://doi.org/10.1063/1.1376144).
- (340) Fleming, G., *Chemical applications of ultrafast spectroscopy*; Oxford University Press, New York, NY: 1986.
- (341) Jonas, D. M.; Lang, M. J.; Nagasawa, Y.; Joo, T.; Fleming, G. R. Pump-Probe Polarization Anisotropy Study of Femtosecond Energy Transfer within the Photosynthetic Reaction Center of Rhodobacter sphaeroides R26. *J. Phys. Chem.* **1996**, *100*, 12660–12673, DOI: [10.1021/jp960708t](https://doi.org/10.1021/jp960708t).
- (342) Hochstrasser, R. M. Two-dimensional IR-spectroscopy: polarization anisotropy effects. *Chem. Phys.* **2001**, *266*, 273–284, DOI: [https://doi.org/10.1016/S0301-0104\(01\)00232-4](https://doi.org/10.1016/S0301-0104(01)00232-4).
- (343) Gaffney, K. J.; Piletic, I. R.; Fayer, M. D. Orientational relaxation and vibrational excitation transfer in methanol–carbon tetrachloride solutions. *J. Chem. Phys.* **2003**, *118*, 2270–2278, DOI: [10.1063/1.1534580](https://doi.org/10.1063/1.1534580).

- (344) Tokmakoff, A. Orientational correlation functions and polarization selectivity for non-linear spectroscopy of isotropic media. I. Third order. *J. Chem. Phys.* **1996**, *105*, 1–12, DOI: 10.1063/1.471856.
- (345) Fano, U. Effects of Configuration Interaction on Intensities and Phase Shifts. *Phys. Rev.* **1961**, *124*, 1866–1878, DOI: 10.1103/PhysRev.124.1866.
- (346) Owrutsky, J. C.; Raftery, D.; Hochstrasser, R. M. Vibrational Relaxation Dynamics in Solutions. *Annu. Rev. Phys. Chem.* **1994**, *45*, 519–555, DOI: 10.1146/annurev.pc.45.100194.002511.
- (347) Kenkre, V. M.; Tokmakoff, A.; Fayer, M. D. Theory of vibrational relaxation of polyatomic molecules in liquids. *J. Chem. Phys.* **1994**, *101*, 10618–10629, DOI: 10.1063/1.467876.
- (348) Stratt, R. M.; Maroncelli, M. Nonreactive Dynamics in Solution: The Emerging Molecular View of Solvation Dynamics and Vibrational Relaxation. *J. Phys. Chem.* **1996**, *100*, 12981–12996, DOI: 10.1021/jp9608483.
- (349) Gruebele, M.; Wolynes, P. G. Vibrational Energy Flow and Chemical Reactions. *Acc. Chem. Res.* **2004**, *37*, 261–267, DOI: 10.1021/ar030230t.
- (350) Nitzan, A., *Chemical Dynamics in Condensed Phases: Relaxation, Transfer and Reactions in Condensed Molecular Systems*; Oxford Graduate Texts; OUP Oxford: 2006.
- (351) May, V.; Kühn, O., *Vibrational Dynamics: Energy Redistribution, Relaxation, and Dephasing In Charge and Energy Transfer Dynamics in Molecular Systems*; John Wiley & Sons, Ltd: 2011; Chapter 5, pp 221–254, DOI: <https://doi.org/10.1002/9783527633791.ch5>.
- (352) Stannard, P. R.; Gelbart, W. M. Intramolecular vibrational energy redistribution. *J. Phys. Chem.* **1981**, *85*, 3592–3599.
- (353) Boyall, D.; Reid, K. L. Modern studies of intramolecular vibrational energy redistribution. *Chem. Soc. Rev.* **1997**, *26*, 223–232, DOI: 10.1039/CS9972600223.
- (354) Nesbitt, D. J.; Field, R. W. Vibrational Energy Flow in Highly Excited Molecules: Role of Intramolecular Vibrational Redistribution. *J. Phys. Chem.* **1996**, *100*, 12735–12756, DOI: 10.1021/jp960698w.

- (355) Elles, C. G.; Bingemann, D.; Heckscher, M. M.; Crim, F. F. Vibrational relaxation of CH₂I₂ in solution: Excitation level dependence. *J. Chem. Phys.* **2003**, *118*, 5587–5595, DOI: 10.1063/1.1554396.
- (356) Sakai, M.; Ishiuchi, S.; Fujii, M. Picosecond time-resolved nonresonant ionization detected IR spectroscopy on 7-azaindole dimer. *Eur. Phys. J. D* **2002**, *20*, 399–402, DOI: 10.1140/epjd/e2002-00162-7.